Review

Severe plastic deformation for producing superfunctional ultrafine-grained and heterostructured materials: An interdisciplinary review

Kaveh Edalati [a,*], Anwar Q. Ahmed [b,c], Saeid Akrami [d], Kei Ameyama [e], Valery Aptukov [f], Rashid N. Asfandiyarov [g,h], Maki Ashida [i], Vasily Astanin [g], Andrea Bachmaier [j], Victor Beloshenko [k], Elena V. Bobruk [g], Krzysztof Bryła [l], José María Cabrera [m,n], Amanda P. Carvalho [o], Nguyen Q. Chinh [b], In-Chul Choi [p], Robert Chulist [q], Jorge M. Cubero-Sesin [r], Gregory Davdian [s], Muhammet Demirtas [t], Sergiy Divinski [u], Karsten Durst [v], Jiri Dvorak [w,x], Parisa Edalati [y], Satoshi Emura [z], Nariman A. Enikeev [g,aa], Ghader Faraji [ab], Roberto B. Figueiredo [o], Ricardo Floriano [ac], Marjan Fouladvind [ad], Daniel Fruchart [ad,ae], Masayoshi Fuji [y,af], Hiroshi Fujiwara [e], Marcell Gajdics [b,ag], Diana Gheorghe [ah], Łukasz Gondek [ai], Joaquín E. González-Hernández [r], Alena Gornakova [s], Thierry Grosdidier [aj,ak], Jenő Gubicza [b], Dmitry Gunderov [g,h], Liqing He [al], Oscar Fabian Higuera [am], Shoichi Hirosawa [an], Anton Hohenwarter [ao], Zenji Horita [ap,aq,ar], Jelena Horky [as], Yi Huang [at,au], Jacques Huot [av], Yoshifumi Ikoma [aw], Tatsumi Ishihara [a,ax], Yulia Ivanisenko [ay], Jae-il Jang [az], Alberto M. Jorge Jr [ba,bb,bc], Mie Kawabata-Ota [bd], Megumi Kawasaki [be], Tarek Khelfa [bf], Junya Kobayashi [bg], Lembit Kommel [bh], Anna Korneva [q], Petr Kral [w,x], Natalia Kudriashova [bi], Shigeru Kuramoto [bg], Terence G. Langdon [au], Dong-Hyun Lee [bj], Valery I. Levitas [bk,bl], Cong Li [bm], Hai-Wen Li [al], Yongtao Li [bn], Zheng Li [bo], Huai-Jun Lin [bp], Klaus-Dieter Liss [bq], Ying Liu [bo], Diana Maritza Marulanda Cardona [br], Kenji Matsuda [bs], Andrey Mazilkin [s], Yoji Mine [bt], Hiroyuki Miyamoto [bu], Suk-Chun Moon [bq], Timo Müller [bv], Jairo Alberto Muñoz [m], Maxim Yu. Murashkin [g,aa], Muhammad Naeem [bw], Marc Novelli [aj,ak], Dániel Olasz [b,ag], Reinhard Pippan [bx], Vladimir V. Popov [by], Elena N. Popova [by], Gencaga Purcek [bz], Patricia de Rango [ad], Oliver Renk [ca], Delphine Retraint [cb], Ádám Révész [b], Virginie Roche [ba], Pablo Rodriguez-Calvillo [cc], Liliana Romero-Resendiz [bw,cd,ce], Xavier Sauvage [cf], Takahiro Sawaguchi [z], Hadi Sena [cg], Hamed Shahmir [ch], Xiaobin Shi [bn], Vaclav Sklenicka [w,x], Werner Skrotzki [ci], Nataliya Skryabina [ae], Franziska Staab [v], Boris Straumal [s], Zhidan Sun [cc], Maciej Szczerba [q], Yoichi Takizawa [cj], Yongpeng Tang [ck], Ruslan Z. Valiev [g,aa], Alina Vozniak [cl], Andrei Voznyak [cm], Bo Wang [cn], Jing Tao Wang [bo], Gerhard Wilde [u], Fan Zhang [cn], Meng Zhang [bp], Peng Zhang [bp], Jianqiang Zhou [co], Xinkun Zhu [bm], Yuntian T. Zhu [cp]

[a] *WPI, International Institute for Carbon-Neutral Energy Research (WPI-I2CNER), Kyushu University, Fukuoka 819-0395, Japan*
[b] *Department of Materials Physics, Eötvös Loránd University, ELTE, Pázmány Péter sétány 1/A, Budapest H-1117, Hungary*
[c] *College of Science, University of Kufa, Najaf 54001, Iraq*

Abbreviations: ARB, Accumulative roll-bonding; BCC, Body-centered cubic; EBSD, Electron backscatter diffraction; ECAP, Equal-channel angular pressing; FCC, Face-centered cubic; GNDs, Geometrically necessary dislocations; HCVD, Hard cyclic viscoplastic deformation; HCP, Hexagonal close-packed; HEA, High-entropy alloy; HPS, High-pressure sliding; HPT, High-pressure torsion; HPTE, High-pressure torsion extrusion; RDAC, Rotational diamond anvil cell; SEM, Scanning electron microscopy; SPD, Severe plastic deformation; SMAT, Surface mechanical attrition treatment; TEM, Transmission electron microscopy; t-HPS, Tube high-pressure shearing; UTS, Ultimate tensile strength; UFG, Ultrafine-grained; XRD, X-ray diffraction.

* Corresponding author.

E-mail address: kaveh.edalati@kyudai.jp (K. Edalati).

[d] *Institutes of Innovation for Future Society, Nagoya University, Nagoya 464-8603, Japan*

[e] *College of Science and Engineering, Ritsumeikan University, Kusatsu 525-8577, Japan*

[f] *Perm State University, Bukireva, Perm 614068, Russia*

[g] *Ufa University of Science and Technology, 32 Zaki Validi str, Ufa 450076, Russia*

[h] *Institute of Molecule and Crystal Physics UFRC RAS, 71 pr. Oktyabrya, Ufa 450054, Russia*

[i] *Seikei University, 3-3-1 Kichijoji-Kitamachi, Musashino-shi, Tokyo 180-8633, Japan*

[j] *Erich Schmid Institute of Materials Science of the Austrian Academy of Sciences, Leoben, 8700, Austria*

[k] *Donetsk Institute for Physics and Engineering Named after O.O. Galkin, National Academy of Sciences of Ukraine, Pr. Nauki, 46, Kyiv 02000, Ukraine*

[l] *Faculty of Mechanical Engineering, Cracow University of Technology, Warszawska 24, Kraków 31-155, Poland*

[m] *Department of Materials Science and Engineering EEBE, Universidad Politécnica de Catalunya, c/Eduard Maristany 10-14, Barcelona 08019, Spain*

[n] *Fundació CIM-UPC, c/Llorens i Artigas 12, Barcelona 08028, Spain*

[o] *Department of Metallurgical and Materials Engineering, Universidade Federal de Minas Gerais, Belo Horizonte, MG 31270-901, Brazil*

[p] *School of Materials Science and Engineering, Kumoh National Institute of Technology, Gumi 39177, Republic of Korea*

[q] *Institute of Metallurgy and Materials Science, Polish Academy of Sciences, Krakow 30-059, Poland*

[r] *Centro de Investigación y Extensión en Materiales (CIEMTEC), Escuela de Ciencia e Ingeniería de los Materiales, Instituto Tecnológico de Costa Rica, Cartago 159-7050, Costa Rica*

[s] *Osipyan Institute of Solid State Physics of the Russian Academy of Sciences, Ac. Osipyan Str. 2, Chernogolovka 142432, Russia*

[t] *Department of Aerospace Engineering, Samsun University, Samsun 55420, Turkey*

[u] *Institute of Materials Physics, University of Münster, Germany*

[v] *Physical Metallurgy (PhM), Materials Science Department, Technical University of Darmstadt, Peter-Grünberg-Str. 2, Darmstadt 64287, Germany*

[w] *Institute of Physics of Materials, Czech Academy of Sciences, Zizkova 22, Brno 616 62, Czech Republic*

[x] *CEITEC – Institute of Physics of Materials, Czech Academy of Sciences, Zizkova 22, Brno 616 62, Czech Republic*

[y] *Department of Life Science and Applied Chemistry, Nagoya Institute of Technology, Tajimi 507-0033, Japan*

[z] *National Institute for Materials Science, 1-2-1 Sengen, Tsukuba, Ibaraki 316-8511, Japan*

[aa] *Laboratory for Dynamics and Extreme Characteristics of Advanced Nanostructured Materials, Saint Petersburg State University, 7-9 Universitetskaya nab., St. Petersburg 199034, Russia*

[ab] *School of Mechanical Engineering, College of Engineering, University of Tehran, Tehran, Iran*

[ac] *School of Applied Sciences, University of Campinas (FCA-UNICAMP), Pedro Zaccaria, 1300, Limeira 13484-350, Brazil*

[ad] *Institut Néel, CNRS & UGA, Grenoble, 38042, France*

[ae] *JOMI-LEMAN SA, 1115 route de St Thomas, La Motte-Fanjas 26217, France*

[af] *Advanced Ceramics Research Center, Nagoya Institute of Technology, Tajimi 507-0033, Japan*

[ag] *Institute for Technical Physics and Materials Science, HUN-REN Centre for Energy Research, Budapest H-1121, Hungary*

[ah] *National Institute for Research and Development in Environmental Protection, 294 Splaiul Independentei, 6th District, Bucharest 060031, Romania*

[ai] *AGH University of Science and Technology, Faculty of Physics and Applied Computer Science, Kraków 30-059, Poland*

[aj] *Université de Lorraine, Laboratoire d'Etude des Microstructures et de Mécanique des Matériaux (LEM3 UMR 7239), 7 rue Félix Savart, BP 15082, Metz F-57073, France*

[ak] *Université de Lorraine, Laboratory of Excellence on Design of Alloy Metals for low-mass Structures (DAMAS), Metz F-57045, France*

[al] *Hefei General Machinery Research Institute Co., Ltd, Hefei 230031, PR China*

[am] *Universidad del Atlántico, Faculty of Engineering, Mechanical Engineering Program, Research Group CONFORMAT, Puerto Colombia, Colombia*

[an] *Department of Mechanical Engineering and Materials Science, Yokohama National University, Yokohama 240-8501, Japan*

[ao] *Department of Materials Science, Montanuniversität Leoben, Jahnstraße 12, Leoben 8700, Austria*

[ap] *Graduate School of Engineering, Kyushu Institute of Technology, Kitakyushu 804-8550, Japan*

[aq] *Magnesium Research Center, Kumamoto University, Kumamoto 860-8555, Japan*

[ar] *Synchrotron Light Application Center, Saga University, Saga 840-8502, Japan*

[as] *RHP-Technology GmbH, Forschungs- und Technologiezentrum, Seibersdorf 2444, Austria*

[at] *Department of Design and Engineering, Faculty of Science and Technology, Bournemouth Univesity, Poole, Dorset BH12 5BB, UK*

[au] *Materials Research Group, Department of Mechanical Engineering, University of Southampton, Southampton SO17 1BJ, UK*

[av] *University of Quebec in Trois-Rivieres (UQTR), 3351 des Forges, Trois-Rivieres G9A 5H7, Canada*

[aw] *Department of Materials Science and Engineering, Kyushu University, Fukuoka 819-0395, Japan*

[ax] *Department of Applied Chemistry, Faculty of Engineering, Kyushu University, Fukuoka 819-0395, Japan*

[ay] *Institute for Nanotechnology, Karlsruhe Institute for Technology, Karlsruhe, 76021, Germany*

[az] *Division of Materials Science and Engineering, Hanyang University, Seoul 04763, Republic of Korea*

[ba] *LEPMI, Univ. Grenoble Alpes, Univ. Savoie Mont Blanc, CNRS, Grenoble INP, LEPMI, Grenoble, 38000, France*

[bb] *SIMAP, Univ. Grenoble Alpes, CNRS, Grenoble INP, SIMaP, Grenoble, 38000, France*

[bc] *DEMa, Federal University of São Carlos, São Carlos, São Paulo 13565-905, Brazil*

[bd] *Ritsumeikan Global Innovation Research Organization, Ritsumeikan University, Kusatsu 525-8577, Japan*

[be] *School of Mechanical, Industrial and Manufacturing Engineering, Oregon State University, Corvallis, OR 97331, USA*

[bf] *Department of Materials Engineering, School of Energy and Electromechanical Engineering, Hunan University of Humanities Science and Technology, Loudi 417000, China*

[bg] *Department of Mechanical and Systems Engineering, Faculty of Engineering, Ibaraki University, 4-121-1 Nakanarusawa, Hitachi, Ibaraki 316-8511, Japan*

[bh] *Department of Mechanical and Industrial Engineering, Tallinn University of Technology (TalTech), Ehitajate tee 5, Tallinn 19086, Estonia*

[bi] *School of Physical Sciences, University of Cambridge, Trinity Lane, Cambridge CB2 1TN, UK*

[bj] *Department of Materials Science and Engineering, Chungnam National University, Daejeon 34134, Republic of Korea*

[bk] *Iowa State University, Departments of Aerospace Engineering and Mechanical Engineering, Ames, IA 50011, USA*

[bl] *Ames National Laboratory, Division of Materials Science & Engineering, Ames, IA 50011, USA*

[bm] *Faculty of Materials Science and Engineering, Kunming University of Science and Technology, Kunming, Yunnan 650093, China*

[bn] *School of Materials Science and Engineering & Low-Carbon New Materials Research Center, Anhui University of Technology, Maanshan 243002, PR China*

[bo] *School of Materials Science and Engineering, Nanjing University of Science & Technology, Nanjing 210014, China*

[bp] *Institute of Advanced Wear & Corrosion Resistance and Functional Materials, Jinan University, Guangzhou 510632, China*

[bq] *School of Mechanical, Materials, Mechatronic and Biomedical Engineering, University of Wollongong, NSW 2522, Australia*

[br] *Faculty of Engineering, Universidad Militar Nueva Granada, Bogotá, Colombia*

[bs] *Graduate School of Science and Engineering, University of Toyama, Toyama 930-8555, Japan*

[bt] *Department of Materials Science and Engineering, Kumamoto University, Kumamoto 860-8555, Japan*

[bu] *Department of Mechanical Engineering, Doshisha University, Kyoto 640-0394, Japan*

[bv] *Anton Paar GmbH, Anton-Paar-Straße 20, Graz 8054, Austria*

[bw] *School of Metallurgy and Materials, University of Birmingham, Birmingham B15 2TT, UK*

[bx] *Erich Schmid Institute of Materials Science, Austrian Academy of Sciences, Jahnstraße 12, Leoben 8700, Austria*

[by] *M.N. Miheev Institute of Metal Physics, Ural Branch of RAS, Ekaterinburg 620108, Russia*

[bz] *Department of Mechanical Engineering, Karadeniz Technical University, Trabzon 61080, Turkey*

[ca] *Department Materials Science, Montanuniversität Leoben, Roseggerstraße 12, Leoben 8700, Austria*

cb *LASMIS, University of Technology of Troyes (UTT), Troyes, 10004, France*
cc *NLMK Belgium Holdings NV, Rue des Rivaux 2, La Louvière 7100, Belgium*
cd *Department of Design and Engineering, Faculty of Science and Technology, Bournemouth University, Poole, Dorset BH12 5BB, UK*
ce *Facultad de Química, Departamento de Ingeniería Metalúrgica, Universidad Nacional Autónoma de México, Mexico City 04510, Mexico*
cf *Univ Rouen Normandie, INSA Rouen Normandie, CNRS, Groupe de Physique des Matériaux UMR 6634, Rouen, 76000, France*
cg *Department of Electrical Engineering, Stanford University, Stanford, CA 94305, USA*
ch *Department of Materials Engineering, Tarbiat Modares University, Tehran, Iran*
ci *Institute of Solid State and Materials Physics, Dresden University of Technology, Dresden, 01062, Germany*
cj *Technology Department, Nagano Forging Co., Ltd, Nagano 381-0003, Japan*
ck *Department of Advanced Materials Science and Engineering, Faculty of Engineering Sciences, Kyushu University, Kasuga, Fukuoka 816-8580, Japan*
cl *Centre of Molecular and Macromolecular Studies, Polish Academy of Sciences, Sienkiewicza Street, 112, Lodz 90001, Poland*
cm *Kryvyi Rih State Pedagogical University, Gagarin av. 54, Kryvyi Rih 50086, Ukraine*
cn *School of Materials Science and Engineering, Shanghai University of Engineering Science, Shanghai 201620, China*
co *School of Mechanical Engineering, Northwestern Polytechnical University, Xi'an 710072, China*
cp *Department of Materials Science and Engineering, Mechanical Behavior Division of Shenyang National Laboratory of Materials Science, City University of Hong Kong, Kowloon, Hong Kong, China*

ARTICLE INFO

ABSTRACT

Ultrafine-grained and heterostructured materials are currently of high interest due to their superior mechanical and functional properties. Severe plastic deformation (SPD) is one of the most effective methods to produce such materials with unique microstructure-property relationships. In this review paper, after summarizing the recent progress in developing various SPD methods for processing bulk, surface and powder of materials, the main structural and microstructural features of SPD-processed materials are explained including lattice defects, grain boundaries and phase transformations. The properties and potential applications of SPD-processed materials are then reviewed in detail including tensile properties, creep, superplasticity, hydrogen embrittlement resistance, electrical conductivity, magnetic properties, optical properties, solar energy harvesting, photocatalysis, electrocatalysis, hydrolysis, hydrogen storage, hydrogen production, CO_2 conversion, corrosion resistance and biocompatibility. It is shown that achieving such properties is not limited to pure metals and conventional metallic alloys, and a wide range of materials are currently processed by SPD, including high-entropy alloys, glasses, semiconductors, ceramics and polymers. It is particularly emphasized that SPD has moved from a simple metal processing tool to a powerful means for the discovery and synthesis of new superfunctional metallic and nonmetallic materials. The article ends by declaring that the borders of SPD have been extended from materials science and it has become an interdisciplinary tool to address scientific questions such as the mechanisms of geological and astronomical phenomena and the origin of life.

Table of Contents

1. Introduction

Severe plastic deformation is receiving significant attention as a powerful process to produce materials with ultrafine grains (UFG) and large fractions of crystal lattice defects such as vacancies, stacking faults, dislocations, twins and grain boundaries [1–3]. These microstructural features of SPD-processed materials lead to their enhanced properties for various applications [4,5]. Although high strength through the Hall-Petch strengthening mechanism is the most known property of SPD-processed materials [6,7], these materials exhibit a wide range of mechanical and functional properties [4,5]. In addition to microstructure control by SPD, the process has other applications such as phase transformation control [8,9], mechanical alloying [10,11] and consolidation of powders [12,13]. The application of SPD has been extended from metallic alloys to a wider range of materials such as polymers [14], carbon [15] ceramics [16], *etc.* Since the properties of such SPD-processed materials are superior compared to conventional engineering materials, the term superfunctional materials has been recently used for them [17]. As shown in Fig. 1, the number of publications about SPD has experienced a gradual increase since the year 2000, and over 1000 papers are currently published about SPD every year.

The historical development of SPD was discussed in a recent review paper by 49 active scientists in the field [5]. Such a historical development can be briefly summarized in Fig. 2 [5]. The SPD was known in ancient times in sword making, and it became popular during the transition from the Bronze Age to the Iron Age [18]. The repeated forging and folding that was used for sword making is considered an ancient form of modern accumulative roll-bonding (ARB) [19]. Another transition in the SPD occurred in the 1930 s [20,21] followed by a book in 1952 [22] when Bridgman could apply SPD to a wide range of materials by the introduction of the high-pressure torsion (HPT) method (see details in [23]). It should be noted that superplastic deformation (severe plastic elongation by thermally-activated deformation mechanisms) was also reported in metallic materials in the 1930 s by Pearson [24], which received the term "super-plasticity" in polymer sciences in the 1930 s [25]. The invention of equal-channel angular extrusion/-pressing (ECAP) and ECAP-conform by Segal and his co-workers in the 1970 s was another important development that resulted in scaling up the size of SPD-processed samples by simple shear [26–28]. The
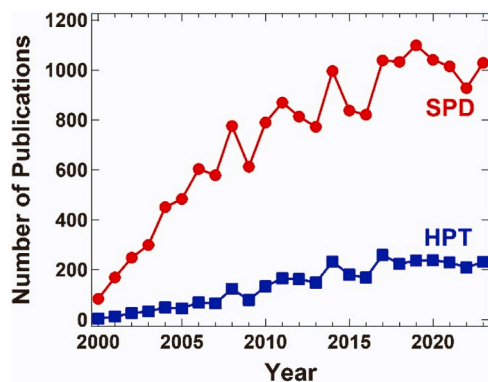
discovery of the formation of UFG microstructure by SPD was another important finding, which was first reported by Bridgman using X-ray diffraction (XRD) [20–22] and later visualized by transmission electron microscopy (TEM) in a few papers in the 1970 s [29,30] and a book written in Polish in 1976 [31] (the content of the book was summarized in English in [32]). The achievement of low-temperature superplasticity by Valiev and his co-workers in the 1980 s was an important finding that showed the interesting properties of SPD-processed materials with UFG structures and a large fraction of high-angle grain boundaries [33]. An extension of this study to Western and Asian countries [34,35] followed by the publication of a review paper in 2000 [1] resulted in the birth of the modern NanoSPD (nanomaterials by severe plastic deformation) field and eventually in the commercialization of the method for biomedical applications [36].

Despite significant progress in the SPD field, there are some arguments regarding the terminology of SPD. The SPD process was defined as the introduction of large strains in a bulk sample without changing its shape [2]. In SPD processes, the applied pressure should be usually high to avoid the fracture of materials, and the temperature should be below the recrystallization temperature when the objective is to produce UFG materials [37,38]. However, there are comments that the strain level (usually over a von Mises equivalent strain of 6) should be considered as a border of SPD regardless of the method used for the application of such strain levels. Such strains can be sometimes applied at low temperatures by conventional methods such as rolling, wire drawing and extrusion [39]. Moreover, there have been long-term efforts to apply such large strain on the surface of bulk materials [40,41] or in powders [42,43]. Since all these processes follow the same principles, SPD methods can be classified into three broad categories: (a) bulk-SPD, (b) surface-SPD and (c) powder-SPD. Despite such classification, a rigid strain border can be hardy defined for SPD because the microstructure-strain relationships of materials are quite different [5]. Moreover, the objective of SPD is not always the formation of UFG (materials with grain sizes below 1000 nm having high angles of misorientation) or nanograined (materials with grain sizes below 100 nm) materials, but it may be used in lower strain levels to control lattice defects [44] or produce heterostructured materials [45].

Despite significant progress in the field of SPD in recent years, there are limited comprehensive review papers about the field [1–5]. Moreover, available review papers are either old or mainly focus on SPD as a metal processing tool. However, the borders of SPD have been extended to non-metallic materials and various disciplines other than metallurgy. By considering the progressive changes of SPD in terms of concept and research direction, a comprehensive review paper is required to discuss the most recent aspects and future direction. Such a review paper should also clarify the classification of the SPD process and discuss the behavior of various types of materials during severe straining. This article, which was prepared by a large number of active researchers in different aspects of SPD, aims to provide a comprehensive overview of the latest concepts and findings in the field of SPD. The article classifies these findings by considering the processing methods, microstructural and structural features, mechanical and functional properties, and processed UFG and heterostructured materials. At the end of the manuscript, the application of SPD as a potential scientific tool for elucidating some natural phenomena such as earthquakes and the origin of life is briefly mentioned.

2. SPD methods

As mentioned in the introduction, the SPD processes can be classified as bulk-SPD, surface-SPD and powder-SPD methods. In bulk-SPD, the goal is to modify the bulk microstructure of a material with reasonably large sizes, although the surface is also affected [1–3]. In surface-SPD, only surface and sub-surface layers are modified, and the core of the sample remains reasonably unchanged [46]. In powder-SPD, the material is in the form of powder, and strain is introduced on the surface layer and core of the powder particles usually by ball milling methods [43].

Fig. 1. Number of publications per year about SPD and HPT [Scopus, January 15, 2024].
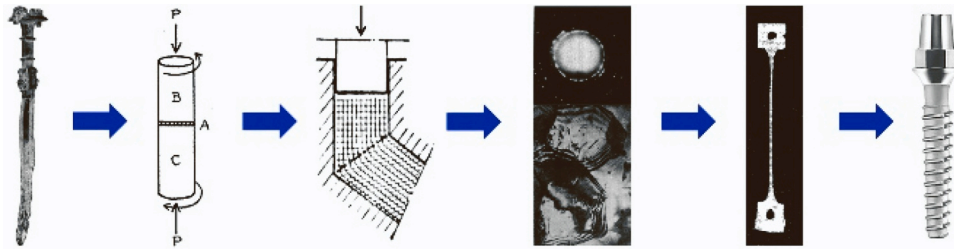
Fig. 2. Illustration of the historical development of SPD. From left to right: sword making by repeated forging and folding (photograph of a sword made in Luristan, Iran, 750–650 BSE), principles of HPT (a drawing by Bridgman, 1935), principles of ECAP (visualization of simple shear by Moire Fringes and coordinate grids reported by Segal, 1970 s), formation of UFG structure by HPT processing (micrographs reported by Erbel, 1976), high strain rate superplasticity in an aluminum alloy processed by ECAP (a work by Valiev, *et al.*, 1997), and commercialization of ECAP-processed titanium for implants [5].

To introduce large levels of strain in the sample, the SPD method should be able to introduce strain at low temperatures without failure of the sample. To satisfy these conditions, high pressure is an important requirement, as indicated by Bridgman decades ago [20–22]. The pressure should be higher than the final yield stress of the material after processing to realize the plastic flow [38]. Furthermore, introducing large shear strains in the material is difficult when the dimensions of the

sample change [2]. For example, if a von Mises strain of 6 is applied by rolling a plate with a thickness of 1 cm, its thickness is reduced to 300 nm, which is not practical. Different methods based on rolling, torsion, forging and extrusion can satisfy the required conditions for SPD processing of bulk material [5]. In most of these methods, the dimensions of the samples remain unchanged; however, some methods result in some dimensional changes in the samples. In this section, SPD
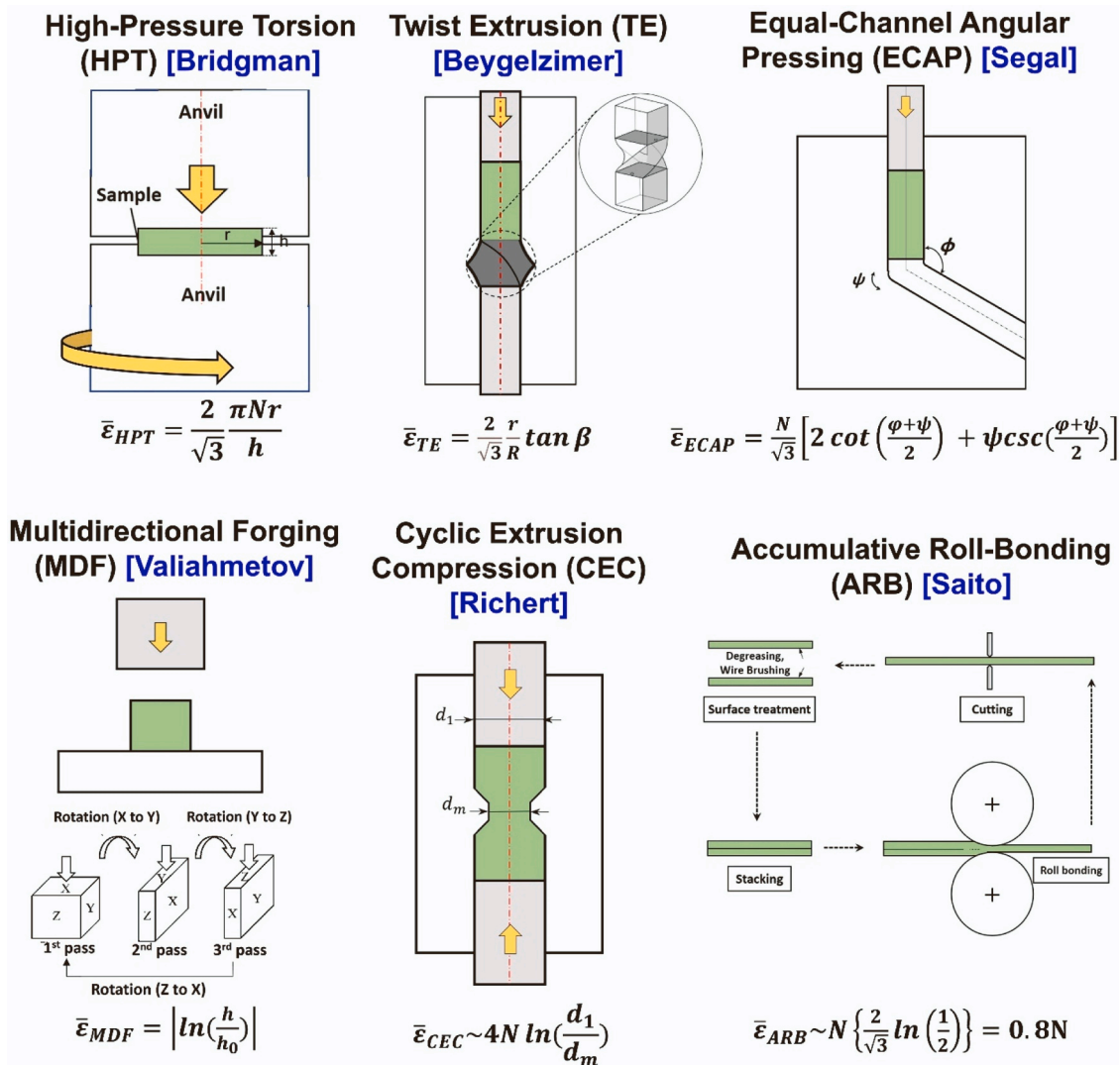
Fig. 3. Schematic illustration of main SPD methods and corresponding equivalent strain [50]. For HPT, N, r and h are the number of turns, distance from the center and disc thickness, respectively. For TE, r, R, and β are radial distance from the center, maximum radial distance from the center, and angle between the extrusion axis and the twist line, respectively. For ECAP, N is the number of passes. For MDF, h_0 and h are the initial and final height of the sample, respectively. For CEC and ARB, N is the number of cycles.

methods are comprehensively reviewed and some recent trends in SPD processing are discussed.

2.1. Bulk-SPD methods

In the majority of SPD methods, and particularly the popular methods such as HPT, ECAP and ARB, the introduction of large strain is possible due to no change in the sample dimensions [47]. HPT is becoming increasingly popular because it works at very high pressure and is therefore suitable for all types of metallic and non-metallic materials. In addition, the process can apply extremely large shear strains which are not achievable with other processes. ECAP has the benefit of the big sample size which makes it appropriate for commercial application. ARB is of interest because it is a simple and continuous process. Fig. 3 shows schematics and equivalent plastic strains of the main SPD methods including HPT [20], twist extrusion (TE) [48], ECAP [26], multi-directional forging (MDF) [49], cyclic extrusion compression (CEC) [50] and ARB [19].

Various methods were developed in recent years mainly by modification of major SPD processes to either improve straining conditions, modify the shape and dimensions of samples, or make the process continuous [50]. In most of these processes, the dimensions of the samples remain unchanged. Die structure and corresponding equivalent plastic strain of such SPD methods are summarized in Table 1 [51–109]. In some limited methods, the introduction of high plastic strain on the sample is associated with cross-section change. These methods are included in Table 2 [110–120].

2.2. Surface-SPD methods

In surface-SPD, gradient microstructures are generated from the treated surface to the core instead of producing a homogeneous plastic deformation within the bulk of the sample. The materials processed by surface-SPD can take advantages of the characteristics of both the refined surface layer and the coarse-grained core of the sample. When surface properties such as biocompatibility, wear resistance and corrosion resistance are of importance, surface-SPD processes have high technical benefits for commercial applications. Over time, several approaches have been designed to generate surface-SPD. Table 3 contains schematic representations of several surface-SPD methods, which are mainly based on peening, grinding, ultrasound and rolling [121–145]. Among these methods, ultrasonic shot peening (USSP or USP) [41] and surface mechanical attrition treatment (SMAT) [134] have received high attention in producing gradient-structured materials. The methods have a high potential for processing large sheets with enhanced properties. At the end of this article, the mechanical and functional properties of surface-SPD-processed materials with gradient microstructure are reviewed.

2.3. Powder-SPD methods

The most known method for inducing SPD in powders is high-energy ball milling, which was developed in the 1960 s [43]. In this method, powders of materials together with some hard balls (steel, tungsten carbide, zirconia, alumina, *etc.*) are introduced into a vial. The strain is introduced by rotation or vibration of the vial which leads to the impact of powders between the balls in dry or wet conditions [146]. In addition to straining, other phenomena such as welding and fracturing occur during the process [43]. The grain sizes achieved by this method are usually smaller than those achieved by bulk-SPD and surface-SPD methods, but the method suffers from contamination by milling media (balls and vial) as well as oxidation [43]. Ball milling followed by high-temperature sintering is a process to make bulk UFG materials, although the size of grains can be large due to the high-temperature effect [147]. Ball milling can be conducted using reactant liquids and gasses which is known as reactive ball milling [148]. Ball milling is

applicable to almost all types of material [149], while bulk-SPD methods (except for HPT) have limited applications to various metallic and non-metallic materials. Ball milling has contributed to the synthesis and discovery of various materials since the last century [150] until now [151,152]. The most popular ball milling methods are shown in Fig. 4, which include attritor milling, vibratory milling, planetary milling and high-pressure gas milling [153].
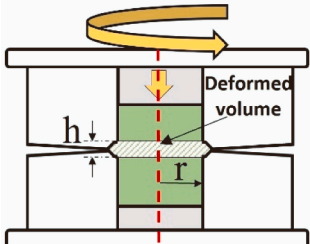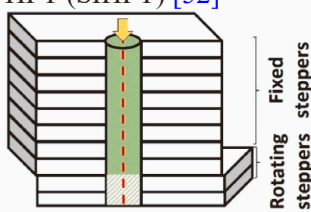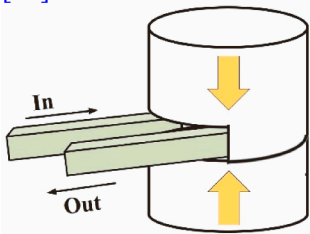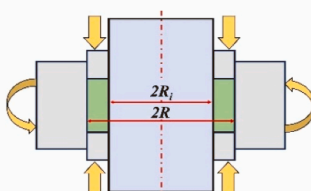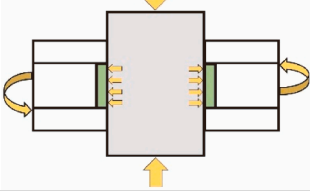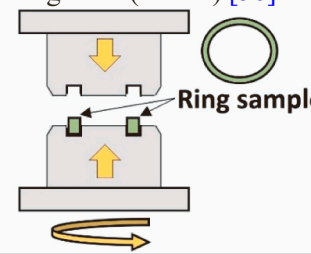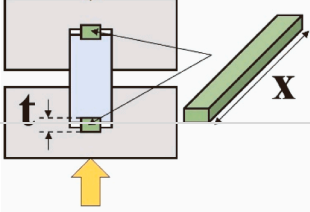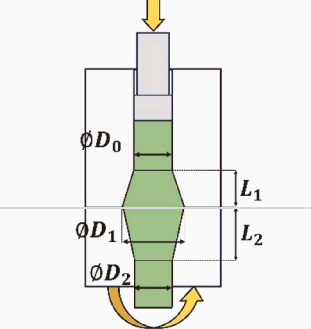
2.4. Recent trends in SPD methods

Although the most focused research direction in the SPD field is the examination of characteristics and properties of SPD-processed materials, there are some efforts on the modification or invention of processing methods. Some efforts focused on making the SPD methods continuous [154]. Despite these efforts, classic methods of ARB [19,155] and ECAP conform [28,156] are still among the most powerful and popular continuous SPD methods. Some studies focused on the application of hydrostatic pressure to make SPD processes more practical in terms of load and energy [157]. Some other studies focused on the modification of the shape and size of the sample to a form that can be more appropriate for practical applications such as rods [158], pipes [159] and sheets [160]. In most of these methods, high pressure plays a critical role. The application of SPD through cyclic viscoelastic deformation is another effort in this regard, although it has been employed by limited groups [161]. SPD processing under extreme processing conditions such as cryogenic temperature [162], ultra-high pressure [15], ultra-high strain rate [163] and ultra-high shear strain (known as ultra-SPD) [164] is another important progress in the field in recent years. In the following sections, some of these recent trends in SPD methods are discussed.

2.4.1. SPD methods with hydrostatic pressure

Despite high attraction in SPD during the last three decades, most SPD methods are limited to laboratory-scale experiments. This matter, which prevents the utilization of SPD methods for industrial goals, is mainly relevant to the higher load when processing longer samples [50]. Total processing load includes deformation load (F_D), friction load (F_f) and required load for the redundant work (F_R) [157]. It should be noted that the magnitude of the total processing load is mainly affected by the friction load portion especially when processing long samples [157]. In this regard, an increase in the sample length leads to higher surface contact between the die and the sample, which consequently increases the total processing load remarkably. An increase in the processing load increases the chance of buckling and yielding of the punch. Therefore, any approach that reduces the total processing load opens the opportunity for processing relatively long samples as a requirement for industrial applications [5]. Using high-pressure fluid instead of a solid punch is one of the best candidates, which was implemented in single-pass hydrostatic deformation processes as modified versions of conventional methods. Single-pass hydrostatic deformation processes include hydrostatic extrusion (HE) [165], hydrostatic extrusion integrated with circular equal channel angular pressing (HECCAP) [166], hydrostatic backward extrusion (HBE) [167] and hydrostatic radial forward tube extrusion (HRFTE) [168]. The presence of high-pressure fluid in the gap between die-sample contact eliminates the friction force which is very huge in processing longer samples. This reduces the processing load and makes it possible to process samples with a higher aspect ratio (length to diameter) compared to conventional methods. It was reported that a sample with an aspect ratio of 0.27 with a processing load of ~264 kN was processed by conventional backward extrusion while only a fifth of this load was required in HBE to process a sample with an aspect ratio of 8.5 [167].
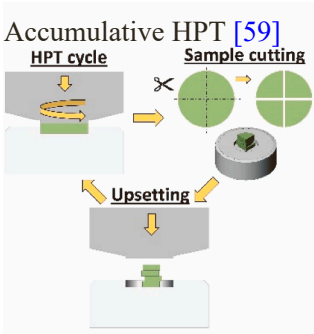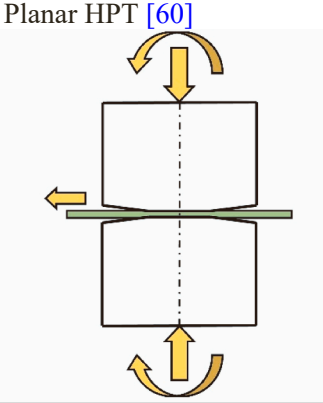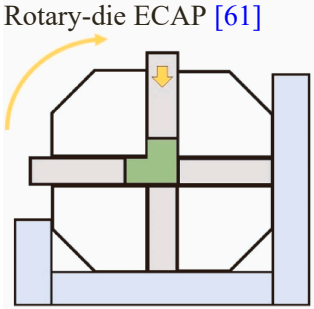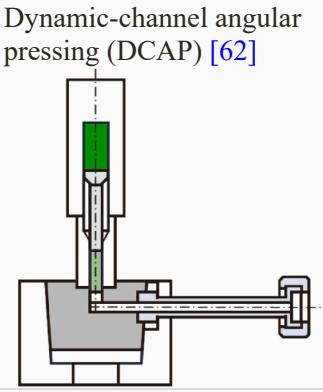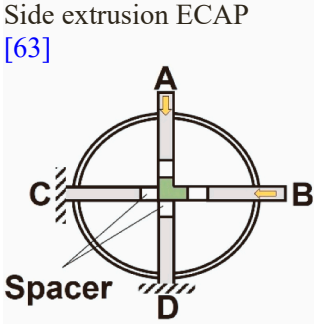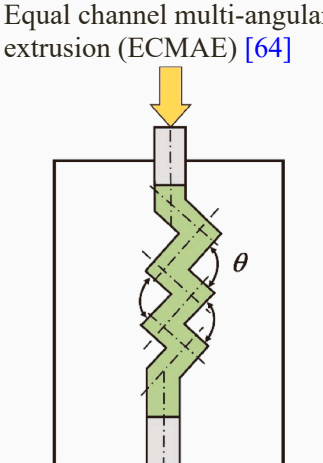
The application of high-pressure fluid to SPD methods leads to the development of hydrostatic SPD methods as new counterparts of conventional SPD processes [157] including equal-channel angular hydro-extrusion (ECAH) [169], hydrostatic cyclic extrusion compression

Table 1
Die structure and equivalent plastic strain of some SPD methods (references do not necessarily refer to the first publication of each method).

Schematics of Process	Equivalent Plastic Strain	Schematics of Process	Equivalent Plastic Strain
Incremental HPT (IHPT) [51]	$$\bar{\varepsilon}_{IHPT} = \frac{2}{\sqrt{3}}\frac{\pi N r}{h}$$	Single-task incremental HPT (SIHPT) [52]	$$\bar{\varepsilon}_{SIHPT} = \bar{\varepsilon}_{IHPT}$$
Continuous HPT (CHPT) [53]	$$\bar{\varepsilon}_{CHPT} = (1-s)\frac{\pi R}{\sqrt{3}t}$$	Tube high-pressure shearing (t-HPS) [54]	$$\bar{\gamma}_{t-HPS} = \frac{\theta}{ln(R/R_i)}$$ $$\bar{\varepsilon}_{t-HPS} = \frac{\theta}{\sqrt{3}ln(R/R_i)}$$
High-pressure tube twisting (HPTT) [55]	$$\bar{\gamma}_{HPTT} = \frac{\beta}{ln\left(\frac{b}{a}\right)}$$	Ring HPT (RHPT) [56]	$$\bar{\varepsilon}_{RHPT} = \bar{\varepsilon}_{HPT}$$
High-pressure sliding (HPS) [57]	$$\bar{\varepsilon}_{HPS} = \frac{x}{\sqrt{3}t}$$	High-pressure torsion extrusion (HPTE) [58]	$$\bar{\varepsilon}_{HPTE} = 4\,ln\frac{D0}{D1} + 2\,ln\frac{D1}{D2} + \frac{\omega \cdot R}{\sqrt{3} \cdot V}\frac{D2}{D1}$$
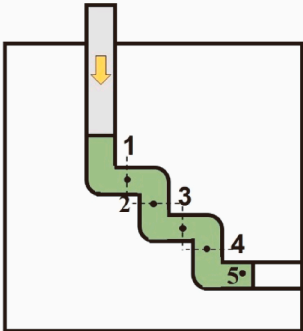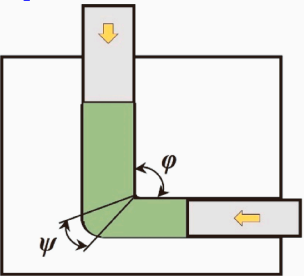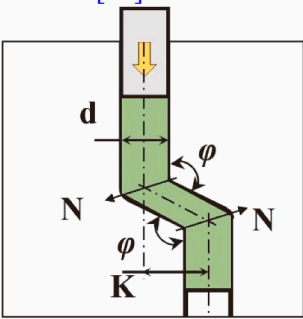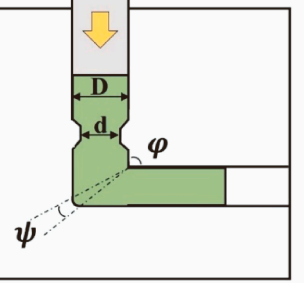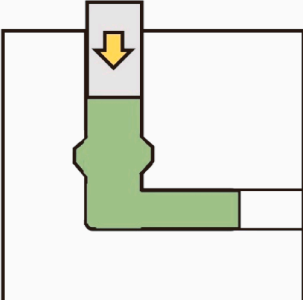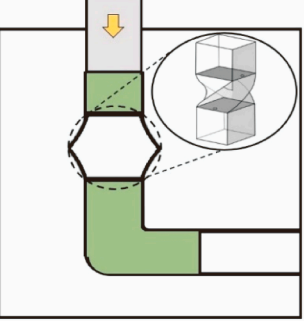
Table 1 (*continued*)

Accumulative HPT [59]	Planar HPT [60] $$\overline{\gamma}_{P-HPT} = \frac{2\pi r}{t}\frac{\varphi}{360°}$$
Rotary-die ECAP [61]	Dynamic-channel angular pressing (DCAP) [62] $$\overline{\varepsilon}_{DCAP} = N\left[\frac{2\cot\left(\frac{\varphi}{2}+\frac{\psi}{2}\right)}{\sqrt{3}} + \frac{\psi\csc\left(\frac{\varphi}{2}+\frac{\psi}{2}\right)}{\sqrt{3}}\right]$$
Side extrusion ECAP [63]	Equal channel multi-angular extrusion (ECMAE) [64] $$\overline{\varepsilon}_{ECMAE} = 2\sum_{i=1}^{n}\frac{\cot\theta_i}{\sqrt{3}}$$
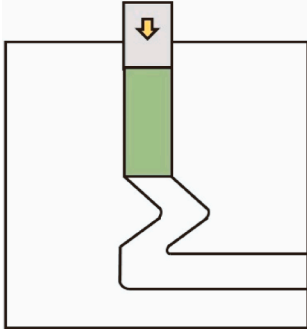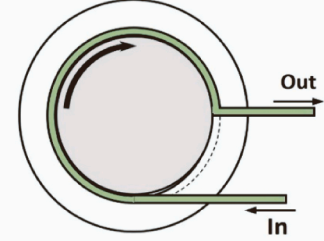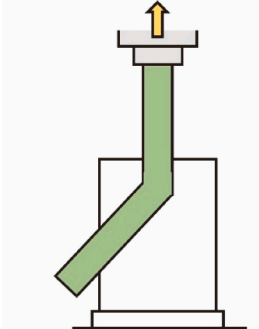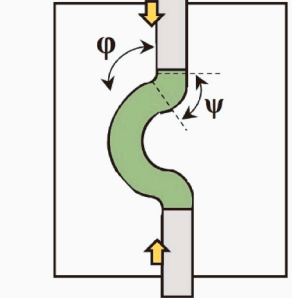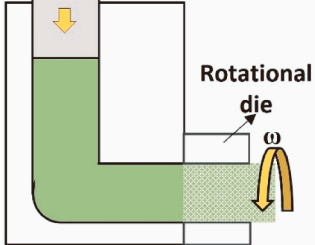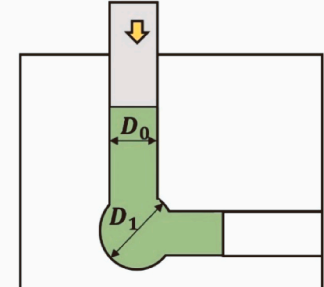
Table 1 (*continued*)

Multi-pass die ECAP [50]	ECAP with back pressure [65]
$\bar{\varepsilon}_{MPECAP} \sim 5\bar{\varepsilon}_{ECAP}$ (for $\varphi = 90°$)	$\bar{\varepsilon}_{ECAPBP} = \bar{\varepsilon}_{ECAP}$
ECAP with parallel channel [66]	Cyclic extrusion compression angular pressing (CECAP) [67]
	$\bar{\varepsilon}_{CECAP} = \varepsilon_{CEC} + \varepsilon_{ECAP}$
Extrusion-expansion channel angular pressing (EECAP) [68]	Twist channel angular pressing (TCAP) [69]
$\bar{\varepsilon}_{EECAP} = \varepsilon_{CEE} + \varepsilon_{ECAP}$	$\bar{\varepsilon}_{TCAP} = \varepsilon_{twist\ extrusion} + \varepsilon_{ECAP}$
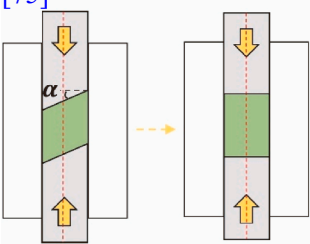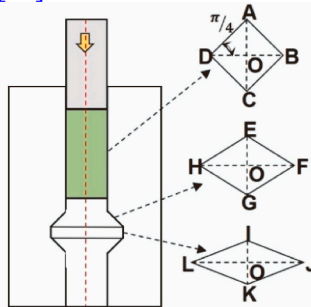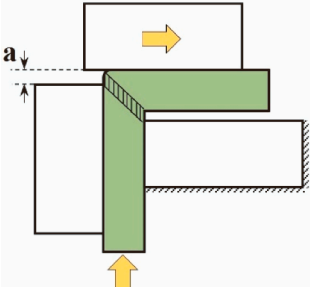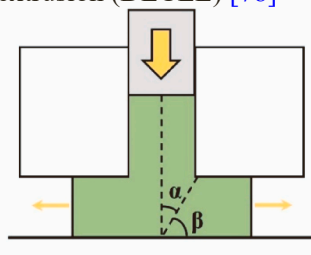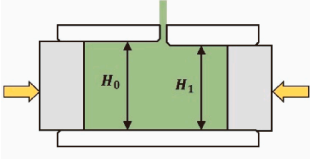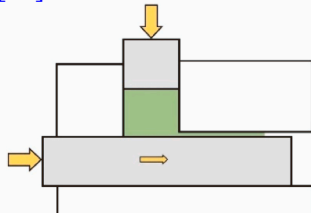
Table 1 (*continued*)

Twist channel multi-angular pressing (TCMAP) [70]	ECAP conform [28]
Equal channel angular drawing (ECAD) [71]	C-shape equal channel reciprocating extrusion (CECRE) [72] $\overline{\varepsilon}_{CECRE} = \overline{\varepsilon}_{ECAP}$
Torsional ECAP [73]	Expansion ECAP (Exp-ECAP) [74] $\overline{\varepsilon}_{Exp-ECAP} = \overline{\varepsilon}_{ECAP} + 4N \ln \dfrac{D_1}{D_0}$
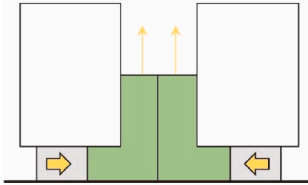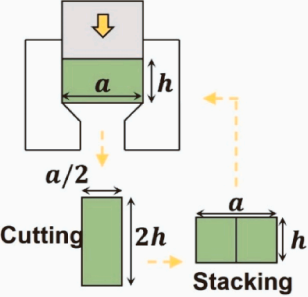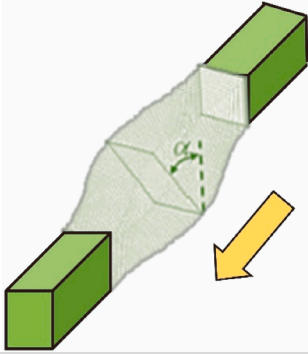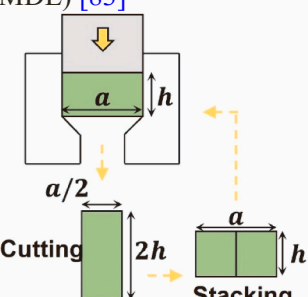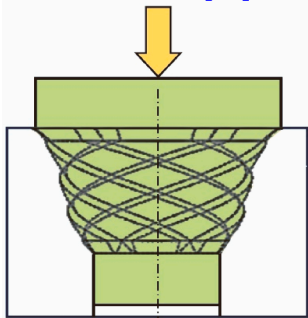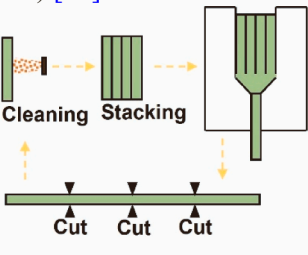
Table 1 (*continued*)

Repetitive forging using inclined punch (RFIP) [75] $\bar{\gamma}_{RFIP} = 2N \tan \alpha$	Pure shear extrusion (PSE) [76] $\bar{\varepsilon}_{PSE} = \frac{2N}{\sqrt{3}} \sqrt{(\ln R)^2 + \left(\frac{R^2-1}{R^2+1}\right)^2}$
Incremental ECAP (IECAP) [77]	Dual equal channel lateral extrusion (DECLE) [78] $\bar{\gamma}_{DECLE} = \cot \alpha + \cot \beta$
Plastic flow machining [79]	Friction-assisted lateral extrusion process (FALEP) [80] $\bar{\gamma}_{FALEP} = \frac{p}{c} + \frac{c}{p}$
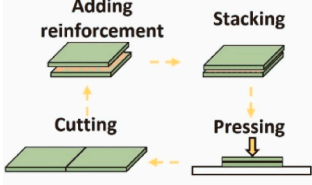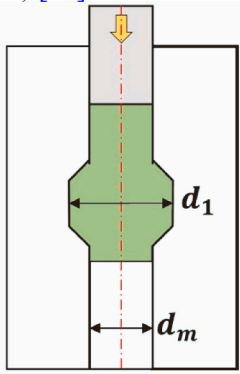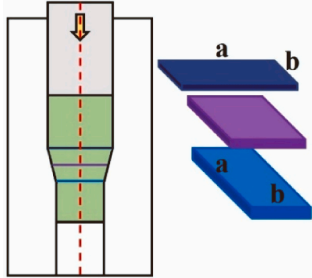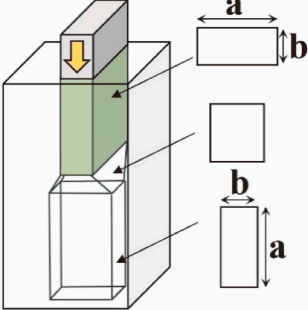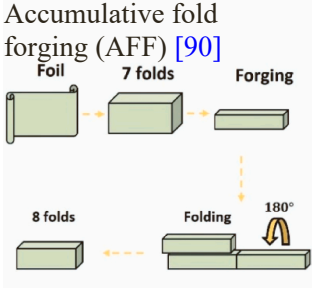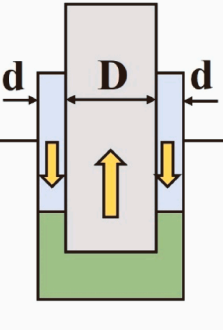
Table 1 (*continued*)

Channel angular pressing with converging billets (CAPCB) [81]

Channel angular pressing with converging billets (CAPCB) [81]

$$\bar{\varepsilon}_{MDE} = \frac{2N}{\sqrt{3}} ln \frac{1}{1-r}$$
$$= \frac{2N}{\sqrt{3}} ln\, 2$$

Multiple direct extrusion (SSE) [82]

$$\bar{\gamma}_{SSE} = 2 \tan \alpha$$
$$\bar{\varepsilon}_{SSE} = \frac{\gamma}{\sqrt{3}}$$

Multiple direct extrusion (MDE) [83]

Vortex extrusion [84]

Accumulated extrusion (AE) [85]
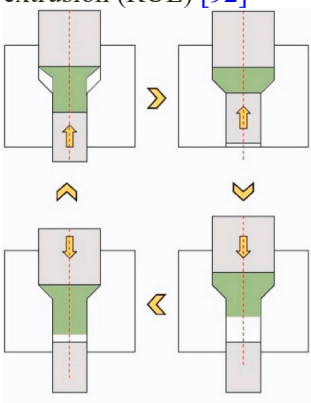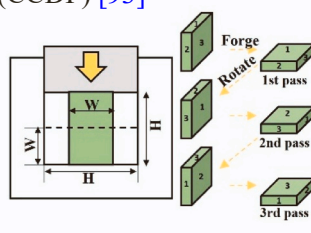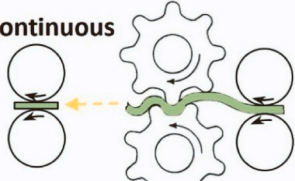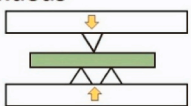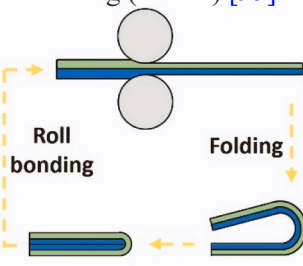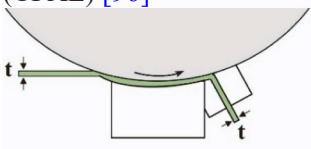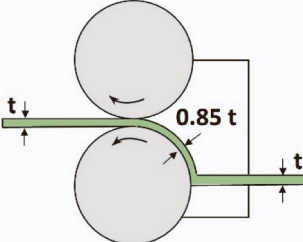
Table 1 (*continued*)

Accumulative press bonding (APB) [86]	Cyclic expansion extrusion (CEE) [87] $$\overline{\varepsilon}_{CEE} = 4N\ln\left(\frac{d_1}{d_m}\right)$$
Severe forward extrusion (SFE) [88]	Equal channel forward extrusion (ECFE) [89]
Accumulative fold forging (AFF) [90]	Accumulative back extrusion (ABE) [91] $$\overline{\varepsilon}_{ABE} = 4N\ln\left(\frac{D+2d}{5d^2+4dD}\right)$$
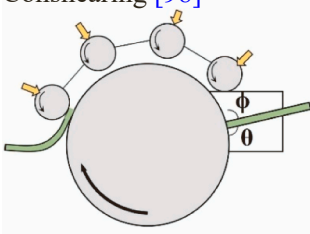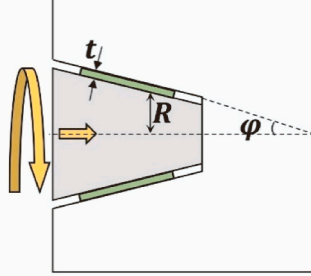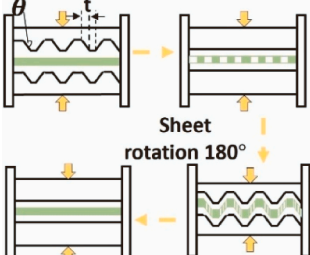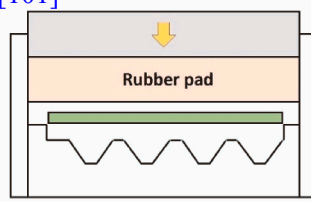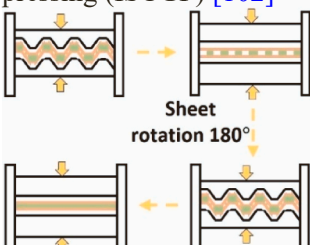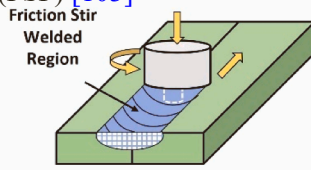
Table 1 (*continued*)

Repetitive upsetting and extrusion (RUE) [92]	Cyclic closed die forging (CCDF) [93] $$\bar{\varepsilon}_{CCDF} = \frac{2N}{\sqrt{3}} \ln\left(\frac{H}{W}\right)$$
Repetitive corrugation and straightening (RCS) [94]	Accumulative roll bonding and folding (ARBF) [95]
Continuous frictional angular extrusion (CFAE) [96]	Equal channel angular rolling (ECAR) [97]

14

Table 1 (*continued*)

Conshearing [98]	Cone–cone method (CCM) [99] $$\bar{\varepsilon}_{CCM} = \frac{2\pi N.R(x)}{\sqrt{3}.t}$$
Constrained groove pressing (CGP) [100] $$\bar{\varepsilon}_{CGP} = \frac{\tan\theta}{\sqrt{3}}$$	Rubber pad-constrained groove pressing (RP-CGP) [101]
Interface sheet constrained groove pressing (ISCGP) [102]	Friction stir processing (FSP) [103]

Table 1 (*continued*)
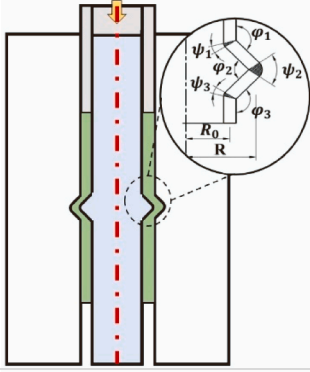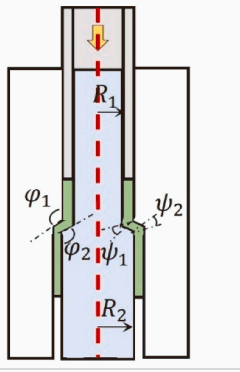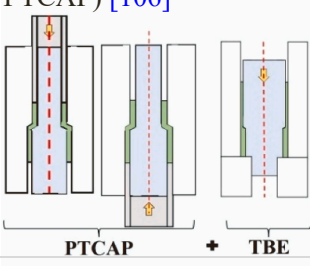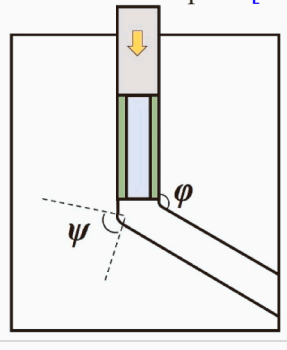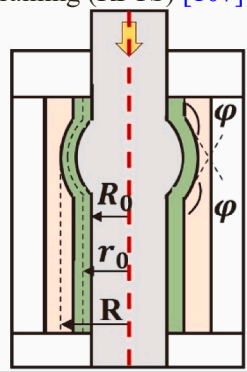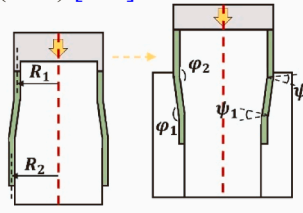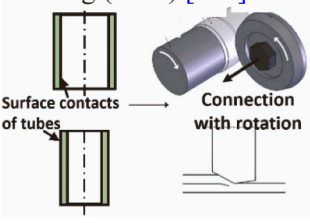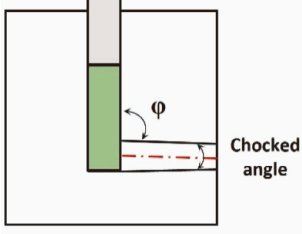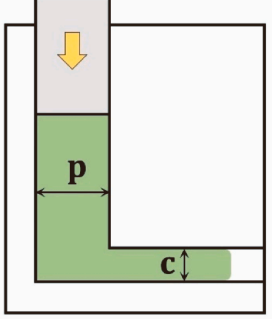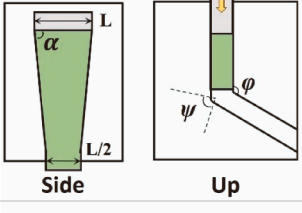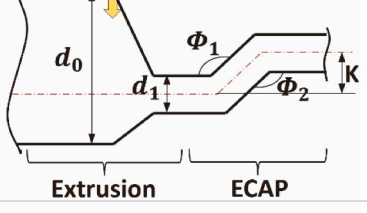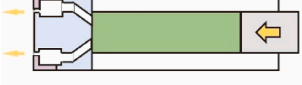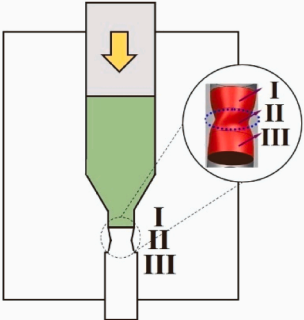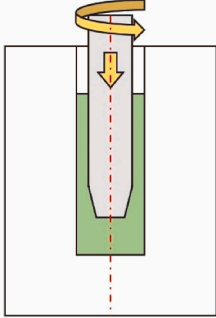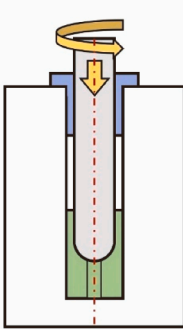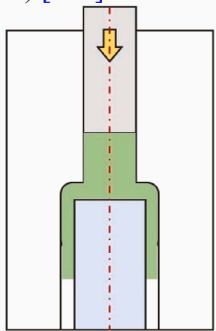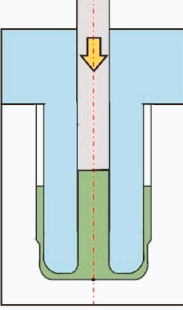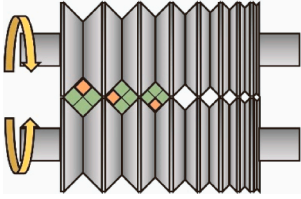
Tubular channel angular pressing process (TCAP) [104]	Parallel tubular channel angular pressing (PTCAP) [105]

$$\bar{\varepsilon}_{TCAP} = \frac{N}{\sqrt{3}}\left\{\sum_{i=1}^{3}\left[2\cot(\frac{\varphi_i+\psi_i}{2}) + \psi_i\mathrm{cosec}(\frac{\varphi_i+\psi_i}{2})\right] + 4\ln\frac{R}{R_0}\right\}$$

$$\bar{\varepsilon}_{PTCAP} = \frac{2}{\sqrt{3}}N\left\{\sum_{i=1}^{2}\left[2\cot((\frac{\phi_i+\psi_i}{2}) + \psi_i\cos e\,c(\frac{\phi_i+\psi_i}{2})\right] + 2\ln\frac{R_2}{R_1}\right\}$$

Combined parallel tubular channel angular pressing (Combined PTCAP) [106]

$$\bar{\varepsilon}_{CPTCAP} = \bar{\varepsilon}_{PTCAP} + \ln\frac{R_0^2 - r_0^2}{R_0^2 - r_f^2}$$

ECAP for hollow parts [55]

$$\bar{\varepsilon}_{ECAPHP} = \bar{\varepsilon}_{ECAP}$$

Rubber pad tube straining (RPTS) [107]

$$\bar{\varepsilon}_{RPTS} = \frac{4}{\sqrt{3}}N\left[\cot\frac{\varphi}{2} + \ln\frac{R_0+R}{R_0+r_0}\right]$$

Cyclic flaring and sinking (CFS) [108]

$$\bar{\varepsilon}_{CFS} = \frac{4}{\sqrt{3}}N\sum_{i=1}^{2}\left[\cot((\frac{\phi_i}{2}) + \ln\frac{R_2}{R_1}\right]$$

Accumulative spin bonding (ASB) [109]

$$\bar{\gamma}_{ASB} = \frac{2(1-r)^2}{r(2-r)}\tan\theta\ln\frac{1}{1-r}$$

Table 2

Die structure and equivalent plastic strain of SPD methods with cross-sectional area change.

Schematics of process	Equivalent plastic strain	Schematics of process	Equivalent plastic strain
ECAP with chocked exit channels (ECAPCEC) [110]	$\bar{\varepsilon}_{ECAPCEC}$ $= \bar{\varepsilon}_{extrusion}$ $+ \bar{\varepsilon}_{ECAP}$	Non-equal channel angular pressing (NECAP) [111]	$\bar{\gamma}_{NECAP}$ $= \dfrac{p}{c} + \dfrac{c}{p}$
Half-channel angular extrusion (HCAE) [112]	$\bar{\varepsilon}_{HCAE}$ $= \bar{\varepsilon}_{extrusion}$ $+ \bar{\varepsilon}_{ECAP}$	Integrated extrusion and ECAP (IEECAP) [113]	$\bar{\varepsilon}_{IEECAP}$ $= \bar{\varepsilon}_{extrusion}$ $+ \bar{\varepsilon}_{ECAP}$
Porthole-equal channel angular pressing (P-ECAP) [114]	$\bar{\varepsilon}_{P-ECAP}$ $= \bar{\varepsilon}_{ECAP} + \bar{\varepsilon}_{PE}$	Integrating forward extrusion and torsion deformation (IFETD) [115]	

Table 2 (*continued*)

Friction stir back extrusion (FSBE) [116]	$\bar{\varepsilon}_{FSBE} = \bar{\varepsilon}_{FSP} + \bar{\varepsilon}_{BE}$	Friction stir tube back extrusion process (FSTBE) [117]	$\bar{\varepsilon}_{FSTBE} = \bar{\varepsilon}_{FSP} + \bar{\varepsilon}_{BE}$
Radial forward extrusion (RFE) [118]	$\bar{\varepsilon}_{RFE} = \bar{\varepsilon}_{FE}$	Radial backward extrusion (RBE) [119]	$\bar{\varepsilon}_{RBE} = \bar{\varepsilon}_{BE}$
Caliber rolling (CAROL) [120]			
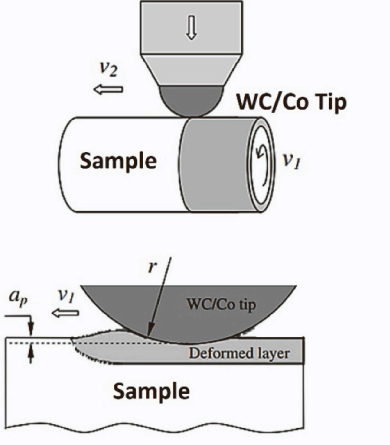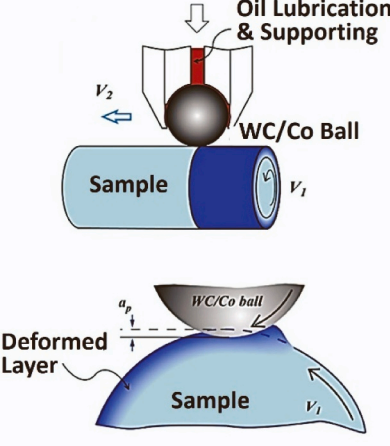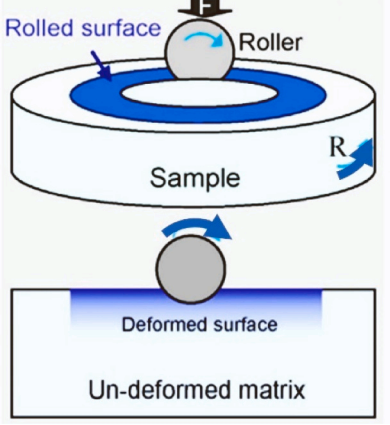
(HCEC) [170], hydrostatic cyclic extrusion expansion (HCEE) [171], hydrostatic twist extrusion (HTE) [172], hydrostatic tube cyclic extrusion compression (HTCEC) [173] and hydrostatic tube cyclic extrusion expansion (HTCEE) [174] as shown schematically in Fig. 5. Five main advantages of utilizing SPD methods with high hydrostatic pressure can be summarized as:

- lower processing load
- higher aspect ratio of the processable sample
- more homogeneous properties
- lower ductility loss
- smaller saturated grain size

Similar to common SPD methods, a decrease in grain size and an increase in dislocation density leads to an increase in yield and ultimate strength in hydrostatic SPD processes [174]. However, in these processes, ductility loss is usually lower than that in common SPD methods. The strength-ductility paradox is one of the challenges ahead of the industrial application of SPD. As an example, it was reported that pure copper with simultaneously higher ductility and strength is achievable by the hydrostatic TCEE method in comparison with other conventional SPD methods like common TCEE, ECAP and ARB [174]. It was also reported that HCEC applies more homogeneous strain to the sample compared to the common CEC method [170], which results in more uniform grain refinement and mechanical properties after HCEC [175]. Since mechanical properties are a function of grain size, the minimum achievable grain size or minimum saturated grain size is a remarkable parameter in SPD methods, which is highly influenced by hydrostatic pressure [50,175]. As an example, HTE [172] was capable of producing samples with a grain size of 800 nm, which was 50% smaller than that of the TE method [176]. Also, among all SPD methods with high hydrostatic pressure, those that create higher hydrostatic pressure
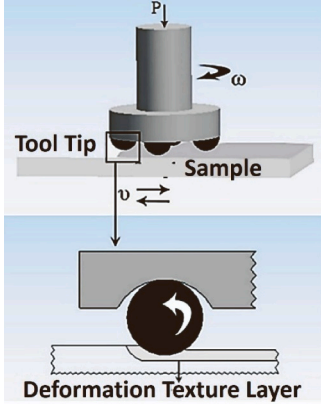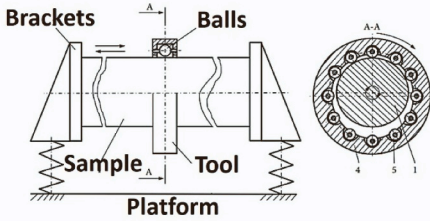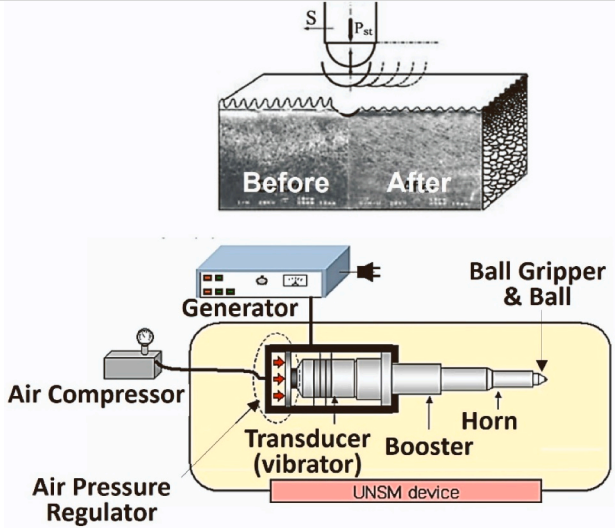
Table 3
Schematic representations of some surface-SPD methods (references do not necessarily refer to the first publication of each method).

Process	Schematics
Spherical motion burnishing (SMB) [121] Surface mechanical grinding treatment (SMGT) [122]	
Conventional deep cold rolling (CDCR) [123] Ultrasonic deep cold rolling (UDCR) [124] Surface mechanical rolling treatment (SMRT) [125]	
High-pressure surface rolling (HPSR) [126]	

Table 3 (*continued*)

Fast multiple rotation rolling (FMRR) [127]	
Vibration-centrifugal hardening (VCH) [128,143]	
Ultrasonic cold forging technology (UCFT) [129] Ultrasonic nanocrystal surface modification (UNSM) [130]	
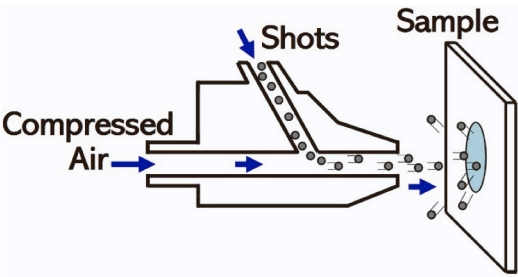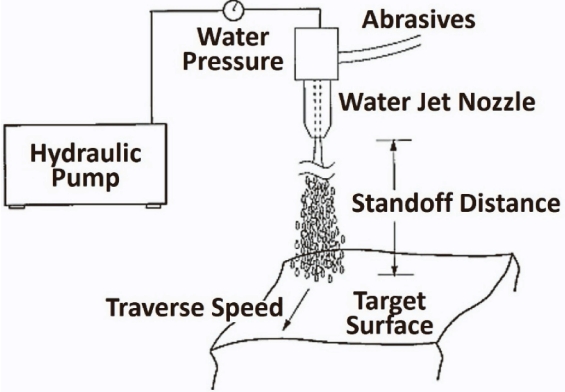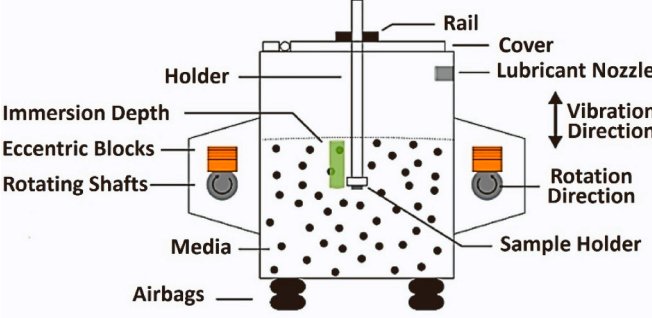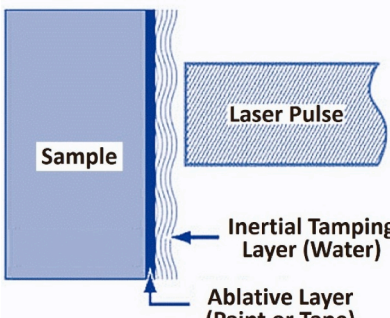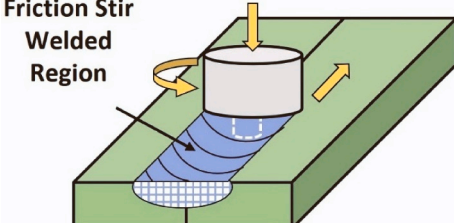
Table 3 (*continued*)

Rotating pins ultrasonic peening (RPUP) [131] Ultrasonic peening (UP) [132] Ultrasonic impact peening (UIP) [133]	
Ultrasonic shot peening (USSP) [41] Surface mechanical attrition treatment (SMAT) [134]	
Surface mechanical impact treatment (SMIT) [135]	

Table 3 (*continued*)

High energy shot peening (HESP) [136] Severe shot peening (SSP) [137] Gradient severe shot peening (GSSP) [138]	
Abrasive waterjet peening (AWJP) [139]	
Vibratory peening (VP) [140, 144]	
Laser shock peening (LSP) [141,145]	
Friction stir processing (FSP) [142]	

Fig. 4. Various types of high-energy ball milling for powder-SPD: (a) attritor milling, (b) vibratory milling, (c,d) planetary milling and (e) high-pressure gas milling [43, 151, 153].

produce samples with better mechanical properties. In this regard, CEC-based methods such as HCEC and HTCEC are more capable of grain refinement compared to CEE-based methods including HCEE and HTCEE [175].

In conclusion, the application of high hydrostatic pressure through a liquid phase provides specific features for scaling up the sample size. Moreover, this strategy improves the microstructure and mechanical properties of the final product.

2.4.2. Upscaling disc sample to rod

It is well known that HPT is the most effective method in terms of reachable strain, versatility of treatable materials, grain refinement and processing costs [177,178], but the size of HPT-processed disc samples is small, which prevents the industrial application of this method. Over the past 30 years, numerous other methods of SPD allowing the production of billets and sheets have been developed. A comprehensive overview of these methods can be found in a recent review publication [179]. Typically, multiple processing passes are required to accumulate a significant strain, which is necessary for refining the microstructure of a billet to the sub-micrometer range (one-pass processing is possible in limited methods like ECAP-conform [156]). As a result, integrating these methods into a technological processing chain is challenging, despite the clear advantages demonstrated by SPD-processed materials [36, 180–182]. There have been some attempts to overcome this problem and the introduction of high-pressure torsion extrusion (HPTE) is one of them.

The HPTE method reproduces the stress-strain conditions similar to HPT conditions (*i.e.* obtaining very high torsional strain in a single pass) but in a rod-shaped sample [183]. The technical detailed description of the method was reported elsewhere [58]. In short, a rod-shaped specimen is deformed by the punch (moving with the velocity *v*) as well as by the containers (one of them rotates with the velocity *ω*) (Fig. 6a) in such a way that the entire length of a specimen is torsionally deformed, as a specimen gradually passes through the shear zone. During the deformation, the plastic flow of the billet material follows a spiral pattern, as evidenced using aluminum marker wires embedded in a copper billet (Fig. 6b) [184,185]. To constrain torsional deformation within a thin layer of a billet, and to prevent slippage of the billet in the die, the die design was modified to include special holding elements (Fig. 6a). Similar to HPT, strain distribution at HPTE is not uniform along the billet radius (as well as along the billet height), as follows from FEM calculations of the strain distribution in the billet [58,184,186]. Therefore, HPTE at low strain levels can be used for the processing of gradient structure in the billet, favorable concerning the good balance of strength and ductility [187,188]. On the other hand, at a high enough strain, the microstructure of the billet can be homogenous due to the saturation of grain refinement phenomenon observed at SPD processing [38,189].

By now HPTE was successfully used for processing commercially pure copper [58,190] and aluminum [191], 6101 Al-based alloy, niobium [192], magnesium as well as ZK30 and ZK60 Mg-based alloys. In each case, the mean grain size of the treated metals and alloys has been effectively refined to the submicrometer range. This is illustrated, for example, in Fig. 7a which highlights the microstructure refinement of copper. Both the microhardness and tensile strength of HPTE-processed metals and alloys are significantly higher than those in the annealed state. Uniform elongation is reduced to a few percent, but total elongation remains rather large, similar to the annealed sample (Fig. 7b). This is in agreement with the "strength-ductility paradox" proclaimed for some SPD-processed materials [193]. Therefore, HPTE
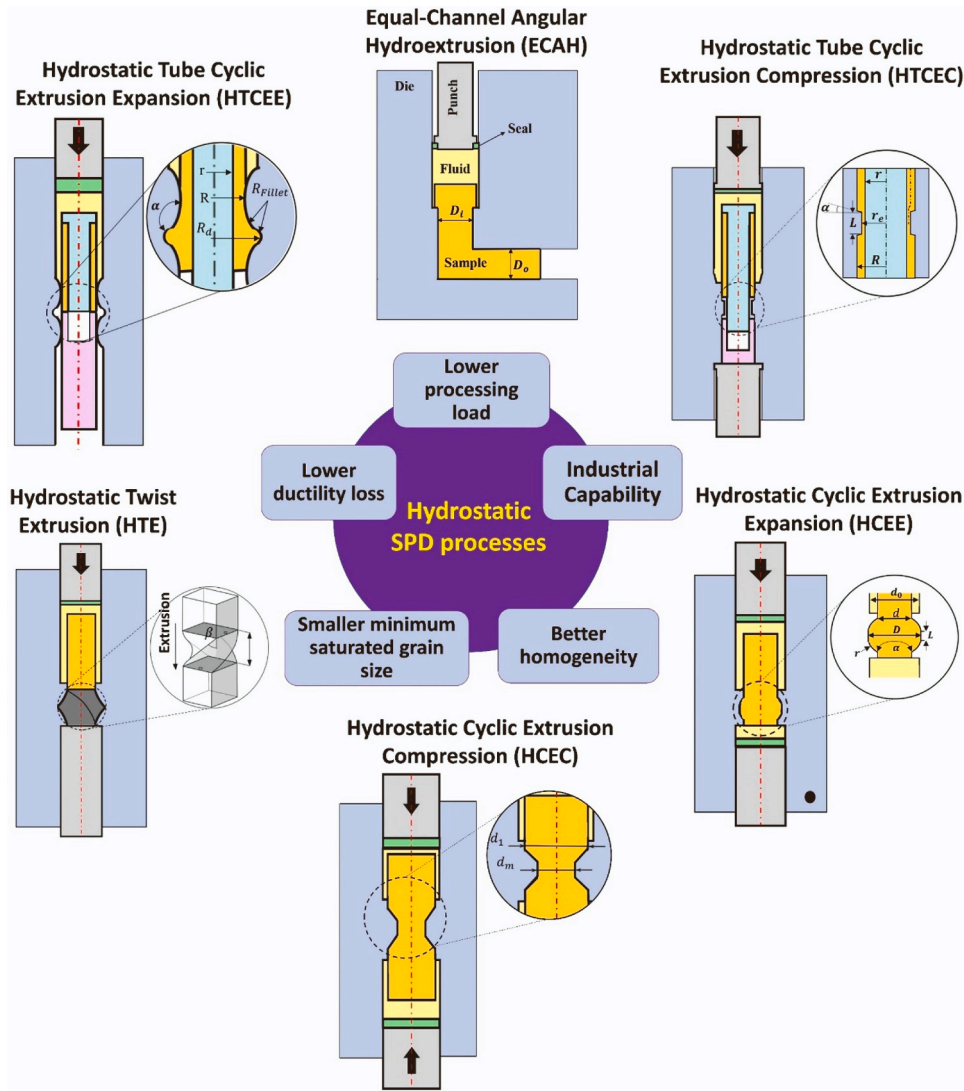
Fig. 5. Schematics of different SPD methods with high hydrostatic pressure [157].
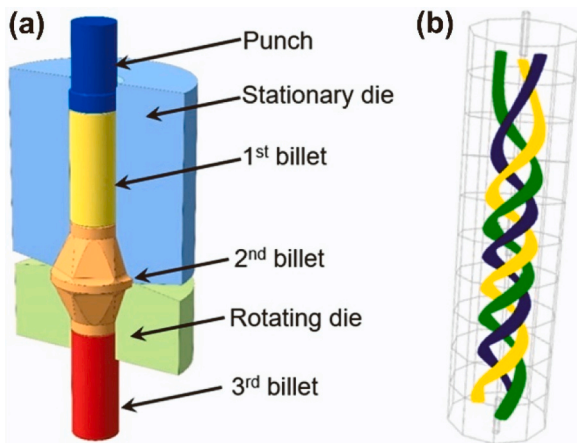
Fig. 6. (a) Schematics of the HPTE process with three billets inside the die [184]. (b) X-ray tomography reconstruction of aluminum wires embedded into the copper billet after HPTE processing with translational velocity $v = 6$ mm/min and rotational velocity $\omega = 1$ rpm (aluminum wires are shown in three different colors for better visualization) [185].

appears to be feasible for fabricating metallic rods with small grain size and enhanced mechanical properties in one pass, while other rod-processing SPD methods like ECAP require several passes [193]. HPTE can be also used for processing architectured (gradient and hybrid) samples [194–196]. Application of HPTE to a rod sample with inserted hardening wires leads to a refinement of the matrix microstructure and transforms the shape of wires from straight to helical (Fig. 6b). Such architectures resemble the morphology of natural tissues having high fracture toughness (bones, shells, *etc.*) [197,198], and can be used for parts operating in special conditions such as shock loading.

In conclusion, there are ways to upscale the sample size and modify the shape by modification of SPD methods, and the HPTE method is one of the successful examples that can be used for processing bulk specimens like rods [158]. The main highlight of this method includes the possibility of accumulating large shear strain in one pass (orders of magnitude larger than in ECAP [27], TE [199] and CEC [87]) under high pressure.

2.4.3. Pipe sample processing

Pipes and tubes are of significance in industrial applications, but as shown in Table 1, quite limited SPD methods are available for the processing of pipes. There have been some attempts in recent years for SPD processing of pipes and tube high-pressure shearing (t-HPS) is one
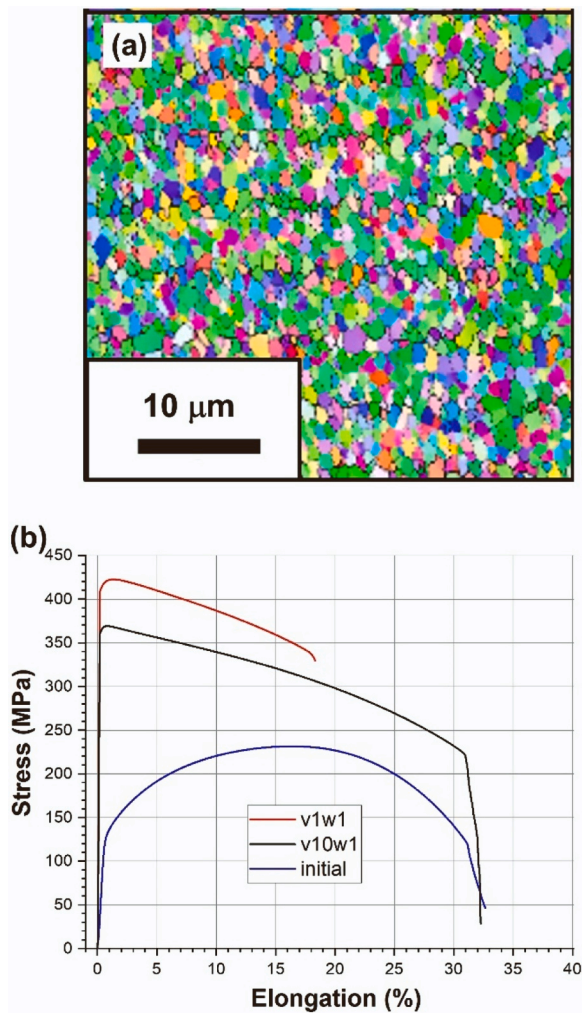
Fig. 7. (a) Inverse pole figure map of the copper microstructure in the longitudinal cross-section of the billet after HPTE at 373 K with a translational velocity of $v = 1$ mm/min and a rotational velocity of $\omega = 1$ rpm [190]. (b) Tensile curves of copper samples in the initial coarse-grained state (initial) and after HPTE at 373 K with a rotational velocity of $\omega = 1$ rpm and translational velocities of $v = 1$ mm/min ($v1\omega1$) and $v = 10$ mm/min ($v10\omega1$) [185].

Fig. 8. Illustration of t-HPS schemes: (a) compression directly applied on two ends of tube by pressure ring in scheme E1 [54,206], (b) compression directly applied on two ends of tube by stepped mandrel together with stepped cylinder in scheme E2 [200,207], (c) a small tapper angle is introduced to tube and die parts so that compression can be directly applied to the tube wall in scheme W [207,208] and (d) compression directly applied to both ends and wall of tube by stepped mandrel together with stepped cylinder in scheme EW [207,208].

successful friction-driven process for such an application [54,159]. The t-HPS is different from other friction-driven processes such as HPT [23], where the strain planarity of simple shear is violated [159,200], and high-pressure sliding (HPS), where the achievable strain level is limited by the plunger stroke [57]. Therefore, t-HPS provides a monotonic deformation process characterized by constant shear direction and strain planarity to high strain levels over 2000 [201]. The development of this SPD technique may be classified into three sectors with different names as rotation shear [202], high-pressure tube twisting [203,204] and t-HPS [54], where they include the same core concept of friction-driven azimuthal shear in the tube and independently developed by three different scientific groups. Continuous processing of t-HPS was also investigated [205]. The principle of t-HPS is depicted schematically in Fig. 8 [54,159,200,206,207]: (i) a tube sample is radially constrained between a central mandrel and an outer cylinder; (ii) a sufficiently high hydrostatic pressure is introduced in the tube wall by the four schemes illustrated in Fig. 8, so that frictional forces at the interfaces between the sample-mandrel and the sample-cylinder are sufficiently high to prevent any localized slip between the interfaces; and (iii) a simple shear strain is then produced in the tube wall by fixing the mandrel and rotating the outer cylinder (or vice versa) [54,202,203]. Although t-HPS is different from HPT by the planarity of shear

deformation [159,200], it has a strain gradient along the radius of the sample, but it is the reverse of HPT [54,200,208,209].

The microstructure evolution upon t-HPS is distinguished between geometrical parameters, such as grain size and aspect ratio versus crystallographic parameters, such as grain boundary misorientation, high-angle grain boundary fractions and texture. The evolution of geometrical parameters is observed to be consistent with those observed in general SPD processes [159,210]. Fig. 9a presents an example of pure aluminum processed by different SPD methods compared to t-HPS [211–220]. Grain size and aspect ratio demonstrate a clear trend of stagnation at a t-HPS equivalent strain of ~30 [220]. This is consistent with the saturation features of many metals during HPT at equivalent strains between 10 and 30 [38]. This general trend was also demonstrated by Shan and Tóth using different materials like commercially pure aluminum [202,204,221], AA5056 alloy, interstitial-free (IF) steel, copper and magnesium [204,210]. Accompanying this stagnation in the geometrical parameters, the crystallographic parameters evolve continuously in contrast. Fig. 9b shows that the average grain boundary misorientation and high-angle grain boundary fractions increase first at low strain levels, passing through a peak at around the equivalent strain of ~9, and decrease thereafter monotonically. The intensity of the texture sharply decreases at low strain levels, passing through a minimum at an equivalent strain of ~20, and increases monotonically thereafter, where a new texture component gradually dominates [220].

The t-HPS method has some advantages. For example, tubes with multilayered structures composed of unitary pieces of metals can be fabricated in one step of t-HPS [200]. A detailed comparison between ARB and t-HPS in multilayered laminate synthesis is given in [200]. Moreover, t-HPS provides a new channel to bypass the phase separation in solidification and to synthesize homogeneous alloys directly from monolithic bulk elements, which provides more freedom in the design and synthesis of alloys with enhanced properties. For example, exceptional superplasticity as shown in Fig. 9c is achieved in a Pb-40Sn (wt%) alloy with off-eutectic composition, synthesized from lead and tin bulks in one step of the t-HPS step [201]. The reason for large superplasticity by t-HPS is bypassing the inherent pre-eutectic Pb-rich phase separation during solidification [222]. A similar effect is also observed in other systems [223,224].
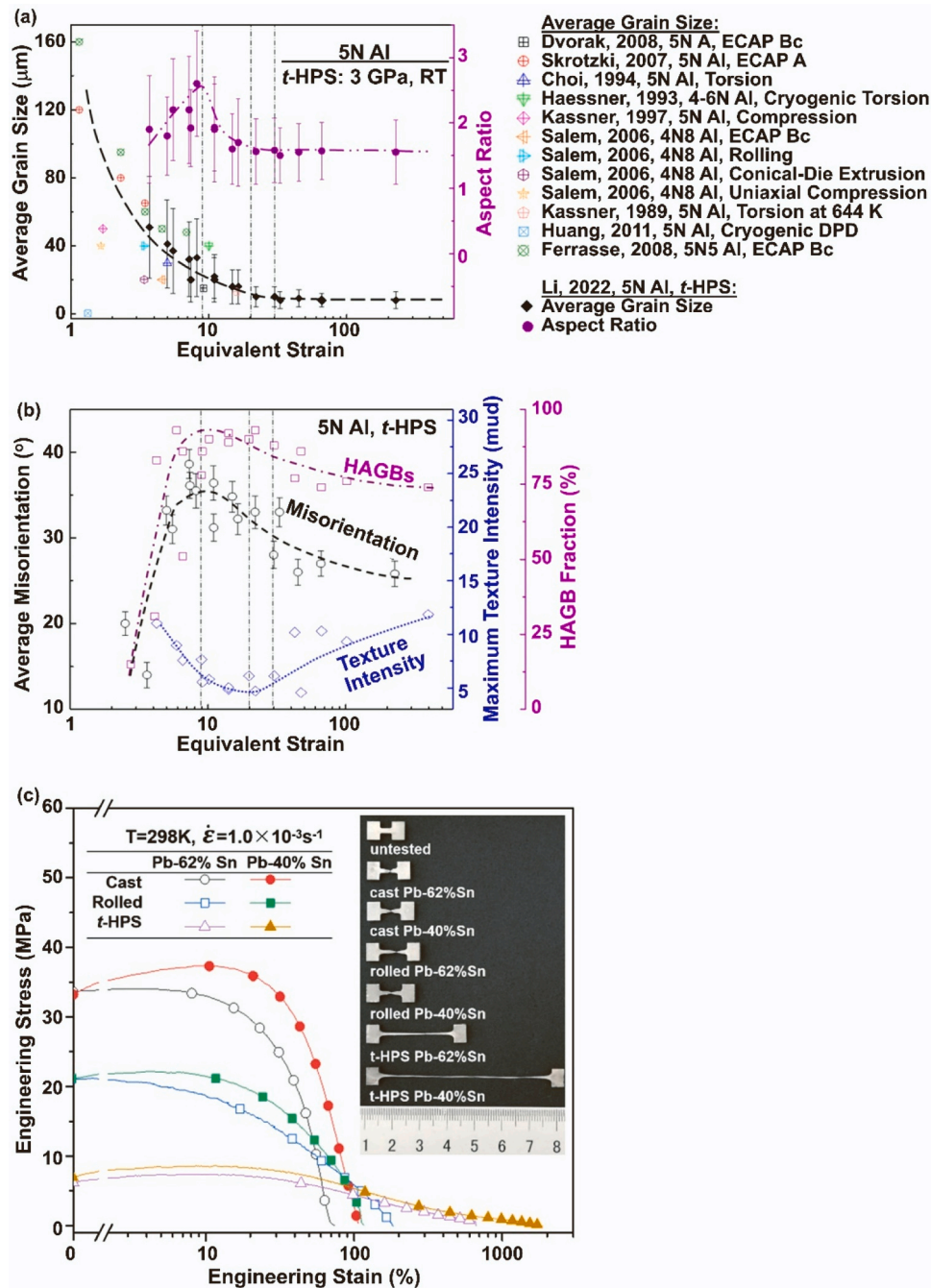
Fig. 9. (a) Evolution of average grain sizes and grain aspect ratios upon increase of t-HPS equivalent strain (grain size obtained from other deformation processing of aluminium with 99.999% purity are also included for comparison) [220]. (b) Evolution of average grain boundary misorientation, high-angle grain boundary fractions and intensity of {$\bar{1}10$}<110> texture upon increase of t-HPS equivalent strain [220]. (c) Engineering stress-strain curves for the Pb-Sn alloys tested at the initial strain rate of 1.0×10^{-3} s^{-1} at room temperature (inset: appearance of the specimens after pulling to failure) [201].

In summary, although there are limited SPD methods for processing pipes, the newly developed ones such as t-HPS exhibit high potential for various applications such as the generation of UFG structure, fabrication of multilayered laminates from monolithic materials, and synthesizing bulk micro-duplex alloys. The high planarity character of SPD methods for processing tubes makes it possible to produce a sole component shear texture, which challenges the long-standing position of a torsion-based method as a typical simple shear method and this may further bring about new challenges to the existing theory of texture evolution for simple shear [225].

2.4.4. Upscaled sheet processing

Despite significant progress in the development of SPD techniques [1–3,32], limited techniques can apply SPD in sheet samples in a continuous process. Among popular methods such as ECAP [193,226], ARB [19,227,228], MDF [229,230] and HPT [20,23], only ARB can process large sheets continuously [154]. There have been various attempts for continuous SPD processing or processing sheets [156, 231–235], but SPD processing of large sheets is still challenging. One of the recent attempts to process large sheets is the application of HPS [57]. The HPS process is similar to HPT because both processes are operated under high pressure, and they are applicable to hard-to-deform and/or less ductile metallic materials due to highly constrained conditions. The
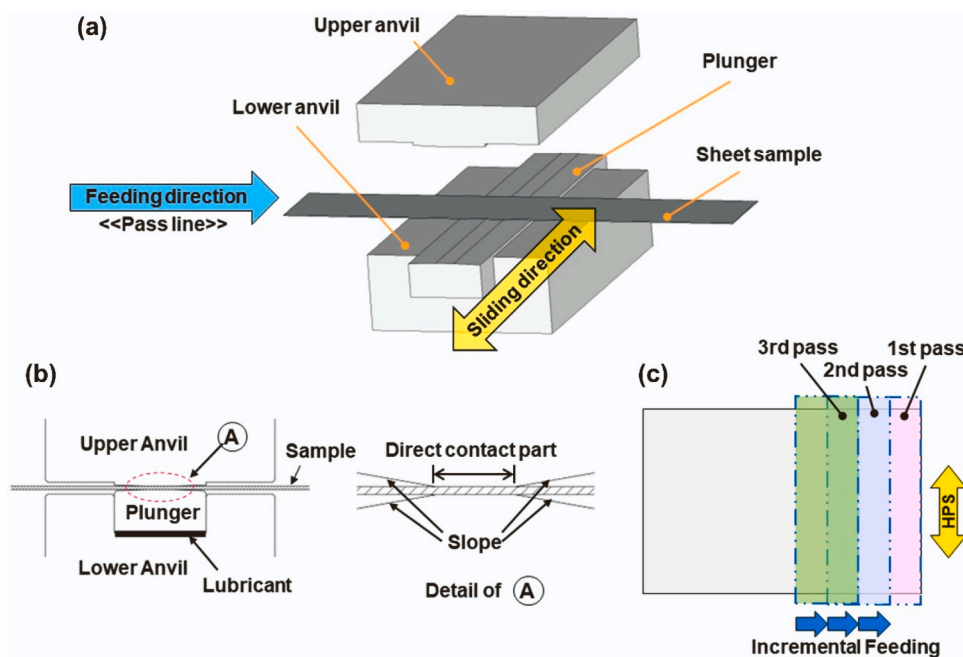
Fig. 10. (a) Schematic illustration, (b) cross-sectional view and (c) incremental feeding pattern for consecutive 1st, 2nd and 3rd passes of incremental-feeding HPS [160].

major difference between the two processes is that, while the HPT process is used with disc or ring forms of the samples [30,56,177,236, 237], the HPS process utilizes the samples in rectangular sheet forms and sometimes in rod or pipe forms [238,239]. The HPS process has more advantages in upscaling the sample size [179].

A typical example of the upscaling of sheet samples by HPS is the development of incremental feeding HPS (IF-HPS) process as illustrated in Fig. 10a. [160,240]. The incremental feeding, which has been combined with HPT in some studies as well [51,58,60,241], has a high potential for upscaling the sample size without any need to increase the machine capacity. Fig. 10b shows a detailed cross-sectional view including a sheet sample between a plunger and anvils, and Fig. 10c illustrates a strained area that is extended to a larger scale by repeating the operation of sliding and successive feeding. The feeding pattern can be made in one- or two-dimensional directions. Until now, IF-HPS has been successful in enlarging the SPD-processed area to 100×100 mm^2 in a Ni-based superalloy (Inconel 718) [160,240]. It should be noted that it is possible to increase the sizes of rods and pipes by adopting a multi-pass HPS [238,239]. In developing the IF-HPS process, the following three points are important as recently described in detail [160, 242]: (i) the use of flat-type anvils to make sample feeding easier and sheet surface smoother, (ii) the control of the sliding mode determined by the sliding distance and the numbers of the reciprocation of the sliding direction and (iii) the control of the feeding pattern determined by the feeding distance and the feeding direction. The performance of the IF-HPS process was demonstrated with the application to a Ni-based superalloy (Inconel 718) [240], a Ti-6Al-7 Nb (wt%) alloy [243] and commercially available aluminum alloys (A1050, A3105, A5052 and A5182) [242].

As an example of the properties of sheets processed by IF-HPS, Fig. 11 shows the stress-strain curves of the Inconel 718 after HPS processing for a single pass under 4 GPa using (a) flat-type anvils and (b) groove-type anvils. The total elongations reached 220% and 710% for the sliding distances of 10 and 15 mm using the flat-type anvils [240], while they exhibited 770 and 670% using the groove-type anvils for the corresponding sliding distances [244]. The difference is significant when the sliding distance is 10 mm but no difference was observed when the sliding distance is longer than 15 mm [160]. The superplastic
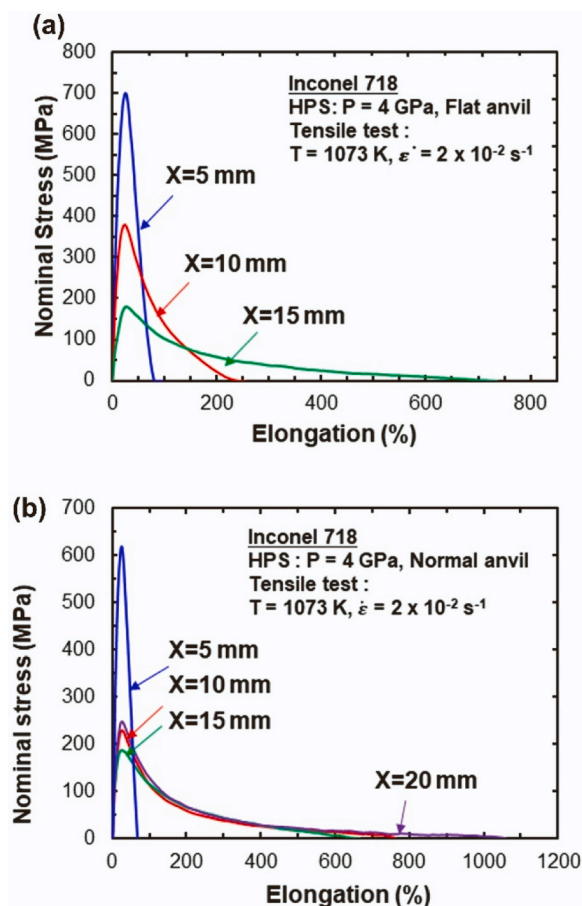
Fig. 11. Stress-strain curves of tensile specimens extracted from samples processed using (a) flat-type and (b) groove-type anvils of incremental-feeding HPS for sliding distances of 5, 10 and 15 mm (tensile tests were performed at 1073 K with an initial strain rate of 2×10^{-2} s^{-1} [160].

behavior of these sheets confirms that SPD could be successfully imparted in them by using IF-HPS.

In conclusion, sheet processing is a key issue in the commercialization of the SPD process. While ARB is still the most practical process for the continuous processing of large sheets, methods like IF-HPS can be used to process large sheets of hard materials under high pressure.

2.4.5. Hard cyclic viscoplastic deformation

Despite the potential of SPD in reducing the grain size [3,22,245, 246] and increasing tensile strength and hardness [247–250], the thermal stability of such materials is relatively low depending on their microstructural evolutions [5,251,252]. To have a better balance between the microstructure, mechanical properties and thermal stability, the evolution of these features should be examined step by step during or after SPD processing [253–255]. To study the microstructure and properties evolution of metallic materials before and after SPD, a processing method, called hard cyclic viscoplastic deformation (HCVD), was developed based on viscoplasticity theory [256–260], cyclic ratcheting [261] and Bauschinger effect [262, 263].

The main parameters of HCVD are a strain-controlled deformation process with an amplitude of tension-compression in the range from $\pm 0.2\%$ to $\pm 3.0\%$ with several cycles from 20 to 30 per strain level and a frequency of 0.5–2.5 Hz of cycles [161, 263–269]. The tension-compression cycle is applied at constant strain amplitude, by a strain-controlled system at room temperature (Fig. 12). The load or stress amplitude, which depends on the mechanical properties of the metallic material, is introduced in the viscoplastic region. During HCVD,

the viscoplastic region parameters affect the microstructure and mechanical, physical and chemical properties of the materials. HCVD can be used to study the stability and viability of metallic materials with different microstructures and grain sizes and to predict their suitability over time in harsh environments such as aerospace and defense applications where the strain amplitude is greater than $\pm 0.2\%$ of the strain [268]. It was shown that the microstructure and properties of the material obtained before or after SPD processes alter in HCVD testing. For example, the initial strength properties of a coarse-grained material increase, but the strength properties of a UFG material may decrease. Also, other features of materials such as electrical conductivity, dislocation density, *etc.*, change during HCVD processing [269, 270]. Changes in physical properties (Figs. 13a and 13b) before material failure were reported during HCVD [267].

In summary, the HCVD method can provide information about the behavior of materials, including SPD-processed materials in various extreme operating conditions such as aerospace and defense applications, when the margin coefficient is very small and the deformation can be increased to 0.2% and higher. Such information provided by HCVD can expand the application of SPD in the industry by clarifying the relationships between microstructure, mechanics, physics and chemistry with processing parameters.

2.4.6. Cryogenic-SPD

An effective way to obtain high-strength UFG materials is by conducting SPD at cryogenic temperature in liquid nitrogen [5, 271–273]. UFG metals and alloys obtained by cryogenic-SPD exhibit exceptional
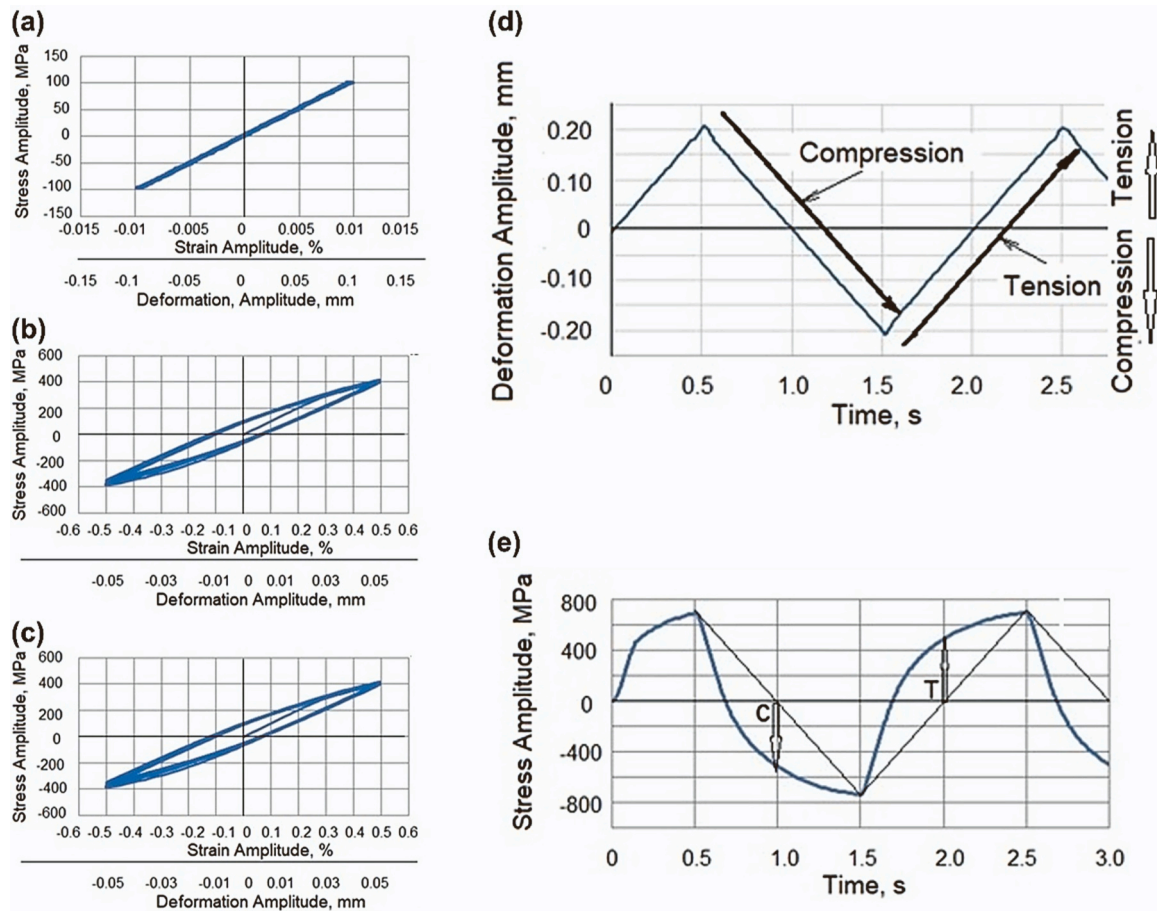
Fig. 12. (a-c) HCVD stress amplitude versus strain amplitude curves of niobium for viscoplastic tension-compression straining at (a) an amplitude of $\varepsilon = \pm 0.1\%$ and corresponding deformation amplitude of $v = \pm 0.01$ mm in the base length of 10 mm in elastic regime, (b) $\varepsilon = \pm 0.5\%$ and $v = \pm 0.05$ mm and (c) $\varepsilon = \pm 2.0\%$ and $v = \pm 0.2$ mm. (d) HCVD stress amplitude versus time curves at $\varepsilon = \pm 2\%$. (e) Effect of elastic-plasticity on the deflection of the curves during the compression (C) and tension (T) cycles [161].
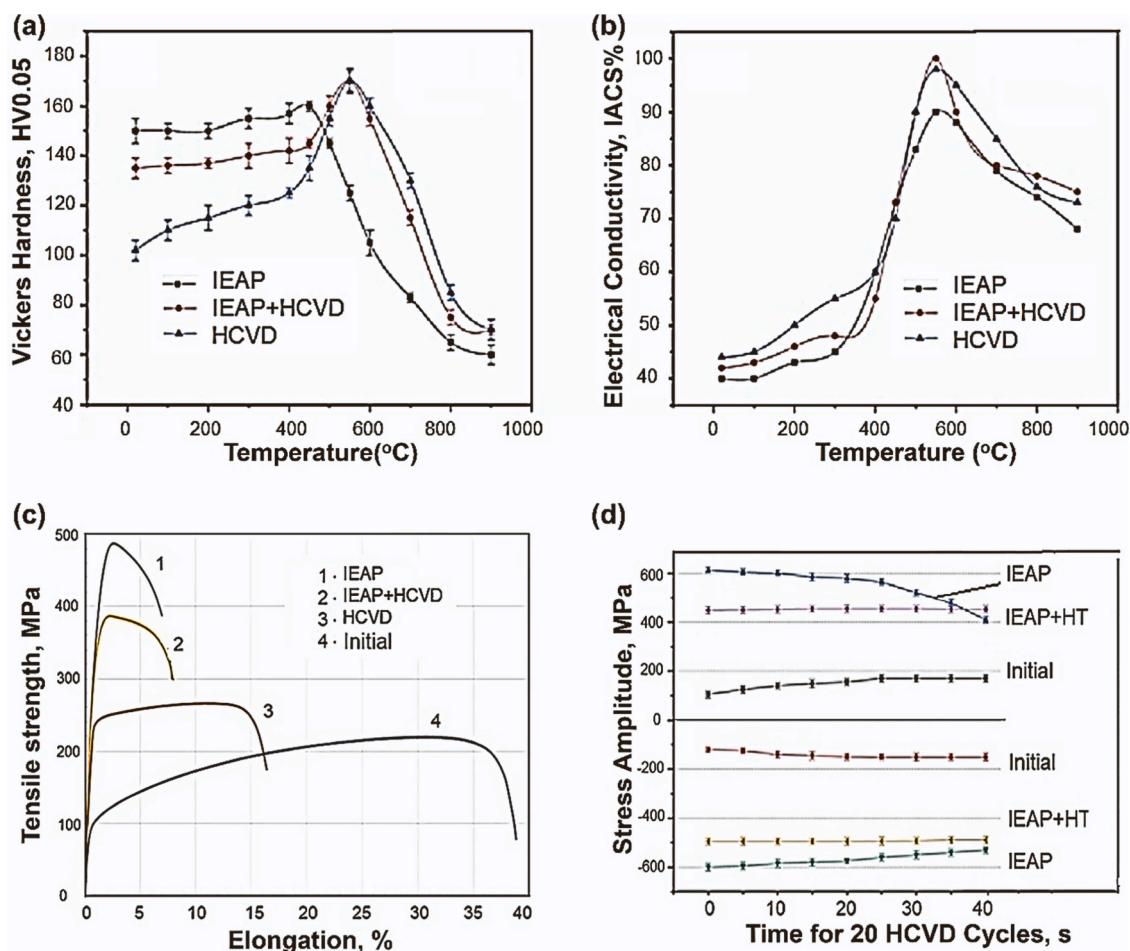
Fig. 13. (a) Variation of Vickers hardness versus aging temperature and (b) electrical conductivity versus aging temperature, (c) tensile strength versus elongation and (d) experimental values of stress amplitudes obtained during HCVD testing for 20 cycles at a frequency of 0.5 Hz and a strain amplitude of $\pm 1\%$ for Cu-0.66Cr-0.03Si-0.02Fe-0.016S (wt%) alloy processed under different conditions (initial coarse-grained sample, SPD by indirect extrusion angular pressing IEAP and SPD followed by heat treatment at 723 K IEAP+HT) [267].

mechanical properties in a wide temperature range, especially at cryogenic temperatures, due to the activation of additional deformation mechanisms, such as twinning and phase transitions [274–276]. The coexistence of several deformation paths affects the evolution of the microstructure and deformation mechanisms during cryogenic-SPD. This section reviews the influence of various methods of cryogenic-SPD (ECAP [193], quasi-hydroextrusion [277], HPT [22]) on the mechanical properties of some metals (titanium, zirconium, cobalt), titanium grade 2 alloy and high-entropy alloys (HEAs). The influence of cryo-rolling on the mechanical properties of titanium is also briefly mentioned [278–282]. A more complete review of the results on this topic was given elsewhere [162].

Cryogenic-SPD has received attention, particularly in recent years [283–289]. Such studies were partly motivated by the effectiveness of cryo-rolling in controlling microstructure [278–282]. Cryo-rolling studies on commercially pure titanium grade 2 showed that the material after cryo-rolling demonstrates a higher rate of hardening (due to the rapid growth of twins and a slower dynamic recovery process) than after rolling at room temperature. Titanium exhibits an increase in strength and a finer nanostructure with an average grain size of 30–80 nm (compared to 200 nm after rolling at room temperature). Commercially pure titanium grade 2 was also processed by cryo-ECAP, which led to a decrease in the average grain size and an increase in strength (by about 10%) compared to ECAP at room temperature [283]. The effect of HPT on the structure and mechanical properties of high-purity titanium was also investigated in [284]. The hardness and

strength of nanostructured titanium treated with cryo-HPT is 10–14% higher compared to room-temperature processing due to the smaller average grain size (100 nm instead of 160 nm). A combination of different SPD methods (ECAP and quasi-hydroextrusion) at cryogenic temperature was also applied to commercially pure titanium in a study [285]. A significant increase in the yield strength by a factor of two (from 0.42 GPa at 300 K to 0.86 GPa at 77 K) was achieved using simple shear via ECAP and axisymmetric deformation via quasi-hydroextrusion at 77 K. These results showed that additional modes of plastic deformation with a different set of working sliding systems significantly affect the microstructure and mechanical properties of titanium.

It was reported that extra strengthening by cryogenic-SPD is not limited to titanium and similar results were reported for other metals such as zirconium and cobalt [286, 287]. After HPT at 77 K and 300 K, the average grain sizes are 80 nm and 200 nm for zirconium and 70 nm and 100 nm for cobalt, respectively. The values of microhardness, yield strength and strength under deformation by uniaxial compression after cryo-HPT (at temperatures of 77 K and 4.2 K) are approximately 10% higher than those after HPT at room temperature. These effects are due to the slowdown in the processes of dynamic recovery during cryo-HPT and an increase in the contribution of the twinning process to grain refinement. The effect of cryo-HPT on the structure and strength properties of HEAs was studied as well[288–291]. After cryo-HPT, both hardening and softening processes are observed in HEAs. In some HEAs (CoCrFeNiMn, CoCrFeNiMnV$_{0.2}$, Co$_{20}$Cr$_{26}$Fe$_{20}$Mn$_{20}$Ni$_{14}$), cryo-HPT results in lower yield strength and microhardness than those after HPT at
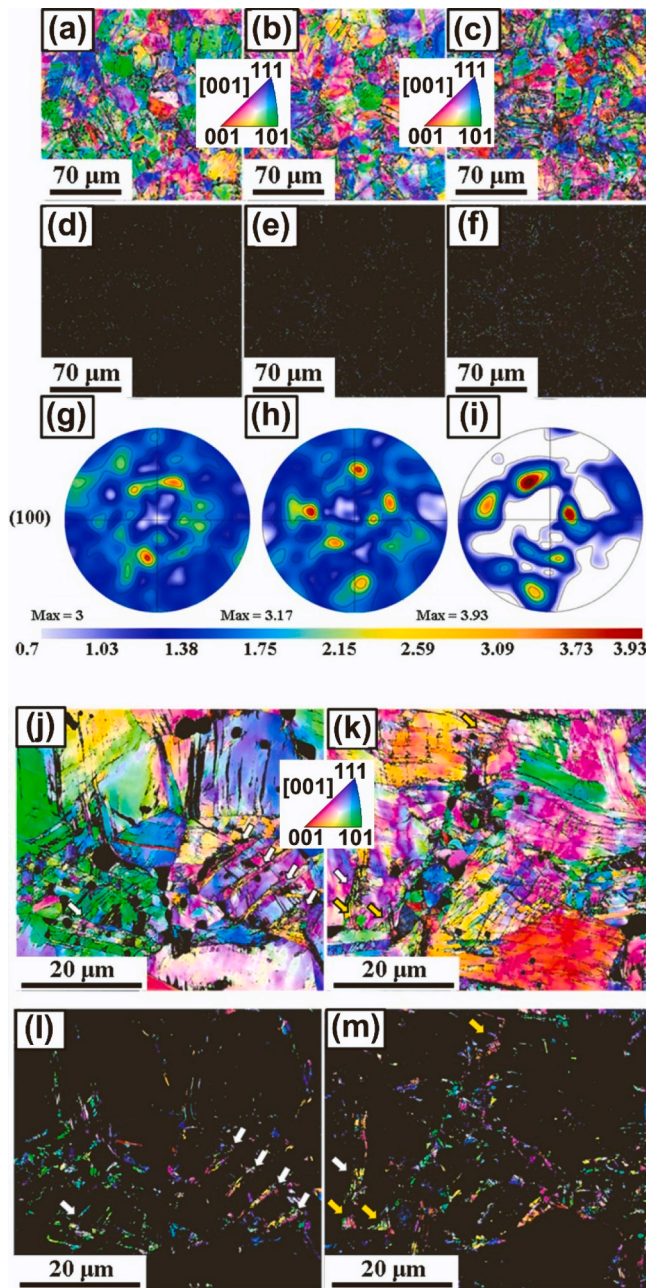
Fig. 14. Inverse pole figure images and (100) pole figures for Co$_{20}$Cr$_{26}$Fe$_{20}$Mn$_{20}$Ni$_{14}$ alloy after cryogenic-SPD via HPT for (a,d,g) 1 rotation, (b,e,h) 3 rotations and (c,f,k) 5 rotations, (d–f) show the grains with sizes smaller than 1 μm (maximum texture intensity is indicated for each pole figure in mrd). (j-m) Inverse pole figure images of Co$_{20}$Cr$_{26}$Fe$_{20}$Mn$_{20}$Ni$_{14}$ alloy after cryogenic-SPD via HPT for (j,l) 1 rotation and (k,m) 5 rotations, where (l,m) show the grains with sizes smaller than 1 μm [288].

room temperature. The reasons for such softening may be related to phase transformations (FCC-HCP) and a decrease in the dislocation density [292–295]. Such transformations during and after cryo-HPT are shown in Figs. 14 and 15 [288]. It should be noted that in nano-structured CoCrFeMnNi [274] obtained at certain values of pressure and number of revolutions, subsequent holding at room temperature leads to reverse structural transformations. Despite reported results on HEAs, cryogenic-SPD can generally be considered an effective method for producing high-strength materials that can be used as materials for structural and functional purposes.
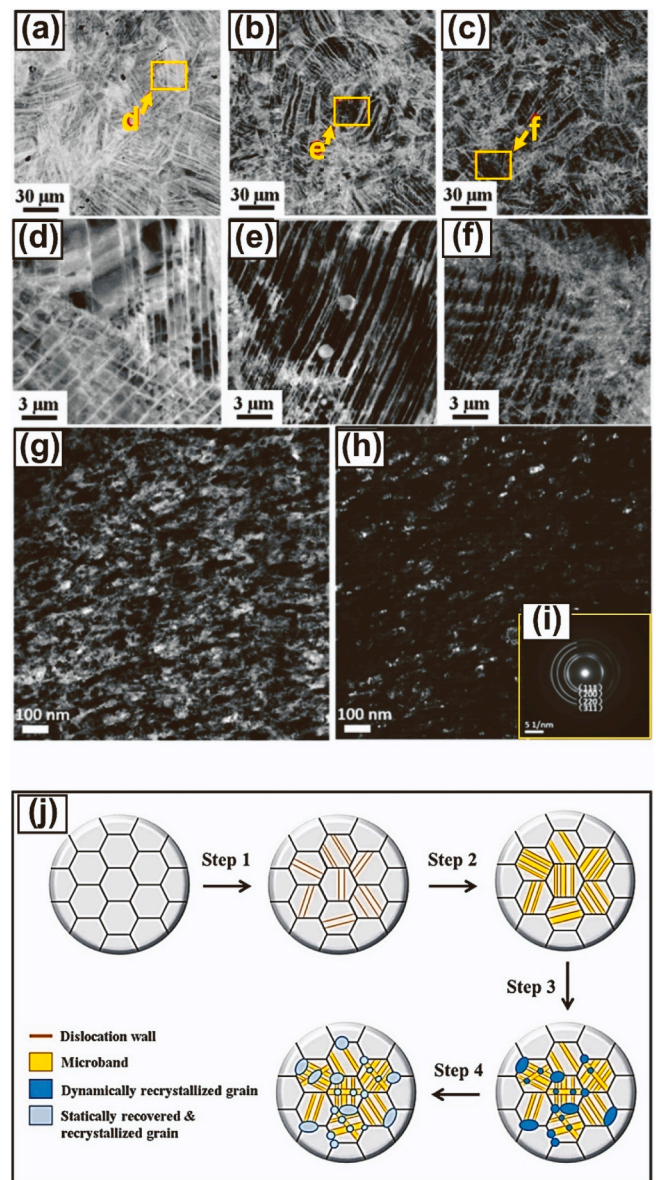
Fig. 15. (a-f) SEM backscatter electron images of Co$_{20}$Cr$_{26}$Fe$_{20}$Mn$_{20}$Ni$_{14}$ alloy after cryogenic-SPD via HPT for (a,d) 1 rotation, (b,e) 3 rotations and (c,f) 5 rotations where (d-f) are the magnified images of the corresponding areas highlighted in (a-c). (g-i) TEM images of the Co$_{20}$Cr$_{26}$Fe$_{20}$Mn$_{20}$Ni$_{14}$ alloy after 5 rotations of HPT at 300 K, where (g) is a bright-field image, (h) is a dark-field image and (i) is the corresponding selected area electron diffraction pattern. (j) Schematics illustrating the microstructural evolution of Co$_{20}$Cr$_{26}$Fe$_{20}$Mn$_{20}$Ni$_{14}$ alloy which accommodates stored strain energy during and after cryo-HPT [288].
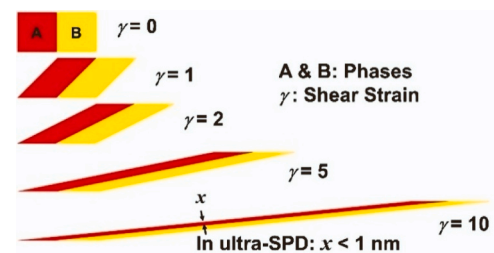
Fig. 16. Schematic illustration of ultra-SPD concept, in which severe shear strains are applied to a material so that the thickness of sheared phases is reduced to the subnanometer level [298].

2.4.7. Ultra-SPD

The ultra-SPD concept was defined in 2017 in an attempt to discover new materials by mechanical alloying via SPD [296]. As schematically illustrated in Fig. 16, ultra-SPD is defined as SPD processes in which the applied shear strain significantly increases so that the thicknesses of phases are reduced to the subnanometer level [296]. The shear strain required to achieve these changes depends on the initial phase dimensions and co-deformation behavior of various phases, but it was suggested that the applied shear strain should be over 1000 in ultra-SPD [178]. Besides the original target of ultra-SPD was the synthesis of new materials, it has also raised questions concerning the deformation behavior of materials at the steady state [38, 45]. It was shown that some deviations from the steady-state hardness occur in a few pure metals after ultra-SPD [178]. These observations suggested that there can be new deformation stages beyond stage V of deformation at extremely large shear strains [297].

Among various bulk-SPD methods [1–3, 37, 299], HPT, which applies to disc [3, 177] or ring [56, 300] samples, is currently the only method used to apply ultra-SPD. There are a few reasons that HPT appears as the best candidate for this application. (i) Shear strain can be continuously enhanced in HPT by increasing the number of rotations of anvils with almost no limitations, a fact that was first recognized by Bridgman [20]. (ii) High pressure in HPT makes it applicable to metals with high hardness such as hafnium [301], molybdenum [302] and tungsten [303] and their powder mixtures for mechanical alloying. (iii) The method is one of the most effective methods to introduce lattice defects [304–306] for enhancing dynamic interdiffusion [307, 308] and controlling solid-state phase transformations [9, 10].

The concept of ultra-SPD has been successfully used to synthesize various materials such as binary alloys [309–312], ternary alloys [313–315], HEAs [316, 317], intermetallics [318–321], hydrides [322], oxides [323–325] and oxynitrides [326, 327]. The materials synthesized by this method exhibit interesting properties such as ultrahigh strength, stability at high temperatures, enhanced superplasticity at room temperature, storage of hydrogen at low temperature, compatibility with biological environments, superconductivity and photocatalytic activity for hydrogen and oxygen production and CO_2 conversion, as reviewed in a few papers [164, 298]. Some of the features of materials processed by ultra-SPD are briefly reviewed below.

- Materials processed by SPD usually exhibit poor thermal stability because of large stored energy [328–331], but ultra-SPD can contribute to thermal stability by the generation of supersaturated solid solution and second-phase precipitation. Ultra-SPD-developed supersaturated alloys of aluminum with calcium [311], iron [310], zirconium [332] and lanthanum and cerium [315] exhibit not only high thermal stability but also strengthening through precipitation hardening.
- A combination of high strain and high pressure and their interaction with lattice defects can lead to the formation of hidden phases [8]. In this regard, ultra-SPD could stabilize large fractions of phases that are not formed in equilibrium phase diagrams. The formation of body-centered cubic (BCC) and face-centered cubic (FCC) phases in magnesium alloyed with titanium [333], zirconium [334] and hafnium [335] are the most highlighted examples because these elements are immiscible in magnesium even in the liquid form.
- Nanograined intermetallics are usually produced by two-step processes such as the production of nanopowders followed by high-temperature sintering [43, 336–338]. On the contrary, ultra-SPD synthesizes bulk nanograined intermetallics in a single step. Mg_2X (X: various elements) [339], AlNi [318], Al_3Ni [319, 320] TiAl [321], FeNi [340] and Ni_2AlTi [341] are some intermetallics synthesized by ultra-SPD from elemental powders.
- Materials for orthopedy should have a combination of low elastic modulus, high hardness and good biocompatibility [342]. SPD-processed biomaterials, which are usually based on titanium,

show high hardness and good biocompatibility but suffer from high elastic modulus [36, 343–345]. In a few attempts to produce biomaterials with high hardness and low elastic modulus, ultra-SPD was employed to synthesize various alloys in the Ti-Zr-Hf-Nb-Ta alloy system [312, 317].
- Superplasticity can be usually achieved at homologous temperatures over 0.5, where grain boundary sliding is dominant [346]. Due to the activation of grain boundary sliding at high homologous temperatures, the achievement of room-temperature superplasticity is not possible in conventional magnesium and aluminum alloys. To reduce the superplastic deformation temperature, two strategies can be used [347]: (i) grain refinement which was employed to attain low-temperature superplasticity by conventional SPD processing [33, 348, 349]; and (ii) enhancement of grain boundary diffusion by the engineering of grain boundaries. The second strategy was realized by ultra-SPD in Mg-Li and Al-Zn alloys to attain room-temperature superplasticity for the first time in magnesium and aluminum alloys [350, 351].
- Nb-Ti alloys are the most used superconductors which are industrially produced by several repetitions of wire drawing and long-time annealing [352–355]. Ultra-SPD provides a single-step process to produce Nb-Ti superconductors with properties similar to industrial products [356].
- The production of magnesium alloys for storing hydrogen at room temperature has been a long-time objective of many research works, but there has been little success in this regard [357, 358]. Ultra-SPD was used for the synthesis of some Mg-based hydrogen storage materials like Mg_2X (X: various elements) [339], Mg-Ti [322, 333],

Table 4

Summary of the application of ultra-SPD to various materials [164].

Alloy	Shear Strain	Characteristics	Ref.
Mg–Li	7800	Superplasticity at room temperature	[351]
Mg_2X (X: 21 elements)	5500	Storing hydrogen	[339]
Mg–Ti	5500	Storing hydrogen	[333]
Mg–Zr	55000	Storing hydrogen in new phases	[334]
Mg–Hf	3900	Biocompatible new phases	[335]
Mg–V–Cr	50000	Storing hydrogen	[313]
Mg_4NiPd	59000	Storing hydrogen at room temperature	[359]
MgTiVCrFe	12000	Storing hydrogen	[314]
$MgTiH_4$	17000	Storing hydrogen	[322]
Al–Ca	39000	Thermal stability	[311]
Al–Fe	39000	Thermal stability	[310]
AlNi	4700	Enhanced microhardness	[318]
Al_3Ni	4700	Enhanced microhardness	[319, 320]
Al–Cu	3900	Quick interdiffusion	[308]
Al–Zn	7800	Superplasticity at room temperature	[351]
Al–Zr	39000	Thermal stability and age hardening	[332]
Al–La–Ce	39000	Thermal stability and age hardening	[315]
TiAl	2000	Enhanced strength/plasticity	[321]
TiV	5500	Storing hydrogen with no activation treatment	[309]
Ti–Nb	5900	Biocompatibility with good strength/elasticity	[312]
TiZrHfNbTa	2000	Biocompatibility with good strength/elasticity	[317]
$TiZHfNbTaO_{11}$	7800	Photocatalytic H_2 evolution and CO_2 conversion	[323, 324]
$TiZrHfNbTaO_6N_3$	3900	Photocatalytic H_2 evolution and CO_2 conversion	[326, 327]
$TiZrNbTaWO_{12}$	3900	Photocatalytic O_2 evolution	[325]
FeNi	3900	Quick phase transition	[340]
Ni_2AlTi	4700	Enhanced microhardness	[341]
Nb–Ti	3900	Superconductivity	[356]

Mg-Zr [334], Mg-V-Cr [313] and Mg-V-Ti-Cr-Fe [314], but the most interesting results were reported for Mg-Ni-Pd which could reversibly store hydrogen at room temperature [359].

- Photocatalysis is a clean technology to produce hydrogen and oxygen from water or convert CO_2 to CO under sunlight [360, 361]. Ultra-SPD contributed to this field by the introduction of the first high-entropy photocatalysts such as $TiZrHfNbTaO_{11}$ [323, 324], $TiZrNbTaWO_{12}$ [325] and $TiZrHfNbTaO_6N_3$ [326, 327].

Table 4 summarizes major studies on the application of ultra-SPD, including the compositions of processed materials, applied shear strain and reported characteristics. All these results suggest the high potential of ultra-SPD in exploring new functional materials.

3. Microstructural features after SPD

SPD induces large plastic deformation in a piece of sample, and thus, significant microstructural changes are introduced. Since such plastic deformations are introduced at temperatures below the traditional recrystallization temperature and under high pressure, the introduced microstructural features are usually unique and can hardly be introduced by other methods [2, 3]. Continuous refinement of grains and the introduction of various defects during SPD increases the internal energy of the material, leading to the reduction of the temperature for continuous dynamic recrystallization to room temperature [362]. This issue finally leads to the saturation of microstructural evolution, the formation of UFG grains with nanometer or submicrometer sizes, the appearance of high-angle grain boundaries and the weakening or randomization of texture [3, 363]. The saturation of grain refinement to the steady state and parameters influencing the steady-state grain size have been a matter of study for a long time [189, 297, 364, 365]. Impurity atoms, alloying, the addition of a second phase, and reduction of homologous temperature (i.e. reducing the processing temperature or increasing the melting point) are well-known factors that reduce the steady-state grain size [189, 297, 364, 365]. It is well established that in materials with covalent or ionic bondings such as ceramics, the steady state grain size can be lower than in metallic materials due to difficult dislocation slip and grain boundary motion in these materials [365]. There have been some suggestions that the materials with low stacking fault energy can have smaller grain sizes [364], while some studies showed that the steady-state grain size is reasonably independent of stacking fault energy [365]. Moreover, steady-state grain size is independent of pressure if no phase transformation occurs [366]. Besides grain refinement, SPD introduces large fractions of lattice defects such as vacancies [306] and dislocations [305]. Grain boundaries formed by SPD have special features usually not in equilibrium conditions [307] and can sometimes be decorated by segregation or dynamic precipitation [304]. In the following sections, after a discussion of features of high-angle grain boundaries, recent advances in the investigation of the microstructure of SPD-processed materials are reviewed.

3.1. Grain boundaries and related phenomena

SPD drives bulk materials far away from equilibrium and opens up new opportunities to explore hitherto uncharted regions of structure-property correlations with respect to grain size, strain and defect density under extreme conditions [5]. The SPD processing involves the interaction of defects of different dimensionality during deformation and their interrelation with fluxes of solute atoms or with segregation fields under complex elastic strain fields, resulting in chemo-mechanical coupling effects especially accompanying nucleation and precipitation of secondary phases [367]. All of these aspects that result from the complex interactions of defects and solutes strongly affect phase equilibria and phase- and microstructure evolution and stability. Naturally, material properties, such as diffusion rates or the plastic response of SPD-processed materials are controlled by the SPD-induced

microstructure, giving rise to new opportunities for "defect engineering" [368]. For such defect engineering, fundamental aspects of the processing-microstructure-property correlations under these boundary conditions have to be addressed. While most SPD-related work has focused on crystalline materials and microstructures [299, 369], amorphization transformations [370, 371] and deformation-induced structure modifications of bulk metallic glasses [372] present new aspects and additional opportunities that expand the spectrum of SPD-engineered materials with superfunctional properties [180].

A prominent aspect of specific and characteristic microstructural features that are induced by SPD processing of crystalline materials is the appearance of so-called "non-equilibrium" or "deformation-modified" grain boundaries as one of the prominent characteristics of SPD processing [307, 373]. The non-equilibrium grain boundaries in SPD-processed materials were suggested to be characterized by increased elastic strains, enhanced diffusivities and elevated grain boundary energies [374–376]. An in-depth analysis of local strains using geometrical phase analysis from TEM images with atomic resolution [377, 378] revealed an accumulation of defects at the grain boundaries
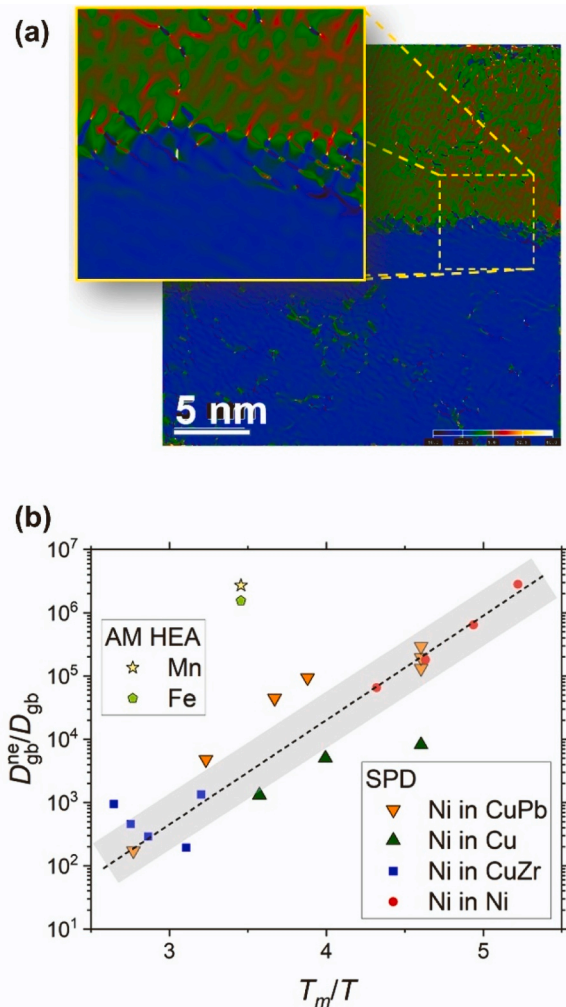
Fig. 17. (a) Strain map showing the in-plane rigid-body rotation ω_{xy} for HPT-processed PdAg alloy [377]. (b) Relative enhancement of diffusion rate for non-equilibrium grain boundaries with respect to diffusion along relaxed general high-angle grain boundaries as they are present in the polycrystalline counterparts for SPD-processed nickel [380], copper [381], Cu-0.17Zr (wt%) [382] and Cu-1Pb (wt%) [383] where inverse homologous temperature scale, T_m/T, is used for proper comparison. The relative enhancements measured for manganese and iron in additively manufactured CoCrFeNiMn HEA are shown in (b) for comparison [384].

with atomic-scale arrangements [379] and the resulting significant accumulation of strains at such grain boundaries (Fig. 17a). Radiotracer measurements of diffusion rates along such interfaces in SPD-processed metals and alloys confirmed a non-equilibrium state of high-angle grain boundaries in terms of severely enhanced diffusion rates (Fig. 17b), orders of magnitude above those typical of polycrystalline counterparts [379–383].

However, recent results clearly demonstrated that the existence of such a non-equilibrium state of grain boundaries is not limited to SPD-processed materials. In fact, similar grain boundary states have recently been discovered in additively manufactured alloys [384–386], where the processing history did not involve externally applied deformation. In the micrograph and energy-dispersive X-ray spectroscopy mapping of Fig. 18a, the non-equilibrium segregation of manganese atoms at both low-angle and high-angle grain boundaries in an additively manufactured CoCrFeMnNi alloy is indicated. The lack of similar segregation and equiatomic concentrations at grain boundaries has been observed in polycrystalline CoCrFeMnNi alloys [387], which are prominent members of the HEA family. Measurements of tracer diffusion in the additively manufactured alloy revealed a significant enhancement of grain boundary diffusion rates by many orders of magnitude, even exceeding the relative enhancement observed for pure metals or highly concentrated binary alloys (Fig. 17b). This enhancement is exemplified for manganese and iron in Fig. 17b. This unexpected result may be related to the larger configuration space of grain boundary structures in complex, multicomponent alloys. For example, segregation must be taken into account and the structure of grain boundary complexions could also be affected by the presence of minute amounts of alloying elements that are not sufficiently concentrated to allow observation of segregation. The strong enhancement of grain boundary diffusion disappears completely after one-hour annealing treatment at a moderate temperature of 773 K, which has been shown to cause no measurable changes in the microstructure [385].

SPD processing can also serve for bonding or mechanical intermixing at low homologous temperatures. Previous work on HPT-processed HEAs has typically been focused on single-phase solid solutions [388–392]. However, recently the potential for fabricating UFG or even nanocrystalline HEA composites via HPT processing has been analyzed

[370]. For this reason, single-phase equiatomic FCC CoCrFeMnNi and BCC HfNbTaTiZr HEAs were severely co-deformed by HPT, enabling the fabrication of a novel generation of HEA nanocomposites. Bulk nanocomposites consisting of alternating elongated nanocrystalline CoCrFeMnNi and amorphous HfNbTaTiZr nano-lamellae with residual crystalline fractions of HfNbTaTiZr developed (Fig. 18b), exhibiting complex microstructures with vortex-like regions and extremely high hardness. The hardness of the co-deformed BCC-FCC-amorphous nanocomposite exceeded both single-phase materials deformed under similar conditions and reached values exceeding 6 GPa. Amorphization during severe co-deformation and the associated defect accumulation and defect interaction at the severely strained heterophase interfaces may represent a rather extreme material response. However, these results highlight the importance of strain-induced modifications that can occur at heterophase interfaces during SPD processing [370].

SPD processing under at least partial confinement and involving high hydrostatic pressure introduces significant structural modifications of metals and crystalline as well as amorphous alloys and drives internal interfaces into states that are denoted as non-equilibrium. The modified grain boundary structure in terms of structural defects (or complexions [393, 394]) affects grain boundary segregation [395, 396] and diffusion [397], and influences strain accumulation [398] or inhibits grain boundary migration by rotational defects [367]. Such modifications are not limited by the SPD processing of materials. Non-equilibrium processing via additive manufacturing drives grain boundaries to similar non-equilibrium states featuring both non-equilibrium segregation and enhanced diffusion [384].

In-depth analysis shows a strong heterogeneity of grain boundary structures [386], segregation response [304, 370, 395, 396], precipitation, amorphization and/or phase decomposition along interfaces with the same macroscopic degrees of freedom [370], and therefore requires new approaches that go beyond purely geometric descriptions of the atomic structure and the related properties of internal interfaces, especially after non-equilibrium processing.

3.2. Investigation of non-equilibrium grain boundaries

As mentioned earlier, SPD allows the production of bulk UFG
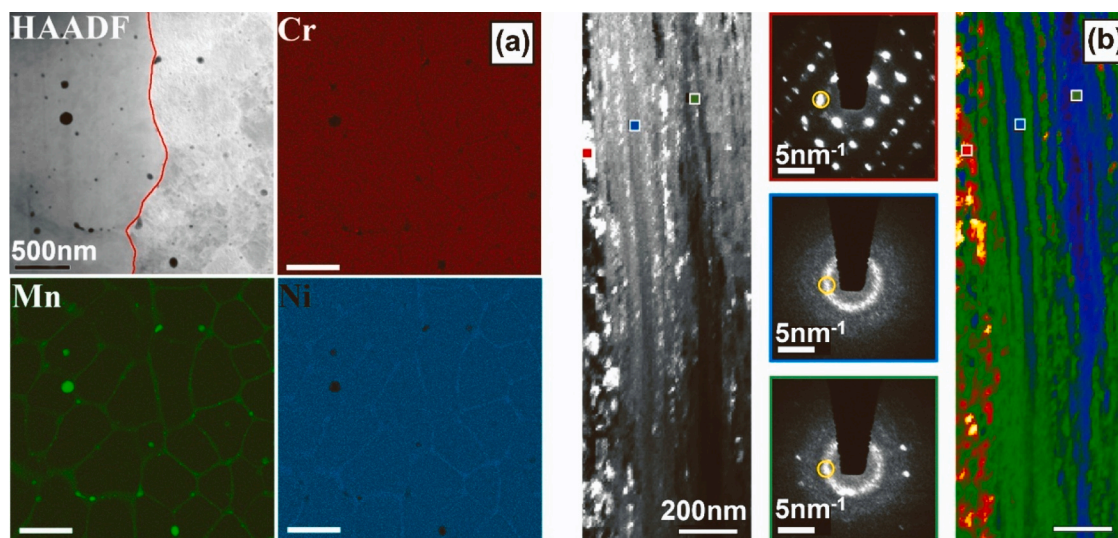
Fig. 18. (a) Microstructure and energy-dispersive X-ray spectroscopy chemical maps of additively manufactured CoCrFeMnNi alloy in the as-printed state with pronounced non-equilibrium segregation of manganese [386]]. (b) A virtual dark-field image reconstructed from nanobeam diffraction mapping of co-deformed FCC/BCC HEA composite (left panel), individual diffraction patterns revealing crystalline reflections of the FCC CoCrFeMnNi phase (red square), an amorphous halo in the Ta-rich (green square) and an amorphous halo with crystalline reflections at the equiatomic HfNbTaTiZr regions (blue square) and color map of the phases using the value of the intensity-weighted mean of the reciprocal diffraction distance around the first strong crystalline reflections of each nano-beam diffraction pattern (right panel) [370]. Homogenous red and yellow regions fit with the FCC phase. The green regions match the BCC phase and/or the mixed phase regions. The blue regions correspond to a Ta-rich amorphous-nanocrystalline composite.

materials with more attractive properties compared to their coarse-grained counterparts [5]. As will be discussed later, these materials demonstrate higher strength and hardness, increased toughness and wear resistance, and enhanced fatigue strength and superplasticity [182, 347, 399–401]. In UFG materials processed by SPD, the role of grain boundaries is especially high not only because of their high density but also due to their specific state [3]. In the present chapter, specific features of grain boundaries in various materials nanostructured by different modes of SPD are considered in detail.

As mentioned in the previous chapter, grain boundaries in UFG materials processed by SPD are in a non-equilibrium state, which is responsible for the improved mechanical properties [394, 402]. Nazarov worked out a theoretical model, according to which modification in the structure and properties of grain boundaries under the SPD results from the absorption of lattice dislocations, and the non-equilibrium grain boundaries are characterized by excess free energy, higher fields of long-range elastic stresses and larger free volume compared to conventional high-angle grain boundaries [376]. In recent publications, the term deformation-modified grain boundaries is used along with non-equilibrium [307, 373]. It was suggested that localized residual strain fields are located in the near-boundary regions of deformation-modified grain boundaries, rather than long-range elastic stress fields [403]. The specific state of deformation-modified grain boundaries can be revealed by various methods.

- Firstly, a conclusion about the non-equilibrium state of boundaries in nanostructured materials was made based on TEM. For example, significant elastic distortions near grain boundaries in nanocrystalline nickel and Ni$_3$Al were observed by high-resolution TEM [404]. In [405] the "zigzag" stepped configurations of grain boundaries in UFG pure copper and Al-3Mg (wt%) alloy processed by HPT were attributed to their non-equilibrium state. An analogous appearance of grain boundaries was observed in HPT-processed niobium and nickel (Figs. 19a and 19b) [406, 407].

- The state of grain boundaries can be assessed qualitatively and quantitatively by emission Mössbauer spectroscopy [408], which reveals the specific deformation-modified state of grain boundaries in molybdenum, tungsten and niobium [406, 409–411]. In Fig. 19c, the isomer shifts of ^{57}Co(^{57}Fe) spectral lines versus annealing temperature are compared for coarse-grained and UFG niobium [406]. In coarse-grained niobium, the isomer shifts of both lines (grain-boundary line – component 1 and volume line – component 2) increase slightly with increasing annealing temperature approaching the isomer shift in the regular lattice. In UFG niobium, the isomer shifts of both lines are noticeably lower, especially at low temperatures (673–723 K), because of an excessive free volume, which is one
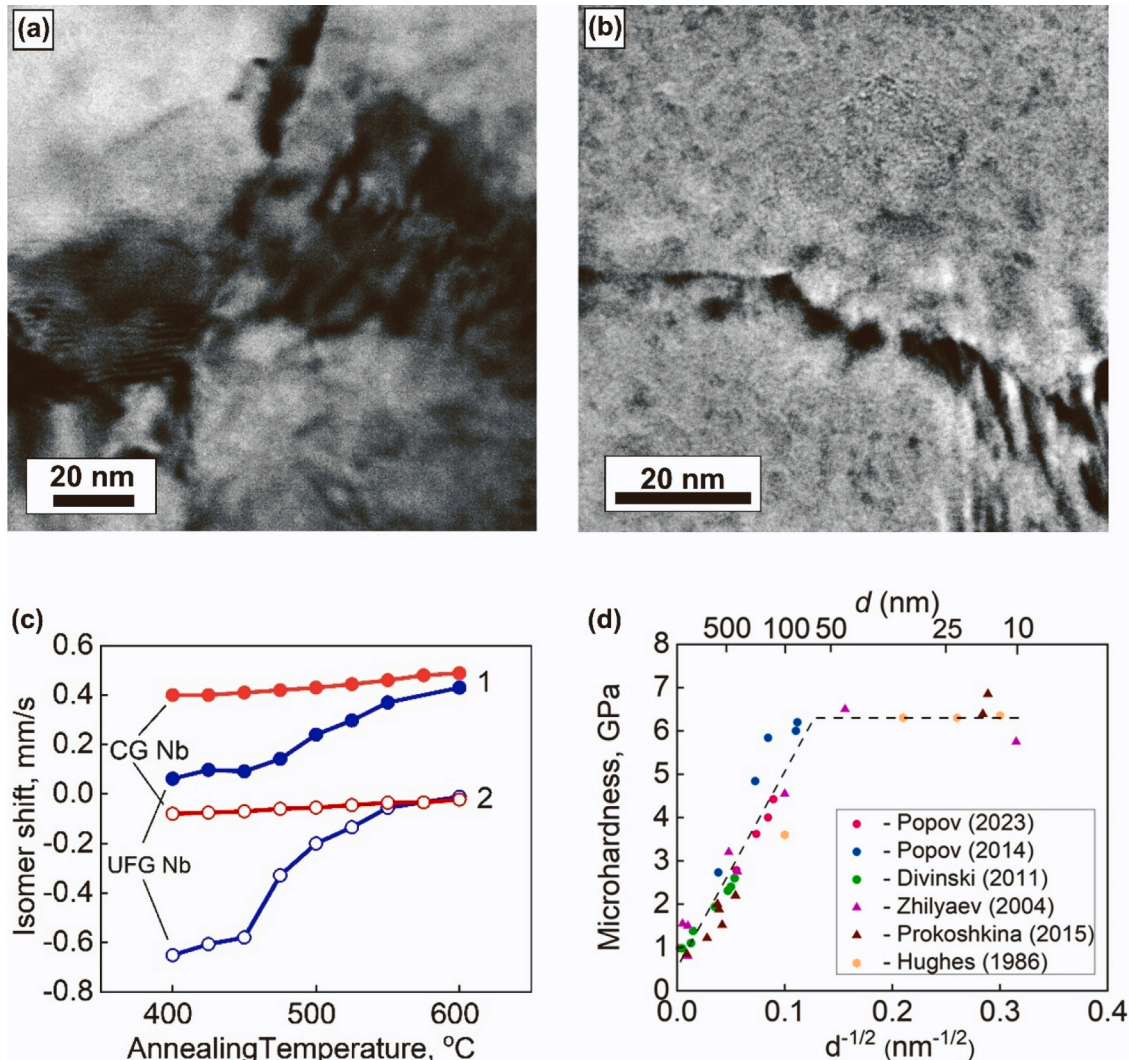
Fig. 19. (a,b) Stepwise boundaries in HPT-processed (a) niobium and (b) nickel [407]. (c) Isomer shifts of ^{57}Co(^{57}Fe) spectral lines versus annealing temperature in coarse-grained niobium (red lines and symbols) and UFG niobium (blue lines and symbols) [406]. (d) Microhardness versus grain size (d) in nickel processed by various techniques [407].

of the main features of the deformation-modified grain boundaries. Above 723 K, the isomer shifts of both lines increase sharply, and after annealing at 873 K, the isomer shift of the volume line of the UFG sample approaches the value for the coarse-grained sample. The increase of isomer shift with increasing annealing temperature is explained by the recovery processes in grain boundaries and near-boundary regions of crystallites.

- The state of grain boundaries can also be revealed by diffusion methods. For example, in [412], an additional free volume was supposed in the deformation-modified boundaries of titanium processed by ECAP based on the tracer diffusion data. In some publications, it was shown that under the SPD processing, a part of high-angle boundaries acquires the deformation-modified state,

characterized by accelerated atomic transfer [380, 403, 413, 414]. As demonstrated in [415–418], the grain-boundary diffusion coefficients of cobalt in UFG nickel and niobium processed by HPT are several orders of magnitude higher than in their coarse-grained counterparts, suggesting that non-equilibrium grain boundaries form under SPD processing.

- Additional information on the specific state of deformation-modified grain boundaries can be obtained from the joint analysis of emission Mössbauer spectroscopy and radiotracer data [419]. Based on this approach, it was shown in [420] that grain boundaries in UFG molybdenum processed by HPT are the ultrafast diffusion paths, the coefficients of which are several orders of magnitude higher than those for grain boundaries of recrystallization origin, and this is a
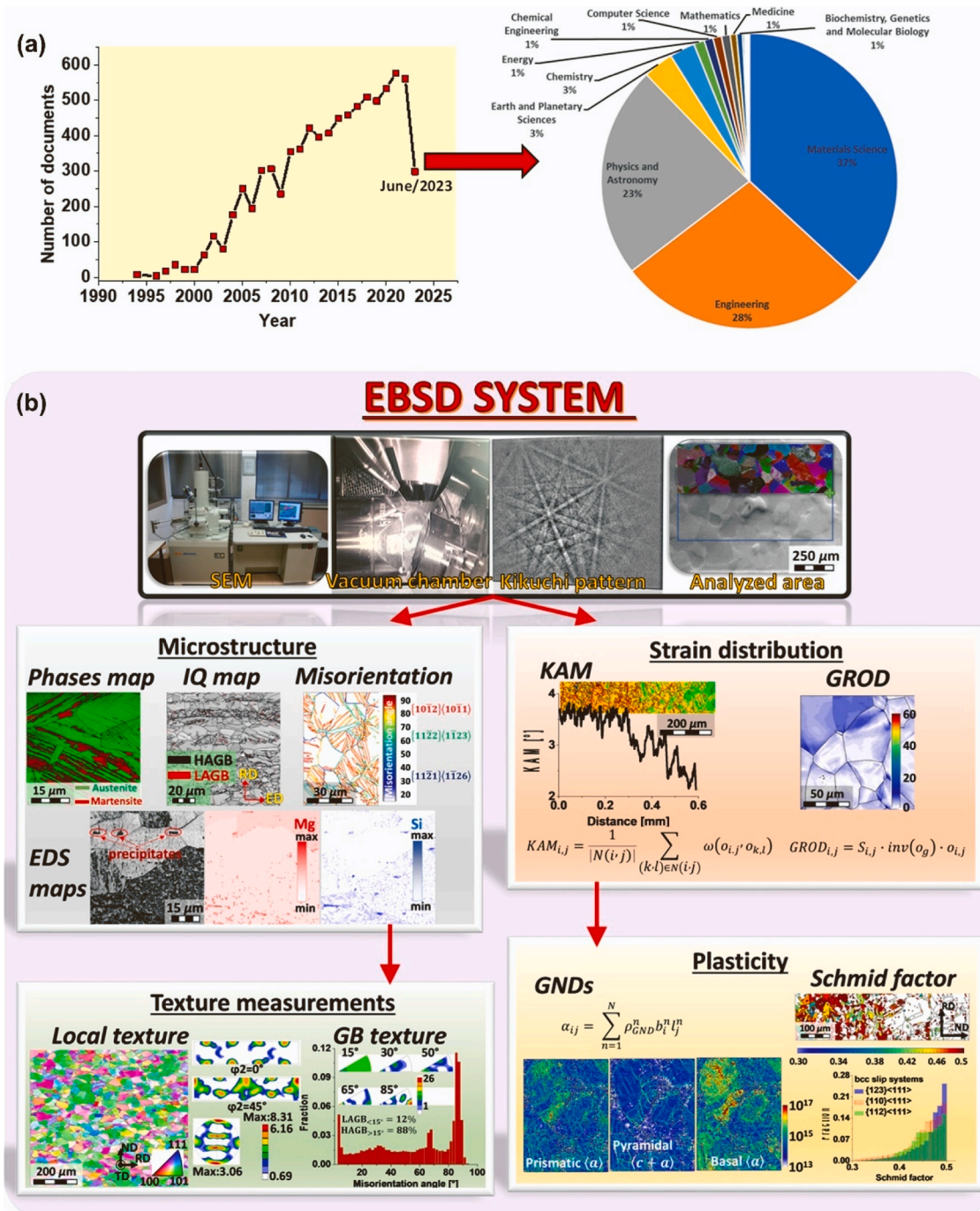
Fig. 20. (a) Number of scientific documents that included EBSD as keyword since 1994 until now and their distribution according to the research field (information obtained from Scopus data base on June 2023). (b) EBSD system and main calculation and representation techniques [437, 439, 442, 443].

direct part of the evidence for the specific non-equilibrium state of grain boundaries.

In [407], tunneling microscopy was additionally applied to reveal the specific state of grain boundaries in HPT-processed nickel. The relative energy of grain boundaries was determined by the method of etching grooves and calculated from the dihedral angle at the bottom of an etching groove by Equation 1.

$$\gamma_{rel} = \frac{\gamma_{gb}}{\gamma_s} = 2\cos\frac{\Psi}{2} \tag{1}$$

where γ_{rel}, γ_{gb} and γ_s are the relative energy of a grain boundary, the grain boundary energy and the energy of a free surface, respectively, and Ψ is the angle at the bottom of the groove. The relative energies of grain boundaries markedly increase with straining, and even at HPT by 0.5 revolutions, γ_{rel} is much higher than in coarse-grained nickel, where it equals 0.30 [421].

Fig. 19d demonstrates the Hall-Petch dependence of microhardness on the square root of the average crystallite size for nickel [329, 380, 407, 422–424], and it is obvious that for grain sizes down to ~ 100 nm the dependence is linear, indicating that the main strengthening factor is grain refinement rather than the specific state of grain boundaries. This conclusion is confirmed by the results of X-ray studies, based on which the level of microstresses was determined. These studies showed that under HPT conditions, the microstress changes from 0.23 GPa for a sample deformed by 0.5 revolutions to 0.35 GPa for a sample deformed by 5 revolutions [407], and this is much less than the total strengthening of nickel after SPD processing.

The main conclusion of this section is that the specific non-equilibrium state of grain boundaries, characterized by excess free energy and larger free volume compared to conventional relaxed high-angle grain boundaries, is formed in metals and alloys under various modes of SPD. This can be revealed by different methods. The contribution of the deformation-modified state of grain boundaries to strengthening is relatively small, and the strengthening mainly results from grain refinement by SPD processing.

3.3. Investigation of microstructure by electron backscatter diffraction

UFG materials produced by SPD methods present complex microstructures involving different phases, high density of defects, heterogeneous grain sizes and local texture variations that cannot be characterized by conventional optical microscopy [425]. In this regard, scanning electron microscopy (SEM) coupled with an electron backscatter diffraction (EBSD) detector has gained importance over the years for a thorough microstructure characterization of polycrystalline materials [426, 427]. Fig. 20a proves the continuously growing interest in this technique as the number of published documents has increased in the last thirty years in diverse research fields such as medicine, mathematics, energy, chemistry, physics and materials science. In this technique, an electron beam strikes the surface of a 70° tilted sample, where the diffracted electrons produce a characteristic pattern known as Kikuchi lines on a phosphorous screen (Fig. 20b) [428–430]. This pattern reflects the crystal structure and orientation of the region from which it was generated, so it is recorded and indexed according to the previously selected database [431]. Various *in situ* and *ex situ* microstructural measurements can be performed inside the SEM vacuum chamber: After the data acquisition, several microstructural representations and calculations can be obtained: phase identification, texture [432], recrystallized fractions (using local strain indicators like kernel average misorientation KAM and image quality IQ) [433, 434], composition distribution [435], grain size distribution, geometrically necessary dislocations GND and Schmid factor quantifications. These techniques enable the study of grain fragmentation and plasticity of materials [436, 437], characterization of grain boundaries, strain

distribution and microstructural heterogeneity (*e.g.* grain reference orientation deviation GROD) [438, 439]. EBSD has evolved tremendously during the last decade in terms of software and hardware due to new detectors that enable fast scans (*i.e.* several samples analyzed in a few hours) and the building up of three-dimensional microstructures at high resolution [440]. Furthermore, the transmission Kikuchi diffraction technique, also known as transmission-electron backscatter diffraction, can overcome some limits of standard EBSD. These constraints include the spatial resolution of around 20 nm and the angular resolution of approximately 1°. This method utilizes TEM samples within the SEM chamber, enabling a greater spatial resolution compared to conventional EBSD. Therefore, it is particularly well-suited for analyzing nanomaterials due to its exceptional sensitivity to small variations in the crystal lattice [441].

EBSD allows for the analysis of several microstructural characteristics. For example, Fig. 21a-c show the microstructure evolution as IQ map with the overlapping low-angle and high-angle grain boundaries for Armco iron after annealing treatment (Fig. 21a) and subsequently ECAP processing by one (Figs. 21b) and 16 ECAP passes (Fig. 21c). This representation highlights the microstructure transformation from the coarse-grained annealed state to a UFG microstructure, passing through a substructure state dominated by a high fraction of low-angle grain boundaries. The transformation from low-angle grain boundaries to high-angle grain boundaries at room temperature (*i.e.* very low homologous temperature) has been described as a continuous dynamic recrystallization process [444]. It is pertinent to note that conducting a successful EBSD analysis necessitates accurately defining microstructural parameters such as the minimum grain size and the minimum grain boundary misorientation to obtain reliable results. Typically, a grain should consist of at least five pixels to be considered as such, and the minimum grain boundary misorientation needed to differentiate between grains falls within the range of 1–5°. It is important to mention that these are general guidelines, and the specific requirements may vary depending on factors such as the crystal structure, sample preparation methods and instrument settings [426].

EBSD representations like GROD and GND can evaluate the microstructure heterogeneity and the lattice curvature following Equations 2 and 3, respectively [436, 448].

$$\boldsymbol{GROD_{i,j}} = \Delta(\boldsymbol{\theta_{ij}}, \quad \boldsymbol{\theta_{avg}}) \tag{2}$$

$$\rho_{GND}^{(2D)} = \frac{1}{b} \quad \sqrt{\alpha_{12}^2 + \alpha_{13}^2 + \alpha_{21}^2 + \alpha_{23}^2 + \alpha_{33}^2} \tag{3}$$

where θ_{ij} is the misorientation at the position (i,j), θ_{avg} represents the grain average misorientation, b is the magnitude of Burgers vector and α_{ij} represents the five components of the Nye's tensor that can be determined from two-dimensional mapping. Fig. 21d-e illustrates the GROD maps of interstitial free steel across the sheet thickness after cold symmetric and asymmetric rolling, respectively. This analysis proves that the asymmetric rolling process gives rise to microstructure heterogeneity across the sheet thickness. At the same time, the deformation on the symmetric rolled material is evenly distributed in different zones of the sheet. The large GROD values close to the sheet surfaces after asymmetric rolling emphasize a higher density of dislocations and faster grain refinement than in the symmetrically rolled sample due to the velocity gradient and the intense shear strain component (*i.e.* faster texture randomization than in symmetric rolling) [442, 449]. In view of GNDs and texture evolution in heterostructured materials, Fig. 21f displays the GND maps considering the slip systems for commercially pure titanium after two passes by equal-channel angular sheet extrusion (an ECAP-based technique applied to sheets to create heterogeneous materials, with a specific focus on plane geometry deformation). These maps and the pole figures suggest that dislocation activity occurs primarily on the basal and prismatic planes rather than pyramidal planes (larger Burgers vector and, therefore, a higher resolved shear stress for
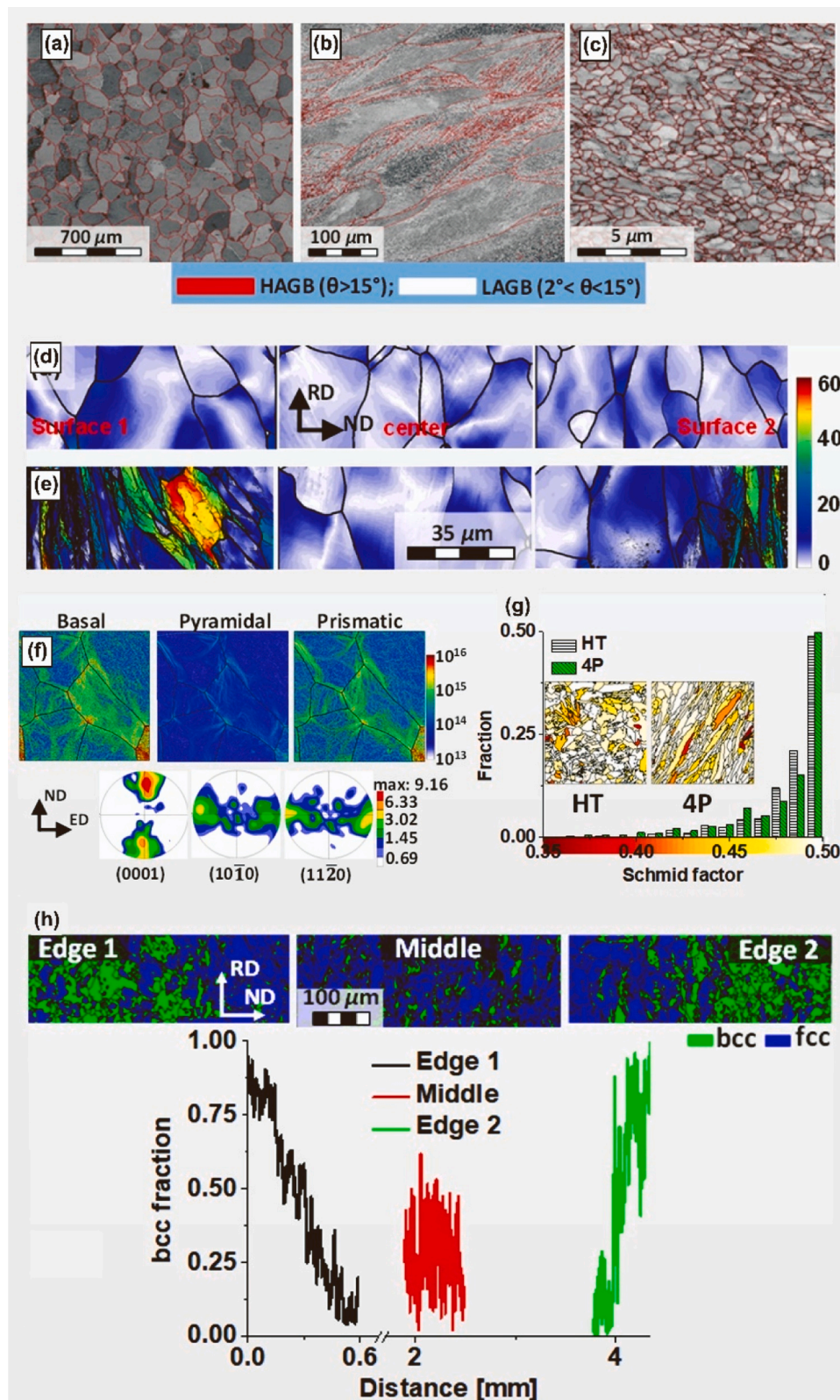
Fig. 21. (a-c) Armco iron processed by (a) zero, (b) one and (c) 16 ECAP passes [445, 446]. (d,e) Grain reference orientation deviation (GROD) maps for interstitial free steel processed by (d) cold symmetric rolling and (e) asymmetric rolling [442]. (f) Geometrically necessary dislocations (GND) and pole figures for commercially pure titanium after two passes of equal-channel angular sheet extrusion (ECASE) [439]. (g) Schmid factor evolution for low-carbon 1020 steel after heat treatment (HT) and four ECAP passes [447]. (h) Phase maps for an austenitic stainless steel processed by one ECASE pass [437].

dislocations to slip), which is indicative of the titanium low formability capacity at room temperature and the strong material anisotropy [439, 450]. Regarding plasticity, Fig. 21g shows the Schmid factor evolution for low-carbon steel processed by ECAP at room temperature. In this plot, the initial heat-treated and four ECAP pass processed materials present similar distributions, indicating that the low-carbon steel can withstand more significant amounts of plastic deformation even when the ductility after four ECAP passes is almost neglectable [447, 451]. EBSD also enables the evaluation of phase transformation from austenite to martensite on steels like the austenitic stainless steel 304 L processed by equal-channel angular sheet extrusion, which creates a heterogeneous material across the sheet thickness, as indicated in Fig. 21h. The aforementioned results demonstrate the efficacy of the EBSD technique in characterizing materials with homogenous coarse, homogeneous UFG, and heterostructured microstructures.

The information obtained by EBSD leads to a better understanding of the microstructural and mechanical properties of different SPD-processed metallic materials. Fig. 22a-c compiles results from different SPD processes, like ECAP, ARB, and HPT, concerning the grain boundary misorientation examined by EBSD [443, 445, 446, 452–475]. Thus, metallic materials processed by ARB present a faster transition from low-angle grain boundaries to high-angle grain boundaries with less accumulated strain than ECAP and HPT. However, all the processes suggest a plateau state after von Mises plastic strains larger than seven, which is associated with the slowing of grain fragmentation, *i.e.* saturation of the grain size reduction and low ductility [445]. In this sense, metallic materials subjected to SPD techniques are characterized by high yield strength but low ductility, limiting their application, as indicated in Fig. 22d. To overcome this strength-ductility paradox, the newly emerging research field of heterostructured materials appears as a solution (Fig. 22d) [443, 452]. EBSD characterization thus plays a crucial

role in understanding the property-microstructure relation and hardening mechanisms of SPD-processed materials.

3.4. Investigation of microstructure by synchrotron X-ray and neutron diffraction

The investigation of microstructure evolution during SPD and under extreme conditions can be accomplished in reciprocal space using various diffraction techniques, including X-ray, synchrotron and neutron diffraction. A portrayal of Laue–Bragg interference is depicted in Fig. 23a [476], where λ is the wavelength, θ is the Bragg angle, k_i and k_f are the incoming and scattered wavevectors, respectively, d is the lattice spacing and G is the reciprocal lattice vector. Lab-scale XRD and its line profile analysis have been effectively employed to study the microstructural evolution and phase transformation of bulk nanostructured metals processed through SPD [477–481]. Such reflection-type XRD, having a limited penetration depth [482], presents unique opportunities to unveil microstructural heterogeneity even when different planes and sections are scanned within SPD-processed metals. Some examples of such capability are different textures at local and global regions of ZK60 discs after HPT [483] and heterogeneous phase transformation and order-to-disorder transformation in a TiAl intermetallic compound through HPT [484]. By contrast, synchrotron X-ray and neutron diffraction techniques, both in penetration-type settings [485, 486], complement each other, providing distinct measurement capabilities and offering valuable insights into dynamic microstructural changes [476, 487].

High-energy synchrotron X-rays enable the penetration of millimeters into metals using a micro- to nano-scale beam, revealing precise local probing of interest with a high reciprocal space resolution providing the through-thickness microstructural information [476,
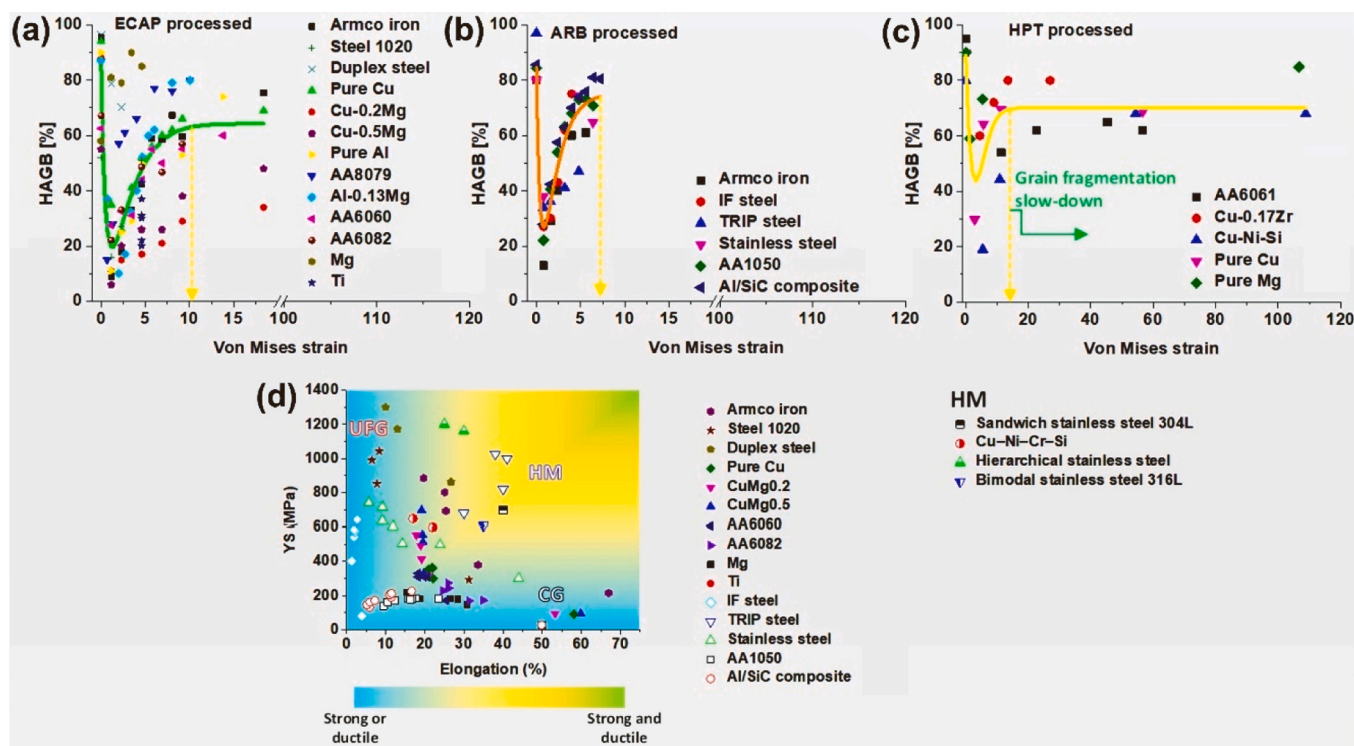
Fig. 22. High-angle grain boundary (HAGB) fractions for different metallic materials processed by (a) ECAP (Armco iron [446], steel 1020 [447], duplex steel [453], pure copper [454], Cu-0.2Mg [455], Cu-0.5Mg [455], pure aluminum [456], AA8079 [457], Al-0.13Mg [457], AA6060 [458], AA6082 [459], Mg-based alloy [460] and commercially pure titanium [461]), (b) ARB (Armco iron [462], interstitial free (IF) steel [463], TRIP (transformation-induced plasticity) steel [464], stainless steel [465], AA1050 [466] and Al/SiC composite [466]) and (c) HPT (AA6061 [467], Cu-0.17Zr [468], Cu-Ni-Si [469], pure copper [470] and pure magnesium [471]). (d) Yield strength and elongation evolution for UFG, coarse-grained and heterostructured materials (sandwich stainless steel [472], Cu-Ni-Cr-Si [473], hierarchical stainless steel [474] and bimodal stainless steel 316 L [475]).
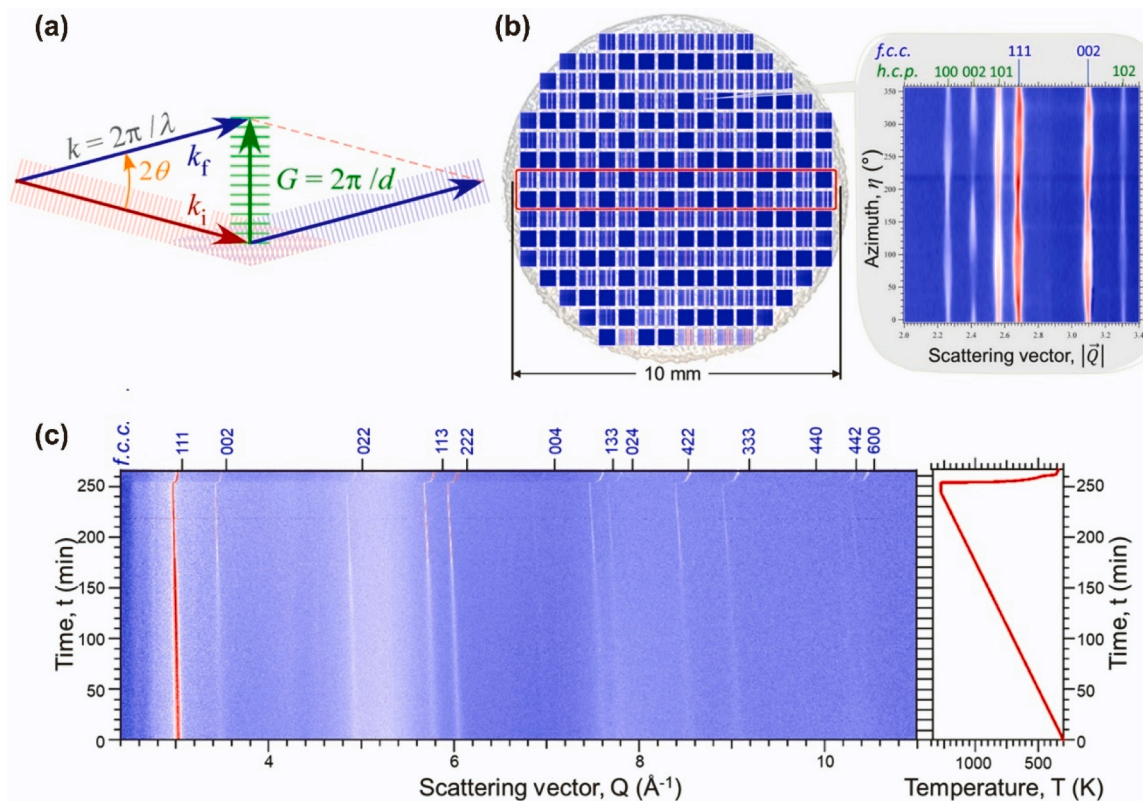
Fig. 23. (a) A portrayal of Laue–Bragg interference [476]. (b) Position-dependent microstructure map constructed by a series of high-energy XRD (HEXRD) patterns with an enlarged representative diffractogram [488]. (c) A contour plot showing neutron diffraction patterns with time and temperature [489].

490]. The technique of high-energy XRD with a micro-beam is utilized at beamline BL02B1, SPring 8, Japan, [491] by scanning the local region of an HPT-induced diffusion-bonded Al-Mg metastable alloy over the disc surface, enabling a mapping of heterogeneous phase fractions and microstructure over the whole sample volume [488]. Fig. 23b showcases the position-dependent microstructure of the HPT-deformed Al-Mg disc, where the map is constructed from a series of high-energy XRD patterns, with an enlarged representative diffractogram aiding in the visualization of heterogeneous phase fractions and microstructure across the

entire sample volume [488]. The polymorphous phase transformation as a function of plastic strain is demonstrated during the nanostructuring and diffusion bonding of aluminum and magnesium through HPT.

Neutrons offer the advantage of integrating over larger sample volumes [476], rendering them highly suitable for targeted investigations, especially in the context of titanium alloys [487, 492], where their diverse diffraction contrasts can effectively detect order and disorder structures. Neutron diffraction characterization facilitates the study of time-resolved structural changes, thereby elucidating the evolution
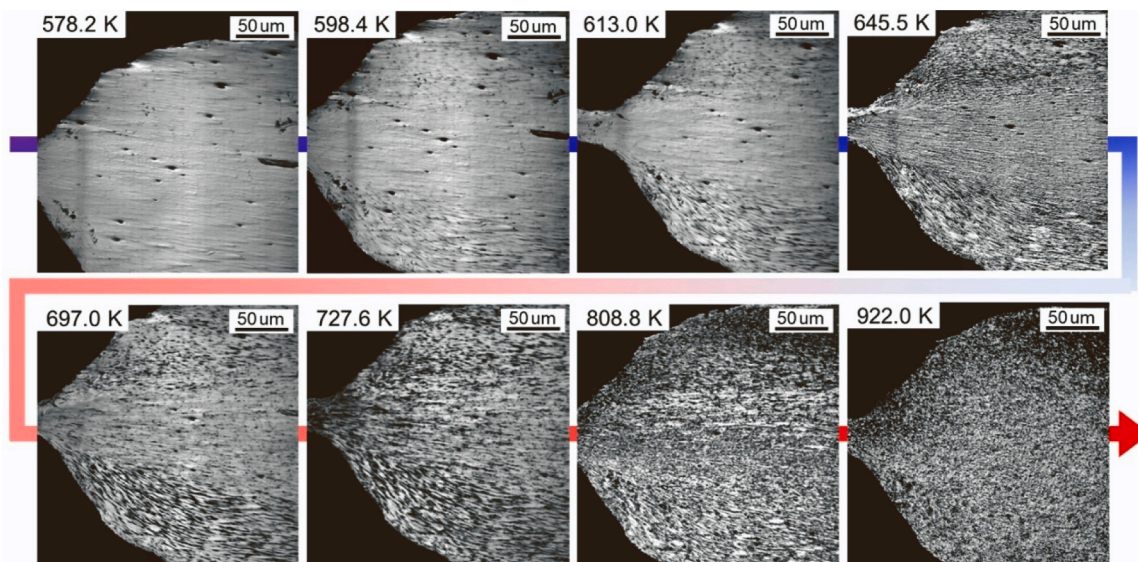
Fig. 24. A heterogeneous phase transformation observed by laser-scanning confocal microscopy (LSCM) at the cross-sections of the HPT-processed CoCrFeNiMn alloy disc edges upon heating [499].

mechanisms and transitions in bulk samples [493]. The incorporation of additional parameters such as heating or cooling enables real-time characterization of crystallographic changes with varying temperatures. A neutron diffraction study on a nanostructured 316 L stainless steel under a heating-cooling cycle was conducted at the iMATERIA beamline BL20 [494, 495] located within J-PARC, Japan [496, 497]. A contour plot showing neutron diffraction patterns against time and temperature is shown in Fig. 23c. The neutron diffraction data were analyzed and the structural evolution in the nanostructured stainless steel is described by the changes in relative lattice expansion and contraction, crystallite size, micro-strain and dislocation density with heating through 1300 K [489]. This technique elucidates the detailed structural relaxation behavior upon heating with detailed transition temperatures of the bulk nanostructured alloy after HPT [498]. A recent report displayed a comprehensive summary of the utilization of the synchrotron X-ray and neutron diffraction techniques on SPD-processed nanostructured materials [499].

In the context of characterization techniques for capturing the heterogeneously appearing microstructural recovery upon heating of nanostructured metals, *in situ* examination by laser-scanning confocal microscopy with a heating system [500–502] demonstrates a preliminary result on a nanostructured CoCrFeNiMn HEA after HPT for 15 turns [499]. A series of micrographs taken at arbitrarily selected temperatures upon heating from 373 to 923 K at a rate of 10 K/min is shown in Fig. 24 displaying a gradual and heterogeneously occurring phase transformation upon heating at a similar disc edge region of the HPT-processed CoCrFeNiMn HEA [499]. Microstructural recovery is visible mainly due to the phase separation of the alloy [503–505]. The delayed multi-phase microstructure formation during recovery is evident in the middle-height region of the nanostructured HEA disc after HPT. At the central section, the morphology of the multi-phases appears more equiaxed, in contrast to the elongated structure along the shear pattern observed in the surface regions. This characterization method serves as an excellent preliminary technique for *in situ* and *ex situ* nanoscale microstructural and mechanical testing and the interpretation of local diffraction studies as previously stated.

In summary, the novel and unique microstructural characterization techniques via synchrotron X-ray and neutron diffraction present not only alternative and complementary approaches but also go beyond by allowing *in situ* observations and incorporating time and temperature scales. This integration of real-time and localized monitoring enhances our ability to gain a deeper understanding of the heterogeneity in nanostructures across multiple length scales.

4. Phase transformations

In addition to microstructural evolutions, crystal structure evolutions through strain-, pressure- and temperature-induced phase transformations are another feature of SPD. The history of SPD has a close relation to phase transformations [20], and the topic is still of high interest [8, 9, 15]. It is well established that SPD can affect both the thermodynamics and kinetics of phase transformations and contribute to the discovery of new phases [8, 9, 15]. The SPD-induced phase transformations were reported in various elements including titanium [506], zirconium [507], hafnium [508], cobalt [509], bismuth [510], carbon [511], silicon [15], germanium [512] and phosphorous [20]. Phase transformations and solid-state reactions in alloying systems containing two or more elements were frequently observed after SPD [10, 11] and particularly in the systems with full immiscibility in the solid and liquid forms (*e.g.* Mg-Ti [333], Mg-Zr [334] and Mg-Hf [335]) after ultra-SPD [164]. Phase transformations by SPD are not limited to metallic materials as such transformations were reported in various nano-metallic materials such as oxides [513], nitrides [514], hydrides [515], *etc.* In this section, after reviewing phase transformations in metallic materials and ceramics, recent findings on coupling theoretical studies with *in situ* experiments are discussed.

4.1. Phase transformations in metallic alloys

Along with grain refinement, SPD can cause various phase transformations in metals and metallic materials [516]. Titanium, zirconium and hafnium, along with iron, cobalt and bismuth, belong to the metals in which allotropic phase transformations occur when temperature or pressure changes. These phase transformations make it possible to design mechanical and heat treatments to control the properties. Metallic alloys after SPD usually do not contain the same phases as before processing with SPD. SPD can drive the phase transformations both in the bulk and in grain boundaries of alloys. In turn, the SPD-driven bulk phase transitions can be divided into three large groups.

- The first group of phenomena includes competition between decomposition and formation of a solid solution. During the decomposition of a supersaturated binary solid solution, particles of a second phase form and grow, and the concentration of the alloying element in the solid solution decreases. During the formation of a supersaturated solid solution, particles of the second phase dissolve during SPD, increasing the concentration of the second component in the solid solution [517–520]. It is well known that during SPD (especially during HPT), a stationary state (or steady state) can be reached with the strain increase [521]. It turns out that, as a rule, when the decomposition and formation of a solid solution compete, a certain stationary concentration is established. Interestingly, this concentration usually is equal to the solubility of the second component at some elevated temperature called effective temperature (T_{eff}) [522]. Most frequently, T_{eff} significantly exceeds the room temperature being usually the temperature of SPD treatment [523].
- The second group of phenomena includes SPD-driven amorphization of crystalline phases [524–527], or nanocrystallization from an amorphous phase [528–530]. Interestingly during HPT, one, two, or several different amorphous phases can appear [531].
- The third class of phase transformations during SPD is observed in metals that possess several allotropic modifications at different temperatures or pressures. In this class of phenomena, the SPD-driven transformations in titanium and its alloys are best studied.

Titanium alloys are one of the most important classes of materials in modern technologies [532–534]. Pure titanium (like zirconium or hafnium) can exist in three crystallographic modifications, namely the low-temperature α-Ti with a hexagonal close-packed crystal structure (space group P63/mmc), the high-temperature β-Ti with a body-centered cubic structure (space group Im3m), and the high-pressure ω-Ti with a hexagonal structure (space group P6/mmm). Many SPD studies are devoted to the change in the properties and structure of titanium and its alloys, such as pure titanium [535–540], binary titanium alloys like Ti-Al [541, 542], Ti-Mg [333, 543], Ti-Fe [544, 545], Ti-Ni [546, 547], Ti-Co [548, 549], Ti-Mo [550, 551], Ti-Nb [552, 553], Ti-Hf [554], Ti-V [309, 555], ternary alloys like Ti-Nb-Zr (TNZ) [556, 557], Ti-Nb-Ta [558], quaternary Ti-Nb-Ta-Zr (TNTZ) [559, 560] and quinary Ti-Al-Zr-Mo-V (TA15) [561]. However, only a small portion of these works concern HPT-induced phase transformations in titanium and its alloys.

In a recent study, HPT processing of various binary titanium alloys with β stabilizers (iron, cobalt, nickel, molybdenum and niobium) was studied [544]. Before HPT, the samples were annealed and contained (i) pure β-phase, (ii) α+β mixture with different portions of phases, (iii) α' or α'' martensites, (iv) the mixture of α-Ti and respective intermetallic phase. It was observed that HPT can lead to various phase transitions in the alloys. In particular, the metastable high-pressure ω phase and α' martensite could form [544]. The orientation relationship between the lattices of β-Ti and α/α'-Ti is described as $(0001)_\alpha \| (110)_\beta; \langle 11\bar{2}0 \rangle_\alpha \| \langle 111 \rangle_\beta$ [562]. As shown in Fig. 25a, at low

iron concentrations, the fraction of the ω phase after HPT is modest and amounts to about 40% [563–566]. With an increase in the iron content, the portion of the ω phase in the alloy after HPT also increases. It reaches almost 100% at an iron concentration of 4 wt%. Then it begins to decrease with increasing iron concentration and drops to 10–30% at 10 wt% of iron. It is important to mention that, despite the diffusion-like mass transfer during HPT, the transformation of the β phase into the ω phase occurs according to the martensitic mechanism and is associated with a certain orientation relationship between the β-phase and the ω-phase. It turns out that the lattice period of the β and ω phases changes with the addition of iron but in different ways. In both cases, the lattice period decreases with the addition of iron, but in the β phase, it decreases more rapidly. Fig. 25b shows that in the Ti-Fe alloys at a concentration of about 4 wt% of iron, the lines for the lattice period a_ω and $\sqrt{2}\, a_\beta$ in β and ω phases intersect. The intersection point corresponds to the lowest lattice mismatch. It greatly facilitates the β-to-ω transformation. As a result, almost 100% of the crystal volume is converted after five HPT revolutions into the ω phase. A micrograph obtained at earlier stages of deformation of Ti-Fe alloy, namely after 1/10 of HPT revolutions, is shown in Fig. 26.and 26b clearly shows how the ω phase (shown in turquoise) surrounds the remains of the α phase (shown in red). Between the α phase and the ω phase, a shell of the β phase is visible (shown in green). It was also shown that the replacement of iron by cobalt in a titanium alloy leads to an increase in the lattice mismatch between α, β and ω phases and to the incomplete transformation of these phases into the ω phase [548].

The composition of phases (similar to their grain size) reaches the steady state value (*e.g.* after about 1.5 HPT revolutions). In some cases, the equifinality of the SPD-driven phase transitions is observed [568]. Equifinality means that the composition and portion of phases after HPT do not depend on the composition and portion of phases before SPD [519]. However, pre-SPD treatment can sometimes influence the phase transformations. For example, if the Ti-based alloys are annealed below the temperature of eutectoid decomposition of the β phase, they contain only α phase or the mixture of α phase with the corresponding intermetallic compound. In this case, the α phase has no chance to "use" the intermediate layer of the β phase to transform into the ω phase during HPT. Thus, the formation of the ω phase is more complicated and can be completely suppressed if the α phase contains enough diluted alloying atoms. Moreover, if the intermetallic compound exists in a certain

Fig. 25. (a) Dependence of the ω phase volume fraction of HPT-treated Ti-Fe alloys on the iron concentration (samples were pre-annealed at 1233 K, 1273 K, 893 K, 873 K) [544]. (b) Data gathered from the literature [545, 563–566] for the lattice periods in Ti-Fe alloys measured for ω-phase (a_ω, filled squares) with the values $\sqrt{2}\, a_\beta$ for β phase (open symbols). Vegard law straight lines are shown in (b) for the β (thin) and ω (thick) phases which intersect at ~4 wt% of iron [567].

Fig. 26. (a) Bright field TEM micrograph of the Ti-4Fe (wt%) sample pre-annealed at 1223 K quenched in water and treated by HPT (7 GPa, 0.1 rot, 1 rpm). (b) Phase map of a red outlined area in (a). The α phase is shown in red, the β phase is shown in green and the ω phase is shown in turquoise. The elongated α grain is surrounded by a layer of β phase embedded in ω matrix. The elemental analysis for the black outlined area is shown in the insets in the upper part of (b) [562].

concentration interval, HPT can lead to the composition change in such solid solution based on the intermetallic compound.

The HPT-driven phase transitions can be martensitic (*i.e.* without or almost without mass transfer) or diffusional (*i.e.* with mass transfer). For example, in the case of martensitic β-to-ω or α-to-ω phase transitions in titanium alloys, certain orientation relations between β and ω or α and ω phases were observed. In the case of diffusional phase transitions, the rate of mass transfer during HPT at room temperature is several orders of magnitude higher than that of conventional bulk diffusion at room temperature [569]. This is especially remarkable since the high pressure itself (*i.e.* without shear strain) decreases the rate of mass transfer [570, 571]. The type of phase transformation (martensitic or diffusional) and chemical composition can affect the thermal stability of phases. The thermal stability of the ω phase obtained by HPT has been studied by the *in situ* XRD at high temperatures. It was shown that the ω phase in the HPT-treated Ti-based alloys with β stabilizers can remain in the samples

up to 773–873 K. This temperature range is much higher than in pure titanium (~453 K). Alloying with niobium or molybdenum increases this temperature to 573–623 K. In Ti−Co alloys, the ω phase remains stable up to 673 K and in the Ti−Fe alloys even up to 823 K [567, 572].

Phase transformations can take place not only in the bulk but also in grain boundaries. They include faceting-roughening transitions [573], as well as wetting [574], prewetting [575–577] or premelting [578, 579] transformations. The significance of SPD-driven grain boundary phase transformations was reported in a few recent studies [580, 581]. The HPT-driven bulk and grain boundary phase transitions open a new way for tailoring, grain size, phase composition and properties of metallic materials. In turn, it gives the new instrument in the hands of engineers to design materials for special applications such as titanium alloys for medical applications.
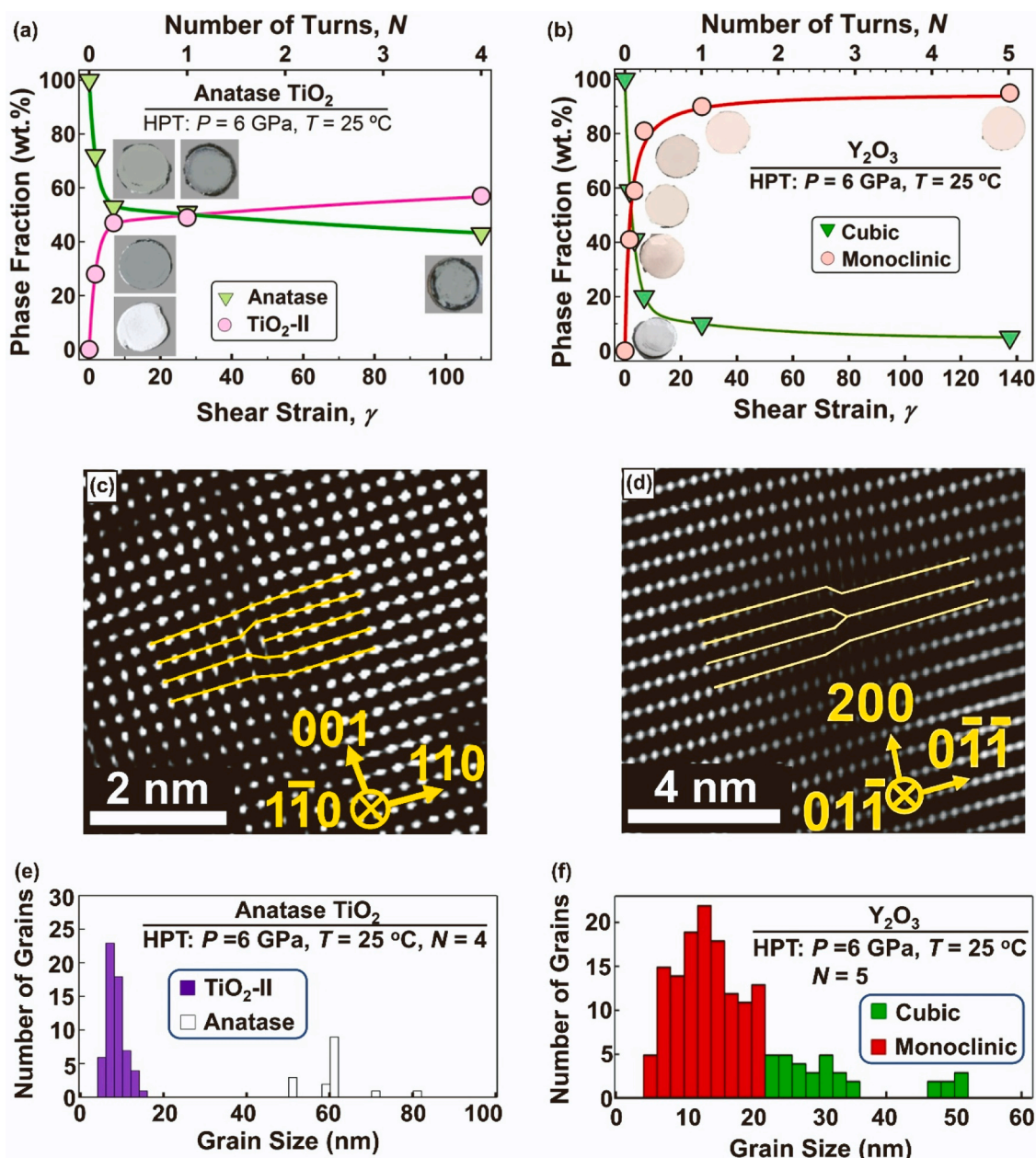
Fig. 27. (a,b) Influence of plastic shear strain on the fraction of high-pressure phases in (a) TiO_2 [582] and (b) Y_2O_3 [583] after HPT processing. (c,d) Formation of dislocations during phase transformations of (c) ZrO_2 [584] and (d) TiO_2 [582] after HPT processing. (e,f) Grain size effect on the stability of high-pressure (e) TiO_2-II [582] and (f) monoclinic Y_2O_3 [583] after HPT processing.

4.2. Phase transformations in ceramics

Phase transformation induced by SPD is not limited to metallic materials and such phase transformations were reported in a wide range of ceramics (*e.g.* ZrO_2, $BaTiO_3$, ZnO, TiO_2, Y_2O_3, SiO_2, Al_2O_3, VO_2, BN, *etc.*). Among bulk-SPD methods, HPT is currently the only method used for controlling phase transformations in ceramics due to the high processing pressure in this method. Processing by HPT provides some unique features for the phase transformation of ceramics. (i) The fraction of the high-pressure phase increases with increasing the applied shear strain, as shown in Fig. 27a for TiO_2 [582] and Fig. 27b for Y_2O_3 [583]. (ii) Phase transformation can occur at a pressure below the transition pressure under static compression (*e.g.* reduction of pressure from 11 to 15–6 GPa in monoclinic-to-cubic phase transformation of Y_2O_3 shown in Fig. 27b). (iii) Dislocations contribute to the acceleration of phase transformation and the reduction of transition pressure (*e.g.* see dislocations observed during phase transformation of ZrO_2 in Fig. 27c [584] and TiO_2 in Fig. 27d [582]). (iv) High-pressure phases formed by HPT can remain stable after releasing pressure, particularly in grains with small nanoscaled sizes, as shown in Fig. 27e for TiO_2 [582] and in Fig. 27f for Y_2O_3 [583]. The stability of HPT-induced phases is a striking issue because such phases can be used for different applications. Zinc oxide (ZnO) is one successful example that its high-pressure phase was utilized for photocatalysis, as described below in detail.

ZnO is a well-known ceramic semiconductor with versatile properties for optoelectronic and biochemical applications [585–590] including applications such as ointment, pigment and vulcanization [591, 592]. ZnO exhibits an allotropic transformation from a wurtzite crystal structure to a rocksalt crystal structure as the pressure increases to more than ~6 GPa according to a pressure-temperature phase diagram [593, 594]. For photovoltaic and photocatalytic applications [595–599], the rocksalt structure is more attractive than the wurtzite structure because its band gap is in the range of 1.2–2.6 eV so that it can absorb visible light [600–602], while the band gap of the wurtzite structure is as high as 3.1–3.4 eV so that its light absorption is limited to the range of UV light [596, 603]. Nevertheless, the rocksalt structure is not stable at ambient pressure, and thus, stabilization at ambient pressure is required for its practical use. A striking report in 2017 [604] that the rocksalt structure can exist at ambient pressure when ZnO is strained under high pressure using HPT, which is mainly known as a metal processing method [2, 20, 23, 177]. Although enhanced photocatalytic activity was realized on the HPT-processed ZnO-containing samples [604–606], the fraction of the rocksalt phase was marginal, and thus, further attempts were made to enhance its fraction.

In a recent study, high pressure was applied to HPT-processed ZnO and the change in the fraction of the rocksalt structure was examined using *in situ* synchrotron high-energy XRD analysis in SPring-8, Japan [607]. A high-pressure application system including a heating unit as illustrated in Fig. 28a [608] is adopted for this XRD experiment, of which principle was introduced earlier [57] and modification was made to this *in situ* experiment [608]. The rocksalt structure in the sample processed by HPT under 6 GPa for 3 turns disappeared with heating to temperatures higher than 433 K under ambient pressure. However, its fraction increased to 100% after heating above 353 K by applying pressures more than ~9 GPa, and remained stable after cooling down to room temperature even after unloading to ambient pressure. In contrast, the formation of the rocksalt phase was considerably suppressed for the ZnO powder without processing by HPT (only a minor fraction was formed above 453 K under 12 GPa). Fig. 28b shows a pressure-temperature phase diagram reproduced from a report by Bayarjargal and Winkler [593]. Open symbols and closed symbols represent phase regions corresponding to the wurtzite structure and the rocksalt structure, respectively. Fig. 28b also includes the results by Decremps *et al.* [594], where the transformation point from rocksalt to the wurtzite structure is marked by open blue squares and that from wurtzite to the rocksalt structure by closed blue squares. The present
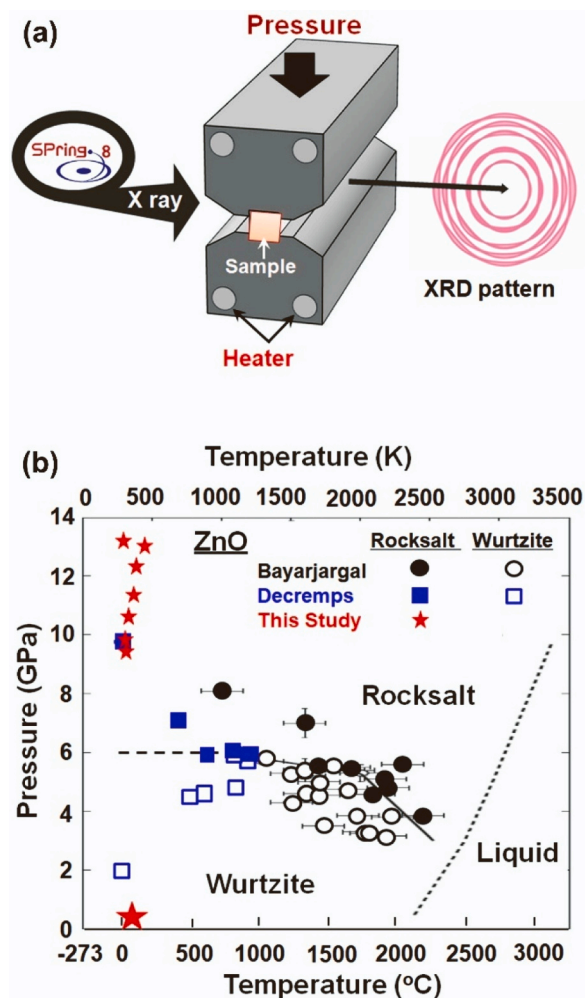
Fig. 28. (a) Schematic illustration of high-pressure application system for *in situ* XRD analysis at SPring-8, Japan [607]. (b) Temperature-pressure phase diagram of ZnO. Open and closed circles are reproduced from Bayarjargal and Winkler [593] for wurtzite and rocksalt structures, respectively. Open and closed blue squares are from Decremps *et al.* [594], representing transformation points from rocksalt to wurtzite structure and from wurtzite to rocksalt structure, respectively. Star symbols represent results of HPT-proceced ZnO in which rocksalt occupies 100% [607].

results are plotted as marked by star symbols in red. Inspection of Fig. 28b reveals that the presence of the rocksalt structure under high pressures is well consistent with the reports by Bayarjargal and Winkler [593] and Decremps *et al.* [594]. However, the presence of the rocksalt structure is also confirmed under ambient pressure and temperature. This exceptional result arose because the strain introduced in the sample by the HPT process generates internal pressure due to the mutual interaction of dislocations as argued in earlier papers [8, 584, 609].

In summary, SPD methods and particularly HPT are powerful tools to control phase transformations in ceramics. Such phase transformations, such as stabilization of 100% of the rocksalt ZnO phase which was confirmed by *in situ* high-energy XRD experiments, open a new path for the employment of these phases in functional applications such as photocatalysis.

4.3. Coupled in situ and theoretical studies of phase transformations

SPD under high pressure is mostly studied postmortem after pressure release, as reflected in old [1], recent [23, 182, 236] and latest [5] reviews. Here, recent *in situ* experimental and theoretical studies of coupled SPD, strain-induced phase transformations under high pressure
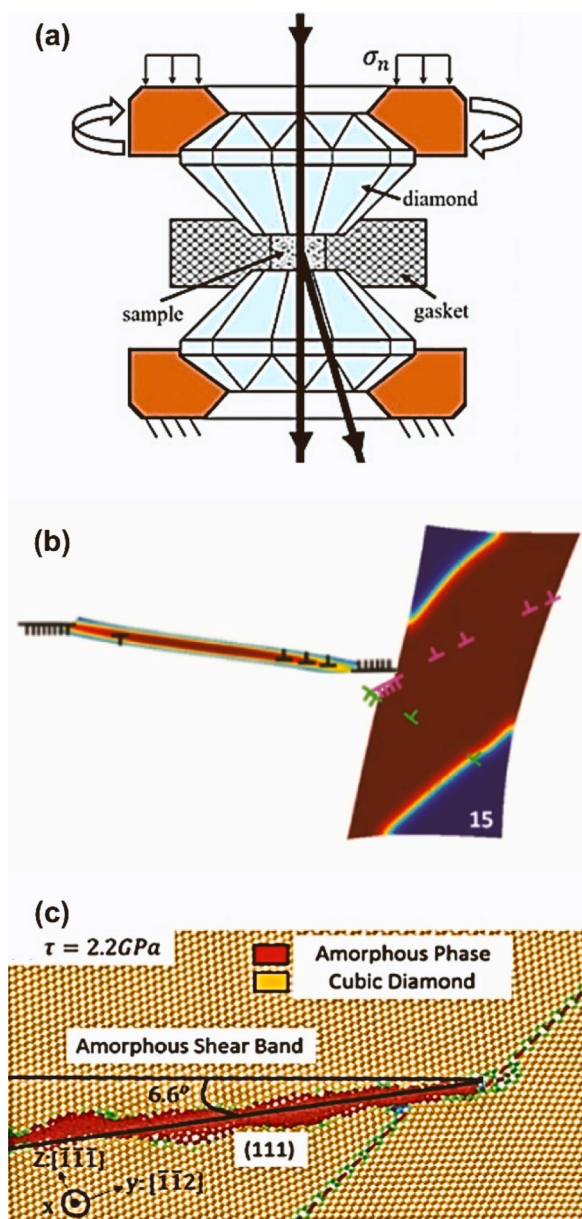
Fig. 29. (a) Schematic of RDAC. (b) Phase-field approach results showing dislocation pileup in the left grain produces a step at the grain boundary (superdislocation) with a strong stress concentrator leading to phase transformation and dislocation slip in the right grain [624]. (c) Molecular dynamics results showing dislocation pileup in the right grain produces a step at the grain boundary in Si-I phase and amorphization in the left grain [623].

obtained under compression in diamond anvil cell (DAC) or compression and torsion in rotational diamond anvil cell (RDAC) [8, 366] are summarized. In RDAC (Fig. 29a), two diamond anvils compress the sample within or without a gasket, like in traditional DAC, to high pressure. Then torque is applied, leading to the superposition of large shear-dominated straining on compression. The X-ray beam is directed along the axial direction for the characterization of the material. The utilization of XRD with synchrotron radiation allowed one to determine the radial distribution of volume fraction of phases and pressure [610–614], dislocation density and crystallite size in each phase [613, 614] and find the main laws of their evolution and interaction. Coupling with the finite element simulations of the sample behavior [615–617] allows the determination of fields of all components of the stress and plastic strain tensors and volume fraction of the high-pressure phase [618, 619] and provides a better understanding of ways to control

occurring transformations and corresponding microstructural evolution. Atomistic [620–622], nanoscale [514, 623–625] (Fig. 29) and scale-free phase-field simulations [626, 627] allow elucidation of the main physical mechanisms of the plastic strain-induced drastic reduction in phase transformation pressure (by one to two orders of magnitude [8, 612, 628, 629]), the appearance of new phases [630–632] and strain-controlled phase transformation kinetics [8, 610, 611, 619] in comparison with hydrostatic loading. Combining *in situ* experiments with multiscale theory potentially leads to the formulation of methods to control strain-induced phase transformation evolution and designing economic synthetic paths for the defect-induced synthesis of desired high-pressure phases, nanostructures and nanocomposites. It should be noted that *in situ* XRD during HPT [633, 634], HPS [608] and compression [607] were also attempted. However, XRD patterns in these cases are averaged over very heterogeneous fields, and just one value is measured for the prescribed load. Thus, it is much less informative than the axial diffraction measurements in RDAC. XRD in perpendicular geometry for the rotational Drickamer apparatus [635–637] has also a large error bar.

It was found that the study of strain-induced phase transformations is significantly simplified when steady states for microstructure and pressure-dependent yield strength are reached before the initiation of strain-induced phase transformations [610, 611]. For such a case, it was shown that (a) the minimum pressure for the strain-induced α-ω phase transformation in zirconium, and the pressure-dependent yield strength $\sigma_y(p)$ of ω-Zr are independent of plastic strain tensor ε_p and strain path ε_p^{path}; (b) crystallite size and dislocation density in a single phase ω-Zr are in addition independent of pressure; (c) crystallite size and dislocation density in ω-Zr and (with some outliers) α-Zr during phase transformation are independent of pressure, plastic strain tensor, and strain path and depend on the volume fraction of the high-pressure phase only. It was also found for zirconium [610, 611] and olivine [613] that there is a correlation between the Hall-Petch effect of the grain/crystallite size on the yield strength [638] and the minimum pressure for the strain-induced phase transformation, with corresponding theoretical justification. Similar results, including correlation for the inverse Hall-Petch effect [638] and the minimum pressure for the strain-induced phase transformations, were found for silicon [612]. Namely, in the region when the yield strength increases with the reduction in grain size, the minimum pressure for the strain-induced phase transformation reduces; while for smaller nanoscale grain sizes, the yield strength reduces, and the minimum pressure for the strain-induced phase transformation increases. These *in situ* results are consistent with results for Y_2O_3 [583], TiO_2 [582, 639] and ZnO [604], obtained with TEM: after phase transformation by HPT processing, the recovered high-pressure phases have smaller grain sizes and initial low-pressure phases have larger grain sizes. However, since TEM results are obtained *ex situ*, various other interpretations are possible [366], *i.e.* they are not conclusive.

The obtained results imply that the factors and mechanisms that affect the steady grain size (see original papers [364, 365, 640–642] and reviews [189, 643, 644]) and dislocation density [645] are important for controlling strain-induced phase transformations. They change the general wisdom that plastic shear is responsible for reducing phase transformation pressure. In fact, any mode of straining and strain paths that belong to some classes lead to the same phase transformation pressure and steady microstructure. For example, variations of crystallite size and dislocation density in the ω-Zr phase after α→ω phase transformations are shown in Figs. 30a and 30b, respectively. Since the plastic strain tensor and its path, as well as pressure strongly vary with radius and increasing load, approximate independence of the crystallite size and dislocation density and of the radius and load indicates that they reached steady values, which are independent of pressure, plastic strain tensor and its path. This issue is further discussed in Fig. 30c in which schematic of the evolution of the yield surface $f(\boldsymbol{s}, \boldsymbol{\varepsilon}_p, \boldsymbol{\varepsilon}_p^{path}) =$
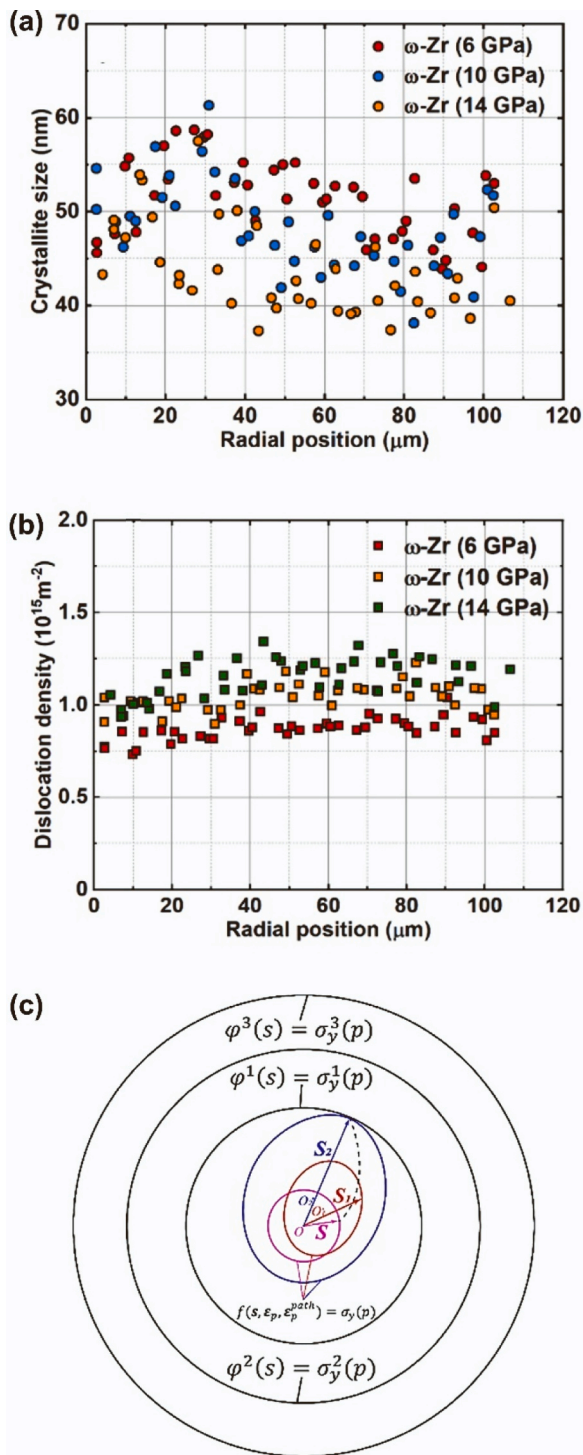
Fig. 30. (a,b) Radial distribution of (a) crystallite size and (b) dislocation density in the ω-Zr phase for three compression steps after full transformation. Pressures in the upper right corner designate maximum pressure at the sample center [614]. (c) Schematic of the evolution of the yield surface $f(s, \varepsilon_p, \varepsilon_p^{path}) = \sigma_y(p)$ until it reaches the fixed surface of perfect plasticity $\varphi(s) = \sigma_y^1(p)$ in "5D" space of deviatoric stresses s at fixed pressure p, after which the material deforms like perfectly plastic, isotropic, and independent of ε_p and ε_p^{path} (for some classes of straining paths, several other fixed surfaces of perfect plasticity $\varphi^i(s) = \sigma_y^i(p)$ with larger yield strengths $\sigma_y^i(p)$ can be reached) [614].

$\sigma_y(p)$ until it reaches the fixed surface of perfect plasticity $\varphi(s) = \sigma_y^1(p)$ in "5D" space of deviatoric stresses s at fixed pressure p is illustrated [614]. The initial yield surface and $\varphi(s) = \sigma_y^1(p)$ are isotropic (circles). Two other yield surfaces depend on ε_p and ε_p^{path}, and acquire strain-induced anisotropy, namely shifted centers O_1 and O_2 (back stress) and ellipsoidal shape due to texture. When the yield surface reaches $\varphi(s) = \sigma_y^1(p)$, the material deforms like perfectly plastic, isotropic with the fixed surface of perfect plasticity. However, for α-Zr for some classes of straining paths, several other fixed surfaces of perfect plasticity $\varphi^i(s) = \sigma_y^i(p)$ with larger yield strengths $\sigma_y^i(p)$ (due to larger steady dislocation density and smaller crystallite size can be reached.

In situ studies [614] lead to a key question: for which classes of plastic strain and strain path (and maybe pressure path), the material remains in each of the steady states, and for which loading classes, the material behavior jumps from one steady state to another? This question is just a translation into the language of plasticity theory of known technological problem: why different SPD technologies lead to different steady microstructures and how to design the loading process to reduce the grain size and phase transformation pressure and increase dislocation density and strength. It is also shown that incomplete phase transformation is a much more effective way to reduce the grain size to produce nanocomposite materials with controllable strength and ductility than SPD alone [366, 610, 611]. In addition, SPD under normal pressure, *e.g.* by rolling, leading to one of the steady states followed by compression or HPT at relatively low pressure, is a more economical way to produce nanostructured high-pressure phases and nanocomposites than HPT of annealed materials. The possibility of manipulating synthetic paths may lead to new economic technologies at relatively low pressures, room temperature, and without catalysts, *e.g.* for cubic and hexagonal diamond, cubic and wurtzite BN, Si-III, *etc.* Application of the concept of plastic strain-induced phase transformations (instead of pressure-induced phase transformations) [8] may also change various geological interpretations, like the mechanism of the deep-focus earthquakes [646] and the appearance of microdiamonds in the Earth's crust [629]. Application of ultra-SPD [178] may lead to discoveries in strain-induced phase transformation. Still, the entire field of fundamental study of SPD and plastic strain-induced phase transformation is in its infancy; one needs to find whether the above results are valid for other materials and material classes and to find a much more detailed theoretical description at each of the four scales.

5. Mechanical properties

The most visible effect of SPD, particularly in metallic materials, is the enhancement of mechanical properties such as strength and hardness, mainly due to the grain refinement effect [3] and the Hall-Petch mechanism [6, 7]. Some studies, however, suggested that the strengthening of these materials by the dislocation hardening mechanism can be quite significant [45]. Hardening by other factors like precipitation, twins, segregation, phase transformation and spinodal decomposition was also reported in these materials [305, 647]. Materials after severe plastic deformation do not always exhibit hardening, and it was shown that softening can occur in pure metals with low melting temperatures, despite a decrease in grain size and an increase in dislocation density [399]. Such behavior, which was reported in lead, tin, indium and aluminum with ultrahigh purity, was attributed to the contribution of thermally-activated phenomena [399, 648]. In magnesium, which also has a low melting temperature, it was shown that storage of HPT-processed samples for several years leads to increasing grain size, decreasing dislocation density and an unusual increase in hardness via anneal hardening [649]. Softening can occur in some metallic alloys by unusual grain coarsening, phase transformation or the activation of thermally-activated phenomena such as grain boundary sliding [38, 650]. Despite some exceptions mentioned above, strength usually

increases after SPD processing and this strengthening is not accompanied by a complete loss of plasticity, as recognized by Segal *et al.* after ECAP processing [27]. HPT studies have also shown that SPD-processed materials can exhibit a good combination of strength and plasticity, although their work hardening and uniform ductility are limited [194]. A large number of studies attempted to enhance the ductility of SPD-processed materials and there is quite good progress on this issue [182, 651].

Studies on the mechanical properties of SPD-processed materials can be classified as: (i) torque measurements which originated from Bridgman's works on HPT in the 1930 s [20], (ii) hardness-strain behaviors which can provide quick information about the microstructural evolution and the occurrence of steady state [400], (iii) tensile, compression and bending properties which are of significance for commercialization of SPD-processed materials [305], (iv) superplasticity which occurs frequently in SPD-processed materials due to large fraction of grain boundaries [652], (v) fatigue properties [653], (vi) creep properties [654], (vii) wear resistance [655], (viii) fracture toughness [656], *etc.* In the following sections, some recent findings on strain hardening, anneal hardening, creep resistance, superplasticity and hydrogen embrittlement resistance of SPD-processed materials are discussed. Other mechanical properties are reviewed in other chapters of this article.

5.1. Strain hardening

As mentioned earlier, SPD is effective not only for grain refinement [1, 657, 658] but also in the generation of various kinds of defects, particularly dislocations [2, 659] which accordingly can enhance

strength. Moreover, SPD can fragment intermetallic phases into nanosized in alloys containing elements with low diffusivity and low solubility [178], such as Al-Fe [310], Al-Ca [311], Al-Zr [332], Al-RE (RE: rare earth elements) [315], Mg-Ca [660], Mg-Ti [322] and Mg-Zr [334], and further enhance the strength. The contribution of grain boundaries to strengthening can be estimated using the Hall-Patch relationship [6, 661, 662].

$$\Delta\sigma_{GB} = \frac{k}{\sqrt{d}} \quad (4)$$

where k is the Hall-Petch coefficient and d is the average grain size. The contribution of dislocations can be estimated through the Bailey-Hirsch relationship [663].

$$\Delta\sigma_{\rho} = \alpha MGb\sqrt{\rho} \quad (5)$$

where α is a constant, M is the Taylor factor, G is the shear modulus, b is the Burgers vector, and ρ is the dislocation density. The HPT process, which is operated under high pressure for processing various materials [181, 512, 609, 664–667], is believed to be the most effective SPD technique for hardening through grain refinement and dislocation generation [668, 669]. However, the sample in the HPT process is a disc that experiences heterogeneous strain distribution [154, 177], but methods such as ARB and HPS produce sheets that experience more homogenous strain [670–672]. HPS has the benefits of HPT for hardening because it can be applied under high pressure, but its merit is that it applies to sheets [673–676], rods [238, 677–679] and pipes [239]. The pressure in ARB is not as high as HPT and HPS, but it is still effective
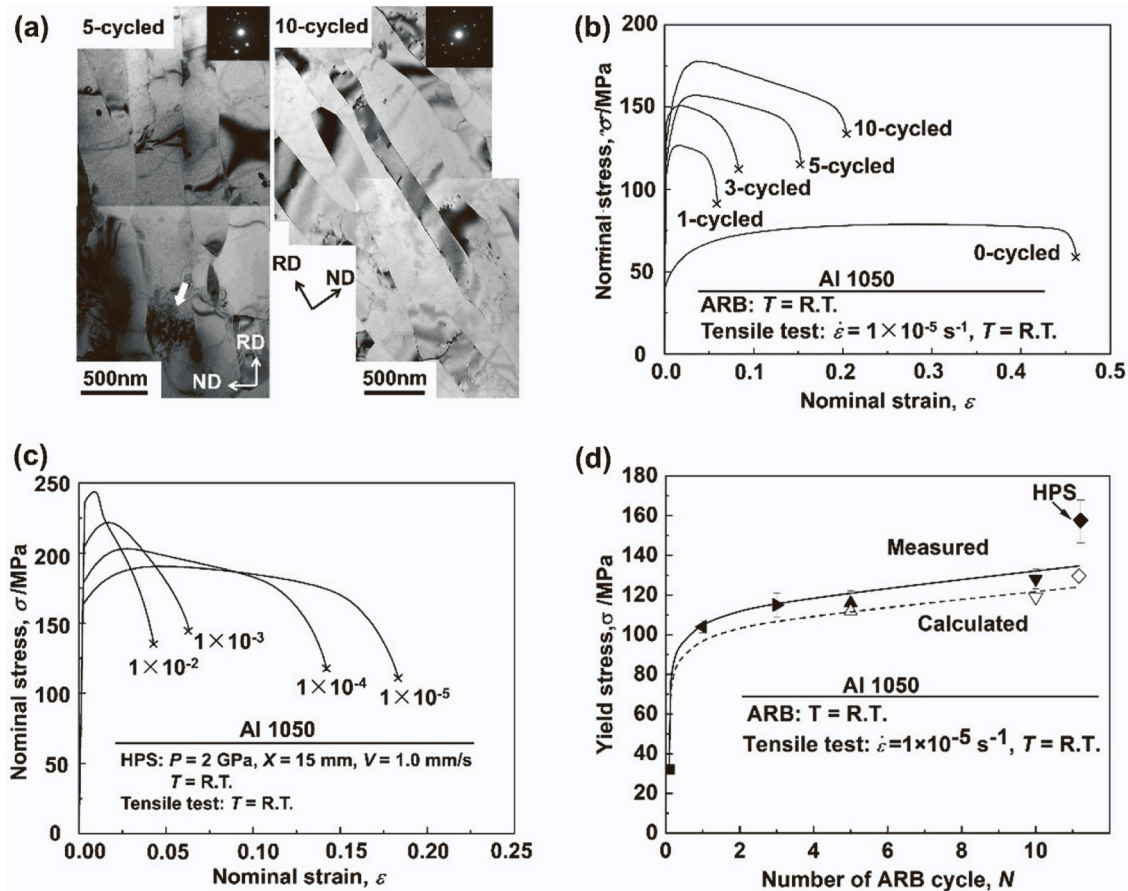
Fig. 31. (a) TEM bright-field images of aluminum after five and 10 ARB cycles. (b) Nominal stress-strain curves at a strain rate of 1×10^{-5} s^{-1} for aluminum after 0, 1, 3, 5 and 10 ARB cycles. (c) Nominal stress-strain curves with strain rates ranging from 1×10^{-2} to 1×10^{-5} s^{-1} for HPS-processed aluminum. (d) Plots of yield stress against the number of ARB cycle at a strain rate of 1×10^{-5} s^{-1}, including value of HPS-processed sample and values calculated by grain boundary and dislocation hardening [675].

in enhancing strain hardening in sheets [19, 227].

Fig. 31a displays typical TEM microstructures of sheets after ARB processing, revealing elongated grains well-developed after five and 10 cycles along the rolling direction, with mean grain thicknesses of 310 and 240 nm, respectively [675]. A significant grain refinement is evident when compared with the mean grain size after annealing, which is 31 μm. Concurrently, Fig. 31b demonstrates a significant strain hardening by increasing ARB cycles. The strain rate dependence of the nominal strength is observed in sheets processed by HPS (Fig. 31c) [675], a fact that was also reported in ARB-processed sheets [679, 680]. A comparison of the yield stress of aluminum processed by HPS and ARB with the calculated strength through Equations 4 and 5, is shown in Fig. 31d. It was shown that yield strength by the HPS process is comparable to those obtained by the ARB process for similar equivalent strains (a sliding distance of 15 mm for HPS compared to 10 ARB cycles).

It is concluded that strain hardening of pure metals can be simply justified through Hall-Petch and dislocation hardening mechanisms when grain sizes are at the submicrometer level. Strain hardening becomes more complicated by the presence of second phases and precipitates [310, 658]. Moreover, breaks in the Hall-Petch mechanisms can occur when grain sizes are reduced to the nanometer level [681].

5.2. Anneal hardening

Cold working increases the strength of metallic materials. Especially for severe plastic strains, strength levels of up to 1/3 of the theoretical

strength can be reached [682, 683]. Subsequent heat treatment generally reduces strength as the microstructure is gradually transferred back to the state before cold deformation [434, 684]. However, for sufficiently fine grain sizes and restricting the heat treatment to the recovery regime (*i.e.* avoiding recrystallization or grain growth), further strengthening instead of a softening, can be observed [671, 685–690]. This extra strengthening increases with annealing temperature until grain coarsening initiates (Fig. 32a). First reports on this subject date back to the 1960 s [691–693] and were related to ordering phenomena. However, examination of nanostructured metals in the past decades indicated that anneal hardening can also occur for single-phase metals and alloys, where decomposition or ordering can be excluded. This is also evident from isothermal annealing curves, showing a constant hardness plateau after a rapid initial increase (Fig. 32b) [685, 694], which contrasts with precipitation or decomposition sequences (*e.g.* see [503]).

For single-phase metals, the hardening is hence a consequence of the reduction of available inter- and intragranular defects, accompanied by solute or impurity segregation to grain boundaries [671,685–687,689, 690]. The required temperatures for the annihilation of dislocations at high-angle boundaries thus perfectly agree with those leading to the maximum anneal hardening increment (Fig. 32c) [695, 696]. The loss of existing dislocation debris requires the activation of dislocation sources after the heat treatment to realize plastic strain [671, 697, 698]. For sufficiently fine grain sizes, these sources are predominantly located at grain boundaries [699] and are relaxed during the annealing treatment
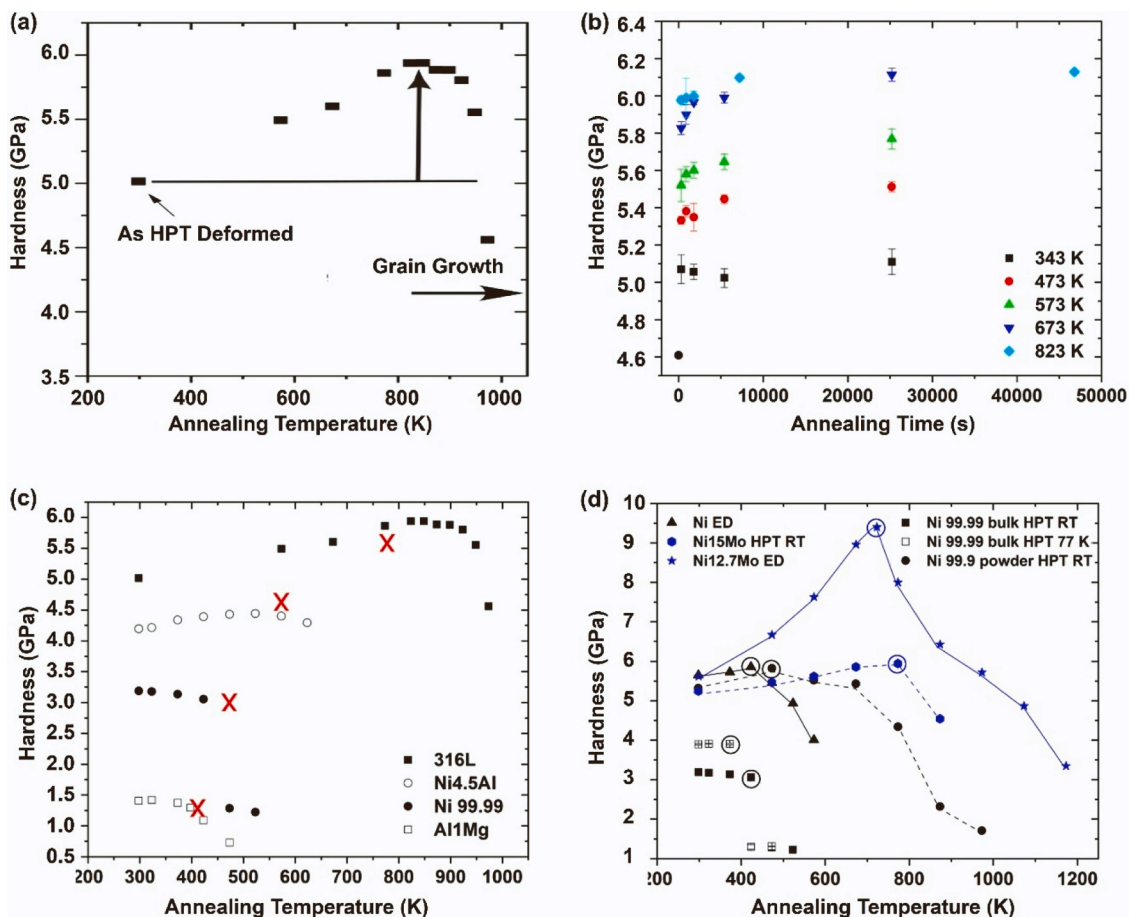
Fig. 32. (a) Hardness after isochronal (30 min) annealing of 316 L steel processed by HPT at ambient temperature (grain growth occurs above 823 K) [687]. (b) Isothermal annealing of 316 L steel processed by HPT for different times [694]. (c) Hardness of several nanostructured FCC materials after 30 min annealing as a function of annealing temperature (temperatures for the annihilation of lattice dislocations in high-angle grain boundaries are highlighted) [695, 696]. (d) Hardness of various nanostructured nickel and Ni-Mo alloys as a function of annealing temperature (annealing time <1 h), indicating that the temperature leading to the maximum hardness stays almost unaffected, despite large differences in grain size [690].

[685, 697, 698, 700], enhancing the stresses needed to operate these sources [697]. The activation stress of a grain boundary source could be additionally affected by solute or impurity segregation [701]. For example, different extents of anneal hardening were reported for different solutes but similar grain sizes such as in Ni-W and Ni-Mo alloys [685, 688]. However, active interactions of segregated atoms with propagating dislocations are not expected from strain rate jump tests at ambient and elevated temperatures. At least for the studied strain rates and temperatures, a positive rate sensitivity was measured in any case [702].

The extent of the anneal hardening can be significant and may even double the strength of the nanostructures [688, 703], making it attractive to further improve the mechanical properties of SPD-processed materials. Apart from a few exceptions [704], the strength increment was found to increase with decreasing grain size [685, 688, 702]. This is reasonable, since according to Equation 6 [705, 706], the time, t, to annihilate dislocations at grain boundaries (apart from material constants such as atomic volume Ω, shear modulus G, and boundary width δ) depends only on the boundary diffusivity, D_{GB} and the grain size d.

$$t \sim \frac{k_B T d^3}{G \Omega \delta D_{GB}} \tag{6}$$

While smaller grain sizes recover faster and thus allow for a larger hardening, the temperatures leading to the maximum hardness increase are not significantly dependent on grain size [690]. This is evident by comparing specimens with different grain sizes, either synthesized by SPD at different temperatures or by comparing SPD-processed alloys with batches prepared by deposition techniques (allowing usually for

smaller grain sizes), as shown in Fig. 32d. The pronounced dependence of boundary diffusivity on temperature may explain this result.

As the microstructural stability is crucial for the fatigue strength of nanostructures [707, 708], and cyclically induced grain coarsening depends on the (micro)plastic strain amplitude [709, 710], anneal hardening should also have a pronounced effect on the fatigue strength. Since the loss of dislocation debris and the hardening of dislocation sources shift the onset of plasticity to higher stress levels, the fatigue limit should be significantly influenced by anneal hardening. Indeed, this has been observed for nanostructured nickel and 316 L austenitic steel [711, 712], allowing for an additional 60% increase in the fatigue strength compared to the as-HPT deformed condition (Fig. 33a) [712, 713].

However, anneal hardening drastically shortens ductility (Fig. 33b) [671, 712, 714]. This is not because of an embrittlement effect (e.g. induced by impurity segregation), as can be deduced from the micro-ductile fracture surfaces for as-deformed and annealed state (Fig. 33c). The loss of ductility and early failure is related to an enhanced tendency for strain localization, as defect generation after the heat treatment softens the material. Allowing grain growth ($d > 500$ nm), the strain softening can be balanced by hardening from dislocation-dislocation interactions [715], but the full strengthening potential is not exploited due to the coarsening. Current research activities aim to identify strategies to avoid strain localization without negating anneal hardening. Manipulation of the grain boundary structure, for instance by introducing nanometer-thick amorphous films [716, 717], or by applying slight plastic strains after the anneal hardening treatment [718, 719], seems promising in this regard (Fig. 33d). Future work should thus elaborate processing strategies to synthesize materials with dedicated
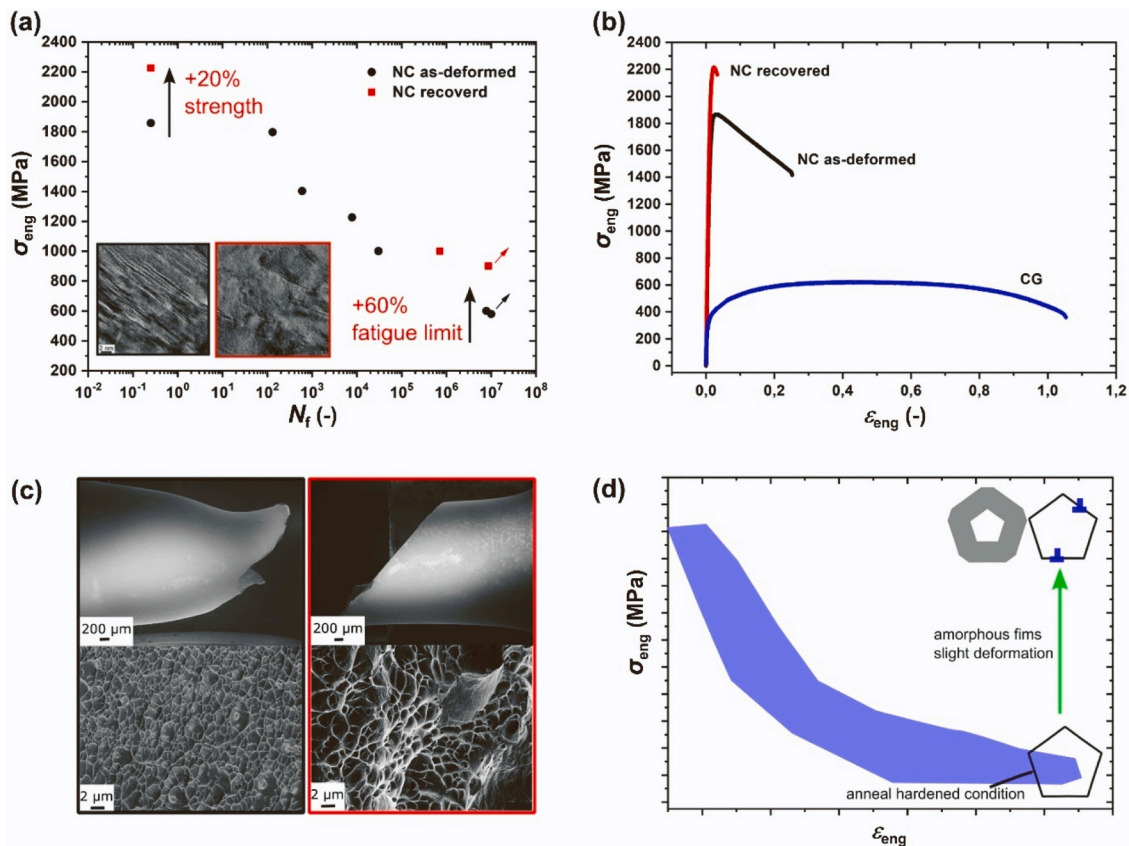
Fig. 33. (a) Fatigue S-N (stress-cycle to failure) curves showing the effect of anneal hardening (recovery) on the quasi-static strength and the fatigue limit of a nanocrystalline 316 L austenitic steel prepared by HPT at room temperature [712]. (b) Representative engineering stress-strain curves of a uniaxial tensile test obtained on the same samples as in (a), indicating that anneal hardening drastically shortens the elongation to failure [712]. (c) Representative images of fractured tensile specimens and the corresponding fracture surfaces of a nanocrystalline 316 L steel in HPT-processed (black) and anneal-hardened (red) conditions [712]. (d) Schematics showing the general problem of the strength-ductility trade-off applying especially for anneal hardened metals, and potential solutions to this problem [690].

boundary structures, but also to understand the effect of post-anneal deformation. This could pave the way towards unprecedented combinations of strength and ductility.

5.3. Creep resistance

Creep is defined as the time-dependent plastic strain under constant applied stress and/or load at a given temperature. The various deformation mechanisms operating during creep can be defined in terms of the creep rate given by an established phenomenological relationship [720].

$$\dot{\varepsilon} = \frac{ADGb}{kT} \left(\frac{b}{d}\right)^P \left(\frac{\sigma}{G}\right)^n \tag{7}$$

where D is the diffusion coefficient, G is the shear modulus, b is the Burgers vector, k is Boltzmann's constant, T is the absolute temperature, d is the grain size, σ is the applied stress, p is the exponent of the inverse grain size. n is the stress exponent which is equal to $1/m$ where m is the strain rate sensitivity and A is an appropriate dimensionless constant. The value of D is given by:

$$D = D_o \exp\left(-\frac{Q}{RT}\right) \tag{8}$$

where D_o is a frequency factor, Q is the activation energy for the creep process and R is the gas constant. It follows, therefore, that the creep mechanism is defined by the specific values of Q, n (or m), p and A and these values may be determined by conducting appropriate creep experiments. A mechanism of creep deformation can be particularly identified through knowledge of the stress exponent n using the following equation [721]:

$$n = (\partial \ln \dot{\varepsilon} / \partial \ln \sigma)T \tag{9}$$

The creep behavior of polycrystalline materials with conventional coarse grain sizes is well described through a series of constitutive equations that delineate different deformation mechanisms [721–724]. According to the value of the stress exponent n, the following types of creep regions can be classified in which corresponding operating deformation mechanisms exist: diffusion-based processes ($n = 1$) [725–727], a combination of diffusion and dislocation-based processes such as grain boundary sliding ($n = 2$) [721, 723, 728, 729] and Harper-Dorn creep ($n = 1$) [730, 731], the power-law controlled mechanisms like viscous glide creep ($n = 3$) [724] and power-law creep by glide and climb of dislocations ($n = 4$–7) [721, 723, 724]. At extremely high applied stresses, a power-law breakdown region with very high values of n is observed [722, 732].

Recent progress in producing UFG materials by SPD processing [5, 180] together with factors like reduced grain sizes, microstructure instability, non-equilibrium grain boundaries, very high intragranular dislocation densities and increasing diffusivity resulted in significantly different creep behavior of UFG materials in comparison with coarse-grained materials. Therefore, questions naturally arise about whether the creep deformation and fracture mechanisms in UFG materials are similar to those operating in coarse-grained counterparts, as reviewed in several publications [654, 733–739]. Most studies were performed on pure metals or model binary alloys to separate the basic mechanisms related to grain refinement and microstructure. However, creep experiments have been limited to a narrow range of testing temperatures and stresses because of the instability of non-equilibrium grain boundaries. Further, the experimental results and their interpretations by different authors are not in agreement with each other due to different SPD processing techniques and routes used [740]. It was reported that in pure aluminum and copper, under the same loading conditions, the measured minimum creep rate $\dot{\varepsilon}_{min}$ in the SPD-processed materials with ultrafine grain size was slower and the time to fracture (creep lives t_f) was longer than in the same material in a coarse-grained

state [5, 735, 738, 740–746]. However, such positive effects dramatically decrease with increasing value of imposed strain. Microstructural analysis showed that after the first ECAP pass grain boundaries were predominantly low-angle ones and high-angle grain boundary fraction in SPD-pressed specimens significantly increased with increasing value of imposed strain [735]. This implies that high-angle grain boundaries have a lower strengthening effect in creep than low-angle grain boundaries [747]. The important conclusion from the creep experiments on UFG pure materials with unstable microstructure is that conventional creep mechanisms, already proposed for coarse-grained materials, may be used also to explain the creep behavior in UFG materials [735–737, 746].

The creep behavior of reasonably stable precipitation and oxide dispersion strengthened structural materials processed by various SPD techniques [654, 748–753] in principle matches the behavior of coarse-grained materials [721–724]. The best way to confirm this view is to compare the resultant creep characteristics of UFG materials with those attained in unprocessed conditions of the same material. To illustrate the creep behavior of polycrystalline materials, it is most informative to use creep curves, which represent graphically the time dependence of creep strain. Fig. 34a shows schematically three creep stages after instantaneous strain ε_0 upon loading: a primary or transient creep (Stage I), a secondary or steady-state creep (Stage II), and a tertiary or accelerated creep (Stage III) ending up creep fracture. Figs. 34b, 34c and 34d show the real creep curves of the precipitate-strengthened Zr-2.5 Nb (wt%) alloy [754], the austenitic stainless S304H steel [755] and the heat-resistant high chromium ferritic-martensitic P92 steel [750, 756], respectively. Inspection of these figures leads to the following observations. First, the processing by SPD has a detrimental effect on creep life. Generally, UFG precipitate-strengthened materials exhibit shorter creep lives than the coarse-grained ones under the same loading conditions which limits their engineering utility. Second, it appears that the pertinent ductility (fracture plasticity) enhancement is associated with the increase in the fraction of high-angle grain boundaries. Third, in some cases, the grain refinement after a higher number of SPD operations (*e.g.* a higher number of ECAP passes) could result in a dramatic decrease in the creep resistance (see Fig. 34b).

In a similar way as in Equation 7, the equation for the time to fracture, t_f is given by [757, 758]:

$$t_f = B (\sigma)^{-m} \exp (Q_f / kT) \tag{10}$$

where B is a material constant, $m = - (\partial \ln t_f / \partial \ln \sigma)_T$ is the stress exponent of the time to fracture, and Q_f is the activation energy for the time to fracture. Fig. 35 shows stress dependences of the minimum creep rate $\dot{\varepsilon}_{min}$ (Figs. 35a and 35c) and the time to fracture (Figs. 35b and 35d) [754, 756, 759–762]. Determined values of the stress exponents n and m imply that UFG structural materials obey the power-law relationship and suggest that occurring creep deformation mechanisms are similar to those operating in the same coarse-grained materials [654, 736]. However, such a conclusion is based on mostly short-term creep experiments at medium and high applied stresses where intergranular (dislocation) mechanisms are dominant. By contrast, diffusion-controlled grain boundary-mediated processes are important at low applied stresses.

In summary, creep mechanisms in UFG structural materials across all stress scales are not clearly resolved at present due to the complexity of the phenomenon. Long-term creep tests should be carried out to properly evaluate the creep strength of UFG materials under service conditions.

5.4. Superplastic deformation

When metal samples are pulled in tension they generally fail at relatively low elongations, typically in the range of ~10–50%. But under some conditions, much larger elongations may be achieved and this
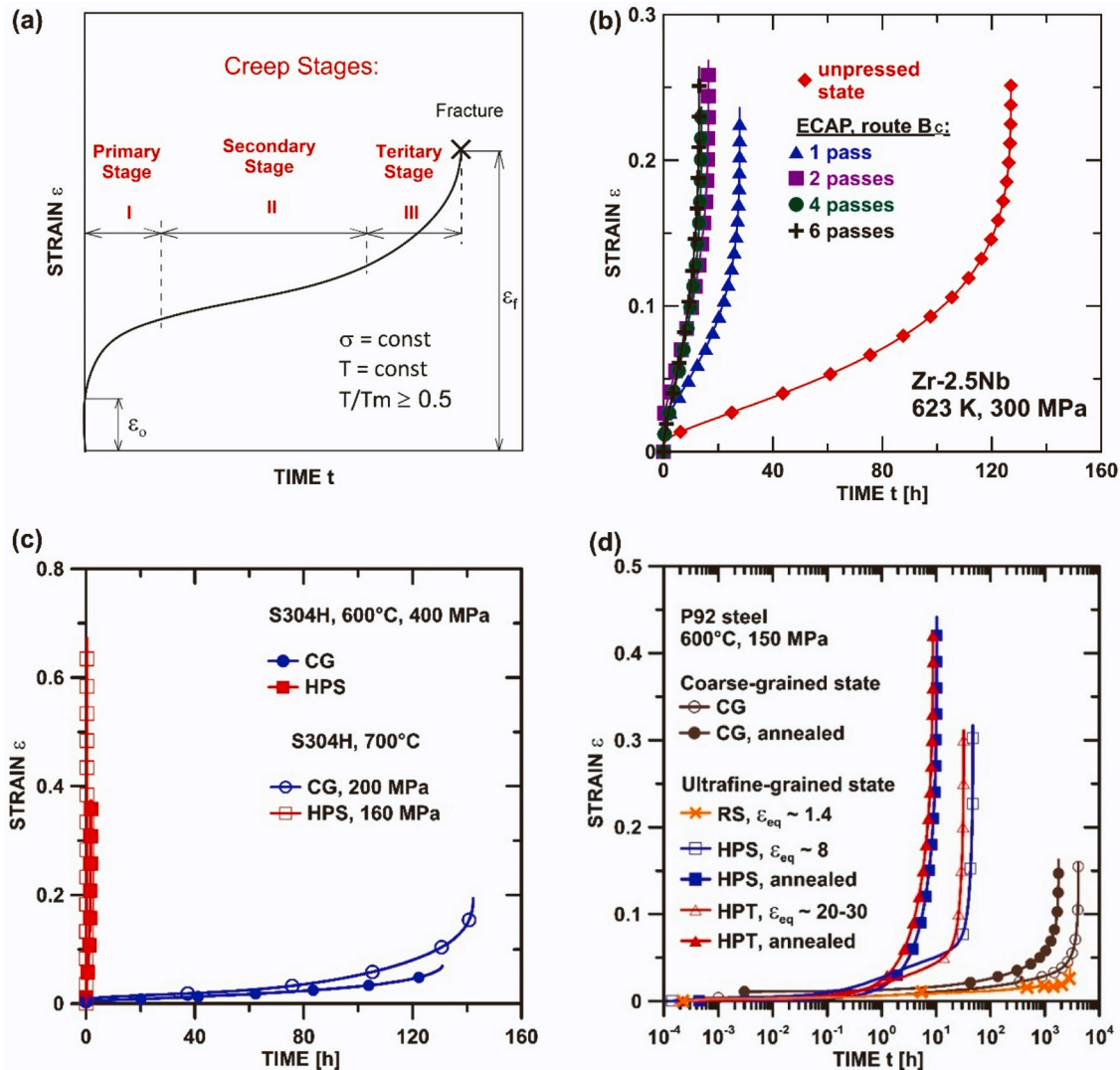
Fig. 34. (a) Schematic representation of a creep curve. (b) Creep curves for Zr-2.5 Nb (wt%) cladding alloy [754]. (c) Creep curves for austenitic S304H steel [755]. (d) Creep curves for creep-resistant P92 steel with 9 wt% Cr [756].

becomes important because of the potential for using these materials in forming operations. Relatively high elongations, of the order of a few hundreds of percent, were first reported in the scientific literature about one hundred years ago [763, 764] but it was only later, in 1934, that a report appeared from Pearson in England documenting a remarkable tensile elongation of ~1950% in a near-eutectic Bi-Sn alloy together with a similar high elongation of ~1505% in a Pb-Sn alloy when these samples were pulled to failure at room temperature [24]. The result for the Bi-Sn alloy is shown in Fig. 36 where the tensile sample has been coiled after failure to facilitate the recording of a photographic record. Although this result was unique and truly remarkable, it attracted little interest in western scientific circles where it remained simply a laboratory curiosity. Nevertheless, similar investigations were undertaken in the Soviet Union and numerous reports appeared in the Russian literature describing the potential for achieving high elongations in various metals when pulling in tension. In fact, it was the translation of the Russian word *sverkhplastichnost'*, meaning "ultrahigh plasticity", that led to the introduction of the new word of "superplasticity" in the English language literature when it first appeared in Chemical Abstracts in 1947 [765].

It was the publicity from these Russian articles, and especially the publication of a comprehensive review of the Russian results [766], that prompted establishing a superplastic testing facility at M.I.T. and the

subsequent demonstration that superplastic forming provided the potential for fabricating, relatively easily, complex curved shapes that may be used for many industrial applications [767]. This represented the nucleus of the modern superplastic forming industry which now processes many thousands of tons of sheet metals and produces beautifully curved products that have many applications in numerous consumer and architectural applications and especially in fabricating the bodies and many major parts for the aerospace and automotive industries. A review was presented earlier describing the transition of superplasticity from a laboratory curiosity to a major tool in modern industrial metal forming operations [768]. Full details of superplastic forming are now available [769, 770] including overviews [771–774] and descriptions of the development of applications in specific industries such as in the manufacture of cars [775].

Superplastic flow is a diffusion-controlled creep process and it is reasonable to anticipate that it will be governed by the conventional rate equation that is used to denote the steady-state creep rate in all crystalline materials. Specifically, in high-temperature creep, the steady-state creep rate for all flow mechanisms is expressed through a general creep relationship (Equation 7) [723, 776], given in the previous chapter. Early tests were conducted in superplasticity where tensile specimens were pulled at the same high temperature but using a different strain rate for each sample and these results showed that the
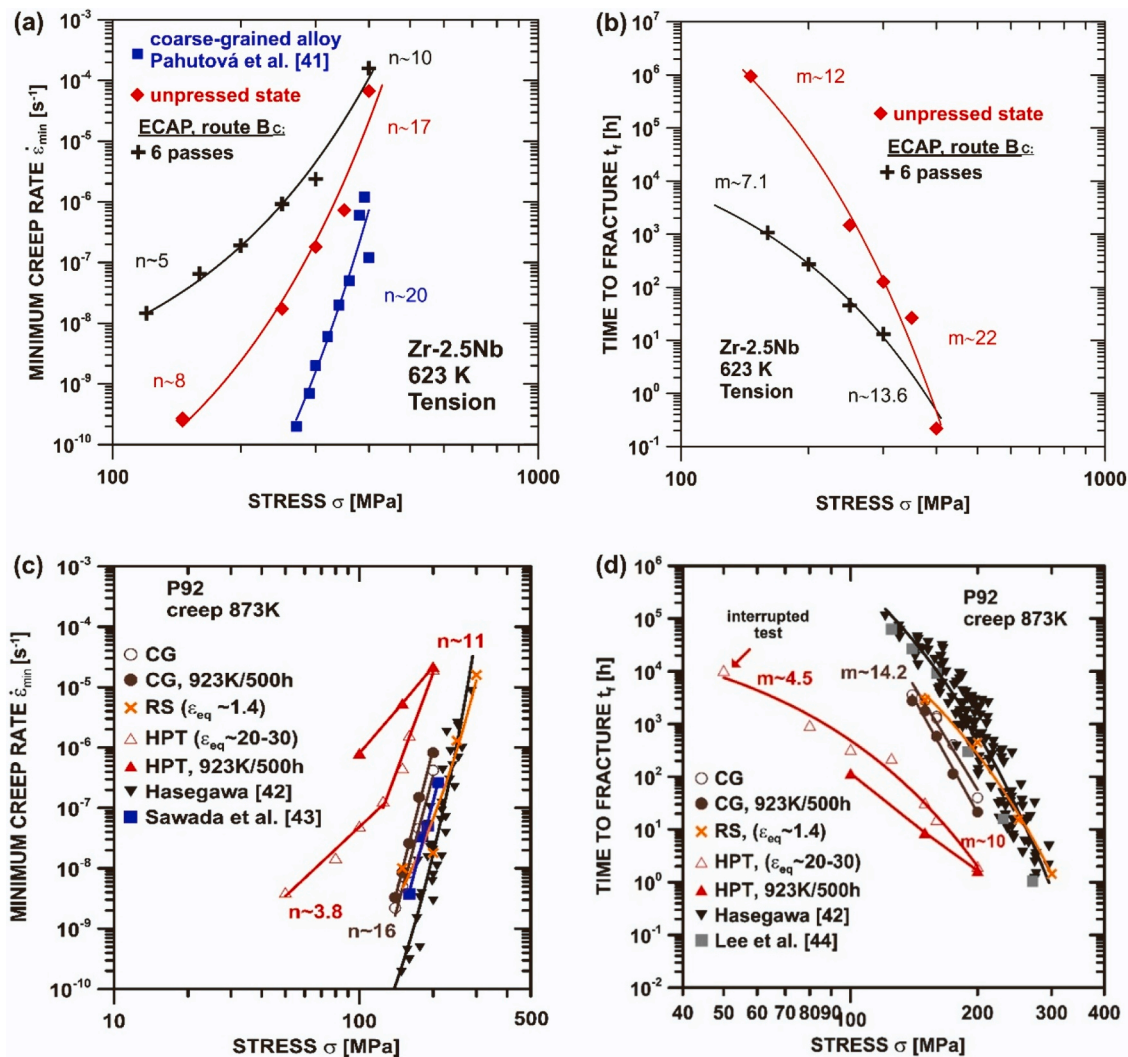
Fig. 35. Stress dependences of (a,c) the minimum creep rate $\dot{\varepsilon}_{min}$, and (b,d) the time to fracture t_f: for (a,b) Zr-2.5 Nb (wt%) alloy [754] and (c,d) P92 steel [756]. The creep results for coarse-grained materials published by Pahutova *et al.* [759], Hasegawa [760], Sawada *et al.* [761], and Lee *et al.* [762] are also listed.
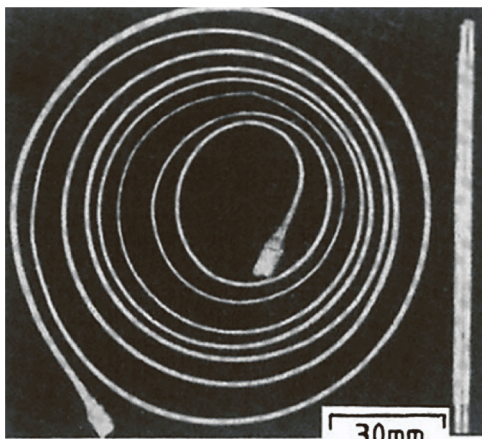
Fig. 36. An exceptional superplastic elongation of ~1950% in a Bi-Sn alloy, reported by Pearson [24].

flow stress varied with the strain rate through three distinct regions where region I at low strain rates was not superplastic with a value of m ≈ 0.2, region II at intermediate strain rates exhibited superplastic flow with m ≈ 0.5 and region III at high strain rates was again not

superplastic with m ≈ 0.2 [777]. These results demonstrate that the strain rate sensitivity is close to ~0.5 in superplastic flow and comprehensive sets of experiments, covering a range of experimental variables, showed that superplastic flow required a small grain size, typically less than ~10 μm, and a temperature typically higher than ~0.5T_m where T_m is the absolute melting temperature [778]. By using experimental data to construct deformation mechanism maps for superplastic materials [779], it was established that the critical grain size delineating the onset of superplastic flow is a grain size equal to or smaller than the equilibrium grain size that forms within the grains under creep conditions. These equilibrium grain sizes are similar for metals [720], ceramics [780] and geological materials [781, 782].

In superplasticity, the polycrystalline grains remain essentially equiaxed so that the dominant flow process is grain boundary sliding [783] but this must be accompanied by the occurrence of some intragranular slip to prevent the opening of cracks at the grain boundaries. Experimental evidence is available confirming the occurrence of this slip [784–787] including some recent reports where tests were conducted on a superplastic Al-Mg-Li alloy [788–790]. Using experimental results, a model for superplasticity was developed where grain boundary sliding occurs on a boundary and thereby produces a stress concentration at a triple point, this leads to slip in the next grain so that the dislocations pass through the grain and pile up at the opposite grain boundary in the absence of any subgrain boundaries and finally the rate of flow is

controlled by the climb of these dislocations into the boundary. For these conditions, the superplastic strain rate is given by the general creep relationship with $D = D_{gb}$ for grain boundary diffusion, $n = 2$, $p = 2$ and with A having a value of ~10. Based on the available experimental data, superplasticity is now defined as an elongation of at least 400% and a strain rate sensitivity close to $m \approx 0.5$ so that the stress exponent is $n \approx 2$ [346].

The requirement of a small grain size for superplasticity was achieved initially in the superplastic forming industry by subjecting metals to appropriate thermo-mechanical treatments but these procedures were not capable of producing grain sizes smaller than ~2–3 μm. This situation changed in 1988 with a Russian publication showing that a much smaller grain size may be achieved using the procedure now known as HPT [33]. This report introduced the processing of metals using SPD techniques and this approach has now been adopted and investigated in many laboratories around the world. Thus, materials have been processed to give submicrometer or nanometer grain sizes using the procedures of HPT [177], ECAP [193] and very recently using the new processing technique of t-HPS [54, 159]. To obtain a direct comparison with the very early work of Pearson [24], recent investigations have been conducted using t-HPS on various Bi-Sn alloys that are close to the eutectic structure [223]. An example of the excellent superplasticity that may be attained by t-HPS is shown in Fig. 37 where an elongation of 2320% was achieved after processing through 100 turns and pulling to failure at room temperature [224].

In summary, superplasticity refers to a tensile elongation of at least 400% and a strain rate sensitivity close to ~0.5. This requires a very fine grain size, typically smaller than ~10 μm, and in practice, exceptionally small grain sizes, in the submicrometer or nanometer range, may be achieved using SPD processing. Recent experiments using these new SPD techniques have demonstrated the potential for achieving excellent superplastic properties.

5.5. Low- and room-temperature superplasticity

As mentioned earlier, high-temperature plastic flow, including superplasticity, can be expressed by the general creep equation (Equation 7) [791]. The temperature dependence of superplasticity arises from the presence of the diffusion coefficient in the general creep equation. The creep equation shows that decreasing grain size increases strain rate and decreases the temperature of superplasticity. Such an effect of grain size on superplasticity leads to two types of superplasticity: low-temperature superplasticity and high-strain rate superplasticity. As the most effective grain refinement techniques, SPD methods have been used effectively to attain significant grain refinement leading to low-temperature superplasticity. Al-, Mg- and Ti-based alloys are the most commonly studied alloy systems to achieve low-temperature superplasticity using SPD. Details of SPD processing of these alloys and principles of grain refinement were described in detail in a previously published overview paper
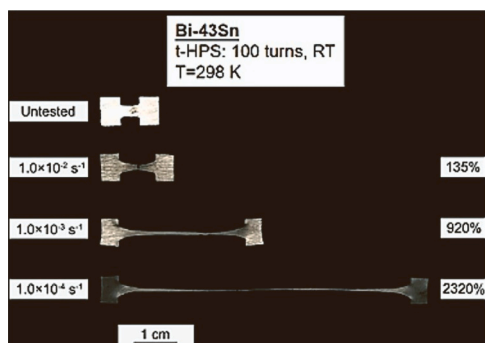
Fig. 37. Appearance of Bi-43Sn (wt%) samples after processing by t-HPS for 100 turns and pulling to failure at 298 K [224]: the elongation of 2320% exceeds the elongation of 1950% reported in early experiments by Pearson [24].

[792]. In this section, superplastic elongation values in the severely deformed alloys and their microstructural origin are described.

Low-temperature superplastic elongations reported in severely deformed alloys are shown in Fig. 38a-d. In general, elongation to failure of Mg-based alloys is scattered in a wide range between 330% and 1330% [793–801] with an exception of 2400% which is the highest low-temperature superplastic elongation in severely-deformed alloys (Fig. 38a). Ti-based alloys, on the other hand, exhibit superplastic elongations between 474% and 1400% (Fig. 38b) [802–809]. Relatively lower superplastic elongations below 700% were reported in the Al-based alloys (Figs. 38c and 38d) [810–823]. As an extreme example of low-temperature superplasticity, some low-melting point alloys exhibited superplastic elongation even at room temperature [824–831]. Mostly, the Al-Zn alloy system has been studied to attain room-temperature superplasticity. The highest elongation at room temperature was reported in the ECAP-processed Zn-0.3Al alloy as 1000% (Fig. 39) [829].

The main reason for high superplastic elongations in the severely deformed alloys was stated to be their equiaxed and UFG microstructure having large grain boundary area leading to easy grain boundary sliding as the main deformation. However, more recently it was shown that engineering grain-boundary composition and diffusion could also be used to achieve low-temperature superplasticity. Diffusion coefficient D in the creep equation should be equal to the coefficient for grain boundary diffusion for grain boundary sliding. The coefficient of diffusion depends strongly on the deformation temperature, and a higher temperature brings about a higher diffusion coefficient. Thus, the diffusion coefficient should be increased without increasing temperature to achieve low-temperature superplasticity. Besides the UFG microstructure, zinc segregation at the difficult-to-slide Al/Al grain boundaries was stated to be the main reason for lowering the superplastic temperature of HPT-processed Al-4.8Zn-1.2Mg-0.14Zr (wt%) alloy [811, 812]. Segregation of zinc at grain boundaries accelerates diffusion and enhances sliding which results in superplasticity at lower temperatures [811, 812]. A similar result was also reported in the friction-stir-processed Mg-9Li-1Zn (wt%) alloy [799, 832]. The β phase (lithium solid solution) particles precipitated at the grain boundaries and triple junctions contributed to the stress relaxation and accommodated grain boundary sliding [832]. It was also specified that lithium segregation at Mg-rich α/α phase boundaries increases the boundary diffusivity and contributes to phase boundary sliding at relatively low temperatures leading to high superplastic elongation of 1104% in Mg-9Li-1Zn alloy [799]. All these results show that besides the UFG formation, controlling the grain boundary composition and grain-boundary segregation using a proper SPD method and alloying element selection is effective for low- and room-temperature superplasticity (*e.g.* addition of lithium, sodium, calcium, strontium, selenium, bismuth and tellurium to magnesium can enhance the diffusivity) [351, 833].

The effect of grain-boundary segregation on the mobility of grain boundaries was reported to lead to the achievement of room-temperature superplasticity in Al-30Zn (at%) [351] and Mg-8Li (wt%) [350] alloys. One of the most interesting results of grain boundary engineering to attain room-temperature superplasticity was reported in the Al-Zn alloy [351]. It was reported that 200 turns of HPT did not cause further grain refinement compared to lower strains but resulted in the segregation of zinc atoms at α/α grain boundaries. High zinc concentration enhanced grain-boundary diffusion along these boundaries and made them favorable for grain boundary sliding. Thus, improved diffusivity at the α/α boundaries activated grain boundary sliding as the main deformation mechanism and brought about high superplastic elongation in Al-30Zn at room temperature [351]. HPT processing of Mg-8Li alloy also resulted in the segregation of lithium atoms at the α/α boundaries and enhanced diffusion capability of these boundaries [350]. Such a modification on the grain boundaries resulted in a high superplastic elongation of 440% at room temperature corresponding to
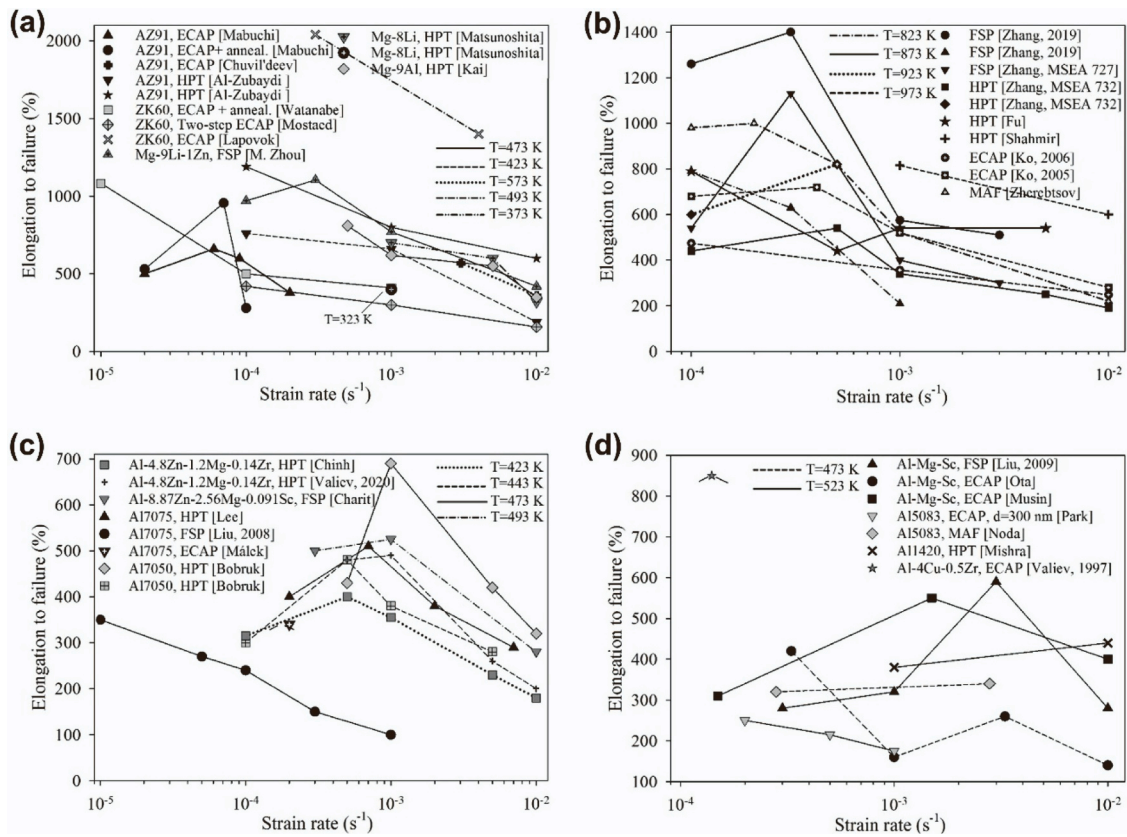
Fig. 38. The variation of superplastic elongation values with strain rate at different temperatures in severely-deformed alloys: (a) Mg-based alloys, (b) Ti-6Al-4 V (wt %) alloy, (c) 7xxx series of Al-based alloys and (d) other Al-based alloys [792].
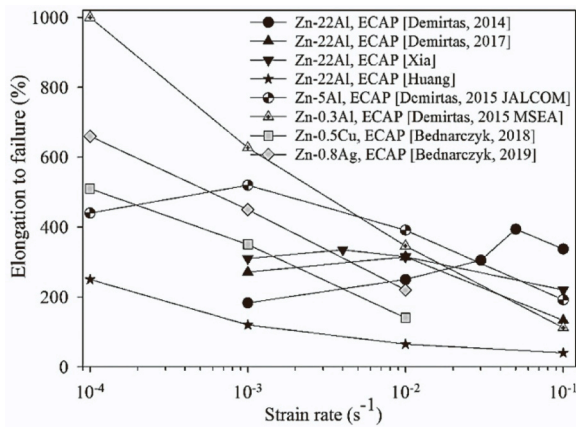
Fig. 39. Room temperature superplastic elongations of some severely deformed alloys [792].

$0.35T_m$ which is the lowest homologous temperature for the low-temperature superplasticity in the severely deformed metals.

Regarding the results summarized above it can be concluded that besides UFG formation, the type and chemical composition of grain boundaries also play an important role in decreasing the temperature for superplasticity. Thus, modification of the grain boundaries via SPD can be considered a promising way to achieve low- and room-temperature superplasticity.

6. Functional properties

Although SPD-processed materials primarily received attention for their mechanical properties, there is a general trend in the field toward functional properties. Since these materials show more than one functionality and their functional properties are superior to conventional engineering materials, they are sometimes referred to as multifunctional or superfunctional materials. A review of the recent literature published on the functional properties of SPD-processed materials suggests that the main investigated functional properties include: electromagnetic properties (electrical conductivity [834, 835], superconductivity [836, 837], thermoelectric properties [838, 839], dielectric properties [840] and magnetic properties [841]), thermal conductivity [842], catalytic properties (catalyst [843], photocatalyst [844] and electrocatalyst [845]). hydrogen-related applications (hydrogen storage [846], hydrogen production [847] and hydrogen embrittlement [848]), corrosion resistance [849], irradiation resistance [850], biocompatibility [851], *etc.* In the following sections, the main functional properties of SPD-processed materials are reviewed.

6.1. Electrical conductivity

Electrical conductivity (σ_E, S/m) is a property of materials defined as the capability to allow electron flow under an applied electric field [852–854], or the inverse of electrical resistivity (ρ, Ωm) and calculated using Equation 11.

$$\sigma_E = \frac{1}{\rho_E} \tag{11}$$

According to the International Annealed Copper Standard (IACS%), the electrical conductivity can be expressed as a percentage of that of annealed copper (100 IACS%). Conductive metallic materials should exhibit high strength and good ductility, with high thermal stability and electrical conductivity. For pure metals, the main scattering mechanism consists of the interaction between conduction electrons and the

vibrating lattice (ρ_{lattice}), which has a strong temperature dependence. However, microstructural features, especially in metallic alloys, can increase the electrical resistivity. Matthiessen's rule expressed in Equation 12 considers the contribution of two components: (i) lattice resistivity (ρ_{lattice}) and (ii) residual resistivity (ρ_{residual}). The latter is associated with local distortion of the lattice, solute atoms, grain boundaries and crystal defects. Their contribution to the total resistivity can be added and designated as *B*, which is weakly dependent on temperature. *A* is a constant independent of temperature [852–854].

$$\rho_{\text{E}} = \rho_{\text{lattice}} + \rho_{\text{residual}} \approx A \bullet T + B \qquad (12)$$

Processing copper and aluminum alloys by SPD increases their strength and decreases the electrical conductivity due to the high density of grain boundaries and crystal defects, which hinder dislocation motion but promote electron scattering mechanisms [180, 236,

855–862]. Traditionally, high strength and highly conductive Cu-based alloys are expected to have ultimate tensile strength (UTS) of 300–800 MPa and electrical conductivity of 50–95 IACS% [856]. Meanwhile, Al-based alloys should achieve at least a UTS of 300 MPa and 52 IACS% [857]. Such ranges of properties are indicated in Figs. 40a and 40b as hatched areas. Copper alloys can be strengthened with restored electrical conductivity through several processing routes. A summary of such results is shown in Fig. 40a.

- Grain refinement by HPT of high-purity copper increases its strength to 440 MPa [859] with electrical conductivity of ~87 IACS% at the steady state [860]. During microstructure evolution high density of dislocations are produced, but the microstructure undergoes dynamic recrystallization with a grain size of ~ 0.2 μm and lower density of dislocations at the steady state.

- Age hardenable Cu-Cr-X alloys processed by SPD with further annealing allow the precipitation of particles rich in chromium. Meanwhile, SPD at high temperatures promotes dynamic strain aging and particle precipitation. The low solute content in the copper matrix reduces the electron scattering and optimizes the electrical conductivity [254, 856, 861–863]. Islamgaliev *et al.* [862] processed a Cu-Cr-Ag alloy by HPT at room temperature followed by aging at 723 K for 1 h and achieved UTS of 840 MPa and conductivity of 85 IACS%, as shown in Fig. 40a.

- Fine grains and nanoscale twins have been shown to minimize the scattering of conduction electrons and still serve as barriers to dislocation motion [864–868]. Fig. 41a shows a bright-field image of high-purity copper with nanoscale twins produced by pulsed electrodeposition (PED), which shows yield stress of ~900 MPa and conductivity of 96.9 IACS%. This result is also shown in Fig. 40a [864].

The mechanical and electrical properties of aluminum alloys have a close relationship with the nature and fraction of alloying elements [834, 855, 870]. UFG Al-based alloys subjected to post-processing heat treatment after SPD or SPD at elevated temperatures have been reported to produce decomposition of supersaturated solid solutions and precipitation of second phase particles of Mg_2Si [870–876], Al_3Fe, Al_6Fe [869, 877–880], $Al_{11}RE_3$ (RE: rare-earth elements) [881, 882] and Al_3Zr [332, 883–886]. A summary of these results is shown in Fig. 40b. For instance, processing AA6201 by HPT at elevated temperatures (403 K, 453 K and 503 K) allowed the precipitation of nano-sized Mg_2Si due to dynamic strain aging and increased electrical conductivity with processing temperature: 55.6 IACS%, 58.4 IACS% and 59.0 IACS% respectively [870]. Consequently, strength decreases to 412, 365 and 275 MPa by annealing, respectively, as shown in Fig. 40b. On the other hand, UFG Al-2Fe (wt%) alloys with nanosized Al_3Fe and Al_6Fe particles, as indicated by arrows in Figs. 41b and 41c were produced by HPT for 20 and 75 revolutions, respectively. Both were peak-aged at 473 K and attained UTS of 600 and 650 MPa with 55 and 54 IACS% respectively [869, 877]. This result is also shown in Fig. 40b.

In summary, the thermal dependence of electrical resistivity, grain boundaries and grain size allows the balance of mechanical and electrical properties by thermomechanical routes, such as SPD complemented by static or dynamic aging [9, 373, 887]. On the other hand, scaling up sample dimensions and optimization of continuous SPD methods can open a new path for the industrial application of high-performance UFG copper and aluminum conductors [154, 164, 179, 241].

Fig. 40. Electrical conductivity with respect to strength in (a) copper and (b) aluminum alloys [834].

6.2. Magnetic properties

Magnetic materials are key materials needed, for the electrification of mobility and the generation and conversion of electrical energy [888]. In recent years, interest in the magnetic properties of SPD-processed materials increased as microstructure strongly influences

Fig. 41. (a) TEM bright-field image of as-deposited copper with diffraction pattern (as inset) [864]. (b,c) TEM bright/dark-field images of Al-2Fe (wt%) alloy after HPT processing for (b) 20 and (c) 75 revolutions at peak-aged condition [869].

Fig. 42. (a) Schematic representation of coercivity (H_c) as a function of grain size (D) for soft (upper graph) and hard magnetic (lower graph) materials (different logarithmic scales for H_c of soft and hard magnetic are used) [888–893]. (b) Powder blends for the HPT process, (c) schematic representation of powder-based HPT processes and (d) schematics of bulk materials produced by HPT from powder blends with enhanced microstructural features [841].

the magnetic properties and HPT can be used to tune it [841]. For example, the coercivity H_c of soft and hard magnetic materials correlates with the grain size (Fig. 42a) [888–893] and HPT leads to strong grain refinement [23, 38, 894]. Other advantages include the potential to form nanostructured composites with a high density of interfaces or supersaturated solid solutions, while at the same time enabling a shear

texture formation through the deformation processes [895, 896]. Powder-based HPT processing (Fig. 42b-d) offers even more interesting and unique opportunities for the fabrication of hard or soft magnetic materials [841]. Using elemental powders or intermetallic phases in the form of powders, a free choice of combinations is possible, without the limitations given by the phase diagrams or, better, by phase formation
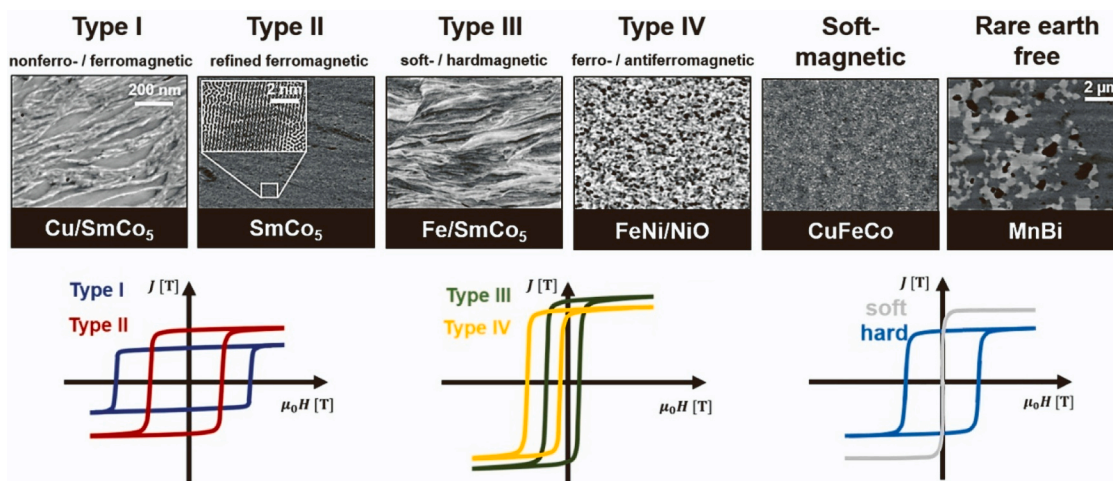
Fig. 43. Different types of microstructures which can be generated by HPT applied to powder/powder blends and their corresponding schematic magnetic hysteresis curves [841].

from a melt as in metallurgical processing routes (Fig. 42b). As mentioned earlier, HPT processing of powders can produce bulk nano-structured materials (*e.g.* nanocomposites), while at the same time processes like mechanical alloying, phase transformations and super-saturations can be used to enhance the magnetic properties [897, 898]. The free choice of starting powders is particularly interesting because thermodynamically metastable chemical compositions and various composite structures can be achieved. Fig. 43 summarizes examples of microstructures of different magnetic materials or nanocomposites that can be obtained by HPT processing of powders [841]. Here some recent findings are reviewed.

Smaller grain sizes compared to single-phase materials can be achieved in HPT-deformed Cu-Co [897–899] and Fe-Cu alloys [900] with supersaturated phases, in which semi-hard, tunable magnetic properties are obtained. Additionally, annealing treatments are used to modify magnetic properties [899]. To achieve soft magnetic properties, ternary Fe-Co-Cu alloys were studied [901]. The addition of iron decreases the magnetocrystalline anisotropy and increases the saturation magnetization [902]. Giant magneto-resistance (GMR) is observed in materials that consist of nanometer-sized ferromagnetic particles dispersed in non-magnetic metallic matrixes (termed 'granular') [903, 904]. In HPT-deformed binary and ternary powder mixtures consisting of different compositions of elemental copper, cobalt, nickel and iron [905–907], similar GMR values as in materials processed with different methods are found. HPT processing of powders is further used to obtain hard magnetic materials. In recent studies, Nd-Fe-B-based bulk materials were processed by HPT from amorphous precursors, in which the deformation-induced texture further led to anisotropic magnetic properties and a maximum energy product of 22.8 MGOe [908, 909].

For nucleation-controlled magnets, the four classical magnetic interaction mechanisms with the different microstructures (type I-IV) can be implemented via powder-based HPT (Fig. 43). Powder blends of $SmCo_5$ and magnetically different binder phases, *i.e.* copper (diamagnetic) [910], iron (ferromagnetic) [911], nickel (ferro), cobalt (ferro), zinc (para), tin (para) and chromium (antiferromagnetic) [841], were deformed by HPT. A type I magnetic material (aligned/textured single-domain ferromagnetic particles are separated by a thin non-magnetic layer leading to magnetic decoupling of ferromagnetic particles) was obtained using copper as a diamagnetic phase [910]. Type II magnets (exchange-coupled ferromagnetic particles) were fabricated as well by deforming SmCo-based intermetallic powders by HPT [841]. An exchange-coupled type III system (a combination of soft and hard magnetic phases) was synthesized using iron in addition to $SmCo_5$ [911]. A type IV ferro-antiferromagnetic composite is processed by deforming $SmCo_5$ and chromium [841]. The highest saturation

magnetization was obtained for the Fe-containing composition (type III) and the lowest for the diamagnetic and antiferromagnetic binder phases (type I and IV). According to Fig. 42a it has been shown that a refinement of the microstructure and grain size of the hard ferromagnetic phase increases the coercivity, whereas the largest coercivity is achieved with copper and chromium as a binder phase [841]. The highest coercivity is obtained in the Cu-$SmCo_5$ system (type I) due to the magnetic decoupling of the $SmCo_5$ particles by copper [910]. Successful processing of type IV magnetic materials by HPT was also reported in the Fe-NiO [912] and Co-NiO [913] systems.

Phase transformations by HPT can also be employed to synthesize different hard magnetic phases such as $L1_0$-FeNi [340], Mn-Al-C [914] and MnBi [915]. Soft magnetic properties in HPT-processed bulk single-phase materials (cobalt [509, 916], nickel [917–919], iron [919–923], Fe-Si [917, 919, 921], FeCo [917, 921], FeNi [921]) have not yet been achieved due to large grain sizes and high density of defects. In HPT-processed hard magnetic materials, grain refinement generally leads to coercivity enhancement [924–928], partial amorphization [924, 929–932] or phase decomposition [933]. By deformation of amorphous magnetic materials [934–939], type III magnetic materials can be obtained [934].

In summary, SPD processing and particularly powder-based HPT offers strong advantages in the design of magnetic microstructures based on the possibility to freely combine hard, soft and non-magnetic phases for forming a textured nanocomposite. SPD processing opens thereby new pathways to future magnetic materials with unique microstructures covering the whole range of soft-to-hard magnetic properties.

6.3. Optical bandgap narrowing and solar energy harvesting

Metal oxides, such as TiO_2 and ZnO, are efficient semiconductors for light harvesting and photocatalysis because they generate a large number of electrons and holes upon light irradiation. However, their efficiency is low under sunlight because their bandgap is large and is in the range of ultraviolet (UV) light and sunlight only contains about 2–3% of UV light. To enhance the efficiency of metal oxide across the solar spectrum, it is necessary to broaden their light absorption to the visible light region by reducing their bandgap. Various approaches, such as doping with anions like nitrogen [940–942], carbon [943], hydrogen [944], fluorine [945], chlorine [945], bromine [945] and iodine [945] and/or cations like tungsten [946, 947], ruthenium [948], tantalum [949], sodium [950], bismuth [951], lanthanum [952], molybdenum [953], zinc [954], calcium [954] and cobalt [955] have been employed to reduce the bandgap of metal oxide semiconductors. When metal oxide is doped with anions like nitrogen or carbon, N 2p states in nitrogen and

C 2p states in carbon couple with O 2p states of the metal oxide, resulting in the formation of acceptor levels above the valence band of the host metal oxide [956]. The formation of such acceptor levels reduces the bandgap of the metal oxide whose valence band is composed of O 2p orbitals. Although doping or co-doping with anions/cations is an effective method for reducing the bandgap of most metal oxides, it has been challenging in some aspects. Dopants often tend to precipitate and alter the chemical composition of the host material. Another limitation is the low solubility of dopants in the host material. Additionally, high temperatures are typically required to enhance the crystallinity of the host material and this can lead to the unintended expulsion of dopants.

An effective method for reducing the bandgap is the introduction of defects into the host material. Taking TiO_2 as an example, defects such as oxygen vacancies have been shown to reduce its bandgap. The major intrinsic defects in TiO_2 include oxygen vacancies, titanium interstitials and titanium vacancies [957–959]. Among these, oxygen vacancies are the most common type of intrinsic defect. Introducing plastic strain by HPT method is shown to be effective for the formation of the oxygen vacancies in many semiconductors such as TiO_2 [582, 639, 960], ZnO [604], Y_2O_3 [583], $BiVO_4$ [961], TiO_2/ZnO [605], $CsTaO_3$ [962], $LiTaO_3$ [962], Bi_2O_3 [963], ZrO_2 [666], GaN/ZnO [606], $BaTiO_3$ [840] and Al_2O_3 [964]. In this method, dopants are not used, while oxygen vacancies are effectively formed. The generation of oxygen vacancies arises from the crystal structure of most oxides including TiO_2. In TiO_2, bridge bonding oxygen atoms are two-fold coordinated and can be easily removed from the lattice by introducing plastic strain. Therefore, oxygen vacancies are known to be the most reactive sites in TiO_2. Generation of one oxygen vacancy leaves two valence electrons that occupy empty Ti 3d levels. As a consequence, energy levels below the conduction band are generated, leading to the bandgap reduction of the metal oxide semiconductor.

Another interesting feature of introducing the simultaneous plastic strain and high pressure is reducing the bandgap of materials by stabilizing the high-pressure phases at ambient pressure. These high-pressure phases have theoretically been calculated to have better light absorbance and narrower bandgaps that coincide with visible light. For example, columbite TiO_2-II with an orthorhombic structure is calculated to have a bandgap of 2.59 eV, but it is stable only at pressures higher than 2 GPa [639, 960]. The application of HPT for stabilizing the TiO_2-II phase showed that the high-pressure phase was stable for at least 6 months. The high-pressure rocksalt phase of ZnO [604] and the monoclinic phase of Y_2O_3 [583] are some successful examples of bandgap reduction through the formation of high-pressure phases. Fig. 44a shows the UV-Vis light absorbance spectra of TiO_2 samples before HPT and after HPT. The absorption edge of the starting TiO_2 powder is 400 nm, while it shifted to 470 nm, after HPT processing. The bandgap of samples was calculated by the Kubelka-Munk equation as shown in Fig. 44b, being 3.1 eV and 2.7 eV for samples before HPT and after HPT processing. Comparing the bandgaps of samples before HPT and after HPT processing, it is clear that the formation of a high-pressure phase is an effective approach for reducing the bandgap of oxides. A schematic illustration of bandgap reduction is shown in Fig. 45. Fig. 45a represents the bandgap of a pure metal oxide, whose bandgap is shown to be wide. Fig. 45b shows the cation-doped oxide, where donor states are responsible for the bandgap narrowing. Fig. 45c shows an anion-doped oxide, where donor states are responsible for bandgap narrowing. Bandgap narrowing through oxygen vacancies produced by HPT processing also falls into this group, with the difference that no dopants are present in this case. Fig. 45d represents the bandgap of a pure metal oxide with high-pressure phases. In this case, the high-pressure phase itself has a narrower bandgap without any donor/acceptor states. Table 5 is a summary of publications in the literature that studied the effect of the HPT method on the bandgap of various semiconductors and ceramics [323–327, 844, 965, 966].

Taken altogether, inducing plastic strain using the SPD is an effective approach for the formation of oxygen vacancies and/or high-pressure
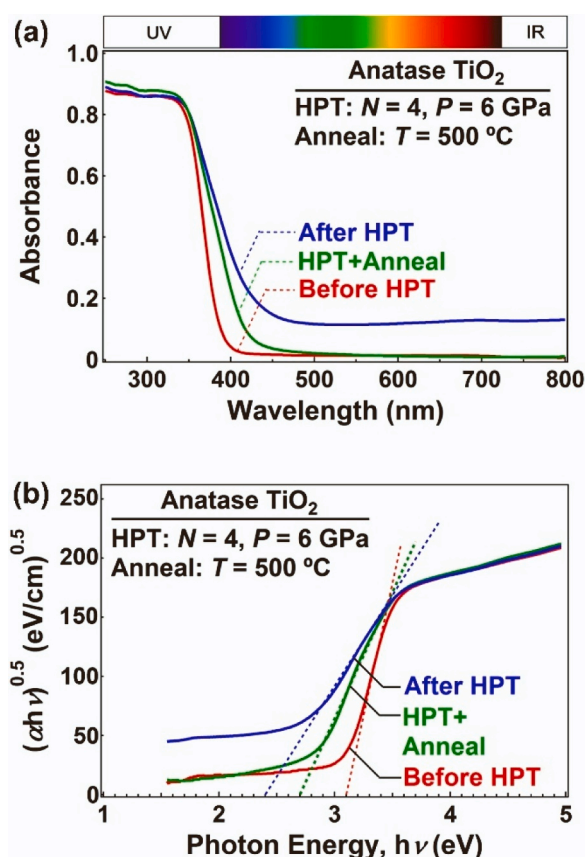
Fig. 44. (a) UV-Vis absorbance spectra and (b) bandgap calculation by the Kubelka-Munk theory for TiO_2 before and after HPT processing and after HPT followed by annealing [639].
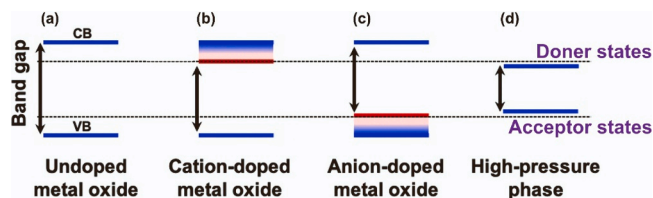
Fig. 45. Schematic illustration of bandgap reduction mechanisms: (a) pure metal oxide, (b) cation-doped oxide in which donor states are responsible for bandgap narrowing, (c) anion-doped oxide in which acceptor states are responsible for bandgap narrowing and (d) high-pressure phases with oxygen vacancies in which bother donor and acceptor states are responsible for bandgap narrowing.

phases in semiconductors to enhance light harvesting via bandgap narrowing. This feature of SPD has opened a pathway for the development of photocatalysts, as will be discussed in the next chapters.

6.4. Photocatalytic CO_2 conversion

Among all scientific attempts to solve the global warming crisis, photocatalytic CO_2 conversion has been introduced as one of the cleanest methods to convert CO_2 to CO and useful organic components [967–969]. Photocatalytic CO_2 conversion reactions are performed on the surface of a semiconductor under solar irradiation where electrons and holes are separated and immigrated to the surface as shown in Fig. 46a [970]. A variety of methods such as doping with impurities [971–974], defect/surface engineering [975, 976] and the introduction of heterojunctions [977, 978] have been reported to enhance the

Table 5
Summary of publications related to the effect of SPD via the HPT method on bandgap of various semiconductors and ceramics.

Material	Bandgap before HPT (eV)	Bandgap After HPT (eV)	Factors Affect Bandgap	Color Before HPT	Color After HPT	Application	Ref.
TiO_2	3.1	2.4	High-pressure phase, Oxygen vacancy	White	Green	Water splitting H_2 production	[582, 639, 960]
ZnO	3.4	1.8	High-pressure phase, Oxygen vacancy	White	Yellow	Dye degradation	[604]
Y_2O_3	5.82	5.69	Phase transformation	White	Pink	Photoluminescence	[583]
$BiVO_4$	2.4	2.1	Defect formation	Yellow	Orange and Rose	CO_2 conversion	[961]
TiO_2-ZnO	3.2	1.6	High-pressure phase, Oxygen vacancy	White	Black	Water splitting H_2 production	[605]
$CsTaO_3$	4.6	3.3	Oxygen vacancy	-	-	Water splitting H_2 production	[962]
$LiTaO_3$	4.7	4.2	Oxygen vacancy	-	-	Water splitting H_2 production	[962]
Bi_2O_3	2.5	2.3	Oxygen vacancy	Yellow	Black	Photocurrent	[963]
ZrO_2	5.1	4.0	High-pressure phase, Oxygen vacancy	White	Black	Water splitting H_2 production	[666]
GaN-ZnO	2.7	2.4	Nitrogen vacancy	Yellow	Magenta	Water splitting H_2 production	[606]
Al_2O_3	5.7	2.5	Oxygen vacancy	White	Black	Dye degradation	[964]
$TiHfZrNbTaO_{11}$	0	2.9	High-entropy phase	Metallic	Orange	Water splitting H_2 production, CO_2 conversion	[323, 324]
$TiZrNbTaWO_{12}$	>3.0	2.3	High-entropy phase	White	Orange	Water splitting O_2 production	[325]
$TiZrHfNbTaO_6N_3$	2.9	1.6	High-entropy phase	Orange	Black	Water splitting H_2 production, CO_2 conversion	[326, 327]
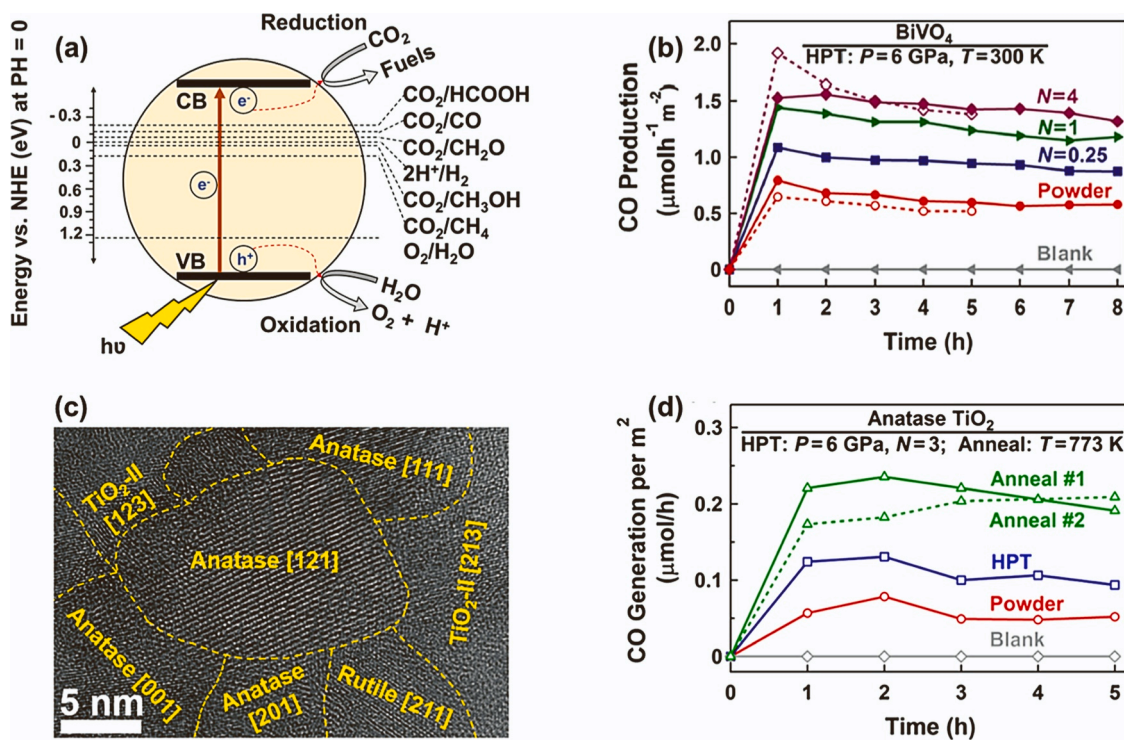
Fig. 46. (a) Schematic of photocatalytic CO_2 conversion mechanism [981]. (b) Photocatalytic CO production rate of $BiVO_4$ versus time for powder and samples processed by HPT with 0.25, 1 and 4 turns [961]. (c) High-resolution TEM image of sample processed by HPT containing TiO_2-II high-pressure phase [985]. (d) Rate of CO generation for TiO_2 samples before HPT, after HPT and after HPT and annealing [985].

efficiency of different photocatalysts, but doping with impurities is the most feasible one. Since this method suffers from the impurity-induced recombination of electrons and holes [974, 979, 980], it is necessary to introduce new strategies to improve the photocatalytic activity. SPD through the HPT method which was employed to improve the photocatalytic dye degradation [604, 956, 964] and water splitting [606, 639, 666], showed high potential to suppress electron-hole recombination and enhance the photocatalytic CO_2 conversion efficiency. SPD enhanced photocatalytic CO2 conversion by the introduction of (i) oxygen vacancies and strain, (ii) high-pressure phases, (iii) defective high-entropy oxides and (iv) low-bandgap high-entropy oxynitrides, as discussed below [981, 982].

- Simultaneous oxygen vacancy generation and strain engineering using the HPT method was employed to improve the properties and photocatalytic activity of $BiVO_4$ for CO_2 conversion [961], due to the high recombination rate and inappropriate conduction band position of this material [983]. Using various characterization tools, it was observed that lattice strain and oxygen vacancies increase in the $BiVO_4$ sample by increasing the HPT turns [961]. These changes resulted in systematically increasing the light absorbance, narrowing the bandgap and suppressing the recombination rates. The

conduction band was also aligned to an upper level of energy which could advance the reactions thermodynamically. The $BiVO_4$ sample processed by HPT showed an improved CO production rate under UV light and the activity increased by increasing the HPT turns due to increasing lattice strain and oxygen vacancy as shown in Fig. 46b [961]. A similar concept was recently employed by HPT processing to produce oxygen vacancy-rich black rookite as an active photocatalyst for CO_2 conversion [984].

- As mentioned in the earlier chapter, columbite TiO_2-II is the high-pressure phase of TiO_2 which was formed by SPD through the HPT method (Fig. 46c) and employed for photocatalytic CO_2 conversion [985]. The resultant material after HPT was annealed to decrease the oxygen vacancy concentration in bulk. The annealed sample containing the TiO_2-II phase showed higher light absorbance in the visible region and lower bandgap. Recombination of electrons and holes suppressed significantly for the annealed sample and it could successfully generate a photocurrent much higher than the initial anatase powder. All these improvements led to considerable photocatalytic activity of anneal sample containing TiO_2-II compared to anatase powder as shown in Fig. 46d [985].

- Since high-entropy ceramics have shown superior properties for various ranges of applications, especially in the catalysis field [986, 987], a defective high-entropy oxide was fabricated using HPT and consequent high-temperature oxidation and examined for photocatalytic CO_2 conversion [324]. The synthesized high-entropy oxide $TiZrNbHfTaO_{11}$ containing nanograin boundaries and defects such as oxygen vacancy and dislocations adsorbed the light in both UV and visible regions with the bandgap value of 3 eV. It showed lower recombination of electrons and holes compared to anatase TiO_2 and $BiVO_4$ as conventional photocatalysts and successfully generated

photocurrent. This material showed a high CO production rate similar to P25 TiO_2 as a benchmark catalyst and lower than anatase TiO_2 and $BiVO_4$. This study reported the first application of high-entropy materials for photocatalytic CO_2 conversion [324].

- By considering the high potential of the mentioned $TiZrNbHfTaO_{11}$ synthesized by HPT for CO_2 photoreduction and the promising low bandgap of metal oxynitrides [988], the $TiZrNbHfTaO_6N_3$ high-entropy oxynitride was fabricated by nitriding the $TiZrNbHfTaO_{11}$ [327]. The material showed an appropriate electronic band structure with an extremely narrow bandgap of 1.6 eV which is lower than P25 TiO_2 and the high-entropy oxide as shown in Fig. 47a [327]. The light absorbance of this high-entropy oxynitride was higher than P25 TiO_2, high-entropy oxide and all corresponding binary oxides (Fig. 47b) [326, 327]. The recombination rate of this material was significantly suppressed compared with P25 TiO_2 and the high-entropy oxide and it adsorbs the CO_2 molecules with both physisorption and chemisorption better than P25 TiO_2 and the high-entropy oxide (Fig. 47c) [327]. The result of these improvements caused by HPT processing was the effective enhancement of photocatalytic CO_2 conversion activity of $TiZrNbHfTaO_6N_3$ compared to P25 TiO_2 as a benchmark photocatalyst, the high-entropy oxide (Fig. 47d) and almost all reported photocatalysts in the literature [327].

In summary, SPD was introduced as an effective tool to improve the structural and optical properties and consequently activity of conventional photocatalysts for CO_2 conversion. This method also showed promising potential to synthesize the new high-entropy ceramics with superior photocatalytic efficiency comparable to benchmark photocatalysts for CO_2 conversion. The ability of HPT to develop these highly
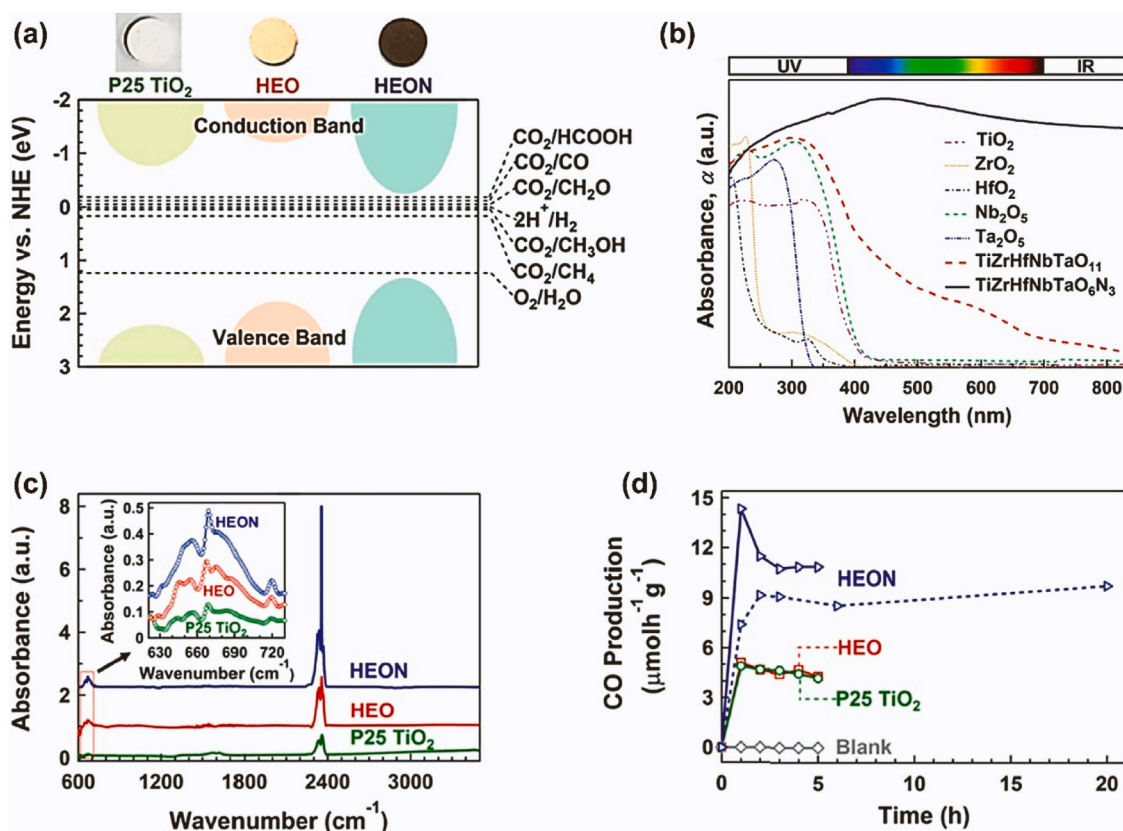
Fig. 47. (a) Electronic band structure of $TiZrNbHfTaO_6N_3$ high-entropy oxynitride (HEON), P25 TiO_2 and $TiZrNbHfTaO_{11}$ high-entropy oxide (HEO) [327]. (b) UV–vis light absorbance spectra for $TiZrNbHfTaO_6N_3$ compared to $TiZrNbHfTaO_{11}$ and corresponding binary oxides [326]. (c) Diffuse reflectance infrared Fourier transform spectra for $TiZrNbHfTaO_6N_3$ compared to P25 and $TiZrNbHfTaO_{11}$ [327]. (d) Rate of CO production for $TiZrNbHfTaO_6N_3$ compared to P25 TiO_2 and $TiZrNbHfTaO_{11}$ [327].

active catalysts for CO_2 photoreduction is attributed to the formation of defects such as oxygen vacancies which act as active sites to adsorb and activate the CO_2 molecules [981, 982]. For the future outlook, the SPD can significantly extend in the field of photocatalysis to develop new and effective catalysts to convert CO_2 to CO and also hydrogenate to other useful components such as CH_4. The HPT method is expected to play the most important role in this regard because the method applies to a wide range of hard-to-deform materials such as optical ceramics [15, 844], semiconductors [512, 989] and oxides [513, 989].

6.5. Photocatalytic hydrogen production

Clean production of hydrogen is a promising alternative to fossil fuel utilization, but its production is still a challenge [990]. Photocatalysis, by splitting water in the presence of light and a photocatalyst [991, 992], produces hydrogen with minimum CO_2 emission. Fig. 48a shows a schematic representation of a photocatalytic process. The main limitation of the photocatalysis is the photocatalyst itself. The photocatalyst must have great light absorbance, narrow bandgap, good efficiency and high stability. Several popular photocatalysts such as TiO_2 [639, 993], ZnO [604, 994, 995], perovskites [323, 962] and oxynitrides [606, 996] show these characteristics; however, various studies demonstrate the necessity of the improvement of activity of these catalysts. SPD processing via HPT [604, 639, 962], ball milling [997–1000] and tubular channel angular pressing (TCAP) [1001] were demonstrated to be beneficial in improving photocatalytic activity. SPD can tune three
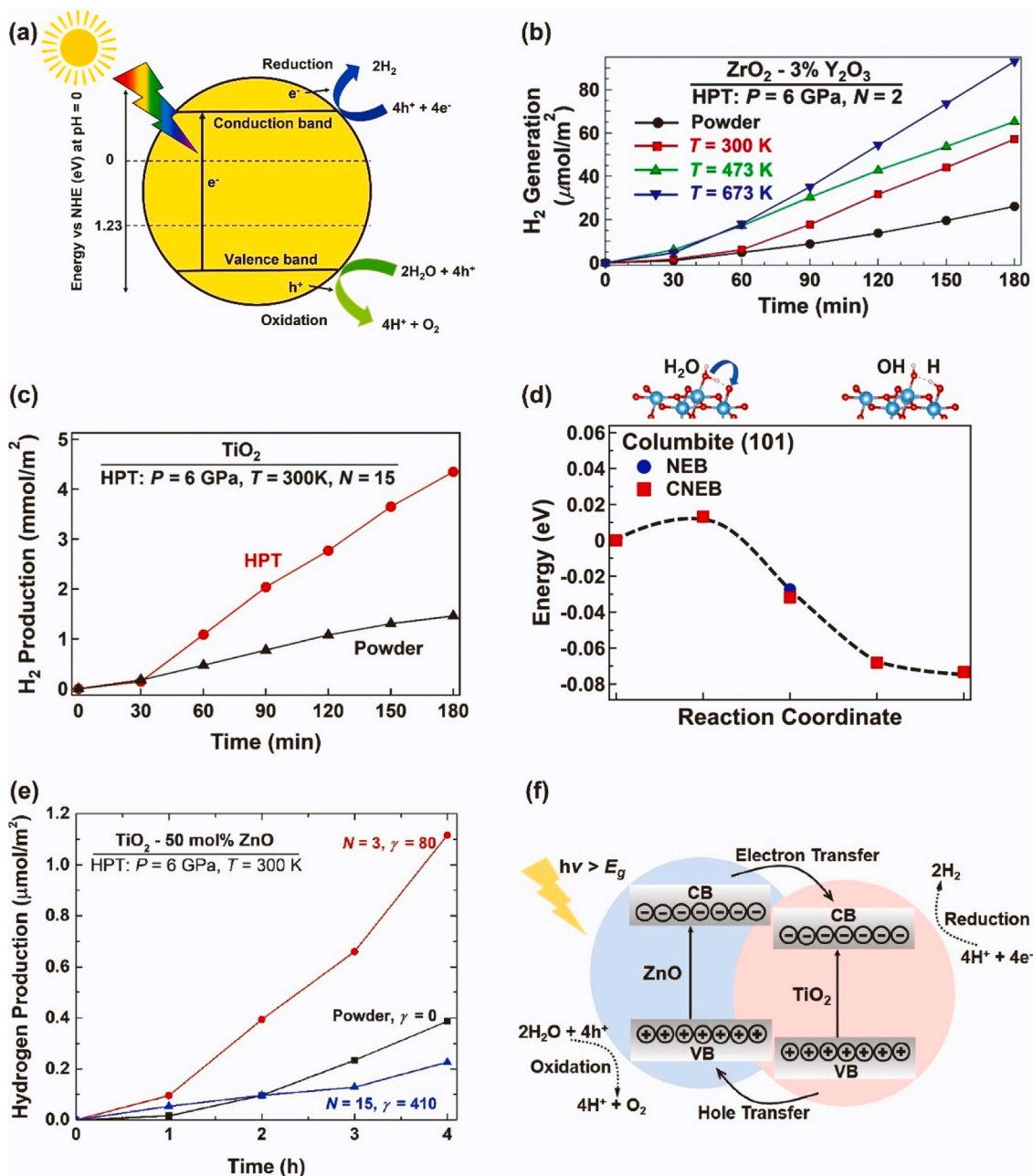
Fig. 48. (a) Schematic representation of the photocatalytic water splitting reaction for hydrogen production. (b) Enhanced photocatalytic activity of zirconia by oxygen vacancy introduction via HPT processing [666]. (c) Enhanced photocatalytic activity TiO_2 by stabilization of high-pressure columbite phase [1002]. (d) Density functional theory calculations, showing high surface activity of the (101) atomic plane of high-pressure columbite for H_2O to OH + H decomposition [1002]. (e) Photocatalytic hydrogen production for TiO_2-ZnO composite under UV light after HPT processing for 3 and 15 turns [605]. (f) Schematic representation of charge separation in TiO_2-ZnO interface boundary as heterojunctions [605].

major characteristics of the photocatalysts: (i) defects introduction [606, 666], (ii) high-pressure phase transformation [604, 639, 1002] and (iii) heterojunctions [325, 605, 997, 998].

Due to the pressure-strain effect, vacancy formation is one of the most common defects when processing ceramics by SPD. A arge concentration of oxygen vacancies was found in black ZrO_2 [666], TiO_2 [639], ZnO [604, 1003], Al_2O_3 [995], $CsTaO_3$ [962] and $LiTaO_3$ [962] and MgO [956] after being processing by SPD. The oxygen vacancies are beneficial for photocatalytic activity in all the cases [604, 666, 956, 962, 995]. The study performed on black ZrO_2 demonstrated that oxygen vacancy concentration can be increased by high-temperature processing [666]. In addition, these strain-induced vacancies improve the hydrogen generation in the sample as shown in Fig. 48b. The oxygen vacancies can enhance the photon absorption, narrow optical bandgap and function as active sites for photocatalytic activity [639, 666, 956, 1002]. Nitrogen vacancies were also observed in GaN-ZnO after HPT [606]. The study concluded that the nitrogen-vacancy complexes can reduce the bandgap by modifying the energy levels above the top of the valence band and below the conduction band [606]. Vacancies generally diminish the electron-hole recombination and narrow the bandgap of the material. The defect introduction by SPD processing not only can improve several properties but also contribute to the stabilization of high-pressure phases.

The transformation to a high-pressure phase can be highly beneficial for photocatalytic activity. For ZnO, the transformation to Rocksalt decreases the bandgap from 3.4 to 1.8 eV [604]. However, as mentioned earlier, the rocksalt phase is only stable under high pressure but could be stabilized in ambient pressure by HPT [604]. Similarly, the TiO_2 high-pressure columbite phase is unstable under ambient pressure; however, it can be stabilized by the shear strain introduced by HPT [1004]. The shear strain induces gradual modifications on the anatase crystal structure until it transforms to ~70% columbite [1004]. Columbite stabilization in combination with the anatase, rutile and intermediate sheared structures significantly improves the water-splitting efficiency (Fig. 48c) [639, 1002, 1004]. Columbite is demonstrated to be highly active for water splitting in the atomic plane (101). The DFT results for the reaction pathway observed in Fig. 48d showed low activation energy for the water-splitting reaction compared to anatase and rutile [1002].

Several composites have been also subjected to plastic deformation or SPD methods to improve their coupling: SnO_2/TiO_2 [997, 1005], p-CuO/n-ZnO [998], p-$CuBi_2O_4$/n-TiO_2 [999], g-C_3N_4/ZnO [1000], $CuFe_2O_4$/$Bi_4Ti_3O_{12}$ [1006] and TiO_2-ZnO [605, 1005]. As shown in Fig. 48e, TiO_2-ZnO after HPT processing for 3 turns showed greater photocatalytic activity compared to TiO_2 and ZnO. Ball milling is commonly utilized to couple the oxides into a composite [997, 1006], but it is also able to generate improvements in the photocatalytic activity of the composites. At an optimum time of milling, the activity is enhanced, but it reduces after increasing the time due to the agglomeration of the powders [998, 999] or reduction of crystallinity [605]. The reason for the enhancement of the photocatalytic activity, as in the HPT, is attributed to the presence of heterojunction for easy electron-hole separation [605, 997, 1000, 1006]. In a TiO_2-ZnO composite, the electron transfer occurs from the conduction band of ZnO to TiO_2, and the holes move from the valence band of TiO_2 to ZnO [605, 1005] (Fig. 48f). When processing TiO_2-ZnO composite by HPT, the stabilization of high-pressure phases generates additional interphase boundaries between phases which positively contribute to the increment of active sites [605]. Therefore, SPD can contribute to the enhancement of photocatalytic hydrogen production through different routes such as the stabilization of vacancies, high-pressure phase transformations and heterojunction formation.

6.6. Electrocatalytic hydrogen production

As mentioned in an earlier chapter, hydrogen is emerging as a new energy carrier and is gaining global acceptance as a potential fuel pathway. Unlike all carbon-based fuels, hydrogen can be truly carbon-neutral [1007–1009]. Electrocatalytic water splitting to produce renewable hydrogen has been widely regarded as a promising strategy for the coming hydrogen society [1010, 1011]. Similar to photocatalytic water splitting discussed earlier, the electrocatalytic water-splitting process is also composed of two half-reactions [1012]. The oxygen evolution reaction (OER) happens at the anode to produce O_2, while the hydrogen evolution reaction (HER) happens at the cathode to produce hydrogen. Equation 13 is the reaction of water splitting which can be separated into two half-cell reactions (Equations 14 and 15).

$$H_2O \rightarrow H_2 + \frac{1}{2} O_2 \quad E° = 1.23V \text{ vs. SHE} \tag{13}$$

$$2H^+ + 2e^- \rightarrow H_2 \quad E° = 0V \tag{14}$$

$$2H_2O \rightarrow O_2 + 4H^+ + 4e^- \quad E° = 1.23V \tag{15}$$
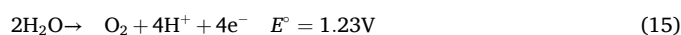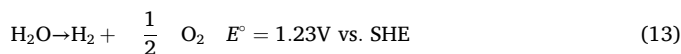
Developing efficient and stable electrocatalysts for HER and OER of water splitting is very important for electrocatalytic hydrogen production [1013, 1014]. Noble metal catalysts, such as Pt-, Pd- and Ru-based compounds have shown excellent electrocatalytic water splitting catalytic performance [1015, 1016], however, their application is limited due to high price, few resources, *etc*. Amorphous alloys, which can be prepared by rapid solidification [1017, 1018], have shown promising catalytic and electrocatalytic properties because of the long-range disordered atomic structure [1019–1022]. Moreover, it was reported that amorphous alloys can show significantly enhanced HER and OER performances of water splitting after being processed by SPD [845]. Fig. 49a shows the schematic illustration for the fabrication of $Fe_{78}Si_9B_{13}$ nanoglass alloy by melt spinning followed by HPT [1023]. Fig. 49b shows that the nanoglass requires an overpotential of only 112 mV to achieve the current density of 10 mA cm^{-2} in 1.0 M KOH, which is much smaller than those of the corresponding amorphous alloy (385 mV) and crystalline alloy (465 mV). Similar improvements in HER properties by HPT can also be seen in the $Fe_{73.5}Si_{13.5}B_9Cu_1Nb_3$ [1024] and $Fe_{75}B_{25}$ [1025] amorphous alloy.

Since the Fe-based amorphous alloys are usually quite hard, the HPT treatment would induce nanocrystallization upon the amorphous matrix, and the effect of nanocrystals on the catalytic performance is difficult to elucidate. A $Pd_{40}Cu_{30}Ni_{10}P_{20}$ amorphous alloy, which is much softer than Fe-based alloys, is subjected to HPT treatment to study the HER catalytic performances. The HPT treatment did not cause crystallization. The overpotentials at 10 mA cm^{-2} of the HPT-treated $Pd_{40}Cu_{30}Ni_{10}P_{20}$ amorphous alloys were 76 mV and 209 mV in 0.5 M H_2SO_4 and 1.0 M KOH, respectively, which were much smaller than those of 179 mV and 379 mV for the melt-spun $Pd_{40}Cu_{30}Ni_{10}P_{20}$ amorphous alloy at the same conditions [1015]. The improved HER performances should be mainly attributed to the significantly increased density of flow units in the amorphous matrix by SPD [1027].

FeOOH nanocrystals have been explored as remarkable OER catalysts in past years [1028, 1029]. Based on a previous study, the HPT-treated $Fe_{78}Si_9B_{13}$ nanoglass with an *in situ* formed FeOOH layer on the surface was prepared by a cathodic corrosion activation method. The FeOOH-covered nanoglass showed excellent OER performances because the FeOOH layer not only exposes more active sites but also generates hydroxyl radicals (OH·) in oxygen vacancies to activate the Fe-based nanoglass matrix. Fig. 49c shows that the FeOOH-covered nanoglass generates an overpotential of only 240 mV at 10 mA cm^{-1} in 1 M KOH, and the Tafel slope is as low as 42 mV dec^{-1} [1026]. The OER catalytic mechanism has been revealed as shown in Fig. 49d. Firstly, under the action of an electric field, electrons are separated from oxygen vacancies to form positively charged oxygen vacancies (Vo$^+$) [1030].

$$Vo \rightarrow e^- + Vo^+ \tag{16}$$

Secondly, Vo$^+$ adsorbs the hydroxide ions and water on the catalyst
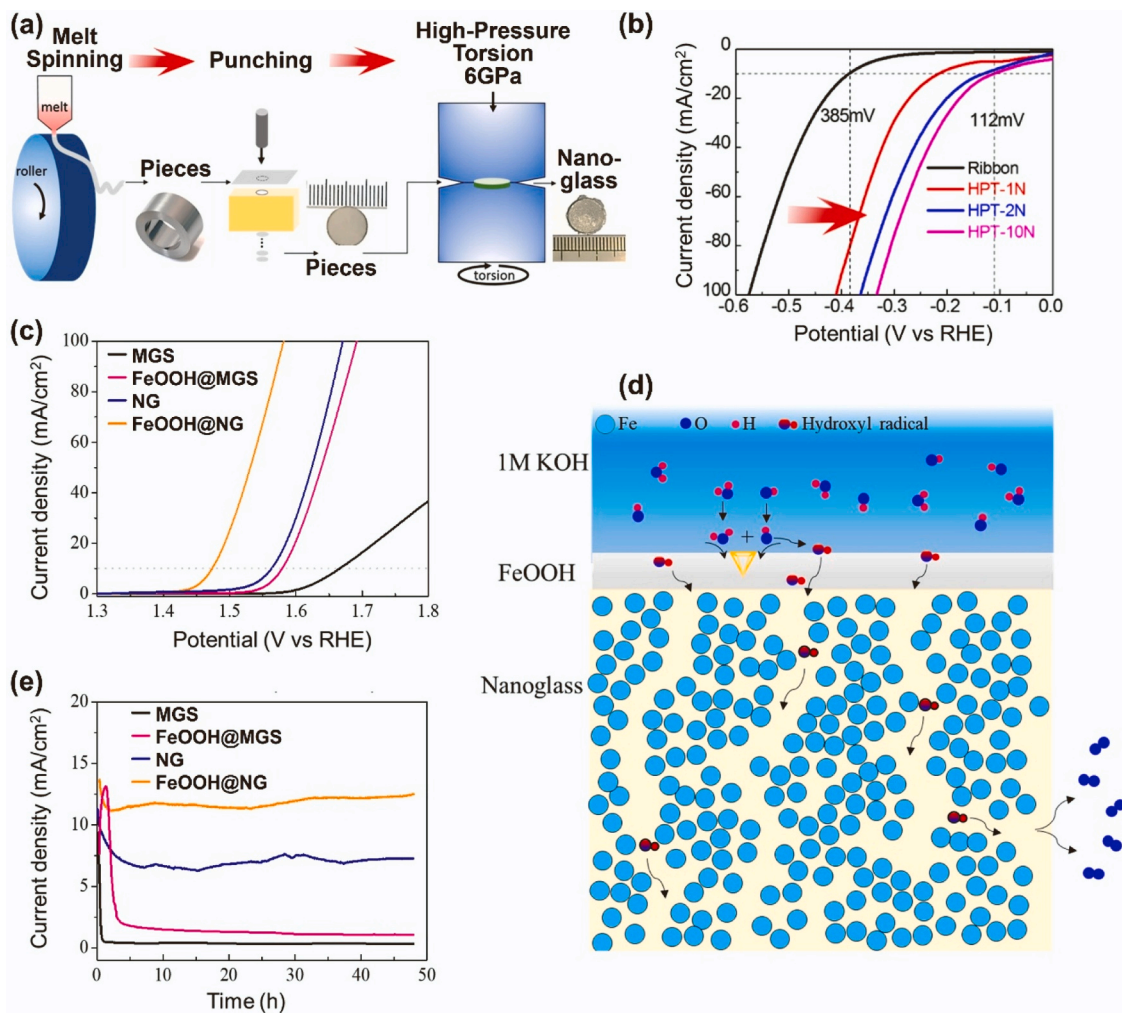
Fig. 49. (a) Schematic illustration for the fabrication of $Fe_{78}Si_9B_{13}$ nanoglass alloy [1023]. (b) Linear sweep voltammetry (LSV) curves of the $Fe_{78}Si_9B_{13}$ amorphous alloy upon HPT treatment [1023]. (c) LSV curves (iR compensation 90%) of melt-spinning glass (MSG), HPT-processed nanoglass (NG), glass covered by FeOOH (FeOOH@MSG) and and nanoglass covered by FeOOH (FeOOH@NG) [1026]. (d) OER catalytic mechanism of the FeOOH@NG [1026]. (e) stability performance obtained from chronoamperometric curves of all samples at the working voltage at 10 mA cm^{-2} [1026].

surface to produce hydroxyl radicals [1031, 1032].

$$OH^- + Vo^+ \rightarrow OH + Vo \qquad (17)$$

$$H_2O + Vo^+ \rightarrow H^+ + OH + Vo \qquad (18)$$

Thirdly, hydroxyl radicals attack Fe (0) to produce Fe (II).

$$Fe (0) + 2OH \rightarrow Fe (II) (OH)_2 \qquad (19)$$

Afterward, Fe (II) continues to be oxidized to produce oxygen molecules [1031, 1033, 1034]:

$$Fe (II) (OH)_2 + OH \rightarrow Fe (II\&III) OOH + H_2O \qquad (20)$$

Fe (II&III) OOH + OH→ Fe (III) ads + O$_2$ + H$_2$O(21)
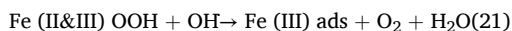
Finally, the reaction products Fe (III) near the amorphous matrix continuously react with Fe (0) to produce intermediate product Fe(II)(OH)$_2$, which participates in the catalytic cycle process [1035, 1036].

$$2Fe (III) ads + Fe (0) \rightarrow 3Fe (II) ads \qquad (22)$$

$$Fe (II) ads + 2OH^- \rightarrow Fe (II) (OH)_2 \qquad (23)$$
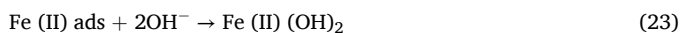
In addition, Fe (III) eventually exists in the alkaline medium as Fe (III) (OH)$_3$ colloids in the absence of Fe (0) by the following reaction.

$$Fe (III)_{ads} + 3OH^- \rightarrow Fe (III) (OH)_3 \qquad (24)$$
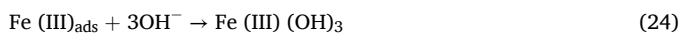
Furthermore, the catalytic performance of the FeOOH-covered nanoglass remains almost unchanged after 50 h continuous reaction (Fig. 49e). In short, the FeOOH-covered nanoglass can perfectly combine self-activation and synergistic catalysis between volume and surface, leading to high activity, fast reaction kinetics and stability of activity for OER. Besides good electrocatalytic activity for hydrogen production, SPD-processed nanoglasses are expected to show good activity for hydrogen storage [1037].

In summary, SPD can greatly enhance electrochemical hydrogen production through the formation of new nanoglass structures. After SPD, the overpotentials at the current density of the amorphous alloys can be greatly reduced, and the stability of HER and OER can be greatly enhanced. It can be predicted that SPD-processed materials will make outstanding contributions to electrochemical catalytic applications.

6.7. Hydrolytic hydrogen production

In recent decades, hydrogen generation from hydrolysis of some special materials has been an important research topic [1038]. Fig. 50a shows the commonly used materials for hydrolytic hydrogen production. Among them, active metals like magnesium and aluminum can react chemically with water with the following fundamental reaction equation:
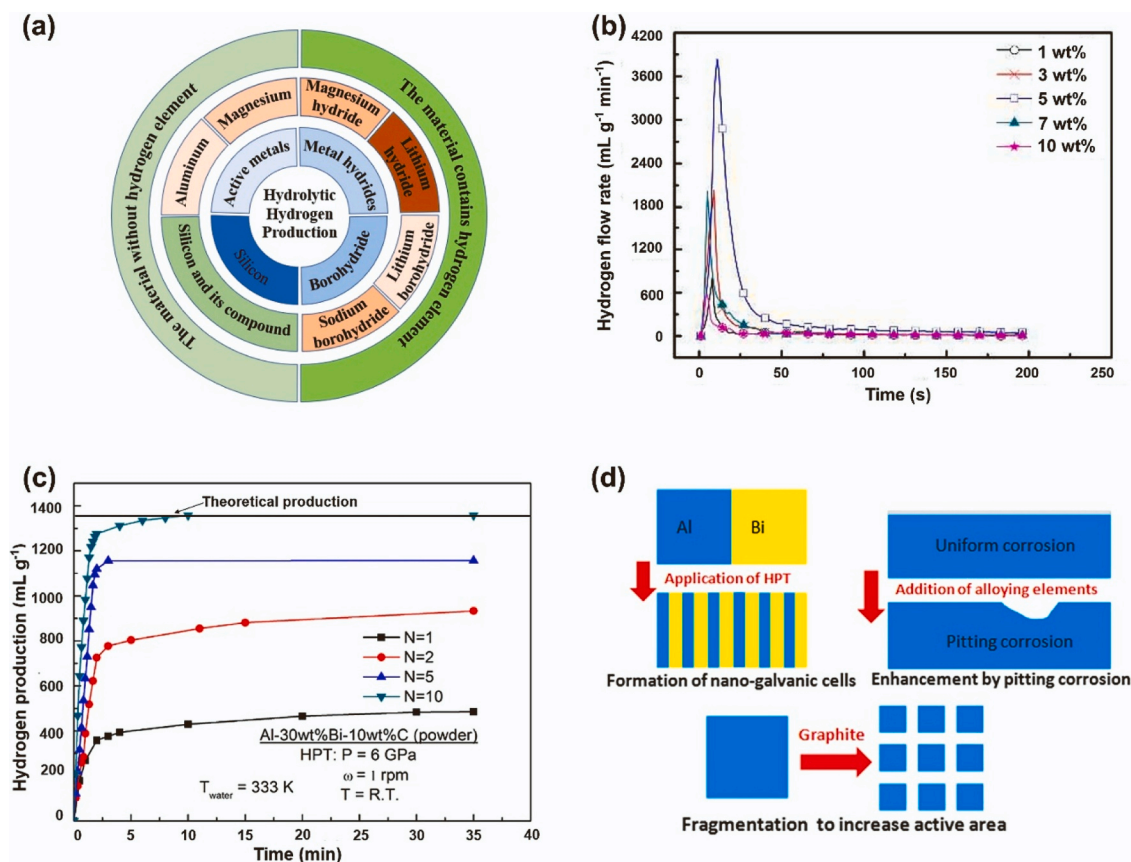
Fig. 50. (a) Materials used for hydrolytic hydrogen production [1038]. (b) Hydrolytic hydrogen flow rate curves of Al - 5 wt% LiH - x wt% Ga$_2$O$_3$ (x = 1, 3, 5, 7 and 10) at 298 K [1039]. (c) Hydrolytic hydrogen production curves of HPT-processed Al-30Bi-10 C (wt%) composite with different HPT turns [1040]. (d) Combination of three strategies to promote aluminum hydrolysis by high-pressure torsion [1040].

$$M + nH_2O \rightarrow M(OH)_n + n/2\ H_2 \qquad (25)$$

where M represents the metal and n stands for the number of electrons transferred in the reaction [1038, 1041]. This hydrolysis reaction, however, is often inhibited by the oxide film on the metal surface. Adding some catalysts or destroying the oxide film via mechanical activation are basic strategies to enhance the hydrogen generation behavior (Fig. 50b) [1038, 1041–1043]. SPD is one of the effective methods that can combine the advantages of the above strategies [846]. Successful attempts have been made in the Al-Sn and Al-Bi systems via HPT [1040, 1044, 1045]. In the Al-Sn binary system [1044], the improved hydrogen generation behavior was mainly attributed to the increased amount of micro-galvanic cells between aluminum and tin after HPT processing. The further addition of zinc to the Al-Sn system can promote pitting corrosion and therefore enhance hydrogen production [1045]. As bismuth can play both the role of tin and zinc, binary Al-Bi alloys show much higher hydrogen yield and hydrogen generation rate than Al-Sn alloys [1040]. The addition of graphite to the Al-Bi alloys can further enhance the hydrolysis speed due to the easy fragmentation of the reaction products (Figs. 50b and 50c).

Currently, most research on hydrogen production from the hydrolysis of Al-based materials is focused on finding materials with high reaction rates. For example, the instantaneous hydrogen flow rate of Al-5LiH-5Ga$_2$O$_3$ (wt%) is as high as 3837 mL H$_2$ min^{-1} g^{-1} (Fig. 50b) [1039]. Although the high rate is important for emergency cases, a stable hydrogen flow rate is more favorable for fuel cells [1046]. An ideal material may be one that can meet these two directions of application with proper treatments. As shown in Fig. 50c, HPT-processed Al-30Bi-10 C (wt%) composite can exhibit high instantaneous (10 HPT turns with a maximum hydrogen flow rate of ~1600 mL min^{-1} g^{-1}) or stable hydrogen flow rate (5 HPT turns with a stable hydrogen flow rate of ~600 mL min^{-1} g^{-1}) depending on HPT turns [1040]. However, the

underlying kinetic as well as the catalytic mechanism of such materials remain complex and need more in-depth studies. For kinetic studies, the shrinking core model is currently a common method to predict and simulate the practical experimental data of the aluminum hydrolysis reaction [1047–1050]. With proper modifications (e.g. considering the impact of single product AlOOH densification with time), this simulating model can correlate well with the actual data [1051–1053]. However, the aqueous solutions of such studies are primarily using acidic or alkaline solutions which is not eco-friendly and few studies have been done on the hydrolysis of bulk materials in neutral solution. Besides the common catalytic effect of catalysts, the catalytic mechanism for the hydrolysis of severely plastic-deformed Al-based materials can be influenced by deformation-induced microstructures. The accelerating effect of micro/nano galvanic cells on aluminum hydrolysis can be mainly attributed to the reduced grain size [1054, 1055]. In addition to the grain size effect, high-angle grain boundaries as well as the deformation texture may also have positive effects on the hydrolysis reaction [1056, 1057]. Several theoretical calculations also pointed out that aluminum hydrolysis can also be improved by some special surface orientations [1058–1060].

As for Mg-based materials, the hydrolysis reaction is similar to the Al-based materials but often occurs at higher temperatures and the passive oxide film is also the key problem. The methods for eliminating the passivation layer include adding acid [1061], reducing particle size [1062], alloying [1063, 1064] and adding strong acids and weak alkaline salts [1065, 1066]. Adding acid can effectively remove the passivation layer, but acid may change the hydrolysis reaction path, which will greatly reduce the theoretical hydrogen yield. Reducing the particle size of magnesium can improve the reaction conversion rate, but too small a particle size increases the difficulty of storage. Adding strong acids and

weak alkaline salts to promote magnesium hydrolysis is a practical and very effective way [1067, 1068]. With the combination of the above strategies, MgLi-10EG (wt%) alloy exhibited a hydrogen yield of ~100% and a maximum hydrogen generation rate of 1147 mL min^{-1} g^{-1} [1069].

In summary, SPD can combine the advantages of several effective strategies for hydrolytic hydrogen production such as the nano-galvanic cell effect, pitting corrosion effect and fragmentation effect, as shown in Fig. 50d. Future work should pay more attention to the kinetic studies and catalytic mechanism of materials with deformation-induced
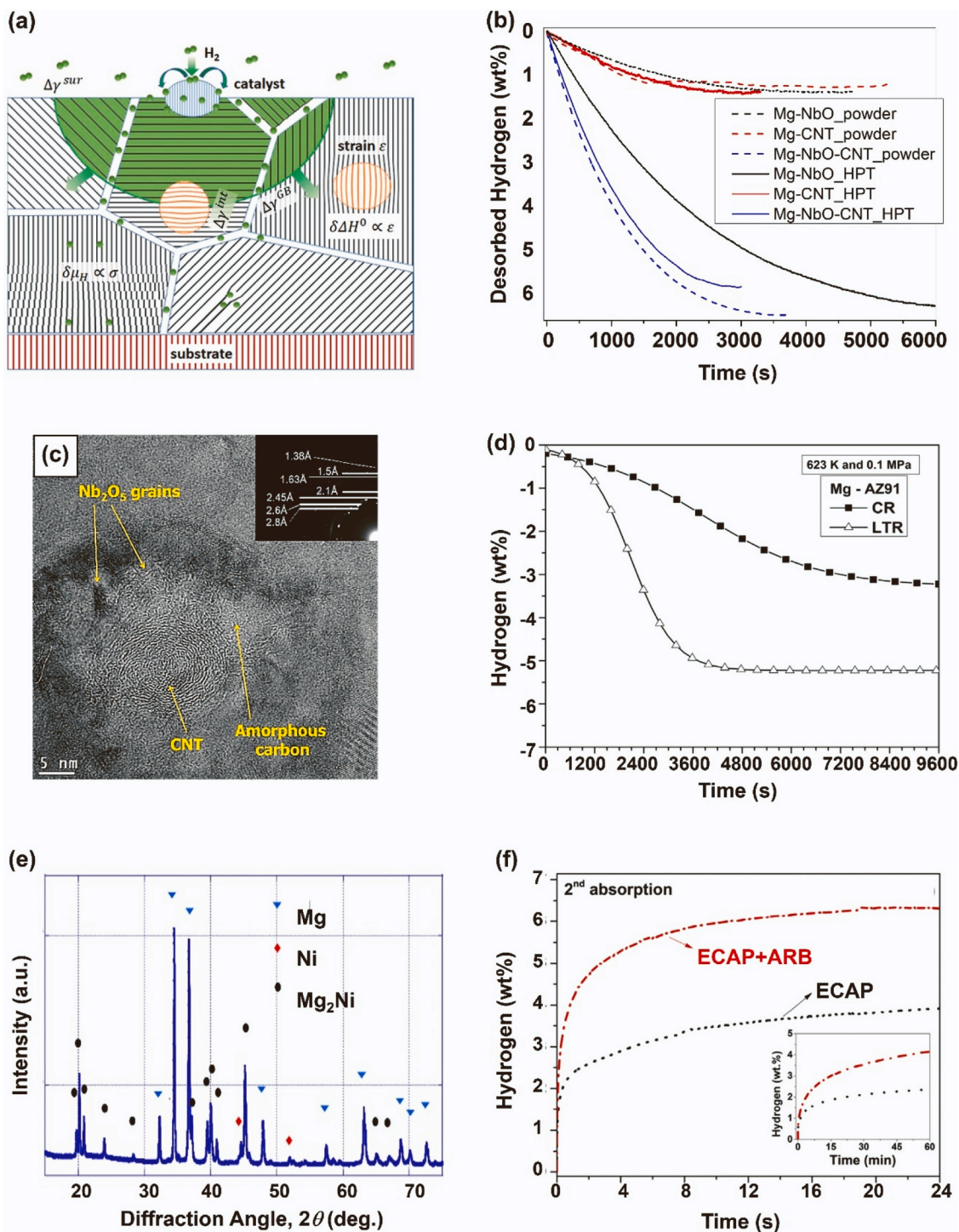
Fig. 51. (a) Structural and geometrical features relevant to hydrogen sorption in nanomaterials [1081]. The growth of the hydride phase, depicted in green, requires H$_2$ dissociation possibly favored by a catalyst, subsurface penetration and H diffusion, which is accelerated along internal interfaces or line defects (dislocations). (b) Dehydrogenation kinetic measurements obtained at 573 K and 1 kPa for nanocrystalline magnesium powders catalyzed by Nb$_2$O$_5$ and/or carbon nanotube (CNT) and for the corresponding HPT-processed discs [1086]. (c) High-resolution lattice image of cycled HPT-processed Mg + Nb$_2$O$_5$ + CNT composite (inset: selected area electron diffraction pattern) [1086]. (d) Hydrogen desorption curves of cold rolled AZ91 alloy at room temperature (CR) and at low temperature (LTR) [1098]. (e) XRD pattern of a Mg-22Ni (wt%) alloy after fast forging at 480°C with the significant formation of Mg$_2$Ni [1102]. (f) Hydrogen absorption kinetic curves of an ECAP and ECAP + ARB processed ZK60 alloy measured at 623 K, under 2 MPa pressure [1103].

microstructures.

6.8. Solid-state hydrogen storage

Hydrogen-based energy storage can be a promising technology shortly [1070, 1071]; however, there are still technological challenges in the way of realizing it in practice. One obstacle is the difficulty of storing hydrogen. A hydrogen storage system has to possess high storage capacity, appropriate charge/discharge rate and long operational cycle life [1072]. In the past decades, a lot of effort was put into the development of material-based hydrogen storage systems, including metal hydrides [1073, 1074], as they generally offer large storage capacity by volume and reversible operation [1075, 1076]. Metal hydrides store hydrogen not only on the surface but in the whole volume of the material as well through a chemisorption reaction [1077–1079]. Thus, hydrogenation/dehydrogenation of these materials involves both long-range diffusion of hydrogen atoms and phase transformations. Structural inhomogeneities, nanostructuring and lattice defects can promote these processes [1080]. It was reported that altering the microstructure by SPD methods is an effective way to enhance the hydrogen absorption and desorption kinetics of these materials, see Fig. 51a [847, 1081, 1082]. Moreover, mechanical treatment by SPD can induce the formation of dislocations and grain boundaries in the oxide layer that is usually present on the surface of metal hydrides, thus making it permeable to hydrogen for easy activation. In this section, various SPD methods applied to hydrogen storage materials are reviewed and the impact of such process on the thermodynamics, kinetics and activation of these materials will be discussed in coming sections.

- HPT can be applied to various hydrogen storage systems, as demonstrated in a recent overview [358]. When MgH_2 powder is deformed by HPT, an intensive nanostructure formation takes place, which positively influences the hydrogen storage performance [1083]. The application of high-energy ball milling before HPT can promote mechanochemical routes, resulting in the formation of intermetallic compounds with advantageous hydrogen storage properties. Plastic strain generated by HPT can increase the maximum hydrogen capacity of ball-milled $Mg_{70}Ni_{30}$ nanopowders by 50 % due to an increased number of defects [1084]. It was established recently that carbon nanotubes (CNTs) can provide fast diffusion channels during hydrogenation and dehydrogenation for the hydrogen atoms through the passivated surface layer into the bulk material [1085]. The addition of Nb_2O_5 to magnesium catalyzed by CNTs plays a crucial role in attaining suitable hydrogen capacity (see Fig. 51b) [1086]. The CNT sections presented in Fig. 51c are preserved during the plastic deformation of ball milling + HPT and subsequent sorption cycling. The hydrogenation behavior of fully disordered systems, like metallic glasses can significantly be improved when the material is subjected to severe shear deformation by HPT [1087, 1088]. The enhanced hydrogen sorption kinetics of a melt-spun $Mg_{65}Ni_{20}Cu_5Ce_{10}$ nanoglass subjected to torsional straining are attributed to the abundant pathways for hydrogen diffusion at the interfaces between the nanoglass regions that are developed during the HPT process [1037].
- ECAP is often used to enhance the hydrogen storage properties of different bulk materials. It was shown that the number of ECAP passes [1089] and the deformation route [1090] have a significant effect on the absorption/desorption time and the maximum reversible capacity of different Mg-based alloys. The improvements were attributed to the increased grain boundary fraction that presents nucleation sites for the hydride and provides fast diffusion channels for hydrogen atoms. The use of ECAP can also induce the crystallization of different second-phase particles (for example, $Mg_{17}Al_{12}$ in AZ61 and AZ31 alloys) that can enhance the absorption/desorption performance of the material as catalysts [1091, 1092]. Improvement

of the long-term cycling stability up to 1000 cycles was demonstrated for ZK60 magnesium alloy after ECAP processing [1093].
- Cold rolling was shown to reduce the necessary activation time for different Mg-based materials [1094, 1095] and the TiFe alloy [1096, 1097]. Rolling can also be performed at cryogenic temperatures, which results in a more refined microstructure and better absorption/desorption kinetics than the sample rolled at room temperature (see Fig. 51d) [1098]. ARB offers the possibility to synthesize composites in which the secondary phase particles can act as nucleation sites as was demonstrated for the Mg-Ti system [1099]. It was shown that cold rolling induces a strong (002) texture in magnesium and this texture promotes the hydrogen absorption capability of the specimen.
- Fast forging, a less conventional SPD technique, can operate at larger scales and shorter times [1100]. Earlier research on the mechanical processing of MgH_2 + 5 wt% Fe by fast forging resulted in a good dispersion of the catalyst particles and significant nanostructuring [1101]. A Mg+Ni powder mixture processed by fast forging exhibits a threshold processing temperature, below which hydrogen absorption is mainly governed by the formation of defects and cracks, enhancing hydrogen diffusion into the bulk, however, forging at elevated temperature yields the solid-state formation of Mg_2Ni nanocrystals that can act as a catalyst, see Fig. 51e [1102].
- Combination of different SPD techniques, for example, ARB + ECAP [1103] and ECAP + cold rolling [1104], can further improve hydrogen storage performance compared to the use of only a single method (see Fig. 51f).

In conclusion, several SPD methods can significantly improve the hydrogen storage capabilities of different classes of materials via refining their microstructure, generating grain boundaries, and inducing lattice defects, hence improving the diffusion of hydrogen and the nucleation of the hydride phase. Nevertheless, the different SPD techniques promote different microstructures (different types and densities of defects, texture, *etc.*) which can result in different hydrogen sorption properties.

6.8.1. Thermodynamic tailoring of hydrogen storage materials

Solid hydrogen storage materials such as solid-state hydrides have been studied for over 50 years [1105], for their uses as energy storage materials [1106–1108]. As discussed in an earlier chapter, the merits of these materials include lower operation pressure and energy consumption, higher volumetric hydrogen density and safety compared with compressed high-pressure or cryogenic liquid hydrogen storage [1109–1116]. A main concern regarding these materials is tailoring their thermodynamics. Hydrogen is reversibly absorbed and desorbed via a chemical reaction accompanied by energy change [1117].

$$M + x/2H_2 \rightleftharpoons MH_x + \Delta H \qquad (26)$$

where M is the metal or alloy, x is the amount of reacted hydrogen and ΔH is the enthalpy change. Fig. 52a illustrates the reversible phase transition process between metal (in the α phase) and metal hydrides (in the β phase) [1118]. Hydrides can be divided into two categories of interstitial and non-interstitial hydrides, which are comprised of metallic and covalent or ionic bonds, respectively [1119]. The dehydrogenation temperatures of solid-state hydrides are positively correlated with bond strength [1120]. This means the dehydrogenation temperature of the hydrides is determined by thermodynamics, which can be obtained from the van't Hoff equation [1121, 1122]:

$$\ln PH2 = -\frac{\Delta H}{RT} + \frac{\Delta S}{R} \qquad (27)$$

In Equation 27, P is hydrogen pressure, T is temperature, R is gas constant and ΔS is the entropy change which is approximately equal to 130 J/(K mol H_2) [1123, 1124]. Fig. 52b indicates the corresponding
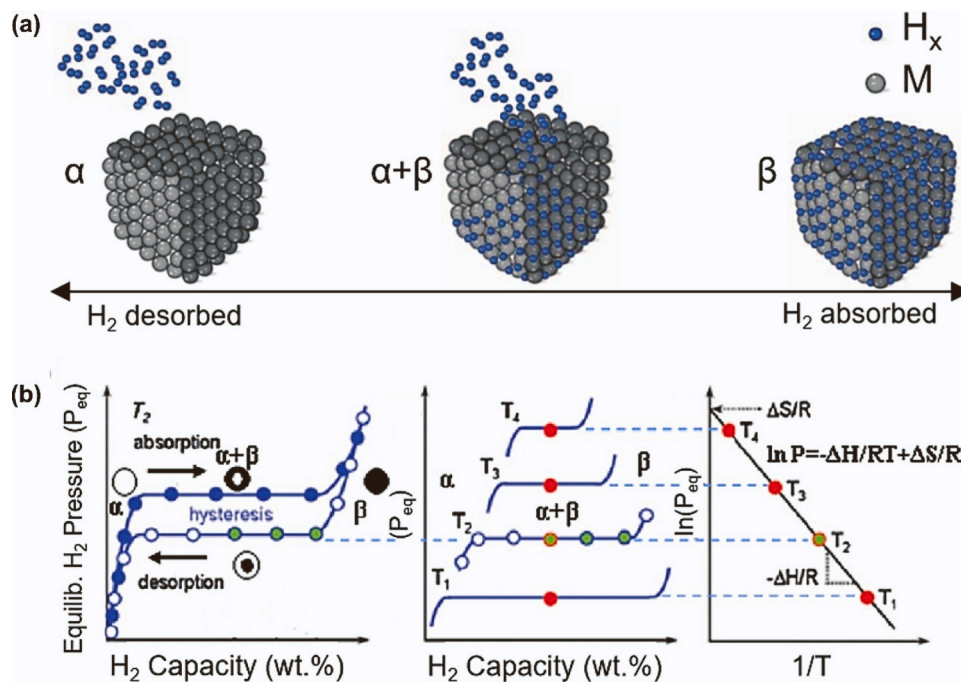
Fig. 52. (a) Diagrammatic representation of phase transition during reversible hydrogen storage process [1118]. (b) Typical pressure-composition isotherm, phase diagram, and van't Hoff plot of a metal hydride [1122, 1123].
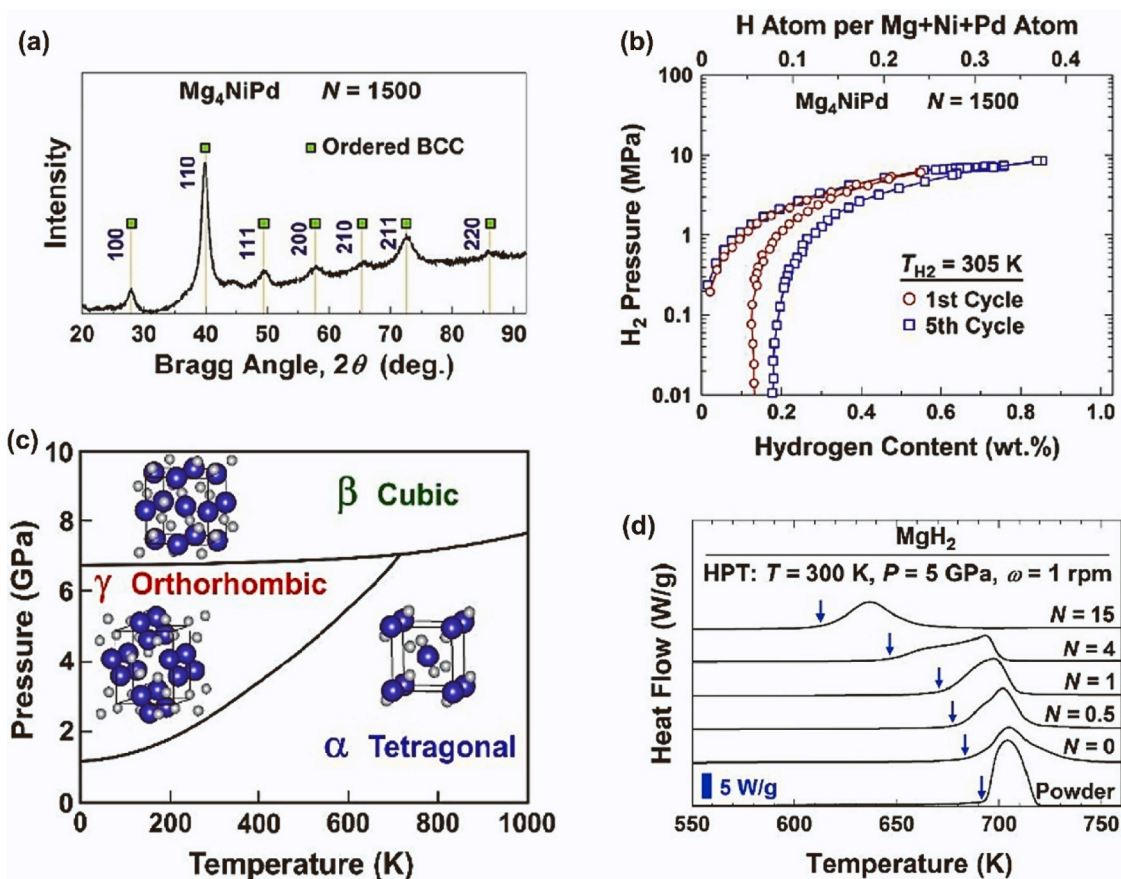
Fig. 53. (a) XRD pattern of Mg_4NiPd after 1500 HPT turns [359]. (b) Pressure-composition isotherm of Mg_4NiPd at 305 K [359]. (c) Pressure-temperature phase diagram of MgH_2 [515]. (d) Heat flow in differential scanning calorimetry for MgH_2 processed by HPT for various turns [515].

relationship between pressure-composition-temperature (PCT) isotherms and the van't Hoff equation [1122, 1123]. For the reversible desorption/absorption of hydrogen at a temperature close to room temperature, the ideal dehydrogenation enthalpies of hydrides are 25–35 kJ/mol H_2 [1124, 1125]. Therefore, thermodynamic tailoring is in great need to design materials for practical applications [1126].

Thermodynamic tailoring can be realized by the following approaches: (i) nanoengineering [1127–1129]; (ii) alloying [1118, 1129–1132]; (iii) phase transition control [1101, 1133]; and (iv) reaction pathway changes [1129, 1134, 1135].

SPD has been proven to be a powerful tool for thermodynamics tailoring, by taking MgH_2 as an example. MgH_2 is widely regarded as a promising hydrogen storage material because (i) its high hydrogen capacity is 7.6 wt%, and (ii) magnesium is the ninth most abundant element in the universe [1129]. High dehydrogenation thermodynamics of 75 kJ/mol H_2 for MgH_2, however, hinders its application at room temperature [1129]. Thermodynamic destabilization of magnesium is a main topic for hydrogen storage at room temperature. Recently, a Mg-based ternary alloy Mg_4NiPd was designed based on the prediction of first-principles calculations. The Mg_4NiPd alloy was expected to have moderate hydrogen binding energy between the Mg_2Ni and Mg_2Pd ones [359, 1077]. It was successfully prepared with an ordered BCC-based structure (Fig. 52a) through 1500 turns of HPT processing and was found to exhibit a reversible 0.7 wt% hydrogen storage capacity at room temperature (Fig. 53a). Among the possible octahedral sites of 4Mg-2Ni, 4Mg-1Ni-1 Pd and 4Mg-2 Pd in Mg_4NiPd, the 4Mg-1Ni-1 Pd site with the hydrogen binding energy of −0.12 eV was found to be responsible for the room-temperature hydrogen storage. Furthermore, a series of alloys with elevated hydrogen storage properties have been fabricated by the HPT process, such as $Mg_{65}Ni_{20}Cu_5Y_{10}$ alloy [1088], $Mg_{65}Ce_{10-}Ni_{20}Cu_5$ nanoglass [1037], MgTiVCrFe HEA [314], *etc.* [1082]. HPT has become a popular technology to improve the performances of many hydrogen storage materials including, but not limited to TiFe alloys [664, 1136, 1137], Mg-based alloys [313, 515, 1083, 1138, 1139], HEAs [1082] and others [192, 309, 322].

Another strategy to tailor the thermodynamics of hydrogen storage materials is through phase transformations. For example, MgH_2 has an α phase with a stable tetragonal structure at ambient pressure and transfers into the γ phase or the β phase at higher pressures (Fig. 53c) [1077, 1133]. A transition from the α phase to the γ phase occurs by HPT processing under 5 GPa, and the proportion of the γ phase increases with the increase of HPT turns. The formation of almost 100% γ phase was obtained after HPT processing for 15 turns. With the increase of the γ phase fraction, the dehydrogenation temperature reduced gradually. The formation of the nanocrystalline γ phase by 15 turns of HPT processing resulted in a decrease of the dehydrogenation temperature by 80 K (Fig. 53d) [515]. The results indicate that HPT processing is also effective in reducing the thermodynamic stability of MgH_2.

In conclusion, SPD is a powerful tool that helps to tailor the thermodynamics of hydrogen storage materials by fabricating metastable alloys or preparing unstable phases. Among the different SPD methods, HPT is currently the most popular method for tailoring the thermodynamics of such materials. However, HPT has main drawbacks to be overcome [1077, 1082]: it is hard to prepare samples on a large scale. In the future, HPT technology and other SPD methods are expected to be further improved for the preparation of samples with not only larger sizes but also improved properties.

6.8.2. Kinetic tailoring of hydrogen storage materials

Kinetics of hydrogen storage in metal hydrides, particularly in magnesium and magnesium-based hydrides, are actively investigated because of their potential for commercial applications [1140]. One way to increase the hydrogenation kinetics in metal hydrides is by mechanical deformation. Many techniques have been used, such as ECAP [1093, 1141–1144], HPT [181, 192, 309, 334, 359, 1139, 1145, 1146] and cold rolling (also called ARB) [5, 1147–1150]. This last technique is arguably the easiest to scale up to the industrial level. However, cold rolling is usually performed in a horizontal fashion which may be problematic for metal hydride materials because they are often in a powder form. The solution to this problem is to perform the rolling vertically. In the cold rolling process, the deformation is mostly plane strain compression. The strain tensor is expressed as ε_{ij} (i, j = 1, 2, 3) where 1 is the rolling

direction (RD), 2 is the transverse direction (TD) and 3 is the normal direction (ND). In the ideal case, the strain in cold rolling is $\varepsilon_{11} = -\varepsilon_{33}$ and all other strains are zeros ($\varepsilon_{22} = \varepsilon_{12} = \varepsilon_{13} = \varepsilon_{23} = 0$). The effective strain is then equal to the von Mises equivalent strain [1151].

$$\varepsilon = \sqrt{\frac{2}{3}}\varepsilon_{11} \tag{28}$$

Magnesium is ductile but has only four slip planes [1152]. This means that magnesium will experience important work hardening after only a few rolling passes. For hydrogen storage applications, this is not a problem because the metal hydrides are usually used in the form of powders. Also, upon hydrogenation/dehydrogenation a metal hydride will decrepitate. Therefore, work hardening is acceptable for metal hydrides. Many groups have investigated the effect of cold rolling on pure magnesium and they found that cold rolling improved the hydrogenation kinetics [1098, 1141, 1153–1156]. The same conclusion was reached from investigations on magnesium alloys such as AZ91 [1098], MRI153 [1157], ZK60 [1158] and Elektron 21 [1156]. Other systems such as Mg-Al [1159], Mg-Cu [1160], Mg-Fe [1161], Mg-Ni [1162] and Mg-Pd [1163] have been also investigated. Fig. 54a shows a comparison of the first hydrogenation of magnesium and two magnesium alloys (MRI153 and AZ91D) after cold rolling while Fig. 54b shows the second hydrogenation [1164]. It is clear that cold rolling is beneficial for the hydrogenation kinetics. A more in-depth discussion of all these systems could be found in a recent review paper [1165]. Cold rolling can be also used on hydrogenated powder. Fig. 54c shows the effect of cold rolling and ball milling on MgH_2 powder [1166]. We see that the hydrogenation kinetics is much faster for the mechanically processed samples. Ball milling produced a sample with a higher hydrogen capacity and faster kinetics. However, the difference is that ball-milled powder should always be under an argon atmosphere while cold-rolled samples are processed in the air.

In conclusion, SPD methods are efficient in improving the hydrogenation kinetics of hydrogen storage materials. In this regard, cold rolling of magnesium alloys is promising because of its potential for scaling up and industrial use, although there are still many technical investigations that need to be done. For example, appropriate magnesium compounds should be searched, and the effect of cold rolling parameters such as rolling speed, number of rolls, temperature of rolling, number of rolling passes, thickness reduction at each pass, *etc.* should be studied. But arguably the most important investigation is to get a more in-depth understanding of the exact mechanism that makes the kinetics of hydrogenation better after SPD processing.

6.8.3. Activation and air resistance of hydrogen storage materials

In addition to thermodynamics and kinetics, activation is another important issue that should be considered for the industrial application of hydrogen storage materials. Difficult activation results in no hydrogenation, even when the material is thermodynamically favorable for hydrogen storage. Difficult activation is usually due to the formation of an oxide layer in air on the surface which hinders hydrogen dissociation and diffusion. The formation of oxide reduces the air resistance of these materials, and thus, they should be usually handled under an inert gas atmosphere. Hydrogen storage materials are activated either by heating to high temperatures under vacuum, chemical or mechanical modification. Perhaps, TiFe is the most famous hydrogen storage material that suffers from difficult activation. TiFe has a B2 crystal structure and is known as a good candidate for stationary (housing) and semi-stationary (submarines) hydrogen storage applications because its hydrogenation is thermodynamically possible at room temperature, its volumetric storage capacity is high and it is reasonably cheap [1167–1172]. Nevertheless, the practical use of TiFe is hindered due to the difficulty of initial activation for the hydrogenation which requires exposure to a vacuum or a hydrogen atmosphere under a pressure of ∼3 MPa at temperatures higher than ∼673 K [1167–1172]. SPD has introduced a
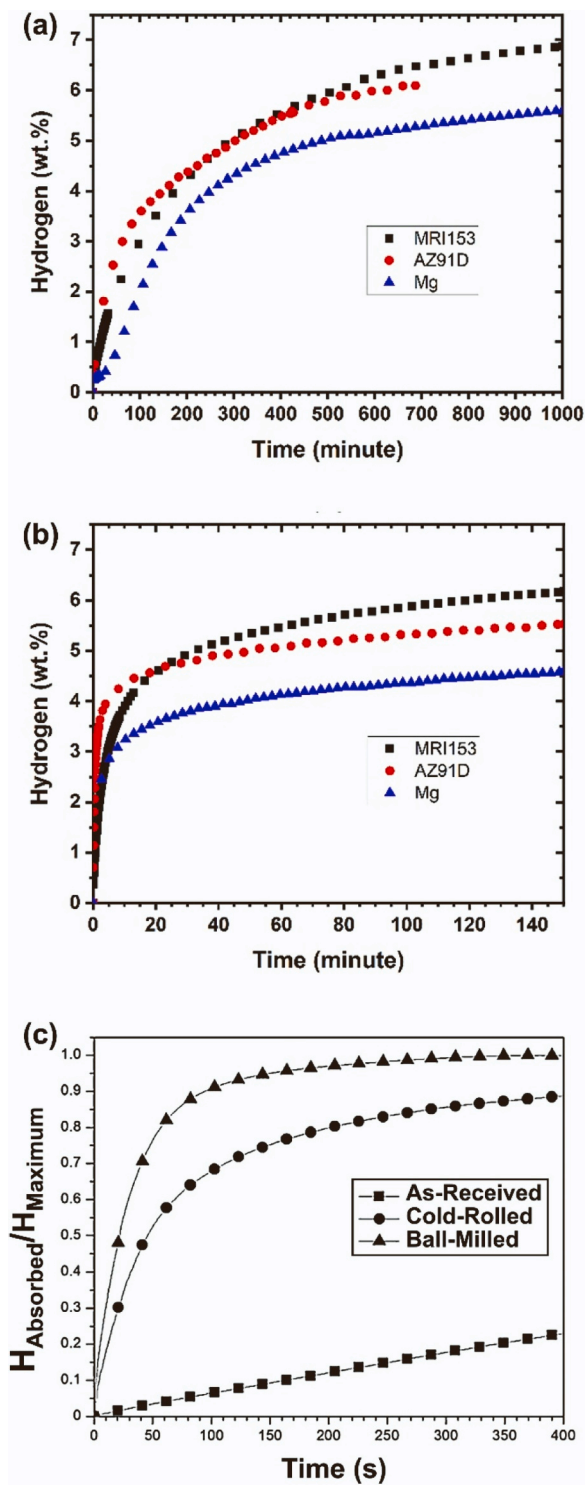
Fig. 54. (a) First and (b) second hydrogenation at 623 K under 2 MPa of hydrogen for cold-rolled pure magnesium, MRI153 and Az91D alloys [1157, 1164]. (c) Normalized kinetic absorption at 623 K and under 2.0 MPa hydrogen pressure for MgH$_2$ in as-received, cold rolled (five passes, CR5X) and mechanically milled for 30 min (BM 30 m) [1166].

Fig. 55. (a) pressure-composition isotherms of TiFe at 303 K for annealed sample, sample processed by compression under 6 GPa ($N = 0$) and samples processed by HPT for $N = 1/4$–10 turns [1136]. (b) Variation of hydrogen content against hydrogenation time at room temperature after the first and second exposure to hydrogen under a pressure of 2 MPa for Ti-Fe-Mn intermetallic processed by HPS including as-received ingot and HPT-processed disc [1186].

new pathway for easy activation of TiFe and many other materials as will be discussed in this section [664, 1136, 1137, 1173].

An example of the effect of SPD on activation is shown in Fig. 55a where TiFe was processed by HPT for different numbers of turns including the samples after annealing and after compression but without rotation [1136]. While hydrogen absorption is essentially negligible in the samples after annealing and after compression, the absorption occurs by 1.6–2.1 wt% after HPT processing. It is important to note that this hydrogen absorption was realized after exposure to air for several hundred days following HPT processing. Moreover, when an HPT-processed sample was left in the air for 400 days, subjected to hydrogenation for five cycles, and left in the air for an extra 30 days, hydrogen absorption still occurred without activation. Such experiments thus demonstrate that HPT-processed TiFe is quite air resistant and hardly deactivated in the air once it is processed by HPT [1136]. Here it should be noted that TiFe is an extremely hard and brittle material, but its SPD processing could be realized by HPT [1, 2, 23, 177, 179]. As discussed earlier, the high processing pressure in HPT makes it applicable not only to metallic materials [177, 674, 1174] but also to hard-to-deform materials such as intermetallics [1175–1178], ceramics [584, 844, 1179] and semiconductors [512, 1180–1185].

Activation of hydrogen storage materials by SPD is not limited to the HPT method. As an alternative to the HPT process, which uses small disc- or ring-shapes, the HPS process has been developed [57]. The HPS utilizes sheets, and thus, it has the potential to upscale the sample size [179, 240, 1187]. As mentioned earlier, the strain in HPS is accumulated by the reciprocation of anvils with respect to the sample [1188], while the rotation of the anvils is adopted in HPT [20]. Because HPS is operated under high hydrostatic pressure as in HPT, its application is also

feasible to hard-to-deform materials [240, 244, 1187]. In a recent study, a TiFe intermetallic containing a minor addition of Mn (TiFe$_{1-x}$Mn$_x$ with $x = 0.3$) was processed by HPS to enhance its hydrogen storage activation [1186]. The addition of Mn to TiFe reduces the hydrogenation pressure and activation temperature [1189, 1190], but the material still needs activation [1173]. Fig. 55b shows the hydrogenation kinetics curves of the HPS-processed strip and an as-received ingot [1186]. For comparison, a hydrogenation curve is also included from the HPT-processed sample [1173]. The hydrogenation occurs quickly in the sample processed by HPS, while no appreciable hydrogenation proceeds in the as-received ingot without the HPS process, at least for the period exposed to the hydrogen atmosphere. Incubation of ~60 min is observed after the first exposure of the HPS-processed sample to hydrogen, but the hydrogenation starts immediately after the second exposure in the HPS-processed sample. The fast hydrogenation for the second exposure without incubation is similar to the one observed in the HPT-processed sample (measured after the fourth hydrogenation cycle) [1173].

The activation of hydrogen storage materials by SPD processing was also reported by cold rolling [1137], rolling and HPT [1191] and ball milling [1192, 1193]. Here, it should be noted that the materials processed by ball milling as a powder-SPD method are not air resistant, while materials processed by cold rolling, HPS and HPT as bulk-SPD methods are quite air resistant. As discussed earlier [1136], the enhanced activation and air resistance by bulk-SPD methods should be due to the formation of a high density of lattice defects such as dislocations and grain boundaries. Particularly, grain boundaries are expected to provide pathways for fast hydrogen diffusion and improve both hydrogenation activation and kinetics [1136]. Future studies are needed to clarify the exact mechanism underlying the positive effect of SPD on hydrogen storage activation.

6.8.4. Mass sample production for hydrogen storage

Magnesium is one of the most appropriate hydrogen storage materials [1194, 1195], while SPD-processed magnesium has both fast kinetics and large hydrogen uptake, as discussed in recent review papers [5, 1077, 1196]. Hydrogen diffusion, restricted solid solution of hydrogen in magnesium and nucleation of hydrides are some issues that are positively affected by SPD processing [1197–1200]. However, mass production of SPD-processed materials is a main challenge for their commercialization in hydrogen storage applications. Besides cold rolling, as reviewed in an earlier chapter, fast forging (high-speed drop forging) and ECAP are two methods with high potential for upscaling, as will be discussed in this section.

The so-called fast forging process (Fig. 56a) was applied to Mg-based materials. The flow of material takes a rather perfect two-dimensional isotropic character in the open die fast forging procedure contrarily to the one-dimensional transformation of the microstructure in cold rolling. Moreover, compared to cold rolling with a 50% thickness reduction, a much higher thickness reduction (90%) can be achieved by fast forging in only one pass [1201]. For example, a cylinder billet of a Mg-rich alloy with 12 mm in diameter and 20 mm in height, transforms into a disc of ~38 mm in diameter and ~2 mm in height (thickness) in one pass of fast forging [1202]. Another benefit of fast forging is that the process is operated fast within 5×10^{-3} s with a flow rate of at least 25 m/s [1100, 1203]. In fast forging, the kinetic energy E of the free-falling load is assumed to expand mostly on the impact energy of plastic deformation ΔW [1204]. The heat flux of the adiabatic process on impact takes the form $\rho c \Delta T \sim k_P \Delta W$ (ρ: density, c: heat capacity, T: Temperature k_P: the coefficient determining the fraction of sample converted by plastic deformation at a given internal heat level). Other specific parameters like energy loss due to external friction with both the hammer and the die, intense friction between grains, formation of cracks and elastic vibrations can be defined by an additional k coefficient, leading to $\Delta T \sim k k_P \Delta W / c = \sim 200$ K. This thermal effect in fast forging enables parts of the sample to reach an intermediate situation between fragile to ductile states [1205, 1206]. It can be shown using the Crockroft and Latham
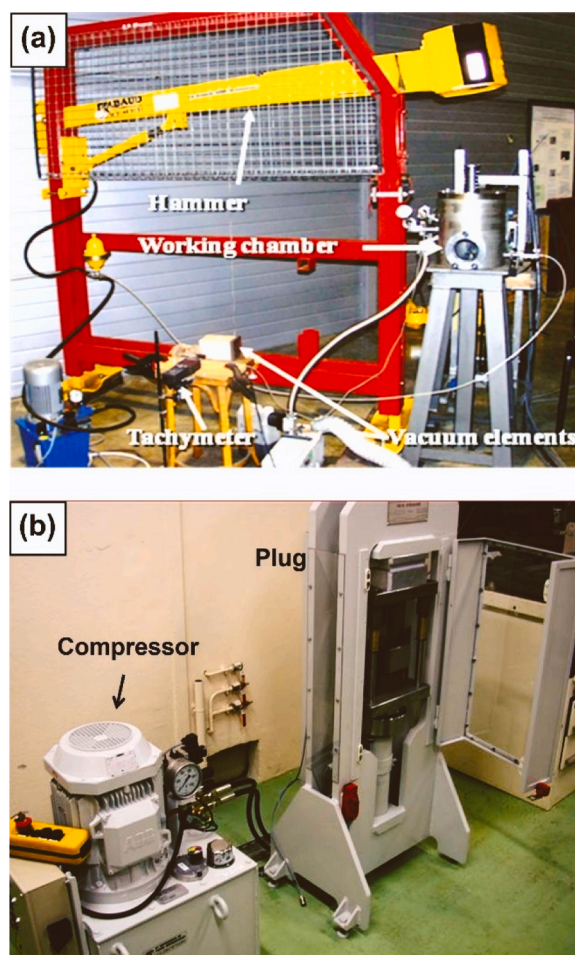
Fig. 56. (a) Fast Forging instrument of the drop type (sample is placed in an argon-filled chamber and can be also heated using an induction coil). (b) ECAP instrument (die can be heated on demand by resistive inserts placed in the die. The deformation rate can be controlled in both instruments by computer-connected sensors [1100].

criterion [1207, 1208] that the thermal effect and non-uniform metal flow may generate porosities, de-cohesion then create extended fractures which are positive features for hydrogen storage materials.

Since the early paper published by Skripnyuk *et al.* [1209], ECAP has been demonstrated as an efficient SPD method for the mass production of Mg-based materials with fast hydrogen sorption kinetic [1045, 1143, 1210–1213]. After most of ECAP procedures, high-energy ball milling is applied to hydrogen storage materials to obtain a higher specific surface, but the time for milling is quite short [1214]. Nevertheless, the ECAP route showed high potential for the delivery of various hydrogen-reactive Mg-based materials such as ZK60 [1103], AZ31 [1215]) or more specific alloys [1216]. However, the sorption kinetics after ECAP are not still as fast as the widely reported data reported in the literature for the ball-milled powders with catalyst addition [1217–1223]. An ECAP instrument used to process hydrogen storage materials at the laboratory scale is shown in Fig. 56.

The performance of fast forging and ECAP for hydrogen storage materials is reasonably comparable notwithstanding the study where powders of pure magnesium (5–20 μm grain size) were compacted and processed by both fast forging and two passes of ECAP [1224]. The mechanically treated materials remained particularly fragile, so no subsequent high-energy ball milling was needed, but only attrition was applied for a few tens of seconds. Table 6 summarizes the results of hydrogen absorption and desorption, indicating the performances of the two methods are reasonably comparable.

Table 6

Hydrogen absorption and times and temperature for magnesium powder processed by ECAP and fast forging [1224].

SPD Process	Absorption (~7 w %)	Time (min.)	Desorption (100 w %)	Time (min.)
ECAP (2B$_C$)	2 MPa, 380°C (cycle 3)	45	15 kPa, 380°C (cycle 3)	30
Fast Forging	2 MPa, 380°C (Cycle 1)	60	15 kPa, 320°C (cycle 1)	60

The reduction of the grain sizes to the UFG level (multiplication of the grains boundaries) and simultaneous creation of pores and cracks appear to be desirable to achieve such enhanced properties. The addition of catalysts during mass production to these UFG materials with pores and cracks can provide additional benefits for hydrogen storage [1225]. It is expected that the knowledge produced in recent years for SPD can facilitate the mass production of metal hydrides, particularly using methods such as cold rolling, fast forging and ECAP.

6.9. Hydrogen embrittlement resistance

The susceptibility to hydrogen embrittlement is markedly increased in high-strength steels with a tensile strength higher than 1.2 GPa. The addition of carbide-forming elements such as titanium, vanadium and molybdenum and subsequent high-temperature tempering are designed not only to contribute to secondary hardening but also to provide irreversible trapping into the martensite matrix to prevent local hydrogen concentration at prior austenite grain boundaries in BCC steels [1226–1228]. The roles of the lattice defects in the hydrogen embrittlement mechanisms are widely varied with different crystal structures, *i.e.* BCC and FCC structures [1229]. For austenitic stainless steel with an FCC structure, titanium-bearing Fe–25Ni–15Cr (wt%) steel is recognized as precipitation-hardened austenitic steel, which is strengthened via the dispersion of fine Ni$_3$(Al,Ti) precipitates. However, this type of steel is susceptible to hydrogen embrittlement despite containing large amounts of rare metal elements [1230]. Solid solution strengthening by interstitial atoms such as nitrogen enhances hydrogen-induced strain localization, which reduces the hydrogen embrittlement resistance [1231]. By contrast, Macadre *et al.* reported that grain refinement to approximately 1 μm mitigated the hydrogen-induced ductility loss in

Fe–16Cr–10Ni steel [1232]. Further, Mine *et al.* investigated [1233, 1234] the hydrogen effects on the tensile properties of UFG stainless steels produced by HPT processing and demonstrated that post-HPT annealing reduced the hydrogen-induced ductility loss while maintaining their high strength by reducing the dislocation density and mixing secondary phases in UFG austenite. Recently, it has been reported that high strength and reduced hydrogen embrittlement susceptibility were attained by introducing UFG and nanotwins into HEAs with an FCC structure [1235, 1236].

For metastable austenitic steels, although transformation-induced plasticity (TRIP) and twinning-induced plasticity (TWIP) phenomena improve the balance between tensile strength and ductility, the mechanical properties are considerably degraded in the presence of hydrogen [1237, 1238]. Park *et al.* and Bai *et al.* reported that grain refinement suppressed the hydrogen embrittlement in the TWIP steels [1239, 1240]. Metastable austenitic stainless steels such as types 301 and 304 with ordinary grain sizes undergo severe hydrogen embrittlement, which is attributed to deformation-induced martensitic transformation during tensile loading [1241, 1242]. Fig. 57 shows the effect of hydrogen on the deformation and fracture morphology of ordinary-grained type 304 stainless steel [1237]. The uncharged specimen exhibits a typical cup-and-cone failure with dimples on the fracture surface (Fig. 57a). The cross-section area is reduced at a part remote from the fracture surface along with a significant uniform elongation (Fig. 57b). Fig. 57c shows the EBSD phase map of the microstructure near the fracture surface at a longitudinal cross-section of the fractured specimen. Grains are substantially elongated along the tensile axis and α' martensite is densely formed at the fracture surface (Fig. 57c). By contrast, the specimen containing ~25 mass ppm of hydrogen exhibited plastic inhomogeneity and less α' martensitic transformation (Fig. 57d) when compared to the uncharged specimen (Fig. 57c). The hydrogen-charged specimen was fractured on the plane macroscopically perpendicular to the loading axis with many microcracks on the free surfaces (Fig. 57e). In addition, the fracture surface of the hydrogen-charged specimen was composed of quasi-cleavages and flat facets (Fig. 57f). Microtension testing studies successfully characterized the hydrogen-induced quasi-cleavage and flat facet formations using single-crystalline and twin bi-crystalline specimens, respectively [1243, 1244]. Hydrogen-induced quasi-cleavages in metastable austenitic stainless steel occurred at the interphase boundaries between the
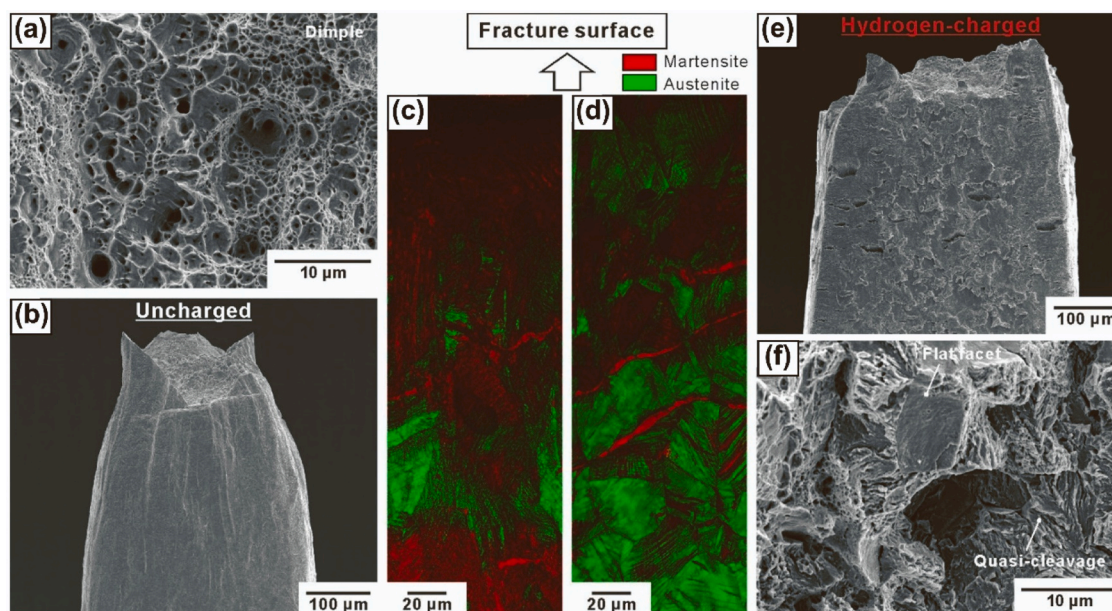
Fig. 57. SEM images of fracture surface, side view and EBSD phase maps at longitudinal cross-section in (a–c) uncharged and (d–f) hydrogen-charged specimens of ordinary-grained type 304 stainless steel [1237].
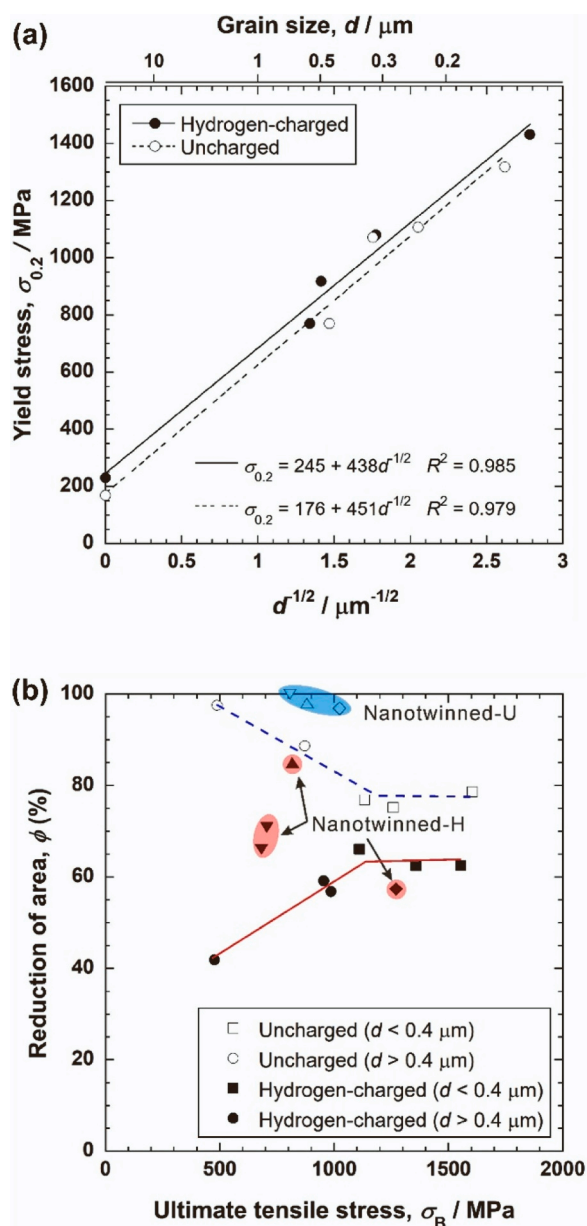
Fig. 58. (a) Grain size dependence of yield stress and (b) relationship between area reduction and ultimate tensile strength for 304 stainless steels with different grain sizes [848].

austenite and α′ martensite formed during the tensile loading, which was triggered by excess hydrogen generated owing to the differences in the hydrogen diffusivity and solubility between the two phases [1245]. The flat facet formation associated with twin boundary separation is the primary mechanism for premature failure concerning hydrogen embrittlement of the metastable austenitic stainless steels [1244, 1246]. It is then hypothesized that the dispersion of dynamic martensitic transformation suppresses the local hydrogen concentration at the interphase and twin boundaries.

Fig. 58 shows the effects of hydrogen charge on the tensile properties of type 304 stainless steels with different grain sizes, which is obtained using microtension testing [848, 1247]. Both uncharged and hydrogen-charged specimens well held the Hall-Petch relationship between yield stress and average grain size (Fig. 58a). The friction stress was increased by 40% by hydrogen charging but the Hall–Petch coefficient was invariable. This indicates that hydrogen strengthens the matrix via the solid solution effect, but does not influence the grain

refinement strengthening. The relationship between the reduction of area and UTS in the uncharged specimens reveals that the area reduction is reduced with increasing UTS in the average grain size range larger than ~0.4 μm, whereas it remains unchanged in the smaller grain sizes (Fig. 58b). The hydrogen-charged specimens have 1–1.5 GPa UTS with 60% area reduction in the UFG microstructures with grain sizes smaller than ~0.4 μm. In other words, ultra-grain refinement not only improves the balance between strength and ductility but also mitigates the hydrogen embrittlement susceptibility in metastable austenitic stainless steel. It has been argued that dynamic α′ martensitic transformation is the crucial factor determining hydrogen embrittlement susceptibility [1245, 1248, 1249]. The saturated hydrogen concentration is lower in α′ martensite than in austenite by an order of magnitude [1250]. When austenite containing hydrogen is transformed to α′ martensite, excess hydrogen can be generated, which corresponds to the difference in the saturated hydrogen concentration between the two phases. Subsequently, excess hydrogen diffuses out of the formed α′ martensite to the surrounding austenite and is accumulated at the interface boundaries because of the extremely high diffusivity of hydrogen in martensite compared to that in austenite. A finite element calculation study by Wang *et al.* supported [1251] that cracking occurs in the austenite region neighboring the formed α′ martensite. UFG austenite formed a single-variant α′ martensite from each grain, whereas ordinary-grained austenite selected several α′ martensite variants with a favorable orientation [1252]. For this reason, excess hydrogen generated from UFG austenite is dispersed, which results in reduced local hydrogen concentration and in turn, mitigates the hydrogen-induced ductility loss. As shown in Fig. 58b, the area reduction and UTS relationship reveals that the nanotwinned microstructures as well as the UFG microstructures can contribute to the strengthening while reducing the hydrogen embrittlement susceptibility in metastable austenitic stainless steel [848, 1253]. This supported that the hydrogen embrittlement resistance was enhanced in type 304 and TWIP steels with bimodal microstructures consisting of nanotwin bundles and recrystallized grains [1254–1256].

In summary, introducing UFG and nanotwins into metastable austenitic stainless steels is effective for mitigation of hydrogen-induced ductility loss through controlling dynamic α′ martensitic transformation. Plastic deformation processes of metastable austenitic steels at controlled moderate temperatures are a promising strategy for obtaining sustainable materials.

6.10. Corrosion resistance

With the advent of SPD, the effect of plastic deformation on corrosion has again come back to being an important topic of materials science [849, 1257, 1258]. In the ultrahigh strain range, microstructural features such as dislocation density, misorientation, and structures of grain boundaries develop progressively into an ultimate form of UFG or nanocrystalline structures which can affect the corrosion resistance [454]. For example, the introduction of a very high strain yields a maximum dislocation density of approximately 10^{15} m^{-2} in pure copper [454, 1259] and iron [446, 1260]. Moreover, the final grain size is copper is reduced to 0.4 μm by ECAP at room temperature [1261, 1262] and 80 nm by HPT at 100 K [1263]. After reaching the complete UFG structure, dislocations inside grains decrease; however, some residual dislocations remain. Such high-density grain boundaries with residual dislocations impact the corrosion behavior even in pure metals or single-phase materials [849]. A similar situation occurs in HEAs or multi-principal elements alloys (MPEAs), which are a new class of materials with superior mechanical properties, and some of them have very high corrosion resistance [1264]. The effect of SPD on the corrosion resistance of metals and conventional alloys is of great importance in scientific and practical viewpoints and the corrosion resistance of SPD-processed HEAs is waiting to be explored [1265]. Although corrosion resistance has been investigated for a wide range of alloys, Fe-based alloys and steel received the most significant attention due to their
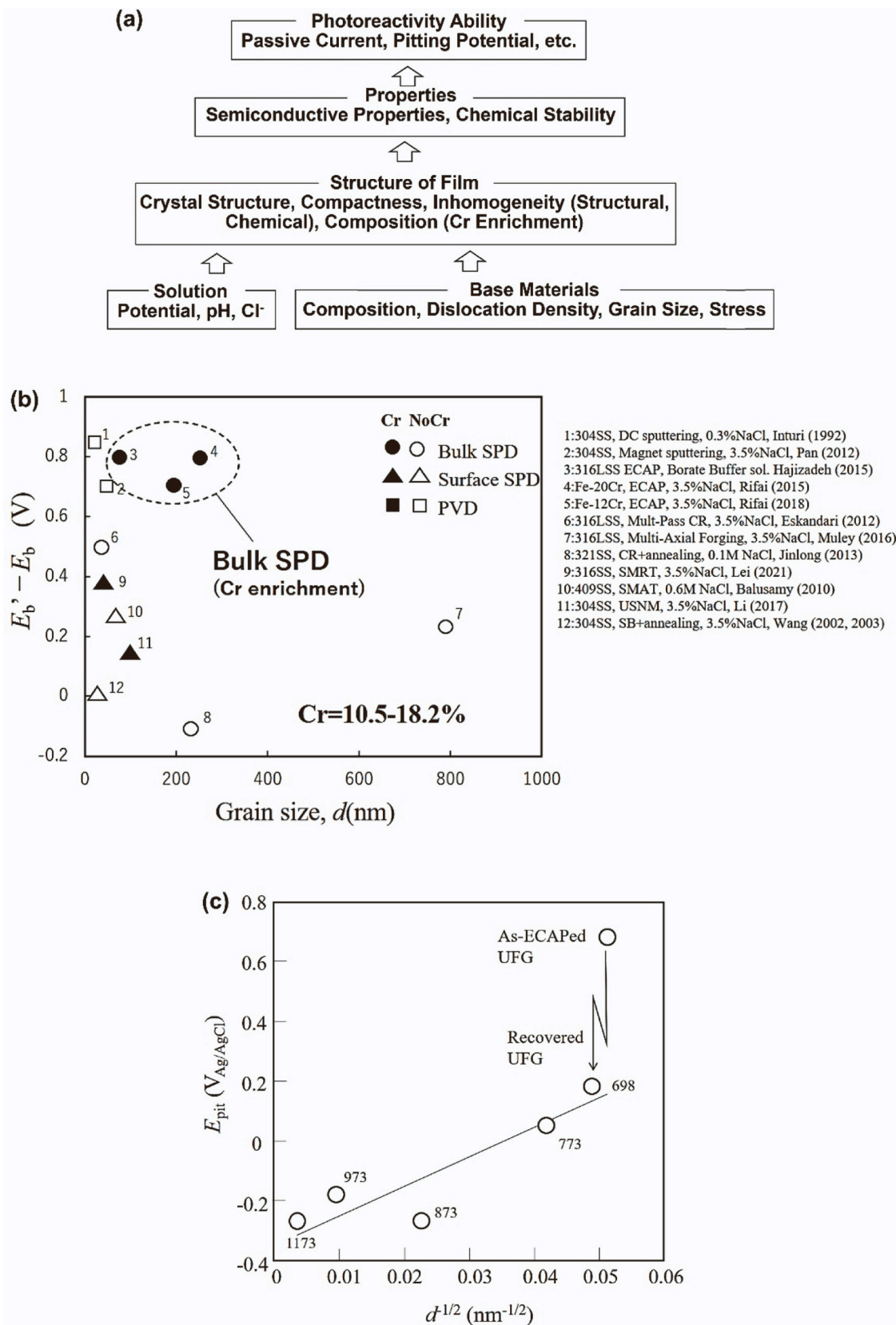
Fig. 59. (a) Hierarchal steps leading to the protective ability of passive films from the corrosive environment and microstructure of base metals [849]. (b) Relation between grain size of UFG stainless steels obtained via various methods versus the difference in pitting potentials of UFG (E_b') and coarse-grained (E_b') materials ("Cr" and "No Cr" indicate that chromium enrichment in passivation films was observed or not) [849]. (c) Relation between the pitting potential of Fe-12Cr (wt%) alloys and grain size after ECAP (eigth passes) and subsequent annealing (the numbers in the figure indicate the annealing temperature) [1275].

practical applications. The formation of a protective "passive film" on the surface and the effect of SPD on this film are the most critical issues studied in recent years. In this section, the features of the passive layer and corrosion resistance of steels are discussed.

6.10.1. Corrosion passive film features

Studies have shown that the corrosion resistance of Fe-based alloys in passive environments is enhanced by grain refinement down into the submicron or nanoscale level [1266]. This beneficial effect in Fe-Cr alloys has been attributed to the enhanced protective nature of the passive film due to a greater chromium enrichment in the film [1266]. Two independent mechanisms for greater chromium enrichment in passive films have been proposed: enhanced selective dissolution of iron and faster chromium diffusion [849, 1257, 1266]. Both mechanisms are supposed to originate from high-density of grain boundaries, as reported using high-resolution observation techniques such as high-angle annular dark-field scanning transmission electron microscopy (STEM) [1267] and *in situ* atomic force microscopy [1268]. Examination of nano-crystalline 316 L stainless steel processed by a surface mechanical rolling treatment (SMRT) has shown that protective passive films with surface chromium enrichment were localized to a zone at grain boundaries with a width of up to 50 nm [1267]. Maurice *et al.* showed the presence of an inhomogeneous chromium distribution that stems from the grain boundaries of the base metal and the granular structure of the passive film using *in situ* atomic force microscopy [1268]. This finding suggests that both these mechanisms, facilitated by grain refinement, might be capable of homogeneous passive film formation over the entire surface if the grain size is extremely small (possibly, <100 nm), which cannot be achieved by most classical SPD methods. Therefore, for the formation of a uniform and homogeneous passive film on all grains, the role of factors other than grain size should be considered. Fig. 59a shows the hierarchal relation between the protective ability of passive films formed on base metals of Fe-Cr alloys and structural parameters [849]. The protective ability is affected by the semi-conductive properties such as ion/point defect transport [1269, 1270] and/or chemical stability against dissolution into the solution [1271]. These properties are further related to crystal structure, compactness, structural or chemical inhomogeneity, and chemical composition. The passivity of Fe-Cr alloys appears in neutral to acidic solutions when the bulk chromium content exceeds approximately 12% [1272]. The passivation involves chromium enrichment in the passive film [1273], which has generally been explained based on the selective dissolution of iron and oxidation of chromium at the surface [1274]. Therefore, the structure of passive films is affected by the environment as well as the structure of the base metal.

Fig. 59b depicts the very low correlation between the difference in the pitting potentials of nanocrystals (E_b') and their coarse-grained counterpart (E_b) and the grain size of nanocrystals obtained using various methods [849]. Bulk-SPD [1275–1277] and physical vapor deposition (PVD) [1278, 1279] resulted in a significantly large improvement, as high as 0.8 V, in UFG materials although there were some exceptions [1280–1282]. Although surface-SPD methods such as SMAT can reduce the grain size to levels comparable to that of PVD [1267, 1283–1286], its effect on corrosion resistance appears to be less, probably owing to the presence of surface defects such as contamination or roughness. In Fig. 59b, the closed dots indicate that the chromium enrichment in the passive film after passivation was confirmed by X-ray photoelectron spectroscopy (XPS) or glow discharge optical emission spectroscopy (GD-OES) whereas the open dots indicate that chromium enrichment was not observed or confirmed. Despite a relatively large grain size and insufficient grain boundary area in the materials processed by bulk-SPD, uniform surface chromium enrichment might be achieved. The residual dislocations and their internal stress are the possible promotors of more uniform protective films over the entire surface. Fig. 59c shows the pitting potential of Fe-12Cr (wt%) alloys after eight ECAP passes and subsequent annealing [1275]. Note that the

pitting potential decreased appreciably after flash annealing at 698 K despite of negligible grain growth. The reduction of the peak-broadening in XRD after this flash annealing indicates that strain associated with residual dislocations, and possibly non-equilibrium grain boundaries was reduced. Thus, stress relaxation associated with structural recovery could degrade corrosion resistance.

The enhancement of the Cr/Fe ratio in the passivation film by the elastic or plastic deformation has been reported in Fe-Cr alloys [1287–1289]. One can consider the effect of dislocations on the Cr/Fe ratio based on the kinetics of the anodic dissolution of iron and chromium. For the anodic dissolution of the Fe-Cr solid-solution system, the degree of preferential dissolution of iron could be estimated by the ratio of the dissolution currents of iron and chromium. Under the stress field of dislocations, the interaction energy, w, arises between the solute chromium and the stress field and affects the dissolution currents of chromium and iron atoms differently according to the following equations.

$$i_{Fe} = A x_{Fe} \exp\left\{ -\frac{\Delta Q_{o,Fe} - (1-\beta)F\mu}{kT} \right\} \tag{29}$$

$$i_{Cr} = A x_{Cr} \exp\left\{ -\frac{\Delta Q_{o,Cr} - (1-\beta)F\mu - w}{kT} \right\} \tag{30}$$

where x_{Fe} and x_{Cr} are the atomic fractions of iron and chromium, respectively, $\Delta Q_{o,Fe}$ and $\Delta Q_{o,Cr}$ are the activation energy at equilibrium, F is the Faraday constant, β is a symmetrical factor, μ is the potential drop, A is constant, k is Boltzmann's constant and T is temperature. A simple estimation of the interaction energy arising from atomic mismatch and modulus misfit between the solute chromium in iron indicates that the interaction energy becomes -0.06 eV at the core of the edge dislocations and -0.07 eV at screw dislocations [849]. The negative value of the interaction energy means that the solute chromium is stabilized near dislocations, which leads to lower dissolution kinetics than iron. Assuming that all solute chromium atoms are positioned at the core of screw dislocations, the selective dissolution, i_{Fe}/i_{Cr}, could reach 2.2×10^4, where i_{Fe} and i_{Cr} are anodic currents corresponding to the dissolution of iron and chromium atoms, respectively. This value is more than 10^2 higher than that for no residual dislocations. The high-density residual dislocations of the order of 10^{15}–10^{16} m^{-2} in UFG can affect the dissolution balance between iron and chromium through their stress field and may promote the local chromium enrichment and protective ability of passive films [849].

6.10.2. Corrosion resistance of steels

As discussed in an earlier chapter, processing steels using SPD techniques enables obtaining UFG-structured steels with improved mechanical properties and corrosion resistance [1290, 1291]. The main mechanism for enhancing corrosion resistance by SPD is the formation of a passive protective layer that is more stable than in coarse-grained (CG) steels, mainly because of the high grain boundary density. The native oxide layer is formed in both coarse-grained and UFG steels, as shown in Fig. 60a. However, the high density of grain boundaries in UFG steels produces a uniform, compacted and well-adhered passive layer. This in turn results in uniform corrosion instead of localized corrosion because there are no preferential sites for cathodic or anodic corrosion [1276, 1292]. In addition, there are high-energy boundaries that also contribute to corrosion enhancement. Although corrosion in steels prefers to take place in the high-energy grain boundary region, there is also high atomic activity through diffusion to the surface as well as long diffusion paths. This influences the re-passivation process forming a thicker and more efficient passive layer [1293]. This mechanism has been also observed for other severely deformed metals [1258, 1294].

Different studies have been performed using SPD techniques to study the enhanced corrosion resistance over a range of steels. For carbon, alloyed and stainless steels, which have been mainly processed using
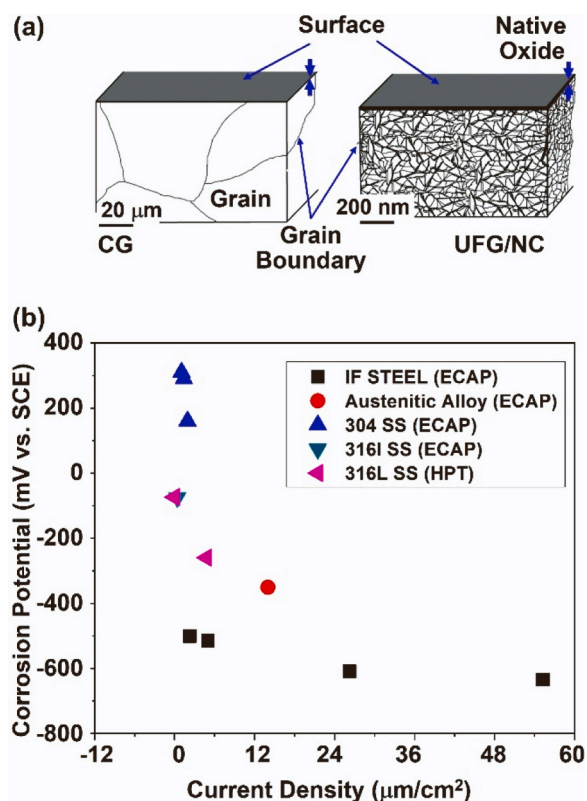
Fig. 60. (a) Differences between coarse grain (CG) and ultrafine/nanograined (UFG/NC) in the formation of native oxide passivation layer in steels [1276]. (b) Comparison of corrosion potential and current density between different steels processed by SPD: IF steel by ECAP [1295], austenitic steel by ECAP [1296], 304 stainless steel by ECAP [1297], 316 L stainless steel by ECAP [1276, 1298] and 316 L stainless steel by HPT [1299, 1300].

ECAP and HPT, the stability of the protective layer has been mainly characterized in neutral and alkaline environments by the corrosion potential (E_{corr}), the corrosion current density (I_{corr}) and the pitting potential (E_{pit}). The corrosion potential indicates the tendency of the steel to corrode, and therefore it should be low. The corrosion current characterizes the rate at which the steel corrodes in a given environment and it also should be low [1301]. The pitting potential indicates the passivity layer breakdown and therefore, it should be high. The enhanced corrosion resistance and the stability of the passive layer in different steels processed using ECAP have been reported in low- and medium-carbon steels [1302, 1303], extremely low-carbon steels [1277], austenitic alloyed steels [1296], mild steels [1304] and interstitial-free (IF) steels [1295]. For stainless steels, although they are commonly characterized by good corrosion resistance, most of the literature also confirms that they can be improved considerably using SPD processing. In particular, the improved corrosion for stainless steels has been reported for 304 SS [1297], 316 L SS [1298, 1305] and F138 SS [1306] after ECAP processing and also for 316 L SS after HPT processing [1299, 1300]. For comparison, Fig. 60b shows some results for E_{corr} and I_{corr} in these steels. It should be noted that surface-SPD techniques such as SMAT [5] were also applied to low-carbon steels [1307], AISI 304 [1308], AISI 316 [1309, 1310] and AISI 316 L [1311]. By SMAT, a decreased grain size can be obtained along with high surface roughness [1312]; however, depending on the surface roughness and defects produced, the passive layer stability would be affected. In this sense, SMAT could be used for providing short-term corrosion protection to steels [1310].

Although there is a notable enhancement in corrosion resistance of steels processed using surface-SPD and bulk-SPD techniques, it is necessary to consider other factors that also influence corrosion

resistance, such as surface roughness, high density of defects and strain-induced martensite. For example, it is known that martensitic steels have lower corrosion resistance, because martensite promotes the pitting sensitivity of the steel, forming or accumulating crack nucleation sites, and as a result, it decreases the stability of the passive film [1313]. In this sense, the strain-induced martensite formed during the SPD process, especially for austenitic stainless steels deteriorates the corrosion resistance [1314, 1315].

6.11. Biomaterials

Biomaterials are defined as materials capable of being introduced into a biological environment to elicit a desired physiological response, such as the promotion of tissue growth or repair. Conversely, they are also expected to not induce any adverse effects, such as inflammation, cytotoxicity, or thrombogenicity [1316–1318]. Biomaterials are intrinsically related to the concept of biocompatibility, which can be defined as the ability of a material to perform with an appropriate host response in a specific application [1319, 1320]. It is important to emphasize that biocompatibility extends beyond the material itself; rather, it encompasses the entire material-host interplay [1321]. The properties of biomaterials are strongly influenced by their composition and grain size and they are available in various forms, including polymers, ceramics, metals and composites. Among these, metallic biomaterials stand out as a pivotal category, finding utility in a broad range of medical devices ranging from dental and orthopedic implants, heart valves and intraocular lenses to artificial hearts, biosensors and pacemakers [1322–1324]. Unquestionably, titanium and its alloys represented the most prominent group within the metallic biomaterials, mainly because of the desired combination of properties required for a biomaterial, such as high strength, low Young's modulus, high corrosion resistance, good fatigue properties, lightweight and good biocompatibility [1325–1328]. While titanium is of high interest for permanent implants, magnesium alloys are receiving significant attention for biodegradable implants. Despite the remarkable achievements with the utilization of titanium, magnesium and their alloys in their microcrystalline form in many different biomedical devices and components, the introduction of these biomaterials in the UFG form is considered the next smart generation of biomaterials [132, 1329, 1330].

When metallic biomaterials are scaled down to the nanometer level, their compatibility and bioactivity with osteoblast and fibroblast cells undergo a remarkable enhancement. This leads to a substantial increase in cell adhesion and proliferation on the surfaces of these materials, as evidenced by various studies [1331–1333]. Moreover, nanostructured materials exhibit higher levels of protein adsorption, cell attachment, proliferation and differentiation when compared to conventional materials [1333]. These physiological processes, involving the interaction of human cells with the surface of biomaterials, are notably enhanced at the nanometer scale, ensuring robust osseointegration [1331–1335]. It has been shown that a surface with nanoscale grain size exhibits higher bone formation efficiency compared with micro-grained surfaces [1334, 1335]. Within this context, SPD techniques have proven to be an outstanding and straightforward method for producing UFG biomaterials [1325, 1329, 1330, 1336]. Numerous studies have highlighted the enhanced properties of nanostructured titanium and its alloys when subjected to SPD methods compared to non-processed titanium. These improvements encompass superior corrosion resistance [1337, 1338], enhanced mechanical attributes including hardness, strength and wear resistance [657, 1329, 1339], enhanced bacterial adhesion [1340, 1341], improved wettability [1342, 1343] and high bioactivity and cell adhesion [1344–1346]. Notably, osteoblast cell proliferation on nanostructured titanium has been reported to be up to 19 times greater than on conventional titanium [1345]. Nanostructured titanium alloys, including Ti-6Al-4 V [1347, 1348], Ti-6Al-7 Nb [1349, 1350], Ti-Nb [312, 1351], Ti-Mo [1352, 1353] and Ti-Nb-Ta-Zr (TNTZ) [1354, 1355], have demonstrated remarkable mechanical properties and

biocompatibility enhancements when prepared using SPD methods such as ECAP or HPT. These materials have showcased advantages over microcrystalline forms of pure titanium and conventional titanium alloys [312, 1347–1355].

In the following sections, the effect of SPD on Ti- and Mg-based biomaterials is reviewed. Moreover, the contribution of SPD to the development of innovative biomaterials such as HEAs [317, 1356] and metal-protein nanocomposites [1357] is briefly discussed.

6.11.1. Biocompatible titanium alloys

Titanium and its alloys are known for their lightweight nature and excellent mechanical properties, corrosion resistance and biocompatibility. Compared to other major metallic biomaterials used in bone replacement implants, such as stainless steel and Co-Cr alloys, titanium demonstrates higher biocompatibility, making it a popular choice in the field of metallic biomaterials. Moreover, titanium stands out as the only metal capable of osseointegration, forming a bond with bone at the optical microscope level. Due to this unique characteristic feature, it finds extensive application in devices that interact with bone, including artificial hip joints, spinal fixation and dental implants. Presently, the most commonly used titanium alloy for biomedical purposes is the $\alpha+\beta$-type Ti-6Al-4 V ELI (extra low interstitial), which boasts greater toughness than the Ti-6Al-4 V alloy [1358]. Pure titanium, such as commercially pure titanium grade 2 [538, 1359–1361] and grade 4 [1362–1364], which have lower strength than Ti-based alloys, have better biocompatibility than alloys, but they suffer from relatively low strength. There have been attempts to strengthen these materials by SPD which resulted in their commercialization. Here, some findings about SPD processing of Ti-based biomaterials are reviewed.

It was reported that the fatigue properties increased to 220 MPa from 180 MPa when etching the surface of UFG titanium grade 4 obtained through ECAP [1362]. Ti-based alloys exhibit high heat treatability, and their initial microstructure can be transformed into a lamellar structure or martensite through SPD, promoting grain refinement. Raab *et al.* conducted a study on titanium grade 4, characterized by a high impurity concentration among pure titanium materials, by quenching from the β region to form martensite [1363]. Subsequently, they subjected the materials to ECAP processing which resulted in a remarkable tensile strength of 1100 MPa and an elongation of 7.2%. The ECAP processing in the state of martensite further contributed to grain refinement by reducing the ability for grain boundary mobility, propagation of dislocations in grain interiors, and stress localization at interphase boundaries.

The $\alpha+\beta$-type Ti-based alloy, such as Ti-6Al-4 V (wt%) alloy [1365–1371], Ti-13 V-3Al (at%) [1372], Ti-6Al-7 Nb (wt%) [1373, 1374], have been also studied by SPD. The strength can be increased in the $\alpha+\beta$ type Ti-based alloy by controlling the initial microstructure. In the Ti-6Al-4 V ELI alloy, Alagić *et al.* reported that both high tensile strength of 1546 MPa and total elongation of 18.8% can be achieved with HPT at 500 °C using the initial microstructure of approximately 90% α' martensite [1375]. In the Ti-6Al-7 Nb alloy, which was developed for medical use by replacing toxic vanadium with biocompatible niobium, Polyakova *et al.* reported 1460 MPa tensile strength and 11% of ductility after ECAP [1373]. Reportedly, 1280 MPa tensile strength and 22% of total elongation were obtained in Ti-6Al-7 Nb after HPT with the bi-modal initial microstructure of equiaxed α and α' grains [1374]. Since high Young's modulus leads to bone resorption, β-type Ti-based alloys with low Young's modulus, such as Ti-3 Nb [1376], Ti-10Mo-8 Nb-6Zr [1377, 1378], Ti-18Zr-15 Nb [1379, 1380], Ti-15Mo [1353], Ti-13 Nb-13Zr [1381, 1382], Ti-29 Nb-13Ta-4.6Zr (TNTZ) [1383], Ti-3.5Al-5Mo-4 V [1384] (all in wt%), have been processed by ECAP or HPT. Recently, Ti-containing HEA TiNbZrTaHf was processed by HPT which showed a high hardness of 564 HV with a low Young's modulus of 79 GPa and good biocompatibility of high entropy alloy after HPT [317].

Grain refinement not only enhances the mechanical properties of
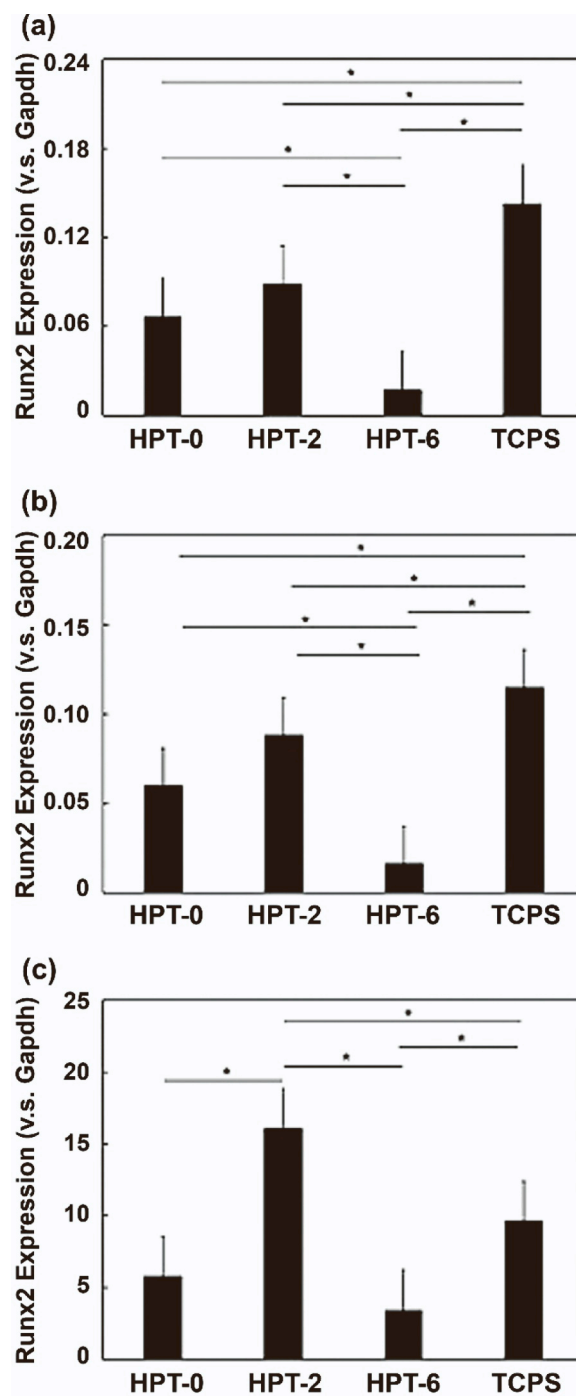
Fig. 61. Histogram of target mRNA expression levels after 7 days of induction in MC3T3-E1 cells cultured on Ti-6Al-7 Nb (wt%) alloy before HPT (HPT-0), after HPT under 2 GPa (HPT-2) and after HPT under 6 GPa (HPT-6) in comparison with tissue-culture-treated polystyrene dishes (TCPS). Expression of (a) Runx2, (b) Col1α1 and (c) Akp2 was detected by real-time RT-PCR [1385].

titanium but also improves corrosion resistance and biocompatibility. The corrosion resistance of UFG pure titanium grade 2 is enhanced through grain refinement by ECAP, leading to the formation of a passive layer on the titanium surface more effectively [1360]. Chen *et al.* reported that grain refinement of Ti-6Al-7 Nb alloy by HPT leads to enhanced osteogenic differentiation, as shown in Fig. 61 [1385]. The SPD process increases the fraction of grain boundaries and dislocations and positively changes the thickness and chemical component of the surface layer for biocompatibility [560, 1385]. All these findings suggest

that SPD techniques provide a powerful means for fabricating advanced biomaterials, holding immense potential for further innovation and development in the biomedical industry.

6.11.2. Biocompatible magnesium alloys

New-generation biodegradable implants possess the potential to supplant permanent medical implants as they assist fractured bones throughout the healing process and subsequently undergo controlled absorption by the body [1386, 1387]. Among the biodegradable metallic materials, magnesium alloys are the most relevant. The fundamental concept of designing Mg-based alloys as biomaterials begins with the formulation of alloy composition, followed by the implementation of manufacturing and processing techniques (*e.g.* utilizing SPD techniques) as well as surface modifications to achieve the desired

properties. This process culminates in the production of finalized products intended for long-term clinical trials, as depicted in Fig. 62a. Magnesium alloys with UFG morphology, produced via SPD techniques such as ECAP and HPT [5, 23, 32, 299, 1388], are especially interesting biomaterials for temporary orthopedic implants as they exhibit enhanced mechanical properties, adequate corrosion resistance and biocompatibility [1389].

ECAP processing of magnesium alloys is especially interesting as this technique can provide large-scale samples allowing the fabrication of bone screws and plates. When doing ECAP of magnesium alloys, not only grain refinement by shear but also dynamic recrystallization plays a substantial role due to the temperature rise during the process, stored energy in deformation-induced defects, and the low deformation rate [1390]. The extent of refinement depends also on the initial grain size.
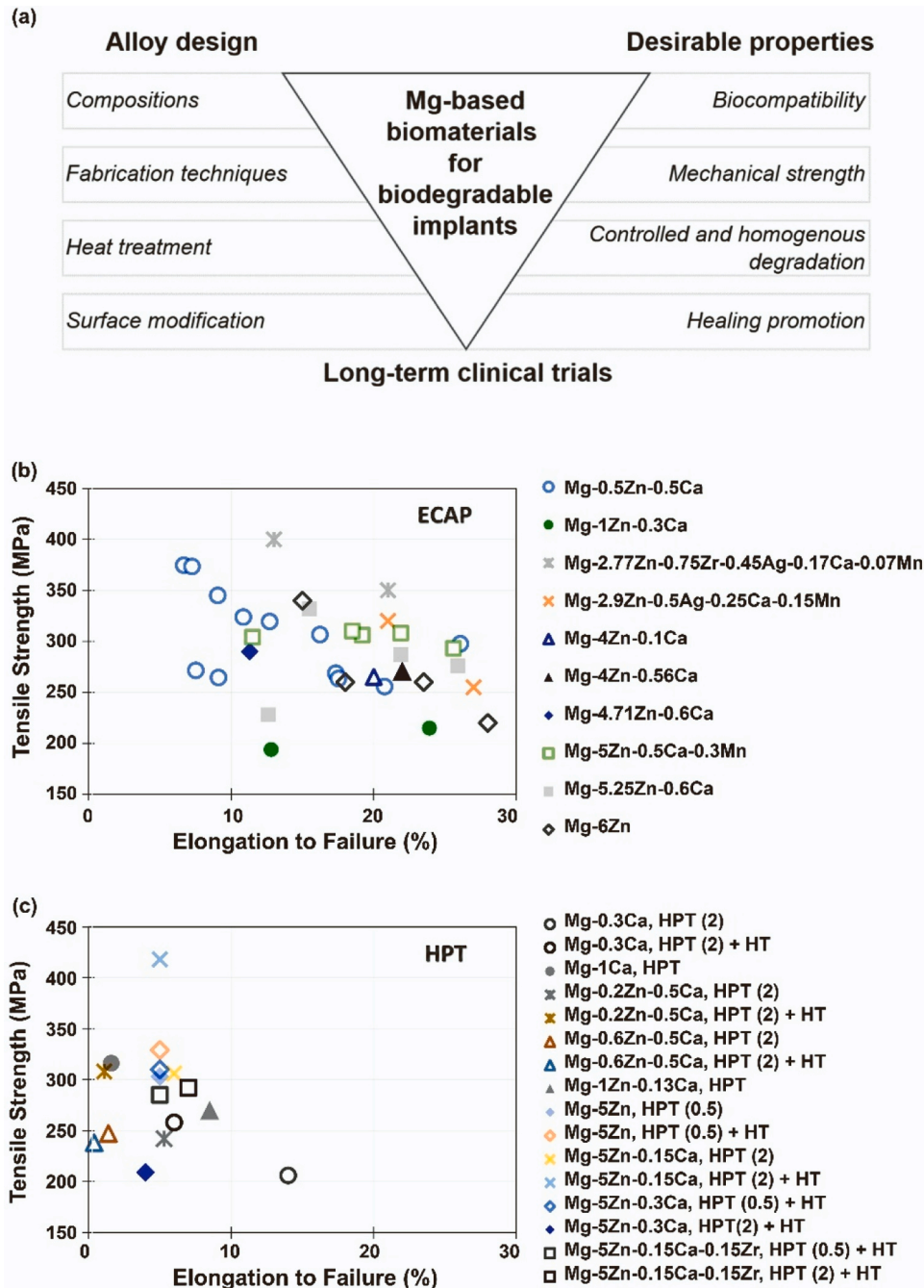
Fig. 62. (a) Concept of designing Mg-based alloys as biomaterials. (b,c) Tensile strength and elongation at fracture for Mg-Zn-Ca alloys processed by (b) ECAP and (c) HPT (the numbers in parentheses for HPT-processed samples indicate the number of rotations and 'HT' indicates a subsequent heat treatment) [1389].

Texture development during ECAP can lead to enhanced ductility and softening effects [1391–1393]. Additionally, ECAP induces fragmentation and redistribution of hard particles within a magnesium matrix, contributing to both, grain refinement and precipitation strengthening [1394–1396]. The popular Mg-Al-based alloys like AZ31 [1397, 1398], AZ91 [1399] or LAE442 [1400–1403] processed by ECAP show significant grain refinement and increased yield and tensile strength. However, the potential use of alloys with aluminum addition as biodegradable implants is limited because the neurotoxic effect of aluminum can cause Alzheimer's disease or dementia when exceeding the daily dose [1404, 1405]. Magnesium alloys containing zinc and calcium are therefore in the research focus of different groups [1406–1412]. They are characterized by excellent biocompatibility and demonstrate attractive properties desirable for medical applications without possible side effects [1406, 1408]. These alloys also exhibit enhanced mechanical properties after ECAP, attributed to grain refinement and precipitation hardening, as shown in Fig. 62b. Rare-earth elements, in general, improve the mechanical properties of magnesium alloys [1395, 1396, 1413–1415] and their corrosion resistance [1416], with some alloys demonstrating good biocompatibility, such as the WE43 alloy containing rare-earth elements and zirconium. However, their content must be controlled to avoid the risk of harmful effects on the human body [1417–1420]. The Mg-Ag alloys, known for their antibacterial properties, exhibit increased strength and ductility after ECAP processing [1421–1425], making an interesting option for biodegradable medical implants to reduce the symptoms of local inflammation or infection that can arise in the first weeks after implantation.

HPT processing of magnesium alloys results in an initially inhomogeneous microstructure, but a gradual evolution towards relatively uniform microstructures due to saturation tendencies occurs [177, 1138, 1426, 1427]. The number of turns required to achieve a homogeneous microstructure depends on the applied pressure during HPT [1426, 1428]. Additionally, HPT induces a strong basal texture with the c-axis parallel to the normal direction of the disc [1427, 1429, 1430]. Particles in the magnesium alloy matrix undergo fragmentation and redistribution during HPT [1431], although the high hydrostatic pressure of the process limits their breakage and spreading. Compared to ECAP, the HPT process of magnesium alloys can be performed at lower temperatures – even at room temperature – and the induced strain is generally higher. For Mg-Al alloys, HPT processing results in significantly smaller grain sizes (100–200 nm) compared to ECAP, thereby resulting in even higher hardness values [1426, 1428, 1432–1434]. HPT-processed Mg-Zn, Mg-Ca and Mg-Zn-Ca alloys (Fig. 62c), which are exclusively alloyed with essential elements found in the human body, exhibit improved mechanical properties through grain refinement and precipitation strengthening [1409, 1435–1437]. Moreover, magnesium alloys containing rare-earth elements [1438–1440], such as the WE43 alloy [1441], exhibit increased hardness, yield stress and tensile strength after HPT processing.

Magnesium alloys have high corrosion rates due to their non-noble nature, which poses challenges for their use in biodegradable implants. The corrosion mechanism involves the formation of hydrogen gas and magnesium hydroxide and subsequent transformations, influenced by factors like chlorine ions [1441] and the presence of impurities [1409, 1442]. Alloying elements and thermomechanical treatments affect corrosion and biodegradation, with galvanic coupling and micro-galvanic corrosion playing a role [1443]. The influence of SPD methods on biodegradation varies depending on the specific alloy and in vitro testing conditions [1412, 1423, 1444–1452]. An increase in the density of grain boundaries and especially changes in particle distribution after SPD processing can positively affect the corrosion rate of magnesium alloys. *In vivo* studies on SPD-processed magnesium alloys are limited but suggest improved degradation resistance and bioactivity compared to untreated alloys [1453–1455].

In conclusion, magnesium alloys, which exhibit good biocompatibility and homogenous and slow biodegradation, can considerably be improved in terms of mechanical behavior by SPD processing to be used for load-bearing medical implants in orthopedics. A heat treatment or a coating to regulate the degradation rate in the first stages of implementation might help to further improve their applicability for biodegradable medical implants. Future *in vivo* studies are needed to clarify the effect of SPD on the biocompatibility of these materials.

6.11.3. Innovative biomaterials

The outstanding performance of nanostructured titanium and magnesium in the biomedical field has inspired ongoing efforts to develop novel biomaterials with even superior mechanical properties and exceptional biocompatibility. Several studies have contributed to this endeavor by harnessing the synergistic benefits of novel compositions and nanostructuring achieved through SPD techniques. Notably, emerging materials like HEAs [317, 1356] and Ti-protein composites [1357] - especially designed for biomedical applications - have emerged as promising candidates. These new biomaterial compositions processed by the HPT method have presented mechanical properties and biocompatibility fairly superior in comparison to traditional biomaterials such as pure titanium, Ti-6Al-4 V, Ti-6Al-7 Nb, Co-Cr-Mo and 316 L alloys. As an example of this innovative approach, exceptional properties including ultrahigh hardness, a low elastic modulus and remarkable cellular activity for functions such as proliferation, viability and cytotoxicity were reported for TiAlFeCoNi alloy after processing by HPT [1356]. As shown in Fig. 63a, the average hardness witnessed a notable increase from 635 Hv to 880 Hv by HPT processing due to grain refinement. Additionally, the elastic modulus is 123 GPa which is comparable to titanium, as shown in Fig. 63b. The cellular metabolic activity of the TiAlFeCoNi alloy surpasses that of pure titanium and the Ti-6Al-7 Nb alloy by an impressive margin ranging from 260% to 1020%.

Since SPD is capable of cold consolidation of powders, a recent study processed the mixture of titanium and small amounts of an endogenous protein BSA (bovine serum albumin) by the HPT method [1357]. This new family of metal-protein nanocomposites exhibited an exceptional combination of high strength and superior biocompatibility. The scanning electron microscope (SEM) images, depicted in Figs. 64a and 64b, show a reasonable mixing between the titanium and BSA particles at the micrometer level and the elemental mapping of Fig. 64c confirms that the black particles correspond to the BSA protein containing carbon atoms which are surrounded by a titanium matrix. After HPT processing, the BSA protein is mixed with titanium particles forming well-defined protein layers that are distributed all over the sample, while the titanium phase keeps its three-dimensional network, as displayed in Fig. 64d-f. The cellular viability after HPT processing was evaluated by *in vitro* cell culture experiments employing the MC3T3-E1 cells, as indicated in the MTT assay in Fig. 64g. As can be seen, the HPT-processed composites present superior biocompatibility in comparison with the coarse-grained titanium reference and the sample with 5 vol% of BSA showing the best biocompatibility performance among other counterparts.

In conclusion, the introduction of innovative biomaterials, such as HEAs and Ti-protein composites, represents a significant stride in the biomedical field by the contribution of SPD. These newly designed materials offer enhanced mechanical properties and biocompatibility compared to conventional counterparts and can be further tuned for particular biomaterial applications.

7. Ultrafine-grained materials processed by SPD

Although SPD processing was preliminarily considered a metal processing technology [1, 2], its application is now extended to a wide range of metallic/nonmetallic materials, inorganic/organic materials and traditional/innovative materials. SPD processing of metals goes
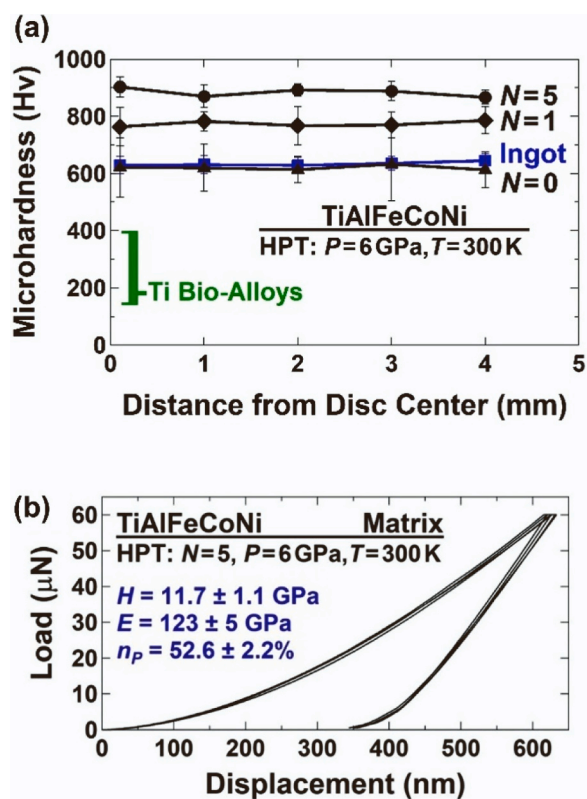
Fig. 63. (a) Variation of Vickers microhardness against distance from disc center for ingot and sample processed by HPT. For comparison, hardness for TiAlFeCoNi after compression ($N = 0$) and $N = 1$ turn of HPT, as well as the hardness range for Ti-based biomaterials, were included. (b) Nanoindentation load against displacement for HPT-processed TiAlFeCoNi sample [1356].

back at least to the Bronze Age and SPD processing of organic materials should have a very old history in food making; however, SPD processing of hard and brittle materials was realized in the 1930 s following the introduction of the HPT method [20, 22]. Although SPD processing is mainly applied to metals (magnesium, aluminum, titanium, iron, *etc.*) and their alloys [1, 2], there are appreciable attempts to design new metallic materials (including, composites, new conventional alloys, HEAs and metallic glasses) using the SPD methods for different functionalities, as discussed in previous chapters. The application of SPD to semiconductors [1456], ceramics [1457] and polymers [14] also experienced significant progress in recent years, although the number of groups actively working on these materials is still limited. In the following section, research activities on various SPD-processed UFG materials are reviewed.

7.1. Magnesium alloys

The inherent brittleness of magnesium sets difficulties for room temperature processing. Therefore, early attempts for processing through ECAP [1458, 1459] and ARB [1460] were carried out at high temperatures. Processing routes which included extrusion followed by ECAP [1461] and the application of a back pressure in ECAP [1462] were developed, enabling the fabrication of UFG magnesium, but the minimum grain sizes achieved were in the range of several hundreds of nanometers. True nanocrystalline magnesium, with grain sizes of ~100 nm or smaller, is only produced via HPT processing at room temperature. Thus, the increase in research groups using HPT in recent years unveiled many interesting aspects of magnesium properties, such as the relationship between flow stress and grain size.

The early reported experimental data were limited to relatively coarse-grained samples and they usually fitted the well-established Hall-
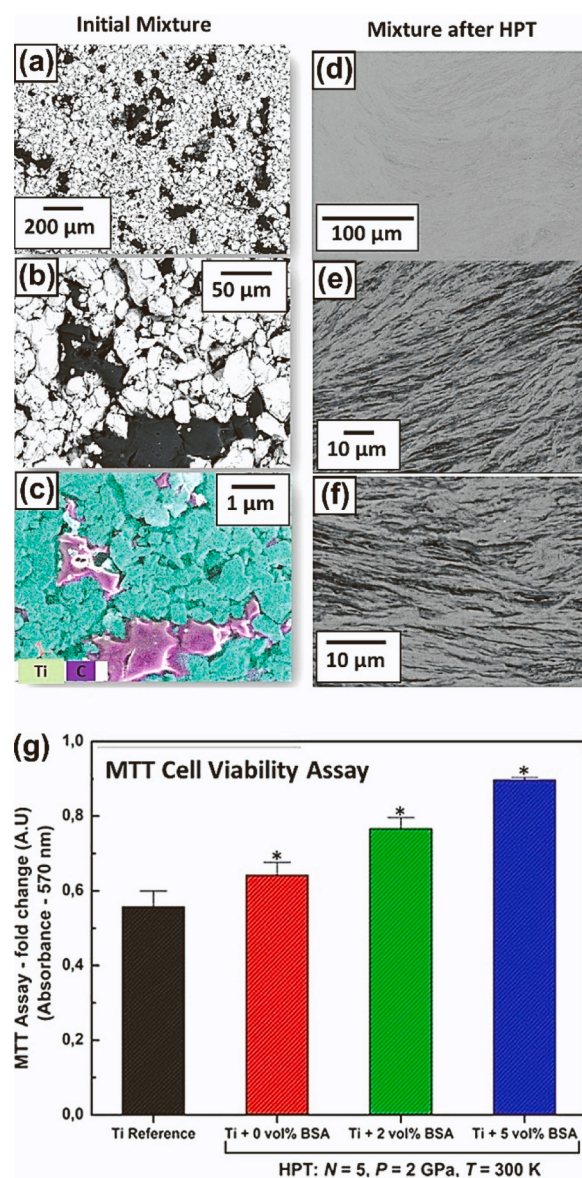
Fig. 64. (a,b) SEM images in backscatter electron mode and (c) corresponding energy-dispersive X-ray spectroscopy elemental mappings of Ti + 5 vol% BSA protein before HPT processing. (d-f) SEM images at different magnifications in backscatter electron mode for Ti + 5 vol% of BSA composite after 5 turns of HPT under 2 GPa. (g) MTT cell viability assay examined by light absorbance at 570 nm for pure titanium and for nanocomposites containing 2 and 5 vol% of BSA protein produced by 5 turns of HPT under 2 GPa in comparison with hardness of coarse-grained annealed titanium [1357].

Petch relationship in which the flow stress is inversely proportional to the square root of the grain size. The proportionality factor, Hall-Petch slope K, was usually high and exhibited a pronounced dependency on temperature [1463, 1464]. Recent studies show that this relationship is not constant for all grain sizes. A change in slope in plots of flow stress vs. grain size and grain refinement softening at small grain sizes have been reported [1465–1469]. A recent review [1470] evaluated multiple magnesium alloys and showed that a change in slope takes place at grain sizes of ~ 4 μm. The data is shown in Fig. 65 and two distinct regimes are observed. Hence, data for coarse-grained magnesium alloys follow a larger slope attributed to twinning-controlled deformation, while data for ultrafine and nanocrystalline follow a reduced slope associated with slip-controlled deformation. It is worth noting that the data in the range of slip-controlled deformation agree with the mechanism of grain
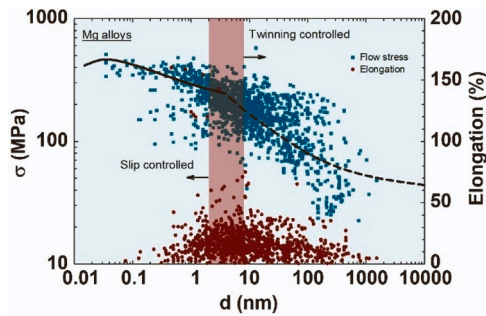
Fig. 65. Flow stress and elongation to failure of magnesium alloys plotted as a function of the grain size [1470].

boundary sliding [1471] in which the flow stress is predicted by Equation 31. This mechanism has shown good agreement with experimental data for multiple materials with different grain sizes and tested at different temperatures and strain rates [739, 1472, 1473].

$$\sigma \approx \sqrt{\frac{3GkT}{2d_s b^2}\ln\left(\frac{\dot{\varepsilon}d_s^3}{10\delta D_{gb}}+1\right)} \tag{31}$$

where σ is the flow stress, G is the shear modulus, k is the Boltzmann's constant, T is the absolute temperature, d_s is the spatial grain size, $\dot{\varepsilon}$ is the strain rate, b is the Burgers vector, δ is the grain boundary width and D_{gb} is the coefficient for grain boundary diffusion. The data in Fig. 65 shows that high strength, in the range of 400 MPa, might be observed in UFG magnesium alloys. The highest strength in a magnesium alloy was reported in a Mg-17Ni-17 Pd (at%) alloy with the BCC structure processed by HPT [296] but this value is not shown in Fig. 65. A noticeable increase in elongation to failure is observed in the grain size range 2–8 μm which is the range for transition in deformation mechanism. Thus, a good combination of strength and ductility is observed in this grain size range.

Early papers showed that ECAP can introduce superplastic behavior in magnesium alloys [796, 798, 1474–1477]. In practice, grain refinement enables a decrease in temperature and/or an increase in strain rate for superplasticity. Also, the elongations reported in magnesium processed by ECAP tend to be larger than in conventional thermo-mechanical processing. Fig. 66a shows the appearance of tensile specimens of a ZK60 alloy processed by different numbers of passes of ECAP and pulled to failure at 473 K. Exceptional elongations of over 1000% were reported, including an elongation of 3050% [1475].

It was shown later that superplasticity is also observed in magnesium processed by HPT [801, 1479, 1480] and analyses of experimental data showed that the strain rate for superplasticity agrees with theoretical predictions from the mechanism of grain boundary sliding [349, 1481]. In addition to the development of high-temperature superplasticity, severe plastic deformation may also introduce exceptional ductility in magnesium at low temperatures and even at room temperature. For instance, superplastic elongations were reported in an AZ91 alloy tested at 423 K [1480] and in an Mg-Li alloy tested at 373 K [800]. Although many magnesium alloys display brittle behavior at room temperature, extraordinary ductility has been reported in UFG pure magnesium [1482] and the Mg-8Li (wt%) alloy processed by HPT [350]. Fig. 66b shows the stress-strain curves of the Mg-8Li (wt%) alloy tested in tension at room temperature in the extruded condition and after 5 and 200 turns of HPT. An increase in elongation is observed after 5 turns of HPT and further processing to 200 turns increases the elongation to over 400%, which is considered a superplastic elongation [350].

As discussed earlier, SPD processing also improves the hydrogen storage performance of magnesium [1077]. It was shown that ECAP processing increases hydrogen desorption kinetics [1143]. It was also demonstrated that HPT processing improves hydrogen storage capacity
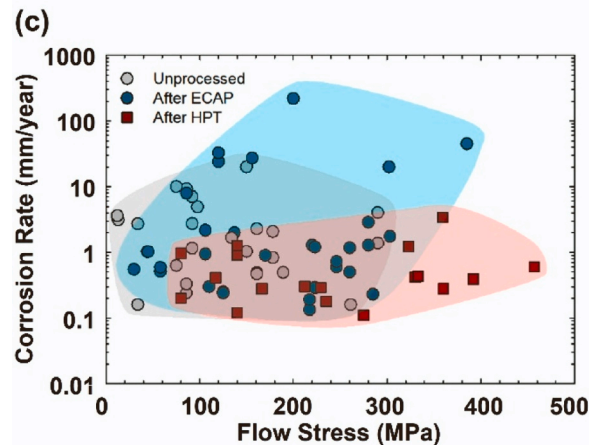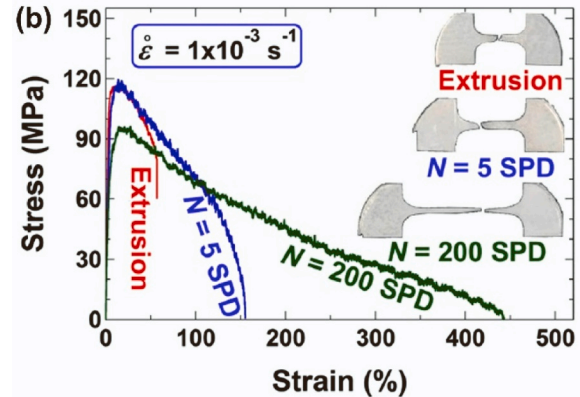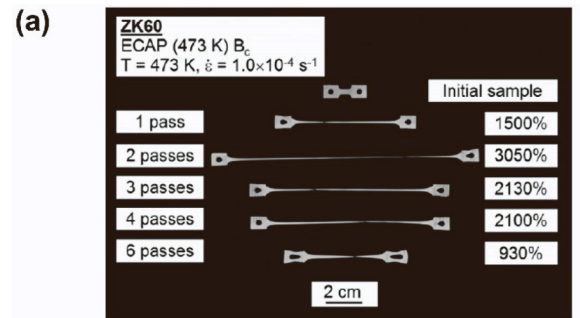
Fig. 66. (a) Appearance of tensile specimens of a ZK60 alloy processed by different number of passes of ECAP and tested at 473 K [1475]. (b) Stress vs. strain curves and appearance of tensile specimens of an Mg-8Li (wt%) alloy processed by extrusion and different number of turns of HPT and tested at room temperature [350]. (c) The corrosion rate of magnesium and magnesium alloys plotted as a function of the flow stress [1478].

[1138]. A significant advance in this field was achieved by mixing magnesium with other metals using ultra-SPD through many turns in HPT. Thus, a Mg₄NiPd alloy with BCC structure processed by 1500 turns of HPT exhibited room-temperature hydrogen storage capability [359]. The hydrogen pressure composition isotherm for tests at 305 K under hydrogen pressures up to 10 MPa shows up to 0.86 wt% of hydrogen adsorption after the fifth cycle with 0.7 wt% reversibility [359]. Besides the improvement in hydrogen storage, it has been suggested that grain refinement can induce pseudo-uniform corrosion due to the increase in the volume fraction of grain boundary area [1258]. Experiments in pure magnesium [1483] and a magnesium alloy [1484] processed by HPT support this suggestion. Also, many papers [1485–1488] reported a decrease in the corrosion rate of magnesium and its alloys after SPD.

These observations suggest that SPD processing can improve the performance of magnesium for biological applications as temporary implants. Fig. 66c shows experimental data of flow stress and corrosion rate for magnesium before and after SPD processing, indicating that HPT processing can increase the strength and decrease the corrosion rate of magnesium [1478].

7.2. Aluminum alloys

Since the early works of the late 20th century and early 21st century on the processing of UFG materials by SPD techniques, much attention has been paid to Al-based materials. They possess a highly attractive combination of functional properties: outstanding strength-to-weight ratio, fair corrosion resistance, notable formability and so on. In addition, aluminum belongs to a limited number of elements that might be used as conductors being the cheapest variant among all. Therefore, Al-based alloys are widely used as constructional and conductive materials in transportation, food, construction, sport and other industries. However, their strength is relatively low while advanced applications require Al-based alloys with improved mechanical and functional performance. Thus, the enhancement of their mechanical and functional properties through nanostructuring by SPD is an important task to develop novel high-performance Al-based alloys for innovative applications. Fundamental studies and recent achievements in this field have been analyzed in the most recent reviews [835, 1489] and are summarized below.

The most important motivation for the application of different SPD
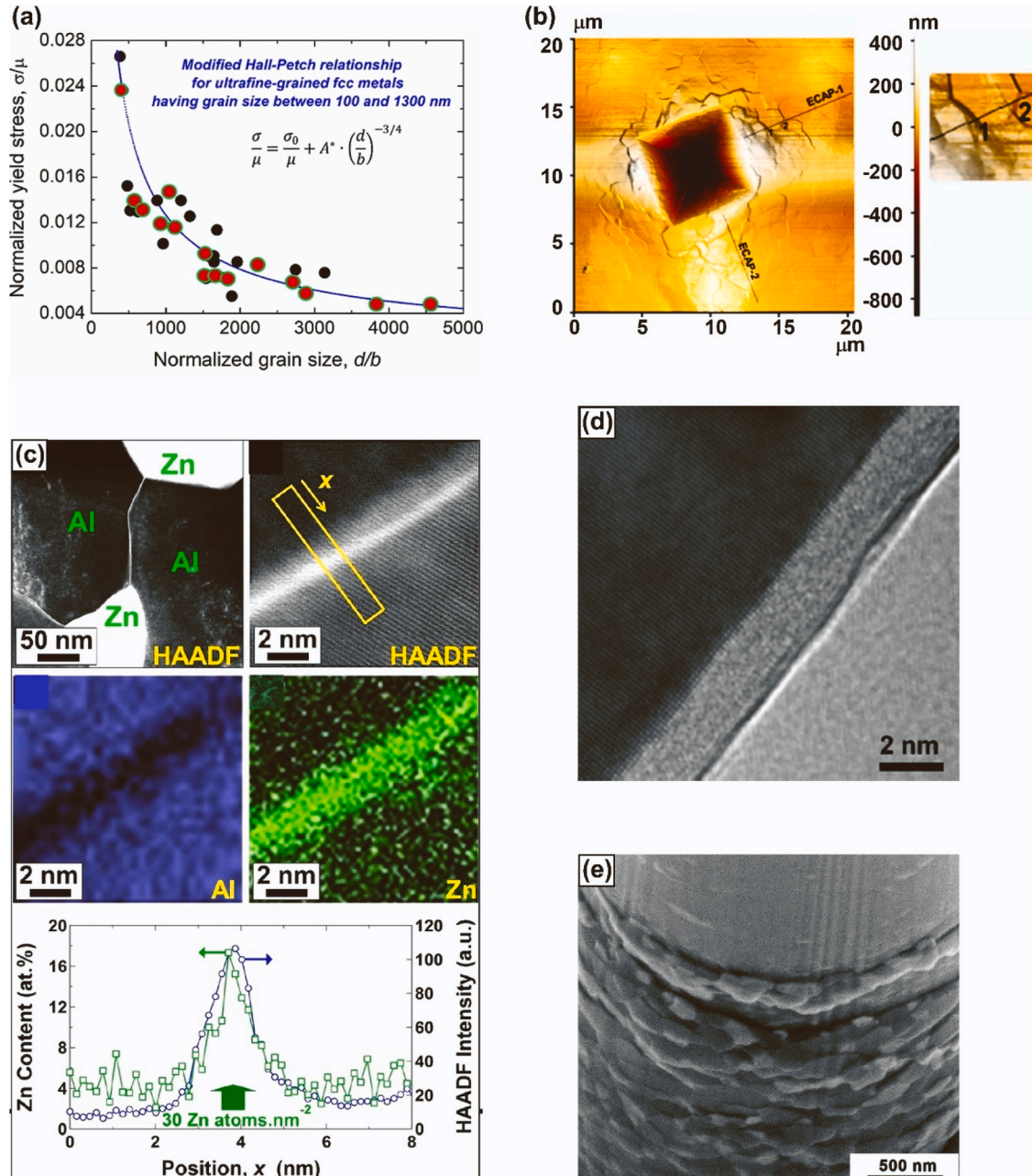
Fig. 67. (a) A possible modification of the Hall-Petch relationship for UFG FCC metals and solid solutions [1497]. (b) Evidence on grain boundary sliding at room temperature in UFG pure Al, shown by three-dimensional atomic force microscopy (AFM) [1498]. (c) The Al/Al boundaries strongly segregated by solute zinc atoms, causing wetted grain boundaries in SPD-processed Al-30Zn (at%) alloys [351]. (d) High-resolution TEM image showing a wetting layer along an Al/Al grain boundary in the HPT-processed Al-30Zn (at%) sample [1499], (e) Surface morphologies of the compressed pillars on the surface of the HPT-processed Al-30Zu (wt%) sample, demonstrating a direct evidence for the occurrence of intensive grain boundary sliding without any deformation localization [1500].

methods comes from the 70-year-old Hall-Petch relationship [661, 1490], describing the improvement of the yield stress with decreasing grain size. The possibility of achieving high-strength states following the Hall-Petch equation, engineering superplastic behavior and other properties of metallic materials by forming UFG structures has traditionally been the motivation for research and development in the SPD field [1491]. Consequently, several early efforts have been made to refine the grain size in aluminum [1492–1495] and its alloys [348, 810, 817, 820, 1492]. Presently, the use of various SPD techniques has become the main approach in obtaining different UFG materials with nanoscale and submicron grain sizes. An important factor for UFG materials is that depending on the SPD processing regimes, different types of grain boundaries are formed in metals and alloys, including aluminum materials, such as low- and high-angle grain boundaries, equilibrium and non-equilibrium ones, as well as the grain boundaries containing significant segregations of alloying elements, which typically has a very strong influence on their properties [304, 373, 1496]. Besides, experimental experience indicates that the conventional Hall-Petch equation cannot be typically maintained in its original form for UFG materials. A possible modification of the original Hall-Petch equation has been suggested [1497] for a uniform description of submicron-sized FCC metals and solid solutions (Fig. 67a).

Together with the strengthening effect, the average grain size also plays an important role in the plastic deformation process, such as superplastic flow, where the main deformation mechanism is grain boundary sliding [791, 1501–1503]. Experimental evidence [1498] on room temperature grain boundary sliding in UFG pure aluminum deformed by Vickers indentation has been detected by using three-dimensional atomic force microscopy (Fig. 67b). Analysis of the pileups formed around the Vickers pattern suggests that the contribution of grain boundary sliding to the total strain in the UFG aluminum sample can reach up to 70% [1504]. Besides the grain-refinement, SPD may result in strong decomposition of the microstructure [351, 817, 1500, 1505–1507] and intensive segregation of solute atoms to grain boundaries (Fig. 67c) [351, 1499, 1508], causing so-called wetted grain boundaries [351, 1499, 1507–1509] in UFG alloys (Fig. 67d). It has been shown that segregated grain boundaries have an enhancing effect on grain boundary diffusion, facilitating grain boundary sliding, as shown in Fig. 67e, and leading to super-ductility [817] or even superplasticity [351, 1510] at room temperature in Al-Zn alloys. The grain boundary segregation also has a unique effect [812] in the case of UFG Al-Zn-Mg-Zr (7xxx) commercial alloys, where conventional materials can show superplastic behavior only at a relatively high homologous temperature of about 0.7–0.8 T_m [315, 810, 814, 1511–1513]. Recent results have demonstrated the significance of enhanced diffusion along grain boundaries at low temperatures in a UFG Al-Zn-Mg-Zr commercial alloy, leading to its superplasticity with a record elongation higher than 500% at 443 K (0.47 T_m) (Fig. 68a), and maintaining relatively high strength after superplastic deformation [1510]. Considering the temperature dependence of the superplasticity of commercial aluminum alloys, the summary graph in Fig. 68b shows the significance of the mentioned new results obtained on the ultralow-temperature superplasticity of the UFG Al-Zn-Mg-Zr alloy.

Combining high mechanical strength with high electrical conductivity has always been a challenge for the aluminum industry, especially for the design of power transmission lines [1514] or for the development of advanced wirings for automotive applications [1515]. Alloying elements in solid solution or precipitates increase the strength but significantly scatter electrons giving rise to an increase of the electrical resistivity. The best compromises achievable by traditional treatments have been demonstrated with 6xxx alloys [857] but the design of UFG structures by SPD processes opens principally new possibilities to expand the limits of the trade-off between strength and conductivity in conductor alloys [834, 835]. There are however some limitations: (i) UFG structures require some stabilizers, solutes or particles that pin grain boundaries and limit grain growth [310]; (ii) grain boundaries are
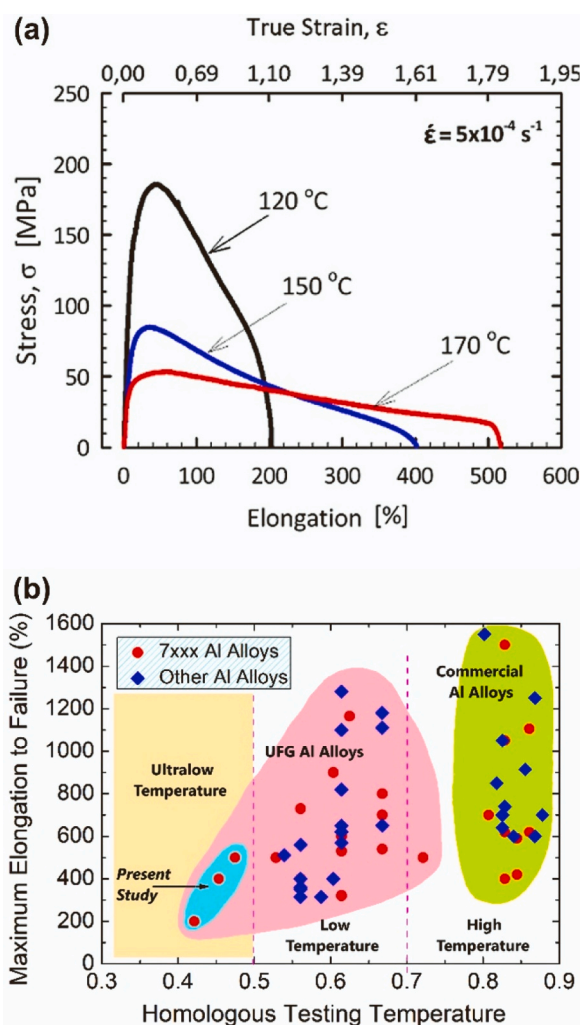
Fig. 68. (a) Deformation curves of an UFG Al-Zn-Mg-Zr (7xxx) alloy, showing a record total elongation higher than 500% at 443 K (homologous temperature: 0.47) [812]. (b) Significance of the UFG structure having grain boundaries segregated by solute atoms, resulting in ultralow-temperature superplasticity in the Al-Zn-Mg-Zr alloy (denoted as Present Study) [812].

known to scatter conduction electrons and when the grain size is below the free mean path of the electrons, the electrical resistivity is significantly affected [1516]. Different strategies involving SPD have been proposed to overcome these barriers. The most straightforward approach (Fig. 69a) is to combine precipitation hardening and grain boundary strengthening in traditional conductor aluminum alloys (such as Al-Mg-Si [872, 1517–1520] or thermally stable Al-Zr-based alloys [884, 1521, 1522]). SPD might be carried out in the solutionized state or after precipitation treatment. In the first case, however, under SPD conditions the crystalline defects and strain-induced segregations [1519] may affect the precipitation and specific heat treatments and/or doping with other elements are required [872, 1518, 1521, 1522].

Alternatively, the potentiality of SPD to tailor new innovative systems has been explored, such as immiscible Al-RE (RE: rare earth) [315, 881, 1523], Al-Fe [310, 869, 877, 879, 880, 1524–1526] or Al-Ca [311, 1527] alloys. As-cast structures with a high-volume fraction of fine intermetallic particles or solute segregations (Fig. 69b) promote the grain refinement and the stability of UFG structures with limited effect on the electrical conductivity. Besides, SPD can additionally expand the limits for the structural design of Al-based alloys by forming grain boundary segregations providing extra-strengthening of the UFG state [1528] or by creating supersaturated solid solutions of elements that are immiscible under near equilibrium conditions [311, 315, 877, 881,
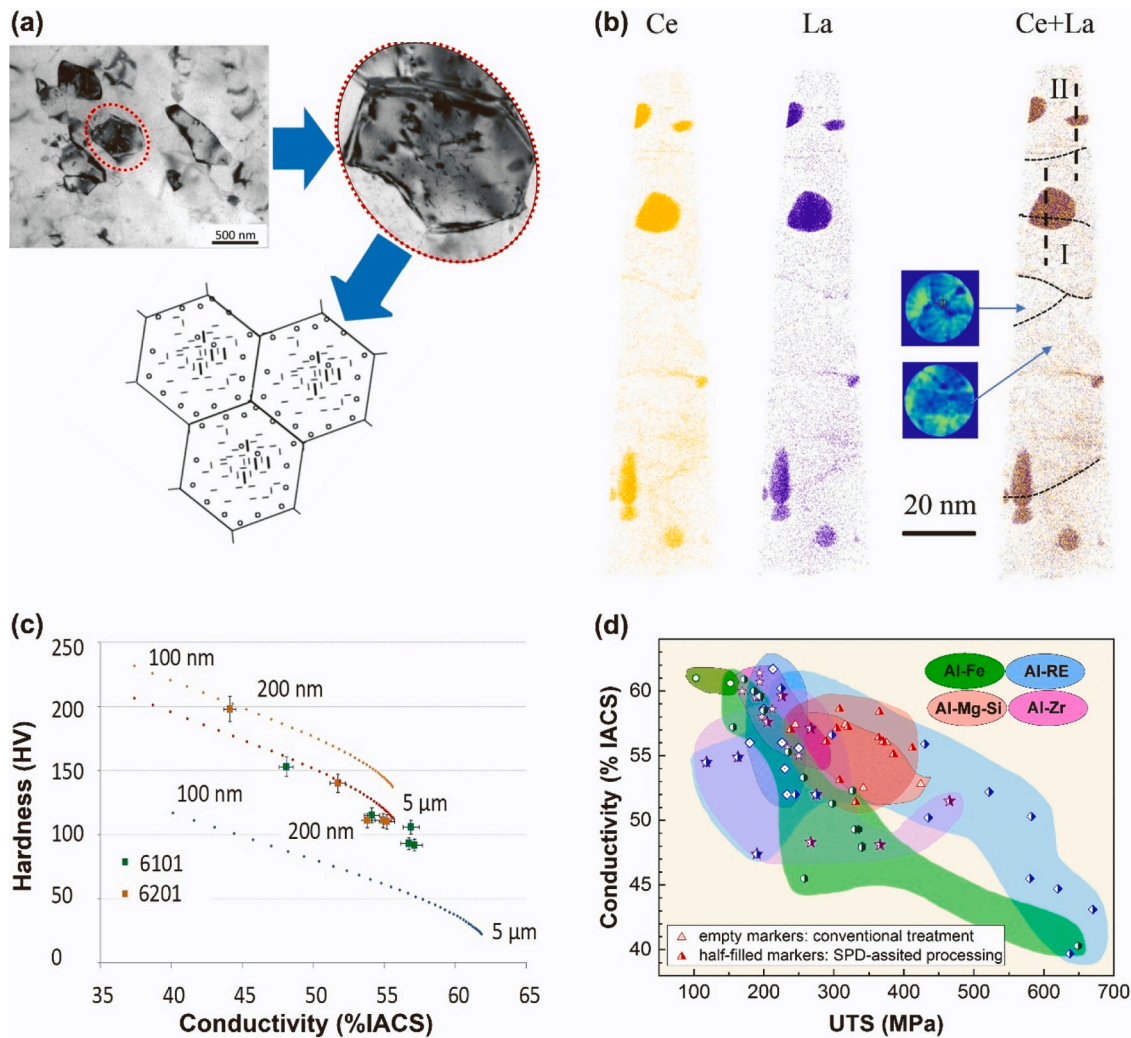
Fig. 69. (a) A strategy to improve the strength-conductivity ratio in age-hardenable aluminum alloys by SPD-controlled nano-precipitation [835]. (b) Grain boundary segregations in SPD-processed immiscible Al-RE (RE: rare earth) alloys [1523]. (c) A theory-based predictive approach to define limits of the hardness-conductivity trade-off in UFG Al-Mg-Si alloys as a function of the grain size and with 0.2 wt% of solutes left in solid solution. Different curves correspond to different contributions considered for the estimations: without precipitates (blue), with precipitates with density corresponding to the conventional T6 (red), with precipitates and maximal measured dislocation density after HPT at room temperature (orange). Green and orange squares correspond to experimental data collected on the 6101 and 6201 alloys, respectively [1519]. (d) A potentiality of SPD to expand the space of improving the strength and conductivity of conductor aluminum alloys [835]. IACS stands for International Annealed Copper Standard [857].

1524], which can transform these alloys to a type of age-hardenable ones. Basic theoretical estimations accounting for structural contributions to yield stress and resistivity can predict the limits of the strength-conductivity ratio for SPD-engineered Al-based alloys as shown in Fig. 69c [1519], but these estimations need to be modernized considering the latest findings.

Note that the morphology of the intermetallic phase in the as-cast state can severely affect the SPD efficiency for immiscible systems [880, 1523]. Here a combination of advanced casting techniques (such as electromagnetic casting [1529]) to disperse intermetallic eutectics before SPD can be fruitful [879, 1523, 1526]. As a result, electromagnetically cast bulk specimens of Al-Fe alloys after complex SPD-assisted treatment demonstrate enhanced thermal stability similar to Al-Zr conductors with a strength/conductivity ratio comparable to advanced Al-Mg-Si alloys [879, 1526]. Moreover, metal matrix composites processed by continuous SPD methods also offer some unique possibilities to achieve conducting wires [1530–1534]. Composites combining different aluminum alloys or Al-Cu alloys are more complex to produce, but extend the possibilities of strength/conductivity combinations. The full range of property combinations that could be expanded using the

different SPD-based approaches is summarized in Fig. 69d (based on the literature data collected in [835]). It is worth noting that there are several issues in the SPD-driven development of high-strength lightweight conductors, which are still poorly documented in the literature. Limited studies address such important properties as fatigue [876, 1515], creep [737, 1535] and corrosion [1515, 1536] behavior of electrotechnical UFG aluminum alloys, vitally important for their industrial applications. Despite the fewer promising results, these areas still wait for comprehensive exploration.

Results obtained on SPD-processed UFG aluminum alloys clearly show the innovation potential of unique grain boundary phenomena, such as the advantage of intensive grain boundary sliding at room temperature for micro-devices, formation of special grain boundary segregations for the combination of high strength and low-temperature superplasticity in commercial aluminum alloys. There is also obviously an open field for the design of unique UFG structures in lightweight Al-based alloys to achieve a full range of exceptional combinations of mechanical strength and electrical conductivity and multifunctional properties [180].

7.3. Titanium alloys

Titanium and its alloys have a special positioning in the SPD field because one of the most important successes in the commercialization of SPD is the use of Ti-based materials for biomedical applications. Application of SPD to pure titanium results in grain refinement to the submicrometer level and enhancement of strength over 1000 MPa. When pure titanium is processed by HPT under high pressure (usually over 4 GPa), it shows a phase transformation to the ω phase which is hard and brittle. SPD is also widely applied to various titanium alloys with different initial phases, leading to grain refinement and phase transformations. Most studies on Ti-based alloys are directed toward biomedical applications by studying the mechanical properties, biocompatibility and corrosion resistance. This section reviews some recent findings on the application of SPD to titanium alloys with a focus on biomedical applications.

Prosthetic devices (Fig. 70a) are growing fast in commercial and medical importance, but progress in implant materials is limited [1537, 1538]. Developing new biomaterials for implants is challenging due to conflicting requirements [1327], as also described in earlier chapters. Prostheses must be biocompatible, free of toxic elements like vanadium, nickel, copper and cobalt [342, 1539, 1540], promote bioactivity, and have high corrosion and wear resistance. They should also possess superior mechanical properties, like a small Young's modulus similar to bone tissue to prevent stress shielding [1541–1544]. Titanium and its alloys are ideal for dental and orthopedic implants due to their biocompatibility and corrosion resistance. They possess a natural oxide

layer [1545] that protects against corrosion but does not promote bone healing or combat infections [1546]. Surface modifications and coatings can improve bone formation and reduce the risk of infections [556, 1350, 1547–1556]. Ti-based implants display exceptional mechanical properties (maximum load, bending, stiffness and fatigue strength) [1547, 1548, 1557]. These properties may effectively promote bone cell phenotypic needs [1558–1560]. Moreover, they have reasonably similar properties to bone tissue [1560]. Pure titanium is corrosion-resistant and is the best material so far for applications such as dentistry. Ti-6Al-4 V alloy has been chosen as a biomaterial because of its mechanical properties; however, there are concerns about its high elastic modulus [1561] and the cytotoxicity effects of aluminum and vanadium ions that can be released into the body due to corrosion or friction [342] and result in adverse bone tissue reactions [342, 1539, 1540]. Therefore, it is imperative to design single-phase β titanium alloys with high strength that are completely non-toxic and free from allergens (β alloys possess a lower elastic modulus intrinsically than α-Ti and the α+β Ti-6Al-4 V alloy) [342, 1557]. More comprehensive and up-to-date insights into the effect of thermomechanical processing on the microstructure and mechanical behavior of Ti-based alloys are given elsewhere [342, 1327].

Grain refining via SPD processes like ECAP and HPT can enhance the mechanical properties of Ti-based alloys. These methods effectively reduce grain sizes to the UFG or even nano-size range [1, 2, 177, 299, 556, 657, 668, 1364, 1549, 1550, 1562, 1564–1567], leading to improved strength, wear resistance and bioactivity. In addition to mechanical strength and stability, appropriate surface
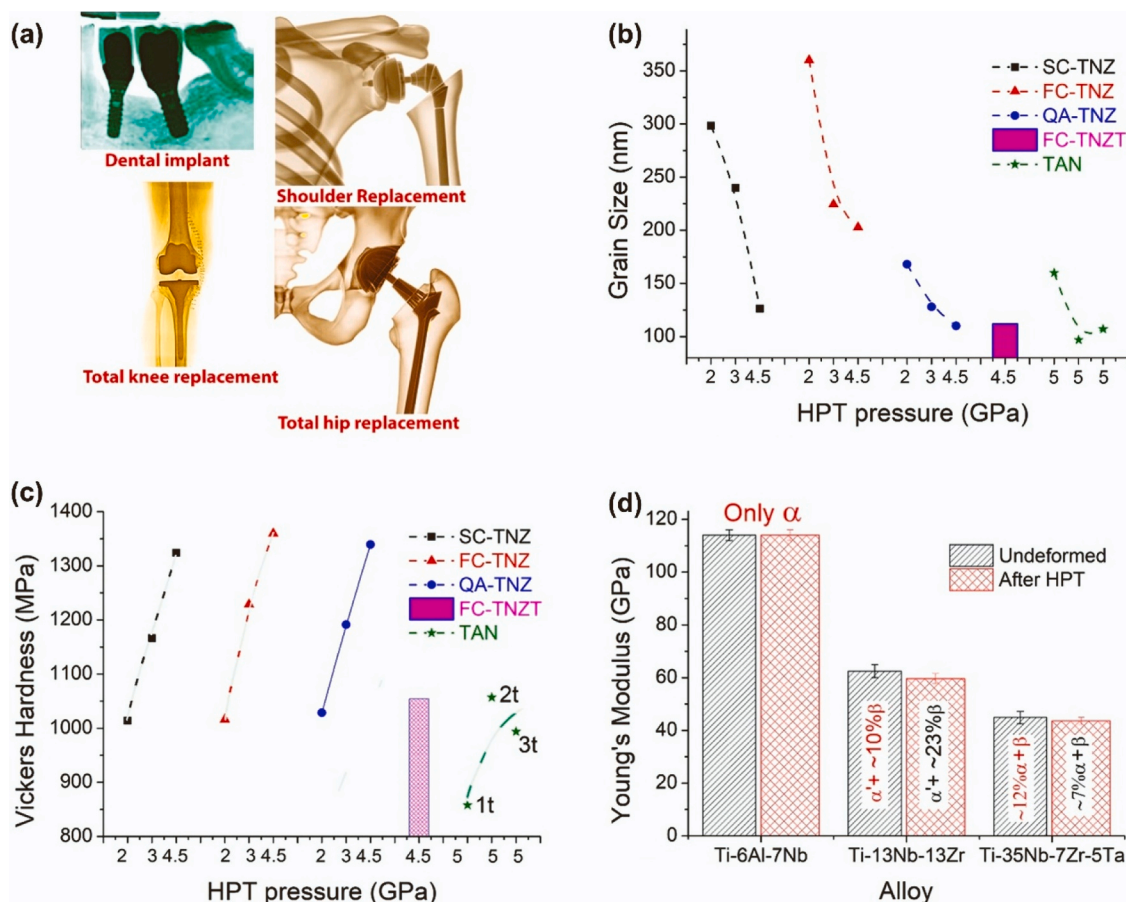
Fig. 70. (a) Examples of prosthetic devices for joint and teeth replacement. (b) Average grain size and (c) hardness in titanium alloys Ti-6Al-7 Nb (TAN), Ti-13-Nb-13Zr (TNZ) and Ti-35 Nb-7Zr-5Ta (TNZT) processed by HPT under different pressures, where 2 t, 3 t and 5 t refers to the number of HPT turns and SC, FC and QA refer to the initial condition before HPT processing (samples were heated treated at 1023 K for 1 h and cooled down; SC: slow cooling from the β phase region in the furnace; FC: fast cooling from the β phase region by water quenching; QA: quenching, aging at 773 K for 5 h and cooling in air). (d) Young's modulus for undeformed and HPT-processed samples of Ti-6Al-7 Nb, Ti-13 Nb-13Zr and Ti-35 Nb-7Zr-5Ta alloys [556, 1562, 1563].

nano/micro-roughness is crucial for producing reliable implants with a low risk of failure incidence [1568]. The high strength of UFG implants allows for smaller sizes and less invasive surgeries while maintaining functionality [851]. In addition to grain refinement, when processing titanium and its alloys through SPD, phase transformations can occur. The formation of metastable phases such as the ω phase and martensite α″ phase [556, 562, 1550, 1569–1571] can impact the tenacity and elastic modulus of titanium alloys [556, 1569, 1572, 1573]. Implants also require stress shielding and corrosion resistance and high bioactivity for a sufficient bone-bonding ability. This can be achieved by creating UFG microstructures through SPD and applying extra surface modifications such as anodization and acid + alkaline treatment.

Different titanium alloys like Ti-6Al-7 Nb (TAN) [1562, 1567], Ti-13-Nb-13Zr (TNZ) [556, 1550, 1566], Ti-35 Nb-7Zr-5Ta (TNZT) [556] and commercially pure titanium [1550, 1553] were subjected to SPD with varying strain rates, applied loads, starting phases and morphologies. An overview of the results of HPT processing, including phase transformations, structural/microstructural characterization, mechanical and corrosion properties, surface treatments (anodization and acid + alkaline treatment) and bioactivity has been compiled in [1563]. Deformation by HPT induces phase transformation in these alloys, which depends on the amounts of α or β stabilizers, the strain rate, applied load, starting phases and α phase morphologies [556, 1550, 1562, 1563, 1566]. When there are high levels of α stabilizers like oxygen or aluminum and α' present, a phase transformation to the ω phase is prevented. If α' is present, the fraction of the β phase increases with decreasing applied pressure. At high pressures, an α phase with a lamellar morphology transforms into the ω phase, while at low pressures, a fine globular α phase transforms into the ω phase (at higher

pressures, β can transform to α as well). The process of HPT is highly effective in achieving high grain refinement in Ti-based alloys down to grain sizes of 120 nm (Fig. 70b) leading to a maximum hardness of 1.4 GPa (Fig. 70c) [556, 1562, 1563]. A Hall-Petch analysis revealed that the strength of titanium alloys is not solely determined by the number of grain boundaries but also by specific characteristics, including different phases and their sizes [1563]. However, Young's modulus is solely affected by the phases, and an increase in the fraction of the β phase leads to a decrease in modulus (Fig. 70d).

To enhance the surface properties of SPD-processed titanium alloys, oxide nanotubes were made via anodization on α or α' phase surfaces [1563]. It was reported that the β phase produces oxide nanopores (thicker-walled tubular morphology), while treatment by acid + alkaline media can change the morphology to sponge-like structures [556, 1350, 1550]. The corrosion properties (Figs. 71a and 71b) indicate that the HPT-processed samples perform the best, although all cases have low current densities, indicating effective control of mass transport through the oxide layer [1550, 1553, 1554, 1563]. Corrosion potentials increased significantly with anodizing the surfaces, suggesting an effective strategy for the further improvement of SPD-processed alloys. Regarding bioactivity (Figs. 71c and 71d), polished surfaces are not bioactive due to their hydrophobic nature. In comparison to hydrophilic anodized alloys, commercially pure titanium hydrophilic anodized surfaces are more bioactive, regardless of the deformation of the surface. Morphologically, surfaces containing nanopores + nanotubes or only nanopores are not promising as well as pure titanium for apatite precipitation. Surface charges have a negative impact on precipitation for both anodized and chemically treated surfaces. For chemically treated surface tentacles to promote apatite formation, a critical dimension is
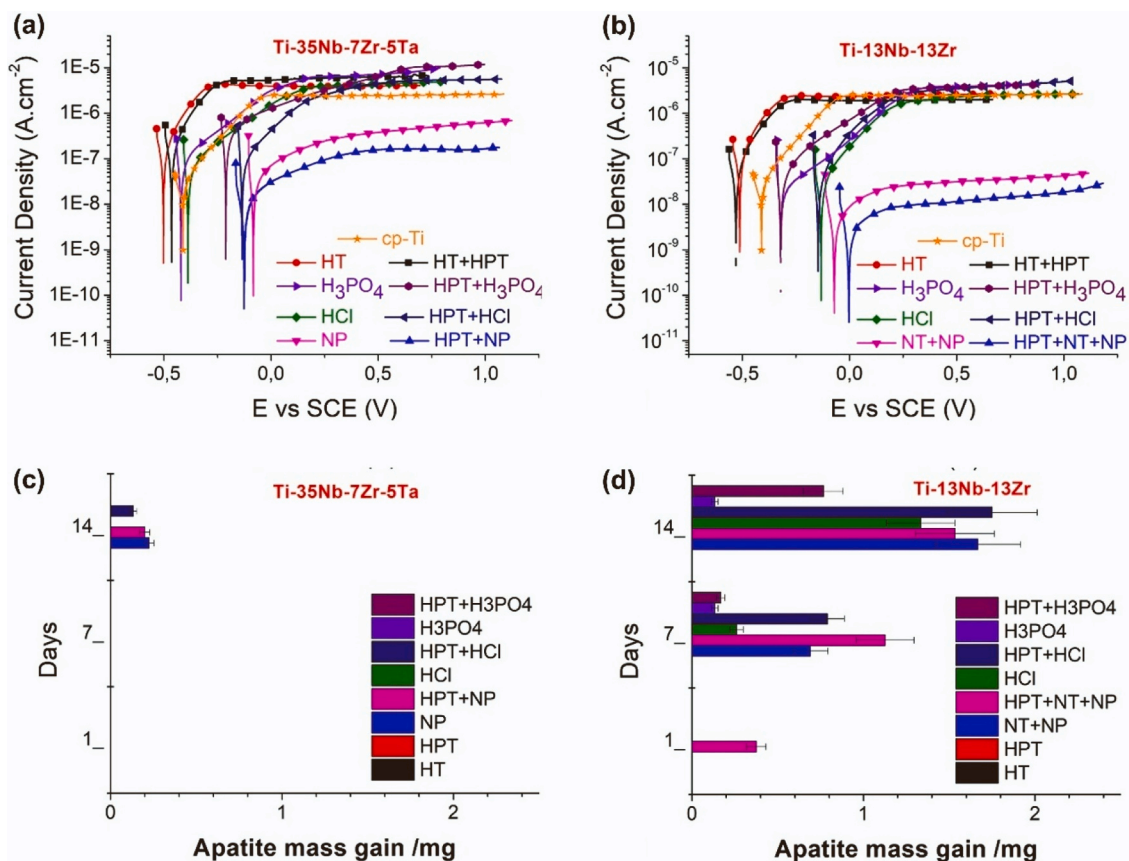
Fig. 71. (a,b) Corrosion behavior shown by potentiodynamic polarization curves recorded in simulated body fluid (SBF) at 310 K for (a) Ti-13-Nb-13Zr (TNZ) and (b) Ti-35 Nb-7Zr-5Ta (TNZT) alloys compared to commercially pure (CP) titanium with and without HPT processing. (c,d) Mass gain of apatite after immersing samples in SBF as a function of the soaking time, comparing treated and untreated surfaces of (c) TNZT and (d) TNZ before and after HPT processing [556, 1550, 1553, 1554, 1563].

necessary for biological fluid bonding. Grain refinement is a crucial factor in surface bioactivation, as proven by the superior results attained by anodized and HCl-treated surfaces of HPT-deformed samples [556, 1550, 1563].

Nanostructuring by SPD effectively improves the properties of titanium and its alloys, particularly for biomedical applications [1563]. While HPT is limited in sample size for medical implant production [53, 177], alternatives like ECAP [1350, 1543, 1549] and ECAP-conform [156, 193] are better suited for commercial processing of Ti-based materials for biomedical applications [1330, 1574].

7.4. Iron alloys and steels

Iron and steel alloys are the most-used engineering metallic materials. These materials have also received high attention in the SPD field and several SPD techniques have been applied to them over the last decades. SPD processing of pure iron, its strength can exceed 1 GPa due to grain refinement. SPD has been applied to various iron alloys and steel. The application of SPD to austenitic stainless steel usually results in martensitic phase transformation and the reduction of grain size below 100 nm. Among iron alloys, carbon-based steels including pearlitic, bainitic and martensitic grades are of special interest to the SPD community because they play a crucial role in our society considering typical engineering applications such as bearings or gear wheels or products for the mobility sector (*e.g.* for railway transportation). In many of these applications contact fatigue and wear arise and may lead to great microstructural changes of the steels [1575]. As a consequence, defects may form and restrict the lifetime of components [1576–1578]. The microstructural changes can be experimentally simulated using SPD in a well-defined manner, as far as the applied strain and temperature are concerned [1579]. In this sense, it represents an industrial application of SPD for testing and ranking materials exposed to contact fatigue. The foundation for this SPD contribution is analyzing the microstructural evolution of such steels for the understanding of material strengthening and changes in ductility [1580], fracture resistance [1581] and fatigue crack growth behavior [1582] along with the connected mechanical anisotropy. This section provides an overview of the underlying structural and mechanical changes of pearlitic, bainitic and martensitic steels subjected to SPD, particularly to HPT [1583].

Although cold wire drawing is sometimes not considered an SPD technique due to the changing sample dimensions [5], it must be mentioned in the context of SPD of steels due to (i) its importance in industry [1584], (ii) its close ability to deform materials of high hardening capacity [1585] and (iii) its status leading to the currently strongest pearlitic steels and therefore the strongest engineering alloy in the world [1586]. Cold-drawn pearlitic steels belong to the best-studied SPD materials and have been studied systematically with the pioneering work of Embury and Fisher in 1966 [1587]. This production route provides thorough insights into the structural evolution up to the highest deformation strains. Different methodologies were used to reveal the loss of the initial colony structure, consisting of alternating ferrite and cementite lamellae, using X-ray-based techniques [1588], TEM [1589] or atom probe tomography [682], as presented in Fig. 72.

The transfer to a single-phase ferrite nanograin structure is accompanied by a severe change in ductility [682] and toughness [683]. Similar observations have been made by studying the structural evolution of pearlitic steels during HPT [1590], although the highest SPD strains are to date not accessible due to experimental restrictions [1591]. However, in any application field in which pearlitic steels and their components are exposed to severe strains (*e.g.* in rails [1592]), one has to deal with these structural changes to better forecast the lifetime or even actively counteract the deterioration of the lifetime by novel alloy design concepts. Deformation in a quasi-constrained setup by HPT also enables to study of the structural changes in bainitic [1593] and martensitic steels [1594]. Especially for the latter case, its inherent brittleness does not allow for cold drawing to elevated strains at ambient conditions. Yet, martensitic steels are imposed to severe straining in bearings, where so-called white etching layers limit their lifetime [1595]. Thus, studying their structural changes at high strains provides important insights into the basic deformation and failure mechanisms during service.

A recent overview demonstrated that severe deformation of the different initial steel microstructures leads finally to a very similar architecture as the limit of deformation, as summarized in Fig. 73 [1583]. The microstructures consist of elongated nano-sized ferritic grains decorated with carbon that stabilizes grain and phase boundaries [1596]. These findings show the importance of carbon distribution, as it has been investigated in martensite for decades [1597]. The evolution in the low and intermediate deformed regime is however strongly dependent on the initial structure, even if the ferrite composite structure consists of a percolating lamellar or randomly distributed carbide structure. It is astonishing that despite the lower carbon concentration in a martensitic Ck10 steel (~0.1 wt% carbon), only slightly coarser lamellar spacings can be achieved in ferrite, as compared to fully
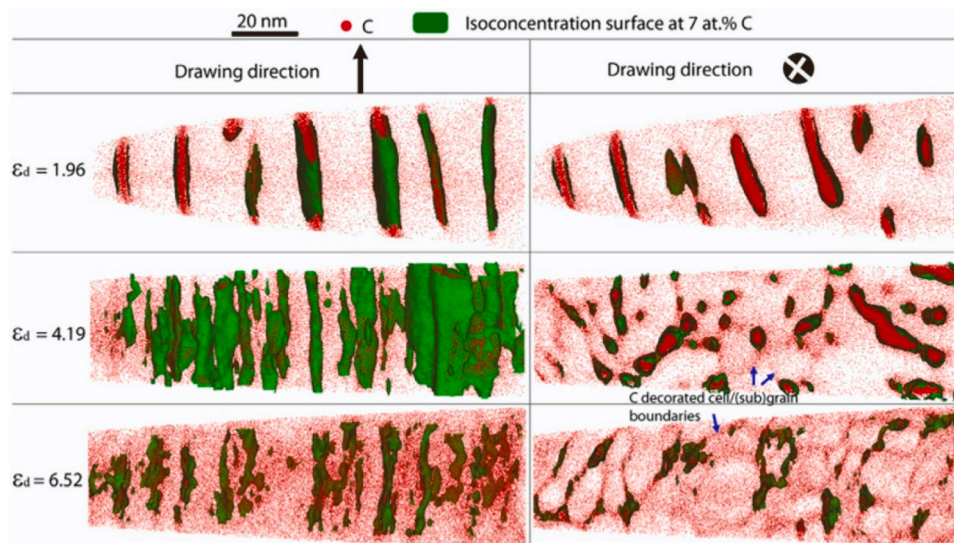
Fig. 72. Evolution from an initially lamellar structure (strain: $\varepsilon_d = 1.96$) to a ferritic subgrain structure with carbon either supersaturated in the matrix or segregated to subgrain boundaries (strain: $\varepsilon_d = 6.52$) by straining [682].
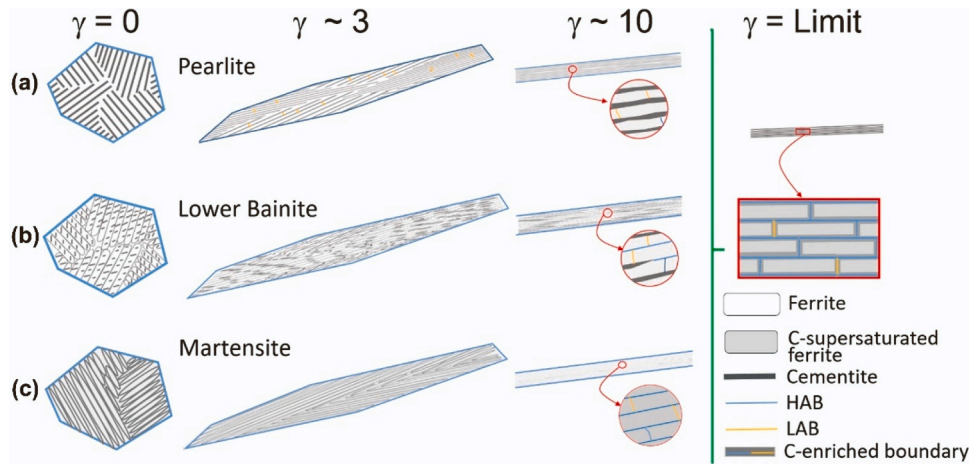
Fig. 73. Schematic illustration of the structural evolution of (a) pearlitic, (b) bainitic and (c) martensitic structures during quasi-constrained HPT deformed up to current technological limits [1583].

pearlitic steel (0.6–0.8 wt% carbon), at the highest HPT strains. These similarities may indicate that white etching layers in pearlitic and martensitic steels, which are subjected to severe strains during service, might be related to similar mechanisms. Along with the microstructural similarities, the mechanical properties of pearlitic and martensitic steels show comparable tendencies within the deformation limits [1596, 1598], which highlights the importance of grain architecture for mechanical properties. Despite these clear trends, there are indications that the interface structure plays a significant role in plasticity, strength and fracture [1599–1601], and thus, further scientific scrutiny is required. The current major restriction to push forward the structural refinement of these steels is however the strength of the HPT anvil materials and the applicable hydrostatic pressure.

7.5. Lattice-softened alloys

Furuta *et al.* reported in 2015 that severely cold worked Fe-24.6Ni-5.8Al-0.4 C (wt%) had a yield strength of 2 GPa and a fracture elongation of 20%, [1602] which attracted attention since such a combination of strength and ductility outperforms the conventional trade-off. They designed the alloy composition by considering the phase stability, where they controlled the averaged valence electron number to generate lattice softening. With these mechanical properties, they also reported that the Lüders-type band propagates multiple times during tensile tests, resulting in high ductility. After the first report by Furuta *et al.*, several high-strength lattice-softened alloys such as Fe-Ni-Al-C, Fe-Mn, Fe-Cr-Ni, Fe-Ni-Mn have been reported to show similar Lüders-type deformation when they are processed by cold working [1603–1613]. Fig. 74a shows the relationship between tensile strength and total elongation, while Fig. 74b shows the relationship between stress of Lüders deformation, σ_L, and Lüders strain. Other reports have been made on these high-strength alloys [1614–1625], but among them, the Fe-Ni-Al-C alloy shows the best strength-ductility balance. There have been limited numbers of reports on the effects of alloy compositions and cold working conditions on mechanical properties and the propagation behavior of the Lüders bands in high-strength steels [1606–1608, 1610–1612, 1626]. However, it has been reported that the stability of the γ phase affects the magnitude of Lüders strain, while the strategies for controlling the microstructure to achieve high strength and high ductility are currently unknown.

Two publications recently reviewed the features of high-strength lattice-softened alloys [1628] and high-strength alloys with Lüders deformation [1627]. Recent experiments attempted to increase the strength of these lattice-softened alloys further by compositional modifications [1627]. A higher amount of aluminum increases the strength

and decreases the ductility in Fe-25Ni-(5.0–6.0)Al-0.3 C (wt%) alloys. The addition of aluminum increases the volume fraction of the B2 phase, Ni-rich second phase, which decreases the γ-phase stability of the matrix and accelerates transformation from γ to α' during cold rolling and tensile deformation. It was also confirmed that the γ-phase stability affects the Lüders strain. Fig. 74c shows tensile stress-strain curves of the specimens after cold rolling by 60% (a-n represent points where Lüders type deformation was confirmed). The alloy with 5.0 wt% Al has a yield point of about 1000 MPa and a total elongation of about 39%, and the alloy with 5.5 wt% Al, has higher strength and lower ductility. Increasing aluminum to 6.0 wt% leads to a higher deformation stress, but the sample fractured at a lower strain. The profiles for local strain along the center line parallel to the tensile axis in the gauge section were determined by digital image correlation (DIC) analysis at each point (a-f in the stress-strain curves of the alloy with 5.0 wt% Al and 60% cold rolling), as shown in Fig. 74d. The local strain increases near 10 mm of the gauge section at point a, after the yield point drop; the local strain profile changes as the nominal strain increases to point c; and the local strain increases and the deformation area expands over the entire test specimen, indicating that typical Lüders-type deformation proceeds. Similar Lüders-type deformation can be seen during the deformation at points d-f. In addition, the higher rolling reduction increased the Lüders strain. For example, severe cold rolling by 80% enabled the prolonged Lüders strain as much as 25% in nominal strain. This prolonged Lüders strain was achieved by multiple propagation of Lüders-type bands.

There exists specific phase stability of the γ phase and deformation texture that enables sustained and prolonged Lüders deformation in lattice-softened alloys. The importance of phase stability on deformation behavior has been also reported in other lattice-softened alloys [1629, 1630]. The stable Lüders deformation suppresses subsequent uniform deformation with large work hardening, which raises the deformation stress and promotes premature fracture. Although the Fe-Ni-Al-C alloy has interstitial carbon, the simple dislocation-locking mechanism cannot explain multiple propagation of Lüders-type bands. Besides the mechanism of dislocation locking, the Lüders deformation has also been found in UFG materials including pure metals [715, 1631–1635] and alloys [1636, 1637], which do not usually show the yield point phenomenon in coarse grain sizes. The microstructure in the SPD-processed lattice-softened Fe-Ni-Al-C specimens is still very complicated [1626], so further investigation on the effect of such microstructure on the Lüders deformation is required in the future.

7.6. High-entropy alloys

The newly developed generation of single-phase, multi-element (five
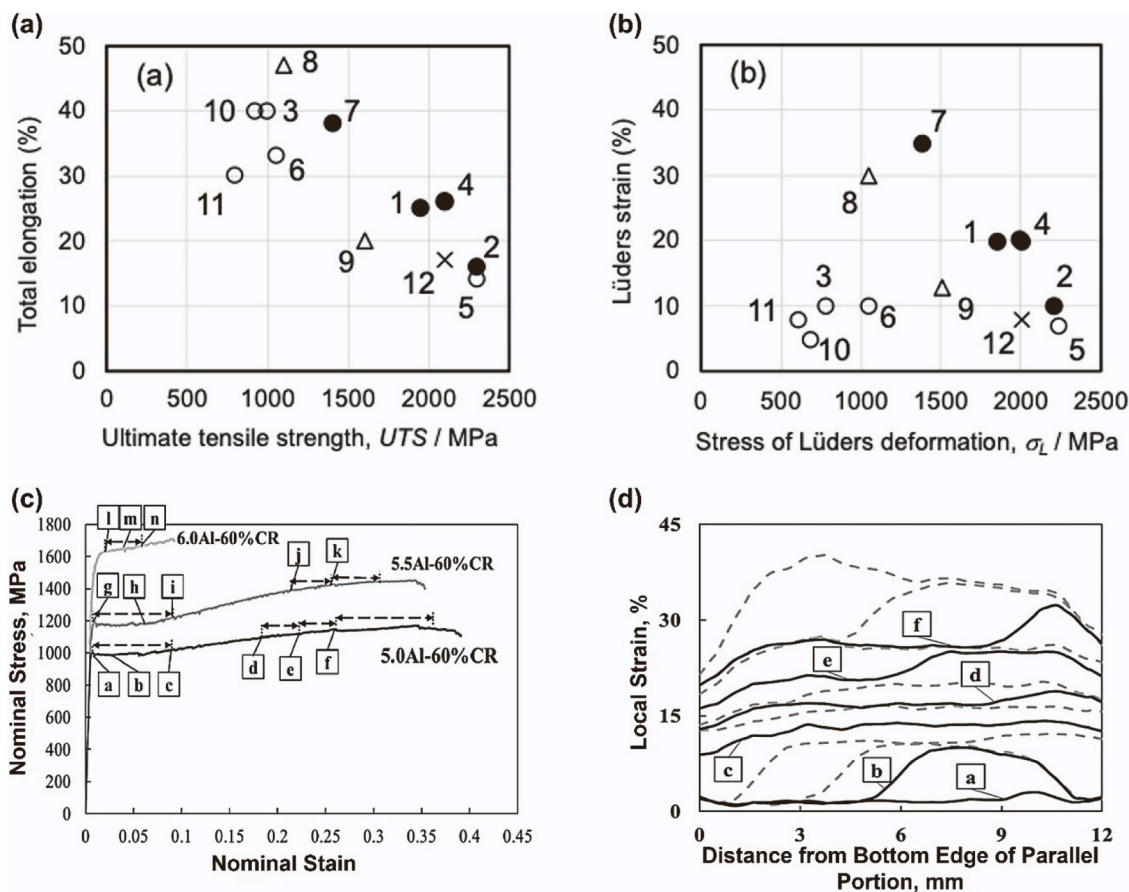
Fig. 74. (a, b) Mechanical properties and Lüders deformation behavior in the literature, where the number indicated at each plot corresponds to the reference number. (a) Total elongation versus ultimate tensile strength, (b) Lüders strain versus stress of Lüders deformation, σ_L. ●: Fe-Ni-Al-C [1602, 1603, 1605, 1608], ○: Fe-Mn [1604, 1606, 1607, 1611, 1612], △: Fe-Cr-Ni [1609, 1610], ×: Fe-Ni-Mn [1613]. (c) Stress-strain curves obtained by tensile tests for specimens rolled by 60% [1627]. (d) Local strain profiles along the tensile axis in the gauge section of the 5.0Al-60% cold-rolled specimen in (c).

or more principal elements) solid solution alloys with concentrations between 5 and 35 at. percent of the individual elements, referred to as high-entropy alloys (HEAs) or multi-principal element alloys (MPEAs), has shifted the design concept away from the corners of phase diagrams toward the center, enabling compositions that go beyond the scope of traditional alloys [1638, 1639]. Such an approach offers unprecedented properties, challenges, and opportunities for a variety of structural and functional applications. HEAs exhibit certain remarkable mechanical properties. One of the most important aspects is the trade-off between strength and ductility, especially as the temperature decreases, resulting in excellent fracture toughness at cryogenic temperatures [1640, 1641].

Since SPD-processed materials with small grain sizes have been shown to have exceptional properties, including high yield strength and moderate ductility, and the ability to undergo superplastic forming [5], many scientists started to apply the SPD methods to HEAs. A current compilation of the publications covering SPD of HEAs is given in [1642]. The compilation shows that most of the work relates to FCC HEAs, mainly the equiatomic Cantor alloy CrMnFeCoNi [1643], a small part to BCC and dual phase FCC + BCC, but not to HCP HEAs. The inspection of publications also indicates that the main SPD process applied to HEAs is HPT. In the following sections, after reviewing the reported results about structural, microstructural and mechanical property changes in Cantor alloys after HPT processing, the hardening behavior, nanomechanical behavior, superplasticity and superficial properties of SPD-processed HEAs are reviewed.

7.6.1. Microstructural and mechanical behavior of Cantor alloy

Most SPD work has concentrated on the HPT processing of the Cantor

alloy [1642]. Therefore, this section aims to provide an overview of the HPT processing of this HEA, with emphasis on microstructure and texture evolution, phase transformation, strength and ductility as well as superplasticity and thermal stability [273]. During HPT processing of the Cantor alloy, a very fast refinement of the FCC microstructure takes place [290, 1644]. The grain size at room temperature and liquid nitrogen temperature (77 K) reaches a very low steady-state value of 24 nm after a shear strain of about 20 (Fig. 75a). Simultaneously, the dislocation density saturates at a high value of 3×10^{16} m^{-2} at room temperature (Fig. 75b), while it is surprisingly lower after cryogenic-SPD at 77 K (10^{16} m^{-2}). The twin density at room temperature reaches a maximum value of 2% at a shear strain of 20 (Fig. 75c). During HPT at 77 K instead of mechanical twinning a deformation-induced phase transformation from FCC to HCP is observed (Fig. 75d) [290]. The onset pressure decreases with decreasing temperature [274], while there is a reverse transformation of the HCP phase produced by HPT at liquid nitrogen during long-term storage under ambient conditions [274]. The textures of HEAs processed by HPT are typical for shear, but they are quite weak [274, 290, 1645].

The room-temperature hardness of the Cantor alloy deformed by HPT at room temperature and in liquid nitrogen increases with shear strain and saturates at a certain strain level depending on pressure and HPT temperature (Fig. 76a) [274, 290]. Surprisingly, samples deformed in liquid nitrogen are softer (about 15%) than those deformed at room temperature. This also holds for compression down to 4 K (Fig. 76b) [291, 295]. The strength anomaly (softening) of the Cantor alloy is related to the martensitic phase transformation. Assuming that during pressure release and/or temperature increase as well as during
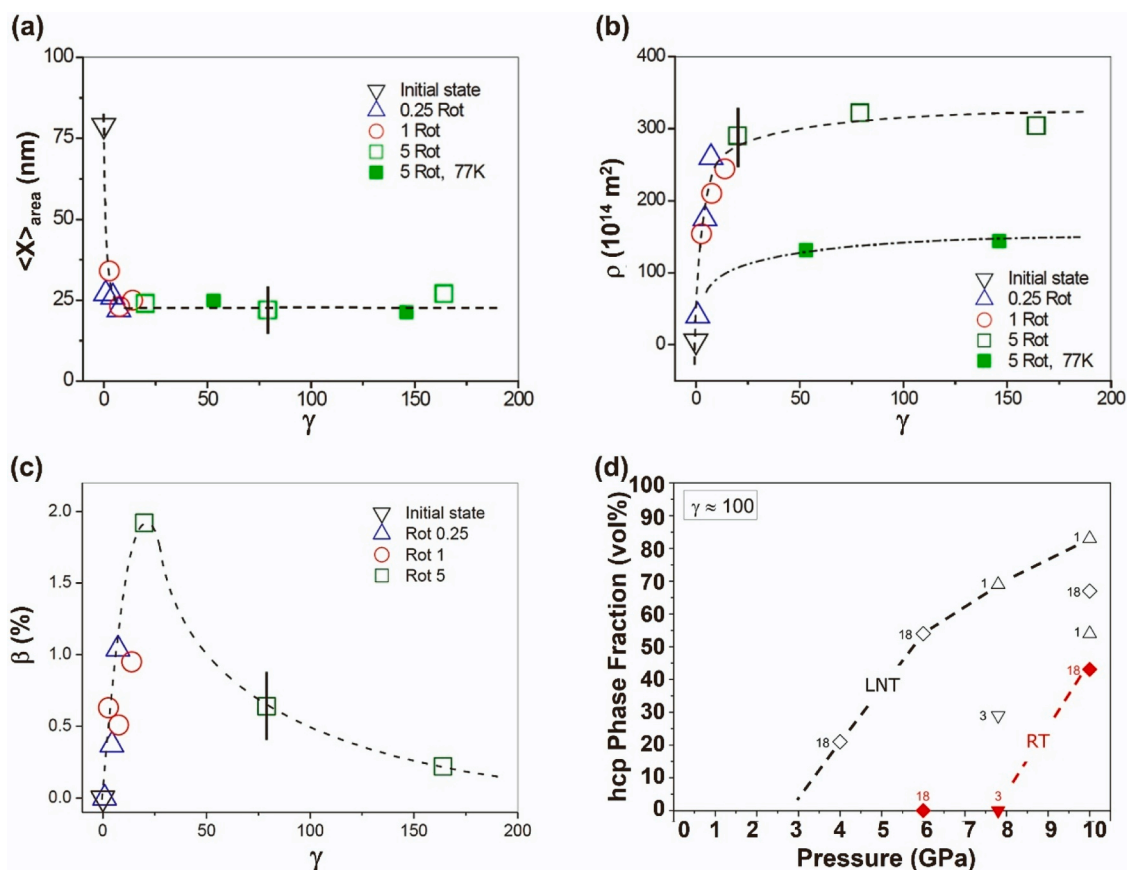
Fig. 75. (a) Crystallite size $<x>_{area}$ (area-weighted mean crystallite size) [290], (b) dislocation density ρ [290] and (c) twin density β as a function of shear strain γ for the Cantor alloy: after HPT processing at room temperature (open) and 77 K (full symbols) [290]. (d) Volume fraction of HCP martensitic phase versus applied pressure for the Cantor alloy after HPT processing at room temperature and in liquid nitrogen (LNT). The symbols represent different series of HPT samples, for which the phase composition was measured after the number of months indicated [274].

room-temperature indentation, the HCP phase becomes unstable, then a reverse transformation is very likely. This process leads to a reduction of internal stresses and the formation of dislocation-free new grains of the FCC phase. Consequently, because of this process, the overall dislocation density of the FCC phase and the hardness of the polyphase aggregate are lowered. Moreover, the microstructure and microhardness become quite inhomogeneous [274]. The strength of the severely deformed Cantor alloy can be further increased by annealing (Fig. 76c) [503]. For this effect, precipitation seems to play a major role, along with other factors discussed in [689, 694, 702, 1646]. The softening above a certain temperature is due to the dissolution of precipitates and grain growth (precipitation leads to a loss of ductility) [503]. Moreover, the nano-crystalline Cantor alloy shows superplasticity above about half the melting temperature (Fig. 76d) [1647–1650]. This deformation mechanism is favored by reduced grain growth due to sluggish diffusion [1651] and/or nanosized precipitates often forming at elevated temperatures [1652, 1653].

In conclusion, similar to traditional metallic alloys, SPD processing of the Cantor alloy leads to UFG microstructures, high dislocation densities and weak textures. This is associated with a high strengthening effect and a loss of ductility. However, due to the multi-element solid solution, the Cantor alloy in the high-energy SPD state becomes quite unstable with respect to phase transformations, grain boundary segregation, and phase decomposition. Due to a defect-enhanced diffusivity [367], the kinetics of the decomposition is increased. This offers the possibility of producing ultra-hard materials by SPD processes or by post-annealing. Reduced grain growth, either caused by sluggish diffusion, segregation or nanoprecipitation, enables extremely high superplasticity at high strain rates [1650]. Although the effect of SPD on

changing properties has been demonstrated mainly for the Cantor alloy [273], a few examples of more complex HEAs indicate the high research potential of this new class of advanced materials in the field of SPD [1642, 1654–1656].

7.6.2. Hardening behavior of high-entropy alloys

The compositions of HEAs correspond to the unexplored middle parts of the phase diagrams; therefore, they exhibit never-before-seen behaviors such as high strength even at elevated temperatures, enhanced wear, oxidation, corrosion and radiation resistance [1638, 1643, 1657–1659]. As mentioned in the earlier chapter, the mechanical properties of these alloys can be further improved by applying SPD techniques. During SPD processing, both grain refinement and an increase in the density of lattice defects (*e.g.* dislocations and planar faults) contribute to the hardening of the as-processed materials [1, 2, 305, 855, 1659, 1660]. The maximum dislocation density and twin fault probability in HEAs achieved by SPD are about 300×10^{14} m^{-2} and 3%, respectively [1661–1665]. The minimum grain sizes for single-phase and multiphase HEAs were about 30 and 10 nm, respectively [1654, 1665]. These values are much smaller than the saturation grain sizes obtained in SPD-processed conventional metals and alloys as shown in Fig. 77, leading to high hardness of HEAs. The saturation state of the microstructure in HEAs is usually achieved at the equivalent strain of about 20 [1657, 1666].

The very high defect density and small grain size in SPD-processed HEAs cause superior hardness compared to conventional metals and alloys as shown in Fig. 78a [1654, 1661–1665]. On the other hand, the lower hardness bound of HEAs can also be achieved by conventional 316 L stainless steel processed by HPT at room temperature [19].
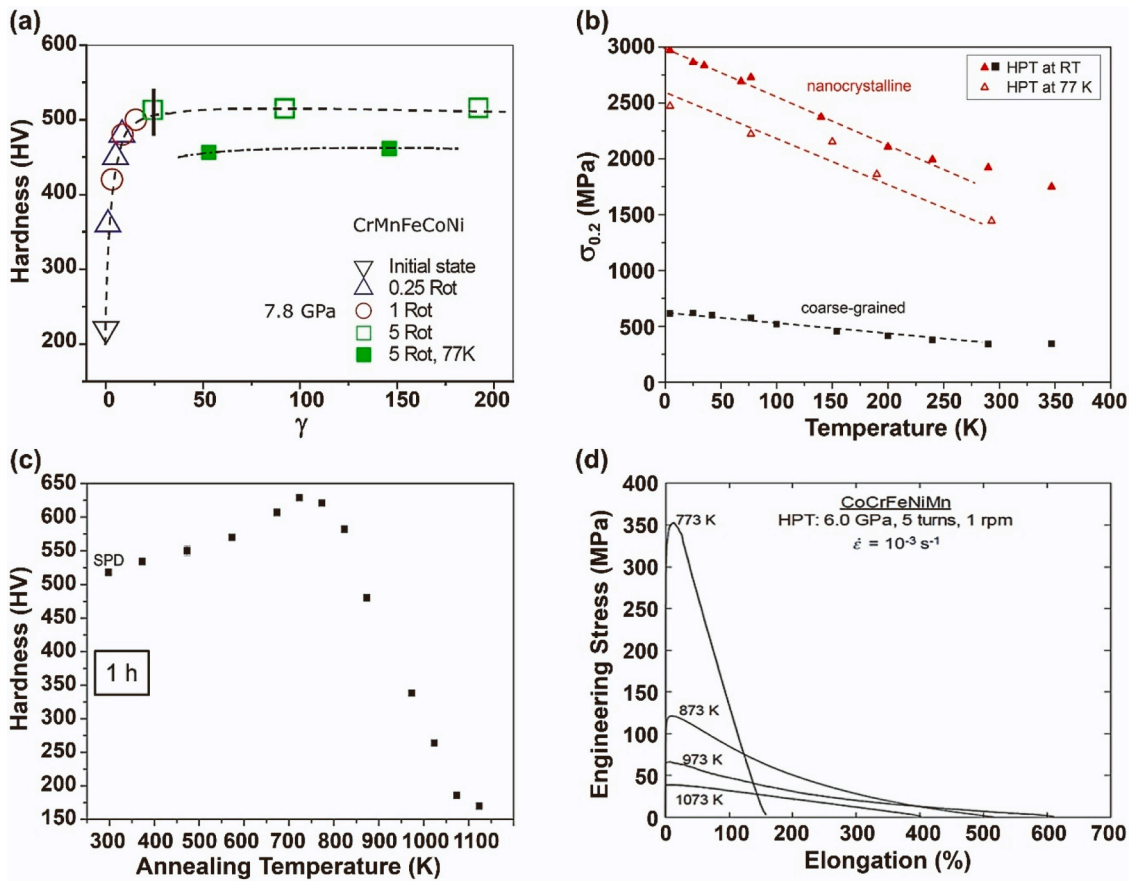
Fig. 76. (a) Room-temperature Vickers hardness as a function of shear strain γ after HPT processing at room temperature (open) and 77 K (full symbols) [290]. (b) Temperature dependence of the yield stress $\sigma_{0.2}$ in nanograined Cantor alloy processed by HPT at room temperature and 77 K in comparison with coarse-grained sample [273]. (c) Vickers hardness of isochronally annealed (1 h) Cantor alloy samples after HPT processing at room temperature [503]. (d) Engineering stress-elongation curves at different temperatures for samples processed by HPT at room temperature [1647].

Multiphase HEAs exhibit much higher hardness values than their single-phase counterparts [503, 1356, 1656, 1667–1677]. SPD-processed AlCrFeCoNiNb showed the highest hardness with a value of about 10 GPa due to the nanosized secondary phase precipitates [1654]. The hardening caused by SPD in the saturation state for different HEAs is shown in Fig. 78a where the hardness measured after SPD processing is plotted as a function of the values obtained before SPD. Fig. 78b reveals that SPD causes a higher relative hardening in HEAs

which had lower initial hardness values before SPD. Namely, below the initial hardness of about 3 GPa, the ratio of the hardness values after and before SPD varies between 1.6 and 4.5 while for HEAs with an initial hardness higher than 3 GPa, the hardening ratio is consistent with the value only of about 1.4. Fig. 78c shows the SPD-induced hardness increase versus the initial hardness in a double-logarithmic scale plot for different MPEAs having initial hardness values smaller than 3 GPa. The points in this plot follow an approximate linear trend which suggests the following relationship.

$$\frac{H_{SPD}}{H_{init}} = A H_{init}{}^{\delta} \tag{32}$$

where H_{SPD} and H_{init} are the hardness values given in MPa unit after and before SPD processing, respectively, and $A = 6870$ and $\delta = -1.05$ [1667].

As mentioned earlier, the high hardness of HEAs caused by SPD can be further enhanced by post-deformation annealing. This phenomenon was also observed for conventional SPD-processed alloys and called anneal hardening, as discussed earlier [689]. This effect was observed after annealing at moderate homologous temperatures between 0.3 and 0.4. Fig. 78d shows the hardness achieved by annealing after SPD versus the hardness observed immediately after SPD for different HEAs. The hardening effect of post-SPD annealing varies between 6% and 75%. Anneal hardening can be attributed to the reduction of mobile dislocation density, the relaxation of grain boundary structure and the formation of precipitates [1670, 1672, 1673, 1675–1677]. The highest hardness of about 11 GPa was achieved in AlNbTiV alloy processed by HPT at room temperature and then heat treated at 973 K [1677]. In this
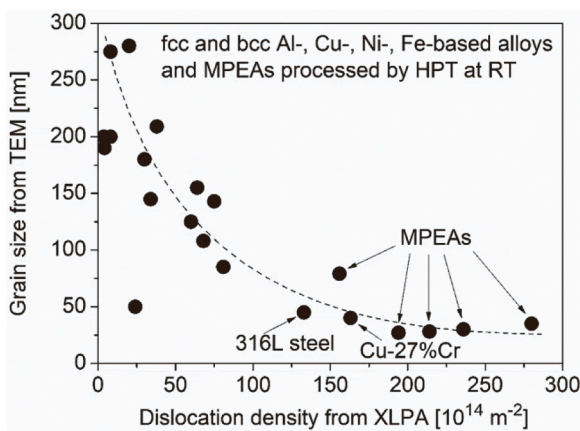
Fig. 77. The grain size versus the dislocation density obtained for FCC and BCC Al-, Cu-, Ni- and Fe-based conventional alloys and multi-principal element alloys (MPEAs) processed by HPT at room temperature [1667].
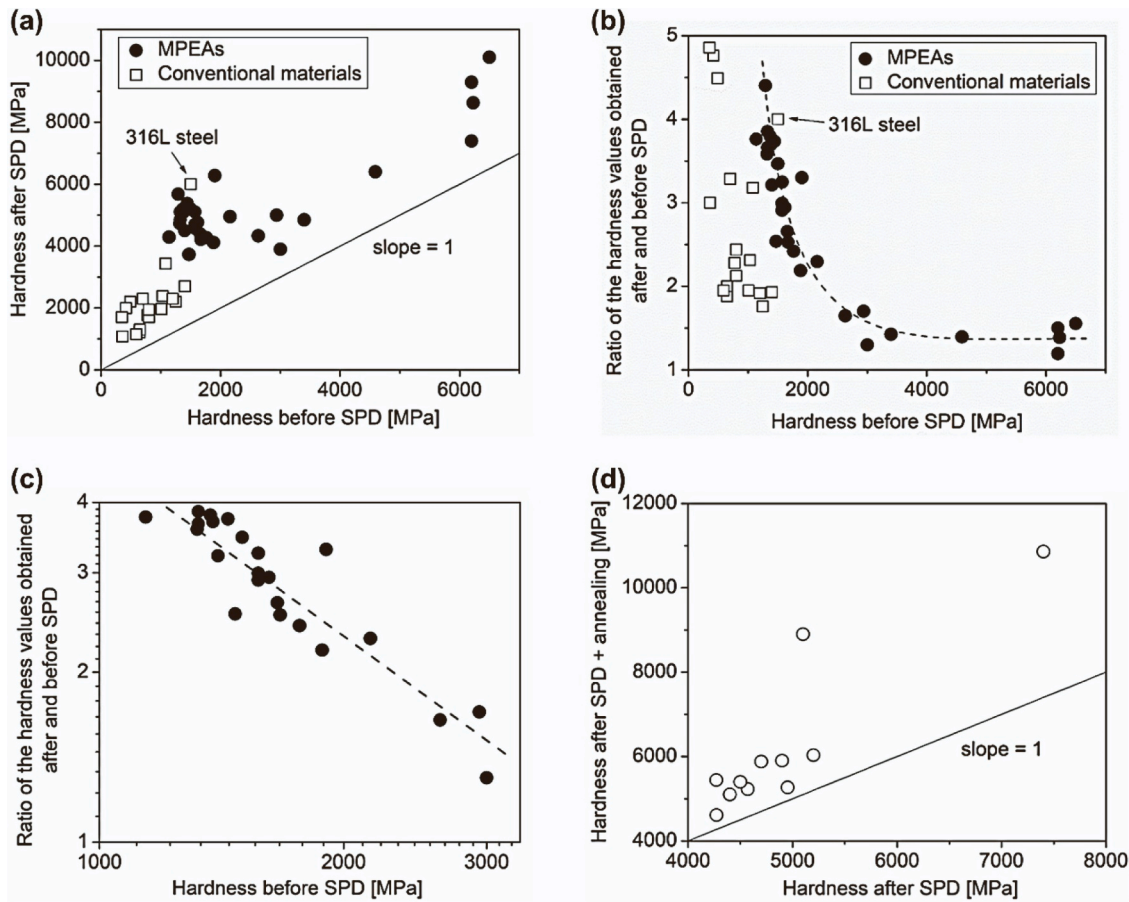
Fig. 78. (a) The maximum hardness measured after SPD processing versus the values obtained before SPD for different conventional materials and multi-principal element alloys (MPEAs). (b) The ratio of the hardness values measured after and before SPD as a function of the hardness determined before SPD for different conventional materials and MPEAs. (c) A double logarithmic plot of the data shown for MPEAs in (b). (d) The maximum hardness obtained due to anneal hardening of SPD-processed MPEAs versus the hardness values measured immediately after SPD [1667].

alloy, anneal hardening was caused by precipitation. Due to superior hardness and strength, SPD-processed HEAs are expected to be used in different applications, *e.g.* as structural materials or surgical implants [1356, 1678].

7.6.3. Nanomechanical behavior of high-entropy alloys

Recently, the nanoindentation technique has been actively applied to characterize the mechanical behavior of HPT-processed medium-entropy alloys (MEAs) and HEAs [1679]. Moreover, employing different strain rates during nanoindentation has allowed the investigation of rate-dependent plasticity in HPT-processed alloys, providing valuable insights into the relationship between microstructural refinement and the enhancement of mechanical properties in these materials [1680]. This section describes the principles of nanoindentation for analyzing the rate-dependent plasticity in HEAs. The study of HEAs by nanoindentation was initially motivated by the relatively limited understanding of the grain refinement effect on rate-dependent plasticity in this new family of alloys compared to conventional materials.

The strain rate sensitivity (m) and activation volume (V^*), which are two important indicators for rate-dependent plastic deformation, provide a clue to a better understanding of thermally-activated deformation mechanisms. According to the power-law response between nanohardness H_N, and indentation strain rate ($\dot{\varepsilon} = h^{-1}(dh/dt)$, where h is displacement and t is time [1681]), the m and V^* values can be determined at a given strain ε, and temperature T, by [1682]:

$$m = \left(\frac{\partial \ln H_N}{\partial \ln \dot{\varepsilon}}\right)_{\varepsilon,T} = \left(\frac{\ln H_{N,2} - \ln H_{N,1}}{\ln \dot{\varepsilon}_2 - \ln \dot{\varepsilon}_1}\right)_{\varepsilon,T} \tag{33}$$

$$V^* = \sqrt{3}kTC\left(\frac{\partial \ln \dot{\varepsilon}}{\partial H_N}\right)_{\varepsilon,T} = \sqrt{3}kTC\left(\frac{\ln \dot{\varepsilon}_2 - \ln \dot{\varepsilon}_1}{H_{N,2} - H_{N,1}}\right)_{\varepsilon,T} \tag{34}$$

where k is Boltzmann's constant and C is the constraint factor. Note that C is often taken as ~3, but it may vary with the material and loading conditions [1683]. In order to obtain m and V^* values using nanoindentation, constant strain rate (CSR) tests and strain rate jump (SRJ) tests are typically employed. The examples of employing CSR and SRJ experiments on a CoCrFeMnNi HEA subjected to the HPT process are shown in Fig. 79. As shown in Figs. 79a and 79b, the HPT process produces a nanocrystalline structure with an average grain size of ~38 nm after 2 turns. In the case of CSR tests, multiple nanoindentation tests with different strain rates are performed and m and V^* values are determined from the slope of a $\ln(H_N)$ versus $\ln(\dot{\varepsilon})$ plot and the slope of the $\ln(\dot{\varepsilon})$ versus H_N plot (Figs. 79c and 79d). On the other hand, for the SRJ test, $\dot{\varepsilon}$ is abruptly changed several times during a single nanoindentation (Figs. 79e and 79f). In order to account for the indentation size effect, H_N immediately before and after each transient change at specific depths is used for estimating m and V^* [505, 1684]. These values are denoted as $H_{N,1}$ and $H_{N,2}$ in Equations 33 and 34, respectively.

To better understand the effect of grain refinement on the deformation mechanisms of M/HEAs, the m and V^* values from the literature [1671, 1674, 1685–1704] are plotted as a function of grain size, d, in Figs. 80a and 80b. Note that only the results for FCC HEAs and MEAs are included in Fig. 80, since the variation in m and V^* values with d in other crystal structures has not been extensively examined for these alloys. In the coarse-grain regime, the m values of HEAs and MEAs are
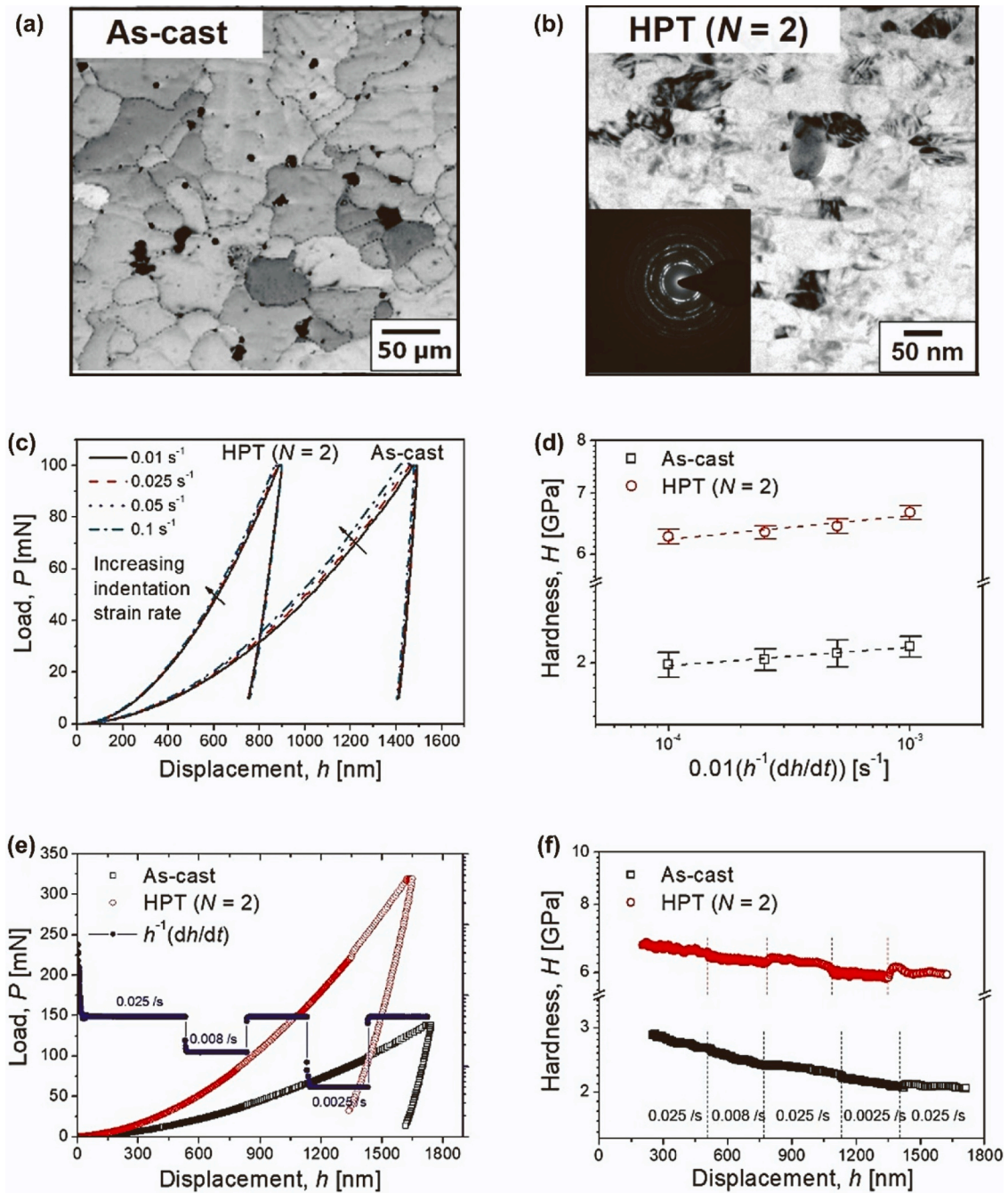
Fig. 79. Microstructures of (a) as-cast and (b) HPT-processed CoCrFeMnNi HEAs [1671] along with corresponding examples of (c,d) constant strain rate (CSR) nanoindentation [1671] and (e,f) strain rate jump (SRJ) nanoindentation [505].

substantially higher than those for pure nickel, whereas HEAs, MEAs and pure nickel show comparable *m* values in the nanocrystalline regime. Compared to pure nickel, FCC HEAs and MEAs exhibit significantly lower V^* values (~ 10–$100\ b^3$), indicating that the short-range of barriers (likely due to high lattice friction stress [1689, 1705] and chemical short-range ordering [1706, 1707]) are predominant. On the other hand, the V^* values for nanocrystalline FCC HEAs and nickel are around $\sim 10\ b^3$, suggesting that the deformation mechanism in the nanocrystalline FCC HEAs is grain-boundary-mediated dislocation activity (*e. g.* dislocation nucleation and/or dislocation depinning at grain boundaries) as in the conventional nanocrystalline FCC metals [1696, 1697].

Fig. 80c shows the change in *m* of nanocrystalline CoCrFeMnNi HEA with testing temperature, suggesting that the *m* value increases abruptly from $T = 473$ K ($\sim 0.3\ T_m$) [505, 1690]. To explore this mechanistic

transition, apparent activation enthalpy, $\Delta \mathscr{H}$, values can be determined by [1708, 1709]:

$$\Delta \mathscr{H} = \frac{H_N V^*}{\sqrt{3} C} \frac{\partial(\ln H_N)}{\partial(1/T)} \tag{35}$$

Using Equation 35 and the *T*-dependent H_N data (the inset of Fig. 80d), the variation in $\Delta \mathscr{H}$ with temperature can be calculated (the main plot of Fig. 80d). The estimated $\Delta \mathscr{H}$ for $T \leq 473$ K is ~ 0.5 eV which indicates that the deformation is primarily governed by grain-boundary-mediated dislocation activities [1696, 1710, 1711]. On the other hand, the estimated $\Delta \mathscr{H}$ for $T > 473$ K approaches that for grain boundary diffusion of nickel in CoCrFeMnNi HEA (~ 2.3 eV [1712]), suggesting that grain boundary diffusion becomes pronounced at higher temperatures.
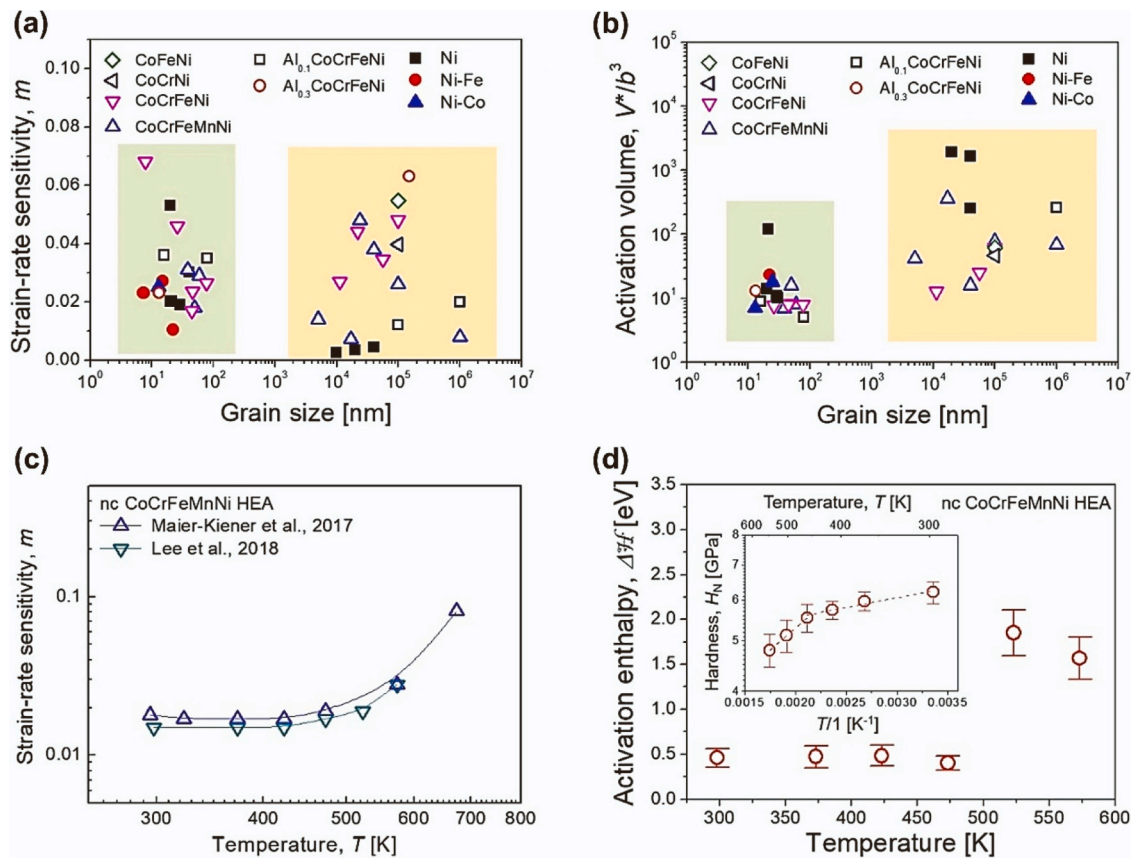
Fig. 80. Variations in (a) strain rate sensitivity and (b) activation volume of various FCC metals and alloys as a function of grain size [1671, 1674, 1685–1704]. (c,d) Results of high-temperature nanoindentation experiments for HPT-processed nanocrystalline CoCrFeMnNi HEA [505, 1690].

In summary, although appropriate for the estimation of strain rate sensitivity, activation volume, and apparent activation energy, nano-indentation provides crucial insights into the deformation mechanisms of SPD-processed HEAs. The results reported so far show that: (i) the deformation mechanism in FCC HEAs transforms from lattice atoms-dislocation interaction to gran-boundary-mediated plasticity as the grain size is reduced to the nanocrystalline regime, and (ii) grain boundary diffusion can become pronounced in nanocrystalline HEAs at homologous temperatures higher than ~0.3 T_m.

7.6.4. Superplasticity of high-entropy alloys

HEAs [1638, 1643, 1713–1720] and SPD processing [54, 159, 177, 193, 200, 224] are two extremes in materials science from the material and processing points of view. This resulted in the fast growth of research works on SPD processing of HEAs to achieve particular microstructures with advanced properties [5, 181, 1669, 1721, 1722]. Since superplasticity has a close connection with the SPD field [346, 770, 778, 783–786, 791], there have been attempts to examine the superplastic behavior of SPD-processed HEAs. The first evidence of superplasticity in HEAs was reported more than ten years ago in a fine multiphase equiaxed structure of an AlCoCrCuFeNi alloy with an average grain size of ~2 μm processed through MDF at 1223 K [1723, 1724]. In these experiments, a maximum elongation of 1240% was achieved when testing at 1273 K at a strain rate of $1.0 \times 10^{-2}\,s^{-1}$. More recently, there have been several reports of high superplastic elongations in HEAs and a detailed tabulation of all results is presented elsewhere [1725]. One of the most striking results available to date includes an elongation of 2000% in a CoCrFeNiMnAl$_{0.5}$ alloy [1650]. Fig. 81 shows results obtained on a Mo$_{7.5}$Fe$_{55}$Co$_{18}$Cr$_{12.5}$Ni$_7$ HEA where tensile tests were conducted at 973 and 1273 K [1726]. As shown in Fig. 81a, this alloy revealed the presence of a rather complex multiphase

microstructure including FCC, BCC, martensite and an Mo-rich μ phase before tensile testing. The results in Fig. 81b demonstrate the occurrence of superplastic elongations of 500% when testing at 1273 K but with an absence of superplasticity at 973 K. The latter result was attributed to the formation of more Mo-rich μ precipitates at the higher testing temperature. Close inspection of the superplastic samples in Fig. 81b shows that they represent true superplasticity because there is no evidence of any additional necking within the gauge lengths [1727].

An important requirement in superplasticity is to test the applicability of the grain boundary sliding model (*i.e.* general creep equation Equation 7) which was first developed for conventional superplastic alloys without processing by SPD techniques. Several analyses demonstrate that there is very good agreement between published data for various conventional Al- and Mg-based alloys and the predictions of the general creep equation for superplasticity [1728–1730]. The results of this analysis are shown in Fig. 82 where the temperature and grain size compensated strain rate is plotted against the normalized stress. The data for Fig. 82 were taken from several published reports [1481, 1647, 1650, 1652, 1653, 1724–1726, 1731–1734] and full details of the analysis were given elsewhere [1725]. The solid line labeled $\dot{\varepsilon}_{sp}$ represents the prediction of the model and it is apparent that there is generally excellent agreement between the experimental datum points and the rates predicted by the superplastic model based on the occurrence of grain boundary sliding [791]. This analysis confirms that superplasticity in HEAs is similar to the superplasticity occurring in other materials both with and without SPD processing.

7.6.5. Superfunctional high-entropy alloys and ceramics

High-entropy materials include two major groups of HEAs and high-entropy ceramics. Similar to HEAs [1735, 1736], high-entropy ceramics are defined as materials with five or more cations or with an entropy of
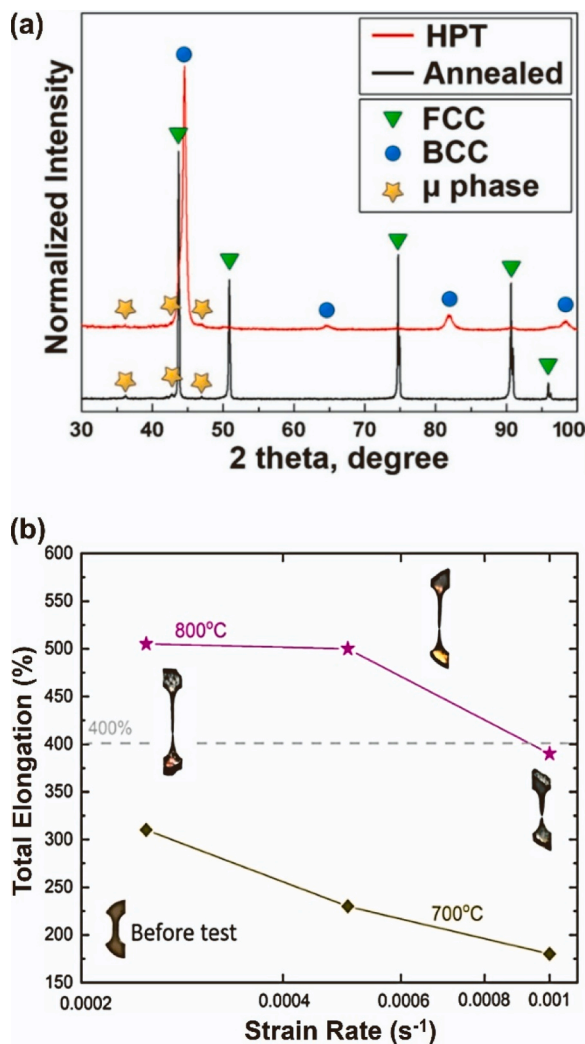
Fig. 81. (a) XRD patterns of $Mo_{7.5}Fe_{55}Co_{18}Cr_{12.5}Ni_7$ HEA before (annealed) and after HPT processing [1650]. (b) Elongation versus strain rate plot for HPT-processed $Mo_{7.5}Fe_{55}Co_{18}Cr_{12.5}Ni_7$ before and after tensile testing at elevated temperatures [1727].

Fig. 82. Temperature and grain size compensated strain rate for SPD-processed HEAs with superplasticity behavior, showing excellent agreement with the theoretical prediction for conventional superplasticity [1650]. $\dot{\varepsilon}_{sp}$: strain rate, k: Boltzmann's constant, T: absolute temperature, D_{gb}: coefficient for grain boundary diffusion, d: grain size, b: Burgers vector, σ: applied stress G: shear modulus). Experimental data were taken from [1481, 1647, 1650, 1652, 1653, 1724–1726, 1731–1734].

mixing more than 1.5R (R: gas constant) (Fig. 83a) [986]. The high entropy of these materials results in low Gibbs free energy and their consequent high stability [983,1732,17333]. High-entropy materials have shown high potential for a varied range of not only mechanical properties but also functional properties due to their superior features including sluggish diffusion, lattice strain and the cocktail effect [1737–1744]. SPD methods, especially HPT, have been employed for processing and synthesizing high-entropy materials mainly for mechanical properties [391, 1236, 1745–1749] and partly for achieving functional properties [1145]. Ultrahigh hardness, hydrogen embrittlement resistance, hydrogen storage capability, biocompatibility, photovoltaic and photocatalysis are the reported functional properties and applications of SPD-processed/synthesized high-entropy materials, which are briefly reviewed below [1642].

- In connection with classic works on SPD processing of conventional materials [4, 38], there have been attempts to improve the mechanical properties of HEAs by SPD methods to levels comparable to those of ceramics [1642]. A combination of the concept of SPD and HEAs resulted in the introduction of the two HEAs processed by HPT with ultrahigh hardness levels up to 10 GPa [1654, 1655]. Among all reported HEAs, carbon-doped AlTiFeCoNi as a dual-phase HEA, which was designed by CALPHAD (calculation of phase diagram)

method and processed by HPT, showed an ultra-high hardness of 950 Hv [1655]. One of the highest hardness values (1030 Hv) was achieved in HPT-processed AlCrFeCoNiNb HEA with six principal elements and two cubic and hexagonal phases (Fig. 83b) [1654]. These high levels of hardness values of HEAs are attributed to the formation of nanograins, dislocation and nanoprecipitates [1642, 1654].

- As mentioned earlier, one critical issue in developing a hydrogen-based energy system is achieving materials with high hydrogen embrittlement resistance [1750]. Enhanced hydrogen embrittlement resistance was observed in some FCC HEAs due to their high plasticity in the presence of hydrogen [1240, 1751], but coarse-grained HEAs suffer from low yield strength. It was reported that HPT was effective in enhancing the yield strength of CrMnFeCoNi HEA as a hydrogen-compatible material, as shown in Fig. 83c [1235, 1752]. Dark-field images and high-resolution TEM images of CrMnFeCoNi after HPT processing show the presence of defects with low mobility such as twins (Fig. 83d), Lomer-Cottrell locks (Fig. 83e) and D-Frank partial dislocations (Fig. 83d) which should be responsible for suppressing hydrogen-enhanced localized plasticity (HELP) mechanism [1752].

- Solid-state hydrogen storage at room temperature is another critical issue in developing a hydrogen-based energy system [1076, 1753]. For the solid hydrogen storage concept, since the SPD methods such as ECAP and HPT could improve the properties of conventional metal hydride in terms of kinetic and thermodynamic [359, 1754], there were some attempts to synthesize new HEAs such as MgTiVCrFe by HPT for hydrogen storage [314]. Although MgTiVCrFe showed low hydrogen storage capacity, this study was a starting point to develop various HEAs for fast and reversible hydrogen storage at room temperature by employing theoretical studies (Fig. 84a): TiZrCrMnFeNi (Fig. 84b) [1755], TiZrNbFeNi [1756], TiZrNbCrFe [1757] and $Ti_xZr_{2-x}CrMnFeNi$ [1758] (x = 0.4–1.6). These materials
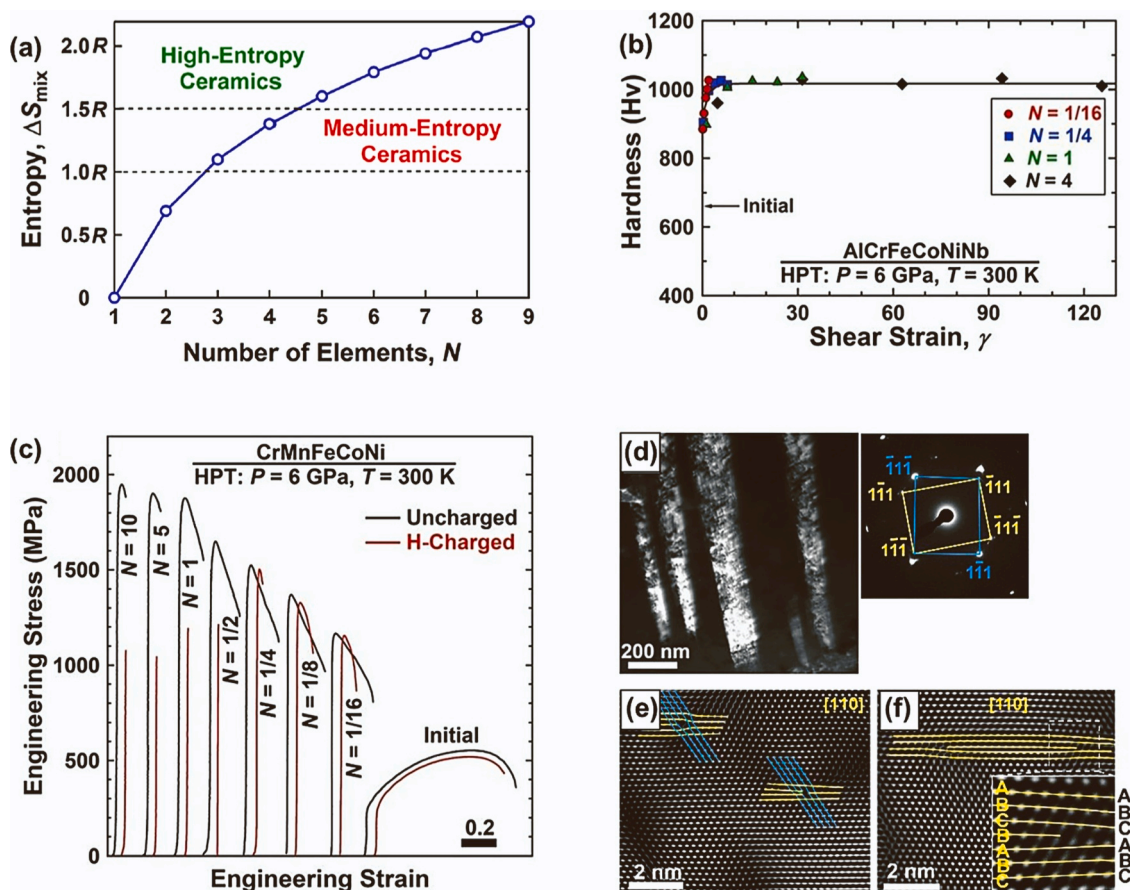
Fig. 83. (a) Entropy of mixing versus number of elements [986]. (b) Hardness of AlCrFeCoNiNb synthesized by HPT for $N = 1/16, 1/4, 1$ and 4 turns [1654]. (c) Engineering stress versus engineering strain before and after hydrogen exposure for CrMnFeCoNi before and after HPT processing with varied turns [1752], (d) Dark-field image of twins with relevant selected area electron diffraction patterns for CrMnFeCoNi after HPT processing for 1/16 [1752]. (e,f) High-resolution lattice images of CrMnFeCoNi after HPT processing for 1/4 turn containing (e) Lomer-Cottrell locks and (f) D-Frank partial dislocations [1752].

also showed a promising potential to be used as anode materials in nickel-metal hydride batteries [1759].

- Biocompatibility is another application of HEAs, which is getting high attention [1760, 1761]. Application of the HPT method to a material designed by CALPHAD calculations (TiAlFeNiCo HEA) was reported to be effective in enhancing the strength, decreasing the elastic modulus (by phase transformation) and improving the biocompatibility of this material [1356]. The material showed a larger microhardness and better biocompatibility (cell proliferation-viability-cytotoxicity activity) compared to coarse-grained and UFG pure titanium and the Ti-6Al-7 Nb alloy representing two conventional biomaterials (Fig. 84c) [1356]. In another report, ultra-SPD with extremely high shear strain was employed to synthesize TiNbZrTaHf HEA with BCC structure as a biomaterial [317]. The material showed higher hardness compared to corresponding binary, ternary and medium-entropy alloys with an elastic modulus better than that of some typical biomaterials [317].

- Photovoltaic and photocatalysis are two functional properties of some high-entropy ceramics. The semiconductors having these two properties can adsorb the light to generate electricity (photovoltaic) and consequently advance a reaction (photocatalysis). TiZrHfNb-TaO$_{11}$ high-entropy oxide [323, 324, 982] and TiZrHfNbTaO$_6$N$_3$ high-entropy oxynitride (HEON) [326, 327, 982] are two high-entropy ceramics synthesized by HPT which could generate the electric current under light as shown in Fig. 84d. The potential of HPT to improve the photovoltaics was also reported in conventional semiconductors [963]. These two high-entropy ceramics also showed activity for photocatalytic hydrogen evolution and the

efficiency of TiZrHfNbTaO$_6$N$_3$ was higher than Ga$_6$ZnON$_6$ as shown in Fig. 84e [323, 326]. High-resolution TEM image of TiZrHfNb-TaO$_6$N$_3$, which contains FCC and monoclinic phases and has higher light absorbance than TiZrHfNbTaO$_{11}$ due to its low bandgap, is shown in Fig. 84f [326, 327]. As mentioned in the earlier chapter, these two materials later were employed for photocatalytic CO$_2$ conversion with high efficiency [324, 327]. TiZrHfNbTaO$_{11}$ showed a high CO production rate the same as P25 TiO$_2$ used as a benchmark photocatalyst [324]. The efficiency of TiZrHfNbTaO$_6$N$_3$ for CO$_2$ photoreduction was even higher than that of P25 TiO$_2$ and all reported photocatalysts in the literature [327]. TiZrNbTaWO$_{12}$ is another HEO synthesized by arc melting and processed by HPT which showed photocatalytic activity for oxygen evolution [325] due to the heterojunction effects [1762].

The combination of the concepts of high-entropy materials and SPD resulted in the discovery of various superfunctional high-entropy materials for various ranges of applications. Perhaps, the introduction of the first high-entropy photocatalysts is the biggest contribution of the SPD field in this regard. Since there are urgent needs for functional biomaterials and energy materials for carbon-neutral energy development, it is expected that the application of SPD in the field of high-entropy materials will be extended from mechanical properties to functional properties in the near future.

7.7. Amorphous and glass materials

Amorphous alloys are one of the most attractive topics of modern
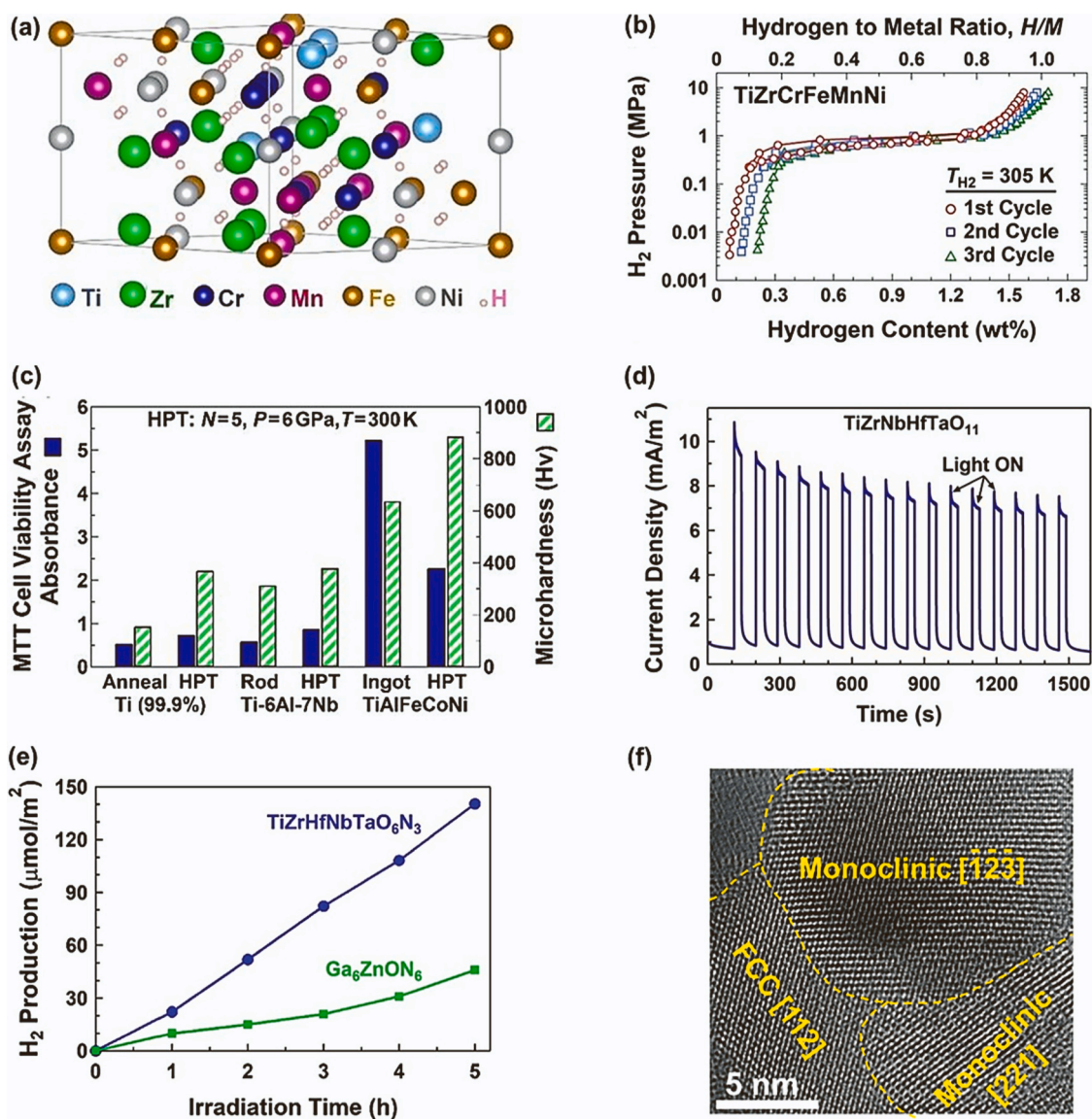
Fig. 84. (a) Lattice structure of $Ti_{0.4}Zr_{1.6}CrMnFeNiH_6$ high-entropy hydride constructed by first-principles calculations [1758]. (b) Hydrogen storage pressure-composition isotherms at room temperature for TiZrCrMnFeNi showing reversible hydrogen storage [1755]. (c) MTT cell viability assay (biocompatibility) and microhardness of TiAlFeCoNi alloy before and after HPT processing compared to titanium and Ti-6Al-7 Nb biomaterials [1356]. (d) Photocurrent generation of $TiZrHfNbTaO_{11}$ versus time [324]. (e) Photocatalytic hydrogen production rate of $TiZrHfNbTaO_6N_3$ versus time compared to convention oxynitride Ga_6ZnON_6 [326]. (f) High-resolution TEM image of $TiZrHfNbTaO_6N_3$ containing nanograins of two phases [326].

materials science [1763–1765]. They are usually obtained as thin ribbons by the rapid quenching from the melt at typical cooling rates of about 10^6 K/s [1763] or in the form of bulk metallic glass (BMG) in the shape of cylinders with diameters of up to several centimeters at lower cooling rates of about 10^2 K/s [1764]. Deformation of amorphous alloys occurs through the formation and propagation of shear bands with a small thickness ($\sim$10 nm). Such behavior leads to extremely low tensile ductility; however, amorphous alloys exhibit some ductility in bending and compression tests. It is possible to improve the ductility of amorphous alloys by increasing the so-called free volume and by creating heterogeneities in the amorphous phase [1765]. A promising way to introduce high strain and therefore, to transform the structure of the glassy metals is the use of SPD through the HPT process [1766]. There are many research groups actively involved in studying the effect of HPT treatment on amorphous alloys and a few reviews were published as well [1087, 1767]. The results obtained can be summarized as follows.

HPT allows the consolidation of amorphous rapid-quenched ribbons and powders into monolithic samples [1768–1770]. The structural changes in amorphous alloys during HPT are determined by their chemical composition. For instance, HPT treatment of Al-rich [1770], Fe-rich [529] and Nd-Fe-B alloys [1771] leads to nanocrystallization in the amorphous phase. In the $Ti_{50}Ni_{25}Cu_{25}$ rapid-quenched alloy TiNi nanocrystals of the B2 phase precipitate in the amorphous phase [1771, 1772]. An attempt to analyze these processes has been reported in [1767, 1773]. In amorphous alloys without a significant excess of the basic element in the composition, for example, in Zr-based BMG, nanocrystallization by HPT is not observed in most cases, but HPT leads to an increase in the free volume and the enthalpy of the amorphous phase (Fig. 85a) [1772, 1774, 1775]. In some cases, a cluster-type structure was formed, which is associated with the chemical separation in the amorphous phase as a result of HPT processing [1776, 1777]. Chemical separation along the shear band in HPT-treated Zr-based amorphous alloy was unveiled by advanced microscopy methods [1778].

Properties of amorphous alloys change significantly by HPT processing, in particular, the microhardness decreases (Fig. 85b) [1774,
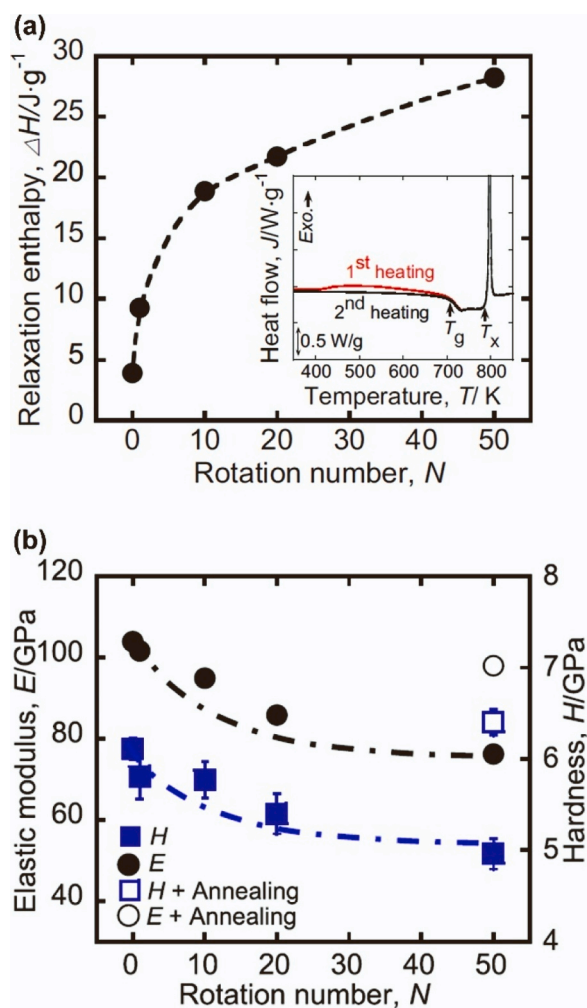
Fig. 85. (a) Structural relaxation enthalpy and (b) elastic modulus (*E*) and hardness (*H*) values as a function of HPT rotation number. The inset in (a) shows differential scanning calorimetry curves of the sample processed with 50 HPT turns, where red and black lines denote the 1st and 2nd heating curves, respectively, and T_g and T_x denote the glass transition temperature and crystallization temperature, respectively. The open symbols in (b) denote the data after annealing at 673 K for 1 h [1774].

[1779] and its distribution over the sample becomes less uniform [1780]. Serrations on the nanoindentation curves of the HPT-processed BMG are not observed unlike for as-cast BMG, and this can be explained by more homogeneous deformation in the former case due to an increase in amorphous phase structure heterogeneity [1775]. HPT leads to a significant 2.5-fold increase in the strain rate sensitivity parameter from 0.014 to 0.036, while the elastic modulus decreases slightly, from 90 to 85 GPa [1775]. Indents analysis suggests that HPT can lead to an increase in the amorphous alloy microplasticity [1781] and improvement of ductility [1782, 1783].

The structural transformation in amorphous alloys by HPT processing is the result of an extremely high density of shear bands propagating through the amorphous matrix. TEM data show that the spacings between shear bands reach 30 nm after HPT processing [1766]. The spacings between shear bands in Zr-based BMG after HPT for 5 turns can vary from 500 nm at the center of the sample to 100 nm at the edge [1784]. Nanohardness measurements across shear bands in the deformed amorphous alloy show noticeable softening on the distances of about tens of microns due to free volume increase [1785]. This means that with the shear band density observed after HPT processing (Figs. 86a and 86b [1786]), the entire amorphous material undergoes

transformations [1787, 1788], despite some possible slippage between anvils and a processed specimen that can occur during HPT of hard BMGs [1784, 1789]. A model has been proposed to explain the strain accumulation in an HPT-processed specimen with an account for slippage [1789]. Furthermore, the accumulative HPT procedure has been implemented for processing BMGs and hard alloys [59, 1790]. It has been shown that a Zr-based amorphous alloy undergoes a more pronounced structural transformation after accumulative HPT as compared to a conventional one. Taken together, SPD provides new opportunities to understand the plastic behavior of brittle amorphous materials. Such understanding can eventually contribute to the design of amorphous materials with improved plasticity and new functionalities.

7.8. Semiconductors

Semiconductors are one of the major components used in the 21st century and silicon is one of the most important semiconductor materials for modern electronic devices [1791]. However, bulk crystalline silicon is not suitable for optical and optoelectronic applications due to its indirect bandgap of 1.1 eV. The well-known way to overcome this limitation is the use of nanostructured silicon, which exhibits photoluminescence in the visible light region associated with the quantum confinement effect [1792]. Recently, allotropes of silicon have been of interest for future electronic devices because they have different electronic structures [1793]. Among several silicon allotropes, metastable phases can be obtained by phase transformation from high-pressure phases. When high pressure is applied to silicon crystals, diamond-cubic Si-I transforms to metallic Si-II with β-Sn structure at about 11 GPa, and then it further transforms to orthorhombic Si-XI (~14 GPa) and simple-hexagonal Si-V (~16 GPa) [1794]. Upon pressure release, Si-II transforms to metastable phases such as rhombohedral Si-XII and BCC Si-III [1795]. These metastable phases can be obtained by high-pressure cells [1795, 1796] and indentation experiments [1797–1799]. However, it is difficult to obtain the bulk samples by these methods. SPD processing of semiconductor materials has attracted attention for altering optical and electrical properties because grain refinement and phase transformation are expected to occur simultaneously. Among several SPD techniques, HPT is suitable for processing brittle semiconductor materials due to constraining in the cavity of anvils. Recently, large-scale samples (> 10 mm in diameter) could be processed by HPT [179]. The first HPT processing of semiconductors was reported by Bridgeman [20] and further investigated by several researchers for silicon [1180, 1183] and germanium [1181, 1182]. HPT processing of semiconductors such as silicon [1184, 1800–1805], germanium [1185, 1806, 1807] and GaAs [1808] were conducted in recent years and the main findings were summarized in some overview articles [512, 1809]. The functional properties of some HPT-processed semiconductors such as silicon [1810, 1811] and $Si_{0.5}Ge_{0.5}$ alloy [1812] were also reported recently.

Fig. 87a shows the XRD profiles of the silicon samples after HPT processing at a nominal pressure of 6 GPa. The XRD profiles consist of Si-III/Si-XII as well as Si-I. The diffraction peak intensities of Si-III/Si-XII increase with increasing the number of anvil rotations. The volume fractions of Si-III and Si-XII after 100 HPT turns are > 0.3 and ~0.2, respectively. The formation of Si-III/Si-XII indicates the strain-induced phase transformation from Si-I to Si-II during HPT processing and phase transformation from Si-II to Si-III/XII during pressure release [8, 1813]. The HPT processing also affects the electrical, optical and thermal properties. The resistivity of the silicon samples (20 Ω·cm) decreases to 0.7 Ω·cm after HPT processing for 100 turns due to the formation of Si-III having a semi-metallic property [1814] with a narrow gap (30 meV) [1815]. A weak broad photoluminescence peak associated with Si-I nanograins appeared in the visible light region after annealing. The thermal conductivity of bulk silicon (~140 W m^{-1} K^{-1}) was reduced to ~3 W m^{-1} K^{-1} after HPT processing for $N \geq 50$ [1810]. To investigate the phase transformation of the metastable phases in
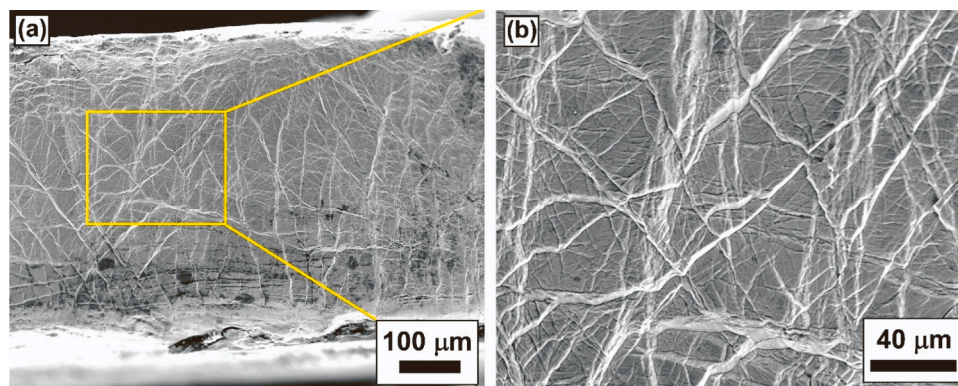
Fig. 86. (a,b) SEM images showing shear bands in a $Zr_{52.5}Cu_{17.9}Ni_{14.6}Al_{10}Ti_5$ metallic glass processed by HPT with 5 rotations, where (b) is a magnified view indicating formation of interacting shear band networks with increaseing strain [1786].

HPT-processed silicon, synchrotron XRD measurements were also performed [1811]. The silicon sample was subjected to HPT processing at a nominal pressure of 24 GPa for 10 turns, and then cut into ~1 mm strips for the XRD measurements. The XRD profiles during annealing showed that the diffraction peaks of Si-III/Si-XII were almost constant up to

Fig. 87. XRD profiles of (a) silicon processed by HPT for different rotations (N) [1810] and (b) $Si_{0.5}Ge_{0.5}$ processed by pure compression (N = 0) and N = 10 turns of HPT [1812].

433 K, and these peaks gradually decreased at 453 K. New diffraction peaks corresponding to hexagonal-diamond Si-IV appeared at 463 K. At 473 K, the Si-IV and Si-I diffraction peaks appeared and Si-III/Si-XII peaks disappeared. These results on the phase transformation of Si-IV from Si-III during annealing indicate that the combination of HPT processing and annealing is effective in obtaining new metastable phases. [1797, 1816, 1817]. It should be noted that Si-IV has been predicted to be a semiconductor having a bandgap of 0.95 eV [1814].

Fig. 87b shows XRD profiles of HPT-processed $Si_{0.5}Ge_{0.5}$ after pure compression and HPT processing for 10 turns. The diffraction peaks correspond to a diamond-cubic phase for the sample without rotation. Additional peaks corresponding to a bc8 phase appear after 10 HPT turns. The formation of bc8-$Si_{0.5}Ge_{0.5}$ is consistent with the high-pressure experiments at high temperatures [1818]. The lattice constant of bc8-$Si_{0.5}Ge_{0.5}$ is 0.678 nm, which is in good agreement with the value found from Vegard's law comprising 0.6784 nm. The electrical resistivity increased from ~9×10^{-3} $\Omega \cdot$cm to ~5×10^{-2} $\Omega \cdot$cm after compression and decreased slightly to ~3×10^{-2} Ω cm after 10 turns of HPT. The decrease in resistivity after HPT is similar to that observed in HPT processing of silicon [1803, 1810], suggesting that bc8-$Si_{0.5}Ge_{0.5}$ has a semi-metallic property [1812].

SPD processing of silicon and related semiconductors appears a promising method to achieve novel functional properties through nanograin refinement and the formation of metastable phases [1456]. Considering the current global crisis concerning semiconductors, such studies deserve to receive higher attention in the SPD field.

7.9. Ceramics

Plastic deformation of ceramics (including oxides, carbides, nitrides, *etc.*) is quite difficult under ambient conditions due to their hard and brittle nature. There have been long-term efforts to process these materials by plastic deformation, particularly because of the importance of this issue in geological studies [1819]. The first success in processing these materials by SPD was reported in 1935 when Bridgman recognized high pressure as the key to the plastic deformation of ceramics [20, 1820]. The introduction of HPT and its use for processing ceramics led to similar studies in the last century by other scientists mainly in the fields of geology [1821–1823] and physics [1824–1827]. The combination of HPT [20] with diamond anvil cells [1828] and the introduction of shear (rotational) diamond anvil cells in the 1980 s [1829, 1830] improved the research in this field because of increasing the level of processing pressure and the possibility of *in situ* examinations [8, 366]. Although high-energy ball milling can also introduce deformation in ceramics, pure plastic deformation can be hardly achieved in ceramics by ball milling due to the limited applied pressure [43]. Following a publication in 2010 [1179], which attempted to consolidate ceramic powders by HPT, SPD processing of ceramics to achieve functional properties

became more popular [513]. As discussed earlier in this manuscript, a wide range of ceramics were processed by HPT to achieve various properties including, high hardness [1179], electrocatalysis [960], photocatalysis [844], photoluminescence [583], photovoltaics [665], dielectric properties [840] and ion conductivity for batteries [1831]. The functional properties of ceramics were reviewed in previous chapters, but it is worth discussing the structural and microstructural evolution of ceramics compared to metals during SPD because there is limited information on this issue.

Phase transformations occur frequently in ceramics, and it was shown that the fraction of both pressure-induced and strain-induced phases increases with increasing strain in ceramics, mainly because of the defect-pressure-strain interactions [1829, 1830]. Fig. 88a shows the phase transformation from the γ phase to the α phase in Al_2O_3 induced by the application of HPT [16]. Moreover, SPD processing has led to the discovery of new hidden or intermediate phases in ceramics [630, 631, 1004]. The structural and phase evolutions in ceramics are principally similar to those in metals and the acceleration of phase transformations by increasing strain during SPD processing of metallic materials was also reported [506, 507].

There are similarities between the microstructural evolution of ceramics and metals, but grain refinement in ceramics is more significant compared to metallic materials [513]. In metallic materials, grain sizes are usually at the submicrometer level [2, 3], except for some dual-phase materials, composites, HEAs and intermetallics [38, 290, 922]; however, grain sizes in SPD-processed ceramics always decrease to the nanometer level (see Fig. 88b for grain sizes in SiO_2 [609]). The reason for smaller grain sizes in ceramics, which usually have a high melting point, is due to their ionic or covalent atomic bondings which make the motion of dislocations and grain boundaries harder than in metals [1832]. Similar to metallic materials, it was shown that dislocations are frequently generated in ceramics, especially at the early stages of straining (see Fig. 88c for a Lomer-Cottrell dislocation lock in TiO_2 [1002]). However, unlike metals in which dislocations cannot stay in nanograins and annihilate at grain boundaries [1833], dislocations can be observed within the grains of nanoceramics due to their slow movement resulting from the strong atomic bonding and high Peierls stress [1832]. Another issue that can be mentioned here is that similar to reports on metallic materials [38], there is a steady state for grain size due to the occurrence of dynamic recrystallization and grain boundary migration in ceramics [513]. When a ceramic with grain sizes smaller than the steady-state grain size is processed by SPD, a grain coarsening rather than a grain refinement occurs (see Fig. 88d for grain coarsening in Al_2O_3 processed by HPT [1831]). Similar grain coarsening was reported during HPT processing of nanograined metals such as copper and nickel [38, 1834]. Finally, it should be noted that the formation of vacancies is also a general phenomenon in HPT-processed ceramics. For example, Fig. 88e shows the formation of vacancies in the TiO_2-ZnO composite confirmed by electron spin resonance spectroscopy [605] and Fig. 88f shows the formation of oxygen vacancies in the high-pressure columbite phase of TiO_2 simulated by the first-principles calculations [1002]. Such vacancies, which were frequently reported in SPD-processed metals [306, 1835, 1836], are responsible for various functionalities of ceramics [513]. Taken together, there are clear similarities between the behavior of metals and ceramics during SPD, but deeper *in situ* studies using XRD and *ex situ* studies using electron microscopy are needed to clarify the mechanisms underlying microstructural evolutions in ceramics.

7.10. Polymers

SPD treatments can significantly affect the structure and properties of polymers. The structural states formed during SPD treatment are characterized by a variety of possible modes of molecular orientation, crystalline lamellar and interlamellar amorphous phase arrangement, degree of macromolecular chain orientation and intermolecular interaction. A distinctive feature of SPD methods compared to conventional polymer processing methods (extrusion, injection molding, forging) is the introduction of uniform, simple shear into the materials, which promotes homogeneous structure and property development throughout the extruded billet and prevents the formation of undesirable so-called skin-core morphology, a reduction in the cross-sectional area of the workpiece, *etc.* Studies have shown that the structural states of polymeric materials formed by SPD and, thus, their physical and mechanical properties, are mainly determined by the magnitude of the accumulated strain. Activation of phase and structural transitions [1837–1840], strain-induced diffusion [1841], and intercalation and exfoliation of organic and inorganic fillers [1842–1844] can occur in polymers at different absolute values of accumulated strain. These changes depend on both SPD parameters (pressure, temperature, intensity and strain rate) and the structure of polymers (amorphous or semi-crystalline; linear, branched, cross-linked, *etc.*). SPD is most commonly performed on polymers by two methods: ECAP [226] and equal-channel multi-angle extrusion (ECMAE) [64]. Most studies on ECAP of polymers were limited to the case of 1–2 strain cycles, corresponding to a true strain of 0.8–2.4 (depending on the channel intersection angle). In contrast, ECMAE was used to reach a higher range of strain (6.7–9.1).

For polymers processed at low values of true strain (0.8–2.4), the increase in their elastic modulus and the decrease in tensile strength and plastic properties with increasing strain are typical [65, 1845–1854]. At the same time, the melting temperature and heat distortion temperature decrease (Table 7). The structure rearrangement in this range of true strains is mainly caused by the processes of molecular orientation and amorphization. The behavior of polymer materials processed in the range of high values of true strain (6.7–9.1) is fundamentally different from that of polymer materials deformed at low values of accumulated strain. At high strain levels, there is an increase in both stiffness and strength [64, 1855–1858]. At the same time, the melting temperature, heat distortion temperature and glass transition temperature increase (Table 7) [1859, 1860]. In semi-crystalline polymers, the amorphization process is replaced by the dynamic recrystallization process (strain-induced crystallization) in this range of strain. The accumulation of large values of strain causes the formation of a larger fraction of the crystalline phase in the deformed polymers. With increasing strain, the conformational transitions in semi-crystalline and amorphous polymers proceed more intensively. As a result, the fraction of oriented polymeric macromolecules, their packing density, and the degree of their orientation increase. This contributes to an additional increase in the stiffness and strength of the deformed polymers [1857]. Fig. 89 shows an example of the dependence of tensile strength and strain at break on accumulated strain for high-density polyethylene subjected to ECMAE.

In polymers capable of polymorphic transformations, activation of phase transitions is observed in high strain levels. As a result of SPD treatment, such polymers have different properties than undeformed polymers or polymers treated with low strain values. For example, an increase in the proportion of the more ductile γ phase due to the α→γ transition in polypropylene and polyamide-6 contributed to an increase in their ductility [1838, 1839], and the transition from the α phase to the β phase in polyvinylidene fluoride manifested the piezoelectric effect [1862]. Several semi-crystalline polymers, such as high-density polyethylene, polyoxymethylene and polytetrafluoroethylene, are characterized by an extremely low coefficient of linear thermal expansion values after SPD with strains of 8.5–9.1, which are close to the values of the coefficient of thermal expansion of invar alloys (Table 7) [1863]. The invar effect is achieved by forming a crystal structure in deformed polymers with a high degree of continuity, an extremely high degree of molecular orientation and a strain-induced degree of crystallization. Polymers deformed to high values of true strain (6.7–9.1) exhibit significant molecular orientation. Varying the deformation route results in different patterns of molecular orientation, in particular a biaxial molecular orientation [1857, 1858]. The latter provides a low anisotropy of elasticity and strength properties and a unique opportunity to improve the plastic properties of deformed polymers (Table 7).
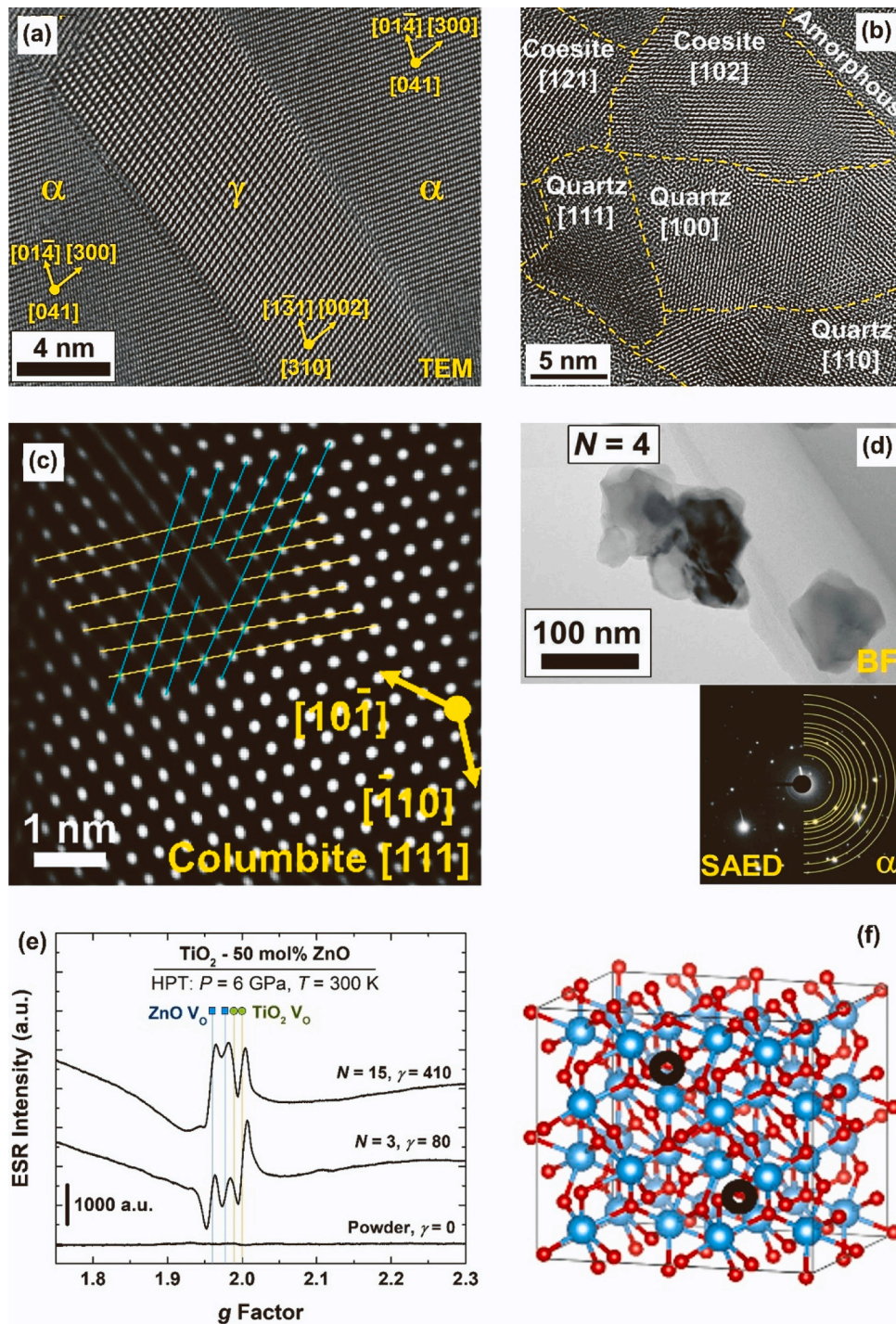
Fig. 88. (a) TEM high-resolution image showing the $\gamma \rightarrow \alpha$ phase transformation in Al_2O_3 by HPT processing for 4 turns at 723 K [16]. (b) TEM High-resolution image showing the formation of nanograins in SiO_2 by HPT processing for 5 turns at 723 K [609]. (c) TEM lattice image of a Lomer-Cottrell dislocation lock formed in TiO_2 by HPT processing for 15 turns at room temperature [1002]. (d) TEM bright-field image (top) and selected area electron diffraction pattern (down), showing grain coarsening from 10 nm to the submicrometer level in Al_2O_3 by HPT processing for 4 turns at 723 K [16]. (e) Electron spin resonance spectra of TiO_2-ZnO composite before and HPT processing for 3 and 5 turns at room temperature, showing the formation of oxygen vacancies in TiO_2 and ZnO [605]. (f) Oxygen vacancies simulated by density functional theory for high-pressure columbite phase of TiO_2 stabilized by HPT processing [1002].

SPD can be also applied to polymer-based composites as well as for the consolidation of polymer powders. SPD-treated polymer composites are characterized by increased physical and mechanical characteristics compared to untreated composites [1842, 1861, 1864, 1865]. Their feature is that an increase in the concentration of the filler does not lead to a decrease in the degree of its dispersion. With an increase in the accumulated plastic deformation, the improvement in the dispersion of

the filler becomes more pronounced (Fig. 90a-f). This fact is because high pressure neutralizes the effect of an increase in melt viscosity with an increase in filler concentration, which hinders the movement of fillers inside the matrix and prevents their dispersion; however, plastic deformation promotes effective exfoliation of filler particles without damage to the polymer matrix. Such a mechanism of filler dispersion leads to an improvement in the physical properties of polymer

Table 7

Effects of accumulated true strain during SPD on physical and mechanical properties of polymers (e: true strain, E: elastic modulus, σ_y - yield strength, ε_b: strain at break, T_m: melting temperature, T_g: glass transition temperature, R: electrical resistance, CLTE: coefficient of linear thermal expansion). The index 0 denotes the corresponding parameters of undeformed polymers [1844, 1861].

Polymer	e	E/E_0	σ_y/σ_{y0}	$\varepsilon_b/\varepsilon_{b0}$	T_m or T_g^*, K	CLTE$\times 10^6$, K^{-1}	R_0/R
High-Density polyethylene	2.18.5	1.703.30	1.403.00	0.930.92	398410	210–7	–
Polyoxymethylene	2.18.5	1.382.28	2.074.04	0.780.94	439443	130–5	–
Polytetrafluoroethylene	2.18.5	1.282.33	1.322.23	1.603.10	–	220–6	–
Polyamide 6	2.18.5	1.292.15	1.612.04	0.870.91	495500	–	–
Poly(methyl methacrylate)	2.18.5	1.191.23	1.101.30	1.501.60	390405	–	–
Linear Low-Density Polyethylene – 10 wt% Carbon Nanotubes	2.18.5	1.201.50	1.221.31	1.501.61	397402	150–6	2416
Cellulose	1.2	1.55	-	-	411	-	-
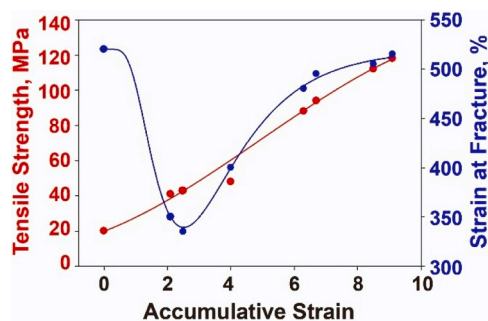
Fig. 89. Influence of the value of accumulated strain on tensile strength and strain at break of high-density polyethylene exposed to ECMAE [1857].

composites. For example, electrical conductivity can be enhanced without a deterioration in mechanical properties with the introduction of conductive nanofillers (carbon nanotubes, carbon nanoplates) into polymers (Table 7) [1844, 1861]. The SPD-consolidated polymer powders (nylon 12, ultra-high molecular weight polyethylene, starch, wood flour, maple hardwood) materials exhibit significantly higher hardness and stiffness compared to reference materials produced by injection molding [1841, 1866–1869]. Strain-induced diffusion, which occurs in this case eliminates the need for the addition of a plasticizer or a binder. Figs. 90g and 90h show SEM images of polypropylene before and after strain-induced consolidation.

In summary, SPD has a high potential to significantly improve the mechanical properties of polymers and achieve new functionalities. The published studies show that SPD-processed polymer materials are characterized by unique physical and mechanical properties that cannot be achieved by other methods, such as (i) an increase in stiffness and strength while maintaining ductility at the level of the original material for semi-crystalline polymers, amorphous polymers and polymer powders, (ii) low coefficient of linear thermal expansion for semi-crystalline polymers and composites, (iii) increased electrical conductivity and strength in the case of polymer composites containing an electrically conductive nanofiller.

8. Heterostructured materials processed by SPD

Heterostructured materials are defined as materials composed of at least two different zones with a large difference in mechanical or physical properties [1870]. For structural heterostructured materials, the disparities can be given by coexisting zones with different order scales, defects densities, crystal structure, chemical composition, or crystallographic orientation [1870]. For multidisciplinary heterostructured materials, the disparities may include electrochemical potential, magnetic sensitivity, optical properties, *etc.* [44]. SPD processing, including bulk-SPD, surface-SPD and powder-SPD, is one solution to produce heterostructured materials. In the following section, after reviewing the fundamentals and properties of heterostructured materials, the features of two kinds of popular heterostructured materials, namely harmonic-structured materials and gradient-structured

materials, are discussed.

8.1. Fundamentals and properties of heterostructured materials

Heterostructured materials are a fast-emerging field that offers a novel solution to various issues in materials science. Increasing both the strength and the strain hardening to avoid the "inevitable" strength-ductility trade-off is one of the most studied issues. Hetero-deformation-induced strengthening and work hardening [1870] by GNDs [1871] serve as the foundation for structural heterostructured materials. The hetero-deformation-induced stress, formerly known as back stress [1872] can be measured by uniaxial loading experiments [1873, 1874]. The hetero-deformation-induced stress accounts for the contribution of both forward stress and back stress [1870]. Back stress cannot be measured from the mechanical testing curves because it cannot be decoupled from the forward stress.
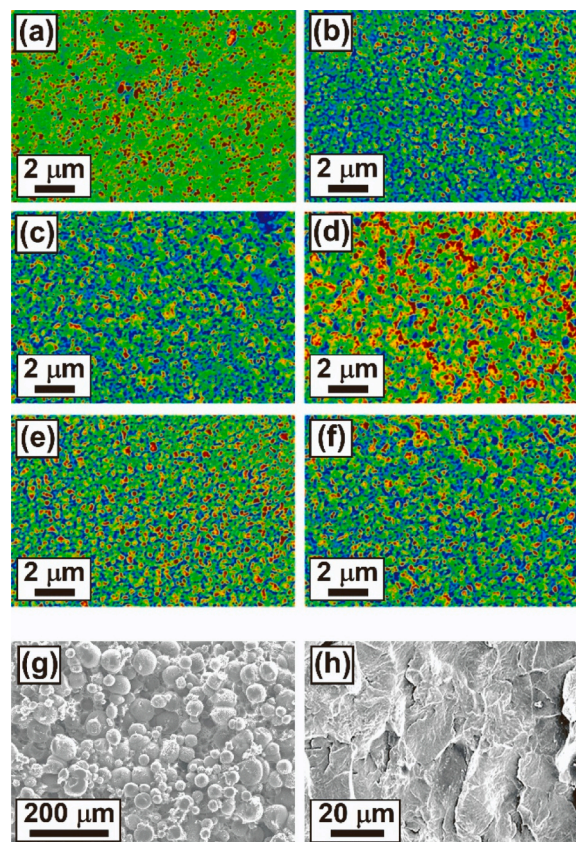
Fig. 90. (a-f): SEM micrographs of nanocomposites of LLDPE polymer with (a-c) 10 wt% of carbon nanotubes and (d-f) 20 wt% of carbon nanotube addition, after true strains of (a,d) $e = 0$, (b,e) $e = 4.4$, (c,f) $e = 8.5$ [1861]. (g,h) Morphologies of compacted polypropylene powders after strains of (g) $e = 0$ and (h) $e = 8.5$ [1841].

The outstanding mechanical properties of heterostructured materials come from the interactive coupling between soft and hard zones (Fig. 91a) [1875]. The differences in flow stress cause a strain gradient between the soft/hard interface and the Frank-Read dislocation source (Fig. 91b) [1875]. To accommodate the strain mismatch near the interfaces, known as zone boundaries in heterostructured materials, GNDs are generated from Frank-Read sources in the soft zone. As a result, hard zones remain elastic while soft zones begin to deform plastically (Fig. 91c) before global yielding. Both soft and hard regions remain under mutual constraints. GNDs pile up against zone boundaries as applied stress increases, causing back stress in soft zones [1870, 1873]. To avoid cross-slip to encourage GND pileup, planar slip promoted by low stacking fault energy or short-range order is desired [1876]. The back stress acts against the dislocation source to curtail the emission of more dislocations [1877]. Simultaneously, the stress exerted by the head of the GND pileup produces forward stress in hard zones [1875, 1878, 1879]. The creation and interaction of GNDs near the zone boundaries will produce a hetero-boundary-affected region [1880]. The back stress strengthens soft zones, while the forward stress makes hard zones easier to deform [44]. As a result, the soft zones sustain larger deformations, while the hard zones act as obstacles to dislocation gliding. Therefore, the heterostructured materials possess higher strain-hardening and strengthening than those obtained in homogeneous nanostructures or coarse materials [1881]. The hetero-deformation-induced strengthening is usually negligibly small in homogeneous materials and not considered in most classical models, such as the rule of mixtures. As a result, the yield strength and strain hardening of heterostructured materials exceed those predicted by the rule of mixtures [1882]. The hetero-deformation-induced strengthening is dominant in heterostructured materials, and their properties come from the synergy of multiple strengthening mechanisms given by microstructural defects, *e. g.* zone boundaries, twins, shear bands, stacking faults, *etc.* [1883–1885].

The main factors to consider during the designing of heterostructured materials can be divided into intrinsic and extrinsic (Fig. 92) [1886]. The former is material-specific and includes crystal structure, crystallographic texture, and those influencing the slip mode, such as stacking fault energy, short-range order, atomic size mismatch and shear modulus. The main extrinsic or processing parameters are stress state, equivalent strain, strain rate, temperature, time and pressure. Intrinsic parameters guide material selection while extrinsic parameters dictate the thermo-mechanical route selection. A description of each effect has been described in detail elsewhere [1886]. The elaboration of heterostructured materials has to be optimized based on their classification: (i) multimodal structures that can be produced by SPD techniques, SPD plus heat treatments, or powder metallurgy, (ii) gradient structure by surface nanostructuring techniques, (iii) harmonic structure by powder metallurgy, powder metallurgy plus heat treatments and additive manufacturing, (iv) heterogeneous lamella structure by cold working (including SPD) plus partial recrystallization annealing, (v) layered
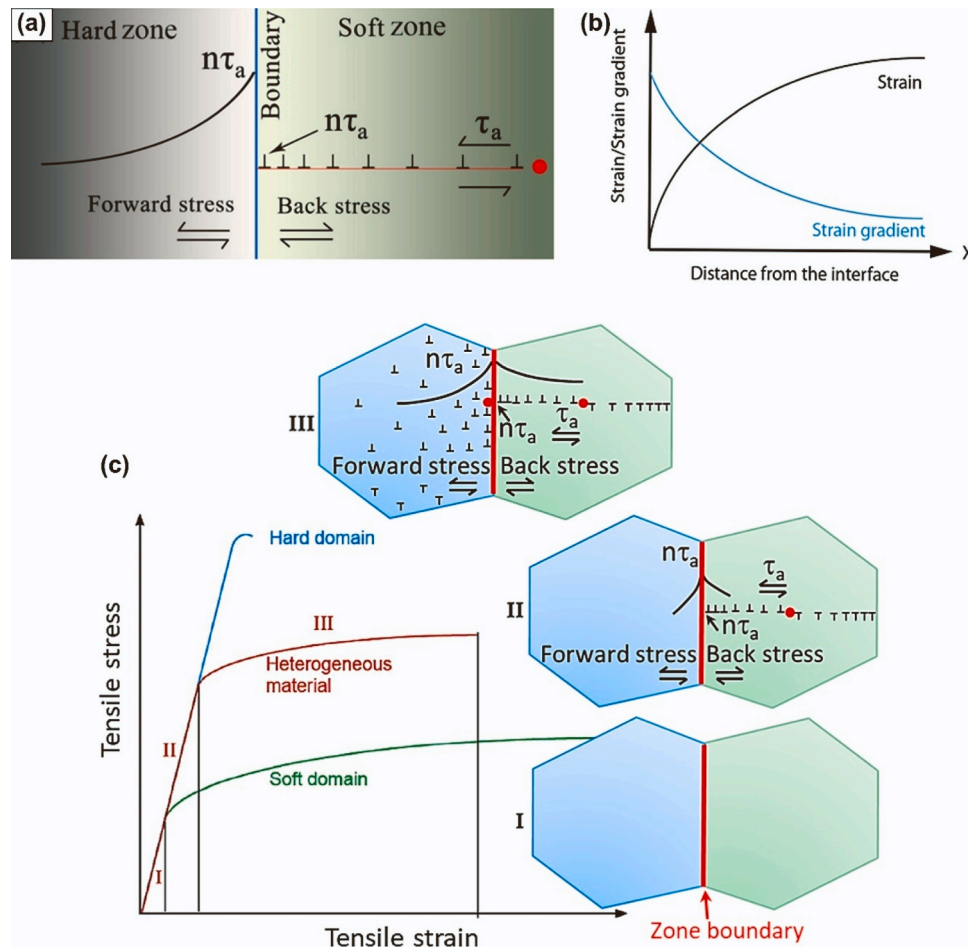
Fig. 91. Fundamental of heterostructured materials. (a) Generation and distribution of long-range back and forward stress by geometrically necessary dislocation (GND) pileups near the zone boundary, including generation of GND pileups from a Frank-Read source that produces hetero-deformation induced (HDI) stress. The curve on the left of the boundary is the distribution of forward stress. (b) Distribution of strain gradient with the distance from the zone boundary. (c) Deformation stages (I, II and III) and their effect on dislocation behavior and HDI stress distribution near a zone boundary (τ_a is the applied shear stress and red circles represent the dislocation source) [44, 1292, 1870].

structure by rolling-based processing, physical or chemical surface deposition, or additive manufacturing, and (vi) multiphase structure by heat treatments, cold working (including SPD), powder metallurgy and additive manufacturing [1887].

Among the key advantages of heterostructured materials is their ability to produce unique property combinations that are not present in their individual zones. So far, the most widely explored combinations are improved mechanical performance with multidisciplinary properties [1292, 1887]. However, other non-structural multidisciplinary materials can also be designed. Heterostructured materials are highly desirable for a wide range of applications, including structural, biomedical [1888–1890], biosafety [1891, 1892], optoelectronics [1893, 1894], energy storage [1895, 1896], catalysis [1891, 1897], photo-electrochemistry [1898], food processing [1890], *etc.* These advances in the development of heterostructured materials contribute to the ongoing efforts to achieve sustainable energy solutions and more efficient multidisciplinary components. More detailed descriptions of fundamentals, properties and perspectives of heterostructured materials can be found in recent literature [44, 1292, 1875, 1899, 1900], including one overview of SPD-processed heterostructured materials [1886].

8.2. Harmonic-structured materials

Powder metallurgy is a widely used technique for producing metallic and ceramic bulk materials by sintering below the melting temperature [1901–1903]. It is easy to produce high melting point materials by powder metallurgy because there is no need to melt materials. In addition, powder metallurgy is suitable for hard-to-deform materials because it is die-forming and does not require cutting or bending. This section introduces harmonic structure design [1904] as a new family of heterostructured materials that can be manufactured by powder-SPD combined with powder metallurgy.

As mentioned earlier in this article, high-energy ball milling is a useful SPD technique for processing powders [43, 153, 1905, 1906]. In ball milling, plastic strain is introduced in powders by rotating, shaking or jetting gases in a closed vessel, and the powder collides with each other or with process media balls. In a single collision, the deformation energy of the powder is quite small, but with repeated collisions in a closed vessel, the deformation energy is accumulated in the powder. For example, in the case of planetary ball milling, Umemoto *et al.* [1907] predicted that in a single collision, the energy imparted to the powder is less than 1 mJ, the equivalent plastic strain is about 1, the increasing temperature is a maximum of 300 K, the collision time is 10^{-5} s, and the strain rate is as high as 10^4 s^{-1}. Therefore, quite a large equivalent

plastic strain and UFG powder formation could be expected by long-time ball milling [1907, 1908]. The ball milling method can also produce powders with heterogeneous grains by applying different levels of strain to the interior and surface of the powder depending on the processing conditions and the size of the powder. Harmonic structure design takes advantage of the inhomogeneity between the interior and surface of the powder [1908].

The harmonic structure is a type of heterogeneous and bimodal grain size microstructure consisting of a three-dimensional UFG network (Shell) surrounding the coarse-grained clusters (Core), as shown in Fig. 93a. Fig. 93b shows a cross-sectional SEM image of a pure titanium powder processed by high-pressure argon gas jet-milling [153], and Fig. 93c shows a TEM image and a selected area diffraction pattern from the TEM image taken from the near-surface region (such as the white square region) shown in Fig. 93b. An equiaxed grain structure with a grain size in the range of 5 µm to 10 µm was observed in the as-received powder, although after high-pressure gas milling, the grain size in the near-surface region became less than 100 nm. A ring-like pattern of the selected area diffraction pattern indicates the existence of high-angle boundaries in the HCP structure. The formation of such nanograins with high-angle boundary structures was attributed to the grain subdivision that occurs in various bulk SPD methods, such as HPT [330, 1909–1911] and ARB [1912–1915]. The ball-milled powder can be consolidated into any shape by powder metallurgy sintering.

The harmonic structure can be introduced to all metallic materials and is expected to combine high strength and high ductility. Compared to the conventional bimodal structure with irregular coarse-grained and UFG distribution, the harmonic structure has a network of UFG structures at the macro scale. The isotopically developed UFG network can provide additional hetero-deformation-induced strengthening in multiple directions during tensile deformation [1870, 1917–1922]. Therefore, it is noteworthy that the harmonic-structured materials do not have anisotropic mechanical properties. In addition, the enhanced strain hardening and suppressed local deformation by the network structure can achieve a good combination of strength and ductility [1904]. The effect of stress partitioning on the UFG network structure during deformation, which is one of the most unique features of harmonic-structured materials, leads to hetero-deformation-induced strengthening, resulting in a synergy of micro- and macro-scale mechanical properties of the materials [1923–1926]. Fig. 93d shows the strength and toughness values of the harmonic-structured materials normalized by the values of the homogeneous coarse-grained structure [153]. All metallic materials show improvement in strength and toughness including titanium [1927–1930], copper [1931, 1932], nickel
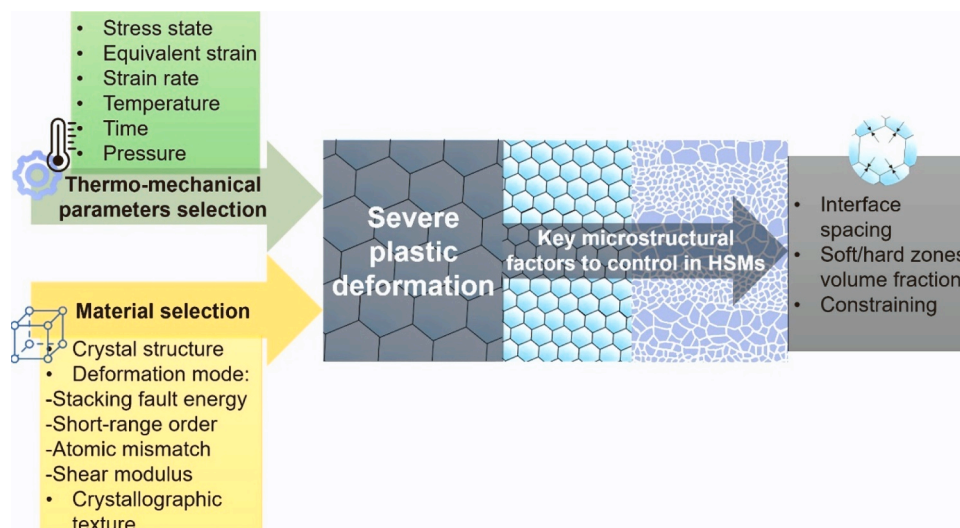
Fig. 92. Main intrinsic and extrinsic parameters to select starting materials and processing routes during the design of heterostructured materials [1886].

[1933, 1934], stainless steel [1916, 1935], and Co-Cr-Mo alloys [1936]. This result suggests that harmonic structure design can be a universal, material-independent design guideline for improving mechanical properties [1876, 1937].

This section, thus, describes harmonic-structured materials as a new family of heterostructured materials with high strength and high ductility which can be produced by the powder-SPD process. Innovative mechanical properties in these materials are achieved through macroscopic periodicity and microscopic heterogeneous microstructures. The harmonic-structured materials not only show improvement in tensile properties but also in fatigue or wear properties [1938–1940]. It is expected that further research will reveal more possibilities for harmonic-structured materials in industrial fields, not only for their mechanical properties but also for their potential functional properties.

8.3. Gradient-structured materials

Gradient-structured materials can be defined as materials with dramatic heterogeneity in strength from one zone area to another [1941]. The gradient-structured materials are classified as a category of heterostructured materials, and thus, the relevant theories of heterostructured materials can be reasonably used to study gradient-structured materials [1942]. Production of gradient-structured materials is currently feasible with various surface-SPD methods developed in recent decades [1941, 1942]. In the following sections, the fundamentals, mechanical properties and functional properties of gradient-structured materials are discussed.

8.3.1. Fundamentals of gradient-structured materials

The application of gradient structures in metal materials could be traced back to the carburizing and nitriding process, but the gradient structure material was not defined at that time. Until now, compositionally graded structures have also played an important role in

structural materials [1943]. Grain size and twinning gradients generated during tensile tests were frequently used in the past [1944–1948]. The relationship between gradient structure and hardness has been shown in Fig. 94 [1949]. Generally, the hardness of the gradient structure gradually decreases from the surface to the core, which has a certain corresponding relationship with the grain size. At present, research on structures such as defect gradient [1950], phase distribution gradient [1951] and texture gradient [1952–1954] is reported. By regulating the gradient structure, materials with excellent strength and ductility are obtained. The microscopic schematic diagram of various gradient structures is shown in Fig. 95 [1955]. Simulations and experiments confirmed that gradient-structured materials have synergistic effects by interactions between the gradient layer and the coarse-grained layer [1882, 1956–1962]. The traditional strengthening mechanism cannot fully explain the superior combination of strength and ductility of gradient-structured materials, and thus, research on their strengthening mechanism remains open for in-depth exploration.

The excellent properties of gradient-structured materials are attributed to the combined action of multiple strengthening theories [1955]. The theory of dislocation and twin strengthening is a common explanation for the good properties of gradient-structured materials. Increasing dislocation density increases the strength, while the pileup of dislocations generally leads to a significant decrease in the ductility of materials. Twins are believed to contribute to dislocation slip and coordinate deformation while increasing strength and improving the ductility of materials [1881, 1941, 1942]. The Zener-Holloman parameter (Z) has been used to express the effect of deformation on microstructure and mechanical properties as shown in Equation 36 [1963].

$$\text{Ln}Z = \text{Ln}\dot{\varepsilon} + \frac{Q}{RT} \tag{36}$$

where Q is the activation energy for diffusion, $\dot{\varepsilon}$ is strain rate and T is deformation temperature (Q is considered to be related to stacking fault
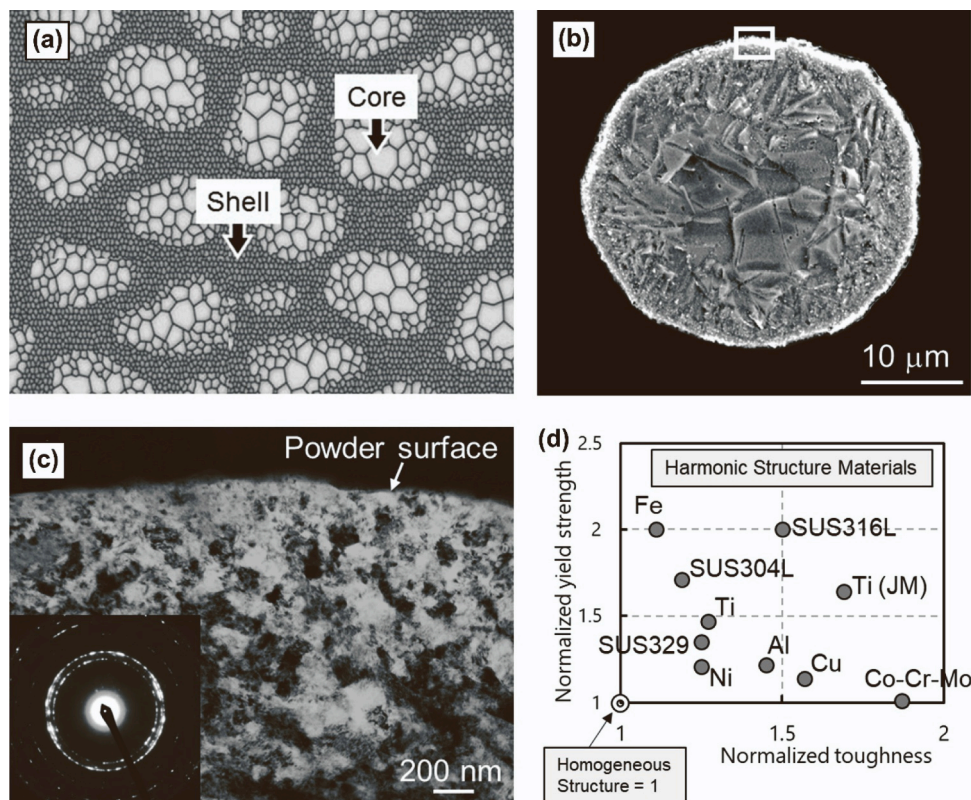
Fig. 93. (a) Schematic representation of the harmonic structure. (b) Cross-sectional image of jet-milled pure titanium powder. (c) TEM image of the near-surface region of jet-milled pure titanium powder. (d) Normalized yield strength and tensile toughness of harmonic structured materials [1916].
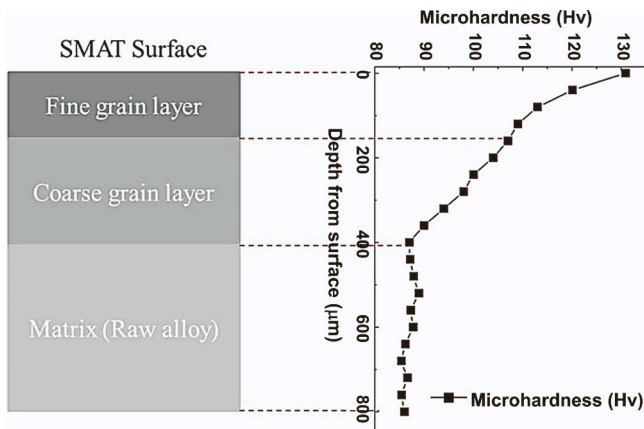
Fig. 94. Schematic diagram of gradient grain structure and corresponding microhardness of metallic samples [1949].

energy [1963]). Stacking fault energy has a considerable influence on the pileup of GNDs, which is closely related to the strengthening of heterostructured materials [44]. Hetero-deformation-induced theory can be used to explain the excellent mechanical properties of heterostructured materials, which has been discussed earlier [188, 1962].

The theory of shear banding and strain delocalization was also used to explain the good ductility of gradient-structured materials. Macroscopically, the orderly and progressive plastic strain of GS material effectively alleviates the local stress concentration of the material, inhibits strain localization, and enables the material to maintain uniform plastic deformation at a higher stress level. Nanometallic materials usually form narrow shear bands after yielding and then fail quickly, while strain localization induced by shear bands seems inevitable. However, in gradient-structured materials, harmful shear bands are used to improve ductility [1941, 1964]. The key mechanical principle to realize the strength-ductility synergistic effect is that the microstructure should be designed by preventing strain localization as far as possible to fully promote the uniformity of plastic flow and realize strain delocalization. This requires that the work hardening capacity or strain rate sensitivity of the material is high enough to stabilize the plastic deformation [1965]. It is difficult for traditional homogeneous materials to meet such requirements, but such effects have been observed in heterostructured materials [1966, 1967].

In summary, the research of gradient-structured materials as a kind of heterostructured materials is just beginning. In the future, a quantitative understanding of structure-property relationships is vital for rational design and optimization of gradient-structured functional materials with desired performance.

8.3.2. Mechanical properties of gradient structures

For materials processed by surface-SPD methods based on impacts [1968–1974], contacts [125, 1975] or shocks [1976–1983], there is a gradient microstructure from the treated surface to the bulk region with three zones: (i) a nanostructured layer, (ii) a transition region where grains are subdivided, (iii) a deformed region where grains are plastically deformed [1984]. For materials that exhibit deformation-induced twinning and/or phase transformation, there is a superposed gradient distribution of twins and transformed phases (see Fig. 96) [1985, 1986]. Due to the induced microstructure and other parameters including residual stresses (Fig. 96), surface-SPD methods are able to enhance mechanical properties such as hardness, tensile properties, fatigue and wear resistance [1951, 1987]. Mechanical properties are mainly determined by the induced nanostructured layer, compressive residual stress, work hardening and surface roughness [1988, 1989]. In general, the first two parameters are beneficial for improving the properties of materials either by retarding crack initiation or delaying crack propagation [1990, 1991], whereas surface roughness degrades it by causing local stress concentration [1991, 1992]. As for work hardening induced by surface-SPD, it is complex due to the multiaxial nature of loading [1976], and it can be divided into isotropic hardening (scalar) and kinematic hardening (tensor) [1993]. Isotropic hardening increases the strength of materials, while kinematic hardening can lower the yield stress of material through back stress [1994].

Under low-cycle fatigue, surface-SPD can significantly enhance mechanical strength and alter the cyclic plasticity (hardening and softening) of gradient-structured materials, depending on imposed stress amplitudes [1995]. In terms of fatigue life, both beneficial and harmful effects of surface-SPD have been observed as a function of the material's type, treatment conditions and load amplitudes [1975, 1995, 1996]. Residual stress relaxation essentially occurs during the first cycles [1997], and the positive effect of compressive residual stress generated by surface-SPD can be quickly reduced or even lost. Significant improvement in fatigue life can thus not be observed, especially for high
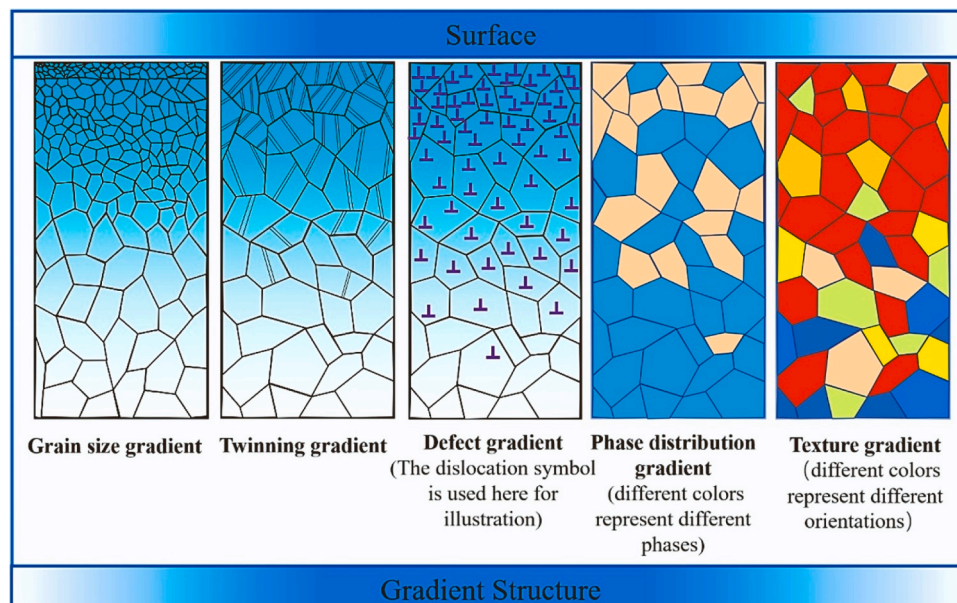
Fig. 95. Micro-schematic diagram of various gradient structures [1955].
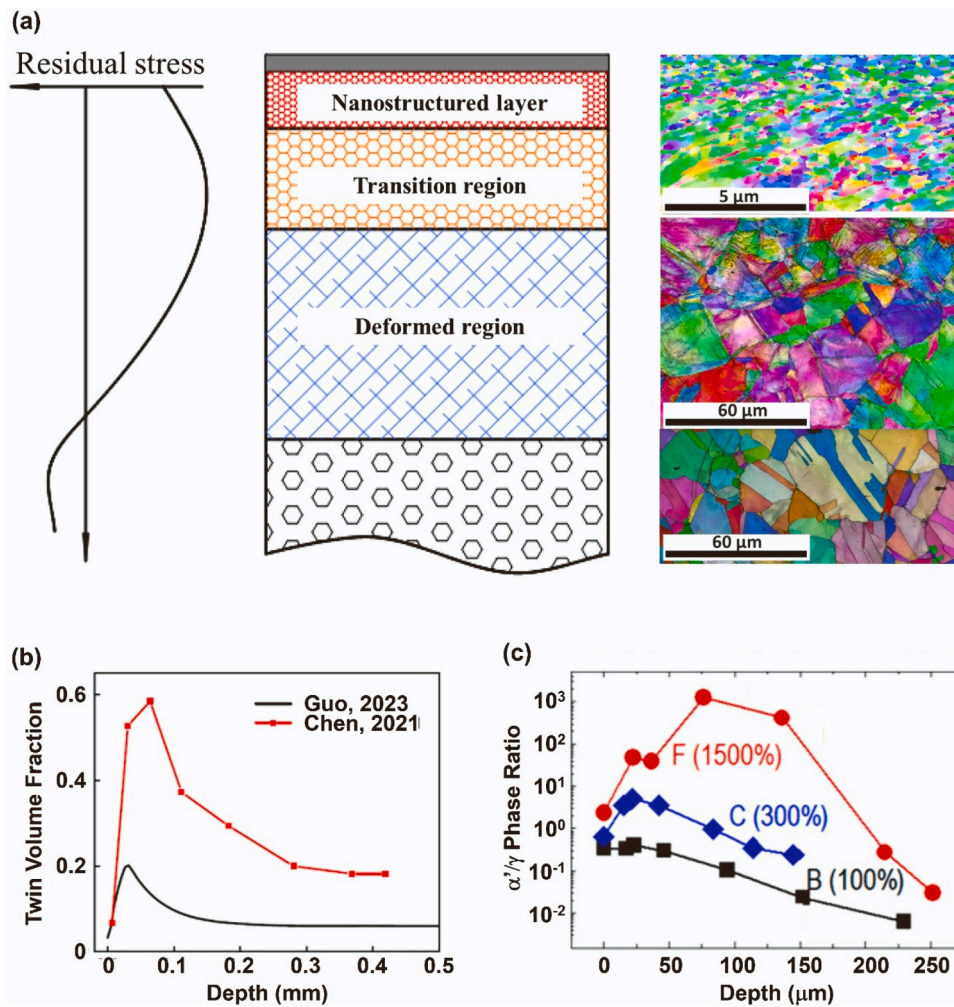
Fig. 96. Generated gradient features including (a) gradient microstructure and residual stress [1971], (b) variation of twin volume fraction [1985] and (c) distribution of phase transformation (B, C and F refer to samples processed by shot peening coverage of 100%, 300% and 1500% respectively) [1986].

load amplitudes [1998]. Improvement in the strength of materials induced by surface-SPD is usually accompanied by a reduction in its ductility [1999, 2000]. Decreased ductility, in some cases, cannot have an improving effect on low-cycle fatigue of materials processed by surface-SPD if the fatigue tests are strain-controlled, especially under high amplitudes [2001].

For high-cycle fatigue, an increase in fatigue resistance due to surface-SPD can usually be observed for various gradient-structured materials under different loading conditions [2002], if no excessive surface defects, such as micro-cracks, are generated by an over-treatment phenomenon. For a given material, the improvement is strongly dependent on treatment conditions which can be optimized according to material behavior [2003]. Under very high-cycle fatigue, extended lives induced by surface-SPD are frequently observed, except for materials with severe surface defects [2004] and excessive interior tensile residual stress [2005, 2006]. For almost all the cyclic loading modes, there is a trend of crack initiation shift from the surface in the high-cycle fatigue regime to the subsurface in the very high-cycle fatigue regime [2004, 2007]. In addition, in the case of subsurface crack initiation, a fish-eye pattern is frequently observed at crack origin, especially for materials that have metallurgical defects such as inclusions and/or crystallographic defects [2008, 2009].

Tribological properties have also been studied for various gradient-structured materials processed by surface-SPD [2010–2013]. In general, a remarkable increase in wear resistance can be observed with respect to coarse-grained counterparts. Several possible mechanisms

potentially involved in improving the tribological performance are: (i) inducing compressive residual stresses [2014, 2015]; (ii) decreasing coefficient of friction [2016, 2017]; (iii) increasing hardness by nano-structured layer and work-hardened region [2018]. However, poor wear resistance of a nanostructured layer can be observed due to its low ductility and toughness easily leading to surface cracks [2019].

Surface-SPD can improve material resistance by retarding crack initiation and delaying crack propagation through strengthened surface and compressive residual stresses. The contributions of grain refinement and that of work hardening to the strength of a structure are rather to increase the crack initiation resistance [1990, 1991]. For crack propagation, however, grain refinement gives rise to a deleterious effect [2020], just like work hardening [2021, 2022], as recapitulated in Fig. 97. As for compressive residual stresses, they usually decrease the crack propagation rate by acting as crack closure stress at the crack tip [2023]. However, the initial residual stresses obtained after surface-SPD cannot be directly used for fatigue analysis because of residual stress relaxation [2024]. In addition, surface-SPD-induced residual stress field and work hardening are associated, and it is difficult to properly separate their contributions through experiments. Their respective effects have thus been investigated using alternative numerical methods [2024, 2025]. The stress-strain curves at different depths can be obtained to provide information about local mechanical behavior. It was highlighted that the presence of residual stress can significantly change the local stress state of materials [2025]. However, more loading modes especially fatigue loading need to be comprehensively investigated in future

work.

8.3.3. Functional properties of gradient structures

There are two general ways to impart SPD to the surface in order to enhance the functional properties of gradient-structured materials: (i) applying a constant load onto the surface to be deformed or (ii) repeatedly impacting the surface with harmers or shots [46, 2026]. Many of the latter family of processes, such as SMAT, are derived from conventional shot peening [2027]. UFG structures generated by SPD are usually produced by the generation and accumulation of lattice defects, dividing and refining the initial microstructure into substructures and ultimately fine grains down to the nanoscale. As mentioned in an earlier section, the gradual cumulative strain applied from the surface creates a gradient microstructure which can be seen as a succession of different affected layers, but with a gradual transition. It goes from a refined surface nanocrystalline + ultrafine grain zone towards the surface to a

"plastically deformed layer" in the depth, via a transition zone where the grains are undergoing the subdivision process [2028, 2029]. The transition depth between the different layers depends on the processing parameters which include also the peening temperature. In addition to the obvious modification of the grain size and density of structural defects (dislocations, twins, etc.) through the depth of the samples, the so-called gradient microstructure is very often the combination of different gradients in terms of local texture, phase distribution and residual stresses [138, 1951, 2030–2034]. For example, when martensite forms by transformation-induced plasticity in SMAT-processed stainless steel, the maximum amount of α′ martensite is never found in the UFG layer at the vicinity of the extreme surface but within the sub-surface; at a depth of 50–100 μm depending on the processing conditions [1951]. SMAT carried out at cryogenic and room temperatures on a 5553 β-metastable Ti-based alloy also promoted a martensitic transformation and kink bands produced essentially at the sub-surface [2034]. All these

(d)	Grain-refined layer	Compressive residual stress	Induced work hardening	Surface roughness
Crack initiation resistance	(+)	(+)	(+/ -)	(-)
Crack propagation resistance	(-)	(+)	(+/ -)	
Wear resistance	(+)	(+)	(+)	(+)

Fig. 97. (a-c) Some typical mechanical properties of gradient-structured materials including (a) low-cycle fatigue of 316 L steel in different states [1995], (b) high-cycle fatigue of 316 L steel in different states [125] and (c) Tribological properties of an AZ91D magnesium alloy [2012]. (d) Roles played by different parameters on fatigue and wear resistance of gradient-structured materials.

microstructural features can affect the functional properties of gradient-structured materials.

The particular property of the UFG structures is the significantly high-volume fraction of high-angle grain boundaries with high energy and free volume resulting in the so-called non-equilibrium grain boundaries. The related increase in intergranular energy densities has an influence on the surface reactivity and the atomic transport along boundaries during chemical diffusion [373]. Thus, in addition to modifying mechanical properties through the influence of UFG, residual compressive stresses and potential stress raisers can be created on the surface by surface-SPD, which would affect the chemical and mechanochemical properties of the materials [2002, 2035–2037]. Consequently, surface-SPD has been used for several applications in which the favored atomic transport is beneficial, as discussed below.

The enhanced diffusion of chemical species after surface-SPD has been used to improve corrosion resistance as well as to optimize thermochemical surface treatments via "duplex" treatments. The most widely investigated process is the nitriding treatment, but pack bromizing, aluminizing, chromizing as well as plasma electrolytic oxidation have also been investigated successfully (See [2038], for further reading). For the case of nitriding, the enhanced atomic mobility after mechanical surface treatment generates a thicker diffusion layer for a given nitriding temperature/duration or allows reducing the nitriding temperature [2038–2040]. The latter is of importance when considering austenitic stainless steels. Indeed, by nitriding at a temperature as low as 573 K, a single-phase expended austenite is created without precipitation of Cr-rich precipitates which are detrimental to corrosion resistance. Also, SMAT carried out before nitriding allows producing a much harder surface layer due to the combination of two hardening mechanisms: strain hardening due to remaining structural defects and solid solution hardening due to the presence of the N-enriched expended austenite [2038]. An important issue with the "duplex" treatments is the contamination that can be introduced during surface-SPD by the peening media that are also able to transfer chemical elements from the working chamber, locally modifying the chemical composition of the treated surfaces [2038, 204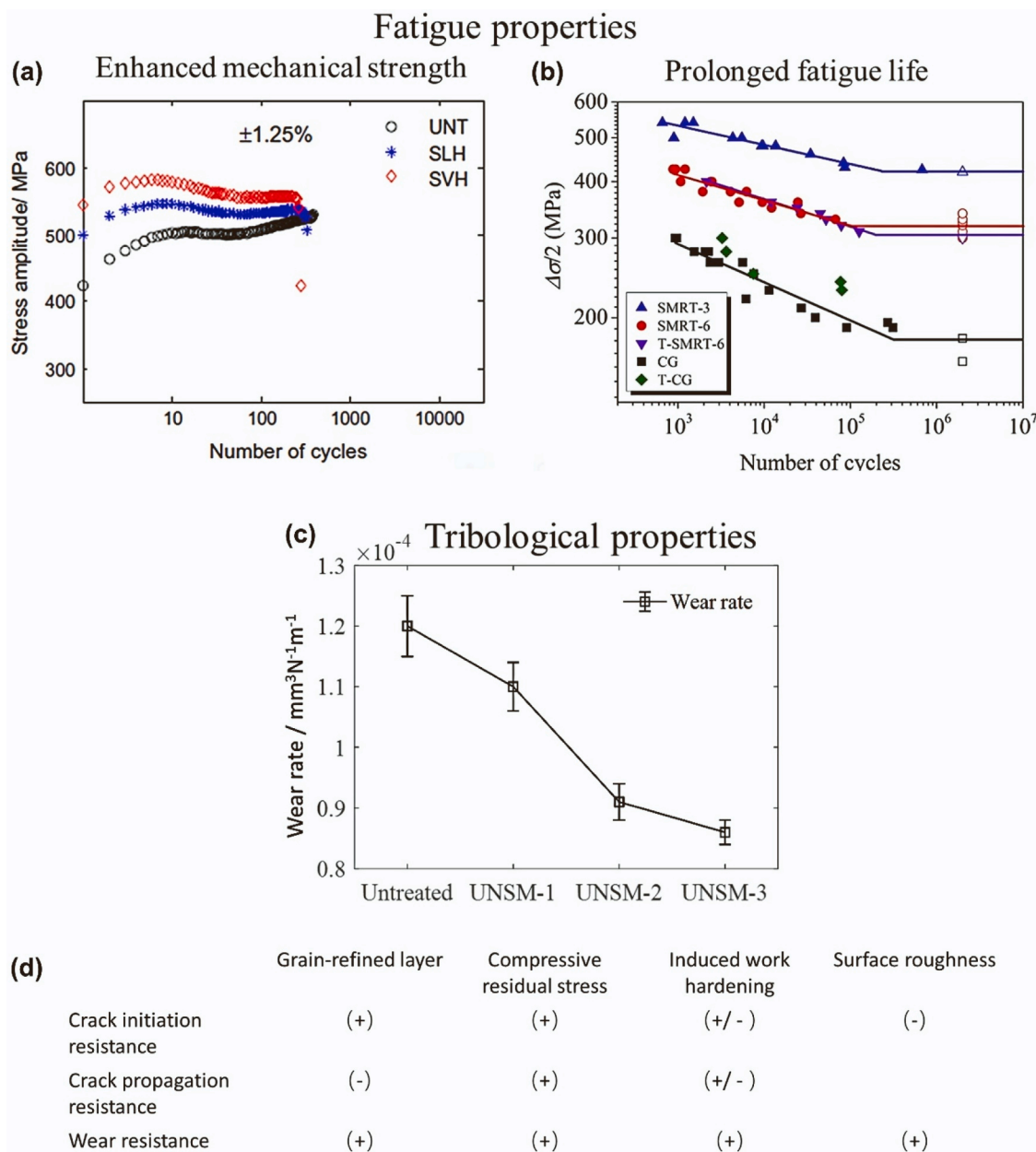1, 2042]. This contamination acts as a barrier to the external atomic flux. For example, it leads to the formation of reduced or discontinuous nitriding layers [2038, 2041] so that the chemical etching [2042] or mechanical polishing [2043, 2044] must be used as an intermediary stage to remove the surface contamination and, thereby, improve further the quality and thickness of the nitrided layers.

Using surface-SPD for modifying the corrosion properties faces the same challenges as nitriding treatment. Plastic deformation improves the corrosion resistance in a passive environment whereas it increases the dissolution rate in a non-passive environment. SMAT has been used for example on a 301 stainless steel to facilitate the diffusion of Cr from the bulk towards the surface to form a stronger passivation film [2045]. Also, the effect of the surface contamination was demonstrated by modifying, for example, the nature of the peening shots during SMAT for a 2024 Al-based alloy [2046]. While the use of ceramic peening balls improved the corrosion resistance by the formation of a dense passive film, the Fe-containing layer induced by SMAT with steel balls led to the diminution in the corrosion resistance.

Surface-SPD is now finding new applications for the hydrogen sector. As hydrogen produces no greenhouse gas emissions when it burns, hydrogen will be the preferred alternative to fossil fuels for decarbonizing both transport and industry. In addition to producing enough green hydrogen near the offtake sites using renewable energies, the storage and transportation of large amounts of hydrogen are other important issues for the hydrogen sector. For hydrogen storage, the objective is to use metallic materials as solid-state hydrogen tanks by storing the hydrogen in reversible metallic hydrides. Bulk-SPD induces structural defects and fine grains in metals which can be used to activate them as well as to optimize their hydrogen absorption/desorption kinetics [1077]. Instead of using high-energy ball milling to introduce structural defects and fine grains, the bulk-SPD techniques have the major advantage of avoiding the complexity of handling highly reactive and pyrophoric powders [1077, 1753, 1754]. A very good example of the high potential of SPD has been demonstrated for the activation of TiFe via groove rolling or HPT [181]. While hydrogen absorption was extremely limited in the coarse-grained TiFe annealed sample because of difficult activation, the HPT-processed samples could fully store hydrogen reversibly at room temperature and were not deactivated by long-time exposure to the air [1137]. However, in some materials like the Ti-V-Cr alloys, the large number of structural defects generated by bulk-SPD can act as trap sites, impeding the hydrogen desorption reversibility. In the case of these Ti-V-Cr materials, the surface-SPD method of SMAT could be used successfully to activate the material while preserving reversibility [2047]. As summarized in Fig. 98, the nanostructure and cracks present at the surface of the SMAT-processed sample could act as a pathway for hydrogen transport through the oxide layer and activate the material while the hydrogen atoms could be stored in the defect-free subsurface and bulk from where reversibility was possible [2047, 2048]. Compared to bulk-SPD, an additional advantage of surface-SPD route is that they can be more easily scaled up. Thus, mechanical surface treatment inducing surface gradients can then be regarded as having a high potential for elaborating activated industrial hydrogen storage materials.

Transportation applications based on hydrogen as a fuel also require preventing the hydrogen embrittlement phenomenon. Since the hydrogen is absorbed and diffused from the surface, surface functionalization has been studied to prevent or reduce phenomena like hydrogen embrittlement. Surface functionalization can take the form of surface chemistry modifications like coatings and mechanical surface treatments [2049]. It was reported that the increase in hydrogen trap sites due to the surface structural refinement associated with the formation of a compressive residual stress gradient is beneficial for limiting the hydrogen embrittlement resistance. It was proposed that the high density of defects associated with the accumulation of hydrogen in the shot-peened deformed layer is responsible for creating a mismatch between the treated surface and the non-deformed core, leading to the formation of sub-surface cracks which will then propagate toward the surface and not the core [2050, 2051]. However, the distinct influence of hydrogen trap site density and residual stress is not clear [2052] and phase transformation may also be of importance [2053]. Fig. 99 illustrates that gradient-structured FCC CrMnFeCoNi HEAs can exhibit a good combination of a high yield stress and good ductility under a hydrogen environment [1235]. Due to the formation of surface nanotwins under SMAT (Figs. 99a and 99b), as opposed to the fully nanostructured sample produced by HPT which led to brittle failure in the presence of hydrogen, the SMAT-processed gradient samples showed a 2-3 times higher yield stress than the coarse-grained material coupled with a fair amount of ductility (Fig. 99c). Such improvement is expected as long as the hydrogen content is kept under a critical level to prevent the hydrogen-enhanced localized plasticity mechanisms. As depicted by the sequence of SEM images given in Fig. 99d-f, the presence of the gradient structure containing nanotwins was associated with a combination of both intergranular (enlarged in Fig. 99e) and transgranular (Fig. 99f) surface cracking mechanisms [1235].

Gradient-structured materials appear to exhibit high potential for various functional applications. Although research in this regard is rather limited compared to the mechanical properties of these materials, there are clear trends to examine the functionality of these materials for various applications and particularly in the energy sector. Despite these gradient-structured materials are currently produced by surface-SPD methods such as SMAT and laser shot peening. which can be operated remotely, various metal forming, machining and welding methods or some SPD methods like equal-channel angular sheet extrusion can be also modified to produce such materials [2054–2057].
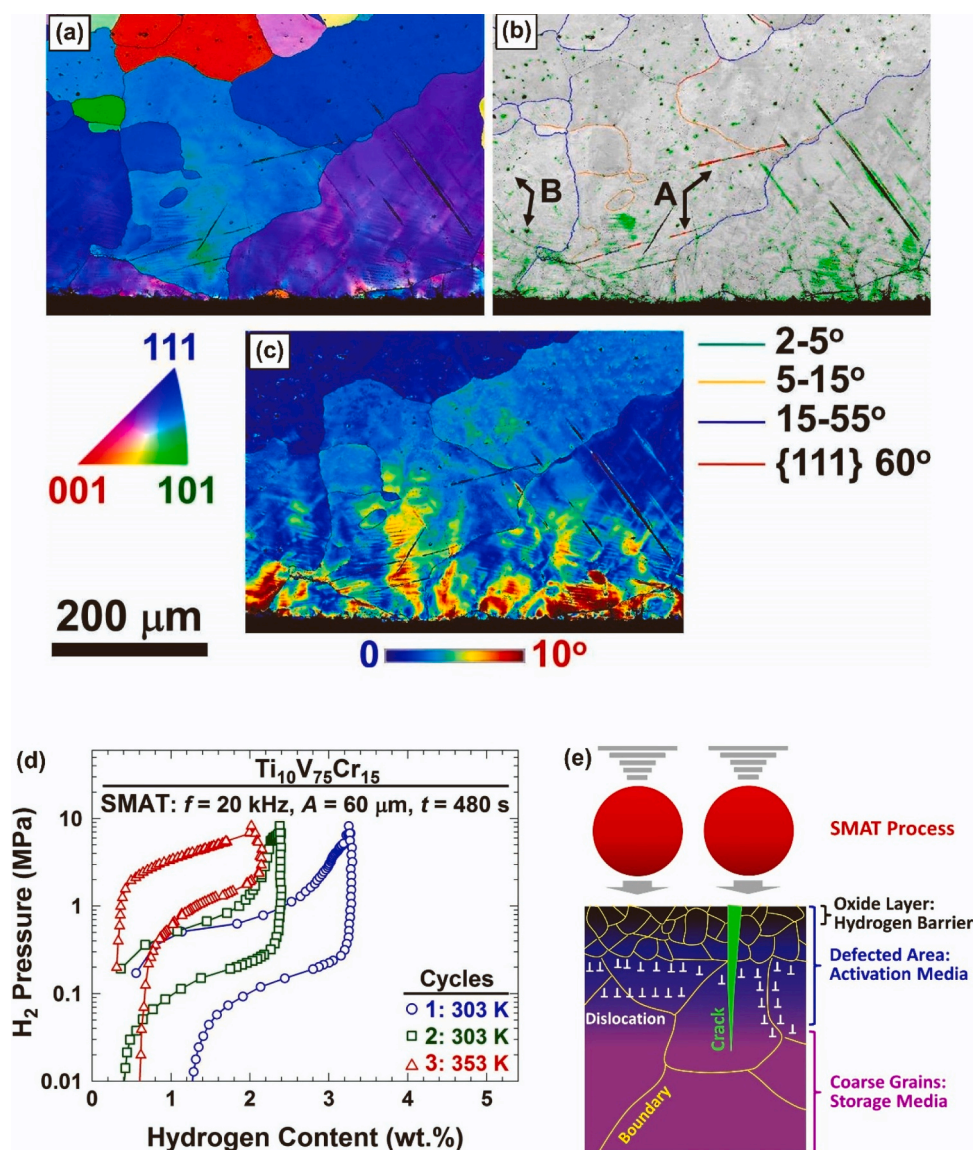
Fig. 98. (a-c) EBSD of cross section of SMAT-processed $Ti_{10}V_{75}Cr_{15}$ where (a) is a misorientation map, (b) is grain boundary map and (c) is internal misorientation map (treated surface is at bottom) [2047]. (d) pressure-composition isotherms for SMAT-processed $Ti_{10}V_{75}Cr_{15}$, indicating reversible hydrogen storage at room temperature without the need to an extra activation treatment [2047]. (e) Schematics of the effect of surface-SPD on hydrogen storage behavior and activation of Ti-V-Cr alloys [2047].

9. SPD from the Bronze Age to 2024

SPD has been a part of human life for centuries and was used first in food-making and later in strategic tool-making. Sword making in the Bronze Age or at least during the transition from the Bronze Age to the Iron Age by Repeated forging and folding is perhaps the first success in commercializing the SPD process [5, 18]. The scientific interests in SPD which originated from geology at the beginning of the last century led to the invention of some new SPD methods such as HPT [20–22] and ECAP [27, 28] which are still the most popular [177, 193] even at the beginning of the year 2024. As discussed in previous chapters, SPD has been expanded in different directions in the 21st century and used to control microstructural and structural features to achieve novel mechanical and functional properties in a wide range of materials. To have an idea about the latest research trends in the SPDD field, some major articles published in 2024 are briefly reviewed in this section.

A review of the paper published in 2024 suggests that there are still attempts to develop new or modified bulk-SPD methods [2057–2061]. These attempts are mainly to enhance the properties, modify the shape

of samples or scale up the final product [2062, 2063]. There are also attempts to develop new surface-SPD methods or combine the existing methods with other processes [2064, 2065]. One issue that can be understood clearly from the literature survey is the high interest of researchers in processing additively manufactured alloys by bulk-SPD [2066, 2067] or surface SPD [2068, 2069]. A combination of 3D printing and SPD was also employed with the objective of enhancing the strength-ductility synergy [2070, 2071]. Cryogenic-SPD to achieve enhanced mechanical properties such as high strength and high ductility is used by some researchers [2072], while the thermal stability of these materials is still a matter of investigation [2073]. There are reports to use the concept of ultra-SPD to synthesize materials and the synthesis of novel Al-Au alloys [2074], HEAs [2075] and high-entropy ceramics [2076] are some reported results. Deep evaluation of microstructure by different *ex situ* characterization methods is still popular as there are still many questions in this regard, but there are clear trends to use *in situ* methods as well [2077, 2078]. Understanding the importance of grain boundaries and related phenomena such as segregation and diffusion are other microstructure-related studies [2079–2081], while there are also
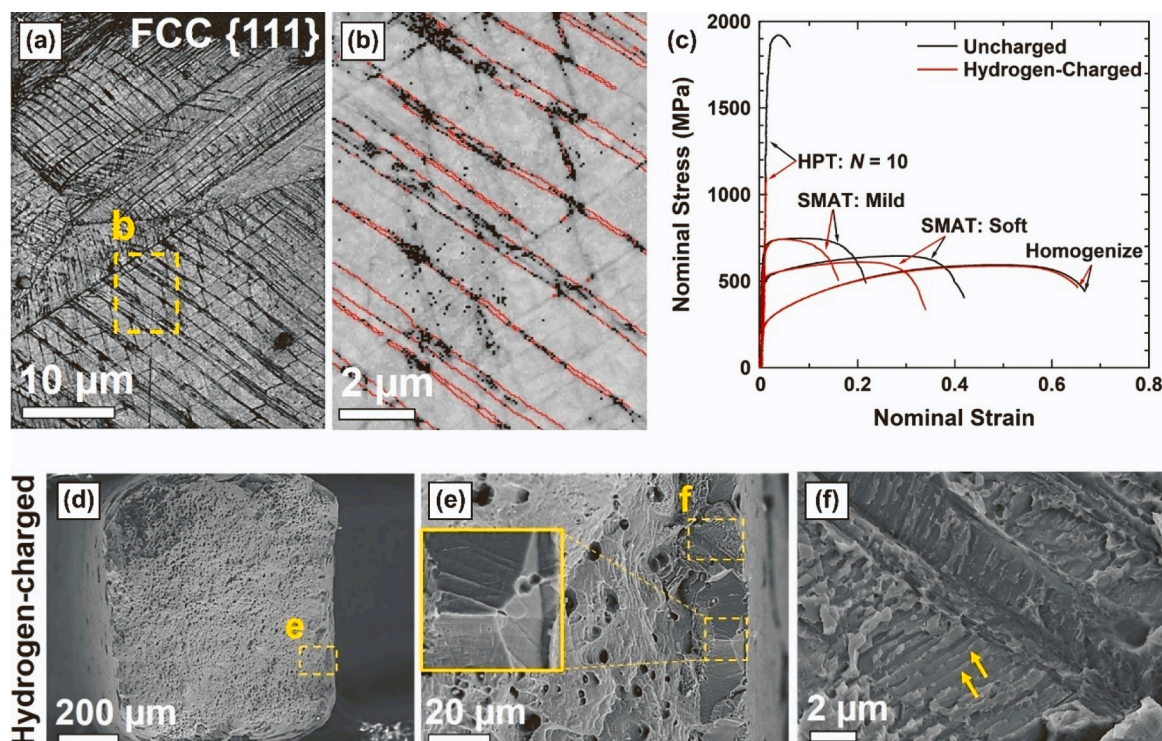
Fig. 99. Illustration of the effect of SMAT on the modification of the hydrogen embrittlement resistance of a CrFeMnCoNi HEA: (a-b) SEM and EBSD images of surface nanotwins induced by SMAT before hydrogen charging, (c) tensile stress-strain curves before (black) and after (red) hydrogen charging for gradient-structured samples produced by two different SMAT processing conditions or fully nanostructured sample produced by HPT, (d-f) SEM images of a fractured specimen after hydrogen charging revealing both intergranular enlarged in (e), and transgranular enlarged in (f) [1235].

various studies on structure-related studies such as phase transformations [2082–2084]. While most of these studies are experimental, there are some efforts to use theoretical or numerical approaches such as atomistic modeling [2085], first-principles calculations [1004, 2086], molecular dynamic simulations [2087], crystal plasticity simulations [2088], finite element analysis [2089] and machine learning [2090].

A survey of publications in 2024 indicates that the investigations of mechanical and functional properties for different applications are the most popular research topics. There are numerous publications on such properties and application after processing by bulk-SPD including hardness [2091], strain hardening [2092], anneal hardening [2093], ductile-brittle fracture transition [2094], fatigue resistance [2095, 2096], creep resistance [2097, 2098], shape memory effect [2099], superconductivity [2100], magnetic properties [2101–2103], electromagnetic interference shielding [2104], thermoelectric properties [2086], battery application [2105, 2106], photocatalytic CO_2 conversion [2076], photocatalytic hydrogen production [2077], solid-state hydrogen storage [2107–2109], corrosion resistance [2110, 2111] and biomedical devices [2112–2114]. Materials processed by surface-SPD were also investigated for different properties including wear resistance [2115, 2116], fatigue resistance [2117, 2118], superplasticity [2119] and corrosion resistance [2120]. There have been also attempts to combine bulk-SPD with laser treatment or replace bulk-SPD with powder-SPD to produce materials that need a large specific surface area such as photocatalysts [2076, 2121]. One of the latest research trends is the application of SPD to biomolecules to simulate their mechanochemical behavior which is of interest in understanding the origin of life [2122]. This last issue will be discussed in more detail in the next session.

10. SPD from earthquake to the origin of life

Although SPD methods are at the early stages of commercialization,

they have significantly contributed to scientific issues regarding the behavior of materials under deformation. Among various SPD methods, HPT is perhaps the most powerful tool for fundamental studies because strain, pressure, temperature and strain rate can be controlled in this method with high precision [20]. Although HPT is currently used mainly for metal processing [23, 2123]; however, high pressure in the method makes it applicable to almost any kind of material including hard-to-deform materials such as ceramics [2124, 2125]. From the historical point of view, Bridgman employed the first HPT facility to process different kinds of metallic and nonmetallic substances including rocks and organic materials [20]. The application of HPT to rocks is accompanied by plastic deformation, phase transformations and snapping, an observation that suggested a mechanism for the occurrence of deep-seated earthquakes by plastic deformation of rocks [20] which is still of interest in geology [646]. The first press release of HPT to the public by Bridgman in 1935 had the title of "Scientist Makes Miniature Earthquake", as shown in Fig. 100a [23]. The HPT has continued its way as a scientific tool in clarification of different phenomena, and understanding the origin of life is one of its latest contributions that was press released in a TV program in 2022, as shown in Figs. 100b and 1c [2126].

One of the most essential biomolecules for life on Earth is protein, but the formation of the first protein molecules from amino acids in the early Earth conditions (about four billion years ago) is not well understood yet. Following the discovery of amino acids in meteorites, particularly Murchison and Tagish Lake meteorites, the hypothesis of delivery of biomolecules and their polymerization by high-pressure impacts through small solar system bodies (meteoroids, asteroids and comets) has received high attention [2127, 2128]. Despite high interest in this hypothesis, simulations of astronomical impacts by high-pressure shock experiments have not led to the formation of proteins from amino acids so far [2129, 2130]. Neglecting the strain effect can be one explanation for little success in the polymerization of amino acids by shock experiments [2131], while straining can practically occur in such

impacts due to high pressure, as schematically shown in Fig. 100b [2132]. Since some studies reported clear changes by straining in organic materials [2133, 2134], the strain effect should be included in the astronomical impact simulations.

For simulating the behavior of biomolecules under astronomical impacts, a recent study processed glycine amino acid by HPT under 1 and 6 GPa at ambient temperature [2126]. A loud explosion occurred during the HPT processing of glycine which can be recognized from the appearance of HPT anvils after the process, as shown in Fig. 100c. The gas phase could not be analyzed in this study, but examination of the solid phase by XRD (Fig. 101a), Raman spectroscopy (Fig. 101b) and nuclear magnetic resonance spectroscopy (Figs. 101c and 101d) indicate the stability of large amounts of glycine and the formation of some amounts of alcohol. The presence of large amounts of glycine after such severe HPT processing conditions justifies the stability of glycine reported in meteorites [2127, 2128]. The detection of ethanol confirmed that polymerization of glycine did not occur but its decomposition to alcohol and nitrogen-containing molecules happened by HPT processing. Despite the absence of polymerization, these findings are of importance because alcohol and nitrogen-containing groups are essential molecules for the development of organic materials on the Earth [2135]. Furthermore, both alcohol and glycine were detected in some comets [2136, 2137] and simulations by HPT suggested a possible mechanism for the formation of alcohol in comets by pressure and strain effects. These findings suggested that further studies by SPD under high pressure can be of importance from the "operational" view [2138] for a better understanding of the origin of life.

11. Concluding remarks and outlook

Severe plastic deformation (SPD) processing and the science of the design and synthesis of ultrafine-grained (UFG) materials by this process continuous its progress, although the focus of the field shows a transition from structural materials with enhanced mechanical properties to superfunctional materials with superior functional properties. This article attempts to highlight the most recent progress in the field and give new insight into the future of SPD. There are now various SPD methods for producing samples with appropriate shapes, large sizes and

continuous processing for commercial applications (Chapter 2). Microstructure and phase transformation of severely deformed materials, which have a significant effect on their properties, are studied much deeper with advanced characterization methods and theoretical studies in recent years (Chapter 3 and 4). Mechanical properties of severely deformed materials including high hardness and strength particularly at room temperature as well as creep resistance and superplasticity particularly at high temperature are widely studied (Chapter 5). However, the general trend is to study the functional properties of these materials for various applications including electric/magnetic properties, catalytic performance, hydrogen-related functionalities (hydrogen production, hydrogen storage and hydrogen embrittlement resistance), corrosion resistance and biocompatibility (Chapter 6). The application of SPD has been now extended from the production of UFG metallic materials such as magnesium, aluminum, titanium and iron alloys to various kinds of metallic and non-metallic materials such as high-entropy alloys, glasses, semiconductors, ceramics and polymers (Chapter 7). Another trend in the SPD field is to produce heterostructured materials including harmonic-structured and gradient-structured materials because these materials can show better properties for some particular applications compared to UFG materials (Chapter 8). These research trends continue to expand in different directions in the year 2024 (Chapter 9), and one of the latest trends in the SPD field is the investigation of the mechanisms behind certain natural phenomena, including the origin of life (Chapter 10).

SPD has shown great potential for the formalization of property-microstructure relationships for a few decades, but the field can move to the discovery of original materials that exhibit unique functionalities for particular applications like energy materials. In this regard, the field needs to be empowered by using various advanced analysis and *in situ* characterization methods. Moreover, close collaboration with theoretical scientists is necessary, particularly for functional properties related to energy applications. Biomaterials and hydrogen-related materials have currently a great positioning in many countries, and interesting findings reported for SPD-processed materials in these applications can lead to a faster transition from the laboratory scale to industry adoption. For such a transition to industry and commercialization, scaling up the sample size by using methods with enlarged processing capacity or with
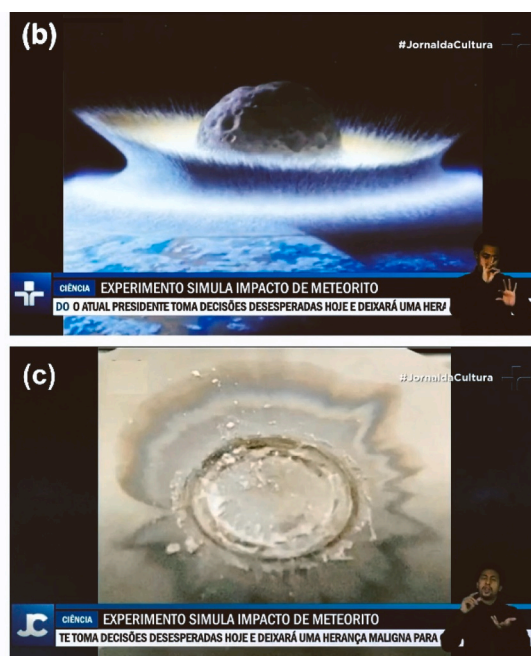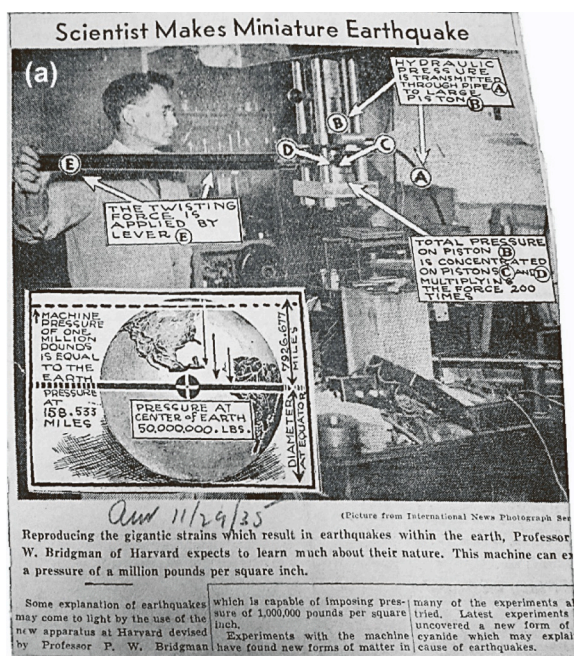
Fig. 100. (a) The first press release about HPT in 1935, highlighting the potential of the method for geological studies and the mechanism of deep-seated earthquakes [23]. (b) A television program on TV Cultura channel in 2022 about the application of HPT for understanding the origin of life [2126].
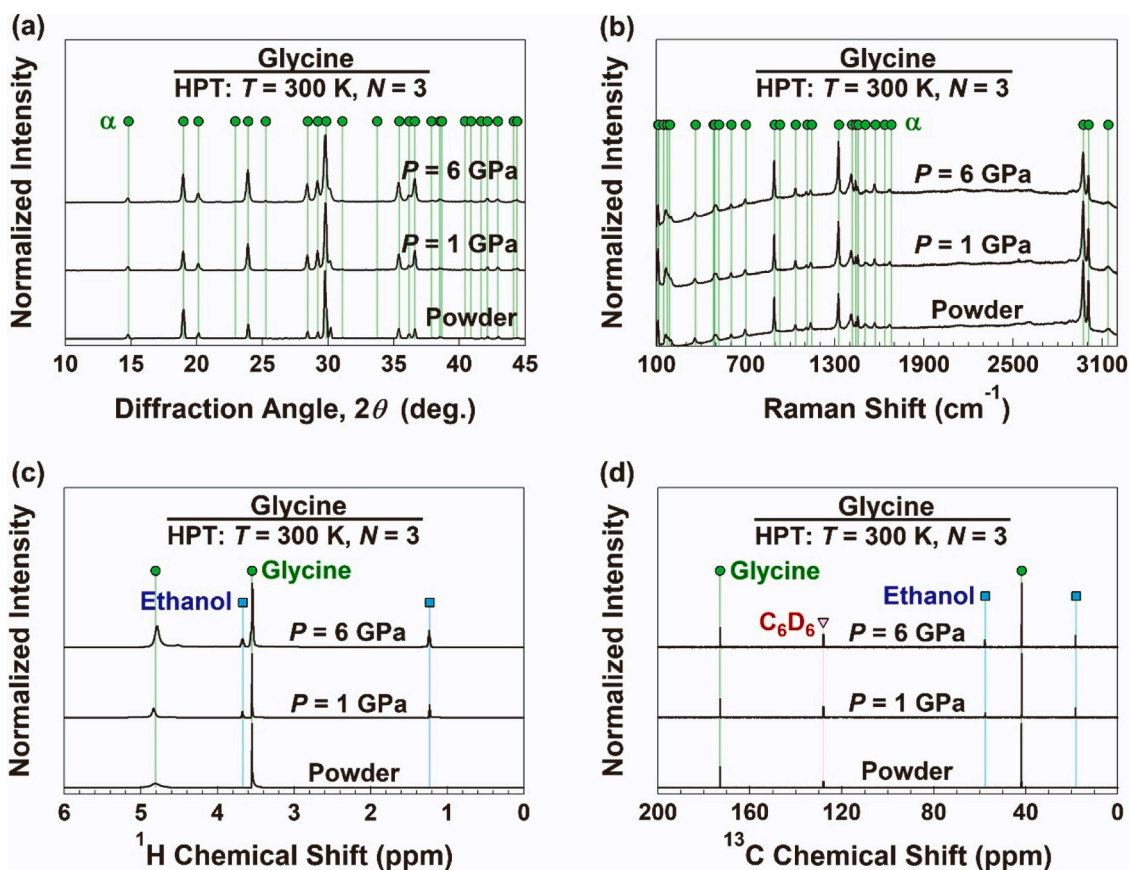
Fig. 101. (a) XRD profiles, (b) Raman spectra and (c,d) nuclear magnetic resonance spectra for glycine amino acid before and after treatment by HPT under 1 and 6 GPa [2126].

continuous processing capability is essential. Studies conducted in very recent years confirm that SPD can move from a metal processing technique to a multidisciplinary tool for various studies that need close connection with scientists from the fields of physics, chemistry, mathematics, geology, astronomy, life sciences and many aspects of engineering.

Declaration of Competing Interest

The authors declare that they have no known competing financial interests or personal relationships that could have appeared to influence the work reported in this paper.

Acknowledgments

References

[1] R.Z. Valiev, R.K. Islamgaliev, I.V. Alexandrov, Bulk nanostructured materials from severe plastic deformation, Prog. Mater. Sci. 45 (2000) 103–189.

[2] R.Z. Valiev, Y. Estrin, Z. Horita, T.G. Langdon, M.J. Zehetbauer, Y.T. Zhu, Producing bulk ultrafine-grained materials by severe plastic deformation, JOM 58 (4) (2006) 33–39.

[3] Y. Estrin, A. Vinogradov, Extreme grain refinement by severe plastic deformation: a wealth of challenging science, Acta Mater. 61 (2013) 782–817.

[4] M. Zehetbauer, R. Grossinger, H. Krenn, M. Krystian, R. Pippan, P. Rogl, T. Waitz, R. Wurschum, Bulk nanostructured functional materials by severe plastic deformation, Adv. Eng. Mater. 12 (2010) 692–700.

[5] K. Edalati, A. Bachmaier, V.A. Beloshenko, Y. Beygelzimer, V.D. Blank, W. J. Botta, K. Bryła, J. Čížek, S. Divinski, N.A. Enikeev, Y. Estrin, G. Faraji, R. B. Figueiredo, M. Fuji, T. Furuta, T. Grosdidier, J. Gubicza, A. Hohenwarter, Z. Horita, J. Huot, Y. Ikoma, M. Janeček, M. Kawasaki, P. Král, S. Kuramoto, T. G. Langdon, D.R. Leiva, V.I. Levitas, A. Mazilkin, M. Mito, H. Miyamoto, T. Nishizaki, R. Pippan, V.V. Popov, E.N. Popova, G. Purcek, O. Renk, Á. Révész, X. Sauvage, V. Sklenicka, W. Skrotzki, B.B. Straumal, S. Suwas, L.S. Toth, N. Tsuji, R.Z. Valiev, G. Wilde, M.J. Zehetbauer, X. Zhu, Nanomaterials by severe plastic deformation: review of historical developments and recent advances, Mater. Res. Lett. 10 (2022) 163–256.

[6] E. Hall, The deformation and ageing of mild steel: III discussion of results, Proc. Phys. Soc. B 64 (1951) 747–752.

[7] N.J. Petch, The orientation relationships between cementite and α-iron, Acta Cryst. 6 (1953) 96-96.

[8] V.I. Levitas, High-pressure phase transformations under severe plastic deformation by torsion in rotational anvils, Mater. Trans. 60 (2019) 1294–1301.

[9] A. Mazilkin, B. Straumal, A. Kilmametov, P. Straumal, B. Baretzky, Phase transformations induced by severe plastic deformation, Mater. Trans. 60 (2019) 1489–1499.

[10] J.K. Han, J.I. Jang, T.G. Langdon, M. Kawasaki, Bulk-state reactions and improving the mechanical properties of metals through high-pressure torsion, Mater. Trans. 60 (2019) 1131–1138.

[11] A. Bachmaier, R. Pippan, High-pressure torsion deformation induced phase transformations and formations: new material combinations and advanced properties, Mater. Trans. 60 (2019) 1256–1269.

[12] J. Sort, D.C. Ile, A.P. Zhilyaev, A. Concustell, T. Czeppe, M. Stoica, S. Surinach, J. Eckert, M.D. Baro, Cold-consolidation of ball-milled Fe-based amorphous ribbons by high pressure torsion, Scr. Mater. 50 (2004) 1221–1225.

[13] Z. Lee, F. Zhou, R.Z. Valiev, E.J. Lavernia, S.R. Nutt, Microstructure and microhardness of cryomilled bulk nanocrystalline Al-7.5%Mg alloy consolidated by high pressure torsion, Scr. Mater. 51 (2004) 209–214.

[14] V. Beloshenko, A. Vozniak, A. Voznyak, Equal channel angular extrusion of polymers: structural changes and their effects on properties, Mater. Trans. 64 (2023) 1325–1330.

[15] V.D. Blank, M.Y. Popov, B.A. Kulnitskiy, The effect of severe plastic deformations on phase transitions and structure of solids, Mater. Trans. 60 (2019) 1500–1505.

[16] I. Fujita, K. Edalati, X. Sauvage, Z. Horita, Grain growth in nanograined aluminum oxide by high-pressure torsion: phase transformation and plastic strain effects, Scr. Mater. 152 (2018) 11–14.

[17] K. Edalati, Z. Horita, Special issue on superfunctional nanomaterials by severe plastic deformation, Mater. Trans. 64 (2023) 1271.

[18] J.T. Wang, Historic retrospection and present status of severe plastic deformation in China, Mater. Sci. Forum 503– 504 (2006) 263–370.

[19] Y. Saito, H. Utsunomiya, N. Tsuji, T. Sakai, Novel ultra-high straining process for bulk materials: Development of the accumulative roll-bonding (ARB) process, Acta Mater. 47 (1999) 579–583.

[20] P.W. Bridgman, Effects of high shearing stress combined with high hydrostatic pressure, Phys. Rev. 48 (1935) 825–847.

[21] P.W. Bridgman, Flow phenomena in heavily stressed metals, J. Appl. Phys. 8 (1937) 328–336.

[22] P.W. Bridgman, Studies in Large Plastic Flow and Fracture, McGraw-Hill,, New York, 1952.

[23] K. Edalati, Z. Horita, A review on high-pressure torsion (HPT) from 1935 to 1988, Mater. Sci. Eng. A 652 (2016) 325–352.

[24] C.E. Pearson, The viscous properties of extruded eutectic alloys of lead-tin and bismuth-tin, J. Inst, Metals 54 (1934) 111–124.

[25] E. Paul, Method of preparing artificial threads, US Pattents (1939) US2145076A.

[26] V.M. Segal, Materials preparation for following processing, USSR Invent. Certif. 575 (1977) 892.

[27] V.M. Segal, V.I. Reznikov, A.E. Drobyshevskiy, V.I. Kopylov, Plastic working of metals by simple shear, Russ. Met. 1 (1981) 99–105.

[28] V.M. Segal, Reznikov, V.I.Kopylov, D.A. Pavlik, V.F. Malyshev, Processes of Plastic Structure Formation in Metals, Nauka I Tehnika, Minsk,1994.

[29] W.A. Jesser, D. Kuhlmann-Wilsdorf, The flow stress and dislocation structure of nickel deformed at very high pressure, Mater. Sci. Eng. 9 (1972) 111–117.

[30] S. Erbel, Mechanical properties and structure of extremely strain-hardened copper, Met. Technol. 6 (1979) 482–486.

[31] S. Erbel, Mechanizm Zmian Własności Metali Poddanych Wielkim Odksztalceniom, Wydawnictwa PW, Warszawa, 1976.

[32] K. Bryła, K. Edalati, Historical studies by Polish scientist on ultrafine-grained materials by severe plastic deformation, Mater. Trans. 60 (2019) 1553–1560.

[33] R.Z. Valiev, O.A. Kaibyshev, R.I. Kuznetsov, R.S. Musalimov, N.K. Tsenev, Low-temperature superplasticity of metallic materials, Dokl. Akad. Nauk. SSSR 301 (1988) 864–866.

[34] R.Z. Valiev, D.A. Salimonenko, N.K. Tsenev, P.B. Berbon, T.G. Langdon, Observations of high strain rate superplasticity in commercial aluminum alloys with ultrafine grain sizes, Scr. Mater. 37 (1997) 1945–1950.

[35] Z. Horita, M. Furukawa, M. Nemoto, A.J. Barnes, T.G. Langdon, Superplastic forming at high strain rates after severe plastic deformation, Acta Mater. 48 (2000) 1633–1640.

[36] T.C. Lowe, R.Z. Valiev, X. Li, B.R. Ewing, Commercialization of bulk nanostructured metals and alloys, MRS Bull. 46 (2021) 265–272.

[37] A. Azushima, R. Kopp, A. Korhonen, D.Y. Yang, F. Micari, G.D. Lahoti, P. Groche, J. Yanagimoto, N. Tsuji, A. Rosochowski, A. Yanagida, Severe plastic deformation (SPD) processes for metals, CRIP Ann. Mauuf. Technol. 57 (2008) 716–735.

[38] R. Pippan, S. Scheriau, A. Taylor, M. Hafok, A. Hohenwarter, A. Bachmaier, Saturation of fragmentation during severe plastic deformation, Annu. Rev. Mater. Res. 40 (2010) 319–343.

[39] J. Gil Sevillano, P. van Houtte, E. Aernoudt, Large strain work hardening and textures, Prog. Mater. Sci. 25 (1981) 69–412.

[40] D.A. Rigney, M.G.S. Naylor, R. Divakar, L.K. Ives, Low energy dislocation structures caused by sliding and by particle impact, Mater. Sci. Eng. 81 (1986) 409–425.

[41] K. Lu, J. Lu, Surface nanocrystallization (SNC) of metallic materials-presentation of the concept behind a new approach, J. Mater. Sci. Technol. 15 (1999) 193–197.

[42] J.S. Benjamin, Mechanical alloying, Sc. Am. 234 (1976) 40–49.

[43] C. Suryanarayana, Mechanical alloying and milling, Prog. Mater. Sci. 46 (2001) 1–184.

[44] Y. Zhu, K. Ameyama, P.M. Anderson, I.J. Beyerlein, H. Gao, H.S. Kim, E. Lavernia, S. Mathaudhu, H. Mughrabi, R.O. Ritchie, N. Tsuji, X. Zhang, X. Wu, Heterostructured materials: superior properties from hetero-zone interaction, Mater. Res. Lett. 9 (2021) 1–31.

[45] M.J. Starink, X.C. Cheng, S. Yang, Hardening of pure metals by high-pressure torsion: a physically based model employing volume-averaged defect evolutions, Acta Mater. 61 (2013) 183–192.

[46] T. Grosdidier, M. Novelli, L. Weiss, Surface severe plastic deformation for improved mechanical/corrosion properties and further applications in the bio-medical and hydrogen sectors, Mater. Trans. 64 (2023) 1695–1708.

[47] A.K. Ghosh, W. Huang, Severe deformation based process for gain subdivision and resulting microstructures, in: T.C. Lowe, R.Z. Valiev (Eds.), Investigations and applications of severe plastic deformation, Springer,, Dordrecht, 2000, pp. 29–36.

[48] Y. Beygelzimer, D. Orlov, V. Varyukhin, A new severe plastic deformation method: twist extrusion, Ultra Graine Mater. II 2002 (2002) 297–304.

[49] J. Richert, M. Richert, A new method for unlimited deformation of metals and alloys, Aluminum 62 (1986) 604–607.

[50] G. Faraji, H.S. Kim, H.T. Kashi, Severe plastic deformation: methods, processing and properties, Elsevier,, 2018.

[51] A. Hohenwarter, Incremental high pressure torsion as a novel severe plastic deformation process: Processing features and application to copper, Mater. Sci. Eng. A 626 (2015) 80–85.

[52] M. Eskandarzade, A. Masoumi, G. Faraji, M. Mohammadpour, X.S. Yan, A new designed incremental high pressure torsion process for producing long nanostructured rod samples, J. Alloy. Compd. 695 (2017) 1539–1546.

[53] K. Edalati, Z. Horita, Continuous high-pressure torsion, J. Mater. Sci. 45 (2010) 4578–4582.

[54] J.T. Wang, Z. Li, J. Wang, T.G. Langdon, Principles of severe plastic deformation using tube high-pressure shearing, Scr. Mater. 67 (2012) 810–813.

[55] G. Faraji, H. Kim, Review of principles and methods of severe plastic deformation for producing ultrafine-grained tubes, Mater. Sci. Technol. 33 (2017) 905–923.

[56] Y. Harai, Y. Ito, Z. Horita, High-pressure torsion using ring specimens, Scr. Mater. 58 (2008) 469–472.

[57] T. Fujioka, Z. Horita, Development of high-pressure sliding process for microstructural refinement of rectangular metallic sheets, Mater. Trans. 50 (2009) 930–933.

[58] Y. Ivanisenko, R. Kulagin, V. Fedorov, A. Mazilkin, T. Scherer, B. Baretzky, H. Hahn, High pressure torsion extrusion as a new severe plastic deformation process, Mater. Sci. Eng. A 664 (2016) 247–256.

[59] D. Gunderov, A. Churakova, V. Astanin, R. Asfandiyarov, H. Hahn, R. Valiev, Accumulative HPT of Zr-based bulk metallic glasses, Mater. Lett. 261 (2020) 127000.

[60] A. Hohenwarter, R. Pippan, Introduction of planar high pressure torsion (P-HPT) for fabrication of nanostructured sheets, Adv. Eng. Mater. 20 (2018) 1800050.

[61] Y. Nishida, H. Arima, J.C. Kim, T. Ando, Rotary-die equal-channel angular pressing of an Al–7 mass% Si–0.35 mass% Mg alloy, Scr. Mater. 45 (2001) 261–266.

[62] V. Popov, E. Popova, D. Kuznetsov, A. Stolbovsky, E. Shorohov, P. Nasonov, K. Gaan, G. Reglitz, S. Divinski, G. Wilde, Evolution of Ni structure at dynamic channel-angular pressing, Mater. Sci. Eng. A 585 (2013) 281–291.

[63] A. Azushima, K. Aoki, Properties of ultrafine-grained steel by repeated shear deformation of side extrusion process, Mater. Sci. Eng. A 337 (2002) 45–49.

[64] V.A. Beloshenko, V.N. Varyukhin, A.V. Voznyak, Y.V. Voznyak, Equal-channel multiangular extrusion of semicrystalline polymers, Polym. Eng. Sci. 50 (2010) 1000–1006.

[65] R. Boulahia, J.M. Gloaguen, F. Zaïri, M. Naït-Abdelaziz, R. Seguela, T. Boukharouba, J.M. Lefebvre, Deformation behaviour and mechanical properties of polypropylene processed by equal channel angular extrusion: effects of back-pressure and extrusion velocity, Polymer 50 (2009) 5508–5517.

[66] Z. Liu, G. Liang, E. Wang, Z. Wang, The effect of cumulative large plastic strain on the structure and properties of a Cu-Zn alloy, Mater. Sci. Eng. A 242 (1998) 137–140.

[67] M. Ensafi, G. Faraji, H. Abdolvand, Cyclic extrusion compression angular pressing (CECAP) as a novel severe plastic deformation method for producing bulk ultrafine grained metals, Mater. Lett. 197 (2017) 12–16.

[68] M. Rassa, G. Azadkoli, M. Eftekhari, A. Fata, G. Faraji, Effects of equal channel angular pressing (ECAP) process with an additional expansion-extrusion stage on microstructure and mechanical properties of Mg-9Al-1Zn, J. Adv. Mater. Process. 9 (2021) 43–52.

[69] R. Kocich, L. Kunčická, P. Král, A. Macháčková, Sub-structure and mechanical properties of twist channel angular pressed aluminium, Mater. Charact. 119 (2016) 75–83.

[70] R. Kocich, A. Macháčková, L. Kunčická, Twist channel multi-angular pressing (TCMAP) as a new SPD process: numerical and experimental study, Mater. Sci. Eng. A 612 (2014) 445–455.

[71] U. Chakkingal, A.B. Suriadi, P.F. Thomson, Microstructure development during equal channel angular drawing of Al at room temperature, Scr. Mater. 39 (1998) 677–684.

[72] Q. Wang, Y. Chen, J. Lin, L. Zhang, C. Zhai, Microstructure and properties of magnesium alloy processed by a new severe plastic deformation method, Mater. Lett. 61 (2007) 4599–4602.

[73] B. Mani, M. Jahedi, M.H. Paydar, Consolidation of commercial pure aluminum powder by torsional-equal channel angular pressing (T-ECAP) at room temperature, Powder Technol. 219 (2012) 1–8.

[74] S. Sepahi-Boroujeni, F. Fereshteh-Saniee, Expansion equal channel angular extrusion, as a novel severe plastic deformation technique, J. Mater. Sci. 50 (2015) 3908–3919.

[75] A. Babaei, G. Faraji, M.M. Mashhadi, M. Hamdi, Repetitive forging (RF) using inclined punches as a new bulk severe plastic deformation method, Mater. Sci. Eng. A 558 (2012) 150–157.

[76] F. Rahimi, A. Eivani, A new severe plastic deformation technique based on pure shear, Mater. Sci. Eng. A 626 (2015) 423–431.

[77] W. Chrominski, L. Olejnik, A. Rosochowski, M. Lewandowska, Grain refinement in technically pure aluminium plates using incremental ECAP processing, Mater. Sci. Eng. A 636 (2015) 172–180.

[78] B. Talebanpour, R. Ebrahimi, K. Janghorban, Microstructural and mechanical properties of commercially pure aluminum subjected to dual equal channel lateral extrusion, Mater. Sci. Eng. A 527 (2009) 141–145.

[79] V.Q. Vu, Y. Beygelzimer, L.S. Toth, J.J. Fundenberger, R. Kulagin, C. Chen, The plastic flow machining: a new SPD process for producing metal sheets with gradient structures, Mater. Charact. 138 (2018) 208–214.

[80] V.Q. Vu, L.S. Toth, Y. Beygelzimer, Y. Zhao, Microstructure, texture and mechanical properties in aluminum produced by friction-assisted lateral extrusion, Materials 14 (2021) 2465.

[81] A. Rosochowski, L. Olejnik, J. Richert, M. Rosochowska, M. Richert, Equal channel angular pressing with converging billets—experiment, Mater. Sci. Eng. A 560 (2013) 358–364.

[82] N. Pardis, R. Ebrahimi, Deformation behavior in simple shear extrusion (SSE) as a new severe plastic deformation technique, Mater. Sci. Eng. A 527 (2009) 355–360.

[83] L. Zaharia, R. Chelariu, R. Comaneci, Multiple direct extrusion: a new technique in grain refinement, Mater. Sci. Eng. A 550 (2012) 293–299.

[84] M. Shahbaz, N. Pardis, R. Ebrahimi, B. Talebanpour, A novel single pass severe plastic deformation technique: vortex extrusion, Mater. Sci. Eng. A 530 (2011) 469–472.

[85] G.K. Muralidharan, B. Verlinden, Novel severe plastic deformation technique—accumulated extrusion (AccumEx), Mater. Sci. Technol. 32 (2016) 547–555.

[86] S. Amirkhanlou, M. Ketabchi, N. Parvin, A. Orozco-Caballero, F. Carreño, Homogeneous and ultrafine-grained metal matrix nanocomposite achieved by accumulative press bonding as a novel severe plastic deformation process, Scr. Mater. 100 (2015) 40–43.

[87] N. Pardis, B. Talebanpour, R. Ebrahimi, S. Zomorodian, Cyclic expansion-extrusion (CEE): a modified counterpart of cyclic extrusion-compression (CEC), Mater. Sci. Eng. A 528 (2011) 7537–7540.

[88] M. Riahi, M. Ehsanian, A. Asgari, F. Djavanroodi, On a novel severe plastic deformation method: severe forward extrusion (SFE), Int. J. Adv. Manuf. Technol. 93 (2017) 1041–1050.

[89] M. Ebrahimi, F. Djavanroodi, Experimental and numerical analyses of pure copper during ECFE process as a novel severe plastic deformation method, Prog. Nat. Sci: Mater. Int. 24 (2014) 68–74.

[90] F. Khodabakhshi, A.P. Gerlich, Accumulative fold-forging (AFF) as a novel severe plastic deformation process to fabricate a high strength ultra-fine grained layered aluminum alloy structure, Mater. Charact. 136 (2018) 229–239.

[91] S.M. Fatemi-Varzaneh, A. Zarei-Hanzaki, Accumulative back extrusion (ABE) processing as a novel bulk deformation method, Mater. Sci. Eng. A 504 (2009) 104–106.

[92] T. Aizawa, K. Tokumitsu, Bulk mechanical alloying for productive processing of functional alloys, J. Metastable Nanocryst. Mater. 2– 6 (1999) 13–22.

[93] J. Metayer, Y. Bing, G. Wei, Q.D. Wang, Z. Hao, F. Mollet, Microstructure and mechanical properties of Mg–Si alloys processed by cyclic closed-die forging, Trans. Nonferrous Met. Soc. China 24 (2014) 66–75.

[94] J. Huang, Y. Zhu, H. Jiang, T. Lowe, Microstructures and dislocation configurations in nanostructured Cu processed by repetitive corrugation and straightening, Acta Mater. 49 (2001) 1497–1505.

[95] M.R. Toroghinejad, R. Jamaati, J. Dutkiewicz, J.A. Szpunar, Investigation of nanostructured aluminum/copper composite produced by accumulative roll bonding and folding process, Mater. Des. 51 (2013) 274–279.

[96] Y. Huang, P. Prangnell, Continuous frictional angular extrusion and its application in the production of ultrafine-grained sheet metals, Scr. Mater. 56 (2007) 333–336.

[97] M. Sedighi, M. Mahmoodi, Residual stresses evaluation in equal channel angular rolled Al 5083 by IHD technique: investigation of two calculation methods, Mater. Manuf. Process. 28 (2012) 85–90.

[98] H. Utsunomiya, Y. Saito, T. Hayashi, T. Sakai, Rolling of T-shaped profiled strip by the satellite mill, J. Mater. Eng. Perform. 6 (1997) 319–325.

[99] O. Bouaziz, Y. Estrin, H.S. Kim, Severe plastic deformation by the cone-cone method: potential for producing ultrafine grained sheet material, Rev. Met. Paris 104 (2007) 318–322.

[100] D.H. Shin, J.J. Park, Y.S. Kim, K.T. Park, Constrained groove pressing and its application to grain refinement of aluminum, Mater. Sci. Eng. A 328 (2002) 98–103.

[101] M. Borhani, F. Djavanroodi, Rubber pad-constrained groove pressing process: experimental and finite element investigation, Mater. Sci. Eng. A 546 (2012) 1–7.

[102] A. Shahmirzaloo, G. Faraji, M. Safari, S. Mohammadinejad, Interface sheet-constrained groove pressing as a modified severe plastic deformation process, Mater. Sci. Technol. 34 (2018) 1669–1678.

[103] R.S. Mishra, M. Mahoney, S. McFadden, N. Mara, A. Mukherjee, High strain rate superplasticity in a friction stir processed 7075 Al alloy, Scr. Mater. 42 (1999) 163–168.

[104] G. Faraji, M.M. Mashhadi, H.S. Kim, Tubular channel angular pressing (TCAP) as a novel severe plastic deformation method for cylindrical tubes, Mater. Lett. 65 (2011) 3009–3012.

[105] G. Faraji, A. Babaei, M.M. Mashhadi, K. Abrinia, Parallel tubular channel angular pressing (PTCAP) as a new severe plastic deformation method for cylindrical tubes, Mater. Lett. 77 (2012) 82–85.

[106] H. Abdolvand, H. Sohrabi, G. Faraji, F. Yusof, A novel combined severe plastic deformation method for producing thin-walled ultrafine grained cylindrical tubes, Mater. Lett. 143 (2015) 167–171.

[107] O. Shapourgan, G. Faraji, Rubber pad tube straining as a new severe plastic deformation method for thin-walled cylindrical tubes, Proc. Inst. Mech. Eng. B: J. Eng. Manuf. 230 (2016) 1845–1854.

[108] H. Torabzadeh, G. Faraji, E. Zalnezhad, Cyclic flaring and sinking (CFS) as a new severe plastic deformation method for thin-walled cylindrical tubes, Trans. Indian Inst. Met. 69 (2016) 1217–1222.

[109] M. Mohebbi, A. Akbarzadeh, Accumulative spin-bonding (ASB) as a novel SPD process for fabrication of nanostructured tubes, Mater. Sci. Eng. A 528 (2010) 180–188.

[110] M. Torabi, A.R. Eivani, H. Jafarian, M.T. Salehi, Die design modification to improve workability during equal channel angular pressing, Adv. Eng. Mater. 18 (2016) 1469–1477.

[111] L.S. Tóth, R. Lapovok, A. Hasani, C. Gu, Non-equal channel angular pressing of aluminum alloy, Scr. Mater. 61 (2009) 1121–1124.

[112] K. Kim, J. Yoon, Evolution of the microstructure and mechanical properties of AZ61 alloy processed by half channel angular extrusion (HCAE), a novel severe plastic deformation process, Mater. Sci. Eng. A 578 (2013) 160–166.

[113] D. Orlov, G. Raab, T.T. Lamark, M. Popov, Y. Estrin, Improvement of mechanical properties of magnesium alloy ZK60 by integrated extrusion and equal channel angular pressing, Acta Mater. 59 (2011) 375–385.

[114] S. Lei, L. Hao, J. Wenzhong, L. Zhiyu, L. Guihua, W. Xiaofeng, Portholes-equal channel angular pressing: novel technique for extrusion of 6061 aluminum alloy tube by subsize billet, Int. J. Adv. Manuf. Technol. 85 (2016) 355–363.

[115] L. Lu, C. Liu, J. Zhao, W. Zeng, Z. Wang, Modification of grain refinement and texture in AZ31 Mg alloy by a new plastic deformation method, J. Alloy. Compd. 628 (2015) 130–134.

[116] F. Abu-Farha, A preliminary study on the feasibility of friction stir back extrusion, Scr. Mater. 66 (2012) 615–618.

[117] M. Ahmadkhanbeigi, O. Shapourgan, G. Faraji, Microstructure and mechanical properties of Al tube processed by friction stir tube back extrusion (FSTBE), Trans. Indian Inst. Met. 70 (2017) 1849–1856.

[118] R. Ebrahimi, M. Reihanian, M. Moshksar, An analytical approach for radial-forward extrusion process, Mater. Des. 29 (2008) 1694–1700.

[119] V. Shatermashhadi, B. Manafi, K. Abrinia, G. Faraji, M. Sanei, Development of a novel method for the backward extrusion, Mater. Des. 62 (2014) 361–366.

[120] P. Rostami, G. Faraji, A. Sadeghi, M. Baghani, Microstructure and mechanical properties of CP-titanium processed by ECAP followed by warm caliber rolling, Trans. Indian Inst. Met. 71 (2018) 1083–1090.

[121] J.T. Maximov, T.V. Kuzmanov, G.V. Duncheva, N. Ganev, Spherical motion burnishing implemented on lathes, Int. J. Mach. Tools Manuf. 49 (2009) 824–831.

[122] W.L. Li, N.R. Tao, K. Lu, Fabrication of a gradient nano-micro-structured surface layer on bulk copper by means of a surface mechanical grinding treatment, Scr. Mater. 59 (2008) 546–549.

[123] K.H. Kloos, J. Adelmann, Effect of deep rolling on fatigue properties of cast irons, J. Mech. Behav. Mater. 2 (1989) 75–86.

[124] A.T. Bozdana, N.N.Z. Gindy, H. Li, Deep cold rolling with ultrasonic vibrations - A new mechanical surface enhancement technique, Int. J. Mach. Tools Manuf. 45 (2005) 713–718.

[125] H.W. Huang, Z.B. Wang, J. Lu, K. Lu, Fatigue behaviors of AISI 316L stainless steel with a gradient nanostructured surface layer, Acta Mater. 87 (2015) 150–160.

[126] M. Liu, J.Y. Li, Y. Ma, T.Y. Yuan, Q.S. Mei, Surface nanocrystallization and property of Ti6Al4V alloy induced by high pressure surface rolling, Surf. Coat. Technol. 289 (2016) 94–100.

[127] P. Chui, K. Sun, C. Sun, C. Wu, H. Wang, Y. Zhao, Effect of surface nanocrystallization induced by fast multiple rotation rolling on mechanical properties of a low carbon steel, Mater. Des. 35 (2012) 754–759.

[128] R.G. Aftanaziv, A.I. Bassarab, Y.B. Kyryliv, Mechanical and corrosion characteristics of 40Kh steel after vibration-centrifugal hardening treatment, Mater. Sci. 38 (2002) 436–441.

[129] I.H. Cho, G.H. Song, C.S. Kim, A. Nobuhide, A. Combs, J. Park, C.M. Suh, J.H. Park, Y.S. Pyoun, Nano structured surface modification of tool steel and its beneficial effects in mechanical properties, J. Mech. Sci. Technol. 19 (2005) 2151–2156.

[130] I. Cho, C.S. Kim, S.G. Jin, J.G. Moon, Y.S. Pyoun, D.H. Jeong, K.B. Lee, Nano surface modification of hub bearing race ways for increasing the dynamic load rating and decreasing the friction loss, SAE Tech. Pap. (2007) 2007–01-3735.

[131] B.N. Mordyuk, G.I. Prokopenko, Fatigue life improvement of α-titanium by novel ultrasonically assisted technique, Mater. Sci. Eng. A 437 (2006) 396–405.

[132] B.N. Mordyuk, G.I. Prokopenko, M.A. Vasylyev, M.O. Iefimov, Effect of structure evolution induced by ultrasonic peening on the corrosion behavior of AISI-321 stainless steel, Mater. Sci. Eng. A 458 (2007) 253–261.

[133] B.N. Mordyuk, G.I. Prokopenko, Ultrasonic impact peening for the surface properties' management, J. Sound Vib. 308 (2007) 855–866.

[134] N.R. Tao, Z.B. Wang, W.P. Tong, M.L. Sui, J. Lu, K. Lu, An investigation of surface nanocrystallization mechanism in Fe induced by surface mechanical attrition treatment, Acta Mater. 50 (2002) 4603–4616.

[135] M. Dehghan, R. Miresmaeili, M. Askari-Paykani, H.R. Shahverdi, Effects of a novel severe plastic deformation approach on microstructural and mechanical characteristics of a medium manganese advanced high strength steel, Met. Mater. Int. 28 (2022) 1232–1245.

[136] S. Bagherifard, I. Fernández-Pariente, R. Ghelichi, M. Guagliano, Fatigue properties of nanocrystallized surfaces obtained by high energy shot peening, Procedia Eng. 2 (2010) 1683–1690.

[137] M. Guagliano, S. Bagherifard, I.F. Parienete, R. Ghelichi, Assessment of severe shot peening on surface characteristics of Al alloys, SDHM Struct. Durab. Heal. Monit. 6 (2010) 31–42.

[138] E. Maleki, S. Bagherifard, O. Unal, M. Bandini, G.H. Farrahi, M. Guagliano, Introducing gradient severe shot peening as a novel mechanical surface treatment, Sci. Rep. 11 (2021) 22035.

[139] D.D. Arola, M.L. McCain, Abrasive waterjet peening: A new method of surface preparation for metal orthopedic implants, J. Biomed. Mater. Res 53 (2000) 536–546.

[140] M.D. Sangid, J.A. Stori, P.M. Ferriera, Process characterization of vibrostrengthening and application to fatigue enhancement of aluminum aerospace components - part I. experimental study of process parameters, Int. J. Adv. Manuf. Technol. 53 (2011) 545–560.

[141] P. Bournot, D. Dufresne, M. Autric, P. Giovanneschi-Testud, C. Coquerelle, Surface treatment by laser generated shock waves, High. Power Lasers 801 (1987), https://doi.org/10.1117/12.941258.

[142] W.M. Thomas, E.D. Nicholas, J.C. Needham, M.G. Murch, P. Templesmith, C.J. Dawes: Friction stir butt welding, G.B. Patent Application, 9125978.8, 1991.

[143] V. Kyryliv, Y. Kyryliv, N. Sas, Formation of surface ultrafine grain structure and their physical and mechanical characteristics using vibration-centrifugal hardening, Adv. Mater. Sci. Eng. 2018 (2018) 3152170.

[144] M. Paques, M.H. Yan, C. Benoit, T. Sylvain, B. Jawad, M. Etienne, Investigation on the relationship between the vibratory peening process parameters and Almen intensity, J. Mach. Eng.;23 (2023) 98–115.

[145] M. Wang, S. Konovalov, F. Dai, X. Chen, Influence of process parameters on laser shock processing effect of aero-engine blades, J. Surf. Investig. 16 (2022) 1208–1220.

[146] H.J. Jung, Y. Sohn, H.G. Sung, H.S. Hyun, W.G. Shin, Physicochemical properties of ball milled boron particles: dry vs. wet ball milling process, Powder Technol. 269 (2015) 548–553.

[147] T.P. Yadav, R.M. Yadav, D.P. Singh, Mechanical milling: a top down approach for the synthesis of nanomaterials and nanocomposites, Nanosci. Nanotechnol. 2 (2012) 22–48.

[148] L. Takacs, Self-sustaining reactions induced by ball milling, Prog. Mater. Sci. 47 (2002) 355–414.

[149] C.C. Koch, D. Whittenberger, Mechanical milling/alloying of intermetallics, Intermetallics 4 (1996) 339–355.

[150] B.S. Murty, S. Ranganathan, Novel materials synthesis by mechanical alloying/ milling, Int. Mater. Rev. 43 (1998) 101–141.

[151] G. Gorrasi, A. Sorrentino, Mechanical milling as a technology to produce structural and functional bio-nanocomposites, Green. Chem. 17 (2015) 2610–2625.

[152] J. Joy, A. Krishnamoorthy, A. Tanna, V. Kamathe, R. Nagar, S. Srinivasan, Recent developments on the synthesis of nanocomposite materials via ball milling approach for energy storage applications, Appl. Sci. 12 (2022) 9312.

[153] M. Ota, S.K. Vajpai, R. Imao, K. Kurokawa, K. Ameyama, Application of high pressure gas jet mill process to fabricate high performance harmonic structure designed pure titanium, Mater. Trans. 56 (2015) 154–159.

[154] G. Faraji, H. Torabzadeh, An overview on the continuous severe plastic deformation methods, Mater. Trans. 60 (2019) 1316–1330.

[155] S.M. Ghalehbandi, M. Malaki, M. Gupta, Accumulative roll bonding - a review, Appl. Sci. 9 (2019) 3627.

[156] G.J. Raab, R.Z. Valiev, T.C. Lowe, Y.T. Zhu, Continuous processing of ultrafine grained Al by ECAP–conform, Mater. Sci. Eng. A382 (2004) 30–34.

[157] A.R.R.M. Zohrevand, M.R. Sabour, E. Taherkhani, G. Faraji, Recent progress on SPD processes empowered by hydrostatic pressure, Mater. Trans. 64 (2023) 1663–1672.

[158] Y. Ivanisenko, Perspectives of scaling up of severe plastic deformation: a case of high pressure torsion extrusion, Mater. Trans. 2023 64 (2023) 1489–1496.

[159] Z. Li, Y. Liu, J.T. Wang, T.G. Langdon, Tube high-pressure shearing: a simple shear path to unusual microstructures and unprecedented properties, Mater. Trans. 64 (2023) 1449–1463.

[160] Y. Takizawa, Z. Horita, Incremental feeding high-pressure sliding (IF-HPS) process for upscaling highly strained areas in metallic materials with enhanced mechanical properties, Mater. Trans. 64 (2023) 1364–1375.

[161] L. Kommel, Microstructure and properties that change during hard cyclic visco-plastic deformation of bulk high purity niobium, Int. J. Refract. Met. Hard Mater. 79 (2019) 10–17.

[162] E. Tabachnikova, T. Hryhorova, S. Shumilin, Y. Semerenko, Y. Huang, T. G. Langdon, Cryo-severe plastic deformation, microstructures and properties of metallic nanomaterials at low temperatures, Mater. Trans. 64 (2023) 1806–1819.

[163] P. Verleysen, H. Lanjewar, Dynamic high pressure torsion: a novel technique for dynamic severe plastic deformation, J. Mater. Process. Techol 276 (2020) 116393.

[164] K. Edalati, Superfunctional materials by ultra-severe plastic deformation, Materials 16 (2023) 587.

[165] W. Sillekens, J. Bohlen, The MAGNEXTRUSCO project: European Community research on hydrostatic extrusion of magnesium, Proceedings of the 6th International Conference Magnesium Alloys and Their Applications, Wiley Online Library, 2003, pp. 1046–1051.

[166] R. Yuan, Z. Wu, H. Cai, L. Zhao, X. Zhang, Effects of extrusion parameters on tensile properties of magnesium alloy tubes fabricated by hydrostatic extrusion integrated with circular ECAP, Mater. Des. 101 (2016) 131–136.

[167] B. Manafi, V. Shatermashhadi, K. Abrinia, G. Faraji, M. Sanei, Development of a novel bulk plastic deformation method: hydrostatic backward extrusion, Int. J. Adv. Manuf. Technol. 82 (2016) 1823–1830.

[168] S. Jamali, G. Faraji, K. Abrinia, Hydrostatic radial forward tube extrusion as a new plastic deformation method for producing seamless tubes, Int. J. Adv. Manuf. Technol. 88 (2017) 291–301.

[169] V. Spuskanyuk, A. Spuskanyuk, V. Varyukhin, Development of the equal-channel angular hydroextrusion, J. Mater. Process. Technol. 203 (2008) 305–309.

[170] A. Siahsarani, G. Faraji, Hydrostatic cyclic extrusion compression (HCEC) process; a new CEC counterpart for processing long ultrafine-grained metals, Arch. Civ. Mech. Eng. 20 (2020) 108.

[171] F. Samadpour, G. Faraji, P. Babaie, S. Bewsher, M. Mohammadpour, Hydrostatic cyclic expansion extrusion (HCEE) as a novel severe plastic deformation process for producing long nanostructured metals, Mater. Sci. Eng. A 718 (2018) 412–417.

[172] M. Haghpanah, A. Esmaeilnia, M. Sabour, E. Taherkhani, M.M. Mashhadi, G. Faraji, Hydrostatic twist extrusion (HTE) for processing relatively long ultrafine grained samples, Mater. Lett. 333 (2022) 133660.

[173] M. Eftekhari, G. Faraji, M. Bahrami, Processing of commercially pure copper tubes by hydrostatic tube cyclic extrusion–compression (HTCEC) as a new SPD method, Arch. Civ. Mech. Eng. 21 (2021) 120.

[174] M.M. Savarabadi, G. Faraji, E. Zalnezhad, Hydrostatic tube cyclic expansion extrusion (HTCEE) as a new severe plastic deformation method for producing long nanostructured tubes, J. Alloy. Compd. 785 (2019) 163–168.

[175] G. Faraji, E. Taherkhani, M.R. Sabour, Cyclic severe plastic deformation processes, Ref. Modul. Mater. Sci. Mater. Eng. (2023) in press. https://doi.org/10.1016/B978-0-323-96020-5.00047-9.

[176] D. Orlov, Y. Beygelzimer, S. Synkov, V. Varyukhin, N. Tsuji, Z. Horita, Plastic flow, structure and mechanical properties in pure Al deformed by twist extrusion, Mater. Sci. Eng. A 519 (2009) 105–111.

[177] A.P. Zhilyaev, T.G. Langdon, Using high-pressure torsion for metal processing: fundamentals and applications, Prog. Mater. Sci. 53 (2008) 893–979.

[178] K. Edalati, Metallurgical alchemy by ultra-severe plastic deformation via high-pressure torsion process, Mater. Trans. 60 (2019) 1221–1229.

[179] Z. Horita, Y. Tang, T. Masuda, Y. Takizawa, Severe plastic deformation under high pressure: upsizing sample dimensions, Mater. Trans. 61 (2020) 1177–1190.

[180] R.Z. Valiev, B. Straumal, T.G. Langdon, Using severe plastic deformation to produce nanostructured materials with superior properties, Ann. Rev. Mater. Res. 52 (2022) 357–382.

[181] K. Edalati, E. Akiba, Z. Horita, High-pressure torsion for new hydrogen storage materials, Sci. Tech. Adv. Mat. 19 (2018) 185–193.

[182] I.A. Ovid'ko, R.Z. Valiev, Y.T. Zhu, Review on superior strength and enhanced ductility of metallic nanomaterials, Prog. Mater. Sci. 94 (2018) 462–540.

[183] V.T. Fedorov, Y. Ivanisenko, B. Baretzky, H. Hahn, Vorrichtung und Verfahren zur Umformung von Bauteilen aus Metallwerkstoffen, Ger. Pat. DE 10 213 (2013) 072.4.

[184] D. Nugmanov, R. Kulagin, O. Perroud, M. Mail, H. Hahn, Y. Ivanisenko, Equivalent strain distribution at high pressure torsion extrusion of pure copper: Finite element modeling and experimental validation, J. Mater. Process. Technol. 315 (2023) 117932.

[185] D. Nugmanov, Hybrid and ultrafine-grained materials produced by high pressure torsion extrusion, PhD Thesis, TU Darmstadt, 2023.

[186] R. Kulagin, Y. Beygelzimer, Y. Estrin, Y. Ivanisenko, B. Baretzky, H. Hahn, A mathematical model of deformation under high pressure torsion extrusion, Metals 9 (2019) 306.

[187] K. Lu, Making strong nanomaterials ductile with gradients, Science 345 (2014) 1455–1456.

[188] X.L. Wu, P. Jiang, L. Chen, F.P. Yuan, Y.T. Zhu, Extraordinary strain hardening by gradient structure, Proc. Natl. Acad. Sci. USA 111 (2014) 7197–7201.

[189] O. Renk, R. Pippan, Saturation of grain refinement during severe plastic deformation of single phase materials: reconsiderations, current status and open questions, Mater. Trans. 60 (2019) 1270–1282.

[190] D. Nugmanov, A. Mazilkin, H. Hahn, Y. Ivanisenko, Structure and tensile strength of pure Cu after high pressure torsion extrusion, Metals 9 (2019) 1081.

[191] B. Omranpour, Y. Ivanisenko, R. Kulagin, L. Kommel, E. Garcia Sanchez, D. Nugmanov, T. Scherer, A. Heczel, J. Gubicza, Evolution of microstructure and hardness in aluminum processed by high pressure torsion extrusion, Mater. Sci. Eng. A 762 (2019) 138074.

[192] B. Omranpour, L. Kommel, E. Garcia Sanchez, Y. Ivanisenko, J. Huot, Enhancement of hydrogen storage in metals by using a new technique in severe plastic deformations, Key Eng. Mater. 799 (2019) 173–178.

[193] R.Z. Valiev, T.G. Langdon, Principles of equal-channel angular pressing as a processing tool for grain refinement Progr, Mater. Sci. 517 (2006) 881–981.

[194] R.Z. Valiev, I.V. Alexandrov, Y.T. Zhu, T.C. Lowe, Paradox of strength and ductility in metals processed by severe plastic deformation, J. Mater. Res 17 (2002) 5–8.

[195] Y. Beygelzimer, Y. Estrin, R. Kulagin, Synthesis of hybrid materials by severe plastic deformation: a new paradigm of SPD processing, Adv. Eng. Mater. 17 (2015) 1853–1861.

[196] Y. Estrin, Y. Beygelzimer, R. Kulagin, Design of architectured materials based on mechanically driven structural and compositional patterning, Adv. Eng. Mat. 21 (2019) 1900487.

[197] U.G.K. Wegst, H. Bai, E. Saiz, A.P. Tomsia, R.O. Ritchie, Bioinspired structural materials, Nat. Mater. 14 (2015) 23–36.

[198] L. Li, J.C. Weaver, Ch Ortiz, Hierarchical structural design for fracture resistance in the shell of the pteropod *Clio pyramidata*, Nat. Comm. 6 (2015) 6216.

[199] Y. Beigelzimer, V. Varyukhin, S. Synkov, D. Orlov, Useful properties of twist extrusion, Mat. Sci. Eng. A 503 (2009) 14–17.

[200] Z. Li, P.F. Zhang, H. Yuan, K. Lin, Y. Liu, D.L. Yin, J.T. Wang, T.G. Langdon, Principle of one-step synthesis for multilayered structures using high pressure shearing, Mater. Sci. Eng. A 658 (2016) 367–375.

[201] K. Lin, Z. Li, Y. Liu, E. Ma, J.T. Wang, T.G. Langdon, Exploiting tube high-pressure shearing to prepare a microstructure in Pb-Sn alloys for unprecedented superplasticity, Scr. Mater. 209 (2022) 114390.

[202] M. Wang, A. Shan, Severe plastic deformation introduced by rotation shear, J. Mater. Process. Technol. 202 (2008) 549–552.

[203] L.S. Tóth, M. Arzaghi, J.J. Fundenberger, B. Beausir, O. Bouaziz, R. Arruffat-Massion, Severe plastic deformation ofmetals by high-pressure tube twisting, Scr. Mater. 60 (2009) 175–177.

[204] M. Arzaghi, J.J. Fundenberger, L.S. Tóth, R. Arruffat, L. Faure, B. Beausir, X. Sauvage, Microstructure, texture and mechanical properties of aluminum processed by high-pressure tube twisting, Acta Mater. 60 (2012) 4393–4408.

[205] R. Lapovok, Y. Qi, H.P. Ng, L.S. Toth, Y. Estrin, Gradient structures in thin-walled metallic tubes produced by continuous high pressure tube shearing process, Adv. Eng. Mater. 19 (2017) 1700345.

[206] J.T. Wang, Z. Li, J. Wang, J.Q. Liu, D.L. Yin, Y. Liu: Tube High-pressure shearing deformation method and the device, Chinese Patent, 201110030903.0, 2011.

[207] J.T. Wang, Z. Li, J. Wang, Y.K. An: Method and device for realizing tube high-pressure shearing by using the wedge principle, Chinese Patent, 201110291933.7, 2011.

[208] J.J. Meng, Z. Li, Y. Liu, Y.B. Zhu, S. Wang, K. Lin, J.Q. Tao, J.T. Wang, Investigation on the strain distribution in tube high-pressure shearing, Matels 9 (2019) 1117.

[209] A. Pougis, L.S. Tóth, O. Bouaziz, J.-J. Fundenberger, D. Barbier, R. Arruffat, Stress and strain gradients in high-pressure tube twisting, Scr. Mater. 66 (2012) 773–776.

[210] L.S. Tóth, C. Chen, A. Pougis, M. Arzaghi, J.J. Fundenberger, R. Massion, S. Suwas, High pressure tube twisting for producing ultra fine grained materials: a review, Mater. Trans. 60 (2019) 1177–1191.

[211] J. Dvorak, V. Sklenicka, Z. Horita, Microstructural evolution and mechanical properties of high purity aluminium processed by equal-channel angular pressing, Mater. Trans. 49 (2008) 15–19.

[212] W. Skrotzki, N. Scheerbaum, C.G. Oertel, H.G. Brokmeier, S. Suwas, L.S. Tóth, Recrystallization of high-purity aluminium during equal channel angular pressing, Acta Mater. 55 (2007) 2211–2218.

[213] C. Choi, O. Changseok, D.N. Lee, J. Jeong, Room temperature recrystallization of 99.999 pct aluminum, Scr. Metall. Mater. 30 (1994) 325–330.

[214] F. Haessner, J. Schmidt, Investigation of the recrystallization of low temperature deformed highly pure types of aluminium, Acta Metall. Mater. 41 (1993) 1739–1749.

[215] M.E. Kassner, J. Pollard, E. Evangelista, E. Cerri, Restoration mechanisms in large-strain deformation of high purity aluminum at ambient temperature and the determination of the existence of steady-state, Acta Metall. Mater. 42 (1994) 3223–3230.

[216] A.A. Salem, T.G. Langdon, T.R. McNelley, S.R. Kalidindi, S.L. Semiatin, Strain-path effects on the evolution of microstructure and texture during the severe-plastic deformation of aluminum, Metall. Mater. Trans. A 37 (2006) 2879–2891.

[217] M.E. Kassner, M.M. Myshlyaev, H.J. McQueen, Large-strain torsional deformation in aluminum at elevated temperatures, Mater. Sci. Eng. A 108 (1989) 45–61.

[218] F. Huang, N.R. Tao, K. Lu, Effects of impurity on microstructure and hardness in pure Al subjected to dynamic plastic deformation at cryogenic temperature, J. Mater. Sci. Technol. 27 (2011) 628–632.

[219] S. Ferrasse, V. Segal, F. Alford, J. Kardokus, S. Strothers, Scale up and application of equal-channel angular extrusion for the electronics and aerospace industries, Mater. Sci. Eng. A 493 (2008) 130–140.

[220] Z. Li, L.Y. Li, Y.B. Zhu, K. Lin, Z.T. Ren, Y. Yang, Y. Liu, J.T. Wang, T.G. Langdon, Evidence for a stable single component sharp texture in high purity aluminum during tube high-pressure shearing at room temperature, Sci. Rep. 12 (2022) 17901.

[221] C. Chen, Y. Beygelzimer, L.S. Tóth, J.J. Fundenberger, Microstructure and strain in protrusions formed during severe plastic deformation of aluminum, Mater. Lett. 159 (2015) 253–256.

[222] D.R. Askeland, W.J. Wright, The Science and Engineering of Materials, Cengage Learning,, 2014, pp. 394–401.

[223] C.T. Wang, Z. Li, Y. He, J.T. Wang, T.G. Langdon, Microstructural evolution and tensile testing of a Bi–Sn (57-43) alloy processed by tube high-pressure shearing, Crystals 11 (2021) 1229.

[224] C.T. Wang, Z. Li, J.T. Wang, T.G. Langdon, New developments in the processing of metallic alloys for achieving exceptional superplastic properties, Mater. Res. Proc. 32 (2023) 3–14.

[225] U.F. Kocks, C.N. Tomé, H.R. Wenk, Texture and Anisotropy: Preferred Orientations in Polycrystals and Their Effect on Materials Properties, Cambridge University Press,, 1998.

[226] V.M. Segal, Materials processing by simple shear, Mater. Sci. Eng. A 197 (1995) 157–164.

[227] Y. Saito, N. Tsuji, H. Utsunomiya, T. Sakai, R.G. Hong, Ultra-fine grained bulk aluminum produced by accumulative roll-bonding (ARB) process, Scr. Mater. 39 (1998) 1221–1227.

[228] N. Tsuji, Y. Saito, H. Utsunomiya, S. Tanigawa, Ultra-fine grained bulk steel produced by accumulative roll-bonding (ARB) process, Scr. Mater. 40 (1999) 795–800.

[229] O. Valiakhmetov, R. Galeyev, G. Salishchev, Mechanical properties of titanium VT8 alloy with submicrocrystalline structure, Fiz. Metal. Met. 10 (1990) 204–206.

[230] G.A. Manjunath, S. Shivakumar, R. Fernandez, R. Nikhil, P.C. Sharath, A review on effect of multi-directional forging/multi-axial forging on mechanical and microstructural properties of aluminum alloy, Mater. Today 47 (2021) 2565–2569.

[231] Z. Xu, S. Schroeder, P. Berbon, T.G. Langdon, Principles of ECAP-conform as a continuous process for achieving grain refinement: application to an aluminum alloy, Acta Mater. 58 (2010) 1379–1386.

[232] G.I. Raab, Plastic flow at equal channel angular processing in parallel channels, Mater. Sci. Eng. A 410– 411 (2005) 230–233.

[233] D. Gunderov, A.V. Polyakov, I.P. Semenova, G.I. Raab, A.A. Churakova, E. I. Gimaltdinova, I. Sabirov, J. Segurado, V.D. Sitdikov, I.V. Alezandrov, N. A. Enikeev, R.Z. Valiev, Evolution of microstructure, macrotexture and mechanical properties of commercially pure Ti during ECAP-conform processing and drawing, Mater. Sci. Eng. A 562 (2013) 128–136.

[234] M. Kamachi, A. Furukawa, Z. Horita, T.G. Langdon, Equal-channel angular pressing using plate samples, Mater. Sci. Eng. A 361 (2003) 258–266.

[235] K. Edalati, Z. Horita, Continuous high-pressure torsion using wires, J. Mater. Sci. 47 (2012) 473–478.

[236] R.Z. Valiev, Y. Estrin, Z. Horita, T.G. Langdon, M.J. Zehetbauer, Y.T. Zhu, Producing bulk ultrafine-grained materials by severe plastic deformation: ten years later, JOM 68 (2016) 1216–1226.

[237] I. Saunders, J. Nutting, Deformation of metals to high strains using combination of torsion and compression, Met. Sci. 18 (1984) 571–575.

[238] Y. Tang, K. Edalati, T. Masuda, Y. Takizawa, M. Yumoto, Z. Horita, Grain refinement and superplasticity of Inconel 718 processed by multi-pass high-pressure sliding, Mater. Let. 300 (2021) 130144.

[239] Y. Tang, K. Matsuda, Y. Takizawa, M. Yumoto, Y. Otagiri, Z. Horita, Grain refinement and superplasticity of pipes processed by high-pressure sliding, Mater. Sci. Techol. 36 (2020) 877–886.

[240] Y. Takizawa, K. Sumikawa, K. Watanabe, T. Masuda, M. Yumoto, Y. Kanai, Y. Otagiri, Z. Horita, Incremental feeding high-pressure sliding for grain refinement of largescale sheets application to Inconel 718, Metall, Mater. Trans. 49 (2018) 1830–1840.

[241] E. Shigeno, T. Komatsu, K. Sumikawa, T. Masuda, Y. Takizawa, M. Yumoto, Y. Otagiri, Z. Horita, Combination of high-pressure torsion with incremental feeding for upsizing sample, Mater. Trans. 59 (2018) 1009–1012.

[242] T. Komatsu, T. Masuda, Y. Tang, I.F. Mohamed, M. Yumoto, Y. Takizawa, Z. Horita, Production of ultrafine-grained aluminum alloys in upsized sheets using process of incremental feeding high-pressure sliding (IF-HPS), Mater. Trans. 64 (2023) 436–442.

[243] Y. Takizawa, K. Watanabe, T. Kajita, K. Sumikawa, T. Masuda, M. Yumoto, Y. Otagiri, Z. Horita, Incremental feeding high-pressure sliding for achieving large area of severe plastic deformation, J. Jpn. Inst. Met. Mater. 82 (2018) 25–31.

[244] Y. Takizawa, T. Kajita, P. Kral, T. Masuda, K. Watanabe, M. Yumoto, Y. Otagiri, V. Sclenicka, Z. Horita, Superplasticity of Inconel 718 after processing by high-pressure sliding (HPS), Mater. Sci. Eng. A 682 (2017) 603–612.

[245] V.M. Segal, Severe plastic deformation: simple shear versus pure shear, Mater. Sci. Eng. A 338 (2002) 331–344.

[246] R.E. Goforth, K.T. Hartwig, L.R. Cornwell, Severe plastic deformation of materials by equal channel angular extrusion (ECAE), in: T.C. Lowe, R.Z. Valiev (Eds.), Investigation and Application of Severe Plastic Deformation, Kluwer Academic Publishers,, 2000, pp. 3–12.

[247] B. Omranpour, L. Kommel, V. Mikli, E. Garcia, J. Huot, Nanostructure development in refractory metals: ECAP processing of niobium and tantalum using indirect-extrusion technique, Int. J. Refract. Met. Hard Mater. 79 (2019) 1–9.

[248] N. Pardis, C. Chen, R. Ebrahimi, L.S. Tóth, C.F. Gu, B. Beausir, L. Kommel, Microstructure, texture and mechanical properties of cyclic expansion-extrusion deformed pure copper, Mater. Sci. Eng. A 628 (2015) 423–432.

[249] J. Calaf-Chica, M.S. Palomar, P.M.B. Díez, M.P. Calzada, Deviations in yield and ultimate tensile strength estimation with the small punch test: numerical analysis of prestraining and Bauschinger effect influence, Mech. Mater. 153 (2021) 103696.

[250] N.S. Martynenko, N.R. Bochvar, P.B. Straumal, D.A. Aksenov, G.I. Raab, S. V. Dobatkin, Effect of equal-channel angular pressing on the structure, mechanical characteristics, and aging behavior of Cu-7%Cr and Cu-10% Fe alloys, Russ. Metall. 2021 (2021) 1085–1092.

[251] L. Kommel, The effect of HCV deformation on hardening/softening of SPD copper, in: Y.T. Zhu, T.G. Langdon, R.Z. Valiev (Eds.), Ultrafine Grained Materials III, The Minerals, Metals & Materials Society,, Charlotte, 2004, pp. 571–576.

[252] L. Kommel, The influence of development of new technology and materials on resource of gas turbine engines, in: S. Hietanen, P. Auersari (Eds.), Proceedings of the International Conference on Condition & Life Management for Power Plants, vol. 1, Finnish Forest Research Institute,, Helsinki, 2001, pp. 173–184.

[253] L. Kommel, A. Pokatilov, Electrical conductivity and mechanical properties of Cu-0.7wt%Cr and Cu-1.0wt% Cr alloys processed by severe plastic deformation, IOP Conf. Ser. Mater. Eng. 63 (2014) 012169.

[254] S.V. Dobatkin, J. Gubicza, D.V. Shangina, N.R. Bochvar, N.Y. Tabachkova, High strength and good electrical conductivity in Cu-Cr alloys processed by severe plastic deformation, Mater. Lett. 153 (2015) 5–9.

[255] L. Kommel, N. Pardis, E. Kimmari, Micromechanical properties and electrical conductivity of Cu and Cu-0.7wt% Cr alloy, I Proceedings of the 9th International DAAAM Baltic Conference "Industrial Engineering", Tallinn, Estonia, 2014, pp. 354–359.

[256] J.T. Yeom, S.J. Williams, I.S. Kim, N.K. Park, Unified viscoplastic models for low cycle fatigue behavior of Waspaloy, Met. Mater. Int. 7 (2001) 233–240.

[257] K. Kenk, On the constitutive modeling of viscoplasticity, In: Proceedings of VIII-th International Conference on Topical Problems of Mechanics, St. Petersburg, 2001, pp. 77–86.

[258] G. Li, A. Shojaei, A viscoplastic theory of shape memory polymer fibres with application to self-healing materials, Proc. R. Soc. A 468 (2012) 2319–2346.

[259] M. Dahlberg, P. Segle, Evaluation of models for cyclic plastic deformation – a literature study, Insp. Technol. AB 45 (2010) 62.

[260] M.K. Darabi, R.K. Abu Al-Rub, E.A. Masad, C.W. Huang, D.N. Little, A modified viscoplastic model to predict the permanent deformation of asphaltic materials under cyclic-compression loading at high temperatures, Int. J. Plast. 35 (2012) 100–134.

[261] L. Zhang, S. Ma, D. Liu, B. Zhou, B. Markert. Fretting wear modelling incorporating cyclic ratcheting deformations and the debris evolution for Ti-6Al-4V, Tribol. Int. 136 (2019) 317–331.

[262] B.K. Chun, J.T. Jinn, J.K. Lee, Modeling the Bauschinger effect for sheet metals, part I: theory, Int. J. Plast. 18 (2002) 571–595.

[263] B.K. Chun, H.Y. Kim, J.K. Lee, Modeling the Bauschinger effect for sheet metals, part II: applications, Int. J. Plast. 18 (2002) 597–616.

[264] L. Kommel, B.O. Shahreza, V. Mikli, Microstructure and physical-mechanical properties evolution of pure tantalum processed with hard cyclic viscoplastic deformation, Int. J. Refract. Met. Hard Mater. 83 (2019) 104983–1049993.

[265] L. Kommel, Effect of hard cyclic viscoplastic deformation on phase's chemical composition and micromechanical properties evolution in single crystal Ni-based superalloy, Acta Phys. Pol. A 128 (2015) 681–684.

[266] L. Kommel, Metals microstructure improving under hard cyclic viscoplastic deformation, Mater. Sci. Forum 584–586 (2008) 349–354.

[267] L. Kommel, J. Hout, B.O. Shahreza, Effect of hard cyclic viscoplastic deformation on the microstructure, mechanical properties, and electrical conductivity of Cu-Cr alloy, J. Mater. Eng. Perform. 31 (2022) 9690–9702.

[268] L. Kommel, Viscoplastic behavior of a single-crystal nickel-based superalloy, Mater. Sci. (Medžiagotyra) 15 (2009) 123–128.

[269] L. Kommel, Metals microstructure improving under hard cyclic viscoplastic deformation, Mater. Sci. Forum 584–586 (2008) 361–366.

[270] L. Kommel, I. Kommel, Damage evolution of structure and fracture of nanocrystalline copper at cyclic deformation. Deformation & Fracture of Materials, Moscow University Press,, 2006, pp. 411–414.

[271] H. Shahmir, M.S. Mehranpour, S.A.A. Shams, T.G. Langdon, Twenty years of the CoCrFeNiMn high-entropy alloy: achieving exceptional mechanical properties through microstructure engineering, J. Mater. Res. Technol. 23 (2023) 3362–3423.

[272] K. Edalati, T. Daio, M. Arita, S. Lee, Z. Horita, A. Togo, I. Tanaka, High-pressure torsion of titanium at cryogenic and room temperatures: grain size effect on allotropic phase transformations, Acta Mater. 68 (2014) 207–213.

[273] W. Skrotzki, R. Chulist, Severe plastic deformation of high-entropy alloys, Mater. Trans. 64 (2023) 1769–1783.

[274] R. Chulist, A. Pukenas, P. Chekhonin, A. Hohenwarter, R. Pippan, N. Schell, W. Skrotzki, Phase transformation induced by high pressure torsion in the high-entropy alloy CrMnFeCoNi, Materials 15 (2022) 8407.

[275] C. Wei, Y. Lu, X. Du, T. Li, T. Wang, P. Liaw, Remarkable strength of a non-equiatomic $Co_{29}Cr_{29}Fe_{29}Ni_{12.5}W_{0.5}$ high-entropy alloy at cryogenic temperatures, Mater. Sci. Eng. A 818 (2021) 141446.

[276] M.S. Mehranpour, H. Shahmir, M. Nili-Ahmadabadi, CoCrFeNiMn high entropy alloy microstructure and mechanical properties after severe cold shape rolling and annealing, Mater. Sci. Eng. A 793 (2020) 139884.

[277] P.A. Khaimovich, Cryodeformation of metals under isotropic compression, Low. Temp. Phys. 44 (2018) 349–370.

[278] V.A. Moskalenko, A.R. Smirnov, A.V. Moskalenko, Cryomechanically obtained nanocrystalline titanium: microstructure and mechanical properties, Low. Temp. Phys. 35 (2009) 905–907.

[279] V.A. Moskalenko, V.I. Betekhtin, B.K. Kardashev, A.G. Kadomtsev, A.R. Smirnov, R.V. Smolyanets, M.V. Narykova, Mechanical properties and structural features of nanocrystalline titanium produced by cryorolling, Phys. Solid State 56 (2014) 1590–1596.

[280] V.A. Moskalenko, A.R. Smirnov, Y.M. Plotnikova, I.S. Braude, R.V. Smolianets, Fundamentals of titanium nanocrystalline structure creation by cryomechanical grain fragmentation, Mater. Sci. Eng. A 700 (2017) 707–713.

[281] S.V. Zherebtsov, G.S. Dyakonov, A.A. Salem, V.I. Sokolenko, G.A. Salishchev, S. L. Semiatin, Formation of nanostructures in commercial-purity titanium via cryorolling, Acta Mater. 61 (2013) 1167–1178.

[282] V.A. Moskalenko, R.V. Smolianets, V.D. Natsik, Y.M. Pohribna, Dislocation mechanisms of low-temperature plasticity of nanocrystalline titanium: the role of impurity and grain boundary strengthening, Low. Temp. Phys. 49 (2023) 268–276.

[283] A.V. Podolskiy, H.P. Ng, I.A. Psaruk, E.D. Tabachnikova, R. Lapovok, Cryogenic equal channel angular pressing of commercially pure titanium: microstructure and properties, J. Mater. Sci. 49 (2014) 6803–6812.

[284] A.V. Podolskiy, C. Mangler, E. Schafler, E.D. Tabachnikova, M.J. Zehetbauer, Microstructure and mechanical properties of high purity nanostructured titanium processed by high pressure torsion at temperatures 300 and 77 K, J. Mater. Sci. 48 (2013) 4689–4697.

[285] E.D. Tabachnikova, A.V. Podolskiy, S.N. Smirnov, M.A. Tikhonovsky, P. A. Khaimovich, N.I. Danylenko, S.A. Firstov, Mechanical properties of the nanostructured Ti processed by combination of the severe plastic deformation methods, Bulletin of KhNU series, Physics 28 (2018) 63–67.

[286] A.V. Podolskiy, E.D. Tabachnikova, B. Bonarski, D. Setman, C. Mangler, E. Schafler, M.J. Zehetbauer, Temperature dependent mechanical properties of zirconium processed by high-pressure torsion at 300 and 77 K, Kov. Mater. 54 (2016) 1–8.

[287] A.V. Podolskiy, D. Geist, E. Schafler, E.D. Tabachnikova, M.J. Zehetbauer, Structure and properties of nanostructured Cobalt processed by high pressure torsion at temperatures of 300 and 77 K, IOP Conf. Ser. Mater. Sci. Eng. 63 (2014) 012103.

[288] J. Moon, Y. Qi, E. Tabachnikova, Y. Estrin, W.M. Choi, S.H. Joo, B.J. Lee, A. Podolskiy, M. Tikhonovsky, H.S. Kim, Microstructure and mechanical properties of high-entropy alloy $Co_{20}Cr_{26}Fe_{20}Mn_{20}Ni_{14}$ processed by high-pressure torsion at 77 K and 300 K, Sci. Rep. 8 (2018) 11074.

[289] A.V. Podolskiy, Y.O. Shapovalov, E.D. Tabachnikova, A.S. Tortika, M. A. Tikhonovsky, B. Joni, E. Ódor, T. Ungar, S. Maier, C. Rentenberger, M. J. Zehetbauer, E. Schafler, Anomalous evolution of strength and microstructure of high-entropy alloy CoCrFeNiMn, after high pressure torsion at 300 and 77 K, Adv. Eng. Mater. 22 (2020) 1900752.

[290] W. Skrotzki, A. Pukenas, E. Odor, B. Joni, T. Ungar, B. Völker, A. Hohenwarter, R. Pippan, E. George, Microstructure, texture, and strength development during high-pressure torsion of CrMnFeCoNi high-entropy alloy, Crystals 10 (2020) 336.

[291] Y. Shapovalov, E.D. Tabachnikova, M.A. Tikhonovsky, A.V. Levenets, M. J. Zehetbauer, E. Schafler, Effect of temperature of severe plastic deformation on mechanical properties of high entropy alloy CoCrFeNiMn, J. Karazin Kharkiv Natl. Univ. Ser. Phys. 32 (2020) 59–64.

[292] J. Moon, Y. Qi, E. Tabachnikova, Y. Estrin, W.M. Choi, S.H. Joo, B.J. Lee, A. Podolskiy, M. Tikhonovsky, H.S. Kim, Deformation-induced phase transformation of $Co_{20}Cr_{26}Fe_{20}Mn_{20}Ni_{14}$ high-entropy alloy during high-pressure torsion at 77 K, Mater. Lett. 202 (2017) 86–88.

[293] H.V. Rusakova, L.S. Fomenko, S.N. Smirnov, A.V. Podolskiy, Y.O. Shapovalov, E. D. Tabachnikova, M.A. Tikhonovsky, M.J. Zehetbauer, E. Schafler, Low temperature micromechanical properties of nanocrystalline CoCrFeNiMn high entropy alloy, Mater. Sci. Eng. A 828 (2021) 142116.

[294] A.V. Levenets, H.V. Rusakova, L.S. Fomenko, Y. Huang, V. Kolodiy, R. L. Vasilenko, E.D. Tabachnikova, M.A. Tikhonovsky, T.G. Langdon, Structure and low-temperature micromechanical properties of as-cast and SPD-processed high-entropy $Co_{25-x}Cr_{25}Fe_{25}Ni_{25}C_x$ alloys, Low. Temp. Phys. 48 (2022) 560–569.

[295] A.V. Podolskiy, E. Schafler, E.D. Tabachnikova, M.A. Tikhonovsky, M. J. Zehetbauer, Thermally activated deformation of nanocrystalline and coarse grained CoCrFeNiMn high entropy alloy in the temperature range 4.2–350 K, Low. Temp. Phys. 44 (2018) 976–982.

[296] K. Edalati, R. Uehiro, K. Fujiwara, Y. Ikeda, H.W. Li, X. Sauvage, R.Z. Valiev, E. Akiba, I. Tanaka, Z. Horita, Ultra-severe plastic deformation: evolution of microstructure, phase transformation and hardness in immiscible magnesium-based systems, Mater. Sci. Eng. A 701 (2017) 158–166.

[297] J.G. Sevillano, Dynamic steady state by unlimited unidirectional plastic deformation of crystalline materials deforming by dislocation glide at low to moderate temperatures, Metals 10 (2020) 66.

[298] K. Edalati, Ultra-severe plastic deformation for room-temperature superplasticity and superfunctionality, Mater. Res. Proc. 32 (2023) 41–52.

[299] V. Segal, Review: modes and processes of severe plastic deformation (SPD), Materials 11 (2018) 1175.

[300] K. Edalati, Z. Horita, Scaling-up of high pressure torsion using ring shape, Mater. Trans. 50 (2009) 92–95.

[301] K. Edalati, Z. Horita, Y. Mine, High-pressure torsion of hafnium, Mater. Sci. Eng. A 527 (2010) 2136–2141.

[302] S. Lee, K. Edalati, Z. Horita, Microstructures and mechanical properties of pure V and Mo processed by high-pressure torsion, Mater. Trans. 51 (2010) 1072–1079.

[303] L. Chen, L. Ping, T. Ye, L. Lingfeng, X. Kemin, Z. Meng, Observations on the ductility and thermostability of tungsten processed from micropowder by improved high-pressure torsion, Rare Met. Mater. Eng. 45 (2016) 3089–3094.

[304] X. Sauvage, A. Duchaussoy, G. Zaher, Strain induced segregations in severely deformed materials, Mater. Trans. 60 (2019) 1151–1158.

[305] J. Gubicza, Lattice defects and their influence on the mechanical properties of bulk materials processed by severe plastic deformation, Mater. Trans. 60 (2019) 1230–1242.

[306] J. Čížek, M. Janeček, T. Vlasák, B. Smola, O. Melikhova, R.K. Islamgaliev, S. V. Dobatkin, The development of vacancies during severe plastic deformation, Mater. Trans. 60 (2019) 1533–1542.

[307] G. Wilde, S. Divinski, Grain boundaries and diffusion phenomena in severely deformed materials, Mater. Trans. 60 (2019) 1302–1315.

[308] K. Oh-ishi, K. Edalati, H.S. Kim, K. Hono, Z. Horita, High-pressure torsion for enhanced atomic diffusion and promoting solid-state reactions in aluminum-copper system, Acta Mater. 61 (2013) 3482–3489.

[309] K. Edalati, H. Shao, H. Emami, H. Iwaoka, Z. Horita, E. Akiba, Activation of titanium-vanadium alloy for hydrogen storage by introduction of nanograins and edge dislocations using high-pressure torsion, Int. J. Hydrog. Energy 41 (2016) 8917–8924.

[310] A. Duchaussoy, X. Sauvage, K. Edalati, Z. Horita, G. Renou, A. Deschamps, F. De Geuser, Structure and mechanical behavior of ultrafine-grained aluminum-iron alloy stabilized by nanoscaled intermetallic particles, Acta Mater. 167 (2019) 89–102.

[311] X. Sauvage, F. Cuvilly, A. Russell, K. Edalati, Understanding the role of Ca segregation on thermal stability, electrical resistivity and mechanical strength of nanostructured aluminum, Mater. Sci. Eng. A 798 (2020) 140108.

[312] A. Campos-Quirós, J.M. Cubero-Sesín, K. Edalati, Synthesis of nanostructured biomaterials by high-pressure torsion: effect of niobium content on microstructure and mechanical properties of Ti-Nb alloys, Mater. Sci. Eng. A 795 (2020) 139972.

[313] K. Fujiwara, R. Uehiro, K. Edalati, H.W. Li, R. Floriano, E. Akiba, Z. Horita, New Mg-V-Cr BCC alloys synthesized by high-pressure torsion and ball milling, Mater. Trans. 59 (2018) 741–746.

[314] M.O. de Marco, Y. Li, H.W. Li, K. Edalati, R. Floriano, Mechanical synthesis and hydrogen storage characterization of MgVCr and MgVTiCrFe high-entropy alloy, Adv. Eng. Mater. 22 (2020) 1901079.

[315] A. Mohammadi, N.A. Enikeev, M.Y. Murashkin, M. Arita, K. Edalati, Examination of inverse Hall-Petch relation in nanostructured aluminum alloys by ultra-severe plastic deformation, J. Mater. Sci. Technol. 91 (2021) 78–89.

[316] A. Kilmametov, R. Kulagin, A. Mazilkin, S. Seils, T. Boll, M. Heilmaier, H. Hahn, High-pressure torsion driven mechanical alloying of CoCrFeMnNi high entropy alloy, Scr. Mater. 158 (2019) 29–33.

[317] J. González-Masís, J.M. Cubero-Sesin, A. Campos-Quirós, K. Edalati, Synthesis of biocompatible high-entropy alloy TiNbZrTaHf by high-pressure torsion, Mater. Sci. Eng. A 825 (2021) 141869.

[318] K. Edalati, S. Toh, M. Watanabe, Z. Horita, In-situ production of bulk intermetallic-based nanocompsites and nanostructured intermetallics by high-pressure torsion, Scr. Mater. 66 (2012) 386–389.

[319] A. Alhamidi, K. Edalati, Z. Horita, Production of nanograined intermetallics using high-pressure torsion, Mater. Res. 16 (2013) 672–678.

[320] A. Alhamidi, K. Edalati, Z. Horita, Effect of temperature on solid-state formation of bulk nanograined intermetallics during high-pressure torsion, Philos. Mag. 94 (2014) 876–887.

[321] K. Edalati, S. Toh, H. Iwaoka, M. Watanabe, Z. Horita, D. Kashioka, K. Kishida, H. Inui, Ultrahigh strength and high plasticity in TiAl intermetallics with bimodal grain structure and nanotwins, Scr. Mater. 67 (2012) 814–817.

[322] K. Kitabayashi, K. Edalati, H.W. Li, E. Akiba, Z. Horita, Phase transformations in MgH2-TiH2 hydrogen storage system by high-pressure torsion process, Adv. Eng. Mater. 22 (2020) 1900027.

[323] P. Edalati, Q. Wang, H. Razavi-Khosroshahi, M. Fuji, T. Ishihara, K. Edalati, Photocatalytic hydrogen evolution on a high-entropy oxide, J. Mater. Chem. A 8 (2020) 3814–3821.

[324] S. Akrami, Y. Murakami, M. Watanabe, T. Ishihara, M. Arita, M. Fuji, K. Edalati, Defective high-entropy oxide photocatalyst with high activity for CO2 conversion, Appl. Catal. B 303 (2022) 120896.

[325] P. Edalati, Y. Itagoe, H. Ishihara, T. Ishihara, H. Emami, M. Arita, M. Fuji, K. Edalati, Visible-light photocatalytic oxygen production on a high-entropy oxide with multiple-heterojunction introduction, J. Photochem. Photobiol. A 433 (2022) 114167.

[326] P. Edalati, X.F. Shen, M. Watanabe, T. Ishihara, M. Arita, M. Fuji, K. Edalati, High-entropy oxynitride as low-bandgap and stable photocatalyst for hydrogen production, J. Mater. Chem. A 9 (2021) 15076–15086.

[327] S. Akrami, P. Edalati, Y. Shundo, M. Watanabe, T. Ishihara, M. Fuji, K. Edalati, Significant CO2 photoreduction on a high-entropy oxynitride, Chem. Eng. J. 449 (2022) 137800.

[328] J. Cubicza, N.Q. Chinh, J.L. Labar, Z. Hegedus, T.G. Langdon, Principles of self-annealing in silver processed by equal-channel angular pressing: the significance of a very low stacking fault energy, Mater. Sci. Eng. A 527 (2010) 752–760.

[329] V.V. Popov, E.N. Popova, D.D. Kuznetsov, A.V. Stolbovskii, V.P. Pilyugin, Thermal stability of nickel structure obtained by high-pressure torsion in liquid nitrogen, Phys. Met. Metallogr. 115 (2014) 682–691.

[330] Y. Huang, S. Sabbaghianrad, A.I. Almazrouee, K.J. Al-Fadhalah, S.N. Alhajeri, T. G. Langdon, The significance of self-annealing at room temperature in high purity copper processed by high-pressure torsion, Mater. Sci. Eng. A 656 (2016) 55–66.

[331] J.A. Muñoz, O.F. Higuera, A.H. Expósito, A. Boulaajaj, R.E. Bolmaro, F. D. Dumitru, P.R. Calvillo, A.M. Jorge Jr, J.M. Cabrera, Thermal stability of ARMCO iron processed by ECAP, Int. J. Adv. Manufact. Technol. 98 (2018) 2917–2932.

[332] A. Mohammadi, N.A. Enikeev, M.Y. Murashkin, M. Arita, K. Edalati, Developing age-hardenable Al-Zr alloy by ultra-severe plastic deformation: significance of supersaturation, segregation and precipitation on hardening and electrical conductivity, Acta Mater. 203 (2021) 116503.

[333] K. Edalati, H. Emami, A. Staykov, D.J. Smith, E. Akiba, Z. Horita, Formation of metastable phases in magnesium-titanium system by high-pressure torsion and their hydrogen storage performance, Acta Mater. 50 (2015) 150–156.

[334] K. Edalati, H. Emami, Y. Ikeda, H. Iwaoka, I. Tanaka, E. Akiba, Z. Horita, New nanostructured phases with reversible hydrogen storage capability in immiscible magnesium-zirconium system produced by high-pressure torsion, Acta Mater. 108 (2016) 293–303.

[335] E.I. Lopez-Gomez, K. Edalati, D.D. Coimbroo, F.J. Antiqueira, G. Zepon, J. M. Cubero-Sesin, W.J. Botta, FCC phase formation in immiscible Mg-Hf (magnesium-hafnium) system by high-pressure torsion, AIP Adv. 10 (2020) 055212.

[336] H. Gleiter, Nanocrystalline materials, Prog. Mater. Sci. 33 (1989) 223–315.

[337] J.A. Haber, J.L. Crane, W.E. Buhro, C.A. Frey, S.M.L. Sastry, J.J. Balbach, M. S. Conradi, Chemical synthesis of nanocrystalline titanium and nickel aluminides from the metal chlorides and lithium aluminum hydride, Adv. Mater. 8 (1996) 163–166.

[338] Y.B. Pithawalla, M.S. El-Shall, S.C. Deevi, Synthesis and characterization of nanocrystalline iron aluminide particles, Intermetallics 8 (2000) 1225–1231.

[339] H. Emami, K. Edalati, A. Staykov, T. Hongo, H. Iwaoka, Z. Horita, E. Akiba, Solid-state reactions and hydrogen storage in magnesium mixed with various elements by high-pressure torsion: experiments and first-principles calculations, RCS Adv. 6 (2016) 11665–11674.

[340] S. Lee, K. Edalati, H. Iwaoka, Z. Horita, T. Ohtsuki, T. Ohkochi, M. Kotsugi, T. Kojima, M. Mizuguchi, K. Takanashi, Formation of FeNi with L10-ordered structure using high-pressure torsion, Philos. Mag. Lett. 94 (2014) 639–646.

[341] K. Edalati, T. Daio, Z. Horita, K. Kishida, H. Inui, Evolution of lattice defects, disordered/ordered phase transformations and mechanical properties in Ni-Al-Ti intermetallics by high-pressure torsion, J. Alloy. Compd. 563 (2013) 221–228.

[342] M. Long, H.J. Rack, Titanium alloys in total joint replacement - a materials science perspective, Biomaterials 19 (1998) 1621–1639.

[343] R. Valiev, I.P. Semenova, E. Jakushina, V.V. Latysh, H.J. Rack, T.C. Lowe, J. Petruželka, L. Dluhoš, D. Hrušák, J. Sochová, Nanostructured SPD processed titanium for medical implants, Mater. Sci. Forum 584- 586 (2008) 49–54.

[344] Y. Estrin, H.E. Kim, R. Lapovok, H.P. Ng, J.H. Jo, Mechanical strength and biocompatibility of ultrafine-grained commercial purity titanium, BioMed. Res. Int. 2013 (2013) 914764.

[345] A.P. Zhilyaev, Y. Huang, J.M. Cabrera, T.G. Langdon, Influence of inhomogeneity on mechanical properties of commercially pure titanium processed by HPT, Defect Diffus. Forum 385 (2018) 284–289.

[346] T.G. Langdon, Seventy-five years of superplasticity: historic developments and new opportunities, J. Mater. Sci. 44 (2009) 5998–6010.

[347] M. Demirtas, G. Purcek, Room temperature superplaticity in fine/ultrafine grained materials subjected to severe plastic deformation, Mater. Trans. 60 (2019) 1159–1167.

[348] R.Z. Valiev, M.Y. Murashkin, A. Kilmametov, B. Straumal, N.Q. Chinh, T. G. Langdon, Unusual super-ductility at room temperature in an ultrafine-grained aluminum alloy, J. Mater. Sci. 45 (2010) 4718–4724.

[349] M. Kawasaki, T.G. Langdon, The contribution of severe plastic deformation to research on superplasticity, Mater. Trans. 60 (2019) 1123–1130.

[350] K. Edalati, T. Masuda, M. Arita, M. Furui, X. Sauvage, Z. Horita, R.Z. Valiev, Room-temperature superplasticity in an ultrafine-grained magnesium alloy, Sci. Rep. 7 (2017) 2662.

[351] K. Edalati, Z. Horita, R.Z. Valiev, Transition from poor ductility to room-temperature superplasticity in a nanostructured aluminum alloy, Sci. Rep. 8 (2018) 6740.

[352] C. Meingast, D.C. Larbalestier, Quantitative description of a very high critical current density Nb-Ti superconductor during its final optimization strain. II. Flux pinning mechanisms, J. Appl. Phys. 66 (1989) 5971–5983.

[353] L.D. Cooley, P.D. Jablonski, P.J. Lee, D.C. Larbalestier, Strongly enhanced critical current density in Nb 47 wt% Ti having a highly aligned microstructure, Appl. Phys. Lett. 58 (1991) 2984–2986.

[354] R.W. Heussner, P.D. Jablonski, P.J. Lee, D.C. Larbalestier, Properties of rod-based artificial pinning center Nb-Ti superconductors, IEEE Trans. Appl. Supercon. 5 (1995) 1705–1708.

[355] V.A. Beloshenko, V.V. Chishko, Deformation-heat treatment of Nb-Ti superconductors using severe plastic deformation methods, Phys. Met. Metallogr. 114 (2013) 992–1002.

[356] K. Edalati, T. Daio, S. Lee, Z. Horita, T. Nishizaki, T. Akune, T. Nojima, T. Sasaki, High strength and superconductivity in nanostructured niobium-titanium alloy by high-pressure torsion and annealing: significance of elemental decomposition and supersaturation, Acta Mater. 80 (2014) 149–158.

[357] I.P. Jain, C. Lal, A. Jain, Hydrogen storage in Mg: a most promising material, Int. J. Hydrog. Energy 35 (2010) 5133–5144.

[358] Á. Révész, M. Gajdics, High-pressure torsion of non-equilibrium hydrogen storage materials: a review, Energies 14 (2021) 819.

[359] K. Edalati, R. Uehiro, Y. Ikeda, H.W. Li, H. Emami, Y. Filinchuk, M. Arita, X. Sauvage, I. Tanaka, E. Akiba, Z. Horita, Design and synthesis of a magnesium alloy for room temperature hydrogen storage, Acta Mater. 149 (2018) 88–96.

[360] K. Maeda, K. Domen, Photocatalytic water splitting: recent progress and future challenges, J. Phys. Chem. Lett. 1 (2010) 2655–2661.

[361] K. Li, B. Peng, T. Peng, Recent advances in heterogeneous photocatalytic CO2 conversion to solar fuels, ACS Catal. 6 (2016) 7485–7527.

[362] T. Sakai, A. Belyakov, R. Kaibyshev, H. Miura, J.J. Jonas, Dynamic and post-dynamic recrystallization under hot, cold and severe plastic deformation conditions, Prog. Mater. Sci. 60 (2014) 130–207.

[363] S. Suwas, S. Mondal, Texture evolution in severe plastic deformation processes, Mater. Trans. 60 (2019) 1457–1471.

[364] F.A. Mohamed, A dislocation model for the minimum grain size obtainable by milling, Acta Mater. 51 (2003) 4107–4119.

[365] K. Edalati, Z. Horita, High-pressure torsion of pure metals: influence of atomic bond parameters and stacking fault energy on grain size and correlation with hardness, Acta Mater. 59 (2011) 6831–6836.

[366] V.I. Levitas, Recent in situ experimental and theoretical advances in severe plastic deformations, strain-induced phase transformations, and microstructure evolution under high pressure, Mater. Trans. 64 (2023) 1866–1878.

[367] G. Wilde, H. Rösner, S. Divinski, Internal interfaces in severely deformed metals and alloys: coupling of kinetics, structure and strain with properties and performance, Mater. Trans. 64 (2023) 1331–1345.

[368] R.Z. Valiev, M.J. Zehetbauer, Y. Estrin, H.W. Höppel, Y. Ivanisenko, H. Hahn, G. Wilde, H.J. Roven, X. Sauvage, T.G. Langdon, The innovation potential of bulk nanostructured materials, Adv. Eng. Mater. 9 (2007) 527–533.

[369] R.N. Harsha, V.M. Kulkarni, B.S. Babu, Severe plastic deformation - a review, Mater. Today Proc. 5 (2018) 22340–22349.

[370] S. Taheriniya, F.A. Davani, S. Hilke, M. Hepp, C. Gadelmeier, M.R. Chellali, T. Boll, H. Rösner, M. Peterlechner, C. Gammer, S.V. Divinski, B. Butz, U. Glatzel, H. Hahn, G. Wilde, High entropy alloy nanocomposites produced by high pressure torsion, Acta Mater. 208 (2021) 116714.

[371] S.K. Mohapatra, V. Ranjan, S. Tripathy, Study of severe plastic deformations of metallic materials:- a move towards amorphization, Mater. Today Proc. 56 (2022) 735–741.

[372] A.I. Bazlov, M.S. Parkhomenko, E.V. Ubyivovk, E.N. Zanaeva, T.A. Bazlova, D. V. Gunderov, Severe plastic deformation influence on the structure transformation of the amorphous Zr$_{62.5}$Cu$_{22.5}$Al$_{10}$Fe$_5$ alloy, Intermetallics 152 (2023) 107777.

[373] X. Sauvage, G. Wilde, S.V. Divinski, Z. Horita, R.Z. Valiev, Grain boundaries in ultrafine grained materials processed by severe plastic deformation and related phenomena, Mater. Sci. Eng. A 540 (2012) 1–12.

[374] A.A. Nazarov, A.E. Romanov, R.Z. Valiev, On the structure, stress fields and energy of nonequilibrium grain boundaries, Acta Met. Mater. 41 (1993) 1033–1040.

[375] V.N. Chuvil'deev, V.I. Kopylov, W. Zeiger, A theory of non-equilibrium grain boundaries and its applications to nano- and micro-crystalline materials processed by ECAP, Ann. De. Chim. Sci. Des. Mat. ériaux 27 (2002) 55–64.

[376] A.A. Nazarov, Review: Nonequilibrium grain boundaries in bulk nanostructured metals and their recovery under the influences of heating and cyclic deformation, Lett. Mater. 8 (2018) 372–381.

[377] H. Rösner, N. Boucharat, K.A. Padmanabhan, J. Markmann, G. Wilde, Strain mapping in a deformation-twinned nanocrystalline Pd grain, Acta Mater. 58 (2010) 2610–2620.

[378] H. Rösner, C. Kübel, Y. Ivanisenko, L. Kurmanaeva, S. Divinski, M. Peterlechner, G. Wilde, Strain mapping of a triple junction in nanocrystalline Pd, Acta Mater. 59 (2011) 7380–7387.

[379] G. Wilde, J. Ribbe, G. Reglitz, M. Wegner, H. Rösner, Y. Estrin, M. Zehetbauer, D. Setman, S. Divinski, Plasticity and grain boundary diffusion at small grain sizes, Adv. Eng. Mater. 12 (2010) 758–764.

[380] S.V. Divinski, G. Reglitz, H. Rösner, Y. Estrin, G. Wilde, Ultra-fast diffusion channels in pure Ni severely deformed by equal-channel angular pressing, Acta Mater. 59 (2011) 1974–1985.

[381] J. Ribbe, D. Baither, G. Schmitz, S.V. Divinski, Network of porosity formed in ultrafine-grained copper produced by equal channel angular pressing, Phys. Rev. Lett. 102 (2009) 165501.

[382] Y. Amouyal, S.V. Divinski, Y. Estrin, E. Rabkin, Short-circuit diffusion in an ultrafine grain copper-zirconium alloy produced by equal channel angular pressing, Acta Mater. 55 (2007) 5968–5979.

[383] J. Ribbe, D. Baither, G. Schmitz, S.V. Divinski, Ultra fast diffusion and internal porosity in ultra fine grain copper–lead alloy prepared by equal channel angular pressing, Scr. Mater. 61 (2009) 129–132.

[384] N. Choi, S. Taheriniya, S. Yang, V.A. Esin, J.H. Yu, J.S. Lee, G. Wilde, S. V. Divinski, 'Non-equilibrium' grain boundaries in additively manufactured CoCrFeMnNi high-entropy alloy: enhanced diffusion and strong segregation, J. Appl. Phys. 132 (2023) 245105.

[385] N. Choi, V. Kulitckii, J. Kottke, B. Tas, J. Choe, J.H. Yu, S. Yang, J.H. Park, J. S. Lee, G. Wilde, S.V. Divinski, Analyzing the 'non-equilibrium state' of grain boundaries in additively manufactured high-entropy CoCrFeMnNi alloy using tracer diffusion measurements, J. Alloy. Compd. 844 (2020) 155757.

[386] S. Taheriniya, N. Choi, S. Yang, R. Sonkusare, J.H. Yu, J.S. Lee, H. Rösner, M. Peterlechner, T. Boll, C. Gammer, H. Hahn, S.V. Divinski, G. Wilde, Additively manufactured equiatomic CoCrFeMnNi high entropy alloy: precipitation-induced heterogeneity by mechano-chemical coupling, J. Alloy. Compd. 938 (2023) 168514.

[387] M. Glienke, M. Vaidya, L. Daum, B. Tas, L. Rogal, K.G. Pradeep, S.V. Divinski, G. Wilde, Grain boundary diffusion in CoCrFeMnNi high entropy alloy: kinetic hints towards a phase decomposition, Acta Mater. 195 (2020) 304–316.

[388] T. Keil, S. Taheriniya, E. Bruder, G. Wilde, K. Durst, Effects of solutes on thermal stability, microstructure and mechanical properties in CrMnFeCoNi based alloys after high pressure torsion, Acta Mater. 227 (2022) 117689.

[389] B. Schuh, B. Völker, J. Todt, N. Schell, L. Perrière, J. Li, J.P. Couzinié, A. Hohenwarter, Thermodynamic instability of a nanocrystalline, single-phase TiZrNbHfTa alloy and its impact on the mechanical properties, Acta Mater. 142 (2018) 201–212.

[390] Q. Lin, X. An, H. Liu, Q. Tang, P. Dai, X. Liao, In-situ high-resolution transmission electron microscopy investigation of grain boundary dislocation activities in a nanocrystalline CrMnFeCoNi high-entropy alloy, J. Alloy. Compd. 709 (2017) 802–807.

[391] S. Zherebtsov, N. Stepanov, Y. Ivanisenko, D. Shaysultanov, N. Yurchenko, M. Klimova, G. Salishchev, Evolution of microstructure and mechanical properties of a CoCrFeMnNi high-entropy alloy during high-pressure torsion at room and cryogenic temperatures, Metals 8 (2018) 123.

[392] J. Čížek, P. Haušild, M. Cieslar, O. Melikhova, T. Vlasak, M. Janeček, R. Kral, P. Harcuba, F. Lukač, J. Zyka, J. Malek, J. Moon, H.S. Kim, Strength enhancement of high entropy alloy HfNbTaTiZr by severe plastic deformation, J. Alloy. Compd. 768 (2018) 924–937.

[393] A.R. Krause, P.R. Cantwell, C.J. Marvel, C. Compson, J.M. Rickman, M.P. Harmer, Review of grain boundary complexion engineering: know your boundaries, J. Am. Ceram. Soc. 102 (2019) 778–800.

[394] P.R. Cantwell, T. Frolov, T.J. Rupert, A.R. Krause, C.J. Marvel, G.S. Rohrer, J. M. Rickman, M.P. Harmer, Grain boundary complexion transitions, Ann. Rev. Mater. Res. 50 (2020) 465–492.

[395] X. Sauvage, A. Ganeev, Y. Ivanisenko, N. Enikeev, M. Murashkin, R. Valiev, Grain boundary segregation in UFG alloys processed by severe plastic deformation, Adv. Eng. Mater. 14 (2012) 968–974.

[396] D.A. Basha, R. Sahara, H. Somekawa, J.M. Rosalie, A. Singh, K. Tsuchiya, Interfacial segregation induced by severe plastic deformation in a Mg–Zn–Y alloy, Scr. Mater. 124 (2016) 169–173.

[397] B. Bian, S. Taheriniya, G. Mohan Muralikrishna, A. Godha, S.K. Makineni, S. Sankaran, B.B. Straumal, Y. Du, G. Wilde, S.V. Divinski, Kinetic and structural insights into the grain boundary phase transitions in Ni-Bi alloys, Acta Mater. 245 (2023) 118632.

[398] S. Sankaran, K.C. Hari Kumar, H. Rösner, M. Peterlechner, V.A. Esin, S. Divinski, G. Wilde, Grain boundary diffusion and grain boundary structures of a Ni-Cr-Fe-alloy: evidences for grain boundary phase transitions, Acta Mater. 195 (2020) 501–518.

[399] K. Edalati, Z. Horita, Significance of homologous temperature in softening behavior and grain size of pure metals processed by high-pressure torsion, Mater. Sci. Eng. A 528 (2011) 7514–7523.

[400] M. Kawasaki, Different models of hardness evolution in ultrafine-grained materials processed by high-pressure torsion, J. Mater. Sci. 49 (2014) 18–34.

[401] R. Pippan, A. Hohenwarter, The importance of fracture toughness in ultrafine and nanocrystalline bulk materials, Mater. Res. Lett. 4 (2016) 127–136.

[402] R.Z. Valiev, V.Y. Gertsman, O.A. Kaibyshev, Grain boundary structure and properties under external influences, Phys. Stat. Sol. A 97 (1986) 11–56.

[403] S.V. Diviski, Grain boundary diffusion in severely deformed metals: state of the art and unresolved issues, Diffus. Found. 5 (2015) 57–76.

[404] R.Z. Valiev, R.S. Musalimov, High-resolution transmission electron microscopy of nanocrystalline materials, Phys. Met. Metallogr. 78 (1994) 666–670.

[405] Z. Horita, T.G. Langdon, Microstructures and microhardness of an aluminum alloy and pure copper after processing by high-pressure torsion, Mater. Sci. Eng. A 410–411 (2005) 422–425.

[406] V.V. Popov, E.V. Osinnikov, R.M. Falakhutdinov, Mössbauer emission spectroscopy of grain boundaries in ultrafine-grained niobium obtained by severe plastic deformation, Phys. Met. Metallogr. 123 (2022) 825–830.

[407] V.V. Popov, E.N. Popova, E.V. Osinnikov, Specific features of grain boundaries in nickel processed by high-pressure torsion, Mater. Trans. 64 (2023) 1401–1409.

[408] V.V. Popov, Mössbauer spectroscopy of interfaces in Metals, Phys. Met. Metallogr. 113 (2012) 1257–1289.

[409] V.V. Popov, Mössbauer spectroscopy studies of grain boundaries in nanostructured metals, Def. Diff, Forum 273–276 (2008) 506–513.

[410] V.V. Popov, Mössbauer spectroscopy of grain boundaries in ultrafine-grained metal materials, Mater. Sci. Forum 783–786 (2014) 2671–2676.

[411] V.V. Popov, E.N. Popova, Behavior of Nb and Cu-Nb composites under severe plastic deformation and annealing, Mater. Trans. 60 (2019) 1209–1220.

[412] J. Fiebig, S.V. Divinski, H. Rösner, Y. Estrin, G. Wilde, Diffusion of Ag and Co in ultrafine-grained α-Ti deformed by equal channel angular pressing, J. Appl. Phys. 110 (2011) 083514.

[413] S.V. Divinski, G. Reglitz, I.S. Golovin, M. Petrlechner, R. Lapovok, Y. Estrin, G. Wilde, Effect of heat treatment on diffusion, internal friction, microstructure and mechanical properties of ultra-fine-grained nickel severely deformed by equal-channel angular pressing, Acta Mater. 82 (2015) 11–21.

[414] F. Emeis, M. Peterlechner, S.V. Divinski, G. Wilde, Grain boundary engineering parameters for ultrafine grained microstructures: proof of principles by a systematic composition variation in the Cu-Ni system, Acta Mater. 150 (2018) 262–272.

[415] V.V. Popov, E.V. Osinnikov, S.A. Murzinova, A.V. Stolbovskiy, R.M. Falahutdinov, Grain-boundary diffusion of ^{57}Co in nickel, J. Phase Equilib. Diffus 41 (2020) 132–137.

[416] E.V. Osinnikov, S.A. Murzinova, A.Y. Istomina, V.V. Popov, A.V. Stolbovskiy, R. M. Falahutdinov, Grain-boundary diffusion of ^{57}Co in ultrafine-grained nickel after severe plastic deformation, Phys. Met. Metallogr. 122 (2021) 976–980.

[417] V.V. Popov, A.Y. Istomina, E.V. Osinnikov, R.M. Falahutdinov, Grain-boundary diffusion of ^{57}Co in niobium, Phys. Met. Metallogr. 124 (2023) 285–289.

[418] V.V. Popov, E.V. Osinnikov, A.Y. Istomina, E.N. Popova, R.M. Falahutdinov, Grain-boundary diffusion of ^{57}Co in ultrafine-grained niobium processed by severe plastic deformation, Phys. Met. Metallogr. 124 (2023) 561–566.

[419] V.V. Popov, A.V. Sergeev, Determination of grain-boundary diffusion parameters based on specified model of grain-boundary diffusion and combined analysis of radiotracer and Mössbauer spectroscopy data, Diffus. Found. 5 (2015) 21–39.

[420] V.V. Popov, A.V. Sergeev, Grain-boundary diffusion of cobalt in submicrocrystalline molybdenum obtained by high-pressure torsion, Phys. Met. Metallogr. 118 (2017) 1091–1096.

[421] P.V. Kuznetsov, T.V. Rakhmatulina, I.V. Belyaeva, A.V. Korznikov, Energy of internal interfaces as a characteristic of the structural evolution of ultrafine-grained copper and nickel after annealing, Phys. Met. Metallogr. 118 (2017) 241–248.

[422] A.P. Zhilyaev, M.D. Baro, Z. Horita, J.A. Szpunar, T.G. Langdon, Microstructure and grain-boundary spectrum of ultrafine-grained nickel produced by severe plastic deformation, Russ. Metall. 1 (2004) 60–74.

[423] D. Prokoshkina, A. Moros, G. Reglitz, G.P. Dinda, D.D. Kuznetsov, V.V. Popov, A. V. Stolbovsky, E. Shorohov, S.V. Divinski, G. Wilde, On the processing pathway dependence of microstructure evolution during severe plastic deformation: nickel as a case example, Adv. Eng. Mater. 17 (2015) 1842–1852.

[424] G.D. Hughes, S.D. Smith, C.S. Pande, H.R. Johnson, R.W. Armstrong, Hall-Petch strengthening for the microhardness of twelve nanometer grain diameter electrodeposited nickel, Scr. Metall. 20 (1986) 93–97.

[425] J.A. Muñoz, T. Khelfa, D. Gheorghe, O.F. Higuera, P. Rodriguez, J.M. Cabrera, Microstructure characterization of metallic materials processed by equal channel angular pressing (ECAP): an electron backscatter diffraction (EBSD) analysis, Mater. Trans. 64 (2023) 1791–1805.

[426] A.J. Schwartz, M. Kumar, B.L. Adams, D.P. Field, Electron Backscatter Diffraction in Materials Science, Springer,, 2009.

[427] J.A. Venables, C.J. Harland, Electron back-scattering patterns - a new technique for obtaining crystallographic information in the scanning electron microscope, Philos. Mag. A 27 (1973) 1193–1200.

[428] K.Z. Baba-Kishi, Review electron backscatter Kikuchi diffraction in the scanning electron microscope for crystallographic analysis, J. Mater. Sci. 37 (2002) 1715–1746.

[429] M.N. Alam, M. Blackman, D.W. Pashley, G.P. Thomson, High-angle Kikuchi patterns, Proc. R. Soc. Lond. Ser. A.: Math. Phys. Sci. 221 (1997) 224–242.

[430] D.G. Coates, Kikuchi-like reflection patterns obtained with the scanning electron microscope, Philos. Mag. A 16 (1967) 1179–1184.

[431] S.I. Wright, J.W. Zhao, B.L. Adams, Automated determination of lattice orientation from electron backscattered Kikuchi diffraction patterns, Textures Micro 13 (1970) 123–131.

[432] O. Engler, V. Randle, Introduction to Texture Analysis: Macrotexture, Microtexture, and Orientation Mapping, CRC press,, 2009.

[433] S.I. Wright, M.M. Nowell, D.P. Field, A review of strain analysis using electron backscatter diffraction, Microsc. Microanal. 17 (2011) 316–329.

[434] F.J. Humphreys, M. Hatherly, Recrystallization and Related Annealing Phenomena, Elsevier,, 2012.

[435] M.M. Nowell, S.I. Wright, Phase differentiation via combined EBSD and XEDS, J. Microsc. 213 (2004) 296–305.

[436] W. Pantleon, Resolving the geometrically necessary dislocation content by conventional electron backscattering diffraction, Scr. Mater. 58 (2008) 994–997.

[437] J.A. Muñoz, A. Komissarov, Back stress and strength contributions evolution of a heterogeneous austenitic stainless steel obtained after one pass by equal channel angular sheet extrusion (ECASE), Int. J. Adv. Manuf. Technol. 109 (2020) 607–617.

[438] A. Kundu, D.P. Field, Influence of microstructural heterogeneity and plastic strain on geometrically necessary dislocation structure evolution in single-phase and two-phase alloys, Mater. Charact. 170 (2020) 110690.

[439] J.A. Muñoz, M. Melia, M. Avalos, R.E. Bolmaro, Equal channel angular sheet extrusion (ECASE) produces twinning heterogeneity in commercially pure titanium, Mater. Charact. 181 (2021) 111460.

[440] S. Kalácska, J. Ast, P.D. Ispánovity, J. Michler, X. Maeder, 3D HR-EBSD characterization of the plastic zone around crack tips in tungsten single crystals at the micron scale, Acta Mater. 200 (2020) 211–222.

[441] G.C. Sneddon, P.W. Trimby, J.M. Cairney, Transmission Kikuchi diffraction in a scanning electron microscope: a review, Mater. Sci. Eng. R. 110 (2016) 1–12.

[442] J.A. Muñoz, M. Avalos, N. Schell, H.G. Brokmeier, R.E. Bolmaro, Comparison of a low carbon steel processed by cold rolling (CR) and asymmetrical rolling (ASR): heterogeneity in strain path, texture, microstructure and mechanical properties, J. Manuf. Process 64 (2021) 557–575.

[443] J.A. Muñoz, O.F.H. Cobos, R. M'Doihoma, M. Avalos, R.E. Bolmaro, Inducing heterogeneity in an austenitic stainless steel by equal channel angular sheet extrusion (ECASE), J. Mater. Res. Technol. 8 (2019) 2473–2479.

[444] L.S. Toth, C. Gu, Ultrafine-grain metals by severe plastic deformation, Mater. Charact. 92 (2014) 1–14.

[445] J.A. Muñoz, R.E. Bolmaro, A.M. Jorge, A. Zhilyaev, J.M. Cabrera, Prediction of generation of high- and low-angle grain boundaries (HAGB and LAGB) during severe plastic deformation, Metall. Mater. Trans. A. 51 (2020) 4674–4684.

[446] J.A. Muñoz, O.F. Higuera, J.A. Benito, D. Bradai, T. Khelfa, R.E. Bolmaro, A. M. Jorge, J.M. Cabrera, Analysis of the micro and substructural evolution during severe plastic deformation of ARMCO iron and consequences in mechanical properties, Mater. Sci. Eng. A 740– 741 (2019) 108–120.

[447] J.A. Muñoz, T. Khelfa, A. Komissarov, J.M. Cabrera, Ductility and plasticity of ferritic-pearlitic steel after severe plastic deformation, Mater. Sci. Eng. A 805 (2020) 140624.

[448] K. Thool, A. Patra, D. Fullwood, K.V.M. Krishna, D. Srivastava, I. Samajdar, The role of crystallographic orientations on heterogeneous deformation in a zirconium alloy: a combined experimental and modeling study, Int. J. Plast. 133 (2020) 102785.

[449] S. Tamimi, J.J. Gracio, A.B. Lopes, S. Ahzi, F. Barlat, Asymmetric rolling of interstitial free steel sheets: Microstructural evolution and mechanical properties, J. Manuf. Process 31 (2018) 583–592.

[450] M.E. Nixon, O. Cazacu, R.A. Lebensohn, Anisotropic response of high-purity α-titanium: Experimental characterization and constitutive modeling, Int. J. Plast. 26 (2010) 516–532.

[451] Y.T. Zhu, X.L. Wu, Ductility and plasticity of nanostructured metals: differences and issues, Mater. Today Nano. 2 (2018) 15–20.

[452] E. Ma, T. Zhu, Towards strength–ductility synergy through the design of heterogeneous nanostructures in metals, Mater. Today 20 (2017) 323–331.

[453] J.A. Muñoz, M. Chand, J.W. Signorelli, J. Calvo, J.M. Cabrera, Strengthening of duplex stainless steel processed by equal channel angular pressing (ECAP), Int. J. Adv. Manuf. Technol. 123 (2022) 2261–2278.

[454] O.F. Higuera-Cobos, J.M. Cabrera, Mechanical, microstructural and electrical evolution of commercially pure copper processed by equal channel angular extrusion, Mater. Sci. Eng. A 571 (2013) 103–114.

[455] P. Rodríguez-Calvillo, N. Ferrer, J.M. Cabrera, Analysis of microstructure and strengthening in CuMg alloys deformed by equal channel angular pressing, J. Alloy. Compd. 626 (2015) 340–348.

[456] M. Kawasaki, Z. Horita, T.G. Langdon, Microstructural evolution in high purity aluminum processed by ECAP, Mater. Sci. Eng. A 524 (2009) 143–150.

[457] P.J. Apps, J.R. Bowen, P.B. Prangnell, The effect of coarse second-phase particles on the rate of grain refinement during severe deformation processing, Acta Mater. 51 (2003) 2811–2822.

[458] T. Khelfa, M.A. Rekik, J.A. Muñoz-Bolaños, J.M. Cabrera-Marrero, M. Khitouni, Microstructure and strengthening mechanisms in an Al-Mg-Si alloy processed by equal channel angular pressing (ECAP), Int. J. Adv. Manuf. Technol. 95 (2017) 1165–1166.

[459] T. Khelfa, J.A. Muñoz-Bolaños, F. Li, J.M. Cabrera-Marrero, M. Khitouni, Microstructure and mechanical properties of AA6082-T6 by ECAP under warm processing, Met. Mater. Int. 26 (2020) 1247–1261.

[460] F.D. Dumitru, O.F. Higuera-Cobos, J.M. Cabrera, ZK60 alloy processed by ECAP: Microstructural, physical and mechanical characterization, Mater. Sci. Eng. A 594 (2014) 32–39.

[461] P. Rodriguez-Calvillo, J.M. Cabrera, Microstructure and mechanical properties of a commercially pure Ti processed by warm equal channel angular pressing, Mater. Sci. Eng. A 625 (2015) 311–320.

[462] E. Bonnot, A.L. Helbert, F. Brisset, T. Baudin, Microstructure and texture evolution during the ultra grain refinement of the Armco iron deformed by accumulative roll bonding (ARB), Mater. Sci. Eng. A 561 (2013) 60–66.

[463] F. Cruz-Gandarilla, A.M. Salcedo-Garrido, R.E. Bolmaro, T. Baudin, N.S. De Vincentis, M. Avalos, J.G. Cabañas-Moreno, H. Mendoza-Leon, Microstructural evolution and mechanical properties on an ARB processed IF steel studied by X-ray diffraction and EBSD, Mater. Charact. 118 (2016) 332–339.

[464] H. Jafarian, Characteristics of nano/ultrafine-grained austenitic TRIP steel fabricated by accumulative roll bonding and subsequent annealing, Mater. Charact. 114 (2016) 88–96.

[465] H.R. Jafarian, S.H.M. Anijdan, A.R. Eivani, N. Park, A comprehensive study of microstructure development and its corresponding tensile properties in nano/ultrafine-grained metastable austenitic steel during accumulative roll bonding (ARB), Mater. Sci. Eng. A 703 (2017) 196–204.

[466] M. Alizadeh, M.H. Paydar, D. Terada, N. Tsuji, Effect of SiC particles on the microstructure evolution and mechanical properties of aluminum during ARB process, Mater. Sci. Eng. A 540 (2012) 13–23.

[467] A. Loucif, T. Baudin, F. Brisset, R.B. Figueiredo, R. Chemam, T.G. Langdon, An investigation of microtexture evolution in an AlMgSi alloy processed by high-pressure torsion, Mater. Sci. Forum 702– 703 (2012) 165–168.

[468] A. Khorashadizadeh, D. Raabe, M. Winning, R. Pippan, Recrystallization and grain growth in ultrafine-grained materials produced by high pressure torsion, Adv. Eng. Mater. 13 (2011) 245–250.

[469] A.Y. Khereddine, F.H. Larbi, H. Azzeddine, T. Baudin, F. Brisset, A.L. Helbert, M. H. Mathon, M. Kawasaki, D. Bradai, T.G. Langdon, Microstructures and textures of a Cu–Ni–Si alloy processed by high-pressure torsion, J. Alloy. Compd. 574 (2013) 361–367.

[470] K.J. Al-Fadhalah, S.N. Alhajeri, A.I. Almazrouee, T.G. Langdon, Microstructure and microtexture in pure copper processed by high-pressure torsion, J. Mater. Sci. 48 (2013) 4563–4572.

[471] C.L.P. Silva, I.C. Tristao, S. Sabbaghianrad, S.A. Torbati-Sarraf, R.B. Figueiredo, T. G. Langdon, Microstructure and hardness evolution in magnesium processed by HPT, Mater. Res. 20 (2017) 2–7.

[472] J.A. Muñoz, A. Komissarov, M. Avalos, R.E. Bolmaro, Mechanical and microstructural behavior of a heterogeneous austenitic stainless steel processed by equal channel angular sheet extrusion (ECASE), Mater. Sci. Eng. A 792 (2020) 139779.

[473] Y.V. Gamin, J.A. Muñoz Bolaños, A.S. Aleschenko, A.A. Komissarov, N.S. Bunits, D.A. Nikolaev, A.V. Fomin, V.V. Cheverikin, Influence of the radial-shear rolling (RSR) process on the microstructure, electrical conductivity and mechanical properties of a Cu–Ni–Cr–Si alloy, Mater. Sci. Eng. A 822 (2021) 141676.

[474] Y. Li, W. Li, S. Li, N. Min, L. Jiang, Q. Zhou, X. Jin, Ensuring the strength and ductility synergy in an austenitic stainless steel: single- or multi-phase hetero-structures design, Scr. Mater. 193 (2021) 81–85.

[475] H.S. Arora, A. Ayyagari, J. Saini, K. Selvam, S. Riyadh, M. Pole, H.S. Grewal, S. Mukherjee, High tensile ductility and strength in dual-phase bimodal steel through stationary friction stir processing, Sci. Rep. 9 (2019) 1972.

[476] K.D. Liss, In-situ neutron and synchrotron methods for the investigation of plastic deformation and annealing in metals, Mater. Res. Proc. 32 (2023) 25–40.

[477] E. Schafler, M. Zehetbauer, Characterization of nanostructured materials by X-ray line profile analysis, Rev. Adv. Mater. Sci. 10 (2005) 28–33.

[478] T. Ungár, Characterization of nanocrystalline materials by X-ray line profile analysis, J. Mater. Sci. 42 (2006) 1584–1593.

[479] J. Gubicza, T. Ungár, Characterization of defect structures in nanocrystalline materials by X-ray line profile analysis, Z. Krist. 222 (2007) 567–579.

[480] M.B. Kerber, M.J. Zehetbauer, E. Schafler, F.C. Spieckermann, S. Bernstorff, T. Ungar, X-ray line profile analysis - an ideal tool to quantify structural parameters of nanomaterials, JOM 63 (2011) 61–70.

[481] E.J., Mittemeijer, P. Scardi, A. Leineweber, U. Welzel (Eds.), Fifth Size Strain Conference. Diffraction Analysis of the Microstructure of Materials, Garmisch-Partenkirchen, October 7–9, 2007, In: Zeitschrift für Kristallographie, Supplemente, Vol. 27; Oldenbourg Wissenschaftsverlag, München, 2008.

[482] N.S. De Vincentis, M.C. Avalos, E.A. Benatti, A. Kliauga, H.G. Brokmeier, R. E. Bolmaro, XRD and EBSD analysis of anisotropic microstructure development in cold rolled F138 stainless steel, Mater. Charact. 123 (2017) 137–152.

[483] H.J. Lee, S.K. Lee, K.H. Jung, G.A. Lee, B. Ahn, M. Kawasaki, T.G. Langdon, Evolution in hardness and texture of a ZK60A magnesium alloy processed by high-pressure torsion, Mater. Sci. Eng. A 630 (2015) 90–98.

[484] X. Li, R.J. Dippenaar, J.K. Han, M. Kawasaki, K.D. Liss, Phase transformation and structure evolution of a Ti-45Al-7.5Nb alloy processed by high-pressure torsion, J. Alloy. Compd. 787 (2019) 1149–1157.

[485] P.J. Withers, Depth capabilities of neutron and synchrotron diffraction strain measurement instruments. I. the maximum feasible path length, J. Appl. Crystallogr 37 (2004) 596–606.

[486] P.J. Withers, Depth capabilities of neutron and synchrotron diffraction strain measurement instruments. II. practical implications, J. Appl. Crystallogr 37 (2004) 607–612.

[487] K.D. Liss, Quantum beam science - applications to probe or influence matter and materials, Quantum Beam Sci. 1 (2017) 1.

[488] J.K. Han, K. Sugimoto, M. Kawasaki, K.D. Liss, Strain-dependent phase transformation mapping of diffusion-bonded nanocrystalline aluminum-magnesium by high-energy synchrotron X-rays, Mater. Lett. 321 (2022) 132414.

[489] M. Kawasaki, J.K. Han, X. Liu, Y. Onuki, Y.O. Kuzminova, S.A. Evlashin, A. M. Pesin, A.P. Zhilyaev, K.D. Liss, In situ heating neutron and X-ray diffraction analyses for revealing structural evolution during postprinting treatments of additive-manufactured 316L stainless steel, Adv. Eng. Mater. 24 (2021) 2100968.

[490] K.D. Liss, A. Bartels, A. Schreyer, H. Clemens, High-energy X-rays: A tool for advanced bulk investigations in materials science and physics, Texture Stress Micro 35 (2003) 219–252.

[491] M. Isshiki, Y. Ohishi, S. Goto, K. Takeshita, T. Ishikawa, High-energy X-ray diffraction beamline: BL04B2 at SPring-8, Nucl. Instrum. Methods Phys. Res. A 467–468 (2001) 663–666.

[492] I.J. Watson, K.D. Liss, H. Clemens, W. Wallgram, T. Schmoelzer, T.C. Hansen, M. Reid, In situ characterization of a Nb and Mo containing γ-TiAl based alloy using neutron diffraction and high-temperature microscopy, Adv. Eng. Mater. 11 (2009) 932–937.

[493] K.D. Liss, Metals challenged by neutron and synchrotron radiation, Metals 7 (2017) 266.

[494] Y. Onuki, A. Hoshikawa, S. Sato, T. Ishigaki, Rapid measurement of texture of metals by time-of-flight neutron diffraction at iMATERIA and its applications, Mater. Sci. Forum 879 (2016) 1426–1430.

[495] Y. Onuki, A. Hoshikawa, S. Sato, P.G. Xu, T. Ishigaki, Y. Saito, H. Todoroki, M. Hayashi, Rapid measurement scheme for texture in cubic metallic materials using time-of-flight neutron diffraction at iMATERIA, J. Appl. Crystallogr. 49 (2016) 1579–1584.

[496] H. Takada, K. Haga, M. Teshigawara, T. Aso, S.I. Meigo, H. Kogawa, T. Naoe, T. Wakui, M. Ooi, M. Harada, M. Futakawa, Materials and life science experimental facility at the Japan proton accelerator research complex I: pulsed spallation neutron source, Quantum Beam, Sci 1 (2017) 8.

[497] K. Nakajima, Y. Kawakita, S. Itoh, J. Abe, K. Aizawa, H. Aoki, H. Endo, M. Fujita, K. Funakoshi, W. Gong, M. Harada, S. Harjo, T. Hattori, M. Hino, T. Honda, A. Hoshikawa, K. Ikeda, T. Ino, T. Ishigaki, Y. Ishikawa, H. Iwase, T. Kai, R. Kajimoto, T. Kamiyama, N. Kaneko, D. Kawana, S. Ohira-Kawamura, T. Kawasaki, A. Kimura, R. Kiyanagi, K. Kojima, K. Kusaka, S. Lee, S. Machida, T. Masuda, K. Mishima, K. Mitamura, M. Nakamura, S. Nakamura, A. Nakao, T. Oda, T. Ohhara, K. Ohishi, H. Ohshita, K. Oikawa, T. Otomo, A. Sano-Furukawa, K. Shibata, T. Shinohara, K. Soyama, J.I. Suzuki, K. Suzuya, A. Takahara, S.I. Takata, M. Takeda, Y. Toh, S. Torii, N. Torikai, N. Yamada, T. Yamada, D. Yamazaki, T. Yokoo, M. Yonemura, H. Yoshizawa, Materials and life science experimental facility (MLF) at the Japan proton accelerator research complex II: neutron scattering instruments, Quantum Beam Sci. 1 (2017) 9.

[498] X. Liu, J.K. Han, Y. Onuki, Y.O. Kuzminova, S.A. Evlashin, M. Kawasaki, K.D. Liss, In situ neutron diffraction investigating microstructure and texture evolution upon heating of nanostructured CoCrFeNi high-entropy alloy, Adv. Eng. Mater. 25 (2023) 2201256.

[499] M. Kawasaki, J.K. Han, X. Liu, S.C. Moon, K.D. Liss, Synchrotron high-energy X-ray & neutron diffraction, and laser-scanning confocal microscopy: in-situ characterization techniques for bulk nanocrystalline metals, Mater. Trans. 64 (2023) 1683–1694.

[500] H. Chikama, H. Shibata, T. Emi, M. Suzuki, "In-situ" real time observation of planar to cellular and cellular to dendritic transition of crystals growing in Fe-C alloy melts, Mater. Trans. JIM 37 (1996) 620–626.

[501] H. Yin, T. Emi, H. Shibata, Morphological instability of δ-ferrite/γ-austenite interphase boundary in low carbon steels, Acta Mater. 47 (1999) 1523–1535.

[502] M. Reid, D. Phelan, R. Dippenaar, Concentric solidification for high temperature laser scanning confocal microscopy, ISIJ Int 44 (2004) 565–572.

[503] B. Schuh, F. Mendez-Martin, B. Volker, E.P. George, H. Clemens, R. Pippan, A. Hohenwarter, Mechanical properties, microstructure and thermal stability of a nanocrystalline CoCrFeMnNi high-entropy alloy after severe plastic deformation, Acta Mater. 96 (2015) 258–268.

[504] V. Maier-Kiener, B. Schuh, E.P. George, H. Clemens, A. Hohenwarter, Nanoindentation testing as a powerful screening tool for assessing phase stability of nanocrystalline high-entropy alloys, Mater. Des. 115 (2017) 479–485.

[505] D.H. Lee, I.C. Choi, G.H. Yang, Z.P. Lu, M. Kawasaki, U. Ramamurty, R. Schwaiger, J.I. Jang, Activation energy for plastic flow in nanocrystalline CoCrFeMnNi high-entropy alloy: A high temperature nanoindentation study, Scr. Mater. 156 (2018) 129–133.

[506] Y. Ivanisenko, A. Kilmametov, H. Rösner, R.Z. Valiev, Evidence of α → ω phase transition in titanium after high pressure torsion, Int. J. Mater. Res 99 (2008) 36–41.

[507] A.P. Zhilyaev, I. Sabirov, G. Gonzales-Doncel, J. Molina-Aldarequia, B. Srinivasarao, M.T. Perez-Prado, Effect of Nb additions on the microstructure, thermal stability and mechanical behavior of high pressure Zr phases under ambient conditions, Mater. Sci. Eng. A 528 (2011) 3496–3505.

[508] C.M. Cepeda-Jiménez, J.I. Beltrán, A. Hernando, M.A. García, F. Ynduráin, A. Zhilyaev, M.T. Pérez-Prado, Tuning the magnetic properties of pure hafnium by high pressure torsion, Acta Mater. 123 (2017) 206–2013.

[509] K. Edalati, S. Toh, M. Arita, M. Watanabe, Z. Horita, High-pressure torsion of pure cobalt: hcp-fcc phase transformations and twinning during severe plastic deformation, Appl. Phys. Lett. 102 (2013) 181902.

[510] K. Edalati, D.J. Lee, T. Nagaoka, M. Arita, H.S. Kim, Z. Horita, R. Pippan, Real hydrostatic pressure in high-pressure torsion measured by bismuth phase transformations and FEM simulations, Mater. Trans. 57 (2016) 533–538.

[511] V.D. Blank, V.D. Churkin, B.A. Kulnitskiy, I.A. Perezhogin, A.N. Kirichenko, S. V. Erohin, P.B. Sorokin, M.Y. Popov, Pressure-induced transformation of graphite and diamond to onions, Crystals 8 (2018) 8.

[512] Y. Ikoma, Severe plastic deformation of semiconductor materials using high-pressure torsion, Mater. Trans. 60 (2019) 1168–1176.

[513] K. Edalati, Review on recent advancement in severe plastic deformation of oxides by high-pressure torsion (HPT), Adv. Eng. Mater. 21 (2019) 1800272.

[514] V.I. Levitas, M. Javanbakht, Phase transformations in nanograin materials under high pressure and plastic shear: nanoscale mechanisms, Nanoscale 6 (2014) 162–166.

[515] K. Edalati, K. Kitabayashi, Y. Ikeda, J. Matsuda, H.W. Li, I. Tanaka, E. Akiba, Z. Horita, Bulk nanocrystalline gamma magnesium hydride with low dehydrogenation temperature stabilized by plastic straining via high-pressure torsion, Scr. Mater. 157 (2018) 54–57.

[516] B.B. Straumal, A.A. Mazilkin, S.G. Protasova, S.V. Dobatkin, A.O. Rodin, B. Baretzky, D. Goll, G. Schütz, Fe–C nanograined alloys obtained by high pressure torsion: Structure and magnetic properties, Mater. Sci. Eng. A 503 (2009) 185–189.

[517] V.V. Stolyarov, R. Lapovok, I.G. Brodova, P.F. Thomson, Ultrafine-grained Al–5 wt% Fe alloy processed by ECAP with backpressure, Mater. Sci. Eng. A 357 (2003) 159–167.

[518] X. Sauvage, F. Wetscher, P. Pareige, Mechanical alloying of Cu and Fe induced by severe plastic deformation of a Cu–Fe composite, Acta Mater. 53 (2005) 2127–2135.

[519] W. Lojkowski, M. Djahanbakhsh, G. Burkle, S. Gierlotka, W. Zielinski, H.J. Fecht, Nanostructure formation on the surface of railway tracks, Mater. Sci. Eng. A 303 (2001) 197–208.

[520] K. Hono, M. Ohnuma, M. Murayama, S. Nishida, A. Yoshie, T. Takahashi, Cementite decomposition in heavily drawn pearlite steel wire, Scr. Mater. 44 (2001) 977–983.

[521] B.B. Straumal, A.R. Kilmametov, Y. Ivanisenko, A.A. Mazilkin, O.A. Kogtenkova, L. Kurmanaeva, A. Korneva, P. Zięba, B. Baretzky, Phase transitions induced by severe plastic deformation: steady-state and equifinality, Int. J. Mater. Res. 106 (2015) 657–664.

[522] B.B. Straumal, A.S. Gornakova, A.A. Mazilkin, O.B. Fabrichnaya, M.J. Kriegel, B. Baretzky, J.Z. Jiang, S.V. Dobatkin, Phase transformations in the severely plastically deformed Zr–Nb alloys, Mater. Lett. 81 (2012) 225–228.

[523] B.B. Straumal, S.G. Protasova, A.A. Mazilkin, E. Rabkin, D. Goll, G. Schütz, B. Baretzky, R.Z. Valiev, Deformation-driven formation of equilibrium phases in the Cu-Ni, Alloy., J. Mater. Sci. 47 (2012) 360–367.

[524] S.D. Prokoshkin, I.Y. Khmelevskaya, S.V. Dobatkin, I.B. Trubitsyna, E.V. Tatyanin, V.V. Stolyarov, E.A. Prokofiev, Alloy composition, deformation temperature, pressure and post-deformation annealing effects in severely deformed Ti–Ni based shape memory alloys, Acta Mater. 53 (2005) 2703–2714.

[525] X. Sauvage, L. Renaud, B. Deconihout, D. Blavette, D.H. Ping, K. Hono, Solid state amorphization in cold drawn Cu/Nb wires, Acta Mater. 49 (2001) 389–394.

[526] T. Miyazaki, D. Terada, Y. Miyajima, C. Suryanarayana, R. Murao, Y. Yokoyama, K. Sugiyama, M. Umemoto, T. Todaka, N. Tsuji, Mesoscopic structural states in plastically deformed nanostructured metal mmaterials, J. Mater. Sci. 46 (2011) 4296–4301.

[527] Á. Révész, S. Hóbor, J.L. Lábár, A.P. Zhilyaev, Z.S. Kovácz, Partial amorphization of a Cu–Zr–Ti alloy by high pressure torsion, J. Appl. Phys. 100 (2006) 103522.

[528] Z. Kovács, P. Henits, A.P. Zhilyaev, Á. Révész, Deformation induced primary crystallization in a thermally non-primary crystallizing amorphous Al85Ce8Ni5Co2 alloy, Scr. Mater. 54 (2006) 1733–1737.

[529] G.E. Abrosimova, A.S. Aronin, S.V. Dobatkin, S.D. Kaloshkin, D.V. Matveev, O. G. Rybchenko, E.V. Tatyanin, I.I. Zverkov, The formation of nanocrystalline structure in amorphous Fe-Si-B alloy by severe plastic deformation, J. Metastab. Nanocryst. Mater. 24 (2005) 69–72.

[530] A.M. Glezer, M.R. Plotnikova, A.V. Shalimova, S.V. Dobatkin, Severe plastic deformation of amorphous alloys: I. structure and mechanical properties, Bull. Russ. Ac. Sci. Phys. 73 (2009) 1233–1239.

[531] A.A. Mazilkin, G.E. Abrosimova, S.G. Protasova, B.B. Straumal, G. Schütz, S. V. Dobatkin, A.S. Bakai, Transmission electron microscopy investigation of boundaries between amorphous "grains" in Ni50Nb20Y30 alloy, J. Mater. Sci. 46 (2011) 4336–4342.

[532] K. Wang, The use of titanium for medical applications in the USA, Mater. Sci. Eng. A 213 (1996) 134–137.

[533] J. Onagawa, Preparation of high corrosion resistant titanium alloys by spark plasma sintering, J. Jpn. Inst. Met. 63 (1999) 1149–1152.

[534] Q. Liu, W.Y. Yang, G.L. Chen, Preparation of high corrosion resistant titanium alloys by spark plasma sintering, Acta Metall. Mater. 43 (1995) 3571–3582.

[535] K. Edalati, Q. Wang, N.A. Enikeev, L.J. Peters, M.J. Zehetbauer, E. Schafler, Significance of strain rate in severe plastic deformation on steady-state microstructure and strength, Mater. Sci. Eng. A 859 (2022) 144231.

[536] H.K. Lin, Y.H. Cheng, G.Y. Li, Y.C. Chen, P. Bazarnik, J. Muzy, Y. Huang, T. G. Langdon, Study on the surface modification of nanostructured Ti alloys and coarse-grained Ti alloys, Metals 12 (2022) 948.

[537] R.B. Figueiredo, T.G. Langdon, Development of an ω-phase in grade 2 titanium processed by HPT at high hydrostatic pressure, Mater. Res. 19 (2016) 1144–1148.

[538] S. Sinha, V.K. Sahu, V. Beura, R. Sonkusare, R. Kalsar, A.K.L. Das, J. Basu, N. P. Gurao, K. Biswas, Initial texture dependence of nanocrystalline omega phase formation during high pressure torsion of commercially pure titanium, Mater. Sci. Eng. A 802 (2021) 140687.

[539] A. Sotniczuk, H. Garbacz, Nanostructured bulk titanium with enhanced properties - strategies and prospects for dental applications, Adv. Eng. Mater. 23 (2021) 2000909.

[540] W.J. Chen, J. Xu, D.T. Liu, J.X. Bao, S. Sabbaghianrad, D.B. Shan, B. Guo, T. G. Langdon, Microstructural evolution and microhardness variations in pure titanium processed by high-pressure torsion, Adv. Eng. Mater. 22 (2020) 1901462.

[541] H. Li, W.C. Zhang, J.L. Yang, J.Q. Pan, W.Z. Chen, G.R. Cui, G.F. Wang, G.N. Chu, Microstructural evolution and mechanical properties of Ti-22Al-25Nb alloy fabricated by high-pressure torsion under ageing treatment, J. Mater. Eng. Perform. 31 (2022) 07465.

[542] P. Bazarnik, A. Bartkowska, Y. Huang, K. Szlazak, B. Adamczyk-Cieslak, J. Sort, M. Lewandowska, T.G. Langdon, Fabrication of hybrid nanocrystalline Al–Ti alloys by mechanical bonding through high-pressure torsion, Mater. Sci. Eng. A 833 (2022) 142549.

[543] M. Alfreider, J. Jeong, R. Esterl, S.H. Oh, D. Kiener, Synthesis and mechanical characterisation of an ultra-fine grained Ti-Mg composite, Materials 9 (2016) 688.

[544] A. Kilmametov, Y. Ivanisenko, B.B. Straumal, A.A. Mazilkin, A.S. Gornakova, M. J. Kriegel, O.B. Fabrichnaya, D. Rafaja, H. Hahn, Transformations of α' martensite in Ti–Fe alloys under high pressure torsion, Scr. Mater. 136 (2017) 46–49.

[545] E.I. Lopez-Gomez, K. Edalati, F.J. Antiqueira, D.D. Coimbrao, G. Zepon, D. R. Leiva, T.T. Ishikawa, J.M. Cubero-Sesin, W.J. Botta, Synthesis of nanostructured TiFe hydrogen storage material by mechanical alloying via high-pressure torsion, Adv. Eng. Mater. 22 (2020) 2000011.

[546] G. Gurau, C. Gurau, F.M. Braz Fernandes, P. Alexandru, V. Sampath, M. Marin, B. M. Galbinasu, Structural characteristics of multilayered Ni-Ti nanocomposite fabricated by high speed high pressure torsion (HSHPT), Metals 10 (2020) 1629.

[547] A. Kilmametov, A. Gornakova, M. Karpov, N. Afonikova, A. Korneva, P. Zięba, B. Baretzky, B. Straumal, Influence of β-stabilizers on the αTi→ωTi transformation in Ti-based alloys, Processes 8 (2020) 1135.

[548] B.B. Straumal, A.R. Kilmametov, Y. Ivanisenko, A.A. Mazilkin, R.Z. Valiev, N. S. Afonikova, A.S. Gornakova, H. Hahn, Diffusive and displacive phase transitions in Ti–Fe and Ti–Co alloys under high pressure torsion, J. Alloy. Compd. 735 (2018) 2281–2286.

[549] B.B. Straumal, A. Korneva, A.R. Kilmametov, L. Lityńska-Dobrzyńska, A. S. Gornakova, R. Chulist, M.I. Karpov, P. Zięba, Structural, mechanical properties of Ti–Co alloys treated by the high pressure torsion, Materials 12 (2019) 426.

[550] K. Bartha, J. Strasky, A. Veverkova, J. Vesely, J. Cizek, J. Malek, V. Polyakova, I. Semenova, M. Janecek, Phase transformations upon ageing in Ti15Mo alloy subjected to two different deformation methods, Metals 11 (2021) 1230.

[551] B.Z. Jiang, S. Emura, K. Tsuchiya, Effect of quasi-hydrostatic pressure on deformation mechanism in Ti-10Mo alloy, Metals 10 (2020) 1387.

[552] C.R.M. Afonso, A. Amigo, V. Stolyarov, D. Gunderov, V. Amigo, From porous to dense nanostructured β-Ti alloys through high-pressure torsion, Sci. Rep. 7 (2017) 13618.

[553] A. Korneva, B. Straumal, A. Gornakova, A. Kilmametov, Ł. Gondek, L. Lityńska-Dobrzyńska, R. Chulist, M. Pomorska, P. Zięba, Formation and thermal stability of the ω-phase in Ti–Nb and Ti–Mo alloys subjected to HPT, Materials 15 (2022) 4136.

[554] A.V. Dobromyslov, N.I. Taluts, V.P. Pilyugin, Severe plastic deformation by high-pressure torsion of Hf and Hf-Ti alloys, Int. J. Refract. Met. Hard Mater. 93 (2020) 105354.

[555] A.S. Gornakova, A.B. Straumal, I.I. Khodos, I.B. Gnesin, A.A. Mazilkin, N. S. Afonikova, B.B. Straumal, Effect of composition, annealing temperature, and high pressure torsion on structure and hardness of Ti–V and Ti–V–Al alloys, J. Appl. Phys. 125 (2019) 082522.

[556] D.A.G. Pérez, A.M. Jorge Junior, V. Roche, J.C. Lepretre, C.R.M. Afonso, D. N. Travessa, G.H. Asato, C. Bolfarini, W.J. Botta, Severe plastic deformation and different surface treatments on the biocompatible Ti13Nb13Zr and Ti35Nb7Zr5Ta alloys: microstructural and phase evolutions, mechanical properties, and bioactivity analysis, J. Alloy. Compd. 812 (2020) 152116.

[557] D.R. Barjaktarevic, V.R. Djokic, J.B. Bajat, I.D. Dimic, I.L. Cvijovic-Alagic, M. P. Rakin, The influence of the surface nanostructured modification on the corrosion resistance of the ultrafine-grained Ti–13Nb–13Zr alloy in artificial saliva, Theor. Appl. Fract. Mech. 103 (2019) 102307.

[558] J. Dutkiewicz, J. Kusnierz, W. Maziarz, M. Lejkowska, H. Garbacz, M. Lewandowska, A.V. Dobromyslov, K.J. Kurzydlowski, Microstructure and mechanical properties of nanocrystalline titanium and Ti–Ta–Nb alloy manufactured using various deformation methods, Phys. Stat. Sol. A 202 (2005) 2309–2320.

[559] T. Maity, O. Balci, C. Gammer, E. Ivanov, J. Eckert, K.G. Prashanth, High pressure torsion induced lowering of Young's modulus in high strength TNZT alloy for bio-implant applications, J. Mech. Beh. Biomed. Mater. 108 (2020) 103839.

[560] H. Yilmazer, M. Sen, M. Niinomi, M. Nakai, H.H. Liu, K. Cho, Y. Todaka, H. Shiku, Matsue, Developing biomedical nano-grained β-type titanium alloys using high pressure torsion for improved cell adherence, RSC Adv. 6 (2016) 7426–7430.

[561] K.M. Xue, J.H. Sun, X.H. Ji, W.W. Guo, P. Li, Effect of high-pressure torsion on microstructure and properties of TA15 titanium alloy, Rare Metal. Mater. Eng. 48 (2019) 1189–1194.

[562] A. Kilmametov, Y. Ivanisenko, A.A. Mazilkin, B.B. Straumal, A.S. Gornakova, O. B. Fabrichnaya, M.J. Kriegel, D. Rafaja, H. Hahn, The α→ω and β→ω phase transformations in Ti–Fe alloys under high-pressure torsion, Acta Mater. 144 (2018) 337–351.

[563] R. Ray, B.C. Giessen, N.J. Grant, The constitution of metastable titanium-rich Ti-Fe alloys, an order-disorder transition, Metall. Trans. 3 (1972) 627–629.

[564] B.W. Levinger, Lattice parameter of beta titanium at room temperature, Trans. Am. Inst. Min. Met. Eng. 197 (1953) 195–200.

[565] S.G. Fedotov, N.F. Kvasova, M.I. Ermolova, Decomposition of the metastable solid solution of titanium with ipron, Dokl. Akad. Nauk SSSR 216 (1974) 363–366.

[566] L.N. Guseva, L.K. Dolinskaya, Metastable phases in titanium alloys with group VIII elements quenched from the β-Region, Izv. Akad. Nauk SSSR Met. 6 (1974) 195–202.

[567] A. Korneva, B. Straumal, A. Kilmametov, L. Lityńska-Dobrzyńska, R. Chulist, P. Gondek, Zięba, The phase transformations induced by high-pressure torsion in Ti–Nb-based alloys, Microsc. Microanal. 28 (2022) 946–952.

[568] B.B. Straumal, A.R. Kilmametov, A.A. Mazilkin, A.S. Gornakova, O. B. Fabrichnaya, M.J. Kriegel, D. Rafaja, M.F. Bulatov, A.N. Nekrasov, B. Baretzky, Formation of the ω phase in the titanium-iron system under shear deformation, JETP Lett. 111 (2020) 568–574.

[569] B.B. Straumal, A.R. Kilmametov, B. Baretzky, O.A. Kogtenkova, P.B. Straumal, L. Lityńska-Dobrzyńska, R. Chulist, A. Korneva, P. Zięba, High pressure torsion of Cu–Ag and Cu–Sn alloys: Limits for solubility and dissolution, Acta Mater. 195 (2020) 184–198.

[570] B.B. Straumal, L.M. Klinger, L.S. Shvindlerman, The influence of pressure on indium diffusion along single tin–germanium interphase boundaries, Scr. Metall. 17 (1983) 275–279.

[571] D.A. Molodov, B.B. Straumal, L.S. Shvindlerman, The effect of pressure on migration of the [001] tilt grain boundaries in the tin bicrystals, Scr. Metall. 18 (1984) 207–211.

[572] A. Korneva, B. Straumal, A. Kilmametov, A. Gornakova, A. Wierzbicka-Miernik, L. Lityńska-Dobrzyńska, R. Chulist, Ł. Gondek, G. Cios, P. Zięba, The α→ω phase transformation in Ti-3wt%Nb alloy subjected to high pressure torsion, Materials 14 (2021) 2262.

[573] E.L. Maksimova, L.S. Shvindlerman, B.B. Straumal, Transformation of Σ17 special tilt boundaries to general boundaries in Sn, Acta Met. 36 (1988) 1573–1583.

[574] B.B. Straumal, A.S. Gornakova, Y.O. Kucheev, B. Baretzky, A.N. Nekrasov, Grain boundary wetting by a second solid phase in the Zr–Nb alloys, J. Mater. Eng. Perform. 21 (2012) 721–724.

[575] L.S. Chang, B.B. Straumal, E. Rabkin, W. Gust, F. Sommer, The solidus line of the Cu–Bi phase diagram, J. Phase Equibl 18 (1997) 128–135.

[576] L.S. Chang, E. Rabkin, B.B. Straumal, S. Hoffmann, B. Baretzky, W. Gust, Grain boundary segregation in the Cu–Bi system, Defect Diff. Forum 156 (1998) 135–146.

[577] D.A. Molodov, U. Czubayko, G. Gottstein, L.S. Shvindlerman, B.B. Straumal, W. Gust, Acceleration of grain boundary motion in Al by small additions of Ga, Philos. Mag. Lett. 72 (1995) 361–368.

[578] O.I. Noskovich, E.I. Rabkin, V.N. Semenov, B.B. Straumal, L.S. Shvindlerman, Wetting and premelting phase transitions in 38° [100] tilt grain boundaries in (Fe–12at%Si) Zn alloy in the vicinity of the A2–B2 bulk ordering in Fe–12at%Si alloy, Acta Metall. Mater. 39 (1991) 3091–3098.

[579] B. Straumal, E. Rabkin, W. Lojkowski, W. Gust, L.S. Shvindlerman, Pressure influence on the grain boundary wetting phase transition in Fe–Si alloys, Acta Mater. 45 (1997) 1931–1940.

[580] Y. Ivanisenko, X. Sauvage, A. Mazilkin, A. Kilmametov, J.A. Beach, B.B. Straumal, Bulk nanocrystalline ferrite stabilized through grain boundary carbon segregation, Adv. Eng. Mater. 20 (2018) 1800443.

[581] A.A. Mazilkin, B.B. Straumal, A.R. Kilmametov, T. Boll, B. Baretzky, O. A. Kogtenkova, A. Korneva, P. Zięba, Competition for impurity atoms between defects and solid solution during high pressure torsion, Scr. Mater. 173 (2019) 46–50.

[582] H. Razavi-Khosroshahi, K. Edalati, M. Arita, Z. Horita, M. Fuji, Plastic strain and grain size effect on high-pressure phase transformations in nanostructured TiO₂ ceramics, Scr. Mater. 124 (2016) 59–62.

[583] H. Razavi-Khosroshahi, K. Edalati, H. Emami, E. Akiba, Z. Horita, M. Fuji, Optical properties of nanocrystalline monoclinic Y₂O₃ stabilized by grain size and plastic strain effects using high-pressure torsion, Inorg. Chem. 56 (2017) 2576–2580.

[584] K. Edalati, S. Toh, Y. Ikoma, Z. Horita, Plastic deformation and allotropic phase transformations in zirconia ceramics during high-pressure torsion, Scr. Mater. 65 (2011) 974–977.

[585] Z.L. Wang, Zinc oxide nanostructures: growth, properties and applications, J. Phys. Condens. Matter 16 (2004) R829.

[586] M.D. McCluskey, S.J. Jokela, Defects in ZnO, J. Appl. Phys. 106 (2009) 071101.

[587] S. Dutta, S. Chattopadhyay, A. Sarkar, M. Chakrabarti, D. Sanyal, D. Jana, Role of defects in tailoring structural, electrical and optical properties of ZnO, Prog. Mater. Sci. 54 (2009) 89–136.

[588] A.B. Djurisic, A.M.C. Ng, X.Y. Chen, (Review) ZnO nanostructures for optoelectronics: Material properties and device applications, Prog. Quant. Elect. 34 (2010) 191–259.

[589] J. Jiang, J. Pi, J. Cai, Review article the advancing of zinc oxide nanoparticles for biomedical applications, Bioinorg. Chem. Appl. 2018 (2018) 1062562.

[590] M.A. Borysiewicz, ZnO as a functional material, a review, Crystals 9 (2019) 505.

[591] A. Moezzi, A.M. McDonagh, M.B. Cortie, Zinc oxide particles: synthesis, properties and applications, Chem. Eng. J. 185–186 (2012) 1–22.

[592] M. Abendrot, U. Kalinowska-Lis, Zinc-containing compounds for personal care applications, Int. J. Cosm. Sci. 40 (2018) 319–327.

[593] L. Bayarjargal, B. Winkler, High (pressure, temperature) phase diagrams of ZnO and AlN from second harmonic generation measurements, Appl. Phys. Lett. 100 (2012) 021909.

[594] F. Decremps, J. Zhang, R.C. Liebermann, New phase boundary and high-pressure thermoelasticity of ZnO, Europhys. Lett. 51 (2000) 268–274.

[595] A.B.F. Martinson, J.W. Elam, J.T. Hupp, M.J. Pellin, ZnO nanotube based dye-sensitized solar cells, Nano Lett. 7 (2007) 2183–2187.

[596] Z.L. Wang, Splendid one-dimensional nanostructures of zinc oxide: a new nanomaterial family for nanotechnology, ACS Nano 2 (2008) 1987–1992.

[597] J. Han, F. Fan, C. Xu, S. Lin, M. Wei, X. Duan, Z.L. Wang, ZnO nanotube-based dye-sensitized solar cell and its application in self-powered devices, Nanotechnology 21 (2010) 405203.

[598] Z. Jiang, S. Soltanian, B. Gholamkhass, A. Aljaafari, P. Servati, Light-soaking free organic photovoltaic devices with sol–gel deposited ZnO and AZO electron transport layers, RSC Adv. 8 (2018) 36542–36548.

[599] D. Liu, T.L. Kelly, Perovskite solar cells with a planar heterojunction structure prepared using room-temperature solution processing techniques, Nat. Photonics 8 (2014) 133–138.

[600] A. Segura, J.A. Sans, F.J. Manjón, A. Muñoz, M.J. Herrera-Cabrera, Optical properties and electronic structure of rock-salt ZnO under pressure, Appl. Phys. Lett. 83 (2003) 278–280.

[601] A. Alvarado, J. Attapattu, Y. Zhang, C. Chen, Thermoelectric properties of rocksalt ZnO from first-principles calculations, J. Appl. Phys. 118 (2015) 165101.

[602] H. Dixit, R. Saniz, D. Lamoen, B. Partoens, The quasiparticle band structure of zincblende and rocksalt ZnO, J. Phys. Condens. Matter 22 (2010) 125505.

[603] V. Srikant, D.R. Clarke, On the optical band gap of zinc oxide, Appl. Phys. 83 (1998) 5447–5451.

[604] H. Razavi-Khosroshahi, K. Edalati, J. Wu, Y. Nakashima, M. Arita, Y. Ikoma, M. Sadakiyo, Y. Inagaki, A. Staykov, M. Yamauchi, Z. Horita, M. Fuji, High-pressure zinc oxide phase as visible-lightactive photocatalyst with narrow band gap, J. Mater. Chem. A 5 (2017) 20298–20303.

[605] J. Hidalgo-Jimenez, Q. Wang, K. Edalati, J.M. Cubero-Sesín, H. Razavi-Khosroshahi, Y. Ikoma, D. Gutiérrez-Fallas, F.A. Dittel-Meza, J.C. Rodríguez-Rufino, M. Fuji, Z. Horita, Phase transformations, vacancy formation and variations of optical and photocatalytic properties in TiO₂-ZnO composites by highpressure torsion, Int. J. Plast. 124 (2020) 170–185.

[606] K. Edalati, R. Uehiro, S. Takechi, Q. Wang, M. Arita, M. Watanabe, T. Ishihara, Z. Horita, Enhanced photocatalytic hydrogen production on GaN–ZnO oxynitride by introduction of strain-induced nitrogen vacancy complexes, Acta Mater. 185 (2020) 149–156.

[607] Z. Horita, Y. Tang, T. Masuda, K. Edalati, Y. Higo, In situ synchrotron high-pressure X-ray analysis for ZnO with rocksalt structure, Mater. Trans.. 64 (2023) 1585–1590.

[608] Z. Horita, D. Maruno, Y. Ikeda, T. Masuda, Y. Tang, M. Arita, Y. Higo, Y. Tange, Y. Ohishi, In situ synchrotron X-ray analysis: application of high-pressure sliding process to Ti allotropic transformation, Mater. Trans. 62 (2021) 167–176.

[609] Q. Wang, K. Edalati, I. Fujita, M. Watanabe, T. Ishihara, Z. Horita, High-pressure torsion of SiO₂ quartz sand: phase transformation, optical properties and significance in geology, J. Am. Ceram. Soc. 103 (2020) 6594–6602.

[610] K.K. Pandey, V.I. Levitas, In situ quantitative study of plastic strain-induced phase transformations under high pressure: example for ultra-pure Zr, Acta Mater. 196 (2020) 338–346.

[611] F. Lin, V.I. Levitas, K.K. Pandey, S. Yesudhas, C. Park, Laws of high-pressure phase and nanostructure evolution and severe plastic flow, (2022) https://doi.org/1 0.21203/rs.3.rs-1998605/v1.

[612] S. Yesudhas, V.I. Levitas, F. Lin, K.K. Pandey, J. Smith, Plastic strain-induced phase transformations in silicon: drastic reduction of transformation pressures, change in transformation sequence, and particle size effect, (2023) ⟨https://arxiv.org/abs/2303.04407⟩.

[613] F. Lin, V.I. Levitas, S. Yesudhas, J. Smith, Plastic strain-induced olivine-ringwoodite phase transformation at room temperature: main rules and the mechanism of the deep-focus earthquake, (2023), https://doi.org/10.4855 0/arXiv.2305.15737.

[614] F. Lin, V.I. Levitas, K.K. Pandey, S. Yesudhas, C. Park, In-situ study of rules of nanostructure evolution, severe plastic deformations, and friction under high pressure, Mater. Res. Lett. 11 (2023) 757–763.

[615] V.I. Levitas, O.M. Zarechnyy, Modeling and simulation of strain-induced phase transformations under compression in a diamond anvil cell, Phys. Rev. B 82 (2010) 174123.

[616] V.I. Levitas, O.M. Zarechnyy, Modeling and simulation of strain-induced phase transformations under compression and torsion in a rotational diamond anvil cell, Phys. Rev. B 82 (2010) 174124.

[617] B. Feng, V.I. Levitas, W. Li, FEM modeling of plastic flow and strain-induced phase transformation in BN under high pressure and large shear in a rotational diamond anvil cell, Int. J. Plast. 113 (2019) 236–254.

[618] V.I. Levitas, M. Kamrani, B. Feng, Tensorial stress-strain fields and large elastoplasticity as well as friction in diamond anvil cell up to 400 GPa, NPJ Comp. Mater. 5 (2019) 94.

[619] V.I. Levitas, A. Dhar, K.K. Pandey, Tensorial stress-plastic strain fields in α-ω Zr mixture, transformation kinetics, and friction in diamond anvil cell, Nat. Comm. 14 (2023) 5955.

[620] V.I. Levitas, H. Chen, L. Xiong, Triaxial-stress-induced homogeneous hysteresis-free first-order phase transformations with stable intermediate phases, Phys. Rev. Lett. 118 (2017) 025701.

[621] V.I. Levitas, H. Chen, L. Xiong, Lattice instability during phase transformations under multiaxial stress: modified transformation work criterion, Phys. Rev. B 96 (2017) 054118.

[622] N.A. Zarkevich, H. Chen, V.I. Levitas, D.D. Johnson, Lattice instability during phase transformations under multiaxial stress: modified transformation work criterion, Phys. Rev. Lett. 121 (2018) 165701.

[623] H. Chen, V.I. Levitas, L. Xiong, Amorphization induced by 60° shuffle dislocation pileup against tilt grain boundaries in silicon bicrystal under shear, Acta Mater. 179 (2019) 287–295.

[624] M. Javanbakht, V.I. Levitas, Phase field simulations of plastic strain-induced phase transformations under high pressure and large shear, Phys. Rev. B 94 (2016) 214104.

[625] V.I. Levitas, M. Javanbakht, Phase field approach to interaction of phase transformation and dislocation evolution, Appl. Phys. Lett. 102 (2013) 251904.

[626] V.I. Levitas, S.E. Esfahani, I. Ghamarian, Scale-free modeling of coupled evolution of discrete dislocation bands and multivariant martensitic microstructure, Phys. Rev. Lett. 121 (2018) 205701.

[627] S.E. Esfahani, I. Ghamarian, V.I. Levitas, Strain-induced multivariant martensitic transformations: a scale-independent simulation of interaction between localized shear bands and microstructure, Acta Mater. 196 (2020) 430–443.

[628] Y. Ma, E. Selvi, V.I. Levitas, J. Hashemi, Effect of shear strain on the α-ε phase transition of iron: a new approach in the rotational diamond anvil cell, J. Phys.: Cond. Matter 18 (2006) 1075–1082.

[629] Y. Gao, Y. Ma, Q. An, V.I. Levitas, Y. Zhang, B. Feng, J. Chaudhuri, W. A. Goddard III, Shear driven formation of nano-diamonds at sub-gigapascals and 300 K, Carbon 146 (2019) 364–368.

[630] V.I. Levitas, Y. Ma, E. Selvi, J. Wu, J. Patten, High-density amorphous phase of silicon carbide obtained under large plastic shear and high pressure, Phys. Rev. B 85 (2012) 054114.

[631] V.D. Blank, E.I. Estrin, Phase Transitions in Solids Under High Pressure, CRC Press,, New York, 2014.

[632] K.K. Pandey, V.I. Levitas, Displacement field measurements in traditional and rotational diamond anvil cells, J. Appl. Phys. 129 (2021) 115901.

[633] A.R. Kilmametov, G. Vaughan, A.R. Yavari, A. LeMoulec, W.J. Botta, R.Z. Valiev, Microstructure evolution in copper under severe plastic deformation detected by in situ X-ray diffraction using monochromatic synchrotron light, Mater. Sci. Eng. A 503 (2009) 10–13.

[634] M.B. Kerber, F. Spieckermann, R. Schuster, C. von Baeckmann, T. Fischer, N. Schell, T. Waitz, E. Schafler, In situ synchrotron x-ray diffraction during high-pressure torsion deformation of Ni and NiTi, Adv. Eng. Mater. 23 (2021) 2100159.

[635] J. Girard, G. Amulele, R. Farla, A. Mohiuddin, S. Karato, Shear deformation of bridgmanite and magnesiowüstite aggregates at lower mantle conditions, Science 351 (2016) 144–147.

[636] Y. Nishihara, D. Tinker, T. Kawazoe, Y. Xu, Z. Jing, K.N. Matsukage, S.I. Karato, Plastic deformation of wadsleyite and olivine at high-pressure and high-temperature using a rotational Drickamer apparatus (RDA), Phys. Earth Planet. Inter. 170 (2008) 156–169.

[637] L. Miyagi, G. Amulele, K. Otsuka, Z. Du, R. Farla, S.I. Karato, Plastic anisotropy and slip systems in ringwoodite deformed to high shear strain in the Rotational Drickamer Apparatus, Phys. Earth Planet. Inter. 228 (2014) 244–253.

[638] G.Z. Voyiadjis, M. Yaghoobi, Size Effects in Plasticity: From Macro to Nano, Academic Press,, Cambridge, 2019.

[639] H. Razavi-Khosroshahi, K. Edalati, M. Hirayama, H. Emami, M. Arita, M. Yamauchi, H. Hagiwara, S. Ida, T. Ishihara, E. Akiba, Z. Horita, M. Fuji, Visible-light-driven photocatalytic hydrogen generation on nanosized TiO₂-II stabilized by high-pressure torsion, ACS Catal. 6 (2016) 5103–5107.

[640] F.A. Mohamed, S.S. Dheda, On the minimum grain size obtainable by high-pressure torsion, Mater. Sci. Eng. A 558 (2012) 59–63.

[641] S. Lu, Q.M. Hu, E.K. Delczeg-Czirjak, B. Johansson, L. Vitos, Determining the minimum grain size in severe plastic deformation process via first-principles calculations, Acta Mater. 60 (2012) 4506–4513.

[642] K. Edalati, Z. Horita, Universal plot for hardness variation in pure metals processed by high-pressure torsion, Mater. Trans. 51 (2010) 1051–1054.

[643] Y. Cao, S. Ni, X. Liao, M. Song, Y. Zhu, Structural evolutions of metallic materials processed by severe plastic deformation, Mater. Sci. Eng. R 133 (2018) 1–59.

[644] Y.T. Zhu, T.G. Langdon, The fundamentals of nanostructured materials processed by severe plastic deformation, JOM 56 (10) (2004) 58–63.

[645] D.J. Lee, E.Y. Yoon, D.H. Ahn, B.H. Park, H.W. Park, L.J. Park, Y. Estrin, H.S. Kim, Dislocation density-based finite element analysis of large strain deformation behavior of copper under high-pressure torsion, Acta Mater. 76 (2014) 281–293.

[646] V.I. Levitas, Resolving puzzles of the phase-transformation-based mechanism of the deep-focus earthquake, Nat. Commun. 13 (2022) 6291.

[647] R.Z. Valiev, N.A. Enikeev, M.Y. Murashkin, V.U. Kazykhanov, X. Sauvage, On the origin of the extremely high strength of ultrafine-grained Al alloys produced by severe plastic deformation, Scr. Mater. 63 (2010) 949–952.

[648] Y. Ito, K. Edalati, Z. Horita, High-pressure torsion of aluminum with ultrahigh purity (99.9999%) and occurrence of inverse Hall-Petch relationship, Mater. Sci. Eng. A 679 (2017) 428–434.

[649] K. Edalati, Y. Hashiguchi, H. Iwaoka, H. Matsunaga, R.Z. Valiev, Z. Horita, Long-time stability of metals after severe plastic deformation: softening and hardening by self-annealing versus thermal stability, Mater. Sci. Eng. A 729 (2018) 340–348.

[650] A.A. Mazilkin, B.B. Straumal, E. Rabkin, B. Baretzky, S. Enders, S.G. Protasova, O. A. Kogtenkova, R.Z. Valiev, Softening of nanostructured Al–Zn and Al–Mg alloys after severe plastic deformation, Acta Mater. 54 (2006) 3933–3939.

[651] P. Kumar, M. Kawasaki, T.G. Langdon, Review: Overcoming the paradox of strength and ductility in ultrafine-grained materials at low temperatures, J. Mater. Sci. 51 (2016) 7–18.

[652] T.G. Langdon, Overview: using severe plastic deformation in the processing of superplastic materials, Mater. Trans. 64 (2023) 1299–1305.

[653] G. Khatibi, J. Horky, B. Weiss, M.J. Zehetbauer, High cycle fatigue behaviour of copper deformed by high pressure torsion, Int. J. Fatigue 32 (2010) 269–278.

[654] V. Sklenicka, P. Kral, J. Dvorak, M. Kvapilova, K. Kucharova, Creep in nanostructured materials, Mater. Trans. 64 (2023) 1566–1574.

[655] N. Gao, C.T. Wang, R.J.K. Wood, T.G. Langdon, Tribological properties of ultrafine-grained materials processed by severe plastic deformation, J. Mater. Sci. 47 (2012) 4779–4797.

[656] A. Hohenwarter, R. Pippan, Fracture and fracture toughness of nanopolycrystalline metals produced by severe plastic deformation, Philos. Trans. R. Soc. A 373 (2015) 20140366.

[657] R.Z. Valiev, Nanostructuring of metals by severe plastic deformation for advanced properties, Nat. Mater. 3 (2004) 511–516.

[658] T. Obata, Y. Tang, H. Iwaoka1, S. Hirosawa, K. Mouri, M. Shimoda, Development of high-strength bolt material of Al-Mg-Si alloy by ECAP and various aging treatments, Mater. Trans. 60 (2019) 1680–1687.

[659] Y. Tang, M. Murayama, K. Edalati, Q. Wang, S. Iikubo, T. Masuda, Y. Higo, Y. Tange, Y. Ohishi, M. Mito, Z. Horita, Phase transformations in Al-Ti-Mg powders consolidated by high-pressure torsion: experiments and first-principles calculations, J. Alloy. Compd. 889 (2021) 161815.

[660] Y. Tang, S. Inoue, M. Mito, T. Masuda, Y. Higo, Y. Tange, Y. Ohishi, Y. Kawamura, Z. Horita, Simultaneous enhancement of strength and ductility in nonflammable Mg alloys through dynamic precipitation using severe plastic deformation under high pressure, Mater. Sci. Eng. A 881 (2023) 145395.

[661] N.J. Petch, The cleavage strength of polycrystals, J. Iron. Steel Inst. 174 (1953) 25–28.

[662] J.W. Wyrzykowski, M.W. Grabski, The Hall–Petch relation in aluminium and its dependence on the grain boundary str ucture, Philos. Mag. 43 (1986) 505–520.

[663] J.E. Bailey, P.B. Hirsch, The dislocation distribution, flow stress, and stored energy in cold-worked polycrystalline silver, Philos. Mag. 5 (1960) 485–497.

[664] K. Edalati, J. Matsuda, H. Iwaoka, S. Toh, E. Akiba, Z. Horita, High-pressure torsion of TiFe intermetallics for activation of hydrogen storage at room temperature with heterogeneous nanostructure, Int. J. Hydrog. Energy 38 (2013) 4622–4627.

[665] Q. Wang, M. Watanabe, K. Edalati, Visible-light photocurrent in nanostructured high-pressure TiO$_2$-II (Columbite) phase, J. Phys. Chem. 124 (2020) 13930–13935.

[666] Q. Wang, K. Edalati, Y. Koganemaru, S. Nakamura, M. Watanabe, T. Ishihara, Z. Horita, Photocatalytic hydrogen generation on low bandgap black zirconia (ZrO$_2$) produced by high pressure torsion, J. Mater. Chem. A 8 (2020) 3643–3650.

[667] Q. Wang, Y. Tang, Z. Horita, S. Iikubo, Structural and thermoelectric properties of CH$_3$NH$_3$SnI$_3$ perovskites processed by applying high pressure with shear strain, Mater. Res. Lett. 10 (2022) 521–529.

[668] A.P. Zhilyaev, G. Nurislamova, B.K. Kim, M. Baró, J. Szpunar, T. Langdon, Experimental parameters influencing grain refinement and microstructural evolution during high-pressure torsion, Acta Mater. 51 (2003) 753–765.

[669] A.P. Zhilyaev, T. McNelley, T. Langdon, Evolution of microstructure and microtexture in fcc metals during high-pressure torsion, J. Mater. Sci. 42 (2007) 1517–1528.

[670] N. Kamikawa, N. Tsuji, X. Huang, N. Hansen, Quantification of annealed microstructures in ARB processed aluminum, Acta Mater. 54 (2006) 3055–3066.

[671] X. Huang, N. Hansen, N. Tsuji, Hardening by annealing and softening by deformation in nanostructured metals, Science 312 (2006) 249–251.

[672] Y. Tang, S. Hirosawa, S. Saikawa, K. Matsuda, S. Lee, Z. Horita, D. Terada, Microstructure and mechanical properties of concurrently strengthened Al-Li-Cu alloy by combining ARB with aging, Adv. Eng. Mater. (2019) 1900561.

[673] Y. Tang, W. Goto, S. Hirosawa, Z. Horita, S. Lee, K. Matsuda, D. Terada, Concurrent strengthening of ultrafine-grained age-hardenable Al-Mg alloy by means of high-pressure torsion and spinodal decomposition, Acta Mater. 131 (2017) 57–64.

[674] Y. Tang, Y. Tomita, Z. Horita, Mechanical properties and microstructure of high Fe-containing Al-Mg-Si alloys processed by severe plastic deformation under high pressure, Mater. Trans. 64 (2023) 448–457.

[675] Y. Tang, T. Fujii, S. Hirosawa, K. Matsuda, D. Terada, Z. Horita, Comparison of mechanical properties in ultrafine grained commercial-purity aluminum (A1050) processed by accumulative roll bonding (ARB) and high-pressure sliding (HPS), Mater. Trans. 64 (2023) 1902–1911.

[676] Y. Tang, T. Komatsu, T. Masuda, M. Arita, Y. Takizawa, M. Yumoto, Y. Otagiri, Z. Horita, Mechanical properties and electrical conductivity of ultrafine-grained aluminum consolidated by high-pressure sliding, Materialia 14 (2020) 100916.

[677] Y. Tang, K. Sumikawa, Y. Takizawa, M. Yumoto, Y. Otagiri, Z. Horita, Multi-pass high-pressure sliding (MP-HPS) for grain refinement and superplasticity in metallic round rods, Mater. Sci. Eng. A 748 (2019) 108–118.

[678] Y. Tang, Y. Takizawa, M. Yumoto, Y. Otagiri, Z. Horita, Achieving grain refinement of upsized Al-3Mg-0.2Sc (mass%) round rods using multi-pass high-pressure sliding (MP-HPS), Mater. Trans. 61 (2020) 1387–1389.

[679] H.W. Höppel, J. May, M. Goken, Enhanced strength and ductility in ultrafine-grained aluminium produced by accumulative roll bonding, Adv. Eng. Mater. 6 (2004) 219–222.

[680] A. Bohner, V. Maier, K. Durst, H.W. Höppel, M. Goken, Macro- and nanomechanical properties and strain rate sensitivity of accumulative roll bonded and equal channel angular pressed ultrafine-grained materials, Adv. Eng. Mater. 13 (2011) 251–255.

[681] S. Dangwal, K. Edalati, R.Z. Valiev, T.G. Langdon, Breaks in the Hall-Petch relationship after severe plastic deformation of magnesium, aluminum, copper and iron, Crystals 13 (2023) 413.

[682] Y. Li, D. Raabe, M. Herbig, P.P. Choi, S. Goto, A. Kostka, H. Yarita, C. Borchers, R. Kirchheim, Segregation stabilizes nanocrystalline bulk steel with near theoretical strength, Phys. Rev. Lett. 113 (2014) 106104.

[683] A. Hohenwarter, B. Völker, M.W. Kapp, Y. Li, S. Goto, D. Raabe, R. Pippan, Ultra-strong and damage tolerant metallic bulk materials: a lesson from nanostructured pearlitic steel wires, Sci. Rep. 6 (2016) 33228.

[684] R.D. Doherty, D.A. Hughes, F.J. Humphreys, J.J. Jonas, D. Juul Jensen, M. E. Kassner, W.E. King, T.R. McNelley, H.J. McQueen, A.D. Rollett, Current issues in recrystallization: a review, Mater. Sci. Eng. A 238 (1997) 219–274.

[685] T.J. Rupert, J.R. Trelewicz, C.A. Schuh, Grain boundary relaxation strengthening of nanocrystalline Ni–W, Alloy., J. Mater. Sci. 27 (2012) 1285–1294.

[686] M.M. Abramova, N.A. Enikeev, R.Z. Valiev, A. Etienne, B. Radiguet, Y. Ivanisenko, X. Sauvage, Grain Bound. Segreg. Induc. Strength. Ultra -Graine austenitic Stainl. Steel 136 (2014) 349–352.

[687] O. Renk, A. Hohenwarter, K. Eder, K.S. Kormout, J.M. Cairney, R. Pippan, Increasing the strength of nanocrystalline steels by annealing: is segregation necessary? Scr. Mater. 95 (2015) 27–30.

[688] J. Hu, Y.N. Shi, X. Sauvage, G. Sha, K. Lu, Grain boundary stability governs hardening and softening in extremely fine nanograined metals, Science 355 (2017) 1292–1296.

[689] J. Gubicza, Annealing-induced hardening in ultrafine-grained and nanocrystalline materials, Adv. Eng. Mater. 22 (2020) 1900507.

[690] O. Renk, R. Pippan, Anneal hardening in single phase nanostructured metals, Mater. Trans. 64 (2023) 1464–1473.

[691] R.R. Hasiguti, A proposed theory of anneal-hardening of cold-worked alpha brass, Mater. Trans. 19 (1955) 103–106.

[692] R.W. Cahn, R.G. Davies, X-ray evidence for segregation of solute to stacking faults in a copper-aluminium alloy, Philos. Mag. A 5 (1960) 1119–1126.

[693] J.M. Popplewell, J. Crane, Order-strengthening in Cu–Al alloys, Metall. Mater. Trans. B 2 (1971) 3411–3420.

[694] O. Renk, A. Hohenwarter, B. Schuh, J.H. Li, R. Pippan, Hardening by annealing: insights from different alloys, IOP Conf. Ser. Mater. Sci. Eng. 89 (2015) 012043.

[695] P.H. Pumphrey, H. Gleiter, The annealing of dislocations in high-angle grain boundaries, Philos. Mag. A. 30 (1974) 593–602.

[696] O. Renk, V. Maier-Kiener, I. Issa, J.H. Li, D. Kiener, R. Pippan, Anneal hardening and elevated temperature strain rate sensitivity of nanostructured metals: their relation to intergranular dislocation accommodation, Acta Mater. 165 (2019) 409–419.

[697] A. Hasnaoui, H. Van Swygenhoven, P.M. Derlet, On non-equilibrium grain boundaries and their effect on thermal and mechanical behaviour: a molecular dynamics computer simulation, Acta Mater. 50 (2002) 3927–3939.

[698] H. Li, S. Gao, Y. Tomota, S. Ii, N. Tsuji, T. Ohmura, Mechanical response of dislocation interaction with grain boundary in ultrafine-grained interstitial-free steel, Acta Mater. 206 (2021) 116621.

[699] A.G. Frøseth, P.M. Derlet, H. Van Swygenhoven, Dislocations emitted from nanocrystalline grain boundaries: nucleation and splitting distance, Acta Mater. 52 (2004) 5863–5870.

[700] M. Alfreider, I. Issa, O. Renk, D. Kiener, Probing defect relaxation in ultra-fine grained Ta using micromechanical spectroscopy, Acta Mater. 185 (2020) 309–319.

[701] N.Q. Vo, J. Schäfer, R.S. Averback, K. Albe, Y. Ashkenazy, P. Bellon, Reaching theoretical strengths in nanocrystalline Cu by grain boundary doping, Scr. Mater. 65 (2011) 660–663.

[702] O. Renk, A. Hohenwarter, V. Maier-Kiener, R. Pippan, Exploring the anneal hardening phenomenon in nanocrystalline Pt-Ru alloys, J. Alloy. Compd. 935 (2023) 168005.

[703] S. Wu, Z. Kou, Q. Lai, S. Lan, S.S. Katnagallu, H. Hahn, S. Taheriniya, G. Wilde, H. Gleiter, T. Feng, Dislocation exhaustion and ultra-hardening of nanograined metals by phase transformation at grain boundaries, Nat. Commun. 13 (2022) 5468.

[704] T. Guo, S. Ke, Q. Zhou, Y. Chen, P. Huang, Anomalous weakened annealing-induced hardening in extremely fine nanograined NiFe alloys, J. Alloy. Compd. 925 (2022) 166597.

[705] L. Priester, On the accommodation of extrinsic dislocations in grain boundaries, Interface Sci. 4 (1997) 205–219.

[706] A.A. Nazarov, Kinetics of grain boundary recovery in deformed polycrystals, Interface Sci. 8 (2000) 315–322.

[707] B.L. Boyce, H.A. Padilla II, Anomalous fatigue behavior and fatigue-induced grain growth in nanocrystalline nickel alloys, Metall. Mater. Trans. A 42 (2011) 1793–1804.

[708] T.A. Furnish, A. Mehta, D. Van Campen, D.C. Bufford, K. Hattar, B.L. Boyce, The onset and evolution of fatigue-induced abnormal grain growth in nanocrystalline Ni–Fe, J. Mater. Sci. 52 (2017) 46–59.

[709] M.W. Kapp, O. Renk, T. Leitner, P. Ghosh, B. Yang, R. Pippan, Cyclically induced grain growth within shear bands investigated in UFG Ni by cyclic high pressure torsion, J. Mater. Res 32 (2017) 4317–4326.

[710] M.W. Kapp, O. Renk, P. Ghosh, T. Leitner, B. Yang, R. Pippan, Plastic strain triggers structural instabilities upon cyclic loading in ultrafine-grained nickel, Acta Mater. 200 (2020) 136–147.

[711] Y. Nakai, R. Takeshige, T. Hirai, S. Kikuchi, Effects of grain size and grain boundary stability on mechanical and fatigue properties of nanocrystalline nickel thin films, Mater. Trans. 62 (2021) 1320–1327.

[712] O. Renk, A. Hohenwarter, C. Gammer, J. Eckert, R. Pippan, Achieving 1 GPa fatigue strength in nanocrystalline 316L steel through recovery annealing, Scr. Mater. 217 (2022) 114773.

[713] O. Renk, A. Hohenwarter, R. Pippan, Cyclic deformation behavior of a 316L austenitic stainless steel processed by high pressure torsion, Adv. Eng. Mater. 14 (2012) 948–954.

[714] Y.M. Wang, S. Cheng, Q.M. Wei, E. Ma, T.G. Nieh, A. Hamza, Effects of annealing and impurities on tensile properties of electrodeposited nanocrystalline Ni, Scr. Mater. 51 (2004) 1023–1028.

[715] Y.Z. Tian, S. Gao, L.J. Zhao, S. Lu, R. Pippan, Z.F. Zhang, N. Tsuji, Remarkable transitions of yield behavior and Lüders deformation in pure Cu by changing grain sizes, Scr. Mater. 142 (2018) 88–91.

[716] Z. Pan, T.J. Rupert, Amorphous intergranular films as toughening structural features, Acta Mater. 89 (2015) 205–214.

[717] A. Khalajhedayati, Z. Pan, T.J. Rupert, Manipulating the interfacial structure of nanomaterials to achieve a unique combination of strength and ductility, Nat. Commun. 7 (2016) 10802.

[718] N.A. Enikeev, I.V. Lomakin, M.M. Abramova, A.M. Mavlyutov, A.A. Lukyanchuk, A.S. Shutov, X. Sauvage, Plasticity of an extra-strong nanocrystalline stainless steel controlled by the "dislocation-segregation" interaction, Mater. Lett. 301 (2021) 130235.

[719] T.S. Orlova, A.M. Mavlyutov, M.Y. Murashkin, N.A. Enikeev, A.D. Evstifeev, D. I. Sadykov, M.Y. Gutkin, Influence of decreased temperature of tensile testing on the annealing-induced hardening and deformation-induced softening effects in ultrafine-grained Al–0.4Zr alloy, Materials 15 (2023) 8429.

[720] J.E. Bird, A.K. Mukherjee, J.E. Dorn, Correlations between high-temperature creep behavior and structure, in: D.G. Brandon, A. Rosen (Eds.), Quantitative Relation Between Properties and Microstructure, Israel, Universities Press,, Jerusalem, Israel, 1959, pp. 255–342.

[721] J. Čadek, Creep in Metallic Materials, Elsevier,, Amsterdam, 1988.

[722] F. Garofalo, Fundamentals of Creep and Creep/Rupture in Metals, McMillan,, New York, USA, 1965.

[723] T.G. Langdon, An analysis of flow mechanisms in high temperature creep and superplasticity, Mater. Trans. 46 (2005) 1951–1956.

[724] M.E. Kassner, Fundamentals of Creep in Metals and Alloys, Elsevier,, Amsterdam, 2009.

[725] F.R.N. Nabarro, Deformation of crystals by the motion of single lonsin, In: Report of Conference on Strength and Solids, The Physical Society. London, England, 1948, pp. 75–90.

[726] C. Herring, Diffusional viscosity of a polycrystalline solid, J. Appl. Phys. 21 (1950) 437–445.

[727] R.L. Coble, A model for boundary diffusion controlled creep in polycrystalline materials, J. Appl. Phys. 34 (1963) 1679–1683.

[728] R.C. Gifkins, Grain boundary sliding and its accommodation during creep and superplasticity, Metall. Trans. A 7 (1976) 1225–1232.

[729] T.G. Langdon, Grain boundary sliding revisited: developments in sliding over four decades, J. Mater. Sci. 41 (2006) 597–609.

[730] J. Harper, J.E. Dorn, Viscous creep in aluminum near its melting temperature, Acta Met. 5 (1957) 654–665.

[731] J. Fiala, J. Novotny, J. Cadek, Coble and Harper-Dorn creep in iron at homologous temperatures of 0.4-0.54, Mater. Sci. Eng. 60 (1983) 195–206.

[732] V. Sklenicka, K. Kucharova, M. Kvapilova, P. Kral, J. Dvorak, The transition from power-law to the power-law breakdown regimes in thermal creep of Zr1% Nb cladding alloys, Kov. Mater. 59 (2021) 279–289.

[733] W. Blum, P. Eisenlohr, V. Sklenicka, Creep behaviour of bulk nanostructured materials – time dependent deformation and deformation kinetics, in: M. Zehetbauer, Z.T. Zhu (Eds.), Bulk Nanostructured Materials, Wiley-VCH,, Weinheim, 2009, pp. 519–537.

[734] W. Yin, Creep and high-temperature deformation in nanostructured metals and alloys, in: S.H. Wang (Ed.), Nanostructured Metals and Alloys: Processing, Microstructure, Mechanical Properties and Application, Woodhead Publishing Ltd,, Oxford, UK, 2011, pp. 594–611.

[735] V. Sklenicka, J. Dvorak, M. Svoboda, P. Kral, M. Kvapilova, Equal-channel angular pressing and creep in ultrafine-grained aluminium and its alloys, in: Z. Ahmad (Ed.), Aluminium Alloys - New Trends in Fabrication and Applications, Chapter 1, INTECH,, Rijeka, Croatia, 2012, pp. 3–45.

[736] M. Kawasaki, T.G. Langdon, Applying conventional creep mechanisms to ultrafine-grained materials, In: I. Charit, Y. Zhu, S. Maloy, O/p. Liaw (Eds.), Mechanical and Creep Behavior of Advanced Materials, The Minerals, Metals & Materials Series, 2017, pp. 117–131.

[737] P. Kral, J. Dvorak, V. Sklenicka, T.G. Langdon, The characteristics of creep in metallic materials processed by severe plastic deformation, in: Mater. Trans., 60, 2019, pp. 1506–1517.

[738] P. Cavaliere, Fatigue and Fracture of Nanostructured Materials, Springer Nature,, Switzerland, 2021.

[739] R.B. Figueiredo, K. Edalati, T.G. Langdon, Effect of creep parameters on the steady-state flow stress of pure metals processed by high-pressure torsion, Mater. Sci. Eng. A 835 (2022) 142666.

[740] V. Sklenicka, J. Dvorak, M. Svoboda, P. Kral, B. Vlach, Effect of processing route on microstructure and mechanical behaviour of ultrafine-grained metals, Mater. Sci. Forum 482 (2005) 83–88.

[741] V. Sklenicka, J. Dvorak, M. Svoboda, Creep in ultrafine-grained aluminium, Mater. Sci. Eng. A 387–389 (2004) 696–701.

[742] V. Sklenicka, J. Dvorak, P. Kral, Z. Stonawska, M. Svoboda, Creep processes in pure aluminium processed by equal-channel angular pressing, Mater. Sci. Eng. A 410–411 (2005) 408–412.

[743] I. Saxl, V. Sklenicka, L. Ilucova, M. Svoboda, J. Dvorak, P. Kral, The link between microstructure and creep in aluminium processed by equal/channel angular pressing, Mater. Sci. Eng. A 502 (2009) 82–85.

[744] W. Blum, Y.J. Li, Creep in ultrafine-grained Al and Cu, in: R.S. Mishra, J. C. Earthman, S.V. Raj, R. Viswanathan (Eds.), Creep Deform. Fract., Des. Life Ext., Symp. . MST05 Fall Meet. (2005) 65–74.

[745] R. Kapoor, Y.J. Li, J.T. Wang, W. Blum, Creep transient during stress changes in ultrafine-grained cooper, Scr. Mater. 54 (2006) 1803–1807.

[746] J. Dvorak, V. Sklenicka, P. Kral, M. Svoboda, I. Saxl, Characterization of creep behaviour and microstructure changes in pure copper processed by equal-channel angular pressing, Rev. Adv. Mater. Sci. 25 (2010) 225–232.

[747] F. Abe, Strengthening mechanisms in steel for creep and creep rupture, in: F. Abe, T.U. Kern, R. Viswanathan (Eds.), Creep-Resistant Steels, Woodhead Publishing Ltd,, Cambridge, England, 2008, pp. 279–304.

[748] A. Kostka, K.G. Tak, G. Eggeler, On the effect of equal-channel angular pressing on tempered martensite ferritic steels, Mater. Sci. Eng. A 481–482 (2008) 723–726.

[749] P. Kral, J. Dvorak, V. Sklenicka, T. Masuda, Z. Horita, K. Kucharova, M. Kvapilova, M. Svobodova, Microstructure and creep behaviour of P92 steel after HPT, Mater. Sci. Eng. A 723 (2018) 287–295.

[750] V. Sklenicka, P. Kral, J. Dvorak, Y. Takizawa, T. Masuda, Z. Horita, K. Kucharova, M. Kvapilova, M. Svobodova, Effects of grain refinement and predeformation impact by severe plastic deformation on creep in P92 martensitic steel, Adv. Eng. Mater. (2019) 1900448.

[751] V. Sklenicka, J. Dvorak, P. Kral, V.I. Betekhtin, A.G. Kadomtsev, M.V. Narykova, S.V. Dobatkin, K. Kucharova, M. Kvapilova, Influence of a prior pressurization treatment on creep behaviour of an ultrafine-grained Zr-2.5%Nb alloy, Mater. Sci. Eng. A 820 (2021) 141570.

[752] P. Kral, J. Dvorak, V. Sklenicka, T. Masuda, Y. Tang, Z. Horita, L. Kuncicka, K. Kucharova, M. Kvapilova, M. Svobodova, Effect of severe plastic deformation on creep behaviour and microstructure changes of P92 at 923K, Kov. Mater. 59 (2021) 141–148.

[753] P. Kral, J. Dvorak, V. Sklenicka, Z. Horita, Y. Takizawa, Y. Tang, L. Kuncicka, M. Kvapilova, M. Ohankova, Influence of high pressure sliding and rotary swaging on creep behavior of P92 steel at 500°C, Metals 11 (2021) 2024.

[754] V. Sklenicka, J. Dvorak, P. Kral, M. Svoboda, V.I. Kopylov, S.A. Nikulin, S. V. Dobatkin, Creep behaviour of a zirconium alloy processed by equal-channel angular pressing, Acta Phys. Pol. A 122 (2012) 485–490.

[755] P. Kral, J. Dvorak, V. Sklenicka, Z. Horita, Y. Takizawa, Y. Tang, L. Kral, M. Kvapilova, P. Roupcova, J. Horvath, Creep resistence of S304H austenitic steel processed by high-pressure sliding, Materials 15 (2022) 331.

[756] P. Kral, J. Dvorak, V. Sklenicka, T. Masuda, Y. Horita, K. Kucharova, M. Kvapilova, M. Svobodova, The effect of ultrafine-grained microstructure on creep behaviour of 9%Cr steel, Materials 11 (2018) 787.

[757] H. Riedel, Fracture at High Temperatures, Springer-Verlag,, Berlin, Germany, 1987.

[758] K. Maruyama, Fracture mechanism map and fundamental aspects of creep fracture, in: F. Abe, T.U. Kern, R. Viswanathan (Eds.), Creep Resistant Steels, Woodhead Publishing Ltd,, Cambridge, UK, 2008, pp. 350–364.

[759] M. Pahutova, J. Cadek, V. Cerny, Steady-state creep rate of Zr-Nb alloys in a temperature interval 350-550°C, J. Nucl. Mater. 61 (1976) 285–296.

[760] Y. Hasegawa, Grade 92 creep-strength-enhanced ferritic steel, in: E. Shibli (Ed.), Coal Power Plant Materials and Life Assessment – Developments, Woodhead Publishing Ltd,, Oxford, UK, 2014, pp. 52–86.

[761] K. Sawada, K. Kubo, F. Abe, Creep behavior and stability of MX precipitates at high temperature in 9Cr-0.5Mo-1.8W-VNb steel, Mater. Sci. Eng. A 319 (2001) 784–787.

[762] J.S. Lee, H.G. Armaki, K. Maruyama, T. Asahi, Causes of breakdown of creep strength in 9Cr-1.8W0.5Mo-VNb steel, Mater. Sci. Eng. A 428 (2006) 270–275.

[763] G.D. Bengough, A study of the properties of alloys at high temperatures, J. Inst, Metals 7 (1912) 123–178.

[764] C.H.M. Jenkins, Strength of Cd-Zn and Sn-Pb alloy solder, J. Inst. Met. 40 (1928) 21–32.

[765] T.G. Langdon. Superplasticity: an historical perspective, In: S. Hori, M. Takizane, N. Furushiro (Eds), Superplasticity in Advanced Materials – ICSAM-91 The Japan Society for Research in Superplasticity, Osaka, Japan, 1991, pp. 3–12.

[766] E.E. Underwood, A review of superplasticity, J. Met. 14 (1962) 914–919.

[767] W.A. Backofen, I.R. Turner, D.H. Avery, Superplasticty in an Al-Zn alloy, Trans. ASM 57 (1964) 980–990.

[768] J. Wongsa-Ngam, T.G. Langdon, Advances in superplasticity from a laboratory curiosity to the development of a superplastic forming industry, Metals 12 (2022) 1921.

[769] A.J. Barnes, Industrial applications of superplastic forming: trends and prospects, Mater. Sci. Forum 357–359 (2001) 3–16.

[770] A.J. Barnes, Superplastic forming 40 years and still growing, J. Mater. Eng. Perform. 16 (2007) 440–454.

[771] Y. Luo, S.G. Luckey, P.A. Friedman, Y. Peng, Development of an advanced superplastic forming process utilizing a mechanical pre-forming operation, Int. J. Mach. Tools Manufact 48 (2008) 1509–1518.

[772] F. Jarrar, D. Sorgente, S. Aksenov, F. Enikeev, On the challenges and prospects of the superplastic forming process, Mater. Sci. Forum 941 (2018) 2343–2348.

[773] R. Chatterjee, J. Mukhopadhyay, A review of superplastic forming, Mater. Today Proc. 5 (2018) 4452–4459.

[774] T.G. Langdon, The background to superplastic forming and opportunities arising from new developments, Solid State Phenom. 306 (2020) 1–8.

[775] P.A. Friedman, S.G. Luckey, W.B. Copple, R. Allor, C.E. Miller, C. Young, Preview of superplastic forming research at Ford Motor Company, J. Mater. Eng. Perform. 13 (2004) 670–677.

[776] T.G. Langdon, Identifying creep mechanisms in plastic flow, Zeit Met. 96 (2005) 522–631.

[777] H. Ishikawa, F.A. Mohamed, T.G. Langdon, The influence of strain rate on ductility in the superplastic Zn-22% Al eutectoid, Philos. Mag. 32 (1975) 1269–1271.

[778] T.G. Langdon, The mechanical properties of superplastic materials, Metall. Trans. A 13 (1982) 689–701.

[779] F.A. Mohamed, T.G. Langdon, Deformation mechanism maps for superplastic materials, Scr. Metall. 10 (1976) 759–762.

[780] W.R. Cannon, T.G. Langdon, Review – creep of ceramics, J. Mater. Sci. 23 (1989) 1–20.

[781] R.J. Twiss, Theory and applicability of a recrystallized grain size paleopiezometer, Pure Appl. Geophys. 115 (1977) 227–244.

[782] S. White, Grain and sub-grain size variations across a mylonite zone, Contrib. Miner. Petrol. 70 (1979) 193–198.

[783] T.G. Langdon, An evaluation of the strain contributed by grain boundary sliding in superplasticity, Mater. Sci. Eng. A 174 (1994) 225–230.

[784] L.K.L. Falk, P.R. Howell, G.L. Dunlop, T.G. Langdon, The role of matrix dislocations in the superplastic deformation of a copper alloy, Acta Met. 34 (1986) 1203–1214.

[785] R.Z. Valiev, T.G. Langdon, An investigation of the role of intragranular dislocation strain in the Pb-62% Sn eutectic alloy, Acta Metall. Mater. 41 (1993) 949–954.

[786] Y. Xun, F.A. Mohamed, Slip-accommodated superplastic flow in Zn-22 wt% Al, Philos. Mag. 83 (2003) 2247–2266.

[787] Y. Xun, F.A. Mohamed, Superplastic behavior of Zn-22% Al containing nano-scale dispersion particles, Acta Mater. 52 (2004) 4401–4412.

[788] M. Myshlyaev, S. Mironov, G. Korznikova, T. Konkova, E. Korznikova, A. Aletdinov, G. Khalikova, EBSD study of superplastically strained Al-Mg-Li alloy, Mater. Lett. 275 (2020) 128063.

[789] M. Myshlyaev, S. Mironov, G. Korznikova, T. Konkova, E. Korznikova, A. Aletdinov, G. Khalikova, G. Raab, S.L. Semiatin, EBSD study of superplasticity: new insight into a well-known phenomenon, J. Alloy. Compd. 898 (2022) 162949.

[790] M. Myshlyaev, G. Korznikova, T. Konkova, E. Korznikova, A. Aletdinov, G. Khalikova, G. Raab, S. Mironov, Microstructural evolution during superplastic deformation of Al-Mg-Li alloy: Dynamic recrystallization or grain-boundary sliding? J. Alloy. Compd. 936 (2023) 168302.

[791] T.G. Langdon, A unified approach to grain boundary sliding in creep and superplasticity, Acta Metall. Mater. 42 (1994) 2437–2443.

[792] M. Demirtas, G. Purcek, An Overview of the principles of low-temperature superplasticity in metallic materials processed by severe plastic deformation, Mater. Trans. 64 (2023) 1724–1738.

[793] M. Mabuchi, H. Iwasaki, K. Yanase, K. Higashi, Low temperature superplasticity of AZ91 magnesium alloy with non-equilibrium grain boundaries, Acta Mater. 47 (1999) 2047–2057.

[794] V.N. Chuvil'deev, T.G. Nieh, M.Y. Gryaznov, A.N. Sysoev, V.I. Kopylov, Low-temperature superplasticity and internal friction in microcrystalline Mg alloys processed by ECAP, Mater. Sci. 50 (2004) 861–865.

[795] A.S.J. Al-Zubaydi, A.P. Zhilyaev, S.C. Wang, P.A.S. Reed, Superplastic behaviour of AZ91 magnesium alloy processed by high-pressure torsion, Mater. Sci. Eng. A 637 (2015) 1–11.

[796] H. Watanabe, T. Mukai, K. Ishikawa, K. Higashi, Low temperature superplasticity of a fine-grained ZK60 magnesium alloy processed by equal-channel-angular extrusion, Scr. Mater. 46 (2002) 851–856.

[797] E. Mostaed, A. Fabrizi, D. Dellasega, F. Bonollo, M. Vedani, Grain size and texture dependence on mechanical properties, asymmetric behavior and low temperature superplasticity of ZK60 Mg alloy, Mater. Charact. 107 (2015) 70–78.

[798] R. Lapovok, R. Cottam, P.F. Thomson, Extraordinary superplastic ductility of magnesium alloy ZK60, J. Mater. Res. 20 (2005) 1375–1378.

[799] M. Zhou, Y. Morisada, H. Fujii, J.Y. Wang, Pronounced low-temperature superplasticity of friction stir processed Mg–9Li–1Zn alloy, Mater. Sci. Eng. A 780 (2020) 139071.

[800] H. Matsunoshita, K. Edalati, M. Furui, Z. Horita, Ultrafine-grained magnesium–lithium alloy processed by high-pressure torsion: low-temperature superplasticity and potential for hydroforming, Mater. Sci. Eng. A 640 (2015) 443–448.

[801] M. Kai, Z. Horita, T.G. Langdon, Developing grain refinement and superplasticity in a magnesium alloy processed by high-pressure torsion, Mater. Sci. Eng. A 488 (2008) 117–124.

[802] W. Zhang, H. Ding, M. Cai, W. Yang, J. Li, Low-temperature superplastic deformation mechanism in Ti–6Al–4V alloy processed by friction stir processing, Mater. Sci. Eng. A 764 (2019) 138261.

[803] W. Zhang, H. Ding, M. Cai, W. Yang, J. Li, Ultra-grain refinement and enhanced low-temperature superplasticity in a friction stir-processed Ti-6Al-4V alloy, Mater. Sci. Eng. A 727 (2018) 90–96.

[804] W. Zhang, H. Ding, P.H.R. Pereira, Y. Huang, T.G. Langdon, Grain refinement and superplastic flow in a fully lamellar Ti-6Al-4V alloy processed by high-pressure torsion, Mater. Sci. Eng. A 732 (2018) 398–405.

[805] J. Fu, H. Ding, Y. Huang, P.H.R. Pereira, W. Zhang, T.G. Langdon, Grain refining of a Ti-6Al-4V alloy by high-pressure torsion and low temperature superplasticity, Lett, Mater 5 (2015) 281–286.

[806] H. Shahmir, F. Naghdi, P.H.R. Pereira, Y. Huang, T.G. Langdon, Factors influencing superplasticity in the Ti-6Al-4V alloy processed by high-pressure torsion, Mater. Sci. Eng. A 718 (2018) 198–206.

[807] Y.G. Ko, C.S. Lee, D.H. Shin, S.L. Semiatin, Low-temperature superplasticity of ultra-fine-grained Ti-6Al-4V processed by equal-channel angular pressing, Metall. Mater. Trans. A 37 (2006) 381–391.

[808] Y.G. Ko, W.G. Kim, C.S. Lee, D.H. Shin, Microstructural influence on low-temperature superplasticity of ultrafine-grained Ti–6Al–4V alloy, Mater. Sci. Eng. A 410 – 411 (2005) 156–159.

[809] S.V. Zherebtsov, E.A. Kudryavtsev, G.A. Salishchev, B.B. Straumal, S.L. Semiatin, Microstructure evolution and mechanical behavior of ultrafine Ti-6Al-4V during low-temperature superplastic deformation, Acta Mater. 121 (2016) 152–163.

[810] I. Charit, R.S. Mishra, Low temperature superplasticity in a friction-stir-processed ultrafine grained Al–Zn–Mg–Sc alloy, Acta Mater. 53 (2005) 4211–4223.

[811] R.Z. Valiev, V.U. Kazykhanov, A.M. Mavlyutov, A.A. Yudakhina, N.Q. Chinh, M.Y. Murashkin, Superplasticity and high strength in Al–Zn–Mg–Zr alloy with ultrafine grains, Adv. Eng. Mater. 22 (2020) 1900555.

[812] N.Q. Chinh, M.Y. Murashkin, E.V. Bobruk, J.L. Lábár, J. Gubicza, Z. Kovács, A.Q. Ahmed, V. Maier-Kiener, R.Z. Valiev, Ultralow-temperature superplasticity and its novel mechanism in ultrafine-grained Al alloys, Mater. Res. Lett. 9 (2021) 475–482.

[813] F.C. Liu, Z.Y. Ma, Low-temperature superplasticity of friction stir processed Al–Zn–Mg–Cu alloy, Scr. Mater. 58 (2008) 667–670.

[814] S. Lee, K. Watanabe, K. Matsuda, Z. Horita, Low-temperature and high-strain-rate superplasticity of ultrafine-grained A7075 processed by high-pressure torsion, Mater. Trans. 59 (2018) 1341–1347.

[815] P. Málek, O. Molnárová, P. Lejček, Low temperature superplasticity of the ECAP Al7075-based alloy, Lett, Mater 8 (2018) 549–553.

[816] E.V. Bobruk, M.Y. Murashkin, I.V. Lomakin, V.U. Kazykhanov, R.Z. Valiev, Low temperature superplasticity of high-strength ultrafine-grained Al 7050 alloy, IOP Conf. Ser. Mater. Sci. Eng. 461 (2019) 012090.

[817] F.C. Liu, Z.Y. Ma, L.Q. Chen, Low-temperature superplasticity of Al–Mg–Sc alloy produced by friction stir processing, Scr. Mater. 60 (2009) 968–971.

[818] S. Ota, H. Akamatsu, K. Neishi, M. Furukawa, Z. Horita, T.G. Langdon, Low-temperature superplasticity in aluminum alloys processed by equal-channel angular pressing, Mater. Trans. 43 (2002) 2364–2369.

[819] F. Musin, R. Kaibyshev, Y. Motohashi, G. Itoh, High strain rate superplasticity in a commercial Al–Mg–Sc alloy, Scr. Mater. 50 (2004) 511–516.

[820] K.T. Park, D.Y. Hwang, S.Y. Chang, D.H. Shin, Low-temperature superplastic behavior of a submicrometer-grained 5083 Al alloy fabricated by severe plastic deformation, Metall. Mater. Trans. A 33 (2002) 2859–2867.

[821] M. Noda, M. Hirohashi, K. Funami, Low temperature superplasticity and its deformation mechanism in grain refinement of Al-Mg alloy by multi-axial alternative forging, Mater. Trans. 44 (2003) 2288–2297.

[822] R.S. Mishra, R.Z. Valiev, S.X. McFadden, R.K. Islamgaliev, A.K. Mukherjee, High-strain-rate superplasticity from nanocrystalline Al alloy 1420 at low temperatures, Philos. Mag. 81 (2001) 37–48.

[823] R.Z. Valiev, Superplastic behaviour of nanocrystalline metallic materials, Mater. Sci. Forum 243–245 (1997) 207–216.

[824] Y. Huang, T.G. Langdon, Characterization of deformation processes in a Zn-22% Al alloy using atomic force microscopy, J. Mater. Sci. 37 (2002) 4993–4998.

[825] M. Demirtas, H. Yanar, G. Purcek, Optimization of RT superplasticity of UFG Zn-22Al alloy by applying ECAP at different temperatures and phase regions, IOP Conf. Ser. Mater. Sci. Eng. 194 (2017) 012033.

[826] M. Demirtas, G. Purcek, H. Yanar, Z.J. Zhang, Z.F. Zhang, Improvement of high strain rate and room temperature superplasticity in Zn–22Al alloy by two-step equal-channel angular pressing, Mater. Sci. Eng. A 620 (2014) 233–240.

[827] S.H. Xia, J. Wang, J.T. Wang, J.Q. Liu, Improvement of room-temperature superplasticity in Zn–22 wt%Al alloy, Mater. Sci. Eng. A 493 (2008) 111–115.

[828] M. Demirtas, G. Purcek, H. Yanar, Z.J. Zhang, Z.F. Zhang, Achieving room temperature superplasticity in Zn–5Al alloy at high strain rates by equal-channel angular extrusion, J. Alloy. Compd. 623 (2015) 213–218.

[829] M. Demirtas, G. Purcek, H. Yanar, Z.J. Zhang, Z.F. Zhang, Effect of equal-channel angular pressing on room temperature superplasticity of quasi-single phase Zn–0.3Al alloy, Mater. Sci. Eng. A 644 (2015) 17–24.

[830] W. Bednarczyk, J. Kawałko, M. Wątroba, P. Bała, Achieving room temperature superplasticity in the Zn-0.5Cu alloy processed via equal channel angular pressing, Mater. Sci. Eng. A 723 (2018) 126–133.

[831] W. Bednarczyk, M. Wątroba, J. Kawałko, P. Bała, Determination of room-temperature superplastic asymmetry and anisotropy of Zn-0.8Ag alloy processed by ECAP, Mater. Sci. Eng. A 759 (2019) 55–58.

[832] Y. Yoshida, L. Cisar, S. Kamado, Y. Kojima, Low temperature superplasticity of ECAE processed Mg-10%Li-1%Zn alloy, Mater. Trans. 43 (2002) 2419–2423.

[833] B.C. Zhou, S.L. Shang, Y. Wang, Z.K. Liu, Diffusion coefficients of alloying elements in dilute Mg alloys: a comprehensive first-principles study, Acta Mater. 103 (2016) 573–586.

[834] J.E. González-Hernández, J.M. Cubero-Sesin, Electrical conductivity of ultrafine-grained cu and al alloys: attaining the best compromise with mechanical properties, Mater. Trans. 64 (2023) 1754–1768.

[835] M.Y. Murashkin, N.A. Enikeev, X. Sauvage, Potency of severe plastic deformation processes for optimizing combinations of strength and electrical conductivity of lightweight Al-based conductor alloys, Mater. Trans. 64 (2023) 1833–1843.

[836] T. Nishizaki, K. Edalati, S. Lee, Z. Horita, T. Akune, T. Nojima, S. Iguchi, T. Sasaki, Critical temperature in bulk ultrafine-grained superconductors of Nb, V, and Ta processed by high-pressure torsion, Mater. Trans. 60 (2019) 1367–1376.

[837] M. Mito, S. Shigeoka, H. Kondo, N. Noumi, Y. Kitamura, K. Irie, K. Nakamura, S. Takagi, H. Deguchi, T. Tajiri, M. Ishizuka, T. Nishizaki, K. Edalati, Z. Horita, Hydrostatic compression effects on fifth-group element superconductors V, Nb, and Ta subjected to high-pressure torsion, Mater. Trans. 60 (2019) 1472–1483.

[838] G. Rogl, M.J. Zehetbauer, P.F. Rogl, The effect of severe plastic deformation on thermoelectric performance of skutterudites, half-Heuslers and Bi-tellurides, Mater. Trans. 60 (2019) 2071–2085.

[839] G. Rogl, P. Rogl, E. Bauer, M. Zehetbauer, Severe plastic deformation, a tool to enhance thermoelectric performance, in: K. Koumoto, T. Mori (Eds.), Thermoelectric Nanomaterials, Springer Series in Materials Science, Volume 182, Springer,, Berlin, Heidelberg, 2013, pp. 193–254.

[840] K. Edalati, M. Arimura, Y. Ikoma, T. Daio, M. Miyata, D.J. Smith, Z. Horita, Plastic deformation of $BaTiO_3$ ceramics by high-pressure torsion and changes in phase transformations, optical and dielectric properties, Mater. Res. Lett. 3 (2015) 216–221.

[841] L. Weissitsch, F. Staab, K. Durst, A. Bachmaier, Magnetic materials via high-pressure torsion of powders, Mater. Trans. 64 (2023) 1537–1550.

[842] M. Tayyebi, M. Alizadeh, Thermal and wear properties of Al/Cu functionally graded metal matrix composite produced by severe plastic deformation method, J. Manufact. Process 85 (2023) 515–526.

[843] E. Menumerov, K.D. Gilroy, M. Hajfathalian, C.J. Murphy, E.R. McKenzie, R. A. Hughes, S. Neretina, Plastically deformed Cu-based alloys as high-performance catalysts for the reduction of 4-nitrophenol, Catal. Sci. Technol. 6 (2016) 5737–5745.

[844] H. Razavi-Khosroshahi, M. Fuji, Development of metal oxide high-pressure phases for photocatalytic properties by severe plastic deformation, Mater. Trans. 60 (2019) 1203–1208.

[845] X. Jian, J. Li, L. He, H.W. Li, M. Zhang, P. Zhang, H.J. Lin, Severe plastic deformation for advanced electrocatalysts for electrocatalytic hydrogen production, Mater. Trans. 64 (2023) 1515–1525.

[846] J. Zhong, F. Zhang, X. Tong, X. Hu, B. Wang, Hydrolytic hydrogen production from severely plastic deformed aluminum-based materials: an overview, Mater. Trans. 64 (2023) 1376–1386.

[847] Á. Révész, M. Gajdics, The effect of severe plastic deformation on the hydrogen storage properties of metal hydrides, Mater. Trans. 64 (2023) 1387–1400.

[848] Y. Mine, Micro-mechanical characterisation of hydrogen embrittlement and fatigue crack growth behaviours in metastable austenitic stainless steels with microstructure refinement, Mater. Trans. 64 (2023) 1474–1488.

[849] H. Miyamoto, Revealing what enhance the corrosion resistance beside grain size in ultrafine grained materials by severe plastic deformation: stainless steels case, Mater. Trans. 64 (2023) 1419–1428.

[850] N.A. Enikeev, V.K. Shamardin, B. Radiguet, Radiation tolerance of ultrafine-grained materials fabricated by severe plastic deformation, Mater. Trans. 60 (2019) 1723–1731.

[851] I.P. Semenova, G.V. Klevtsov, N.A. Klevtsova, G.S. Dyakonov, A.A. Matchin, R. Z. Valiev, Nanostructured titanium for maxillofacial mini-implants, Adv. Eng. Mater. 18 (2016) 1216–1224.

[852] S.O. Kasap. Principles of Electronic Materials and Devices, 4th Edition, McGraw Hill Education,, New York, 2006.

[853] P.L. Rossiter, The Electrical Resistivity of Metals and Alloys, Cambridge University Press,, Cambridge, 1991.

[854] K. Taguchi, T. Shimada, J. Yoshimoto, T. Kuwabara, Y. Akasofu, High-strength aluminum wires for low-voltage automotive engine wiring harnesses, SEI, Tech. Rev. 84 (2017) 125–130.

[855] R.Z. Valiev, A.P. Zhilyaev, T.G. Langdon, Bulk Nanostructured Materials: Fundamentals and Applications, TMS Wiley,, New York, 2014.

[856] H. Yang, Z. Ma, C. Lei, L. Meng, Y. Fang, J. Liu, H. Wang, High strength and high conductivity Cu alloys: a review, Sci. China Technol. Sci. 63 (2020) 2505–2517.

[857] Y. Wang, L. Zhu, G. Niu, J. Mao, Conductive Al alloys: the contradiction between strength and electrical conductivity, Adv. Eng. Mater. 23 (2021) 2001249.

[858] M.J. Zehetbauer, Y.T. Zhu, Bulk Nanostructured Materials, Wiley-VCH,, Weinheim, 2009.

[859] K. Edalati, T. Fujioka, Z. Horita, Microstructure and mechanical properties of pure Cu processed by high-pressure torsion, Mater. Sci. Eng. A 497 (2008) 168–173.

[860] K. Edalati, K. Imamura, T. Kiss, Z. Horita, Equal-channel angular pressing and high-pressure torsion of pure copper: evolution of electrical conductivity and hardness with strain, Mater. Trans. 53 (2012) 123–127.

[861] D.A. Aksenov, R.N. Asfandiyarov, G.I. Raab, E.I. Fakhretdinova, M. A. Shishkunova, influence of the chromium content in low-alloyed Cu–Cr alloys on the structural changes, phase transformations and properties in equal-channel angular pressing, Metals 11 (2021) 1795.

[862] R.K. Islamgaliev, K.M. Nesterov, J. Bourgon, Y. Champion, R.Z. Valiev, Nanostructured Cu-Cr alloy with high strength and electrical conductivity, J. Appl. Phys. 115 (2014) 194301.

[863] Z.Q. Chu, K.X. Wei, I.V. Alexandrov, X.L. An, D.D. Wang, X.K. Liu, Simultaneously enhancing mechanical properties and electrical conductivity of Cu-0.5%Cr alloy as 5G connector material, J. Alloy. Compd. 948 (2023) 169750.

[864] L. Lu, Y. Shen, X. Chen, L. Qian, K. Lu, Ultrahigh strength and high electrical conductivity in copper, Science 304 (2004) 422–426.

[865] X.H. Chen, L. Lu, K. Lu, Electrical resistivity of ultrafine-grained copper with nanoscale growth twins, J. Appl. Phys. 102 (2007) 083708.

[866] X. Zhang, H. Wang, X.H. Chen, L. Lu, K. Lu, R.G. Hoagland, A. Misra, High-strength sputter-deposited Cu foils with preferred orientation of nanoscale growth twins, Appl. Phys. Lett. 88 (2006) 173116.

[867] Y. Zhang, Y.S. Li, N.R. Tao, K. Lu, High strength and high electrical conductivity in bulk nanograined Cu embedded with nanoscale twins, Appl. Phys. Lett. 91 (2007) 211901.

[868] L.X. Sun, N.R. Tao, K. Lu, A high strength and high electrical conductivity bulk CuCrZr alloy with nanotwins, Scr. Mater. 99 (2015) 73–76.

[869] J.M. Cubero-Sesin, M. Arita, Z. Horita, High strength and electrical conductivity of Al-Fe alloys produced by synergistic combination of high-pressure torsion and aging, Adv. Eng. Mater. 17 (2015) 1792–1803.

[870] R.Z. Valiev, M.Y. Murashkin, I. Sabirov, A nanostructural design to produce high-strength Al alloys with enhanced electrical conductivity, Scr. Mater. 76 (2014) 13–16.

[871] Z. Pakieła, K. Ludwichowska, J. Ferenc, M. Kulczyk, Mechanical properties and electrical conductivity of Al 6101 and 6201 alloys processed by hydro-extrusion, IOP Conf. Ser. Mater. Sci. Eng. 63 (2014) 012120.

[872] M. Murashkin, A. Medvedev, V. Kazykhanov, A. Krokhin, G. Raab, N. Enikeev, R. Z. Valiev, Enhanced mechanical properties and electrical conductivity in ultrafine-grained al 6101 alloy processed via ECAP-conform, Metals 5 (2015) 2148–2164.

[873] K. Majchrowicz, Z. Pakieła, W. Chrominski, M. Kulczyk, Enhanced strength and electrical conductivity of ultrafine-grained Al-Mg-Si alloy processed by hydrostatic extrusion, Mater. Charact. 135 (2018) 104–114.

[874] R.C. Meagher, M.L. Hayne, J. DuClos, C.F. Davis, T.C. Lowe, T. Ungár, B. Arfaei, Increasing the strength and electrical conductivity of AA6101 aluminum by nanostructuring, Light Met 2019 (2019) 1507–1513.

[875] Y. Qi, A. Kosinova, E. Lakin, V.V. Popov Jr, E. Rabkin, R. Lapovok, Effect of SPD processing on the strength and conductivity of AA6061 alloy, Adv. Eng. Mater. 21 (2019) 1801370.

[876] A.E. Medvedev, A. Arutyunyan, I. Lomakin, A. Bondarenko, V. Kazykhanov, N. Enikeev, M. Murashkin, Fatigue properties of ultra-fine grained Al-Mg-Si wires with enhanced mechanical strength and electrical conductivity, Metals 8 (2018) 1034.

[877] J.M. Cubero-Sesin, H. In, M. Arita, H. Iwaoka, Z. Horita, High-pressure torsion for fabrication of high-strength and high-electrical conductivity Al micro-wires, J. Mater. Sci. 49 (2014) 6550–6557.

[878] T. Masuda, S. Hirosawa, Z. Horita, Continuous high-pressure torsion of pure Al and Al-2 wt% Fe alloy using multi-wires, J. Mater. Sci. 56 (2021) 8679–8688.

[879] A.E. Medvedev, O.O. Zhukova, V.U. Kazykhanov, A.F. Shaikhulova, N.A. Enikeev, V.N. Timofeev, M.Y. Murashkin, On the effect of ECAP and subsequent cold rolling on the microstructure and properties of electromagnetically cast Al-Fe alloys, Int. J. Lightweight Mater. Manuf. 5 (2022) 484–495.

[880] A.E. Medvedev, M. Murashkin, N. Enikeev, E. Medvedev, X. Sauvage, Influence of morphology of intermetallic particles on the microstructure and properties evolution in severely deformed Al-Fe alloys, Metals 11 (2021) 815.

[881] M.Y. Murashkin, I. Sabirov, A.E. Medvedev, N.A. Enikeev, W. Lefebvre, R. Z. Valiev, X. Sauvage, Mechanical and electrical properties of an ultrafine grained Al–8.5 wt% RE (RE= 5.4 wt% Ce, 3.1 wt% La) alloy processed by severe plastic deformation, Mater. Des. 90 (2016) 433–442.

[882] A.E. Medvedev, M.Y. Murashkin, N.A. Enikeev, R.Z. Valiev, P.D. Hodgson, R. Lapovok, Enhancement of mechanical and electrical properties of Al-RE alloys by optimizing rare-earth concentration and thermo-mechanical treatment, J. Alloy Compd. 745 (2018) 696–704.

[883] A.M. Mavlyutov, T.A. Latynina, M.Y. Murashkin, R.Z. Valiev, T.S. Orlova, The impact of severe plastic deformation on the microstructure and physicomechanical properties of Al–0.4Zr, Inorg. Mater. Appl. Res. 10 (2019) 7–14.

[884] T.S. Orlova, T.A. Latynina, A.M. Mavlyutov, M.Y. Murashkin, R.Z. Valiev, Effect of annealing on microstructure, strength and electrical conductivity of the pre-aged and HPT-processed Al-0.4Zr alloy, J. Alloy. Compd. 784 (2019) 41–48.

[885] T.S. Orlova, T.Y. Latynina, M.Y. Murashkin, V.U. Kazykhanov, The effect of additional severe plastic deformation at elevated temperatures on the microstructure, functional properties of the ultrafine-grained Al–0.4Zr Alloy, Phys. Solid State 61 (2019) 2509–2519.

[886] T.S. Orlova, A.M. Mavlyutov, T.A. Latynina, E.V. Ubyivovk, M.Y. Murashkin, R. Schneider, R.Z. Valiev, Influence of severe plastic deformation on microstructure, strength and electrical conductivity of aged al–0.4zr(wt%) alloy, Rev. Adv. Mater. Sci. 55 (2018) 92–101.

[887] A. Duchaussoy, X. Sauvage, A. Deschamps, F. Geuser, G.Z. Horita, RenouComplex interactions between precipitation, grain growth and recrystallization in a severely deformed Al-Zn-Mg-Cu alloy and consequences on the mechanical behavior, Materialia 15 (2021) 101028.

[888] O. Gutfleisch, M.A. Willard, E. Brück, C.H. Chen, S.G. Sankar, J.P. Liu, Magnetic materials and devices for the 21st century: stronger, lighter, and more energy efficient, Adv. Mater. 23 (2011) 821–842.

[889] D. Goll, H. Kronmüller, High-performance permanent magnets, Naturwissenschaften 87 (2000) 423–438.

[890] G. Herzer, Soft magnetic nanocrystalline materials, Scr. Metall. Mater. 33 (1995) 1741–1756.

[891] J.S. Lee, J.M. Cha, H.Y. Yoon, J.K. Lee, Y.K. Kim, Magnetic multi-granule nanoclusters: a model system that exhibits universal size effect of magnetic coercivity, Sci. Rep. 5 (2015) 12135.

[892] K. Hono, H. Sepehri-Amin, Strategy for high-coercivity Nd–Fe–B magnets, Scr. Mater. 67 (2012) 530–535.

[893] H. Tang, M.A.H. Mamakhel, M. Christensen, Enhancing the coercivity of SmCo$_5$ magnet through particle size control, J. Mater. Chem. C. 8 (2020) 2109–2116.

[894] K. Edalati, D. Akama, A. Nishio, S. Lee, Y. Yonenaga, J.M. Cubero-Sesin, Z. Horita, Influence of dislocation–solute atom interactions and stacking fault energy on grain size of single-phase alloys after severe plastic deformation using high-pressure torsion, Acta Mater. 69 (2014) 68–77.

[895] K.S. Kormout, R. Pippan, A. Bachmaier, Deformation-induced supersaturation in immiscible material systems during high-pressure torsion, Adv. Eng. Mater. 19 (2017) 1600675.

[896] A. Bachmaier, R. Pippan, Generation of metallic nanocomposites by severe plastic deformation, Int. Mater. Rev. 58 (2013) 41–62.

[897] M. Stückler, H. Krenn, R. Pippan, L. Weissitsch, S. Wurster, A. Bachmaier, Magnetic binary supersaturated solid solutions processed by severe plastic deformation, Nanomater 9 (2018) 6.

[898] A. Bachmaier, H. Krenn, P. Knoll, H. Aboulfadl, R. Pippan, Tailoring the magnetic properties of nanocrystalline Cu-Co alloys prepared by high-pressure torsion and isothermal annealing, J. Alloy. Compd. 725 (2017) 744–749.

[899] M. Stückler, H. Krenn, P. Kürnsteiner, B. Gault, F. de Geuser, L. Weissitsch, S. Wurster, R. Pippan, A. Bachmaier, Intermixing of Fe and Cu on the atomic scale by high-pressure torsion as revealed by DC- and AC-SQUID susceptometry and atom probe tomography, Acta Mater. 196 (2020) 210–219.

[900] M. Stückler, L. Weissitsch, S. Wurster, P. Felfer, H. Krenn, R. Pippan, A. Bachmaier, Magnetic dilution by severe plastic deformation, AIP Adv. 10 (2020) 15210.

[901] M. Stückler, L. Weissitsch, S. Wurster, H. Krenn, R. Pippan, A. Bachmaier, Sampling the Cu–Fe–Co phase diagram by severe plastic deformation for enhanced soft magnetic properties, J. Mater. Res. Technol. 12 (2021) 1235–1242.

[902] M. Stückler, S. Wurster, R. Pippan, A. Bachmaier, In situ AC-hysteresis measurements of SPD-processed Cu$_{20}$(Fe$_{15}$Co$_{85}$)$_{80}$, AIP Adv. 11 (2021) 15033.

[903] J.Q. Xiao, J.S. Jiang, C.L. Chien, Giant magnetoresistance in nonmultilayer magnetic systems, Phys. Rev. Lett. 68 (1992) 3749–3752.

[904] A.E. Berkowitz, J.R. Mitchell, M.J. Carey, A.P. Young, S. Zhang, F.E. Spada, F.T. Parker, A. Hutten, G. Thomas, Giant magnetoresistance in heterogeneous Cu-Co alloys, Phys. Rev. Lett. 68 (1992) 3745–3748.

[905] S. Wurster, L. Weissitsch, M. Stückler, P. Knoll, H. Krenn, R. Pippan, A. Bachmaier, Tuneable magneto-resistance by severe plastic deformation, Metals 9 (2019) 1188.

[906] S. Wurster, M. Stückler, L. Weissitsch, T. Müller, A. Bachmaier, Microstructural changes influencing the magnetoresistive behavior of bulk nanocrystalline materials, Appl. Sci. 10 (2020) 5094.

[907] M. Kasalo, S. Wurster, M. Stückler, M. Zawodzki, L. Weissitsch, R. Pippan, A. Bachmaier, Magnetoresistive behaviour of ternary Cu-based materials processed by high-pressure torsion, IOP Conf. Ser. Mater. Sci. Eng. 1249 (2022) 12047.

[908] D.V. Gunderov, A.G. Popov, N.N. Schegoleva, V.V. Stolyarov, A.R. Yavary, Phase transformation in crystalline and amorphous rapidly quenched Nd-Fe-B alloys under SPD, in: M. Zehetbauer, R.Z. Valiev (Eds.), Nanomaterials by Severe Plastic Deformation, Wiley-VCH Verlag GmbH & Co. KGaA,, Weinheim, 2004, pp. 165–169.

[909] F. Hou, Y. Hua, G. Zhang, M. Li, L. Lou, Q. Zhang, G. Huang, W. Li, X. Li, Evolution of microstructures and magnetic properties in bulk Nd-Fe-Cu-B nanocomposites prepared by high pressure thermal deformation, J. Magn. Magn. Mater. 499 (2020) 166271.

[910] F. Staab, E. Bruder, L. Schäfer, K. Skokov, D. Koch, B. Zingsem, E. Adabifiroozjaei, L. Molina-Luna, O. Gutfleisch, K. Durst, Hard magnetic SmCo$_5$-Cu nanocomposites produced by severe plastic deformation, Acta Mater. 246 (2023) 118709.

[911] L. Weissitsch, M. Stückler, S. Wurster, P. Knoll, H. Krenn, R. Pippan, A. Bachmaier, Strain induced anisotropic magnetic behaviour and exchange coupling effect in Fe-SmCo$_5$ permanent magnets generated by high pressure torsion, Crystals 10 (2020) 1026.

[912] M. Zawodzki, L. Weissitsch, H. Krenn, S. Wurster, A. Bachmaier, Exchange bias demonstrated in bulk nanocomposites processed by high-pressure torsion, Nanomater 13 (2023) 344.

[913] E. Menéndez, J. Sort, V. Langlais, A. Zhilyaev, J.S. Muñoz, S. Suriñach, J. Nogués, M.D. Baró, Cold compaction of metal–ceramic (ferromagnetic–antiferromagnetic) composites using high pressure torsion, J. Alloy. Compd. 434-435 (2007) 505–508.

[914] V.V. Popov, F. Maccari, I.A. Radulov, A. Kovalevsky, A. Katz-Demyanetz, M. Bamberger, Microstructure and magnetic properties of Mn-Al-C permanent magnets produced by various techniques, Manuf. Rev. 8 (2021) 10.

[915] L. Weissitsch, S. Wurster, T. Müller, H. Krenn, R. Pippan, A. Bachmaier, Synthesis of hard magnetic α-MnBi phase by high pressure torsion and field assisted annealing, J. Mag. Mag. Mater. 584 (2023) 171082.

[916] K.Y. Mulyukov, G.F. Korznikova, R.F. Valiev, Microstructure and magnetic properties of submicron grained cobalt after large plastic deformation and their variation during annealing, Phys. Stat. Sol. A 125 (1991) 609–614.

[917] S. Scheriau, M. Kriegisch, S. Kleber, N. Mehboob, R. Grössinger, R. Pippan, Magnetic characteristics of HPT deformed soft-magnetic materials, J. Magn. Magn. Mater. 322 (2010) 2984–2988.

[918] K. Mulyokov, G.F. Korznikova, R.Z. Abdulov, R.Z. Valiev, Magnetic hysteretic properties of submicron grained nickel and their variations upon annealing, J. Magn. Magn. Mater. 89 (1990) 207–213.

[919] R. Groessinger, N. Mehboob, M. Kriegisch, A. Bachmaier, R. Pippan, Frequency dependence of the coercivity of soft magnetic materials, IEEE Trans. Magn. 48 (2012) 1473–1476.

[920] R.Z. Valiev, R.R. Mulyukov, V.V. Ovchinnikov, Direction of a grain-boundary phase in submicrometre-grained iron, Philos. Mag. Lett. 62 (1990) 253–256.

[921] S. Scheriau, K. Rumpf, S. Kleber, R. Pippan, Tailoring the magnetic properties of ferritic alloys by HPT, Mater. Sci. Forum 584-586 (2008) 923–928.

[922] A. Hosokawa, H. Ohtsuka, T. Li, S. Ii, K. Tsuchiya, Micostructure and magnetic properties in nanostructured Fe and Fe-based intermetallics produced by high-pressure torsion, Mater. Trans. 55 (2014) 1286–1291.

[923] Y. Oba, N. Adachi, Y. Todaka, E.P. Gilbert, H. Mamiya, Anomalous magnetic anisotropy and magnetic nanostructure in pure Fe induced by high-pressure torsion straining, Phys. Rev. Res. 2 (2020) 033473.

[924] S. Taskaev, K. Skokov, V. Khovaylo, D. Gunderov, D. Karpenkov, Influence of severe plastic deformation on magnetic properties of Fe$_{48}$Ni$_{48}$Zr$_4$, Fe$_{49.5}$Co$_{16.5}$B$_{33}$Ta and Co$_{80}$Zr$_{16}$B$_4$ alloys, Phys. Procedia 75 (2015) 1404–1409.

[925] A. Chbihi, X. Sauvage, C. Genevois, D. Blavette, D. Gunderov, A.G. Popov, Optimization of the magnetic properties of FePd alloys by severe plastic deformation, Adv. Eng. Mater. 12 (2010) 708–713.

[926] I. Shchetinin, I. Bordyuzhin, V. Menushenkov, R. Sundeev, A. Kamynin, V. Verbetskii, A. Savchenko, Magnetic properties of nitrides Sm2Fe17 compound after severe plastic deformation by torsion at 77K, In: METAL 2019 Conference Prooeedings, TANGER Ltd, 2019, pp. 816–820.

[927] P.Z. Si, C.J. Choi, J. Park, H.L. Ge, J. Du, Phase transformation and enhanced coercivity in B-N-doped MnAl nanocrystalline bulk alloys prepared by high pressure torsion, AIP Adv. 10 (2020) 15320.

[928] P.Z. Si, J.T. Lim, J. Park, H.H. Lee, H. Ge, H. Lee, S. Han, H.S. Kim, C.J. Choi, High coercivity in MnAl disc prepared by severe plastic deformation, Phys. Stat. Sol. B 257 (2020) 1900356.

[929] B.B. Straumal, A.R. Kilmametov, A.A. Mazilkin, S.G. Protasova, K.I. Kolesnikova, P.B. Straumal, B. Baretzky, Amorphization of Nd–Fe–B alloy under the action of high-pressure torsion, Mater. Lett. 145 (2015) 63–66.

[930] V.V. Stolyarov, D.V. Gunderov, A.G. Popov, V.S. Gaviko, A.S. Ermolenko, Structure evolution and changes in magnetic properties of severe plastic deformed Nd(Pr)–Fe–B alloys during annealing, J. Alloy. Compd. 281 (1998) 69–71.

[931] I.S. Tereshina, I.A. Pelevin, E.A. Tereshina, G.S. Burkhanov, K. Rogacki, M. Miller, N.V. Kudrevatykh, P.E. Markin, A.S. Volegov, R.M. Grechishkin, S.V. Dobatkin, L. Schultz, Magnetic hysteresis properties of nanocrystalline (Nd,Ho)-(Fe,Co)-B alloy after melt spinning, severe plastic deformation and subsequent heat treatment, J. Alloy. Compd. 681 (2016) 555–560.

[932] B.B. Straumal, A.A. Mazilkin, S.G. Protasova, D.V. Gunderov, G.A. López, B. Baretzky, Amorphization of crystalline phases in the Nd–Fe–B alloy driven by the high-pressure torsion, Mater. Lett. 161 (2015) 735–739.

[933] I.V. Shchetinin, I.G. Bordyuzhin, R.V. Sundeev, V.P. Menushenkov, A.V. Kamynin, V.N. Verbetsky, A.G. Savchenko, Structure and magnetic properties of Sm$_2$Fe$_{17}$N$_x$ alloys after severe plastic deformation by high pressure torsion, Mater. Lett. 274 (2020) 127993.

[934] A.G. Popov, V.S. Gaviko, N.N. Shchegoleva, L.A. Shreder, D.V. Gunderov, V.V. Stolyarov, W. Li, L.L. Li, X.Y. Zhang, Effect of high-pressure torsion deformation and subsequent annealing on structure and magnetic properties of overquenched melt-spun Nd$_9$Fe$_{85}$B$_6$ alloy, J. Iron Steel Res. Int 13 (2006) 160–165.

[935] W. Li, D. Guo, X. Li, Y. Chen, D.V. Gunderov, V.V. Stolyarov, X. Zhang, Bulk α-Fe/Nd$_2$Fe$_{14}$B nanocomposite magnets produced by severe plastic deformation combined with thermal annealing, J. Appl. Phys. 108 (2010) 053901.

[936] W. Li, L. Li, Y. Nan, Z. Xu, X. Zhang, A.G. Popov, D.V. Gunderov, V.V. Stolyarov, Nanocrystallization and magnetic properties of amorphous Nd$_9$Fe$_{85}$B$_6$ subjected to high-pressure torsion deformation upon annealing, J. Appl. Phys. 104 (2008) 23912.

[937] W. Li, L. Li, Y. Nan, X. Li, X. Zhang, D.V. Gunderov, V.V. Stolyarov, A.G. Popov, Controllable nanocrystallization in amorphous Nd$_9$Fe$_{85}$B$_6$ via combined application of severe plastic deformation and thermal annealing, Appl. Phys. Lett. 91 (2007) 062509.

[938] H. Li, W. Li, Y. Zhang, D.V. Gunderov, X. Zhang, Phase evolution, microstructure and magnetic properties of bulk α-Fe/Nd$_2$Fe$_{14}$B nanocomposite magnets prepared by severe plastic deformation and thermal annealing, J. Alloy. Compd. 651 (2015) 434–439.

[939] A. Musiał, Z. Śniadecki, N. Pierunek, Y. Ivanisenko, D. Wang, M.H. Fawey, B. Idzikowski, Tuning of the magnetic properties of Hf$_2$Co$_{11}$B alloys through a combined high pressure torsion and annealing treatment, J. Alloy. Compd. 787 (2019) 794–800.

[940] R.V. Nair, V.S. Gummaluri, M.V. Matham, V. C, A review on optical bandgap engineering in TiO$_2$ nanostructures via doping and intrinsic vacancy modulation towards visible light applications, J. Phys. D: Appl. Phys. 55 (2022) 313003.

[941] E. Lee, C. Park, D.W. Lee, G. Lee, H.Y. Park, J.H. Jang, H. Kim, Y. Sung, Y. Tak, S.J. Yoo, Tunable synthesis of N,C-codoped Ti^{3+}-enriched titanium oxide support for highly durable PEMFC cathode, ACS Catal. 10 (2020) 12080–12090.

[942] S.A. Ansari, M.M. Khan, M.O. Ansari, M.H. Cho, Nitrogen-doped titanium dioxide (N-doped TiO$_2$) for visible light photocatalysis, N. J. Chem. 40 (2016) 3000–3009.

[943] X. Zhou, N. Liu, P. Schmuki, Photocatalysis with TiO$_2$ nanotubes: "colorful" reactivity and designing site-specific photocatalytic centers into TiO$_2$ nanotubes, ACS Catal. 7 (2017) 3210–3235.

[944] X. Yu, B. Kim, Y.K. Kim, Highly enhanced photoactivity of anatase TiO$_2$ nanocrystals by controlled hydrogenation-induced surface defects, ACS Catal. 3 (2013) 2479–2486.

[945] H. Razavi-Khosroshahi, S. Mohammadzadeh, M. Hojamberdiev, S. Kitano, M. Yamauchi, M. Fuji, BiVO$_4$/BiOX (X= F, Cl, Br, I) heterojunctions for degrading organic dye under visible light, Adv. Powder Technol. 30 (2019) 1290–1296.

[946] H. Choi, D. Shin, B.C. Yeo, T. Song, S.S. Han, N. Park, S. Kim, Simultaneously controllable doping sites and the activity of a W-N codoped TiO$_2$ photocatalyst, ACS Catal. 6 (2016) 2745–2753.

[947] C. Takai-Yamashita, M. Ando, H. Razavi-Khosroshahi, M. Fuji, Acceleration of tungsten doping on vanadium dioxide (VO$_2$) by alkali species, Colloids Surf. A 567 (2019) 1–6.

[948] T.D. Nguyen-Phan, S. Luo, D. Vovchok, J. Llorca, J. Graciani, J.F. Sanz, S. Sallis, W. Xu, J. Bai, L.F.J. Piper, D.E. Polyansky, E. Fujita, S.D. Senanayake, D.J. Stacchiola, J.A. Rodriguez, Visible light-driven H$_2$ production over highly dispersed ruthenia on rutile TiO$_2$ nanorods, ACS Catal. 6 (2016) 407–417.

[949] H. Razavi-Khosroshahi, S. Mohammadzadeh, M. Hojamberdiev, S. Kitano, M. Yamauchi, M. Fuji, Visible light active Bi$_3$TaO$_7$ nanosheets for water splitting, Dalton Trans. 48 (2019) 9284–9290.

[950] X. Xu, R. Wang, X. Sun, M. Lv, S. Ni, Layered perovskite compound NaLaTiO$_4$ modified by nitrogen doping as a visible light active photocatalyst for water splitting, ACS Catal. 10 (2020) 9889–9898.

[951] H. Razavi-Khosroshahi, S. Mohammadzadeh, M. Fuji, Bi$_4$TaO$_8$Cl/Graphene nanocomposite for photocatalytic water splitting, Adv. Powder Technol. 31 (2020) 381–386.

[952] X. Sun, Y. Mi, F. Jiao, X. Xu, Activating layered perovskite compound Sr$_2$TiO$_4$ via La/N codoping for visible light photocatalytic water splitting, ACS Catal. 8 (2018) 3209–3221.

[953] Y. Liu, W. Shu, K. Chen, Z. Peng, W. Chen, Enhanced photothermocatalytic synergetic activity toward gaseous benzene for Mo+C-codoped titanate nanobelts, ACS Catal. 2 (2012) 2557–2565.

[954] A. Yamakata, J.J.M. Vequizo, T. Ogawa, K. Kato, S. Tsuboi, N. Furutani, M. Ohtsuka, S. Muto, A. Kuwabara, Y. Sakata, Core–shell double doping of Zn and Ca on β-Ga$_2$O$_3$ photocatalysts for remarkable water splitting, ACS Catal. 11 (2021) 1911–1919.

[955] Y. Yang, L.C. Kao, Y. Liu, K. Sun, H. Yu, J. Guo, S.Y.H. Liou, M.R. Hoffmann, Cobalt-doped black TiO$_2$ nanotube array as a stable anode for oxygen evolution and electrochemical wastewater treatment, ACS Catal. 8 (2018) 4278–4287.

[956] I. Fujita, K. Edalati, Q. Wang, M. Arita, M. Watanabe, S. Munetoh, T. Ishihara, Z. Horita, High-pressure torsion to induce oxygen vacancies in nanocrystals of magnesium oxide: enhanced light absorbance, photocatalysis and significance in geology, Materialia 11 (2020) 100670.

[957] I. Ali, M. Suhail, Z.A. Alothman, A. Alwarthan, Recent advances in syntheses, properties and applications of TiO$_2$ nanostructures, RSC Adv. 8 (2018) 30125–30147.

[958] V. Etacheri, C. Di Valentin, J. Schneider, D. Bahnemann, S.C. Pillai, Visible-light activation of TiO$_2$ photocatalysts: advances in theory and experiments, J. Photochem. Photobiol. C. 25 (2015) 1–29.

[959] O.A. Ibhadon, P. Fitzpatrick, Heterogeneous photocatalysis: recent advances and applications, Catalysts 3 (2013) 189–218.

[960] K. Edalati, Q. Wang, H. Eguchi, H. Razavi-Khosroshahi, H. Emami, M. Yamauchi, M. Fuji, Z. Horita, Impact of TiO$_2$-II phase stabilized in anatase matrix by high-pressure torsion on electrocatalytic hydrogen production, Matter Res. Lett. 7 (2019) 334–339.

[961] S. Akrami, Y. Murakami, M. Watanabe, T. Ishihara, M. Arita, Q. Guoe, M. Fuji, K. Edalati, Enhanced CO$_2$ conversion on highly-strained and oxygen-deficient BiVO$_4$ photocatalyst, Chem. Eng. J. 442 (2022) 136209.

[962] K. Edalati, K. Fujiwara, S. Takechi, Q. Wang, M. Arita, M. Watanabe, X. Sauvage, T. Ishihara, Z. Horita, Improved photocatalytic hydrogen evolution on tantalate perovskites CsTaO$_3$ and LiTaO$_3$ by strain-induced vacancies, ACS Appl. Energy Mater. 3 (2020) 1710–1718.

[963] I. Fujita, P. Edalati, Q. Wang, M. Watanabe, M. Arita, S. Munetoh, T. Ishihara, K. Edalati, Novel black bismuth oxide (Bi$_2$O$_3$) with enhanced photocurrent generation, produced by high-pressure torsion straining, Scr. Mater. 187 (2020) 366–370.

[964] K. Edalati, I. Fujita, S. Takechi, Y. Nakashima, K. Kumano, H. Razavi-Khosroshahi, M. Arita, M. Watanabe, X. Sauvage, T. Akbay, T. Ishihara, M. Fuji, Z. Horita, Photocatalytic activity of aluminum oxide by oxygen vacancy generation using high-pressure torsion straining, Scr. Mater. 173 (2019) 120–124.

[965] H. Sena, M. Fuji, Band gap engineering of semiconductors and ceramics by severe plastic deformation for solar energy harvesting, Mater. Trans. 64 (2023) 1497–1503.

[966] H. Sena, Stabilization of high-pressure phase semiconductors by plastic strain, J. Soc. Powder Technol. Jpn. 58 (2021) 66–72.

[967] M. Forkel, N. Carvalhais, C. Rodenbeck, R. Keeling, M. Heimann, K. Thonicke, S. Zaehle, M. Reichstein, Enhanced seasonal CO$_2$ exchange caused by amplified plant productivity in northern ecosystems, Science 351 (2016) 696–699.

[968] A.J. Morris, G.J. Meyer, E. Fujita, Molecular approaches to the photocatalytic reduction of carbon dioxide for solar fuels, Acc. Chem. Res. 42 (2009) 1983–1994.

[969] H. Tong, S. Ouyang, Y. Bi, N. Umezawa, M. Oshikiri, J. Ye, Nano-photocatalytic materials: possibilities and challenges, Adv. Mater. 24 (2012) 229–251.

[970] X. Li, J. Yu, C. Jiang, Chapter 1 - principle and surface science of photocatalysis, Interface, Sci. Technol. 31 (2020) 1–38.

[971] O. Ola, M.M. Maroto-Valer, Synthesis, characterization and visible light photocatalytic activity of metal based TiO$_2$ monoliths for CO$_2$ reduction, Chem. Eng. J. 283 (2016) 1244–1253.

[972] A. Akhundi, A. Habibi-Yangjeh, M. Abitorabi, S.R. Pouran, Review on photocatalytic conversion of carbon dioxide to value-added compounds and renewable fuels by graphitic carbon nitride-based photocatalysts, Catal. Rev. Sci. Eng. 61 (2019) 595–628.

[973] K. Wang, L. Zhang, Y. Su, S. Sun, Q. Wang, H. Wang, W. Wang, Boosted CO$_2$ photoreduction to methane via Co doping in bismuth vanadate atomic layers, Catal., Sci. Technol. 8 (2018) 3115–3122.

[974] G.J. Lee, S. Anandan, S.J. Masten, J.J. Wu, Photocatalytic hydrogen evolution fromwater splitting using Cu doped ZnS microspheres under visible light irradiation, Renew, Energy 89 (2016) 18–26.

[975] S. Bai, N. Zhang, C. Gao, Y. Xiong, Defect engineering in photocatalytic materials, Nano Energy 53 (2018) 293–336.

[976] X. Cai, F. Wang, R. Wang, Y. Xi, An Wang, J. Wang, B. Teng, S. Bai, Synergism of surface strain and interfacial polarization on Pd@Au core-shell cocatalysts for highly efficient photocatalytic CO$_2$ reduction over TiO$_2$, J. Mater. Chem. A 8 (2020) 7350–7359.

[977] Y. Li, W.N. Wang, Z. Zhan, M.H. Woo, C.Y. Wu, P. Biswas, Photocatalytic reduction of CO$_2$ with H$_2$O on mesoporous silica supported Cu/TiO$_2$ catalysts, Appl. Catal. B 100 (2010) 386–392.

[978] S. Cao, B. Shen, T. Tong, J. Fu, J. Yu, 2D/2D heterojunction of ultrathin MXene/ Bi$_2$WO$_6$ nanosheets for improved photocatalytic CO$_2$ reduction, Adv. Funct. Mater. 28 (2018) 1800136.

[979] B. Liu, L. Ye, R. Wang, J. Yang, Y. Zhang, R. Guan, L. Tian, X. Chen, Phosphorus-doped graphitic carbon nitride nanotubes with amino-rich surface for efficient CO$_2$ capture, enhanced photocatalytic activity, and product selectivity, ACS Appl. Mater. Interfaces 10 (2018) 4001–4009.

[980] A.T. Kuvarega, R.W.M. Krause, B.B. Mamba, Nitrogen/palladium-codoped TiO$_2$ for efficient visible light photocatalytic dye degradation, J. Phys. Chem. C. 115 (2011) 22110–22120.

[981] S. Akrami, T. Ishihara, M. Fuji, K. Edalati, Advanced photocatalysts for CO$_2$ conversion by severe plastic deformation (SPD), Materials 16 (2023) 1081.

[982] S. Akrami, P. Edalati, M. Fuji, K. Edalati, High-pressure torsion for highly-strained and high-entropy photocatalysts, KONA Powder Part. J. 41 (2024) 123–139.

[983] J. Wu, L. Xiong, Y. Hu, Y. Yang, X. Zhang, T. Wang, Z. Tang, A. Sun, Y. Zhoud, J. Shen, Z. Zou, Organic half-metal derived erythroid-like BiVO$_4$/hm-C$_4$N$_3$ Z-scheme photocatalyst, Reduction sites upgrading and rate-determining step modulation for overall CO$_2$ and H$_2$O conversion, Appl. Catal. B 295 (2021) 120277.

[984] M. Katai, P. Edalati, J. Hidalgo-Jimenez, Y. Shundo, T. Akbay, T. Ishihara, M. Arita, M. Fuji, K. Edalati, Black brookite rich in oxygen vacancies as an active photocatalyst for CO$_2$ conversion: experiments and first-principles calculations, J. Photochem. Photobio. A 449 (2024) 115409.

[985] S. Akrami, M. Watanabe, T.H. Ling, T. Ishihara, M. Arita, M. Fuji, K. Edalati, High pressure TiO$_2$-II polymorph as an active photocatalyst for CO$_2$ to CO conversion, Appl. Catal. B 298 (2021) 120566.

[986] S. Akrami, P. Edalati, K. Edalati, M. Fuji, High-entropy ceramics: a review of principles, production and applications, Mater. Sci. Eng. R. 146 (2021) 100644.

[987] C. Oses, C. Toher, S. Curtarolo, High-entropy ceramics, Nat. Rev. Mater. 5 (2020) 295–309.

[988] T. Takata, C. Pan, K. Domen, Recent progress in oxynitride photocatalysts for visible-light-driven water splitting, Sci. Technol. Adv. Mater. 16 (2015) 033506.

[989] K. Edalati, I. Fujita, X. Sauvage, M. Arita, Z. Horita, Microstructure and phase transformations of silica glass and vanadium oxide by severe plastic deformation via high-pressure torsion straining, J. Alloy. Compd. 779 (2019) 394–398.

[990] T. Bak, J. Nowotny, M. Rekas, C. Sorrell, Photo-electrochemical hydrogen generation from water using solar energy. materials-related aspects, Int. J. Hydrog, Energy 27 (2002) 991–1022.

[991] A. Fujishima, K. Honda, Electrochemical photolysis of water at a semiconductor electrode, Nature 238 (1972) 37–38.

[992] B. Ohtani, Photocatalysis A to Z - What we know and what we do not know in a scientific sense, J. Photochem. Photobiol. C. 11 (2010) 157–178.

[993] K. Nakata, A. Fujishima, TiO$_2$ photocatalysis: design and applications, J. Photochem. Photobiol. C. 13 (2012) 169–189.

[994] K.M. Lee, C.W. Lai, K.S. Ngai, J.C. Juan, Recent developments of zinc oxide based photocatalyst in water treatment technology: a review, Water Res 88 (2016) 428–448.

[995] A. Dong, L. Lin, R. Mu, R. Li, K. Li, C. Wang, Y. Cao, Y. Ling, Y. Chen, F. Yang, X. Pan, Q. Fu, X. Bao, Modulating the formation and evolution of surface hydrogen species on ZnO through Cr addition, ACS Catal. 12 (2022) 6255–6264.

[996] K. Maeda, T. Takata, M. Hara, N. Saito, Y. Inoue, H. Kobayashi, K. Domen, GaN: ZnO solid solution as a photocatalyst for visible-light-driven overall water splitting, J. Am. Chem. Soc. 127 (2005) 8286–8287.

[997] C. Shifu, C. Lei, G. Shen, C. Gengyu, The preparation of coupled SnO$_2$/TiO$_2$ photocatalyst by ball milling, Mater. Chem. Phys. 98 (2006) 116–120.

[998] B.B. Sapkota, S.R. Mishra, A simple ball milling method for the preparation of p-CuO/n-ZnO nanocomposite photocatalysts with high photocatalytic activity, J. Nanosci. Nanotechnol. 13 (2013) 6588–6596.

[999] L. Wei, C. Shifu, Z. Sujuan, Z. Wei, Z. Huaye, Y. Xiaoling, Preparation and characterization of p-n heterojunction photocatalyst p-CuBi$_2$O$_4$/n-TiO$_2$ with high photocatalytic activity under visible and UV light irradiation, J. Nanopart. Res. 12 (2010) 1355–1366.

[1000] J. Zhou, M. Zhang, Y. Zhu, Preparation of visible light-driven g-C₃N₄@ZnO hybrid photocatalyst via mechanochemistry, Phys. Chem. Chem. Phys. 16 (2014) 17627–17633.

[1001] M. Mesbah, M. Sarraf, A. Dabbagh, B. Nasiri-Tabrizi, S. Paria, S. M. Banihashemian, A.R. Bushroa, G. Faraji, T. Tsuzuki, H.R.Madaah Hosseini, Synergistic enhancement of photocatalytic antibacterial effects in high-strength aluminum/TiO₂ nanoarchitectures, Ceram. Int. 46 (2020) 24267–24280.

[1002] J. Hidalgo-Jiménez, T. Akbay, T. Ishihara, K. Edalati, Understanding high photocatalytic activity of the TiO₂ high-pressure columbite phase by experiments and first-principles calculations, J. Mater. Chem. A 11 (2023) 23523–23535.

[1003] Y. Qi, Y. Kauffmann, A. Kosinova, A.R. Kilmametov, B.B. Straumal, E. Rabkin, Gradient bandgap narrowing in severely deformed ZnO nanoparticles, Mater. Res. Lett. 9 (2021) 58–64.

[1004] J. Hidalgo-Jiménez, T. Akbay, Y. Ikeda, T. Ishihara, K. Edalati, Mechanism of anatase-to-columbite TiO₂ phase transformation via sheared phases: first-principles calculations and high-pressure torsion experiments, J. Mater. Sci. 59 (2024) 5995–6007.

[1005] M.L.A. Kumari, L.G. Devi, G. Maia, T.W. Chen, N. Al-Zaqri, M.A. Ali, Mechanochemical synthesis of ternary heterojunctions TiO₂(A)/TiO₂(R)/ZnO and TiO₂(A)/TiO₂(R)/SnO₂ for effective charge separation in semiconductor photocatalysis: a comparative study, Environ. Res. 203 (2022) 111841.

[1006] W. Zhao, Y. Jin, C.H. Gao, W. Gu, Z.M. Jin, Y.L. Lei, L.S. Liao, A simple method for fabricating p-n junction photocatalyst CuFe₂O₄/Bi₄Ti₃O_R and its photocatalytic activity, Mater. Chem. Phys. 143 (2014) 952–962.

[1007] H. Ishaq, I. Dincer, C. Crawford, A review on hydrogen production and utilization: challenges and opportunities, Int. J. Hydrog. Energy 47 (2022) 26238–26264.

[1008] Z.X. Yang, X.G. Li, Q.L. Yao, Z.H. Lu, N. Zhang, J. Xia, K. Yang, Y.Q. Wang, K. Zhang, H.Z. Liu, L.T. Zhang, H.J. Lin, Q.J. Zhou, F. Wang, Z.M. Yu, J.M. Ma, 2022 roadmap on hydrogen energy from production to utilizations, Rare Met 41 (2022) 3251–3267.

[1009] T. Yusaf, A.S. Faisal Mahamude, K. Kadirgama, D. Ramasamy, K. Farhana, H. Al Dhahad, A.B.D.R.Abu Talib, Sustainable hydrogen energy in aviation? a narrative review, Int. J. Hydrog, Energy 52 (2024) 1026–1045.

[1010] B. You, Y. Sun, Innovative strategies for electrocatalytic water splitting, Acc. Chem. Res. 51 (2018) 1571–1580.

[1011] S. Anantharaj, S.R. Ede, K. Karthick, S. Sam Sankar, K. Sangeetha, P.E. Karthik, S. Kundu, Precision and correctness in the evaluation of electrocatalytic water splitting: revisiting activity parameters with a critical assessment, Energ. Environ. Sci. 11 (2018) 744–771.

[1012] Y. Zheng, Y. Jiao, A. Vasileff, S.Z. Qiao, The hydrogen evolution reaction in alkaline solution: from theory, single crystal models, to practical electrocatalysts, Angew. Chem. 57 (2018) 7568–7579.

[1013] Y. Wang, B. Kong, D. Zhao, H. Wang, C. Selomulya, Strategies for developing transition metal phosphides as heterogeneous electrocatalysts for water splitting, Nano Today 15 (2017) 26–55.

[1014] J. Zhang, Q. Zhang, X. Feng, Support and interface effects in water-splitting electrocatalysts, Adv. Mater. 31 (2019) 1808167.

[1015] Y.C. Hu, Y.Z. Wang, R. Su, C.R. Cao, F. Li, C.W. Sun, Y. Yang, P.F. Guan, D. W. Ding, Z.L. Wang, W.H. Wang, A highly efficient and self-stabilizing metallic-glass catalyst for electrochemical hydrogen generation, Adv. Mater. 28 (2016) 10293–10297.

[1016] Z. Jia, T. Yang, L. Sun, Y. Zhao, W. Li, J. Luan, F. Lyu, L.C. Zhang, J.J. Kruzic, J. J. Kai, J.C. Huang, J. Lu, C.T. Liu, A novel multinary intermetallic as an active electrocatalyst for hydrogen evolution, Adv. Mater. (2020) 2000385.

[1017] W.H. Wang, Bulk metallic glasses with functional physical properties, Adv. Mater. 21 (2009) 4524–4544.

[1018] A. Inoue, A. Takeuchi, Recent development and application products of bulk glassy alloys, Acta Mater. 59 (2011) 2243–2267.

[1019] Z.J. Wang, M.X. Li, J.H. Yu, X.B. Ge, Y.H. Liu, W.H. Wang, Low-iridium-content IrNiTa metallic glass films as intrinsically active catalysts for hydrogen evolution reaction, Adv. Mater. 32 (2020) 1906384.

[1020] X. Liu, P. Zou, L. Song, B. Zang, B. Yao, W. Xu, F. Li, J. Schroers, J. Huo, J. Q. Wang, Combinatorial high-throughput methods for designing hydrogen evolution reaction catalysts, ACS Catal. 12 (2022) 3789–3796.

[1021] C. Pei, S. Chen, T. Zhao, M. Li, Z. Cui, B. Sun, S. Hu, S. Lan, H. Hahn, T. Feng, Nanostructured metallic glass in highly upgraded energy state contributing to efficient catalytic performance, Adv. Mater. 34 (2022) 2200850.

[1022] F.Y. Gao, S.N. Liu, J.C. Ge, X.L. Zhang, L. Zhu, Y.R. Zheng, Y. Duan, S. Qin, W. Dong, X. Yu, R.C. Bao, P.P. Yang, Z.Z. Niu, Z.G. Ding, W. Liu, S. Lan, M. R. Gao, Y. Yan, S.H. Yu, Nickel-molybdenum-niobium metallic glass for efficient hydrogen oxidation in hydroxide exchange membrane fuel cells, Nat. Catal. 5 (2022) 993–1005.

[1023] K. Wu, Y. Meng, J. Xu, K. Edalati, H. Shao, W. Li, H.J. Lin, Novel Fe-based nanoglass as efficient noble-metal-free electrocatalyst for alkaline hydrogen evolution reaction, Scr. Mater. 188 (2020) 135–139.

[1024] F. Chu, K. Wu, Y. Meng, K. Edalati, H.J. Lin, Effect of high-pressure torsion on the hydrogen evolution performances of a melt-spun amorphous Fe₇₃.₅Si₁₃.₅B₉Cu₁Nb₃ alloy, Int. J. Hydrog. Energy 46 (2021) 25029–25038.

[1025] F. Chu, X. Jian, K. Edalati, Y. Yan, H. Ke, P. Zhang, H.J. Lin, Nanoscale heterogeneous FeB metallic glass as highly active and stable catalyst for hydrogen evolution, J. Alloy. Compd. 960 (2023) 170964.

[1026] K. Wu, F. Chu, Y. Meng, K. Edalati, Q. Gao, W. Li, H.J. Lin, Cathodic corrosion activated Fe-based nanoglass as a highly active and stable oxygen evolution catalyst for water splitting, J. Mater. Chem. A 9 (2021) 12152–12160.

[1027] F. Chu, B. Han, K. Edalati, J. Ma, Y. Meng, C. Wang, F. Yang, P. Zhang, H.J. Lin, Severe plastic deformed Pd-based metallic glass for superior hydrogen evolution in both acidic and alkaline media, Scr. Mater. 204 (2021) 114145.

[1028] J.X. Feng, S.H. Ye, H. Xu, Y.X. Tong, G.R. Li, Design and synthesis of FeOOH/CeO₂ heterolayered nanotube electrocatalysts for the oxygen evolution reaction, Adv. Mater. 28 (2016) 4698–4703.

[1029] J. Chen, F. Zheng, S.J. Zhang, A. Fisher, Y. Zhou, Z. Wang, Y. Li, B.B. Xu, J.T. Li, S.G. Sun, Interfacial interaction between FeOOH and Ni-Fe LDH to modulate the local electronic structure for enhanced OER electrocatalysis, ACS Catal. 8 (2018) 11342–11351.

[1030] Y. Jing, S. Almassi, S. Mehraeen, R.J. LeSuer, B.P. Chaplin, The roles of oxygen vacancies, electrolyte composition, lattice structure, and doping density on the electrochemical reactivity of Magneli phase TiO₂ anodes, J. Mater. Chem. A 6 (2018) 23828–23839.

[1031] T. Reier, H.N. Nong, D. Teschner, R. Schlogl, P. Strasser, Electrocatalytic oxygen evolution reaction in acidic environments reaction mechanisms and catalysts, Adv. Energy Mater. 7 (2017) 1601275.

[1032] M. Tang, Q. Ge, Mechanistic understanding on oxygen evolution reaction on γ-Fe OOH (010) under alkaline condition based on DFT computational study, Chin. J. Catal. 38 (2017) 1621–1628.

[1033] T.R. Cook, D.K. Dogutan, S.Y. Reece, Y. Surendranath, T.S. Teets, D.G. Nocera, Solar energy supply and storage for the legacy and nonlegacy worlds, Chem. Rev. 110 (2010) 6474–6502.

[1034] A. Grimaud, O. Diaz-Morales, B. Han, W.T. Hong, Y.L. Lee, L. Giordano, K. A. Stoerzinger, M.T. Koper, Y. Shao-Horn, Activating lattice oxygen redox reactions in metal oxides to catalyse oxygen evolution, Nat. Chem. 9 (2017) 457–465.

[1035] N.T. Suen, S.F. Hung, Q. Quan, N. Zhang, Y.J. Xu, H.M. Chen, Electrocatalysis for the oxygen evolution reaction: recent development and future perspectives, Chem. Soc. Rev. 46 (2017) 337–365.

[1036] S. Zhao, R. Jin, H. Abroshan, C. Zeng, H. Zhang, S.D. House, E. Gottlieb, H. J. Kim, J.C. Yang, R. Jin, Gold nanoclusters promote electrocatalytic water oxidation at the nanocluster/CoSe₂ interface, J. Am. Chem. Soc. 139 (2017) 1077–1080.

[1037] C. Xu, H.J. Lin, K. Edalati, W. Li, L. Li, Y. Zhu, Superior hydrogenation properties in a Mg₆₅Ce₁₀Ni₂₀Cu₅ nanoglass processed by melt-spinning followed by high-pressure torsion, Scr. Mater. 152 (2018) 137–140.

[1038] M. Liu, Z. Yao, J. Gu, C. Li, X. Huang, L. Zhang, Z. Huang, M. Fan, Issues and opportunities facing hydrolytic hydrogen production materials, Chem. Eng. J. 461 (2023) 141918.

[1039] P. Li, F. Xu, L. Sun, Y. Xia, J. Chen, X. Yang, Y. Wu, F. Yu, Y. Luo, Hydrogen generation performance of novel Al–LiH–metal oxides, Inorg. Chem. Front. 5 (2018) 1700–1706.

[1040] F. Zhang, K. Edalati, M. Arita, Z. Horita, Fast hydrolysis and hydrogen generation on Al-Bi alloys and Al-Bi-C composites synthesized by high-pressure torsion, Int. J. Hydrog. Energy 42 (2017) 29121–29130.

[1041] L. Ouyang, J. Jiang, K. Chen, M. Zhu, Z. Liu, Hydrogen production via hydrolysis and alcoholysis of light metal-based materials: a review, Nano-Micro Lett. 13 (2021) 134.

[1042] H.Z. Wang, D.Y.C. Leung, M.K.H. Leung, M. Ni, A review on hydrogen production using aluminum and aluminum alloys, Renew. Sust. Energy Rev. 13 (2009) 845–853.

[1043] X. Huang, T. Gao, X. Pan, D. Wei, C. Lv, L. Qin, Y. Huang, A review: feasibility of hydrogen generation from the reaction between aluminum and water for fuel cell applications, J. Power Sources 229 (2013) 133–140.

[1044] F. Zhang, R. Yonemoto, M. Arita, Z. Horita, Hydrogen generation from pure water using Al–Sn powders consolidated through high-pressure torsion, J. Mater. Res 31 (2016) 775–782.

[1045] F. Zhang, K. Edalati, M. Arita, Z. Horita, Hydrolytic hydrogen production on Al–Sn–Zn alloys processed by high-pressure torsion, Materials 11 (2018) 1209.

[1046] P. Edwards, V. Kuznetsov, W. David, N. Brandon, Hydrogen and fuel cells: towards a sustainable energy future, Energy Policy 36 (2008) 4356–4362.

[1047] V.K. Milinchuk, E.R. Klinshpont, V.I. Belozerov, Standalone hydrogen generator based on chemical decomposition of water by aluminum, Nucl. Energy Technol. 1 (2015) 259–266.

[1048] C. Ho, Hydrolytic reaction of waste aluminum foils for high efficiency of hydrogen generation, Int. J. Hydrog. Energy 42 (2017) 19622–19628.

[1049] A.L. Martinez-Salazar, J.A. Melo-Banda, M.A. Coronel-Garcia, J. Gonzalez-Barbosa, J.M. Dominguez-Esquivel, Hydrogen generation by aluminum alloy corrosion in aqueous acid solutions promoted by nanometal: kinetics study, Renew. Energy 146 (2020) 2517–2523.

[1050] S.P. Tekade, D.Z. Shende, K.L. Wasewar, Hydrogen generation in an annular micro-reactor: an experimental investigation of water splitting reaction using aluminum in presence of potassium hydroxide, Int. J. Chem. React. Eng. 17 (2019) 20180104.

[1051] S.P. Tekade, D.Z. Shende, K.L. Wasewar, Hydrogen generation in water splitting reaction using aluminum: effect of NaOH concentration and reaction modelling using SCM, Int. J. Chem. React. Eng. 16 (2018) 20170250.

[1052] X. Wang, G. Li, R. Eckhoff, Kinetics study of hydration reaction between aluminum powder and water based on an improved multi-stage shrinking core model, Int. J. Hydrog. Energy 46 (2021) 33635–33655.

[1053] S.S. Razavi-Tousi, J.A. Szpunar, Modification of the shrinking core model for hydrogen generation by reaction of aluminum particles with water, Int. J. Hydrog. Energy 41 (2016) 87–93.

[1054] F. Xiao, R. Yang, J. Li, Hydrogen generation from hydrolysis of activated aluminum/organic fluoride/bismuth composites with high hydrogen generation rate and good aging resistance in air, Energy 170 (2019) 159–169.

[1055] F. Xiao, R. Yang, W. Gao, J. Hu, J. Li, Effect of carbon materials and bismuth particle size on hydrogen generation using aluminum-based composites, J. Alloy. Compd. 817 (2020) 152800.

[1056] X. Hu, G. Zhu, Y. Zhang, Y. Wang, M. Gu, S. Yang, P. Song, X. Li, H. Fang, G. Jiang, Z. Wang, Hydrogen generation through rolling using Al-Sn alloy, Int. J. Hydrog. Energy 37 (2012) 11012–11020.

[1057] K. Cheng, R. Fu, D. Sang, L. Jing, Y. Li, A novel method to prepare Al–Ga alloy with intergranular penetrating, Mater. Lett. 129 (2014) 84–87.

[1058] J. Liu, X. Zhang, M. Chen, L. Li, B. Zhu, J. Tang, S. Liu, DFT study on surface properties and dissolution trends of Al(100) surfaces doped with Zn, Ga, In, Sn and Pb, Appl. Surf. Sci. 257 (2011) 4004–4009.

[1059] P. Hai, C. Wu, X. Ding, Y. Li, Coverage-dependent adsorption and dissociation of H_2O on Al surfaces, Phys. Chem. Chem. Phys. 25 (2023) 13041–13048.

[1060] F. Xu, L. Sun, X. Lan, H. Chu, Y. Sun, H. Zhou, F. Li, L. Yang, X. Si, Jian Zhang, Serge Walter, Zelimir Gabelica. Mechanism of fast hydrogen generation from pure water using Al-SnCl₂ and bi-doped Al-SnCl₂ composites, Int. J. Hydrog. Energy 39 (2014) 5514–5521.

[1061] S. Pighin, G. Urretavizcaya, J. Bobet, Nanostructured Mg for hydrogen production by hydrolysis obtained by MgH_2 milling and dehydriding, J. Alloy. Compd.. 827 (2020) 154000.

[1062] Z. Tan, L. Ouyang, J. Liu, H. Wang, H. Shao, M. Zhu, Hydrogen generation by hydrolysis of Mg-Mg₂Si composite and enhanced kinetics performance from introducing of $MgCl_2$ and Si, Int. J. Hydrog, Energy 43 (2018) 2903–2912.

[1063] J. Jiang, L. Ouyang, H. Wang, J. Liu, H. Shao, M. Zhu, Controllable hydrolysis performance of MgLi alloys and their hydrides, ChemPhysChem 20 (2019) 1316–1324.

[1064] X. Hou, K. Hou, J. Bai, L. Yang, Q. Shu, Q. Cao, L. Feng, G. Suo, X. Ye, L. Zhang, Y. Yang, Mg alloy waste modified by $(Mg_{10}Ni)_{90}Ce_{10}$: a green hydrolysis hydrogen production strategy, Fuel 311 (2022) 122517.

[1065] D. Gan, Y. Liu, J. Zhang, Y. Zhang, C. Cao, Y. Zhu, L. Li, Kinetic performance of hydrogen generation enhanced by AlCl₃ *via* hydrolysis of MgH_2 prepared by hydriding combustion synthesis, Int. J. Hydrog, Energy 43 (2018) 10232–10239.

[1066] Z. Zhao, Y. Zhu, L. Li, Efficient catalysis by MgCl₂ in hydrogen generation *via* hydrolysis of Mg-based hydride prepared by hydriding combustion synthesis, Chem. Commun. 48 (2012) 5509–5511.

[1067] J. Zheng, D. Yang, W. Li, H. Fu, X. Li, Promoting H_2 generation from the reaction of Mg nanoparticles and water using cations, Chem. Commun. 49 (2013) 9437–9439.

[1068] M. Tegel, S. Schöne, B. Kieback, L. Röntzsch, An efficient hydrolysis of MgH_2-based materials, Int. J. Hydrog, Energy 42 (2017) 2167–2176.

[1069] K. Chen, J. Jiang, L. Ouyang, H. Wang, J. Liu, H. Shao, M. Zhu, Enhanced hydrogen generation from hydrolysis of MgLi doped with expanded graphite, J. Magnes. Alloy. 9 (2021) 2185–2193.

[1070] J.O. Abe, A.I.P. Popoola, E. Ajenifuja, O.M. Popoola, Hydrogen energy, economy and storage: review and recommendation, Int. J. Hydrog. Energy 44 (2019) 15072–15086.

[1071] A. Kovac, M. Paranos, D. Marcius, Hydrogen in energy transition: a review, Int, . J. Hydrog. Energy 46 (2021) 10016–10035.

[1072] US DOE Target Explanation Document, Onboard hydrogen storage for light-duty fuel cell vehicles. ⟨https://www.energy.gov/eere/fuelcells/doe-technical-targe ts-onboard-hydrogen-storage-light-duty-vehicles⟩.

[1073] L. Ouyang, F. Liu, H. Wang, J. Liu, X.S. Yang, L. Sun, Min Zhu, Magnesium-based hydrogen storage compounds: a review, J. Alloy. Compd. 832 (2020) 154865.

[1074] Á. Révész, M. Gajdics, Improved H-storage performance of novel Mg-based nanocomposites prepared by high-energy ball milling: a review, Energies 14 (2021) 6400.

[1075] N.A.A. Rusman, M. Dahari, A review on the current progress of metal hydrides material for solid-state hydrogen storage applications, Int. J. Hydrog. Energy 41 (2016) 12108–12126.

[1076] J.B. von Colbe, J.R. Ares, J. Barale, M. Baricco, C. Buckley, G. Capurso, N. Gallandat, D.M. Grant, M.N. Guzik, I. Jacob, E.H. Jensen, T. Jensen, J. Jepsen, T. Klassen, M.V. Lototskyy, K. Manickam, A. Montone, J. Puszkiel, S. Sartori, D. A. Sheppard, A. Stuart, G. Walker, C.J. Webb, H. Yang, V. Yartys, A. Züttel, M. Dornheim, Application of hydrides in hydrogen storage and compression: achievements, outlook and perspectives, Int. J. Hydrog. Energy 44 (2019) 7780–7808.

[1077] K. Edalati, E. Akiba, W.J. Botta, Y. Estrin, R. Floriano, D. Fruchart, T. Grosdidier, Z. Horita, J. Huot, H.W. Li, H.J. Lin, Á. Révész, M.J. Zehetbauer, Impact of severe plastic deformation on kinetics and thermodynamics of hydrogen storage in magnesium and its alloys, J. Mater. Sci. Technol. 146 (2023) 221–239.

[1078] Y. Jia, C. Sun, S. Shen, J. Zou, S.S. Mao, X. Yao, Combination of nanosizing and interfacial effect: future perspective for designing Mg-based nanomaterials for hydrogen storage, Renew. Sust. Energy Rev. 44 (2015) 289–303.

[1079] T. Sadhasivam, H.T. Kim, S. Jung, S.H. Rohd, J.H. Park, H.Y. Jung, Dimensional effects of nanostructured Mg/MgH₂ for hydrogen storage applications: a review, Renew. Sust. Energy Rev. 72 (2017) 523–534.

[1080] H.J. Lin, Y.S. Lu, L.T. Zhang, H.Z. Liu, K. Edalati, Á. Révész, Recent advances in metastable alloys for hydrogen storage: a review, Rare Met 41 (2022) 1797–1817.

[1081] L. Pasquini, Design of Nanomaterials for Hydrogen Storage, Energies 13 (2020) 3503.

[1082] L. He, X. Shi, X. Li, J. Huang, T. Cheng, X. Wang, Y. Li, H. Lin, K. Edalati, H. W. Li, Severe plastic deformation through high-pressure torsion for preparation of hydrogen storage materials - a review, Mater. Trans. 64 (2023) 1575–1584.

[1083] D.R. Leiva, A.M. Jorge, T.T. Ishikawa, J. Huot, D. Fruchart, S. Miraglia, C. S. Kiminami, W.J. Botta, Nanoscale grain refinement and H-sorption properties of MgH_2 processed by high-pressure torsion and other mechanical routes, Adv. Eng. Mater. 12 (2010) 786–792.

[1084] Á. Révész, Zs Kánya, T. Verebélyi, P.J. Szabó, A.P. Zhilyaev, T. Spassov, The effect of high-pressure torsion on the microstructure and hydrogen absorption kinetics of ball-milled $Mg_{70}Ni_{30}$, J. Alloy. Compd. 504 (2010) 83–88.

[1085] X. Hou, R. Hu, T. Zhang, H. Kou, J. Li, Hydrogenation thermodynamics of melt-spun magnesium rich Mg–Ni nanocrystalline alloys with the addition of multiwalled carbon nanotubes and TiF₃, J. Power Sources 306 (2016) 437–447.

[1086] M. Gajdics, T. Spassov, V.K. Kis, E. Schafler, Á. Révész, Microstructural and morphological investigations on Mg-Nb₂O₅-CNT nanocomposites processed by high-pressure torsion for hydrogen storage applications, Int. J. Hydrog. Energy 45 (2020) 7917–7928.

[1087] Á. Révész, Z.S. Kovács, Severe plastic deformation of amorphous alloys, Mater. Trans. 60 (2019) 1283–1293.

[1088] Á. Révész, Á. Kis-Tóth, L.K. Varga, E. Schafler, I. Bakonyi, T. Spassov, Hydrogen storage of melt-spun amorphous $Mg_{65}Ni_{20}Cu_5Y_{10}$ alloy deformed by high-pressure torsion, Int. J. Hydrog. Energy 37 (2012) 5769–5776.

[1089] S.J. Huang, C. Chiu, T.-Y. Chou, E. Rabkin, Effect of equal channel angular pressing (ECAP) on hydrogen storage properties of commercial magnesium alloy AZ61, Int. J. Hydrog. Energy 43 (2018) 4371–4380.

[1090] C. Chiu, S.-J. Huang, T.-Y. Chou, E. Rabkin, Improving hydrogen storage performance of AZ31 Mg alloy by equal channel angular pressing and additives, J. Alloy. Compd. 743 (2018) 437–447.

[1091] S.J. Huang, M.P. Mose, V. Rajagopal, Effect of microstructure on the hydrogenation behavior of AZ61 magnesium alloy with silicon carbide and nickel additives, processed by equal channel angular pressing, Int. J. Hydrog. Energy 46 (2021) 4211–4221.

[1092] S.J. Huang, V. Rajagopal, A.N. Ali, Influence of the ECAP and HEBM processes and the addition of Ni catalyst on the hydrogen storage properties of AZ31-x Ni (x = 0, 2, 4) alloy, Int. J. Hydrog. Energy 44 (2019) 1047–1058.

[1093] M. Krystian, M.J. Zehetbauer, H. Kropik, B. Mingler, G. Krexner, Hydrogen storage properties of bulk nanostructured ZK60 Mg alloy processed by equal channel angular pressing, J. Alloy. Compd. 509S (2011) S449–S455.

[1094] S.D. Vincent, J. Huot, Effect of air contamination on ball milling and cold rolling of magnesium hydride, J. Alloy. Compd. 509 (2011) L175–L179.

[1095] R. Floriano, D.R. Leiva, J.A. Carvalho, T.T. Ishikawa, W.J. Botta, Cold rolling under inert atmosphere: a powerful tool for Mg activation, Int. J. Hydrog. Energy 39 (2014) 4959–4965.

[1096] L.E.R. Vega, D.R. Leiva, R.M. Leal Neto, W.B. Silva, R.A. Silva, T.T. Ishikawa, C. S. Kiminami, W.J. Botta, Mechanical activation of TiFe for hydrogen storage by cold rolling under inert atmosphere, Int. J. Hydrog. Energy 43 (2018) 2913–2918.

[1097] J. Manna, B. Tougas, J. Hout, Mechanical activation of air exposed TiFe+ 4 wt% Zr alloy for hydrogenation by cold rolling and ball milling, Int. J. Hydrog. Energy 43 (2018) 20795–20800.

[1098] R. Floriano, D.R. Leiva, G.C. Melo, T.T. Ishikawa, J. Huot, M. Kaufman, S.J. A. Figueroa, L.A. Mendoza-Zélis, L.C. Damonte, W.J. Botta, Low temperature rolling of AZ91 alloy for hydrogen storage, Int. J. Hydrog. Energy 42 (2017) 29394–29405.

[1099] M. Danaie, C. Mauer, D. Mitlin, J. Huot, Hydrogen storage in bulk Mg–Ti and Mg–stainless steel multilayer composites synthesized via accumulative roll-bonding (ARB), Int. J. Hydrog. Energy 39 (2011) 3022–3036.

[1100] P. de Rango, D. Fruchart, V. Aptukov, N. Skryabina, Fast forging: a new SPD method to synthesize Mg-based alloys for hydrogen storage, Int. J. Hydrog. Energy 45 (2020) 7912–7916.

[1101] D.R. Leiva, R. Floriano, J. Huot, A.M. Jorge, C. Bolfarini, C.S. Kiminami, T. T. Ishikawa, W.J. Botta, Nanostructured MgH_2 prepared by cold rolling and cold forging, J. Alloy. Compd. 509 (2011) S444–S448.

[1102] P. de Rango, J. Wen, N. Skryabina, L. Laversenne, D. Fruchart, M. Borges, Hydrogen storage properties of Mg-Ni alloys processed by fast forging, Energies 13 (2020) 3509.

[1103] A.A.C. Asselli, D.R. Leiva, J. Huot, M. Kawasaki, T.G. Langdon, W.J. Botta, Effects of equal-channel angular pressing and accumulative roll-bonding on hydrogen storage properties of a commercial ZK60 magnesium alloy, Int. J. Hydrog. Energy 40 (2015) 16971–16976.

[1104] J. Soyama, M.R.M. Triques, D.R. Leiva, A.M. Jorge Jr., E.P. Silva, H.C. Pinto, C. Bolfarini, C.S. Kininami, W.J. Botta, Hydrogen storage in heavily deformed ZK60 alloy modified with 2.5 wt% Mm addition, Int. J. Hydrog. Energy 41 (2016) 4177–4184.

[1105] J.J. Reilly Jr, R.H. Wiswall Jr, Reaction of hydrogen with alloys of magnesium and nickel and the formation of Mg₂NiH₄, Inorg. Chem. 7 (1968) 2254–2256.

[1106] F. Cuevas, M. Amdisen, M. Baricco, C.E. Buckley, Y.W. Cho, P. De Jongh, L. M. De Kort, J.B. Grinderslev, V. Gulino, B.C. Hauback, Metallic and complex hydride-based electrochemical storage of energy, Prog, Energy 4 (2022) 032001.

[1107] L. Pasquini, K. Sakaki, E. Akiba, M.D. Allendorf, E. Alvares, J.R. Ares, D. Babai, M. Baricco, J.B. von Colbe, M. Bereznitsky, Magnesium-and intermetallic alloys-based hydrides for energy storage: modelling, synthesis and properties, Prog. Energy 4 (2022) 032007.

[1108] L. He, H.W. Li, H. Nakajima, N. Tumanov, Y. Filinchuk, S.J. Hwang, M. Sharma, H. Hagemann, E. Akiba, Synthesis of a bimetallic dodecaborate LiNaB₁₂H₁₂ with outstanding superionic conductivity, Chem. Mater. 27 (2015) 5483–5486.

[1109] E.M. Dematteis, M.B. Amdisen, T. Autrey, J. Barale, M.E. Bowden, C.E. Buckley, Y.W. Cho, S. Deledda, M. Dornheim, P. De Jongh, Hydrogen storage in complex hydrides: past activities and new trends, Prog. Energy 4 (2022) 032009.

[1110] C. Zhou, H. Wang, L. Ouyang, M. Zhu, The state of the art of hydrogen storage materials for high-pressure hybrid hydrogen vessel, Mater. Rep. 33 (2019) 117–126.

[1111] Z. Chen, Z. Ma, J. Zheng, X. Li, E. Akiba, H.W. Li, Perspectives and challenges of hydrogen storage in solid-state hydrides, Chin. J. Chem. Eng. 29 (2021) 1–12.

[1112] L. He, H.W. Li, S.J. Hwang, E. Akiba, Facile solvent-free synthesis of anhydrous alkali metal dodecaborate $M_2B_{12}H_{12}$ (M = Li, Na, K), J. Phys. Chem. C. 118 (2014) 6084–6089.

[1113] Y. Yan, H.W. Li, H. Maekawa, M. Aoki, T. Noritake, M. Matsumoto, K. Miwa, S. I. Towata, S.I. Orimo, Formation process of $[B_{12}H_1^{2]2-}$ from $[BH_4]^-$ during the dehydrogenation reaction of Mg $(BH_4)_2$, Mater. Trans. 52 (2011) 1443–1446.

[1114] H.W. Li, E. Akiba, S.I. Orimo, Comparative study on the reversibility of pure metal borohydrides, J. Alloy Compd. 580 (2013) S292–S295.

[1115] W. Zhang, X. Zhang, Z. Huang, H.W. Li, M. Gao, H. Pan, Y. Liu, Recent development of lithium borohydride-based materials for hydrogen storage, Adv. Energy Sustain. Res. 2 (2021) 2100073.

[1116] L. Ouyang, K. Chen, J. Jiang, X.S. Yang, M. Zhu, Hydrogen storage in light-metal based systems: a review, J. Alloy Compd. 829 (2020) 154597.

[1117] M. Dornheim, Thermodynamics of metal hydrides: tailoring reaction enthalpies of hydrogen storage materials, in: J.C. Moreno-Pirajan (Ed.), Thermodynamics - Interaction Studies - Solids, Liquids and Gases, IntechOpen,, 2011, pp. 891–918.

[1118] P. Modi, K.F. Aguey-Zinsou, Room temperature metal hydrides for stationary and heat storage applications: a review, Front. Energy Res. 9 (2021) 616115.

[1119] J. Hauck, H. Schenk, The coordination of hydrogen in transition metal hydrides, J. Less-Common Met 51 (1977) 251–258.

[1120] W. Grochala, P.P. Edwards, Thermal decomposition of the non-interstitial hydrides for the storage and production of hydrogen, Chem. Rev. 104 (2004) 1283–1316.

[1121] G. Sandrock, A panoramic overview of hydrogen storage alloys from a gas reaction point of view, J. Alloy Compd. 293 (1999) 877–888.

[1122] J. Yang, A. Sudik, C. Wolverton, D.J. Siegel, High capacity hydrogen storage materials: attributes for automotive applications and techniques for materials discovery, Chem. Soc. Rev. 39 (2010) 656–675.

[1123] Y. Liu, H. Pan, New and future developments in catalysis. Hydrogen storage materials, Elsevier Inc,, 2013, pp. 377–405.

[1124] I. Saldan, A prospect for $LiBH_4$ as on-board hydrogen storage, Cent. Eur. J. Chem. 9 (2011) 761–775.

[1125] Z. Jing, Q. Yuan, Y. Yu, X. Kong, K.C. Tan, J. Wang, Q. Pei, X.B. Wang, W. Zhou, H. Wu, A. Wu, T. He, P. Chen, Developing ideal metalorganic hydrides for hydrogen storage: from theoretical prediction to rational fabrication, ACS Mater. Lett. 3 (2021) 1417–1425.

[1126] H.W. Li, Y. Yan, S.I. Orimo, A. Züttel, C.M. Jensen, Recent progress in metal borohydrides for hydrogen storage, Energies 4 (2011) 185–214.

[1127] R.W. Wagemans, J.H. van Lenthe, P.E. de Jongh, A.J. Van Dillen, K.P. de Jong, Hydrogen storage in magnesium clusters: quantum chemical study, J. Am. Chem. Soc. 127 (2005) 16675–16680.

[1128] J. Lu, Y.J. Choi, Z.Z. Fang, H.Y. Sohn, E. Ronnebro, Hydrogen storage properties of nanosized MgH_2-0.1TiH_2 prepared by ultrahigh-energy-high-pressure milling, J. Am. Chem. Soc. 131 (2009) 15843–15852.

[1129] M. Zhu, Y. Lu, L. Ouyang, H. Wang, Thermodynamic tuning of Mg-based hydrogen storage alloys: a review, Materials 6 (2013) 4654–4674.

[1130] R. Griessen, T. Riesterer, Heat of formation models, In: Hydrogen in Intermetallic Compounds I: Electronic, Thermodynamic, and Crystallographic Properties, 2005, pp. 219–284.

[1131] H. Liu, I.I. Naumov, R. Hoffmann, N. Ashcroft, R.J. Hemley, Potential high-Tc superconducting lanthanum and yttrium hydrides at high pressure, Proc. Natl. Acad. Sci. USA 114 (2017) 6990–6995.

[1132] Q. Li, Y. Lu, Q. Luo, X. Yang, Y. Yang, J. Tan, Z. Dong, J. Dang, J. Li, Y. Chen, Thermodynamics and kinetics of hydriding and dehydriding reactions in Mg-based hydrogen storage materials, J. Magnes. Alloy 9 (2021) 1922–1941.

[1133] D. Moser, G. Baldissin, D. Bull, D. Riley, I. Morrison, D. Ross, W. Oates, D. Noreus, The pressure–temperature phase diagram of MgH_2 and isotopic substitution, J. Phys. -Condens. Mat. 23 (2011) 305403.

[1134] J.J. Vajo, S.L. Skeith, F. Mertens, Reversible storage of hydrogen in destabilized $LiBH_4$, J. Phys. Chem. B 109 (2005) 3719–3722.

[1135] M. Aoki, K. Miwa, T. Noritake, G. Kitahara, Y. Nakamori, S. Orimo, S. Towata, Destabilization of $LiBH_4$ by mixing with $LiNH_2$, Appl. Phys. A 80 (2005) 1409–1412.

[1136] K. Edalati, J. Matsuda, M. Arita, T. Daio, E. Akiba, Z. Horita, Mechanism of activation of TiFe intermetallics for hydrogen storage by severe plastic deformation using high-pressure torsion, Appl. Phys. Lett. 103 (2013) 143902.

[1137] K. Edalati, J. Matsuda, A. Yanagida, E. Akiba, Z. Horita, Activation of TiFe for hydrogen storage by plastic deformation using groove rolling and high-pressure torsion: similarities and differences, Int. J. Hydrog. Energy 39 (2014) 15589–15594.

[1138] K. Edalati, A. Yamamoto, Z. Horita, T. Ishihara, High-pressure torsion of pure magnesium: evolution of mechanical properties, microstructures and hydrogen storage capacity with equivalent strain, Scr. Mater. 64 (2011) 880–883.

[1139] T. Hongo, K. Edalati, M. Arita, J. Matsuda, E. Akiba, Z. Horita, Significance of grain boundaries and stacking faults on hydrogen storage properties of Mg_2Ni intermetallics processed by high-pressure torsion, Acta Mater. 92 (2015) 46–54.

[1140] Y. Sun, C. Shen, Q. Lai, W. Liu, D.W. Wang, K.F. Aguey-Zinsou, Tailoring magnesium based materials for hydrogen storage through synthesis: current state of the art, Energy Stor. Mater. 10 (2018) 168–198.

[1141] A.M. Jorge Jr, G. Ferreira de Lima, M.R. Martins Triques, W.J. Botta, C. S. Kiminami, R.P. Nogueira, A.R. Yavari, T.G. Langdon, Correlation between hydrogen storage properties and textures induced in magnesium through ECAP and cold rolling, Int. J. Hydrog. Energy 39 (2014) 3810–3821.

[1142] J. Huot, N.Y. Skryabina, D. Fruchart, Application of severe plastic deformation techniques to magnesium for enhanced hydrogen sorption properties, Metals 2 (2012) 329–343.

[1143] V.M. Skripnyuk, E. Rabkin, Y. Estrin, R. Lapovok, Improving hydrogen storage properties of magnesium based alloys by equal channel angular pressing, Int. J. Hydrog. Energy 34 (2009) 6320–6324.

[1144] V. Skripnyuk, E. Buchman, E. Rabkin, Y. Estrin, M. Popov, S. Jorgensen, The effect of equal channel angular pressing on hydrogen storage properties of a eutectic Mg-Ni alloy, J. Alloy. Compd. 436 (2007) 99–106.

[1145] K. Edalati, H.W. Li, A. Kilmametov, R. Floriano, C. Borchers, High-pressure torsion for synthesis of high-entropy alloys, Metals 11 (2021) 1263.

[1146] R.B. Strozi, J. Ivanisenko, N. Koudriachova, J. Huot, Effect of HPT on the first hydrogenation of $LaNi_5$ metal hydride, Energies 14 (2021) 6710.

[1147] J.Y. Jung, J.O. Fadonougbo, J.Y. Suh, Y.S. Lee, J.Y. Huh, Y.W. Cho, Synthesis of Mg_2FeH_6 by hydrogenation of Mg/Fe powder mixture prepared by cold roll milling in air: effects of microstructure and oxygen distribution, Int. J. Hydrog. Energy 43 (2018) 16758–16765.

[1148] J. Dufour, J. Huot, Rapid activation, enhanced hydrogen sorption kinetics and air resistance in laminated Mg-Pd2.5at%, J. Alloy. Compd. 439 (2007) L5–L7.

[1149] S. Pedneault, L. Roué, J. Huot, Synthesis of metal hydrides by cold rolling, Mater. Sci. Forum 570 (2008) 33–38.

[1150] J. Huot, Enhancing Hydrogen Storage Properties of Metal Hydrides, Springer,, 2016.

[1151] J.J. Nah, H.G. Kang, M.Y. Huh, O. Engler, Effect of strain states during cold rolling on the recrystallized grain size in an aluminum alloy, Scr. Mater. 58 (2008) 500–503.

[1152] K. Fukuda, Y. Koyanagi, M. Tsushida, H. Kitahara, T. Mayama, S. Ando, Activation stress for slip systems of pure magnesium single crystals in pure shear test, Mater. Trans. 58 (2017) 587–591.

[1153] J. Lang, A. Asselli, N. Hebert, J. Huot, The influence of morphology on the hydrogen storage properties of magnesium based materials processed by cold rolling, Adv. Mater. Res. 922 (2014) 400–405.

[1154] D.R. Leiva, J. Huot, T.T. Ishikawa, C. Bolfarini, C.S. Kiminami, A.M. Jorge, W. J. Botta, Hydrogen activation behavior of commercial magnesium processed by different severe plastic deformation routes, Mater. Sci. Forum 667– 669 (2011) 1047–1051.

[1155] M.S. El-Eskandarany, N. Ali, S.M. Al-Salem, Solid-state conversion of magnesium waste to advanced hydrogen-storage nanopowder particles, Nanomater 10 (2020) 1037.

[1156] G. Donadey, S. Caillaud, P. Coeuret, M. Moussa, L. Cuzacq, J.L. Bobet, Hydrogen generation from Mg wastes by cold rolling and ball milling by hydrolysis reaction: elektron 21 (UNS-M12310) in simulated seawater, Metals 12 (2022) 1821.

[1157] S. Amira, J. Huot, Effect of cold rolling on hydrogen sorption properties of die-cast and as-cast magnesium alloys, J. Alloy. Compd. 520 (2012) 287–294.

[1158] J. Soyama, R. Floriano, D.R. Leiva, Y. Guo, A.M. Jorge Junior, E. Pereira da Silva, H.C. Pinto, C. Bolfarini, C.S. Kiminami, W.J. Botta, Severely deformed ZK60 + 2.5% Mm alloy for hydrogen storage produced by two different processing routes, Int. J. Hydrog. Energy 41 (2016) 11284–11292.

[1159] K. Suganuma, H. Miyamura, S. Kikuchi, N. Takeichi, K. Tanaka, H. Tanaka, N. Kuriyama, T.T. Ueda, M. Tsukahara, Hydrogen storage properties of Mg-Al alloy prepared by super lamination technique, Adv. Mater. Res. 26–28 (2007) 857–860.

[1160] N. Takeichi, K. Tanaka, H. Tanaka, T.T. Ueda, Y. Kamiya, M. Tsukahara, H. Miyamura, S. Kikuchi, The hydrogen storage properties of Mg/Cu and Mg/Pd laminate composites and metallographic structure, J. Alloy. Compd. 446–447 (2007) 543–548.

[1161] F.J. Antiqueira, D.R. Leiva, T.T. Ishikawa, A.M. Jorge Junior, W.J. Botta, Severe plastic deformation and additive distribution in Mg-Fe to improve hydrogen storage properties, Mater. Res. 20 (2017) 61–70.

[1162] T.B. Ameur, A.R. Yavari, Solid state amorphization of MgNi multilayers, Collq. Phys. C. 4 (1990) 219.

[1163] N. Takeichi, K. Tanaka, H. Tanaka, T.T. Ueda, M. Tsukahara, H. Miyamura, S. Kikuchi, Hydrogen storage properties and corresponding phase transformations of Mg/Pd laminate composites prepared by a repetitive-rolling method, Mater. Trans. 48 (2007) 2395–2398.

[1164] J. Huot, S. Amira, J. Lang, N. Skryabina, D. Fruchart, Improvement of hydrogen storage properties of magnesium alloys by cold rolling and forging, IOP Conf. Ser. Mater. Sci. Eng. 63 (2014) 012114.

[1165] N. Kudriashova, J. Huot, Effect of cold rolling on magnesium-based metal hydrides, Mater. Trans. 64 (2023) 1879–1885.

[1166] J. Lang, J. Huot, A new approach to the processing of metal hydrides, J. Alloy. Compd. 509 (2011) L18–L22.

[1167] J.J. Reilly, R.H. Wiswall, Formation and properties of iron titanium hydride, Inorg. Chem. 13 (1974) 218–222.

[1168] L. Schlapbach, A. Seiler, Y. Stucki, Surface segregation in FeTi and its catalytic effect on the hydrogenation II: AES and XPS studies, Mater. Res. Bull. 13 (1978) 1031–1037.

[1169] T. Schober, D.G. Westlake, The activation of FeTi for hydrogen storage: a different view, Scr. Metall. 15 (1981) 913–918.

[1170] J.Y. Lee, C.N. Park, S.M. Pyun, The activation processes and hydriding kinetics of FeTi, J. Less-Common Met 89 (1989) 163–168.

[1171] L. Schlapbach, T. Riesterer, The activation of FeTi for hydrogen absorption, Appl. Phys. A 32 (1983) 169–182.

[1172] H. Inui, T. Yamamoto, M. Hirota, M. Yamaguchi, Lattice defects introduced during hydrogen absorption–desorption cycles and their effects on P-C characteristics in some intermetallic compounds, J. Alloy. Compd. 330- 332 (2002) 117–124.

[1173] K. Edalati, M. Matsuo, H. Emami, S. Itano, A. Alhamid, A. Staykov, D.J. Smith, S. Orimo, E. Akiba, Z. Horita, Impact of severe plastic deformation on microstructure and hydrogen storage of titanium-iron-manganese intermetallics, Scr. Mater. 124 (2016) 108–111.

[1174] P. Ma, T. Masuda, S. Hirosawa, Z. Horita, Development of high-strength Al–Cu–Mg alloy by combined application of high-pressure torsion and aging treatment, Mater. Trans.. 64 (2023) 514–521.

[1175] T. Waitz, V. Kazykhanov, H.P. Karnthaler, Martensitic phase transformations in nanocrystalline NiTi studied by TEM, Acta Mater. 52 (2004) 137–147.

[1176] J.Y. Huang, Y.T. Zhu, X.Z. Liao, R.Z. Valiev, Amorphization of TiNi induced by high-pressure torsion, Philos. Mag. Lett. 84 (2004) 183–190.

[1177] C. Rentenberger, T. Waitz, H.P. Karnthaler, Formation and structures of bulk nanocrystalline intermetallic alloys studied by transmission electron microscopy, Mater. Sci. Eng. A 462 (2007) 283–288.

[1178] C. Mangler, C. Gammer, H.P. Karnthaler, C. Rentenberger, Structural modifications during heating of bulk nanocrystalline FeAl produced by high-pressure torsion, Acta Mater. 58 (2010) 5631–5638.

[1179] K. Edalati, Z. Horita, Application of high-pressure torsion for consolidation of ceramic powders, Scr. Mater. 63 (2010) 174–177.

[1180] V.D. Blank, B.A. Kulnitskiy, Crystallogeometry of polymorphic transitions in silicon under pressure, High. Press. Res. 15 (1996) 31–42.

[1181] R.K. Islamgaliev, F. Chmelik, I.F. Gibadullin, W. Biegel, R.Z. Valiev, The nanocrystalline structure formation in germanium subjected to severe plastic deformation, Nanostruct. Mater. 4 (1994) 387–395.

[1182] R.K. Islamgaliev, R. Kuzel, E.D. Obraztsova, J. Burianek, F. Chmelik, R.Z. Valiev, TEM, XRD and Raman scattering of germanium processed by severe deformation, Mater. Sci. Eng. A 249 (1998) 152–157.

[1183] R.K. Islamgaliev, R. Kuzel, S.N. Mikov, A.V. Igo, J. Burianek, F. Chmelik, R. Z. Valiev, Structure of silicon processed by severe plastic deformation, Mater. Sci. Eng. A 266 (1999) 205–210.

[1184] Y. Ikoma, K. Hayano, K. Edalati, K. Saito, Q. Guo, Z. Horita, Phase transformation and nanograin refinement of silicon by processing through high-pressure torsion, Appl. Phys. Lett. 101 (2012) 121908.

[1185] Y. Ikoma, K. Kumano, K. Edalati, M.R. McCartney, D.J. Smith, Z. Horita, High-resolution transmission electron microscopy analysis of nanograined germanium produced by high-pressure torsion, Mater. Charact. 132 (2017) 132–138.

[1186] Z. Horita, Y. Tang, M. Matsuo, K. Edalati, M. Yumoto, Y. Takizawa, Enhancement of activation and hydrogen storage kinetics of TiFe(Mn) using high-pressure sliding (HPS) process, Mater. Trans. 64 (2023) 1920–1923.

[1187] Y. Takizawa, T. Masuda, K. Fujimitsu, T. Kajita, K. Watanabe, M. Yumoto, Y. Otagiri, Z. Horita, Scaling up of high-pressure sliding (HPS) for grain refinement and superplasticity, Metall. Mater. Trans. A 47 (2016) 4669–4681.

[1188] T. Masuda, K. Fujimitsu, K. Sumikawa, T. Kajita, Y. Tang, S. Hirosawa, Y. Takizawa, M. Yumoto, Y. Otagiri, Z. Horita, Homogeneous strain introduction using reciprocation technique in high-pressure sliding, Metall. Mater. Trans. A 52 (2021) 3860–3870.

[1189] H. Nagai, K. Kitagaki, K. Shoji, Microstructure and hydriding characteristics of FeTi alloys containing manganese, J. Less-Common Met 134 (1987) 275–286.

[1190] S.M. Lee, T.P. Perng, Effect of the second phase on the initiation of hydrogenation of TiFe$_{1-x}$M$_x$ (M = Cr,Mn) alloys, Int. J. Hydrog. Energy 19 (1994) 259–263.

[1191] J. Hidalgo-Jiménez, J.M. Cubero-Sesín, K. Edalati, S. Khajavi, J. Huot, Effect of high-pressure torsion on first hydrogenation of Laves phase Ti$_{0.5}$Zr$_{0.5}$(Mn$_{1-x}$Fe$_x$)Cr$_1$ (x = 0, 0.2 and 0.4) high entropy alloy, J. Alloy. Compd. 969 (2023) 172243.

[1192] M.L. Trudeau, L. Dignard-Bailey, R. Schulz, P. Tessier, L. Zaluski, D.H. Ryan, J. O. Strom-Olsen, The oxidation of nanocrystalline FeTi hydrogen storage compounds, Nanostruct. Mater. 1 (1992) 457–464.

[1193] T. Haraki, K. Oishi, H. Uchida, Y. Miyamoto, M. Abe, T. Kokaji, S. Uchida, Properties of hydrogen absorption by nano-structured FeTi alloys, Int. J. Mater. Res 99 (2008) 507–512.

[1194] J.C. Crivello, B. Dam, R.V. Denys, M. Dornheim, D.M. Grant, J. Huot, T. R. Jensen, P. de Jongh, M. Latroche, C. Milanese, D. Milčius, G.S. Walker, C. J. Webb, C. Zlotea, V.A. Yartys, Review of magnesium hydride-based materials: development and optimization, J. Appl. Phys. A 122 (2016) 97.

[1195] V.A. Yartys, M.V. Lototskyy, E. Akiba, R. Albert, V.E. Antonov, J.R. Ares, M. Baricco, N. Bourgeois, C.E. Buckley, J.M. Bellosta von Colbe, J.-C. Crivello, F. Cuevas, R.V. Denys, M. Dornheim, M. Felderhoff, D.M. Grant, B.C. Hauback, T. D. Humphries, I. Jacob, T.R. Jensen, P.E. de Jongh, J.-M. Joubert, M.A. Kuzovnikov, M. Latroche, M. Paskevicius, L. Pasquini, L. Popilevsky, V.M. Skripnyuk, E. Rabkin, M.V. Sofianos, A. Stuart, G. Walker, H. Wang, C.J. Webb, M. Zhu, Magnesium based materials for hydrogen based energy storage: past, present and future, Int. J. Hydrog. Energy 44 (2019) 7809–7859.

[1196] D. Fruchart, N. Skryabina, P. de Rango, M. Fouladvind, V. Aptukov, Severe plastic deformation by fast forging to easy produce hydride from bulk Mg-based alloys, Mater. Trans. 64 (2023) 1886–1893.

[1197] C. Nishimura, M. Komaki, M. Amano, Hydrogen permeation through magnesium, J. Alloy. Compd. 293- 295 (1999) 329–333.

[1198] P. Spatz, H.A. Aebischer, A. Krozerand, L. Schlapbach, The diffusion of H in Mg and the nucleation and growth of MgH$_2$ in thin films, Zeit . F. üR. Phys. Chem. 181 (1993) 393–397.

[1199] A. San-Martin, F.D. Manchester, The H−Mg (Hydrogen-Magnesium) system, J. Phase Equilibria 8 (1987) 431–437.

[1200] K. Zeng, T. Klassen, W. Oelerich, R. Bormann, Critical assessment and thermodynamic modeling of the Mg-H system, Int. J. Hydrog. Energy 24 (1999) 989–1004.

[1201] J.R. Davis. Handbook: Forming and Forging, 9th Edition, ASM International,, 1989.

[1202] D. Fruchart, M. Jehan, N. Skryabina, P. de Rango, Hydrogen solid state storage on MgH$_2$ compacts for mass applications, Metals 13 (2023) 992.

[1203] S. Rivoirard, D. Chateigner, P. de Rango, D. Fruchart, R. Perrier de la Bâthie, J. L. Soubeyroux, Texture investigation of hot-forged Nd–Fe–B magnets, Philos. Mag. A 80 (2000) 1955–1966.

[1204] V.N. Aptukov, I.I. Tsirulnik, N.E. Skryabina, D. Fruchart, Importance of thermal conductivity and stress level during a phase (hydride) transformation in magnesium, PNRPU Mech. Bull. 2 (2022) 25–38.

[1205] N. Skryabina, V.N. Aptukov, P. de Rango, D. Fruchart, Effect of temperature on fast forging process of Mg-Ni samples for fast formation of Mg$_2$Ni for hydrogen storage, Int. J. Hydrog, Energy 45 (2020) 3008–3015.

[1206] A. Gaikwad1, S. Kirwai, P. Koley, G. Balachandran, R. Singh, Theoretical study on cold open die forging process optimization for multipass workability, MATEC Web Conf. 80 (2016) 13002.

[1207] M.G. Cockroft, D.J. Latham, Ductility and the workability of metals, J. Inst. Met. 96 (1968) 33–39.

[1208] T. Kvačkaj, J. Tiža, J. Bacsó, A. Kováčová, R. Kočiško, R. Pernis, M. Fedorčáková, P. Purcz., Cockcroft-Latham ductile fracture criteria for non-ferrous materials, Mater. Sci. Forum 782 (2014) 373–378.

[1209] V.M. Skripnyuk, E. Rabkin, Y. Estrin, R. Lapovok, The effect of ball milling and equal channel angular pressing on the hydrogen absorption/desorption properties of Mg-4.95 wt% Zn-0.71 wt% Zr (ZK60) alloy, Acta Mater. 52 (2004) 405–414.

[1210] Y. Estrin, R. Hellmig, Improving the properties of magnesium alloys by equal channel angular pressing, Meter Sci. Heat. Treat. 48 (2006) 504–507.

[1211] D.R. Leiva, D. Fruchart, M. Bacia, G. Girard, N. Skryabina, A.C.S. Villela, S. Miraglia, D.S. Santos, W.J. Botta, Mg alloy for hydrogen storage processed by SPD, Int. J. Mater. Res 100 (2009) 1739–1746.

[1212] M. Avvari, S. Narendranath, H.S. Nayaka, A review on wrought magnesium alloys processed by equal channel angular pressing, Int. J. Mater. Product. Technol. 51 (2015) 139–164.

[1213] L. Wang, J. Jiang, A. Ma, Y. Li, D. Song, A critical review of Mg-based hydrogen storage materials processed by equal channel angular pressing, Metals 7 (2017) 324.

[1214] K. Nakashima, Z. Horita, M. Nemoto, T.G. Langdon, Influence of channel angle on the development of ultrafine grains in equal-channel angular pressing, Acta Mater. 46 (1998) 1589–1599.

[1215] N. Skryabina, V. Aptukov, P. Romanov, D. Fruchart, P. de Rango, G. Girard, C. Grandini, H. Sandim, J. Huot, J. Lang, R. Cantelli, F. Leardini, Microstructure optimization of Mg-alloys by the ECAP process including numerical simulation, SPD treatments, characterization, and hydrogen sorption properties, Molecules 24 (2019) 89.

[1216] R. Floriano, D.R. Leiva, S. Deledda, B.C. Hauback, W.J. Botta, Cold rolling of MgH$_2$ powders containing different additives, Int. J. Hydrog. Energy 38 (2013) 16193–16198.

[1217] E. Ivanov, I. Konstanchuk, A. Stepanov, V. Boldyrev, Magnesium mechanical alloys for hydrogen storage, J. Less-Common Met 131 (1987) 25–29.

[1218] Y. Chen, J.S. Williams, Formation of metal hydrides by mechanical alloying, J. Alloy. Compd. 217 (1995) 181–184.

[1219] R. Schulz, S. Boily, L. Zaluski, A. Zaluska, P. Tessier, J.O. Strom-Olsen, Nanocrystalline materials for hydrogen storage. The Proceedings of the International Conference on Composite Materials and Energy, Technomic Publishing Co,, Lancaster, PA, 1995, pp. 529–535.

[1220] L. Zaluski, A. Zaluska, J.O. Ström-Olsen, Nanocrystalline metal hydrides, J. Alloy. Compd. 253- 254 (1997) 70–79.

[1221] B. Bogdanovic, M. Schwickardi, Ti-doped alkali metal aluminium hydrides as potential novel reversible hydrogen storage materials, J. Alloy. Compd. 253–254 (1997) 1–9.

[1222] R.A. Dunlap, Z.H. Cheng, G.R. MacKay, J.W. O'Brien, D.A. Small, Preparation of nanocrystalline metal hydrides by ball milling, Hyperfine Inter. 130 (2000) 109–126.

[1223] J.L. Bobet, B. Chevalier, B. Darriet, Effect of reactive mechanical grinding on chemical and hydrogen sorption properties of the Mg+10 wt% Co mixture, J. Alloy. Compd. 330- 332 (2002) 738–742.

[1224] A. Molotnikov, R. Lapovok, T. Peng, Y. Estrin, Comparison of different extrusion methods for compaction of powders, Mater. Sci. Forum 667–669 (2010) 57–62.

[1225] J. Wen, P. de Rango, N. Allain, L. Laversenne, T. Grosdidier, Improving hydrogen storage performance of Mg-based alloy through microstructure optimization, J. Power Sources 480 (2020) 228823.

[1226] G.M. Pressouyre, I.M. Bernstein, A kinetic trapping model for hydrogen-induced cracking, Acta Met. 27 (1979) 89–100.

[1227] F.G. Wei, K. Tsuzaki, Quantitative analysis on hydrogen trapping of TiC particles in steel, Metall. Mater. Trans. A 37 (2006) 331–353.

[1228] T. Depover, K. Verbeken, Evaluation of the effect of V_4C_3 precipitates on the hydrogen induced mechanical degradation in Fe-C-V alloys, Mater. Sci. Eng. A 675 (2016) 299–313.

[1229] J.Y. Lee, S.M. Lee, Hydrogen trapping phenomena in metals with B.C.C. and F.C. C. crystals structures by the desorption thermal analysis technique, Surf. Coat. Technol. 28 (1986) 301–314.

[1230] A.W. Thompson, J.A. Brooks, Hydrogen performance of precipitation-strengthened stainless steels based on A-286, Metall. Trans. A 6 (1975) 1431–1442.

[1231] M. Koyama, K. Habib, T. Masumura, T. Tsuchiyama, H. Noguchi, Gaseous hydrogen embrittlement of a Ni-free austenitic stainless steel containing 1 mass % nitrogen: effects of nitrogen-enhanced dislocation planarity, Int. J. Hydrog. Energy 45 (2020) 10209–10218.

[1232] A. Macadre, N. Nakada, T. Tsuchiyama, S. Takaki, Critical grain size to limit the hydrogen-induced ductility drop in a metastable austenitic steel, Int. J. Hydrog. Energy 40 (2015) 10697–10703.

[1233] Y. Mine, K. Tachibana, Z. Horita, Effect of hydrogen on tensile properties of ultrafine-grained type 310S austenitic stainless steel processed by high-pressure torsion, Metall. Mater. Trans. A 42 (2011) 1619–1624.

[1234] Y. Mine, K. Tachibana, Z. Horita, Effect of high-pressure torsion processing and annealing on hydrogen embrittlement of type 304 metastable austenitic stainless steel, Metall. Mater. Trans. A 41 (2010) 3110–3120.

[1235] A. Mohammadi, M. Novelli, M. Arita, J.W. Bae, H.S. Kim, T. Grosdidier, K. Edalati, Gradient-structured high-entropy alloy with improved combination of strength and hydrogen embrittlement resistance, Corros. Sci. 200 (2022) 110253.

[1236] A. Mohammadi, P. Edalati, M. Arita, J.W. Bae, H.S. Kim, K. Edalati, High strength and high ductility of a severely deformed high-entropy alloy in the presence of hydrogen, Corros. Sci. 216 (2023) 111097.

[1237] Y. Mine, Z. Horita, Hydrogen effects on ultrafine-grained steel processed by high-pressure torsion, Mater. Trans. 53 (2012) 773–785.

[1238] M. Koyama, E. Akiyama, Y. Lee, D. Raabe, K. Tsuzaki, Overview of hydrogen embrittlement in high-Mn steels, Int. J. Hydrog. Energy 42 (2017) 12706–12723.

[1239] I. Park, S. Lee, H. Jeon, Y. Lee, The advantage of grain refinement in the hydrogen embrittlement of Fe–18Mn–0.6C twinning-induced plasticity steel, Corros. Sci. 93 (2015) 63–69.

[1240] Y. Bai, Y. Momotani, M.C. Chen, A. Shibata, N. Tsuji, Effect of grain refinement on hydrogen embrittlement behaviors of high-Mn TWIP steel, Mater. Sci. Eng. A 651 (2016) 935–944.

[1241] D. Eliezer, D.G. Chakrapani, C.J. Altstetter, E.N. Pugh, The influence of austenite stability on the hydrogen embrittlement and stress-corrosion cracking of stainless steel, Metall. Trans. A 10 (1979) 935–941.

[1242] S. Singh, C. Altstetter, Effect of hydrogen concentration on slow crack growth in stainless steels, Metall. Trans. A 13 (1982) 1799–1808.

[1243] Y. Mine, K. Koga, O. Kraft, K. Takashima, Mechanical characterization of hydrogen-induced quasi-cleavage in a metastable austenitic steel using micro-tensile testing, Scr. Mater. 113 (2016) 176–179.

[1244] S. Ueki, K. Koga, Y. Mine, K. Takashima, Crystallographic characterisation of hydrogen-induced twin boundary separation in type 304 stainless steel using micro-tensile testing, ISIJ Int 59 (2019) 927–934.

[1245] Y. Mine, Z. Horita, Y. Murakami, Effect of hydrogen on martensite formation in austenitic stainless steels in high-pressure torsion, Acta Mater. 57 (2009) 2993–3002.

[1246] C. San March, T. Michler, K.A. Nibur, B.P. Somerday, On the physical differences between tensile testing of type 304 and 316 austenitic stainless steels with internal hydrogen and in external hydrogen, Int. J. Hydrog. Energy 35 (2010) 9736–9745.

[1247] Y. Mine, N. Horita, Z. Horita, K. Takashima, Effect of ultrafine grain refinement on hydrogen embrittlement of metastable austenitic stainless steel, Int. J. Hydrog. Energy 42 (2017) 15415–15425.

[1248] L. Zhang, Z. Li, J. Zheng, Y. Zhao, P. Xu, C. Zhou, X. Li, Effect of strain-induced martensite on hydrogen embrittlement of austenitic stainless steels investigated by combined tension and hydrogen release methods, Int. J. Hydrog. Energy 38 (2013) 8208–8214.

[1249] Y. Mine, K. Koga, K. Takashima, Z. Horita, Mechanical characterisation of microstructural evolution in 304 stainless steel subjected to high-pressure torsion with and without hydrogen pre-charging, Mater. Sci. Eng. A 661 (2016) 87–95.

[1250] Y. Mine, C. Narazaki, T. Kanezaki, S. Matsuoka, Y. Murakami, Fatigue behaviour of metallic materials exposed to high pressure hydrogen environments, in: E. E. Gdoutos (Ed.), Fracture of Nano and Engineering Materials and Structures, Springer,, Netherlands, 2006, pp. 907–908.

[1251] Y. Wang, X. Li, D. Dou, L. Shen, J. Gong, FE analysis of hydrogen diffusion around a crack tip in an austenitic stainless steel, Int. J. Hydrog. Energy 41 (2016) 6053–6063.

[1252] Y. Matsuoka, T. Iwasaki, N. Nakada, T. Tsuchiyama, T. Takaki, Effect of grain size on thermal and mechanical stability of austenite in metastable austenitic stainless steel, ISIJ Int 53 (2013) 1224–1230.

[1253] S. Ueki, R. Oura, Y. Mine, K. Takashima, Micro-mechanical characterisation of hydrogen embrittlement in nano-twinned metastable austenitic stainless steel, Int. J. Hydrog. Energy 45 (2020) 27950–27957.

[1254] X. Chen, L. Ma, C. Zhou, Y. Hong, H. Tao, J. Zheng, L. Zhang, Improved resistance to hydrogen embrittlement of warm-deformed 304 austenitic stainless steel in high-pressure hydrogen atmosphere, Corros. Sci. 148 (2019) 159–170.

[1255] Y.H. Fan, F. Cui, L. Lu, B. Zhang, A nanotwinned austenite stainless steel with high hydrogen embrittlement resistance, J. Alloy. Compd. 788 (2019) 1066–1075.

[1256] A. Mohammadi, K. Edalati, D.D. Coimbrao, W.J. Botta, H. Noguchi, Influence of nanotwins on hydrogen embrittlement of TWIP (twinning-induced plasticity) steel processed by high-pressure torsion, Mater. Sci. Eng. A 783 (2020) 139273.

[1257] H. Miyamoto, Corrosion of ultrafine grained materials by severe plastic deformation, an overview, Mater. Trans. 57 (2016) 559–572.

[1258] H. Miyamoto, M. Yuasa, M. Rifai, H. Fujiwara, Corrosion behavior of severely deformed pure and single-phase materials, Mater. Trans. 60 (2019) 1243–1255.

[1259] Y. Miyajima, M. Mitsuhara, S. Hata, H. Nakashima, N. Tsuji, Quantification of internal dislocation density using scanning transmission electron microscopy in ultrafine grained pure aluminum fabricated by severe plastic deformation, Mater. Sci. Eng. A 528 (2010) 776–779.

[1260] J.A. Muñoz, O.F. Higuera, J.M. Cabrera, Microstructural and mechanical study in the plastic zone of ARMCO iron processed by ECAP, Mater. Sci. Eng. A 697 (2017) 24–36.

[1261] A. Mishra, B.K. Kad, F. Gregori, M.A. Meyers, Microstructural evolution in copper subjected to severe plastic deformation: experiments and analysis, Acta Mater. 55 (2007) 13–28.

[1262] N. Lugo, N. Llorca, J.M. Cabrera, Z. Horita, Microstructures and mechanical properties of pure copper deformed severely by equal-channel angular pressing and high-pressure torsion, Mater. Sci. Eng. A 477 (2008) 366–371.

[1263] K. Edalati, J.M. Cubero-Sesin, A. Alhamidi, I.F. Mohamed, Z. Horita, Influence of severe plastic deformation at cryogenic temperature on grain refinement and softening of pure metals: investigation using high-pressure torsion, Mater. Sci. Eng. A 613 (2014) 103–110.

[1264] H. Cheng, Z. Pan, Y. Fu, X. Wang, Y. Wei, H. Luo, X. Li, Corrosion-resistant high-entropy alloy coatings: a review, J. Electrochem. Soc. 168 (2021) 111502.

[1265] H. Shimizu, M. Yuasa, H. Miyamoto, K. Edalati, Corrosion behavior of ultrafine-grained CoCrFeMnNi high-entropy alloys fabricated by high-pressure torsion, Materials 15 (2022) 1007.

[1266] R.K. Gupta, N. Birbilis, The influence of nanocrystalline structure and processing route on corrosion of stainless steel: a review, Corr. Sci. 92 (2015) 1–15.

[1267] Y.B. Lei, Z.B. Wang, B. Zhang, Z.P. Luo, J. Lu, K. Lu, Enhanced mechanical properties and corrosion resistance of 316L stainless steel by pre-forming a gradient nanostructured surface layer and annealing, Acta Mater. 208 (2021) 116773.

[1268] V. Maurice, P. Marcus, Progress in corrosion science at atomic and nanometric scales, Prog. Mater. Sci. 95 (2018) 132–171.

[1269] D.D. Macdonald, The point defect model for the passive state, J. Electrochem. Soc. 139 (1992) 3434–3449.

[1270] K. Sugimoto, S. Matsuda, Passive and transpassive films on Fe-Cr alloys and neutral solutions, Mater. Sci. Eng. 42 (1980) 181–189.

[1271] N. Hara, K. Hirabayashi, Y. Sugawara, I. Muto, Improvement of pitting corrosion resistance of type 316L stainless steel by potentiostatic removal of surface MnSi inclusions, Int. J. Corr. 2012 (2012) 482730.

[1272] H.H. Uhlig, Passivity in metals and alloys, Corr. Sci. 19 (1979) 777–791.

[1273] K. Asami, K. Hashimoto, S. Shimodaira, An XPS study of the passivity of a series of iron-chromium alloys in sulphuric acid, Corr. Sci. 18 (1978) 151–160.

[1274] R. Kirchheim, B. Heine, H. Fischmeister, S. Hofmann, H. Knote, U. Stolz, The passivity of iron-chromium alloys, Corr. Sci. 29 (1989) 899–917.

[1275] M. Rifai, M. Yuasa, H. Miyamoto, Effect of deformation structure and annealing temperature on corrosion of ultrafine-grain Fe-Cr alloy prepared by equal channel angular pressing, Int. J. Corr. 2018 (2018) 15.

[1276] K. Hajizadeh, H. Maleki-Ghaleh, A. Arabi, Y. Behnamian, E. Aghaie, A. Farrokhi, M.G. Hosseini, M.H. Fathi, Corrosion and biological behavior of nanostructured 316L stainless steel processed by severe plastic deformation, Surf. Interface Anal. 47 (2015) 978–985.

[1277] M. Rifai, H. Miyamoto, H. Fujiwara, Effects of strain energy and grain size on corrosion resistance of ultrafine grained Fe-20%Cr steels with extremely low C and N fabricated by ECAP, Int. J. Corr. 2015 (2015) 386865.

[1278] R.B. Inturi, Z. Szklarska-Smialowska, Localized corrosion of nanocrystalline 304 type stainless steel films, Corrosion 48 (1992) 398–403.

[1279] C. Pan, L. Liu, Z. Bin, F. Wang, The electrochemical corrosion behavior of nanocrystalline 304 stainless steel prepared by magnetron sputtering, J. Electrochem. Soc. 159 (2012) C453–C460.

[1280] M. Eskandari, M. Yeganeh, M. Motamedi, Investigation in the corrosion behavior of bulk nanocrystalline 316L austenitic stainless steel in NaCl solution, Micro Nano Lett. 7 (2012) 380–383.

[1281] S.V. Muley, A.N. Vidvans, G.P. Chaudhari, S. Udainiya, An assessment of ultrafine grained 316L stainless steel for implant applications, Acta Biomater. 30 (2016) 408–419.

[1282] L. Jinlong, L. Hongyun, Comparison of corrosion properties of passive films formed on phase reversion induced nano/ultrafine-grained 321 stainless steel, Appl. Surf. Sci. 280 (2013) 124–131.

[1283] T. Balusamy, S. Kumar, T.S.N. Sankara Narayanan, Effect of surface nanocrystallization on the corrosion behavior of AISI 409 stainless steel, Corr, Sci 52 (2010) 3826–3834.

[1284] S. Li, Z. Ren, Y. Dong, C. Ye, G. Cheng, H. Cong, Enhanced pitting corrosion resistance of 304 SS in 3.5 wt% NaCl by ultrasonic nanocrystal surface modification, J. Electrochem. Soc. 164 (2017) C682–C689.

[1285] X.Y. Wang, D.Y. Li, Mechanical and electrochemical behavior of nanocrystalline surface of 304 stainless steel, Electrochim. Acta 47 (2002) 3939–3947.

[1286] X.Y. Wang, D.Y. Li, Mechanical, electrochemical and tribological properties of nano-crystalline surface of 304 stainless steel, Wear 255 (2003) 836–845.

[1287] C. Man, C. Dong, T. Liu, D. Kong, D. Wang, X. Li, The enhancement of microstructure on the passive and pitting behaviors of selective laser melting 316L SS in simulated body fluid, Appl. Surf. Sci. 467–468 (2019) 193–205.

[1288] V. Vignal, O. Delrue, O. Heintz, J. Peultier, Influence of the passive film properties and residual stresses on the micro-electrochemical behavior of duplex stainless steels, Electrochim. Acta 55 (2010) 7118–7125.

[1289] D.J. Sprouster, W. Streit Cunningham, G.P. Halada, H. Yan, A. Pattammattel, X. Huang, D. Olds, M. Tilton, Y.S. Chu, E. Dooryhee, G.P. Manogharan, J. R. Trelewicz, Dislocation microstructure and its influence on corrosion behavior in laser additively manufactured 316L stainless steel, Addit. Manuf. 47 (2021) 102263.

[1290] X. Guo, P.E. Vullum, H.J. Venvik, Inhibition of metal dusting corrosion on Fe-based alloy by combined near surface severe plastic deformation (NS-SPD) and thermochemical treatment, Corros. Sci. 190 (2021) 109702.

[1291] D.M. Marulanda, F.E. Castillejo, An overview on the corrosion behavior of steels processed by severe plastic deformation, Mater. Trans. 64 (2023) 1317–1324.

[1292] L. Romero-Resendiz, M. El-Tahawy, T. Zhang, M.C. Rossi, D.M. Marulanda-Cardona, T. Yang, V. Amigó-Borrás, Y. Huang, H. Mirzadeh, I.J. Beyerlein, J. C. Huang, T.G. Langdon, Y.T. Zhu, Heterostructured stainless steel: properties, current trends, and future perspectives, Mater. Sci. Eng. R. 150 (2022) 100691.

[1293] A. Hemasian Ettefagh, S. Guo, J. Rausch, Corrosion performance of additively manufactured stainless steel parts: a review, Addit. Manuf. 37 (2021) 101689.

[1294] H.S. Kim, S.J. Yoo, J.W. Ahn, D.H. Kim, W.J. Kim, Ultrafine grained titanium sheets with high strength and high corrosion resistance, Mater. Sci. Eng. A 528 (2011) 8479–8485.

[1295] B. Hadzima, M. Janeček, Y. Estrin, H.S. Kim, Microstructure and corrosion properties of ultrafine-grained interstitial free steel, Mater. Sci. Eng. A 462 (2007) 243–247.

[1296] Z. Wu, J. Chen, N. Piao, C. Sun, W. Hassan, X. Zhang, Y. Xie, Electrochemical corrosion behavior of bulk ultra-fine grained Fe−Ni−Cr alloy, Trans. Nonferrous Met. Soc. China 24 (2014) 1989–1994.

[1297] Z.J. Zheng, Y. Gao, Y. Gui, M. Zhu, Corrosion behaviour of nanocrystalline 304 stainless steel prepared by equal channel angular pressing, Corros. Sci. 54 (2012) 60–67.

[1298] H. Maleki-Ghaleh, K. Hajizadeh, E. Aghaie, S. Alamdari, M. Hosseini, M. Fathi, K. Ozaltin, K. Kurzydlowski, The effect of equal channel angular pressing (ECAP) process on the corrosion behavior of 316L stainless steel in Ringer's solution, Corrosion 71 (2015) 367–375.

[1299] S. Mohd Yusuf, M. Nie, Y. Chen, S. Yang, N. Gao, Microstructure and corrosion performance of 316L stainless steel fabricated by selective laser melting and processed through high-pressure torsion, J. Alloy. Compd. 763 (2018) 360–375.

[1300] P. Zhang, W. Han, Z. Huang, G. Li, M. Zhang, J. Li, Microstructure evolution and corrosion behavior of 316L stainless steel subjected to torsion, Mater. Res. Express 8 (2021) 086519.

[1301] F.E. Castillejo, D.M. Marulanda, J.J. Olaya, J.E. Alfonso, Wear and corrosion resistance of niobium–chromium carbide coatings on AISI D2 produced through TRD, Surf. Coat. Technol. 254 (2014) 104–111.

[1302] J.O. Braga, J.F. Lins, G.P.D. Castro, H.A.D. Almeida Junior, I.C. dos Santos, G. H. Sousa, I.L. Criscuolo, C.M. Santana, U.C. Pereira, Corrosion behavior of low carbon steel processed by ECAP in neutral and alkaline environment, Technol. Metal. Mater. Min. 18 (2021) e2340.

[1303] O.M. Irfan, H.M. Omar, Influence of Grain Refinement by ECAP on mechanical and erosion corrosion properties of AISI 4130 steel: experimental and prediction approach, Metall. Mater. Trans. A 50 (2019) 4232–4244.

[1304] L. Zhang, A. Ma, J. Jiang, D. Yang, D. Song, J. Chen, Sulphuric acid corrosion of ultrafine-grained mild steel processed by equal-channel angular pressing, Corros. Sci. 75 (2013) 434–442.

[1305] D.N. Awang Sh'ri, Z.S. Zahari, A. Yamamoto, Effect of ECAP die angle on mechanical properties and biocompatibility of SS316L, Metals 11 (2021) 1513.

[1306] A.M. Kliauga, V.L. Sordi, M. Ferrante, C.A. Rovere, S.E. Curi, Mechanical and corrosion properties of a F138 austenitic stainless steel after deformation by equal channel angular pressing, Mater. Sci. Forum 783- 786 (2014) 837–841.

[1307] S. Singh, K.K. Pandey, S.K. Bose, A.K. Keshri, Role of surface nanocrystallization on corrosion properties of low carbon steel during surface mechanical attrition treatment, Surf. Coat. Technol. 396 (2020) 125964.

[1308] T. Balusamy, T.S.N. Sankara Narayanan, K. Ravichandran, I.S. Park, M.H. Lee, Influence of surface mechanical attrition treatment (SMAT) on the corrosion behaviour of AISI 304 stainless steel, Corros. Sci. 74 (2013) 332–344.

[1309] T. Olugbade, J. Lu, Enhanced corrosion properties of nanostructured 316 stainless steel in 0.6 M NaCl solution, J. Bio. Tribo. Corros. 5 (2019) 38.

[1310] M. Ran, C. Zhang, L. Wen, H. Zhou, W. Zheng, Effect of surface mechanical attrition treatment on stainless steel corrosion, Surf. Eng. 37 (2021) 739–748.

[1311] E. Rajabi, R. Miresmaeili, M. Aliofkhazraei, The effect of surface mechanical attrition treatment (SMAT) on plastic deformation mechanisms and mechanical properties of austenitic stainless steel 316L, Mater. Res. Express 6 (2020) 1250g8.

[1312] T.O. Olugbade, E.O. Olutomilola, B.J. Olorunfemi, Review of passivity and electrochemical properties of nanostructured stainless steels obtained by surface mechanical attrition treatment (SMAT): trend and progress, Corros. Rev. 40 (2022) 189–203.

[1313] Z.X. Li, L.M. Zhang, I.I. Udoh, A.L. Ma, Y.G. Zheng, Deformation-induced martensite in 304 stainless steel during cavitation erosion: effect on passive film stability and the interaction between cavitation erosion and corrosion, Tribol. Int. 167 (2022) 107422.

[1314] L. Jinlong, L. Hongyun, L. Tongxiang, G. Wenli, The effects of grain refinement and deformation on corrosion resistance of passive film formed on the surface of 304 stainless steels, Mater. Res. Bull. 70 (2015) 896907.

[1315] V.I. Kopylov, A.V. Nokhrin, N.A. Kozlova, M.K. Chegurov, M.Y. Gryaznov, S. V. Shotin, N.V. Melekhin, N.Y. Tabachkova, K.E. Smetanina, V.N. Chuvil'deev, Effect of σ-phase on the strength, stress relaxation behavior, and corrosion resistance of an ultrafine-grained austenitic steel AISI 321, Metals 12 (2022) 45.

[1316] A.F.V. Recum, J.E. Jacobi. Handbook of Biomaterials Evaluation: Scientific, Technical and Clinical Testing of Implant Materials, 2nd Edition, Taylor & Francis,, London, UK, 1999.

[1317] B.D. Ratner, A.S. Hoffman, F.J. Schoen, J.E. Lemons, Biomaterials Science: An Introduction to Materials in Medicine, Academic Press,, New York, 2004.

[1318] D.F. Williams, On the nature of biomaterials, Biomater 30 (2009) 5897–5909.

[1319] R.D. Buddy, The biocompatibility of implant materials, in: S.F. Badylak (Ed.), Host Response to Biomaterials, Academic Press,, 2015, pp. 37–51.

[1320] D.F. Williams, General concepts of biocompatibility, in: J. Black, G.W. Hastings (Eds.), Handbook of Biomaterials Properties. Part III, Chapman and Hall,, New York, 1998, pp. 482–489.

[1321] A.E. Nel, L. Madler, D. Velegol, T. Xia, E.M. Hoek, P. Somasundaran, F. Klassig, V. Castranova, M. Thomps, Understanding biophysicochemical interactions at the nano–bio interface, Nat. Mater. 8 (2009) 543–557.

[1322] L. Mingjun, Yang Lei, Biomedical metallic materials based on nanocrystalline and nanoporous microstructures: properties and applications. Woodhead Publishing Series in Biomaterials, Nanomedicine, 2nd Edition, Woodhead Publishing,, 2023, pp. 555–584.

[1323] G.I. Im, Biomaterials in orthopaedics: the past and future with immune modulation, Biomater. Res. 24 (2020) 1–4.

[1324] Q. Chen, G.A. Thouas, Metallic implant biomaterials, Mater. Sci. Eng. R. 87 (2015) 1–57.

[1325] R. Floriano, K. Edalati, Effects of severe plastic deformation on advanced biomaterials for biomedical applications: a brief overview, Mater. Trans. 64 (2023) 1673–1682.

[1326] M. Niinomi, T. Narushima, M. Nakai, Advances in metallic biomaterials. Series in Biomaterials Science and Engineering, Springer,, Berlin/Heidelberg, Germany, 2015, p. 351.

[1327] M. Geetha, A.K. Singh, R. Asokamani, A.K. Gogia, Ti based biomaterials, the ultimate choice for orthopaedic implants - a review, Prog. Mater. Sci. 54 (2009) 397–425.

[1328] Y. Li, C. Yang, H. Zhao, S. Qu, X. Li, Y. Li, New developments of Ti-based alloys for biomedical applications, Materials 7 (2014) 1709–1800.

[1329] T.C. Lowe, R.Z. Valiev, Frontiers for Bulk Nanostructured Metals in Biomedical Applications, Scrivener Publishing LLC,, 2014.

[1330] R.Z. Valiev, I. Sabirov, E.G. Zemtsova, E.V. Parfenov, L. Dluhoš, T.C. Lowe, in: Titanium in medical and dental applications, Woodhead Publishing,, Duxford, UK, 2018, pp. 393–418.

[1331] K. Kalantari, B. Saleh, B.T.J. Webster, Biological applications of severely plastically deformed nano-grained medical devices: a review, Nanomater 11 (2021) 748.

[1332] Y. Sharkeev, A. Eroshenko, E. Legostaeva, Z. Kovalevskaya, O. Belyavskaya, M. Khimich, M. Epple, O. Prymak, V. Sokolova, Q. Zhu, Z. Sun, H. Zhang, Development of ultrafine–grained and nanostructured bioinert alloys based on titanium, zirconium and niobium and their microstructure, mechanical and biological properties, Metals 12 (2022) 1136.

[1333] D.M. Brunette, P. Tengvall, M. Textor, P. Thomsen, Titanium in medicine: material science, surface science, engineering, biological responses and medical applications. Engineering Materials, Springer,, Berlin/Heidelberg, Germany, 2001, pp. 145–162.

[1334] T.J. Webster, J.U. Ejiofor, Increased osteoblast adhesion on nanophase metals: Ti, Ti6Al4V, and CoCrMo, Biomater 25 (2004) 4731–4739.

[1335] B.C. Ward, T.J. Webster, Increased functions of osteoblasts on nanophase metals, Mater. Sci. Eng. C. 27 (2007) 575–578.

[1336] S. Ramakrishna, M. Ramalingam, T.S.S. Kumar, W.O. Soboyejo, Biomaterials: A Nano Approach, CRC Press,, Taylor & Francis, Boca Raton, 2010.

[1337] A. Balyanov, J. Kutnyakova, N.A. Amirkhanova, V.V. Stolyarov, R.Z. Valiev, X. Z. Liao, Y.H. Zhao, Y.B. Jiang, H.F. Xu, T.C. Lowe, Y.T. Zhu, Corrosion resistance of ultra fine-grained Ti, Scr. Mater. 51 (2004) 225–229.

[1338] I. Dimić, I. Cvijović-lagić, A. Hohenwarter, R. Pippan, V. Kojić, J. Bajat, M. Rakin, Electrochemical and biocompatibility examinations of high-pressure torsion processed titanium and Ti–13Nb–13Zr alloy, J. Biomed. Mater. Res. B 106 (2018) 1097–1107.

[1339] B.R. Sunil, A. Thirugnanam, U. Chakkingal, T.S.S. Kumar, Nano and ultra fine grained metallic biomaterials by severe plastic deformation techniques, Mater. Technol. 31 (2016) 743–755.

[1340] V.K. Truong, R. Stuart, R. Lapovok, Y. Estrin, J.Y. Wang, C.C. Berndt, D. G. Barnes, C.J. Fluke, R.J. Crawford, E.P. Ivanova, Effect of ultrafine-grained titanium surfaces on adhesion of bacteria, Appl. Microbiol. Biotechnol. 83 (2009) 925–937.

[1341] V.K. Truong, R. Lapovok, Y.S. Estrin, S. Rundell, J.Y. Wang, C.J. Fluke, R. J. Crawford, E.P. Ivanova, The influence of nano-scale surface roughness on bacterial adhesion to ultrafine-grained titanium, Biomater 31 (2010) 3674–3683.

[1342] A. Thirugnanam, T.S.S. Kumar, U. Chakkingal, Tailoring the bioactivity of commercially pure titanium by grain refinement using groove pressing, Mat. Sci. Eng. C. 30 (2010) 203–208.

[1343] P. Jojibabu, B.R. Sunil, T.S.S. Kumar, U. Chakkingal, V. Nandakumar, M. Doble, Wettability and in vitro bioactivity studies on titanium rods processed by equal channel angular pressing, Trans. Indian Inst. Met. 66 (2013) 299–304.

[1344] S. Faghihi, F. Azari, A. Zhilyaev, J. Szpunar, H. Vali, M. Tabrizian, Cellular and molecular interactions between MC3T3-E1 pre-osteoblasts and nanostructured titanium produced by high-pressure torsion, Biomater 28 (2007) 3887–3895.

[1345] Y. Estrin, C. Kasper, S. Diederichs, R. Lapovok, Accelerated growth of preosteoblastic cells on ultrafine-grained titanium, J. Biomed. Mater. Res. A 90 (2009) 1239–1242.

[1346] Y. Estrin, E.P. Ivanova, A. Michalska, V.K. Truong, R. Lapovok, R. Boyd, Accelerated stem cell attachment to ultrafine-grained titanium, Acta Biomater. 7 (2011) 900–906.

[1347] I.P. Semenova, L.R. Saitova, G.I. Raab, A.I. Korshunov, Y.T. Zhu, T.C. Lowe, R. Z. Valiev, Microstructural features and mechanical properties of the Ti-6Al-4V ELI alloy processed by severe plastic deformation, Mater. Sci. Forum 503- 504 (2006) 757–762.

[1348] L. Saitova, H.W. Höppel, M. Göken, I. Semenova, R.Z. Valiev, Cyclic deformation behavior and fatigue lives of ultrafine-grained Ti-6AL-4V ELI alloy for medical use, Int. J. Fatigue 31 (2009) 322–331.

[1349] V. Polyakova, I. Semenova, R.Z. Valiev, Influence of annealing on the structure and mechanical properties of ultrafine-grained alloy Ti-6Al-7Nb, processed by severe plastic deformation, Mater. Sci. Forum 667– 669 (2011) 943–948.

[1350] D.P. Oliveira, E. Prokofiev, L.F.R. Sanches, V. Polyakova, R.Z. Valiev, W.J. Botta, A.M.J. Junior, C. Bolfarini, Surface chemical treatment of ultrafine-grained Ti–6Al–7Nb alloy processed by severe plastic deformation, J. Alloy. Compd. 643 (2015) S241–S245.

[1351] M. Delshadmanesh, G. Khatibi, M.Z. Ghomsheh, M. Lederer, M. Zehetbauer, H. Danninger, Influence of microstructure on fatigue of biocompatible β-phase Ti-45Nb, Mater. Sci. Eng. A 706 (2017) 83–94.

[1352] K. Bartha, J. Stráský, A. Veverková, P. Barriobero-Vila, F. Lukáč, P. Doležal, P. Sedlák, P.V. Polyakova, I.P. Semenova, M. Janeček, Effect of the high-pressure torsion (HPT) and subsequent isothermal annealing on the phase transformation in biomedical Ti15Mo alloy, Metals 9 (2019) 1194.

[1353] K. Bartha, A. Veverková, J. Stráský, J. Veselý, P. Minárik, C.A Correa, P.V. Polyakova, I. P. Semenova, M. Janeček, Effect of the severe plastic deformation by ECAP on microstructure and phase transformations in Ti-15Mo alloy, Mater. Today Commun. 22 (2020) 100811.

[1354] H. Yilmazer, M. Niinomi, M. Nakai, J. Hieda, Y. Todaka, T. Akahori, T. Miyazaki, Heterogeneous structure and mechanical hardness of biomedical-type Ti–29Nb–13Ta–4.6Zr subjected to high-pressure torsion, J. Mech. Behav. Biomed. Mater. 10 (2012) 235–245.

[1355] Z. Lin, L. Wang, X. Xue, W. Lu, J. Qin, D. Zhang, Microstructure evolution and mechanical properties of a Ti–35Nb–3Zr–2Ta biomedical alloy processed by equal channel angular pressing (ECAP), Mater. Sci. Eng. C 33 (2013), 5551–4561.

[1356] P. Edalati, R. Floriano, Y. Tang, A. Mohammadi, K.D. Pereira, A.D. Luchessi, K. Edalati, Ultrahigh hardness and biocompatibility of high-entropy alloy TiAlFeCoNi processed by high-pressure torsion, Mater. Sci. Eng. C 112 (2020) 110908.

[1357] R. Floriano, K. Edalati, K.D. Pereira, A.D. Luchessi, Titanium-protein nanocomposites as new biomaterials produced by high-pressure torsion, Sci. Rep. 13 (2023) 470.

[1358] M. Ninomi (Ed.), Metals for Biomedical Devices, 2nd Edition, Woodhead Publishing,, 2019.

[1359] K. Tesař, M. Koller, D. Vokoun, O. Tyc, J. Čech, P. Sedlák, Texture, elastic anisotropy and thermal stability of commercially pure titanium prepared by room temperature ECAP, Mater. Des. 226 (2023) 111678.

[1360] P.M. Hashemi, E. Borhani, M.S. Nourbakhsh, Commercially pure titanium modification to enhance corrosion behavior and osteoblast response by ECAP for biomedical applications, J. Appl. Biomat. Funct. Mater. 20 (2022), https://doi.org/10.1177/22808000221095234.

[1361] B. Völker, S. Wurster, R. Pippan, A. Hohenwarter, Fracture of severely plastically deformed titanium, Mater. Lett. 309 (2022) 131–382.

[1362] A.V. Polyakov, G.I. Raab, I.P. Semenova, R.Z. Valiev, Mechanical properties of UFG titanium: Notched fatigue and impact toughness, Mater. Lett. 302 (2021) 130366.

[1363] G.I. Raab, I.S. Kodirov, D.A. Aksenov, R.Z. Valiev, The formation of a high-strength state in martensitic Ti grade 4 by ECAP, J. Alloy. Compd. 922 (2022) 166205.

[1364] R.K. Islamgaliev, V.U. Kazyhanov, L.O. Shestakova, A.V. Sharafutdinov, R. Z. Valiev, Microstructure and mechanical properties of titanium (grade 4) processed by high-pressure torsion, Mater. Sci. Eng. A 493 (2008) 190–194.

[1365] H. Arabi, M. Ketabchi, S.H.N. Alhosseini, Mechanical and microstructural variations in ECAP of Ti–6Al–4V alloy with equiaxed microstructure, Rare Met 41 (2022) 2732–2738.

[1366] S. Rzepa, Z. Trojanová, J. Džugan, R.Z. Valiev, M. Koukolíková, D. Melzer, M. Brázda, Effect of ECAP processing on microstructure and mechanical behaviour of Ti-6Al-4V manufactured by directed energy deposition, Mater. Charact. 196 (2023) 112622.

[1367] I.P. Semenova, A.V. Polyakov, M.V. Pesin, A.G. Stotskiy, Y.M. Modina, R. Z. Valiev, T.G. Langdon, Strength and fatigue life at 625 K of the ultrafine-grained Ti-6Al-4V alloy produced by equal-channel angular pressing, Metals 12 (2022) 1345.

[1368] D. Wojtas, K. Wierzbanowski, R. Chulist, W. Pachla, M. Bieda-Niemiec, A. Jarzębska, J. Maj, M. Kawałko, M. Marciszko-Wiąckowska, K. Wroński, Sztwiertnia, Microstructure-strength relationship of ultrafine-grained titanium manufactured by unconventional severe plastic deformation process, J. Alloy. Compd. 837 (2020) 155576.

[1369] P.S. Sahoo, A. Meher, M.M. Mahapatra, P.R. Vundavilli, C. Pandey, Analysis of mechanical and microstructural characteristics of plunger-assisted ECAP strengthened Ti-6Al-4V alloy sheets, Arch. Civ. Mech. Eng. 23 (2023) 194.

[1370] A. Tevlek, H.M. Aydin, E. Maleki, R. Varol, O. Unal, Effects of severe plastic deformation on pre-osteoblast cell behavior and proliferation on AISI 304 and Ti-6Al-4V metallic substrates, Surf. Coat. Technol. 366 (2019) 204–213.

[1371] S. Xu, Y. Cao, B. Duan, H. Liu, J. Wang, C. Si, Enhanced strength and sliding wear properties of gas nitrided Ti-6Al-4V alloy by ultrasonic shot peening pretreatment, Surf. Coat. Technol. 458 (2023) 129–325.

[1372] K. Sun, B. Sun, X. Yi, X. Yaqian, X. Meng, Z. Gao, W. Cai, The microstructure and martensitic transformation of Ti-13V–3Al light weight shape memory alloy deformed by high-pressure torsion, J. Alloy. Compd. 895 (2022) 162612.

[1373] V.V. Polyakova, V.N. Anumalasetty, I.P. Semenova, R.Z. Valiev, Influence of UFG structure formation on mechanical and fatigue properties in Ti-6Al-7Nb alloy, IOP Conf. Ser. Mater. Sci. Eng. 63 (2014) 012162.

[1374] M. Ashida, Effects of high-pressure torsion on mechanical properties of biocompatible Ti–6Al–7Nb alloy, Mater. Trans. 64 (2023) 1784–1790.

[1375] I. Cvijović-Alagić, Z. Cvijović, J. Maletaškić, M. Rakin, Initial microstructure effect on the mechanical properties of Ti-6Al-4V ELI alloy processed by high-pressure torsion, Mater. Sci. Eng. A 736 (2018) 175–192.

[1376] A. Korneva, B. Straumal, A. Kilmametov, S. Kopacz, M. Szczerba, Ł. Gondek, G. Cios, L. Lityńska-Dobrzyńska, R. Chulist, Phase transitions and mechanical behavior of Ti-3wt%Nb alloy after high pressure torsion and low-temperature annealing, Mater. Sci. Eng. A 857 (2022) 144096.

[1377] D.V. Gunderov, A.A. Churakova, A.V. Polyakov, A.G. Raab, S.D. Gunderova, Y. A. Lebedev, A.P.R.A. Claro, The influence of equal channel angular pressing on structure and mechanical properties of new β-Ti alloy Ti–10Mo–8Nb–6Zr, Russ. J. Non-Ferr. Met. 63 (2022) 664–670.

[1378] D. Gunderov, A. Churakova, S. Kiseleva, S. Gunderova, J. Pedro, A.P.R.A. Claro, Structure and micro-hardness of titanium alloy Ti10Mo8Nb6Zr after high-pressure torsion, AIP Conf. Proc. 2533 (2022) 020013.

[1379] D.V. Gunderov, K.A. Kim, A.A. Churakova, V.A. Sheremet`ev, M.A. Derkach, Y. A. Lebedev, A.G. Raab, The structure and mechanical properties of the Ti–18Zr–15Nb alloy subjected to equal channel angular pressing at different temperatures, Phys. Met. Metallogr. 123 (2022) 1031–1040.

[1380] D. Gunderov, K. Kim, S. Gunderova, A. Churakova, Y. Lebedev, R. Nafikov, M. Derkach, K. Lukashevich, V. Sheremetyev, S. Prokoshkin, Effect of high-pressure torsion and annealing on the structure, phase composition, and microhardness of the Ti-18Zr-15Nb (at%) alloy, Materials 16 (2023) 1754.

[1381] L. Klinge, C. Siemers, L. Kluy, P. Groche, Nanostructured Ti–13Nb–13Zr for dental implant applications produced by severe plastic deformation, J. Mater. Res 37 (2022) 2581–2588.

[1382] D. Barjaktarević, B. Medjo, P. Štefane, N. Gubeljak, I. Cvijović-Alagić, V. Djokić, M. Rakin, Tensile and corrosion properties of anodized ultrafine-grained Ti–13Nb–13Zr biomedical alloy obtained by high-pressure torsion, Met. Mater. Int. 27 (2021) 3325–3341.

[1383] H. Yilmazer, M. Niinomi, M. Nakai, K. Cho, J. Hieda, Y. Todaka, T. Miyazaki, Mechanical properties of a medical β-type titanium alloy with specific microstructural evolution, Mater. Sci. Eng. C 864 (2021) 158–828.

[1384] S.J. Liu, S. Xiang, Y.B. Tan, F. Liu, W. Shi, S. Hu, L. Luo, Exceptional strength-plasticity synergy in β-Ti alloy via HPT and short-period annealing, J. Alloy. Compd. 25 (2023) 170–173.

[1385] P. Chen, M. Ashida, H. Doi, Y. Tsutsumi, Z. Horita, T. Hanawa, Cytocompatibility of Ti–6Al–7Nb through high-pressure torsion processing, Mater. Trans. 57 (2016) 2020–2025.

[1386] S. Agarwal, J. Curtin, B. Duffy, S. Jaiswal, Biodegradable magnesium alloys for orthopaedic applications: A review on corrosion, biocompatibility and surface modifications, Mater. Sci. Eng. C 68 (2016) 948–963.

[1387] J. Walker, S. Shadanbaz, T.B.F. Woodfield, M.P. Staiger, G.J. Dias, Magnesium biomaterials for orthopedic application: a review from a biological perspective, J. Biomed. Mater. Res. B 102 (2014) 1316–1331.

[1388] Z. Horita, K. Edalati, Severe plastic deformation for nanostructure controls, Mater. Trans. 61 (2020) 2241–2247.

[1389] K. Bryła, J. Horky, Magnesium alloys processed by severe plastic deformation (SPD) for biomedical applications: an overview, Mater. Trans. 64 (2023) 1709–1723.

[1390] R.B. Figueiredo, T.G. Langdon, Grain refinement and mechanical behavior of a magnesium alloy processed by ECAP, J. Mater. Sci. 45 (2010) 4827–4836.

[1391] S.R. Agnew, J.A. Horton, T.M. Lillo, D.W. Brown, Enhanced ductility in strongly textured magnesium produced by equal channel angular processing, Scr. Mater. 50 (2004) 377–381.

[1392] T. Mukai, M. Yamanoi, H. Watanabe, K. Higashi, Ductility enhancement in AZ31 magnesium alloy by controlling its grain structure, Scr. Mater. 45 (2001) 89–94.

[1393] S. Seipp, M.F.X. Wagner, K. Hockauf, I. Schneider, L.W. Meyer, M. Hockauf, Microstructure, crystallographic texture and mechanical properties of the magnesium alloy AZ31B after different routes of thermo-mechanical processing, Int. J. Plast. 35 (2012) 155–166.

[1394] H. Wang, K. Zhou, G. Xie, X. Liang, W. Liang, Y. Zhao, Microstructure and mechanical properties of an Mg-10Al alloy fabricated by Sb-alloying and ECAP processing, Mater. Sci. Eng. A 560 (2013) 787–791.

[1395] K. Bryła, M. Krystian, J. Horky, B. Mingler, K. Mroczka, P. Kurtyka, L. Lityńska-Dobrzyńska, Improvement of strength and ductility of an EZ magnesium alloy by applying two different ECAP concepts to processable initial states, Mater. Sci. Eng. A 737 (2018) 318–327.

[1396] K. Bryła, Microstructure and mechanical characterisation of ECAP-ed ZE41A alloy, Mater. Sci. Eng. A 772 (2020) 138750.

[1397] M. Gzyl, A. Rosochowski, S. Boczkal, L. Olejnik, The role of microstructure and texture in controlling mechanical properties of AZ31B magnesium alloy processed by I-ECAP, Mater. Sci. Eng. A 638 (2015) 20–29.

[1398] K. Bryła, J. Dutkiewicz, L. Lityńska-dobrzyńska, L.L. Rokhlin, P. Kurtyka, Influence of number of ECAP passes on microstructure and mechanical properties of AZ31 magnesium alloy, Arch. Metall. Mater. 57 (2012) 711–717.

[1399] B. Chen, D.L. Lin, L. Jin, X.Q. Zeng, C. Lu, Equal-channel angular pressing of magnesium alloy AZ91 and its effects on microstructure and mechanical properties, Mater. Sci. Eng. A 483– 484 (2008) 113–116.

[1400] F. Witte, J. Fischer, J. Nellesen, H.A. Crostack, V. Kaese, A. Pisch, F. Beckmann, H. Windhagen, In vitro and in vivo corrosion measurements of magnesium alloys, Biomater 27 (2006) 1013–1018.

[1401] M. Thomann, C. Krause, D. Bormann, N. Von Der Höh, H. Windhagen, A. Meyer-Lindenberg, Comparison of the resorbable magnesium alloys LAE442 und MgCa$_{0.8}$ concerning their mechanical properties, their progress of degradation and the bone-implant-contact after 12 months implantation duration in a rabbit model, Materwiss Werksttech 40 (2009) 82–87.

[1402] W.D. Mueller, M. Lucia Nascimento, M.F. Lorenzo De Mele, Critical discussion of the results from different corrosion studies of Mg and Mg alloys for biomaterial applications, Acta Biomater. 6 (2010) 1749–1755.

[1403] B. Heublein, R. Rohde, V. Kaese, M. Niemeyer, W. Hartung, A. Haverich, Biocorrosion of magnesium alloys: a new principle in cardiovascular implant technology? Heart 89 (2003) 651–656.

[1404] S.S. Abd El-Rahman, Neuropathology of aluminum toxicity in rats (glutamate and GABA impairment), Pharmacol. Res. 47 (2003) 189–194.

[1405] P.C. Ferreira, K. De Almeida Piai, A.M. Magosso Takayanagui, Aluminum as a risk factor for alzheimer's disease, Rev. Lat. Am. Enferm. 16 (2008) 151–157.

[1406] Y. He, H. Tao, Y. Zhang, Y. Jiang, S. Zhang, C. Zhao, J. Li, B. Zhang, Y. Song, X. Zhang, Biocompatibility of bio-Mg-Zn alloy within bone with heart, liver, kidney and spleen, Chin. Sci. Bull. 54 (2009) 484–491.

[1407] S. Zhang, X. Zhang, C. Zhao, J. Li, Y. Song, C. Xie, H. Tao, Y. Zhang, Y. He, Y. Jiang, Y. Bian, Research on an Mg-Zn alloy as a degradable biomaterial, Acta Biomater. 6 (2010) 626–640.

[1408] M.R. Sahu, T.S.S. Kumar, U. Chakkingal, A review on recent advancements in biodegradable Mg-Ca alloys, J. Magnes. Alloy. 10 (2022) 2094–2117.

[1409] J. Hofstetter, E. Martinelli, S. Pogatscher, P. Schmutz, E. Povoden-Karadeniz, A. M. Weinberg, P.J. Uggowitzer, J.F. Löffler, Influence of trace impurities on the in vitro and in vivo degradation of biodegradable Mg-5Zn-0.3Ca alloys, Acta Biomater. 23 (2015) 347–353.

[1410] M. Cihova, E. Martinelli, P. Schmutz, A. Myrissa, R. Schäublin, A.M. Weinberg, P.J. Uggowitzer, J.F. Löffler, The role of zinc in the biocorrosion behavior of resorbable Mg-Zn-Ca alloys, Acta Biomater. 100 (2019) 398–414.

[1411] S.Y. Cho, S.W. Chae, K.W. Choi, H.K. Seok, Y.C. Kim, J.Y. Jung, S.J. Yang, G. J. Kwon, J.T. Kim, M. Assad, Biocompatibility and strength retention of biodegradable Mg-Ca-Zn alloy bone implants, J. Biomed. Mater. Res. B 101 (2013) 201–212.

[1412] J. Horky, K. Bryła, M. Krystian, G. Mozdzen, B. Mingler, L. Sajti, Improving mechanical properties of lean Mg-Zn-Ca alloy for absorbable implants via double equal channel angular pressing (D-ECAP), Mater. Sci. Eng. A 826 (2021) 142002.

[1413] K. Bryła, J. Dutkiewicz, L.L. Rokhlin, L. Lityńska-Dobrzyńska, K. Mroczka, P. Kurtyka, Microstructure and mechanical properties of Mg-2.5%Tb-0.78%Sm alloy after ECAP and ageing, Arch. Metall. Mater. 58 (2013) 481–487.

[1414] N.S. Martynenko, E.A. Lukyanova, V.N. Serebryany, M.V. Gorshenkov, I. V. Shchetinin, G.I. Raab, S.V. Dobatkin, Y. Estrin, Increasing strength and ductility of magnesium alloy WE43 by equal-channel angular pressing, Mater. Sci. Eng. A 712 (2018) 625–629.

[1415] L. Zhou, Y. Liu, J. Zhang, Z. Kang, Microstructure and mechanical properties of equal channel angular pressed Mg-Y-RE-Zr alloy, Mater. Sci. Technol. 32 (2016) 969–975.

[1416] E. Willbold, X. Gu, D. Albert, K. Kalla, K. Bobe, M. Brauneis, C. Janning, J. Nellesen, W. Czayka, W. Tillmann, Y. Zheng, F. Witte, Effect of the addition of low rare earth elements (lanthanum, neodymium, cerium) on the biodegradation and biocompatibility of magnesium, Acta Biomater. 11 (2015) 554–562.

[1417] F. Feyerabend, J. Fischer, J. Holtz, F. Witte, R. Willumeit, H. Drücker, C. Vogt, N. Hort, Evaluation of short-term effects of rare earth and other elements used in magnesium alloys on primary cells and cell lines, Acta Biomater. 6 (2010) 1834–1842.

[1418] Y. Nakamura, Y. Tsumura, Y. Tonogai, T. Shibata, Y. Ito, Differences in behavior among the chlorides of seven rare earth elements administered intravenously to rats, Fundam. Appl. Toxicol. 37 (1997) 106–116.

[1419] K.T. Rim, K.H. Koo, J.S. Park, Toxicological evaluations of rare earths and their health impacts to workers: a literature review, Saf. Health Work 4 (2013) 12–26.

[1420] S. Hirano, K.T. Suzuki, Exposure, Metabolism, and toxicity of rare earths and related compounds, Environ. Health Perspect. 104 (1996) 85–95.

[1421] D. Tie, F. Feyerabend, W.D. Müller, R. Schade, K. Liefeith, K. Kainer, R. Willumeit, Antibacterial biodegradable Mg-Ag alloys, Eur. Cell. Mater. 25 (2013) 284–298.

[1422] Z. Liu, F. Feyerabend, J. Bohlen, R. Willumeit-Römer, D. Letzig, Mechanical properties and degradation behavior of binary magnesium-silver alloy sheets, J. Phys. Chem. Sol. 133 (2019) 142–150.

[1423] K. Bryła, J. Horky, M. Krystian, L. Lityńska-Dobrzyńska, B. Mingler, Microstructure, mechanical properties, and degradation of Mg-Ag alloy after equal-channel angular pressing, Mater. Sci. Eng. C 109 (2020) 110543.

[1424] B. Straumal, N. Martynenko, D. Temralieva, V. Serebryany, N. Tabachkova, I. Shchetinin, N. Anisimova, M. Kiselevskiy, A. Kolyanova, G. Raab, R. Willumeit-Römer, S. Dobatkin, Y. Estrin, The effect of equal-channel angular pressing on microstructure, mechanical properties, and biodegradation behavior of magnesium alloyed with silver and gadolinium, Crystals 10 (2020) 918.

[1425] Y. Estrin, N. Martynenko, N. Anisimova, D. Temralieva, M. Kiselevskiy, V. Serebryany, G. Raab, B. Straumal, B. Wiese, R. Willumeit-Römer, S. Dobatkin, The effect of equal-channel angular pressing on the microstructure, the mechanical and corrosion properties and the anti-tumor activity of magnesium alloyed with silver, Materials 12 (2019) 3832.

[1426] J. Stráská, M. Janeček, J. Gubicza, T. Krajňák, E.Y. Yoon, H.S. Kim, Evolution of microstructure and hardness in AZ31 alloy processed by high pressure torsion, Mater. Sci. Eng. A 625 (2015) 98–106.

[1427] A.A. Khaleghi, F. Akbaripanah, M. Sabbaghian, K. Máthis, P. Minárik, J. Veselý, M. El-Tahawy, J. Gubicza, Influence of high-pressure torsion on microstructure, hardness and shear strength of AM60 magnesium alloy, Mater. Sci. Eng. A 799 (2021) 140158.

[1428] J. Xu, J. Wang, M. Shirooyeh, G. Xing, D. Shan, B. Guo, T.G. Langdon, Microhardness, microstructure and tensile behavior of an AZ31 magnesium alloy processed by high-pressure torsion, J. Mater. Sci. 50 (2015) 7424–7436.

[1429] Y. Huang, R.B. Figueiredo, T. Baudin, F. Brisset, T.G. Langdon, Evolution of strength and homogeneity in a magnesium AZ31 alloy processed by high-pressure torsion at different temperatures, Adv. Eng. Mater. 14 (2012) 1018–1026.

[1430] A. Hanna, H. Azzeddine, R. Lachhab, T. Baudin, A.L. Helbert, F. Brisset, Y. Huang, D. Bradai, T.G. Langdon, Evaluating the textural and mechanical properties of an Mg-Dy alloy processed by high-pressure torsion, J. Alloy. Compd. 778 (2019) 61–71.

[1431] K. Bryła, J. Morgiel, M. Faryna, K. Edalati, Z. Horita, Effect of high-pressure torsion on grain refinement, strength enhancement and uniform ductility of EZ magnesium alloy, Mater. Lett. 212 (2018) 323–326.

[1432] T. Masuda, Z. Horita, Grain refinement of AZ31 and AZ61 Mg alloys through room temperature processing by up-scaled high-pressure torsion, Mater. Trans. 60 (2019) 1104–1110.

[1433] L.R.C. Malheiros, R.B. Figueiredo, T.G. Langdon, Grain size and microhardness evolution during annealing of a magnesium alloy processed by high-pressure torsion, J. Mater. Res. Technol. 4 (2015) 14–17.

[1434] A.S.J. Al-Zubaydi, A.P. Zhilyaev, S.C. Wang, P. Kucita, P.A.S. Reed, Evolution of microstructure in AZ91 alloy processed by high-pressure torsion, J. Mater. Sci. 51 (2016) 3380–3389.

[1435] O.B. Kulyasova, R.K. Islamgaliev, Y. Zhao, R.Z. Valiev, Enhancement of the mechanical properties of an Mg-Zn-Ca alloy using high-pressure torsion, Adv. Eng. Mater. 17 (2015) 1738–1741.

[1436] A. Ojdanic, E. Schafler, J. Horky, D. Orlov, M. Zehetbauer, Strengthening of a biodegradable Mg-Zn-Ca alloy ZX50 after processing by HPT and heat treatment. Minerals, Metals and Materials Series, Springer International Publishing,, 2018, pp. 277–282.

[1437] J. Horky, A. Ghaffar, K. Werbach, B. Mingler, S. Pogatscher, R. Schäublin, D. Setman, P.J. Uggowitzer, J.F. Löffler, M.J. Zehetbauer, Exceptional strengthening of biodegradable Mg-Zn-Ca alloys through high pressure torsion and subsequent heat treatment, Materials 12 (2019) 2460.

[1438] S.V. Dobatkin, L.L. Rokhlin, E.A. Lukyanova, M.Y. Murashkin, T.V. Dobatkina, N.Y. Tabachkova, Structure and mechanical properties of the Mg-Y-Gd-Zr alloy after high pressure torsion, Mater. Sci. Eng. A 667 (2016) 217–223.

[1439] X. Liu, R. Xu, Achieving ultra-high hardness of Mg-Sm-Ca alloy with the unique nanostructure, Mater. Sci. Eng. A 825 (2021) 141929.

[1440] E.A. Lukyanova, N.S. Martynenko, V.N. Serebryany, A.N. Belyakov, L.L. Rokhlin, S.V. Dobatkin, Y.Z. Estrin, Structure and mechanical and corrosion properties of a magnesium Mg-Y-Nd-Zr alloy after high pressure torsion, Russ. Metall. 2017 (2017) 912–921.

[1441] A. Atrens, M. Liu, N.I.Zainal Abidin, Corrosion mechanism applicable to biodegradable magnesium implants, Mater. Sci. Eng. B 176 (2011) 1609–1636.

[1442] H. Waizy, J. Diekmann, A. Weizbauer, J. Reifenrath, I. Bartsch, V. Neubert, R. Schavan, H. Windhagen, In vivo study of a biodegradable orthopedic screw (MgYREZr-alloy) in a rabbit model for up to 12 months, J. Biomater. Appl. 28 (2014) 667–675.

[1443] G.L. Song, Corrosion of magnesium (Mg) alloys: concluding remarks, in: G. Song (Ed.), Corrosion of Magnesium Alloys, Woodhead Publishing,, 2011, pp. 615–617.

[1444] N. Martynenko, E. Lukyanova, V. Serebryany, D. Prosvirnin, V. Terentiev, G. Raab, S. Dobatkin, Y. Estrin, Effect of equal channel angular pressing on structure, texture, mechanical and in-service properties of a biodegradable magnesium alloy, Mater. Lett. 238 (2019) 218–221.

[1445] J. Vrátná, B. Hadzima, M. Bukovina, M. Janeček, Room temperature corrosion properties of AZ31 magnesium alloy processed by extrusion and equal channel angular pressing, J. Mater. Sci. 48 (2013) 4510–4516.

[1446] J. Zhang, Z. Kang, F. Wang, Mechanical properties and biocorrosion resistance of the Mg-Gd-Nd-Zn-Zr alloy processed by equal channel angular pressing, Mater. Sci. Eng. C 68 (2016) 194–197.

[1447] D. Song, A. Bin Ma, J. Jiang, P. Lin, D. Yang, J. Fan, Corrosion behavior of equal-channel-angular-pressed pure magnesium in NaCl aqueous solution, Corros. Sci. 52 (2010) 481–490.

[1448] M. Němec, A. Jäger, K. Tesař, V. Gärtnerová, Influence of alloying element Zn on the microstructural, mechanical and corrosion properties of binary Mg-Zn alloys after severe plastic deformation, Mater. Charact. 134 (2017) 69–75.

[1449] Z. Li, S. Jie Zhou, N. Huang, Effects of ECAE processing temperature on the microstructure, mechanical properties, and corrosion behavior of pure Mg, Int. J. Miner. Metall. Mater. 22 (2015) 639–647.

[1450] P. Minárik, R. Král, M. Janeček, Effect of ECAP processing on corrosion resistance of AE21 and AE42 magnesium alloys, Appl. Surf. Sci. 281 (2013) 44–48.

[1451] A. Witecka, A. Bogucka, A. Yamamoto, K. Máthis, T. Krajňák, J. Jaroszewicz, W. Święszkowski, In vitro degradation of ZM21 magnesium alloy in simulated body fluids, Mater. Sci. Eng. C. 65 (2016) 59–69.

[1452] C.Z. Zhang, S.J. Zhu, L.G. Wang, R.M. Guo, G.C. Yue, S.K. Guan, Microstructures and degradation mechanism in simulated body fluid of biomedical Mg-Zn-Ca alloy processed by high pressure torsion, Mater. Des. 96 (2016) 54–62.

[1453] B. Ratna Sunil, T.S. Sampath Kumar, U. Chakkingal, V. Nandakumar, M. Doble, V. Devi Prasad, M. Raghunath, In vitro and in vivo studies of biodegradable fine grained AZ31 magnesium alloy produced by equal channel angular pressing, Mater. Sci. Eng. C. 59 (2016) 356–367.

[1454] W. Li, X. Liu, Y. Zheng, W. Wang, W. Qiao, K.W.K. Yeung, K.M.C. Cheung, S. Guan, O.B. Kulyasova, R.Z. Valiev, In vitro and in vivo studies on ultrafine-grained biodegradable pure Mg, Mg-Ca alloy and Mg-Sr alloy processed by high-pressure torsion, Biomater. Sci. 8 (2020) 5071–5087.

[1455] W. Li, Y. Shen, J. Shen, D. Shen, X. Liu, Y. Zheng, K.W.K. Yeung, S. Guan, O. B. Kulyasova, R.Z. Valiev, In vitro and in vivo studies on pure Mg, Mg-1Ca and Mg-2Sr alloys processed by equal channel angular pressing, Nano Mater. Sci. 2 (2020) 96–108.

[1456] Y. Ikoma, Structural and functional properties of Si and related semiconducting materials processed by high-pressure torsion, Mater. Trans. 64 (2023) 1346–1352.

[1457] K. Edalati, H. Iwaoka, S. Toh, K. Sasaki, Z. Horita, Application of high-pressure torsion to WC-Co ceramic-based composites for improvement of consolidation, microstructure and hardness, Mater. Trans. 54 (2013) 1540–1548.

[1458] M. Mabuchi, H. Iwasaki, K. Yanase, K. Higashi, Low temperature superplasticity in an AZ91 magnesium alloy processed by ECAE, Scr. Mater. 36 (1997) 681–686.

[1459] A. Yamashita, Z. Horita, T.G. Langdon, Improving the mechanical properties of magnesium and a magnesium alloy through severe plastic deformation, Mater. Sci. Eng. A 300 (2001) 142–147.

[1460] J.A. del Valle, M.T. Pérez-Prado, O.A. Ruano, Accumulative roll bonding of a Mg-based AZ61 alloy, Mater. Sci. Eng. A 410–411 (2005) 353–357.

[1461] K. Matsubara, Y. Miyahara, Z. Horita, T.G. Langdon, Developing superplasticity in a magnesium alloy through a combination of extrusion and ECAP, Acta Mater. 51 (2003) 3073–3084.

[1462] C. Xu, K. Xia, T.G. Langdon, Processing of a magnesium alloy by equal-channel angular pressing using a back-pressure, Mater. Sci. Eng. A 527 (2009) 205–211.

[1463] N. Ono, R. Nowak, S. Miura, Effect of deformation temperature on Hall–Petch relationship registered for polycrystalline magnesium, Mater. Lett. 58 (2004) 39–43.

[1464] M.R. Barnett, Z. Keshavarz, A.G. Beer, D. Atwell, Influence of grain size on the compressive deformation of wrought Mg–3Al–1Zn, Acta Mater. 52 (2004) 5093–5103.

[1465] R. Zheng, J.P. Du, S. Gao, H. Somekawa, S. Ogata, N. Tsuji, Transition of dominant deformation mode in bulk polycrystalline pure Mg by ultra-grain refinement down to sub-micrometer, Acta Mater. 198 (2020) 35–46.

[1466] H. Somekawa, T. Mukai, Hall–Petch breakdown in fine-grained pure magnesium at low strain rates, Metall. Mater. Trans. A 46 (2015) 894–902.

[1467] A.P. Carvalho, R.B. Figueiredo, The contribution of grain boundary sliding to the deformation in an ultrafine-grained Mg–Al–Zn alloy, J. Mater. Sci. 58 (2023) 8130–8142.

[1468] A.P. Carvalho, R.B. Figueiredo, The effect of ultragrain refinement on the strength and strain rate sensitivity of a ZK60 magnesium alloy, Adv. Eng. Mater. 24 (2022) 2100846.

[1469] M.M. Castro, P.H.R. Pereira, A. Isaac, T.G. Langdon, R.B. Figueiredo, Inverse Hall–Petch behaviour in an AZ91 alloy and in an AZ91–Al₂O₃ composite consolidated by high-pressure torsion, Adv. Eng. Mater. 22 (2020) 1900894.

[1470] A.P. Carvalho, R.B. Figueiredo, An overview of the effect of grain size on mechanical properties of magnesium and its alloys, Mater. Trans. 64 (2023) 1272–1283.

[1471] R.B. Figueiredo, T.G. Langdon, Deformation mechanisms in ultrafine-grained metals with an emphasis on the Hall-Petch relationship and strain rate sensitivity, J. Mater. Res. Technol. 14 (2021) 137–159.

[1472] R.B. Figueiredo, M. Kawasaki, T.G. Langdon, Seventy years of Hall-Petch, ninety years of superplasticity and a generalized approach to the effect of grain size on flow stress, Prog. Mater. Sci. 137 (2023) 101131.

[1473] R.B. Figueiredo, T.G. Langdon, Effect of grain size on strength and strain rate sensitivity in metals, J. Mater. Sci. 57 (2022) 5210–5229.

[1474] R.B. Figueiredo, T.G. Langdon, Developing superplasticity in a magnesium AZ31 alloy by ECAP, J. Mater. Sci. 43 (2008) 7366–7371.

[1475] R.B. Figueiredo, T.G. Langdon, Record superplastic ductility in a magnesium alloy processed by equal-channel angular pressing, Adv. Eng. Mater. 10 (2008) 37–40.

[1476] Z. Horita, K. Matsubara, K. Makii, T.G. Langdon, A two-step processing route for achieving a superplastic forming capability in dilute magnesium alloys, Scr. Mater. 47 (2002) 255–260.

[1477] R.B. Figueiredo, T.G. Langdon, Achieving superplastic properties in a ZK10 magnesium alloy processed by equal-channel angular pressing, J. Mater. Res. Technol. 6 (2017) 129–135.

[1478] M.P. Medeiros, D.R. Lopes, M. Kawasaki, T.G. Langdon, R.B. Figueiredo, An overview on the effect of severe plastic deformation on the performance of magnesium for biomedical applications, Materials 16 (2023) 2401.

[1479] T. Masuda, Y. Tang, I.F. Mohamed, Z. Horita, Ultrafine-grained AZ61 alloy produced by high-pressure torsion: advent of superplasticity and effect of anisotropy, Mater. Sci. Eng. A 879 (2023) 145240.

[1480] R.B. Figueiredo, T.G. Langdon, Using high-pressure torsion to achieve superplasticity in an AZ91 magnesium alloy, Metals 10 (2020) 681.

[1481] M. Kawasaki, T.G. Langdon, Review: achieving superplastic properties in ultrafine-grained materials at high temperatures, J. Mater. Sci. 51 (2016) 19–32.

[1482] R.B. Figueiredo, S. Sabbaghianrad, A. Giwa, J.R. Greer, T.G. Langdon, Evidence for exceptional low temperature ductility in polycrystalline magnesium processed by severe plastic deformation, Acta Mater. 122 (2017) 322–331.

[1483] C.L.P. Silva, M.A. Camara, A. Hohenwarter, R.B. Figueiredo, Mechanical behavior and in vitro corrosion of cubic scaffolds of pure magnesium processed by severe plastic deformation, Metals 11 (2021) 1791.

[1484] J.H. Gao, S.K. Guan, Z.W. Ren, Y.F. Sun, S.J. Zhu, B. Wang, Homogeneous corrosion of high pressure torsion treated Mg-Zn-Ca alloy in simulated body fluid, Mater. Lett. 65 (2011) 691–693.

[1485] C. op't Hoog, N. Birbilis, Y. Estrin, Corrosion of pure Mg as a function of grain size and processing route, Adv. Eng. Mater. 10 (2008) 579–582.

[1486] D. Orlov, K.D. Ralston, N. Birbilis, Y. Estrin, Enhanced corrosion resistance of Mg alloy ZK60 after processing by integrated extrusion and equal channel angular pressing, Acta Mater. 59 (2011) 6176–6186.

[1487] E.V. Parfenov, O.B. Kulyasova, V.R. Mukaeva, B. Mingo, R.G. Farrakhov, Y. V. Cherneikina, A. Yerokhin, Y.F. Zheng, R.Z. Valiev, Influence of ultra-fine grain structure on corrosion behaviour of biodegradable Mg-1Ca alloy, Corros. Sci. 163 (2020) 108303.

[1488] C.L.P. Silva, A.C. Oliveira, C.G.F. Costa, R.B. Figueiredo, M. de Fátima Leite, M. M. Pereira, V.F.C. Lins, T.G. Langdon, Effect of severe plastic deformation on the biocompatibility and corrosion rate of pure magnesium, J. Mater. Sci. 52 (2017) 5992–6003.

[1489] N.Q. Chinh, D. Olasz, A.Q. Ahmed, E.V. Bobruk, R.Z. Valiev, Review on grain size- and grain boundary phenomenon in unusual mechanical behavior of ultrafine-grained Al alloys, Mater. Trans. 64 (2023) 1844–1855.

[1490] E.O. Hall, Variation of hardness of metals with grain size, Nature 173 (1954) 948–949.

[1491] R.Z. Valiev, Y. Estrin, Z. Horita, T.G. Langdon, M.J. Zehetbauer, Y.T. Zhu, Fundmentals of superior properties in bulk nanoSPD materials, Mater. Res. Lett. 4 (2016) 1–21.

[1492] Y. Iwahashi, Z. Horita, M. Nemoto, T.G. Langdon, The process of grain refinement in equal-channel angular pressing, Acta Mater. 46 (1998) 3317–3331.

[1493] N. Tsuji, S. Okuna, T. Matsuura, Y. Koizumi, Y. Minamino, Mechanical properties as a function of grain size in ultrafine grained aluminum and iron fabricated by ARB and annealing process, Mater. Sci. Forum 426–432 (2003) 2667–2672.

[1494] R.W. Hayes, D. Witkin, F. Zhou, E.J. Lavernia, Deformation and activation volumes of cryomilled ultrafine-grained aluminum, Acta Mater. 52 (2004) 4259–4271.

[1495] X. Chen, G. Huang, S. Liu, T. Han, B. Jiang, A. Tang, Y. Zhu, F. Pan, Grain refinement and mechanical properties of pure aluminum processed by accumulative extrusion bonding, Trans. Nonferrous Met. Soc. China 29 (2019) 437–447.

[1496] R.Z. Valiev, N.A. Enikeev, T.G. Langdon, Towards superstrength of nanostructured metals and alloys produced by SPD, Kov. Mater. 49 (2011) 1–9.

[1497] N.Q. Chinh, D. Olasz, A.Q. Ahmed, G. Sáfrán, J. Lendvai, T.G. Langdon, Modification of the Hall-Petch relationship for submicron-grained fcc metals, Mater. Sci. Eng. A 862 (2023) 144419.

[1498] N.Q. Chinh, P. Szommer, T. Csanádi, T.G. Langdon, Flow processes at low temperatures in ultrafine-grained aluminum, Mater. Sci. Eng. A 434 (2006) 326–334.

[1499] B.B. Straumal, X. Sauvage, B. Baretzky, A.A. Mazilkin, R.Z. Valiev, Grain boundary films in Al-Zn alloys after high pressure torsion, Scr. Mater. 70 (2014) 59–62.

[1500] N.Q. Chinh, R.Z. Valiev, X. Sauvage, G. Varga, K. Havancsák, M. Kawasaki, B. B. Straumal, T.G. Langdon, Grain boundary phenomena in an ultrafine-grained Al-Zn alloy with improved mechanical behavior for micro-devices, Adv. Eng. Mater. 16 (2014) 1000–1009.

[1501] J.W. Edington, K.N. Melton, C.P. Cutler, Superplasticity, Prog. Mater. Sci. 21 (1976) 61–170.

[1502] T.G. Nieh, J. Wadsworth, O.D. Sherby, Superplasticity in Metals and Ceramics, Cambridge University Press,, Cambridge, 1997.

[1503] N.Q. Chinh, P. Szommer, J. Gubicza, M. El-Tahawy, E.V. Bobruk, M. Y. Murashkin, R.Z. Valiev, Characterizing microstructural and mechanical properties of Al-Zn alloys processed by high-pressure torsion, Adv. Eng. Mater. 22 (2020) 1900672.

[1504] N.Q. Chinh, P. Szommer, Z. Horita, T.G. Langdon, Experimental evidence for grain-boundary sliding in ultrafine-grained aluminum processed by severe plastic deformation, Adv. Mater. 18 (2006) 34–39.

[1505] X. Sauvage, M.Y. Murashkin, B.B. Straumal, E.V. Bobruk, R.Z. Valiev, Ultrafine-grained structures resulting from SPD-induced phase transformation in Al-Zn alloys, Adv. Eng. Mater. 17 (2015) 1821–1827.

[1506] A. Alhamidi, K. Edalati, Z. Horita, S. Hirosawa, K. Matsuda, D. Terada, Softening by severe plastic deformation and hardening by annealing of aluminum-zinc alloy: significance of elemental and spinodal decompositions, Mater. Sci. Eng. A 610 (2014) 17–27.

[1507] A.Q. Ahmed, J. Ugi, J. Lendvai, M.Y. Murashkin, E.V. Bobruk, R.Z. Valiev, N. Q. Chinh, Effect of Zn content on microstructure evolution in Al–Zn alloys processed by high-pressure torsion, J. Mater. Res 38 (2023) 3602–3612.

[1508] Z. Song, R. Niu, X. Cui, E.V. Bobruk, M.Y. Murashkin, N.A. Enikeev, J. Gu, M. Song, V. Bhatia, S.P. Ringer, R.Z. Valiev, X. Liao, Mechanism of room-temperature superplasticity in ultrafine-grained Al–Zn alloys, Acta Mater. 246 (2023) 118671.

[1509] N.Q. Chinh, T. Csanádi, T. Győri, R.Z. Valiev, B.B. Straumal, M. Kawasaki, T. G. Langdon, Strain rate sensitivity studies in an ultrafine-grained Al-30wt%Zn alloy using micro-and nanoindentation, Mater. Sci. Eng. A 543 (2012) 117–120.

[1510] E.V. Bobruk, X. Sauvage, N.A. Enikeev, R.Z. Valiev, Influence of fine scale features on room temperature superplastic behavior of an ultrafine-grained Al-30Zn alloy, Mater. Lett. 254 (2019) 329–331.

[1511] Y.I. Duan, G.F. Xu, X.Y. Peng, Y. Deng, Z. Li, Z.M. Yin, Effect of Sc and Zr additions on grain stability and superplasticity of the simple thermal-mechanical processed AlZnMg alloy sheet, Mater. Sci. Eng. A 648 (2015) 80–91.

[1512] M. Abo-Elkhier, M.S. Soliman, Superplastic characteristics of fine-grained 7475 auminum alloy, J. Mater. Eng. Perform. 15 (2006) 76–80.

[1513] Z. Guan, M. Ren, P. Zhao, P. Ma, Q. Wang, Constitutive equations with varying parameters for superplastic flow behavior of Al-Zn-Mg-Zr alloy, Mater. Des. 54 (2014) 906–913.

[1514] F. Kiessling, P. Nefzger, J.F. Nolasco, U. Kaintzyk, Overhead Power Lines: Planning, Design, Construction, Springer,, Berlin, 2003.

[1515] C. Rochet, E. Andrieu, B. Arfaei, J.P. Harouard, A. Laurino, T.C. Lowe, G. Odemer, C. Blanc, Influence of equal-channel angular pressing on the corrosion fatigue behaviour of an Al-Mg-Si aluminium alloy for automotive conductors, Int. J. Fatigue 140 (2020) 105812.

[1516] A.F. Mayadas, M. Shatzkes, J.F. Janak, Electrical resistivity model for polycrystalline films: the case of specular reflection at external surfaces, Appl. Phys. Lett. 14 (1969) 345–347.

[1517] E.V. Bobruk, M.Y. Murashkin, V.U. Kazykhanov, R.Z. Valiev, Aging behavior and properties of ultrafine grained aluminum alloys of Al-Mg-Si system, Rev. Adv. Mater. Sci. 31 (2012) 109–115.

[1518] N. Zhao, C. Ban, H. Wang, J. Cui, Optimized combination of strength and eectrical conductivity of Al-Mg-Si alloy processed by ECAP with two-step temperature, Materials 13 (2020) 1511.

[1519] X. Sauvage, E.V. Bobruk, M.Y. Murashkin, Y. Nasedkina, N.A. Enikeev, R. Z. Valiev, Optimization of electrical conductivity and strength combination by structure design at the nanoscale in Al-Mg-Si alloys, Acta Mater. 98 (2015) 355–366.

[1520] M. Murashkin, I. Sabirov, V. Kazykhanov, E. Bobruk, A. Dubravina, R.Z. Valiev, Enhanced mechanical properties and electrical conductivity in ultra-fine grained Al alloy processed via ECAP-PC, J. Mater. Sci. 48 (2013) 4501–4509.

[1521] M.Y. Murashkin, A.E. Medvedev, V.U. Kazykhanov, G.I. Raab, I.A. Ovid`ko, R. Z. Valiev, Microstructure, strength, electrical conductivity, and heat resistance of an Al-Mg-Zr alloy after ECAP-conform and cold drawing, Rev. Adv. Mater. Sci. 47 (2016) 16–25.

[1522] A.V. Nokhrin, G.S. Nagicheva, V.N. Chuvil`deev, V.I. Kopylov, A.A. Bobrov, N. Y. Tabachkova, Effect of Er, Si, Hf and Nb additives on the thermal stability of microstructure, electrical resistivity and microhardness of fine-grained aluminum alloys of Al-0.25%Zr, Materials 16 (2023) 2114.

[1523] A.E. Medvedev, M.Y. Murashkin, N.A. Enikeev, I. Bikmukhametov, R.Z. Valiev, P.D. Hodgson, R. Lapovok, Effect of the eutectic Al-(Ce,La) phase morphology on microstructure, mechanical properties, electrical conductivity and heat resistance of Al-4.5 (Ce, La) alloy after SPD and subsequent annealing, J. Alloy. Compd. 796 (2019) 321–330.

[1524] A.E. Medvedev, M.Y. Murashkin, N.A. Enikeev, R.Z. Valiev, P.D. Hodgson, R. Lapovok, Optimization of strength-electrical conductivity properties in Al-2Fe alloy by severe plastic deformation and heat treatment, Adv. Eng. Mater. 20 (2017) 1700867.

[1525] G.L. Shuai, Z. Li, D.T. Zhang, Y.X. Tong, L. Li, The mechanical property and electrical conductivity evolution of Al-Fe alloy between room temperature and elevated temperature ECAP, Vacuum 183 (2021) 109813.

[1526] A. Medvedev, O. Zhukova, N. Enikeev, V. Kazykhanov, V. Timofeev, M. Murashkin, The effect of casting technique and severe straining on the microstructure, electrical conductivity, mechanical properties and thermal stability of the Al–1.7 wt% Fe alloy, Materials 16 (2023) 3067.

[1527] L. Tian, A. Russell, T. Riedemann, S. Mueller, I. Anderson, A deformation-processed Al-matrix/Ca-nanofilamentary composite with low density, high strength, and high conductivity, Mater. Sci. Eng. A 690 (2017) 348–354.

[1528] S.V. Bobylev, N.A. Enikeev, A.G. Sheinerman, R.Z. Valiev, Strength enhancement induced by grain boundary solute segregations in ultrafine-grained alloys, Int. J. Plast. 123 (2019) 133–144.

[1529] N.O. Korotkova, N.A. Belov, V.N. Timofeev, M.M. Motkov, S.O. Cherkasov, Influence of heat treatment on the structure and properties of an Al–7% REM conductive aluminum alloy casted in an electromagnetic crystallizer, Phys. Met. Metallogr. 121 (2020) 173–179.

[1530] Y. Qi, R. Lapovok, Y. Estrin, Microstructure and electrical conductivity of aluminium/steel bimetallic rods processed by severe plastic deformation, J. Mater. Sci. 51 (2016) 6860–6875.

[1531] R. Lapovok, M. Dubrovsky, A. Kosinova, G. Raab, Effect of severe plastic deformation on the conductivity and strength of copper-clad aluminium conductors, Metals 9 (2019) 960.

[1532] R. Lapovok, V.V. Popov, Y. Qi, A. Kosinova, A. Berner, C. Xu, E. Rabkin, R. Kulagin, J. Ivanisenko, B. Baretzky, O.V. Prokof`eva, A.N. Sapronov, D. V. Prilepo, Y. Beygelzimer, Architectured hybrid conductors: aluminium with embedded copper helix, Mater. Des. 187 (2019) 108398.

[1533] C. Yang, N. Masquellier, C. Gandiolle, X. Sauvage, Multifunctional properties of composition graded Al wires, Scr. Mater. 189 (2020) 21–24.

[1534] M.Y. Murashkin, D.I. Sadykov, A.M. Mavlyutov, D.K. Magomedova, V. U. Kazykhanov, Strength, thermal resistance and electrical conductivity of aluminum-based composite wire, J. Phys: Conf. Ser. 2231 (2022) 012005.

[1535] M. Kawasaki, V. Sklenička, T.G. Langdon, An evaluation of creep behavior in ultrafine-grained aluminum alloys processed by ECAP, J. Mater. Sci. 45 (2010) 271–274.

[1536] C. Rochet, M. Veron, E.F. Rauch, T.C. Lowe, B. Arfaei, A. Laurino, J.P. Harouard, C. Blanc, Influence of equal-channel angular pressing on the microstructure and corrosion behaviour of a 6xxx aluminium alloy for automotive conductors, Corros. Sci. 166 (2020) 108453.

[1537] B.A. Baker, An old problem: aging and skeletal-muscle-strain injury, J. Sport Rehabil. 26 (2017) 180–188.

[1538] M.P. Soares dos Santos, R.M.C. Bernardo, Bioelectronic multifunctional bone implants: recent trends, Bioelectron. Med. 8 (2022) 15.

[1539] P.G. Laing, A.B. Ferguson, E.S. Hodge, Tissue reaction in rabbit muscle exposed to metallic implants, J. Biomed. Mater. Res 1 (1967) 135–149.

[1540] M. Niinomi, Recent metallic materials for biomedical applications, Metall. Mater. Trans. A 33 (2002) 477–486.

[1541] T. Albrektsson, A. Wennerberg, Oral implant surfaces: part 1 - review focusing on topographic and chemical properties of different surfaces and in vivo responses to them, Int. J. Prosthodont. 17 (2004) 536–543.

[1542] R. Junker, A. Dimakis, M. Thoneick, J.A. Jansen, Effects of implant surface coatings and composition on bone integration: a systematic review, Clin. Oral. Implants Res 20 (2009) 185–206.

[1543] C.M. Agrawal, Reconstructing the human body using biomaterials, JOM 50 (1998) 31–35.

[1544] I. Sabirov, N.A. Enikeev, M.Y. Murashkin, R.Z. Valiev, Bulk Nanostructured Materials with Multifunctional Properties, Springer International Publishing,, Cham, 2015.

[1545] J.M. Hernández-López, A. Conde, J. de Damborenea, M.A. Arenas, Correlation of the nanostructure of the anodic layers fabricated on Ti13Nb13Zr with the electrochemical impedance response, Corros. Sci. 94 (2015) 61–69.

[1546] R. Hazan, R. Brener, U. Oron, Bone growth to metal implants is regulated by their surface chemical properties, Biomater 14 (1993) 570–574.

[1547] R. Bosco, E.R.U. Edreira, J.G.C. Wolke, S.C.G. Leeuwenburgh, J.J.J.P. van den Beucken, J.A. Jansen, Instructive coatings for biological guidance of bone implants, Surf. Coat. Technol. 233 (2013) 91–98.

[1548] R. Bosco, J. Van Den Beucken, S. Leeuwenburgh, J. Jansen, Surface engineering for bone implants: a trend from passive to active surfaces, Coatings 2 (2012) 95–119.

[1549] D. Pedreira de Oliveira, T.V. Toniato, R. Ricci, F.R. Marciano, E. Prokofiev, R. Z. Valiev, A.O. Lobo, A.M. Jorge, Junior, Biological response of chemically treated surface of the ultrafine-grained Ti–6Al–7Nb alloy for biomedical applications, Int. J. Nanomed. 14 (2019) 1725–1736.

[1550] D.A.G. Pérez, A.M. Jorge Junior, G.H. Asato, J.C. Lepretre, V. Roche, C. Bolfarini, W.J. Botta, Surface anodization of the biphasic Ti13Nb13Zr biocompatible alloy: Influence of phases on the formation of TiO₂ nanostructures, J. Alloy. Compd. 796 (2019) 93–102.

[1551] J.E. Berger, A.M. Jorge Jr., G.H. Asato, V. Roche, Formation of self-ordered oxide nanotubes layer on the equiatomic TiNbZrHfTa high entropy alloy and bioactivation procedure, J. Alloy. Compd. 865 (2021) 158837.

[1552] V.P. Ricci, C.R.M. Afonso, R.F.M. dos Santos, A.M. Jorge, Junior, V. Roche, Anodic growth and pre-calcification on β-Ti-40Nb alloy: effects on elastic modulus, electrochemical properties, and bioactivity, Ceram. Int. 48 (2022) 27575–27589.

[1553] F. Hilario, V. Roche, R.P. Nogueira, A.M. Jorge, Junior, Influence of morphology and crystalline structure of TiO₂ nanotubes on their electrochemical properties and apatite-forming ability, Electrochim. Acta 245 (2017) 337–349.

[1554] R.P. Nogueira, J. Deuzimar Uchoa, F. Hilario, G. de, F. Santana-Melo, L.M.R. de Vasconcellos, F.R. Marciano, V. Roche, A.M. Jorge, A.O. Lobo, Characterization of optimized TiO₂ nanotubes morphology for medical implants: biological activity and corrosion resistance, Int. J. Nanomed. 16 (2021) 667–682.

[1555] C.A. Escobar Claros, L. Contri Campanelli, A.M. Jorge, Junior, J-C. Leprêtre, C. Bolfarini, V. Roche, Corrosion behaviour of biomedical β-titanium alloys with the surface-modified by chemical etching and electrochemical methods, Corros. Sci. 188 (2021) 109544.

[1556] G.V.B. da Rocha, J.H. Lopes, V. Roche, A.M. Jorge, R. Riva, A.C. de Oliveira, D. N. Travessa, An innovative strategy for bioactivation of β-Ti12Mo6Zr2Fe alloy surface by dip-coating method with potential application in the biomedical field, Appl. Surf. Sci. 603 (2022) 154460.

[1557] C. Leinenbach, D. Eifler, Fatigue and cyclic deformation behaviour of surface-modified titanium alloys in simulated physiological media, Biomater 27 (2006) 1200–1208.

[1558] A.J. Engler, S. Sen, H.L. Sweeney, D.E. Discher, Matrix elasticity directs stem cell lineage specification, Cell 126 (2006) 677–689.

[1559] G.C. Reilly, A.J. Engler, Intrinsic extracellular matrix properties regulate stem cell differentiation, J. Biomech. 43 (2010) 55–62.
[1560] W.R. Wagner, S.E. Sakiyama-Elbert, G. Zhang, M.J. Yaszemski (Eds.), Biomaterials Science: An Introduction to Materials in Medicine, 4th Edition, Academic Press,, 2020.
[1561] S.W.H.E. Wintermantel, Medizintechnik: Life Science Engineering, Springer Science & Business Media, Springer Berlin Heidelberg,, Berlin, Heidelberg, 2009.
[1562] T.S. Pinheiro, J. Gallego, C. Bolfarini, C.S. Kiminami, A.M. Jorge Jr., W.J. Botta Filho, Microstructural evolution of Ti-6Al-7Nb alloy during high pressure torsion, Mater. Res. 15 (2012) 792–795.
[1563] A.M. Jorge Junior, V. Roche, D.A.G. Pérez, R.Z. Valiev, Nanostructuring Ti-alloys by HPT: phase transformation, mechanical and corrosion properties, and bioactivation, Mater. Trans. 64 (2023) 1306–1316.
[1564] M. Niinomi, Fatigue characteristics of metallic biomaterials, Int. J. Fatigue 29 (2007) 992–1000.
[1565] V.V. Stolyarov, L.O. Shestakova, Y.T. Zhu, R.Z. Valiev, Formation of metastable states in nanostructured Al- and Ti-based alloys by the SPTS technique, Nanostruct. Mater. 12 (1999) 923–926.
[1566] D.A.G. Pérez, A.M. Jorge Junior, C.S. Kiminami, C. Bolfarini, W.J. Botta, Ultrafine-grained Ti-13Nb-13Zr alloy produced by severe plastic deformation, Mater. Res. 20 (2017) 404–410.
[1567] J. Gallego, T.S. Pinheiro, R.Z. Valiev, V. Polyakova, C. Bolfarini, C.S. Kiminami, A.M. Jorge Jr, W.J. Botta, Microstructural characterization of Ti-6Al-7Nb alloy after severe plastic deformation, Mater. Res. 15 (2012) 786–791.
[1568] H.S. Ryu, C. Namgung, J.H. Lee, Y.J. Lim, The influence of thread geometry on implant osseointegration under immediate loading: a literature review, J. Adv. Prosthodont 6 (2014) 547.
[1569] Y.B. Wang, Y.H. Zhao, Q. Lian, X.Z. Liao, R.Z. Valiev, S.P. Ringer, Y.T. Zhu, E.J. Lavernia, Grain size and reversible beta-to-omega phase transformation in a Ti alloy, Scr. Mater. 63 (2010) 613–616.
[1570] K. Edalati, E. Matsubara, Z. Horita, Processing pure Ti by high-pressure torsion in wide ranges of pressures and strain, Metall. Mater. Trans. A 40 (2009) 2079–2086.
[1571] R.B. Figueiredo, F.L. Sicupira, L.R.C. Malheiros, M. Kawasaki, D.B. Santos, T.G. Langdon, Formation of epsilon martensite by high-pressure torsion in a TRIP steel, Mater. Sci. Eng. A 625 (2015) 114–118.
[1572] H.J. Rack, J.I. Qazi, Titanium alloys for biomedical applications, Mater. Sci. Eng. C. 26 (2006) 1269–1277.
[1573] Q. Guo, Y. Zhan, H. Mo, G. Zhang, Aging response of the Ti–Nb system biomaterials with β-stabilizing elements, Mater. Des. 31 (2010) 4842–4846.
[1574] A.A. Matchin, E.V. Nosov, A.A. Stadnikov, G.V. Klevtsov, L.R. Rezyapova, N.A. Sayapina, E.V. Blinova, R.Z. Valiev, In vivo studies of medical implants for maxillofacial surgery produced from nanostructured titanium, ACS Biomater. Sci. Eng. 9 (2023) 6138–6145.
[1575] G. Baumann, H.J. Fecht, S. Liebelt, Formation of white-etching layers on rail treads, Wear 191 (1996) 133–140.
[1576] E. Magel, P. Mutton, A. Ekberg, A. Kapoor, Rolling contact fatigue, wear and broken rail derailments, Wear 366–367 (2016) 249–257.
[1577] U. Zerbst, R. Lundén, K.O. Edel, R.A. Smith, Introduction to the damage tolerance behaviour of railway rails – a review, Eng. Fract. Mech. 76 (2009) 2563–2601.
[1578] I. Grossoni, P. Hughes, Y. Bezin, A. Bevan, J. Jaiswal, Observed failures at railway turnouts: Failure analysis, possible causes and links to current and future research, Eng. Fail. Anal. 119 (2021) 104987.
[1579] F. Wetscher, R. Stock, R. Pippan, Changes in the mechanical properties of a pearlitic steel due to large shear deformation, Mater. Sci. Eng. A 445–446 (2007) 237–243.
[1580] M.W. Kapp, O. Renk, J. Eckert, R. Pippan, The importance of lamellar architecture to obtain ductility in heavily cold-worked pearlitic steels revealed by microbending experiments, Acta Mater. 232 (2022) 117935.
[1581] C. Kammerhofer, A. Hohenwarter, S. Scheriau, H.P. Brantner, R. Pippan, Influence of morphology and structural size on the fracture behavior of a nanostructured pearlitic steel, Mater. Sci. Eng. A 585 (2013) 190–196.
[1582] T. Leitner, G. Trummer, R. Pippan, A. Hohenwarter, Influence of severe plastic deformation and specimen orientation on the fatigue crack propagation behavior of a pearlitic steel, Mater. Sci. Eng. A 710 (2018) 260–270.
[1583] M.W. Kapp, A. Hohenwarter, A. Bachmaier, T. Müller, R. Pippan, SPD deformation of pearlitic, bainitic and martensitic steels, Mater. Trans. 64 (2023) 1353–1363.
[1584] D. Raabe, P.P. Choi, Y. Li, A. Kostka, X. Sauvage, F. Lecouturier, K. Hono, R. Kirchheim, R. Pippan, D. Embury, Metallic composites processed via extreme deformation: toward the limits of strength in bulk materials, MRS Bull. 35 (2010) 982–991.
[1585] C. Borchers, R. Kirchheim, Cold-drawn pearlitic steel wires, Prog. Mater. Sci. 82 (2016) 405–444.
[1586] Y.J. Li, P. Choi, S. Goto, C. Borchers, D. Raabe, R. Kirchheim, Evolution of strength and microstructure during annealing of heavily cold-drawn 6.3 GPa hypereutectoid pearlitic steel wire, Acta Mater. 60 (2012) 4005–4016.
[1587] J.D. Embury, R.M. Fisher, The structure and properties of drawn pearlite, Acta Met. 14 (1966) 147–159.
[1588] S. Djaziri, Y. Li, G.A. Nematollahi, B. Grabowski, S. Goto, C. Kirchlechner, A. Kostka, S. Doyle, J. Neugebauer, D. Raabe, G. Dehm, Deformation-induced martensite: a new paradigm for exceptional steels, Adv. Mater. 28 (2016) 7753–7757.
[1589] G. Langford, Deformation of pearlite, Metall. Mater. Trans. A 8 (1977) 861–875.
[1590] F. Wetscher, R. Pippan, S. Sturm, F. Kauffmann, C. Scheu, G. Dehm, TEM investigations of the structural evolution in a pearlitic steel deformed by high-pressure torsion, Metall. Mater. Trans. A 37 (2006) 1963–1968.
[1591] A. Hohenwarter, A. Bachmaier, B. Gludovatz, S. Scheriau, R. Pippan, Technical parameters affecting grain refinement by high pressure torsion, Inter, J. Mater. Res. 100 (2009) 1653–1661.
[1592] R. Stock, R. Pippan, Rail grade dependent damage behaviour – characteristics and damage formation hypothesis, Wear 314 (2014) 44–50.
[1593] H.K.D.H. Bhadeshia, J.W. Christian, Bainite in steels, Metall. Trans. A 21 (1990) 767–797.
[1594] A.S. Schulz-Beenken, Martensite in steels: its significance, recent developments and trends, J. Phys. IV (1997) C5–359-366.
[1595] J. Lai, K. Stadler, Investigation on the mechanisms of white etching crack (WEC) formation in rolling contact fatigue and identification of a root cause for bearing premature failure, Wear 364– 365 (2016) 244–256.
[1596] T. Müller, M.W. Kapp, A. Bachmaier, P. Felfer, R. Pippan, Ultrahigh-strength low carbon steel obtained from the martensitic state via high pressure torsion, Acta Mater. 166 (2019) 168–177.
[1597] D. Kalish, E.M. Roberts, On the distribution of carbon in martensite, Metall. Trans. 2 (1971) 2783–2790.
[1598] M.W. Kapp, A. Hohenwarter, S. Wurster, B. Yang, R. Pippan, Anisotropic deformation characteristics of an ultrafine- and nanolamellar pearlitic steel, Acta Mater. 106 (2016) 239–248.
[1599] M. Guziewski, S.P. Coleman, C.R. Weinberger, Atomistic investigation into the mechanical properties of the ferrite-cementite interface: the Bagaryatskii orientation, Acta Mater. 144 (2018) 656–665.
[1600] M. Guziewski, S.P. Coleman, C.R. Weinberger, Atomistic investigation into interfacial effects on the plastic response and deformation mechanisms of the pearlitic microstructure, Acta Mater. 180 (2019) 287–300.
[1601] T. Shimokawa, T. Niiyama, M. Okabe, J. Sawakoshi, Interfacial-dislocation-controlled deformation and fracture in nanolayered composites: toward higher ductility of drawn pearlite, Acta Mater. 164 (2019) 602–617.
[1602] T. Furuta, S. Kuramoto, T. Ohsuna, K. Oh-ishi, K. Horibuchi, Die-hard plastic deformation behavior in an ultrahigh-strength Fe–Ni–Al–C alloy, Scr. Mater. 101 (2015) 87–90.
[1603] K. Edalati, T. Furuta, T. Daio, S. Kuramoto, Z. Horita, High strength and high uniform ductility in a severely deformed iron alloy by lattice softening and multimodal-structure formation, Mater. Res. Lett. 3 (2015) 197–202.
[1604] X.G. Wang, L. Wang, M.X. Huang, In-situ evaluation of Lüders band associated with martensitic transformation in a medium Mn transformation-induced plasticity steel, Mater. Sci. Eng. A 674 (2016) 59–63.
[1605] Y. Ma, M. Yang, P. Jiang, F. Yuan, X. Wu, Plastic deformation mechanisms in a severely deformed Fe-Ni-Al-C alloy with superior tensile properties, Sci. Rep. 7 (2017) 15619.
[1606] B.B. He, B. Hu, H.W. Yen, G.J. Cheng, Z.K. Wang, H.W. Luo, M.X. Huang, High dislocation density–induced large ductility in deformed and partitioned steels, Science 357 (2017) 1029–1032.
[1607] Y. Zhang, L. Wang, K.O. Findley, J.G. Speer, Influence of temperature and grain size on austenite stability in medium manganese steels, Metall. Mater. Trans. A 48 (2017) 2140–2149.
[1608] I. Miyazaki, T. Furuta, K. Oh-ishi, T. Nakagaki, S. Kuramoto, A. Shibata, N. Tsuji, Overcoming the strength–ductility trade-off via the formation of a thermally stable and plastically unstable austenitic phase in cold-worked steel, Mater. Sci. Eng. A 721 (2018) 74–80.
[1609] S. Gao, Y. Bai, R. Zheng, Y. Tian, W. Mao, A. Shibata, N. Tsuji, Mechanism of huge Lüders-type deformation in ultrafine grained austenitic stainless steel, Scr. Mater. 159 (2019) 28–32.
[1610] Y. Hosoya, Y. Matsumura, Y. Tomota, Y. Onuki, S. Harjo, Mechanism of improved ductility of 1500 MPa-class ultra-high strength cold-rolled steel sheet produced by rolling and partitioning method, ISIJ Int 60 (2020) 2097–2106.
[1611] M. Koyama, T. Yamashita, S. Morooka, T. Sawaguchi, Z. Yang, T. Hojo, T. Kawasaki, S. Harjo, Microstructure and plasticity evolution during Lüders deformation in an Fe-5Mn-0.1C medium-Mn steel, ISIJ Int 62 (2022) 2036–2042.
[1612] M. Koyama, T. Yamashita, S. Morooka, Z. Yang, R.S. Varanasi, T. Hojo, T. Kawasaki, S. Harjo, Hierarchical deformation heterogeneity during Lüders band propagation in an Fe-5Mn-0.1C medium Mn steel clarified through in situ scanning electron microscopy, ISIJ Int 62 (2022) 2043–2053.
[1613] H. Du, Y. Gong, Y. Xu, Q. Zeng, L. Xiong, Y. Li, Y. Nie, J. Wang, X. Jin, Obtaining ultrastrong and ductile steel with hierarchical lamellar duplex phase microstructure by two-stage martensitic transformation mechanism, Metall. Mater. Trans. A 53 (2022) 1613–1629.
[1614] Y. Zhang, H. Ding, Ultrafine also can be ductile: On the essence of Lüders band elongation in ultrafine-grained medium manganese steel, Mater. Sci. Eng. A 733 (2018) 220–223.
[1615] X.G. Wang, C.H. Liu, B.B. He, C. Jiang, M.X. Huang, Microscopic strain partitioning in Lüders band of an ultrafine-grained medium Mn steel, Mater. Sci. Eng. A 761 (2019) 138050.
[1616] B. Sun, Y. Ma, N. Vanderesse, R.S. Varanasi, W. Song, P. Bocher, D. Ponge, D. Raabe, Macroscopic to nanoscopic in situ investigation on yielding mechanisms in ultrafine grained medium Mn steels: Role of the austenite-ferrite interface, Acta Mater. 178 (2019) 10–25.
[1617] Y. Ma, B. Sun, A. Schökel, W. Song, D. Pong, D. Raabe, W. Bleck, Phase boundary segregation-induced strengthening and discontinuous yielding in ultrafine-grained duplex medium-Mn steels, Acta Mater. 200 (2020) 389–403.

[1618] C.Y. Hung, Y. Bai, N. Tsuji, M. Murayama, Grain size altering yielding mechanisms in ultrafine grained high-Mn austenitic steel: advanced TEM, Investig., J. Mater. Sci. Technol. 86 (2021) 192–203.

[1619] R.S. Varanasi, S. Zaefferer, B. Sun, D. Ponge, Localized deformation inside the Lüders front of a medium manganese steel, Mater. Sci. Eng. A 824 (2021) 141816.

[1620] C. Lei, X. Li, X. Deng, Z. Wang, G. Wang, Deformation mechanism and ductile fracture behavior in high strength high ductility nano/ultrafine grained Fe-17Cr-6Ni austenitic steel, Mater. Sci. Eng. A 709 (2018) 72–81.

[1621] G. Sun, J. Liu, Y. Zhu, Heterostructure alleviates Lüders deformation of ultrafine-grained stainless steels, Mater. Sci. Eng. A 848 (2022) 143393.

[1622] H. Du, Y. Gong, T. Liang, Y. Li, Y. Xu, X. Lu, Q. Zeng, X. Jin, Enhancement of impact toughness via tailoring deformation compatibility of constituent phases in duplex Q&P steel with excellent strength and ductility, Metall. Mater. Trans. A 51 (2020) 2097–2117.

[1623] H. Du, Y. Gong, Z. Li, X. Lu, X. Jin, Investigation into competitive mechanism of carbon partitioning and pseudospinodal decomposition of supersaturated martensite in Q&P steel containing high silicon, Metall. Mater. Trans. A 52 (2021) 2123–2130.

[1624] H. Du, Y. Gong, Q. Zeng, Y. Li, N. Min, X. Jin, Interpretation of dynamic strain aging in an intercritical annealed steel by dislocation multiplication induced by martensitic transformation, Metall. Mater. Trans. A 52 (2021) 5258–5273.

[1625] H. Du, Y. Gong, B. Liu, Y. Xu, Y. Li, X. Jin, Discontinuous yielding mechanisms in tempered hierarchical duplex phase steel with high-density dislocations, Metall. Mater. Trans. A 53 (2022) 2331–2337.

[1626] T. Furuta, I. Miyazaki, K. Oh-ishi, S. Kuramoto, A. Shibata, N. Tsuji, Characterization of cold-rolled heterogeneous microstructure formed by multimodal deformation in an Fe-Ni-Al-C alloy with lattice softening, Mater. Des. 153 (2018) 166–176.

[1627] S. Kuramoto, Y. Kawano, Y. Mori, J. Kobayashi, S. Emura, T. Sawaguchi, Mechanical properties and deformation behavior in severely cold-rolled Fe-Ni-Al-C alloys with Lüders deformation - overview with recent experimental results, Mater. Trans. 64 (2023) 1410–1418.

[1628] S. Kuramoto, T. Furuta, Severe plastic deformation to achieve high strength and high ductility in Fe–Ni based alloys with lattice softening, Mater. Trans. 60 (2019) 1116–1122.

[1629] S. Kuramoto, T. Furuta, N. Nagasako, Z. Horita, Lattice softening for producing ultrahigh strength of iron base nanocrystalline alloy, Appl. Phys. Lett. 95 (2009) 211901.

[1630] K. Edalati, S. Toh, T. Furuta, S. Kuramoto, M. Watanabe, Z. Horita, Development of ultrahigh strength and high ductility in nanostructured iron alloys with lattice softening and nanotwins, Scr. Mater. 67 (2012) 511–514.

[1631] S. Gao, M. Chen, S. Chen, N. Kamikaze, A. Shibata, N. Tsuji, Yielding behavior and its effect on uniform elongation of fine grained IF steel, Mater. Trans. 55 (2014) 73–77.

[1632] F. Pöhl, Pop-in behavior and elastic-to-plastic transition of polycrystalline pure iron during sharp nanoindentation, Sci. Rep. 9 (2019) 15350.

[1633] X.H. An, S.D. Wu, Z.F. Zhang, R.B. Figueiredo, N. Gao, T.G. Langdon, Enhanced strength–ductility synergy in nanostructured Cu and Cu–Al alloys processed by high-pressure torsion and subsequent annealing, Scr. Mater. 66 (2012) 227–230.

[1634] N. Kamikawa, X. Huang, N. Tsuji, N. Hansen, Strengthening mechanisms in nanostructured high-purity aluminium deformed to high strain and annealed, Acta Mater. 57 (2009) 4198–4208.

[1635] Z. Li, L. Fu, B. Fu, A. Shan, Yield point elongation in fine-grained titanium, Mater. Lett. 96 (2013) 1–4.

[1636] D. Drozdenko, K. Fekete, P. Dobroň, M. Knapek, K. Máthis, P. Minárik, M. Yamasaki, Y. Kawamura, The yield point phenomenon in ultrafine-grained dilute Mg-Zn-Y alloys, Mater. Lett. 330 (2023) 133315.

[1637] C.X. Huang, G. Yang, C. Wang, Z.F. Zhang, S.D. Wu, Mechanical behaviors of ultrafine-grained 301 austenitic stainless steel produced by equal-channel angular pressing, Metall. Mater. Trans. A 42 (2011) 2061–2071.

[1638] J.W. Yeh, S.K. Chen, S.J. Lin, J.Y. Gan, T.S. Chin, T.T. Shun, C.H. Tsau, S. Y. Chang, Nanostructured high-entropy alloys with multiple principal elements: novel alloy design concepts and outcomes, Adv. Eng. Mater. 6 (2004) 299–303.

[1639] J.W. Yeh, Alloy design strategies and future trends in high-entropy alloys, JOM 65 (2013) 1759–1771.

[1640] B. Gludovatz, A. Hohenwarter, D. Catoor, E.H. Chang, E.P. George, R.O. Ritchie, A fracture-resistant high-entropy alloy for cryogenic applications, Science 345 (2014) 1153–1158.

[1641] E.P. George, W.A. Curtin, C.C. Tasan, High entropy alloys: a focused review of mechanical properties and deformation mechanisms, Acta Mater. 188 (2020) 435–474.

[1642] P. Edalati, M. Fuji, K. Edalati, Superfunctional high-entropy alloys and ceramics by severe plastic deformation, Rare Met 42 (2023) 3246–3258.

[1643] B. Cantor, I.T.H. Chang, P. Knight, A.J.B. Vincent, Microstructural development in equiatomic multicomponent alloys, Mater. Sci. Eng. A 375–377 (2004) 213–218.

[1644] W. Skrotzki, A. Pukenas, B. Joni, E. Odor, T. Ungar, A. Hohenwarter, R. Pippan, E.P. George, Microstructure and texture evolution during severe plastic deformation of CrMnFeCoNi high-entropy alloy, IOP Conf. Ser. Mater. Sci. Eng. 194 (2017) 012028.

[1645] G.D. Sathiaraj, A. Pukenas, W. Skrotzki, Texture formation in face-centered cubic high entropy alloys, J. Alloy. Compd. 826 (2020) 154183.

[1646] B. Schuh, I. Issa, T. Müller, T. Kremmer, C. Gammer, R. Pippan, A. Hohenwarter, Deformation induced structure and property changes in a nanostructured multiphase CrMnFeCoNi high-entropy alloy, Nanomater 13 (2023) 924.

[1647] H. Shahmir, J. He, Z. Lu, M. Kawasaki, T.G. Langdon, Evidence for superplasticity in a CoCrFeNiMn high-entropy alloy processed by high-pressure torsion, Mater. Sci. Eng. A 685 (2017) 342–348.

[1648] H. Shahmir, M. Kawasaki, T.G. Langdon, Developing superplasticity in high-entropy alloys by severe plastic deformation, Mater. Sci. Forum 941 (2018) 1059–1064.

[1649] R. Motabelli, Z. Savaedi, H. Mirzadeh, Superplasticity of high-entropy alloys: a review, Arch. Civ. Mech. Eng. 22 (2022) 20.

[1650] H. Shahmir, M.S. Mehranpour, M. Kawasaki, T.G. Langdon, Superplasticity in severely deformed high-entropy alloys, Mater. Trans. 64 (2023) 1526–1536.

[1651] K.Y. Tsai, M.H. Tsai, J.W. Yeh, Sluggish diffusion in Co-Cr-Fe-Mn-Ni high entropy alloys, Acta Mater. 61 (2013) 4887–4897.

[1652] H. Shahmir, M. Nili-Ahmadabadi, A. Shafie, T.G. Langdon, Effect of a minor titanium addition on the superplastic properties of a CoCrFeNiMn high-entropy alloy processed by high-pressure torsion, Mater. Sci. Eng. A 718 (2018) 468–476.

[1653] N.T. Nguyen, J. Moon, P. Sathiyamoorthi, P. Asghari-Rad, G.H. Kim, C.S. Lee, H. S. Kim, Superplasticity of $V_{10}Cr_{15}Mn_5Fe_{35}Co_{10}Ni_{25}$ high-entropy alloy processed using high-pressure torsion, Mater. Sci. Eng. A 764 (2019) 138198.

[1654] P. Edalati, A. Mohammadi, M. Ketabchi, K. Edalati, Ultrahigh hardness in nanostructured dual-phase high-entropy alloy AlCrFeCoNiNb developed by high-pressure torsion, J. Alloy. Compd. 884 (2021) 161101.

[1655] P. Edalati, A. Mohammadi, M. Tang, R. Floriano, M. Fuji, K. Edalati, Phase transformation and microstructure evolution in ultrahard carbon-doped AlTiFeCoNi high-entropy alloy by high-pressure torsion, Mater. Lett. 302 (2021) 130368.

[1656] P. Edalati, A. Mohammadi, M. Ketabchi, K. Edalati, Microstructure and microhardness of dual-phase high-entropy alloy by high-pressure torsion: twins and stacking faults in FCC and dislocations in BCC, J. Alloy. Compd. 894 (2022) 162413.

[1657] D.B. Miracle, J.D. Miller, O.N. Senkov, C. Woodward, M.D. Uchic, J. Tiley, Exploration and development of high entropy alloys for structural applications, Entropy 16 (2014) 494–525.

[1658] Y. Zou, H. Ma, R. Spolenak, Ultrastrong ductile and stable high-entropy alloys at small scales, Nat. Commun. 6 (2015) 7748.

[1659] O. Senkov, J. Scott, S. Senkova, F. Meisenkothen, D. Miracle, C. Woodward, Microstructure and elevated temperature properties of a refractory TaNbHfZrTi alloy, J. Mater. Sci. 47 (2012) 4062–4074.

[1660] J. Gubicza, Defect Structure and Properties of Nanomaterials, Woodhead Publishing,, Duxford, 2017.

[1661] A. Heczel, M. Kawasaki, J.L. Lábár, J.I. Jang, T.G. Langdon, J. Gubicza, Defect structure and hardness in nanocrystalline CoCrFeMnNi high-entropy alloy processed by high-pressure torsion, J. Alloy. Compd. 711 (2017) 143–154.

[1662] J. Gubicza, P.T. Hung, M. Kawasaki, J.K. Han, Y. Zhao, Y. Xue, J.L. Lábár, Influence of severe plastic deformation on the microstructure and hardness of a CoCrFeNi high-entropy alloy: a comparison with CoCrFeNiMn, Mater. Charact. 154 (2019) 304–314.

[1663] J. Gubicza, A. Heczel, M. Kawasaki, J.K. Han, Y. Zhao, Y. Xue, S. Huang, J. L. Lábár, Evolution of microstructure and hardness in $Hf_{25}Nb_{25}Ti_{25}Zr_{25}$ high-entropy alloy during high-pressure torsion, J. Alloy. Compd. 788 (2019) 318–328.

[1664] K. Kishore, A.K. Chandan, P.T. Hung, S. Kumar, M. Kawasaki, J. Gubicza, On the enhanced hardening ability and plasticity mechanisms in a novel Mn-added CoCrNi medium entropy alloy during high-pressure torsion, J. Alloy. Compd. 904 (2022) 163941.

[1665] A.K. Chandan, K. Kishore, P.T. Hung, M. Ghosh, S.G. Chowdhury, M. Kawasaki, J. Gubicza, Effect of nickel addition on enhancing nano-structuring and suppressing TRIP effect in $Fe_{40}Mn_{40}Co_{10}Cr_{10}$ high entropy alloy during high-pressure torsion, Int. J. Plast. 150 (2022) 103193.

[1666] P.T. Hung, M. Kawasaki, Á. Szabó, J.L. Lábár, Z. Hegedűs, J. Gubicza, Influence of degree of severe plastic deformation on thermal stability of an HfNbTiZr multi-principal element alloy processed by high-pressure torsion, Nanomater 12 (2022) 3371.

[1667] J. Gubicza, P.T. Hung, Nanostructuring of multi-principal element alloys by severe plastic deformation: from fundamentals to an improved functionality, Mater. Trans. 64 (2023) 1284–1298.

[1668] J. Gubicza, M. El-Tahawy, Y. Huang, H. Choi, H. Choe, J.L. Lábár, T.G. Langdon, Microstructure, phase composition and hardness evolution in 316L stainless steel processed by high-pressure torsion, Mater. Sci. Eng. A 657 (2016) 215–223.

[1669] H. Shahmir, P. Asghari-Rad, M.S. Mehranpour, F. Forghani, H.S. Kim, M. Nili-Ahmadabadi, Evidence of FCC to HCP and BCC-martensitic transformations in a CoCrFeNiMn high-entropy alloy by severe plastic deformation, Mater. Sci. Eng. A 807 (2021) 140875.

[1670] P. Asghari-Rad, P. Sathiyamoorthi, N.T.C. Nguyen, J.W. Bae, H. Shahmir, H. S. Kim, Fine-tuning of mechanical properties in $V_{10}Cr_{15}Mn_5Fe_{35}Co_{10}Ni_{25}$ high-entropy alloy through high-pressure torsion and annealing, Mater. Sci. Eng. A 771 (2020) 138604.

[1671] D.H. Lee, I.C. Choi, M.Y. Seok, J. He, Z. Lu, J.Y. Suh, M. Kawasaki, T.G. Langdon, J.I. Jang, Nanomechanical behavior and structural stability of a nanocrystalline CoCrFeNiMn high-entropy alloy processed by high-pressure torsion, J. Mater. Res 30 (2015) 2804–2815.

[1672] N. Liang, R. Xu, G. Wu, X. Gao, Y. Zhao, High thermal stability of nanocrystalline $FeNi_2CoMo_{0.2}V_{0.5}$ high-entropy alloy by twin boundary and sluggish diffusion, Mater. Sci. Eng. A 848 (2022) 143399.

[1673] H. Shahmir, E. Tabachnikova, A. Podolskiy, M. Tikhonovsky, T.G. Langdon, Effect of carbon content and annealing on structure and hardness of

CrFe₂NiMnV₀.₂₅ high-entropy alloys processed by high-pressure torsion, J. Mater. Sci. 53 (2018) 11813–11822.

[1674] P. Yu, H. Cheng, L. Zhang, H. Zhang, Q. Jing, M. Ma, P. Liaw, G. Li, R. Liu, Effects of high pressure torsion on microstructures and properties of an Al₀.₁CoCrFeNi high-entropy alloy, Mater. Sci. Eng. A 655 (2016) 283–291.

[1675] Q. Tang, Y. Huang, Y. Liao, X. Liao, T. Langdon, P. Dai, Hardening of an Al₀.₃CoCrFeNi high entropy alloy via high-pressure torsion and thermal annealing, Mater. Lett. 151 (2015) 126–129.

[1676] Q. Zhang, M. Li, B. Han, S. Zhang, Y. Li, C. Hu, Investigation on microstructures and properties of Al₁.₅CoCrFeMnNi high entropy alloy before and after ultrasonic impact treatment, J. Alloy. Compd. 884 (2021) 160989.

[1677] B. Schuh, B. Völker, V. Maier-Kiener, J. Todt, J. Li, A. Hohenwarter, Phase decomposition of a single phase AlTiVNb high-entropy alloy after severe plastic deformation and annealing, Adv. Eng. Mater. 19 (2017) 1600674.

[1678] S. Wang, D. Wu, H. She, M. Wu, D. Shu, A. Dong, H. Lai, B. Sun, Design of high-ductile medium entropy alloys for dental implants, Mater. Sci. Eng. C 113 (2020) 110959.

[1679] D.H. Lee, I.C. Choi, M. Kawasaki, T.G. Langdon, J.I. Jang, A review of recent research on nanoindentation of high-entropy alloys processed by high-pressure torsion, Mater. Trans. 64 (2023) 1551–1565.

[1680] I.C. Choi, J.I. Jang, A survey of nanoindentation studies on HPT-processed materials, Adv. Eng. Mater. 22 (2020) 1900648.

[1681] B.N. Lucas, W.C. Oliver, Indentation power-law creep of high purity indium, Metall. Mater. Trans. A 30A (1999) 601–610.

[1682] V. Maier, C. Schunk, M. Göken, K. Durst, Microstructure-dependent deformation behaviour of bcc-metals–indentation size effect and strain rate sensitivity, Philos. Mag. 95 (2015) 1766–1779.

[1683] V. Maier, K. Durst, J. Mueller, B. Backes, H.W. Höppel, M. Göken, Nanoindentation strain-rate jump tests for determining the local strain-rate sensitivity in nanocrystalline Ni and ultrafine-grained Al, J. Mater. Res. 26 (2011) 1421–1430.

[1684] Y. Zhao, J.M. Park, K. Murakami, S. Komazaki, M. Kawasaki, K. Tsuchiya, J. Y. Suh, U. Ramamurty, J.I. Jang, Exploring the hydrogen absorption and strengthening behavior in nanocrystalline face-centered cubic high-entropy alloys, Scr. Mater. 203 (2021) 114069.

[1685] Y. Zhao, X. Wang, T. Cao, J.K. Han, M. Kawasaki, J.I. Jang, H.N. Han, U. Ramamurty, L. Wang, Y. Xue, Effect of grain size on the strain rate sensitivity of CoCrFeNi high-entropy alloy, Mater. Sci. Eng. A 782 (2020) 139281.

[1686] S. Gangireddy, B. Gwalani, V. Soni, R. Banerjee, R.S. Mishra, Contrasting mechanical behavior in precipitation hardenable AlₓCoCrFeNi high entropy alloy microstructures: single phase FCC vs. dual phase FCC-BCC, Mater. Sci. Eng. A 739 (2019) 158–166.

[1687] G. Laplanche, J. Bonneville, C. Varvenne, W.A. Curtin, E.P. George, Thermal activation parameters of plastic flow reveal deformation mechanisms in the CrMnFeCoNi high-entropy alloy, Acta Mater. 143 (2018) 257–264.

[1688] W. Zhao, J.K. Han, Y.O. Kuzminova, S.A. Evlashin, A.P. Zhilyaev, A.M. Pesin, J. I. Jang, K.D. Liss, M. Kawasaki, Significance of grain refinement on micro-mechanical properties and structures of additively-manufactured CoCrFeNi high-entropy alloy, Mater. Sci. Eng. A 807 (2021) 140898.

[1689] Z. Wu, Y. Gao, H. Bei, Thermal activation mechanisms and Labusch-type strengthening analysis for a family of high-entropy and equiatomic solid-solution alloys, Acta Mater. 120 (2016) 108–119.

[1690] V. Maier-Kiener, B. Schuh, E.P. George, H. Clemens, A. Hohenwarter, Insights into the deformation behavior of the CrMnFeCoNi high-entropy alloy revealed by elevated temperature nanoindentation, J. Mater. Res 32 (2017) 2658–2667.

[1691] W. Huo, F. Fang, X. Liu, S. Tan, Z. Xie, J. Jiang, Remarkable strain-rate sensitivity of nanotwinned CoCrFeNi alloys, Appl. Phys. Lett. 114 (2019) 101904.

[1692] M. Shabani, J. Indeck, K. Hazeli, P.D. Jablonski, G.J. Pataky, Effect of strain rate on the tensile behavior of CoCrFeNi and CoCrFeMnNi high-entropy alloys, J. Mater. Eng. Perform. 28 (2019) 4348–4356.

[1693] X.B. Feng, W. Fu, J.Y. Zhang, J.T. Zhao, J. Li, K. Wu, G. Liu, J. Sun, Effects of nanotwins on the mechanical properties of AlₓCoCrFeNi high entropy alloy thin films, Scr. Mater. 139 (2017) 71–76.

[1694] M. Komarasamy, N. Kumar, R.S. Mishra, P.K. Liaw, Anomalies in the deformation mechanism and kinetics of coarse-grained high entropy alloy, Mater. Sci. Eng. A 654 (2016) 256–263.

[1695] S. Gangireddy, B. Gwalani, R.S. Mishra, Grain size dependence of strain rate sensitivity in a single phase FCC high entropy alloy Al₀.₃CoCrFeNi, Mater. Sci. Eng. A 736 (2018) 344–348.

[1696] Y.M. Wang, A.V. Hamza, E. Ma, Temperature-dependent strain rate sensitivity and activation volume of nanocrystalline Ni, Acta Mater. 54 (2006) 2715–2726.

[1697] C.D. Gu, J.S. Lian, Q. Jiang, W.T. Zheng, Experimental and modelling investigations on strain rate sensitivity of an electrodeposited 20 nm grain sized Ni, J. Phys. D. 40 (2007) 7440–7446.

[1698] F. Dalla Torre, H. Van Swygenhoven, M. Victoria, Nanocrystalline electrodeposited Ni: microstructure and tensile properties, Acta Mater. 50 (2002) 3957–3970.

[1699] R. Schwaiger, B. Moser, M. Dao, N. Chollacoop, S. Suresh, Some critical experiments on the strain-rate sensitivity of nanocrystalline nickel, Acta Mater. 51 (2003) 5159–5172.

[1700] Y.M. Wang, A.V. Hamza, E. Ma, Activation volume and density of mobile dislocations in plastically deforming nanocrystalline Ni, Appl. Phys. Lett. 86 (2005) 241917.

[1701] F. Dalla Torre, P. Spätig, R. Schäublin, M. Victoria, Deformation behaviour and microstructure of nanocrystalline electrodeposited and high pressure torsioned nickel, Acta Mater. 53 (2005) 2337–2349.

[1702] T. Guo, P. Huang, K.W. Xu, F. Wang, T.J. Lu, Solid solution effects on hardness and strain rate sensitivity of nanocrystalline NiFe alloy, Mater. Sci. Eng. A 676 (2016) 501–505.

[1703] H. Li, H. Choo, P.K. Liaw, The effect of temperature on strain rate sensitivity in a nanocrystalline Ni–Fe alloy, J. Appl. Phys. 101 (2007) 063536.

[1704] C. Gu, J. Lian, Q. Jiang, Z. Jiang, Ductile–brittle–ductile transition in an electrodeposited 13 nanometer grain sized Ni–8.6 wt% Co alloy, Mater. Sci. Eng. A 459 (2007) 75–81.

[1705] J. Moon, S.I. Hong, J.B. Seol, J.W. Bae, J.M. Park, H.S. Kim, Strain-rate sensitivity of high-entropy alloys and its significance in deformation, Mater. Res. Lett. 7 (2019) 503–509.

[1706] L. Li, Z. Chen, S. Kuroiwa, M. Ito, K. Yuge, K. Kishida, H. Tanimoto, Y. Yu, H. Inui, E.P. George, Evolution of short-range order and its effects on the plastic deformation behavior of single crystals of the equiatomic Cr-Co-Ni medium-entropy alloy, Acta Mater. 243 (2023) 118537.

[1707] Z. He, Y. Guo, L. Sun, H.L. Yan, X. Guan, S. Jiang, Y. Shen, W. Yin, X. Zhao, Z. Li, N. Jia, Interstitial-driven local chemical order enables ultrastrong face-centered cubic multicomponent alloys, Acta Mater. 243 (2023) 118495.

[1708] H. Conrad, Grain size dependence of the plastic deformation kinetics in Cu, Mater. Sci. Eng. A 341 (2003) 216–228.

[1709] J.R. Trelewicz, C.A. Schuh, Hot nanoindentation of nanocrystalline Ni–W alloys, Scr. Mater. 61 (2009) 1056–1059.

[1710] R.J. Asaro, S. Suresh, Mechanistic models for the activation volume and rate sensitivity in metals with nanocrystalline grains and nano-scale twins, Acta Mater. 53 (2005) 3369–3382.

[1711] P. Gu, M. Dao, R.J. Asaro, S. Suresh, A unified mechanistic model for size-dependent deformation in nanocrystalline and nanotwinned metals, Acta Mater. 59 (2011) 6861–6868.

[1712] M. Vaidya, K.G. Pradeep, B.S. Murty, G. Wilde, S.V. Divinski, Radioactive isotopes reveal a non sluggish kinetics of grain boundary diffusion in high entropy alloys, Sci. Rep. 7 (2017) 12293.

[1713] P.K. Huang, J.W. Yeh, T.T. Shun, S.K. Chen, Multi-principal-element alloys with improved oxidation and wear resistance for thermal spray coating, Adv. Eng. Mater. 6 (2004) 74–78.

[1714] C.J. Tong, Y.L. Chen, J.W. Yeh, S.J. Lin, S.K. Chen, T.T. Shun, C.H. Tsau, S. Y. Chang, Microstructure characterization of AlₓCoCrCuFeNi high-entropy alloy system with multiprincipal elements, Metall. Mater. Trans. A 36 (2005) 881–893.

[1715] U. Hsu, U. Hung, J. Yeh, S. Chen, Y. Huang, C. Yang, Alloying behavior of iron, gold and silver in AlCoCrCuNi-based equimolar high-entropy alloys, Mater. Sci. Eng. A 460 (2007) 403–408.

[1716] J.W. Yeh, Recent progress in high entropy alloys, Ann. Chim. Sci. Mater. 31 (2006) 633–648.

[1717] M.H. Tsai, J.W. Yeh, High-entropy alloys: a critical review, Mater. Res. Lett. 2 (2014) 107–123.

[1718] D.B. Miracle, O.N. Senkov, A critical review of high entropy alloys and related concepts, Acta Mater. 122 (2017) 448–511.

[1719] Z. Li, S. Zhao, R.O. Ritchie, M.A. Meyers, Mechanical properties of high-entropy alloys with emphasis on face-centered cubic alloys, Prog. Mater. Sci. 102 (2019) 296–345.

[1720] H. Inui, K. Kishida, Z. Chen, Recent progress in our understanding of phase stability, atomic structures and mechanical and functional properties of high-entropy alloys, Mater. Trans. 63 (2022) 394–401.

[1721] H. Shahmir, M. Nili-Ahmadabadi, Y. Huang, J.M. Jung, H.S. Kim, T.G. Langdon, Shape memory effect in nanocrystalline NiTi alloy processed by high-pressure torsion, Mater. Sci. Eng. A 626 (2015) 203–206.

[1722] H. Shahmir, T.G. Langdon, An evaluation of the hexagonal close-packed to face-centered cubic phase transformation in a Ti-6Al-4V alloy during high-pressure torsion, Mater. Sci. Eng. A 704 (2017) 212–217.

[1723] A.V. Kuznetsov, D.G. Shaysultanov, N.D. Stepanov, G.A. Salishchev, O. N. Senkov, Tensile properties of an AlCrCuNiFeCo high-entropy alloy in as-cast and wrought conditions, Mater. Sci. Eng. A 533 (2012) 107–118.

[1724] D. Shaysultanov, N. Stepanov, A. Kuznetsov, G. Salishchev, O. Senkov, Phase composition and superplastic behavior of a wrought AlCoCrCuFeNi high-entropy alloy, JOM 65 (2013) 1815–1828.

[1725] A.V. Kuznetsov, D.G. Shaisultanov, N. Stepanov, G.A. Salishchev, O.N. Senkov, Superplasticity of AlCoCrCuFeNi high entropy alloy, Mater. Sci. Forum 735 (2013) 146–151.

[1726] N.T.C. Nguyen, P. Asghari-Rad, P. Sathiyamoorthi, A. Zargaran, C.S. Lee, H. S. Kim, Ultrahigh high-strain-rate superplasticity in a nanostructured high-entropy alloy, Nat. Commun. 11 (2020) 2736.

[1727] N.T.C. Nguyen, P. Asghari-Rad, J.W. Bae, P. Sathiyamoorthi, H.S. Kim, Superplastic behavior in high-pressure torsion-processed Mo₇.₅Fe₅₅Co₁₈Cr₁₂.₅Ni₇ medium-entropy alloy, Metal. Mater. Trans. A 52 (2021) 1–7.

[1728] T.G. Langdon, Fracture processes in superplastic flow, Met. Sci. 16 (1982) 175–183.

[1729] M. Kawasaki, T.G. Langdon, Principles of superplasticity in ultrafine-grained materials, J. Mater. Sci. 42 (2007) 1782–1796.

[1730] M. Kawasaki, T.G. Langdon, Review: achieving superplasticity in metals processed by high-pressure torsion, J. Mater. Sci. 49 (2014) 6487–6496.

[1731] N.D. Stepanov, D.G. Shaysultanov, G.A. Salishchev, O.N. Senkov, Mechanical behavior and microstructure evolution during superplastic deformation of the

fine-grained AlCoCrCuFeNi high entropy alloy, Mater. Sci. Forum 838- 839 (2016) 302–307.

[1732] H. Jeong, W.J. Kim, Calculation and construction of deformation mechanism maps and processing maps for CoCrFeMnNi and Al$_{0.5}$CoCrFeMnNi high-entropy alloys, J. Alloy. Compd. 869 (2021) 159256.

[1733] P. Asghari-Rad, N.T.C. Nguyen, A. Zargaran, P. Sathiyamoorthi, H.S. Kim, Deformation-induced grain boundary segregation mediated high-strain rate superplasticity in medium entropy alloy, Scr. Mater. 207 (2022) 114239.

[1734] S.R. Reddy, S. Bapari, P.P. Bhattacharjee, A.H. Chokshi, Superplastic-like flow in a fine-grained equiatomic CoCrFeMnNi high-entropy alloy, Mater. Res. Lett. 5 (2017) 408–414.

[1735] E.P. George, D. Raabe, R.O. Ritchie, High-entropy alloys, Nat. Rev. Mater. 4 (2019) 515–534.

[1736] Y. Zhang, T.T. Zuo, Z. Tang, M.C. Gao, K.A. Dahmen, P.K. Liaw, Z.P. Lu, Microstructures and properties of high-entropy alloys, Prog. Mater. Sci. 61 (2014) 1–93.

[1737] F. Otto, A. Dlouhý, Ch Somsen, H. Bei, G. Eggeler, E.P. George, The influences of temperature and microstructure on the tensile properties of a CoCrFeMnNi high-entropy alloy, Acta Mater. 61 (2013) 5743–5755.

[1738] Y. Zhang, D. Wang, S. Wang, High-entropy alloys for electrocatalysis: design, characterization, and applications, Small 18 (2022) 2104339.

[1739] W. Li, D. Xie, D. Li, Y. Zhang, Y. Gao, P.K. Liaw, Mechanical behavior of high-entropy alloys, Prog. Mater. Sci. 118 (2021) 100777.

[1740] J.X. Yang, B.H. Dai, C.Y. Chiang, I.C. Chiu, C.W. Pao, S.Y. Lu, I.Y. Tsao, S.T. Lin, C.T. Chiu, J.W. Yeh, P.C. Chang, W.H. Hung, Rapid fabrication of high-entropy ceramic nanomaterials for catalytic reactions, ACS Nano 15 (2021) 12324–12333.

[1741] A. Sarkar, Q. Wang, A. Schiele, M.R. Chellali, S.S. Bhattacharya, D. Wang, T. Brezesinski, H. Hahn, L. Velasco, B. Breitung, High-entropy oxides: fundamental aspects and electrochemical properties, Adv. Mater. 31 (2019) 1806236.

[1742] A. Sarkar, L. Velasco, D. Wang, Q. Wang, G. Talasila, L. de Biasi, C. Kübel, T. Brezesinski, S.S. Bhattacharya, H. Hahn, B. Breitung, High entropy oxides for reversible energy storage, Nat. Commun. 9 (2018) 3400.

[1743] D. Bérardan, S. Franger, D. Dragoe, A.K. Meena, N. Dragoe, Colossal dielectric constant in high entropy oxides, Phys. Stat. Sol. Rapid Res. Lett. 10 (2016) 328–333.

[1744] N. Qiu, H. Chen, Z. Yang, S. Sun, Y. Wang, Y. Cui, A high entropy oxide (Mg$_{0.2}$Co$_{0.2}$Ni$_{0.2}$Cu$_{0.2}$Zn$_{0.2}$O) with superior lithium storage performance, J. Alloy. Compd. 777 (2019) 767–774.

[1745] V.H. Hammond, M.A. Atwater, K.A. Darling, H.Q. Nguyen, L.J. Kecskes, Equal-channel angular extrusion of a low-density high-entropy alloy produced by high-energy cryogenic mechanical alloying, JOM 66 (2014) 2021–2029.

[1746] A. Heczel, L. Lilensten, J. Bourgon, L. Perrière, J.P. Couzinié, I. Guillot, G. Dirras, Y. Huang, T.G. Langdon, J. Gubicza, Influence of high-pressure torsion on the microstructure and the hardness of a Ti-rich high-entropy alloy, Mater. Sci. Forum 879 (2017) 732–737.

[1747] R. Zheng, J. Chen, W. Xiao, C. Ma, Microstructure and tensile properties of nanocrystalline (FeNiCoCu)$_{1-x}$Ti$_x$Al$_x$ high entropy alloys processed by high pressure torsion, Intermetallics 74 (2016) 38–45.

[1748] J.W. Won, S. Lee, S.H. Park, M. Kang, K.R. Lim, C.H. Park, Y.S. Na, Ultrafine-grained CoCrFeMnNi high-entropy alloy produced by cryogenic multi-pass caliber rolling, J. Alloy. Compd. 742 (2018) 290–295.

[1749] R. Sonkusare, N. Khandelwal, P. Ghosh, K. Biswas, N.P. Gurao, A comparative study on the evolution of microstructure and hardness during monotonic and cyclic high pressure torsion of CoCuFeMnNi high entropy alloy, J. Mater. Res 34 (2019) 732–743.

[1750] S.K. Dwivedi, M. Vishwakarma, Hydrogen embrittlement in different materials: a review, Int. J. Hydrog. Energy 43 (2018) 21603–21616.

[1751] Y. Mine, D. Haraguchi, T. Ideguchi, N. Horita, Z. Horita, K. Takashima, Hydrogen embrittlement of ultrafine-grained austenitic stainless steels processed by high-pressure torsion at moderate temperature, ISIJ Int 56 (2016) 1083–1090.

[1752] A. Mohammadi, P. Edalati, M. Arita, J.W. Bae, H.S. Kim, K. Edalati, Microstructure and defect effects on strength and hydrogen embrittlement of high-entropy alloy CrMnFeCoNi processed by high-pressure torsion, Mater. Sci. Eng. A 844 (2022) 143179.

[1753] M. Hirscher, V.A. Yartys, M. Baricco, J.B. von Colbe, D. Blanchard, R. C. Bowman Jr., D.P. Broom, C.E. Buckley, F. Chang, P. Chen, Y.W. Cho, J. C. Crivello, F. Cuevas, W.I.F. David, P.E. de Jongh, R.V. Denys, M. Dornheim, M. Felderhoff, Y. Filinchuk, G.E. Froudakis, D.M. Grant, E.M.A. Gray, B. C. Hauback, T. He, T.D. Humphries, T.R. Jensen, S. Kim, Y. Kojima, M. Latroche, H.W. Li, M.V. Lototskyy, J.W. Makepeace, K.T. Møller, L. Naheed, P. Ngene, D. Noréus, M.M. Nygård, S. Orimo, M. Paskevicius, L. Pasquini, D.B. Ravnsbæk, M.V. Sofianos, T.J. Udovic, T. Vegge, G.S. Walker, C.J. Webb, C. Weidenthaler, C. Zlotea, Materials for hydrogen-based energy storage - past, recent progress and future outlook, J. Alloy. Compd. 827 (2020) 153548.

[1754] J. Huot, F. Cuevas, S. Deledda, K. Edalati, Y. Filinchuk, T. Grosdidier, B. C. Hauback, M. Heere, T.R. Jensen, M. Latroche, S. Sartori, Mechanochemistry of metal hydrides: recent advances, Materials 12 (2019) 2778.

[1755] P. Edalati, R. Floriano, A. Mohammadi, Y. Li, G. Zepon, H.W. Li, K. Edalati, Reversible room temperature hydrogen storage in high-entropy alloy TiZrCrMnFeNi, Scr. Mater. 178 (2020) 387–390.

[1756] R. Floriano, G. Zepon, K. Edalati, G.L.B.G. Fontana, A. Mohammadi, Z. Ma, H. W. Li, R. Contieri, Hydrogen storage in TiZrNbFeNi high entropy alloys,

designed by thermodynamic calculations, Int. J. Hydrog. Energy 45 (2020) 33759–33770.

[1757] R. Floriano, G. Zepon, K. Edalati, G.L.B.G. Fontana, A. Mohammadi, Z. Ma, H. W. Li, R.J. Contieri, Hydrogen storage properties of new A$_3$B$_2$-type TiZrNbCrFe high-entropy alloy, Int. J. Hydrog. Energy 46 (2021) 23757–23766.

[1758] A. Mohammadi, Y. Ikeda, P. Edalati, M. Mito, B. Grabowski, H.W. Li, K. Edalati, High-entropy hydrides for fast and reversible hydrogen storage at room temperature: binding-energy engineering via first-principles calculations and experiments, Acta Mater. 236 (2022) 118117.

[1759] P. Edalati, A. Mohammadi, Y. Li, H.W. Li, R. Floriano, M. Fuji, K. Edalati, High-entropy alloys as anode materials of nickel - metal hydride batteries, Scr. Mater. 209 (2022) 114387.

[1760] S.P. Wang, J. Xu, TiZrNbTaMo high-entropy alloy designed for orthopedic implants: as-cast microstructure and mechanical properties, Mater. Sci. Eng. C 73 (2017) 80–89.

[1761] T. Nagase, M. Todai, T. Hori, T. Nakano, Microstructure of equiatomic and non-equiatomic Ti-Nb-Ta-Zr-Mo high-entropy alloys for metallic biomaterials, J. Alloy. Compd. 753 (2018) 412–421.

[1762] S.J.A. Moniz, S.A. Shevlin, D.J. Martin, Z.X. Guo, J. Tang, Visible-light driven heterojunction photocatalysts for water splitting - a critical review, Energy Environ. Sci. 8 (2015) 731–759.

[1763] A.L. Greer, Metallic glasses, Science 267 (1995) 1947–1953.

[1764] D.V. Louzguine-Luzgin, A. Inoue, Bulk metallic glasses, In: K.H.J. Buschow (Ed.), Handb. Magn. Mater. 21 (2013) 131–171.

[1765] E. Ma, J. Ding, Tailoring structural inhomogeneities in metallic glasses to enable tensile ductility at room temperature, Mater. Today 19 (2016) 568–579.

[1766] X.D. Wang, Q.P. Cao, J.Z. Jiang, H. Franz, J. Schroers, R.Z. Valiev, Y. Ivanisenko, H. Gleiter, H.J. Fecht, Atomic-level structural modifications induced by severe plastic shear deformation in bulk metallic glasses, Scr. Mater. 64 (2011) 81–84.

[1767] D. Gunderov, V. Astanin, Influence of HPT deformation on the structure and properties of amorphous alloys, Metals 10 (2020) 415.

[1768] K. Edalati, Y. Yokoyama, Z. Horita, High-pressure torsion of machining chips and bulk discs of amorphous Zr$_{50}$Cu$_{30}$Al$_{10}$Ni$_{10}$, Mater. Trans. 51 (2010) 23–26.

[1769] T. Czeppe, G. Korznikova, J. Morgiel, A. Korznikov, N.Q. Chinh, P. Ochin, A. Sypień, Microstructure and properties of cold consolidated amorphous ribbons from (NiCu)ZrTiAlSi alloys, J. Alloy. Compd. 483 (2009) 74–77.

[1770] N. Boucharat, R.J. Hebert, H. Rösner, G. Wilde, Deformation-induced nanocrystallization in Al-rich metallic glasses, Solid State Phenom. 114 (2006) 123–132.

[1771] R. Valiev, D. Gunderov, A.P. Zhilyaev, A.G. Popov, V. Pushin, Nanocrystallization induced by severe plastic deformation of amorphous alloys, J. Metastable Nanocryst. Mater. 22 (2004) 21–26.

[1772] R.V. Sundeev, A.M. Glezer, A.V. Shalimova, Are the abilities of crystalline alloys to amorphization upon melt quenching and severe plastic deformation identical or different? Mater. Lett. 175 (2016) 72–74.

[1773] E.I. Teitel', L.S. Metlov, D.V. Gunderov, A.V. Korznikov, On the structural and phase transformations in solids induced by severe plastic deformation, Phys. Met. Metallogr. 113 (2012) 1162–1168.

[1774] F. Meng, K. Tsuchiya, Y. Seiichiro, Yokoyama, Reversible transition of deformation mode by structural rejuvenation and relaxation in bulk metallic glass, Appl. Phys. Lett. 101 (2012) 121914.

[1775] E.V. Boltynjuk, D.V. Gunderov, E.V. Ubyivovk, M.A. Monclús, L.W. Yang, J. M. Molina-Aldareguia, A.I. Tyurin, A.R. Kilmametov, A.A. Churakova, A. Y. Churyumov, R.Z. Valiev, Enhanced strain rate sensitivity of Zr-based bulk metallic glasses subjected to high pressure torsion, J. Alloy. Compd. 747 (2018) 595–602.

[1776] D.V. Gunderov, V.Y. Slesarenko, A.A. Churakova, A.V. Lukyanov, E. P. Soshnikova, V.G. Pushin, R.Z. Valiev, Evolution of the amorphous structure in melt-spun Ti$_{50}$Ni$_{25}$Cu$_{25}$ alloy subjected to high pressure torsion deformation, Intermetallics 66 (2015) 77–81.

[1777] A.I. Bazlov, M.S. Parkhomenko, E.V. Ubyivovk, E.N. Zanaeva, D.V. Gunderov, D. V. Louzguine-Luzgin, Evolution of the Zr$_{42.5}$Cu$_{42.5}$Al$_{10}$Fe$_5$ amorphous alloy structure during the HPT process, J. Non-Cryst. Solids 576 (2022) 121220.

[1778] X. Mu, M.R. Chellali, E. Boltynjuk, D. Gunderov, X. Wang, H. Hahn, C. Kübel, Y. Ivanisenko, L. Velasco, Unveiling the local atomic arrangements in the shear band regions of metallic glass, Adv. Mater. 33 (2021) 2007267.

[1779] B. Sarac, F. Spieckermann, A. Rezvan, C. Gammer, L. Krämer, J.T. Kim, J. Keckes, R. Pippan, J. Eckert, Annealing-assisted high-pressure torsion in Zr$_{55}$Cu$_{30}$Al$_{10}$Ni$_5$ metallic glass, J. Alloy. Compd. 784 (2019) 1323–1333.

[1780] X.L. Bian, D. Zhao, J.T. Kim, D. Şopu, G. Wang, R. Pippan, J. Eckert, Controlling the distribution of structural heterogeneities in severely deformed metallic glass, Mater. Sci. Eng. A 752 (2019) 36–42.

[1781] A.M. Glezer, D.V. Louzguine-Luzgin, I.A. Khriplivets, R.V. Sundeev, D. V. Gunderov, A.I. Bazlov, Y.S. Pogozhev, Effect of high-pressure torsion on the tendency to plastic flow in bulk amorphous alloys based on Zr, Mater. Lett. 256 (2019) 126631.

[1782] S.H. Joo, D.H. Pi, A.D.H. Setyawan, H. Kato, M. Janecek, Y.C. Kim, S. Lee, H. S. Kim, Work-hardening induced tensile ductility of bulk metallic glasses via high-pressure torsion, Sci. Rep. 5 (2015) 9660.

[1783] Y. Dong, S. Liu, J. Biskupek, Q. Cao, X. Wang, J.Z. Jiang, R. Wunderlich, H. J. Fecht, Improved tensile ductility by severe plastic deformation for nano-structured metallic glass, Materials 12 (2019) 1611.

[1784] D.V. Gunderov, A.A. Churakova, E.V. Boltynjuk, E.V. Ubyivovk, V.V. Astanin, R. N. Asfandiyarov, R.Z. Valiev, W. Xioang, J.T. Wang, Observation of shear bands in the Vitreloy metallic glass subjected to HPT processing, J. Alloy. Compd. 800 (2019) 58–63.

[1785] J. Pan, Q. Chen, L. Liu, Y. Li, Softening and dilatation in a single shear band, Acta Mater. 59 (2011) 5146–5158.

[1786] D. Gunderov, Unpublished Work, 2024.

[1787] D. Gunderov, R. Asfandiyarov, V. Titov, S. Gunderova, V. Astanin, V, Some slippage issues in high-pressure torsion using Cu and Ti samples as an example, Materials 16 (2023) 162.

[1788] N. Adachi, Y. Todaka, Y. Yokoyama, M. Umemoto, Cause of hardening and softening in the bulk glassy alloy $Zr_{50}Cu_{40}Al_{10}$ after high-pressure torsion, Mater. Sci. Eng. A 627 (2015) 171–181.

[1789] W. Dmowski, Y. Yokoyama, A. Chuang, Y. Ren, M. Umemoto, K. Tsuchiya, A. Inoue, T. Egami, Structural rejuvenation in a bulk metallic glass induced by severe plastic deformation, Acta Mater. 58 (2010) 429–438.

[1790] D. Gunderov, S. Prokoshkin, A. Churakova, V. Sheremetyev, I. Ramazanov, Effect of HPT and accumulative HPT on structure formation and microhardness of the novel $Ti_{18}Zr_{15}Nb$ alloy, Mater. Lett. 283 (2021) 128819.

[1791] L. Venema, Silicon electronics and beyond, Nature 479 (2011) 309.

[1792] L. Canham, Introductory lecture: origins and applications of efficient visible photoluminescence from silicon-based nanostructures, Faraday Discuss. 222 (2020) 10–81.

[1793] S. Wippermann, Y. He, M. Vörös, G. Galli, Novel silicon phases and nanostructures for solar energy conversion, Appl. Phys. Rev. 3 (2016) 040807.

[1794] G.A. Voronin, C. Pantea, T.W. Zerda, L. Wang, Y. Zhao, In situ x-ray diffraction study of silicon at pressures up to 15.5 GPa and temperatures up to 1073 K, Phys. Rev. B 68 (2003) 020102.

[1795] J. Crain, G.J. Ackland, J.R. Maclean, R.O. Piltz, P.D. Hatton, G.S. Pawley, Reversible pressure-induced structural transitions between metastable phases of silicon, Phys. Rev. B 50 (1994) 13043–13046.

[1796] R.O. Piltz, J.R. Maclean, S.J. Clark, G.J. Ackland, P.D. Hatton, J. Crain, Structure and properties of silicon XII: a complex tetrahedrally bonded phase, Phys. Rev. B 52 (1995) 4072–4085.

[1797] A. Kailer, Y.G. Gogotsi, K.G. Nickel, Phase transformations of silicon caused by contact loading, J. Appl. Phys. 81 (1997) 3057–3063.

[1798] J.E. Bradby, J.S. Williams, J. Wong-Leung, Mechanical deformation in silicon by micro-indentation, J. Mater. Res 16 (2001) 1500–1507.

[1799] J. Jang, M.J. Lance, S. Wen, T.Y. Tsui, G.M. Pharr, Indentation-induced phase transformations in silicon: influences of load, rate and indenter angle on the transformation behavior, Acta Mater. 53 (2005) 1759–1770.

[1800] Y. Ikoma, K. Hayano, K. Edalati, K. Saito, Q. Guo, Z. Horita, T. Aoki, D.J. Smith, Fabrication of nanograined silicon by high-pressure torsion, J. Mater. Sci. 49 (2014) 6565–6569.

[1801] S. Harish, M. Tabara, Y. Ikoma, Z. Horita, Y. Takata, D.G. Cahill, M. Kohno, Thermal conductivity reduction of crystalline silicon by high-pressure torsion, Nanoscale Res. Lett. 9 (2014) 326.

[1802] Y. Fukushima, Y. Ikoma, K. Edalati, B. Chon, D.J. Smith, Z. Horita, High-resolution transmission electron microscopy analysis of bulk nanograined silicon processed by high-pressure torsion, Mater. Charact. 129 (2017) 163–168.

[1803] B. Chon, Y. Ikoma, M. Kohno, J. Shiomi, M.R. McCartney, D.J. Smith, Z. Horita, Impact of metastable phases on electrical properties of Si with different doping concentrations after processing by high-pressure torsion, Scr. Mater. 157 (2018) 120–123.

[1804] Y. Ikoma, B. Chon, T. Yamasaki, K. Takahashi, K. Saito, Q. Guo, Z. Horita, Crystal and electronic structural changes during annealing in severely deformed Si containing metastable phases formed by high-pressure torsion, Appl. Phys. Lett. 113 (2018) 101904.

[1805] C. Shao, K. Matsuda, S. Ju, Y. Ikoma, M. Kohno, J. Shiomi, Phonon transport in multiphase nanostructured silicon fabricated by high-pressure torsion, J. Appl. Phys. 129 (2021) 085101.

[1806] Y. Ikoma, T. Toyota, Y. Ejiri, K. Saito, Q. Guo, Z. Horita, Allotropic phase transformation and photoluminescence of germanium nanograins processed by high-pressure torsion, J. Mater. Sci. 51 (2016) 138–143.

[1807] Y. Ikoma, K. Kumano, K. Edalati, K. Saito, Q. Guo, Z. Horita, Phase transformation of germanium by processing through high-pressure torsion: strain and temperature effects, Philos. Mag. Lett. 97 (2017) 27–34.

[1808] Y. Ikoma, Y. Ejiri, K. Hayano, K. Saito, Q. Guo, Z. Horita, Nanograin formation of GaAs by high-pressure torsion, Philos. Mag. Lett. 94 (2014) 1–8.

[1809] Y. Ikoma, Production of nanograins and metastable phases in bulk Si and Ge semiconductors using severe plastic deformation under high pressure, Mater. Jpn. 60 (2021) 706–711.

[1810] Y. Ikoma, K. Matsuda, K. Yoshida, M. Takaira, M. Kohno, Electric, thermal, and optical properties of severely deformed Si processed by high-pressure torsion, J. Appl. Phys. 132 (2022) 215101.

[1811] Y. Ikoma, T. Yamasaki, T. Masuda, Y. Tange, Y. Higo, Y. Ohishi, M. R. McCartney, D.J. Smith, Z. Horita, Synchrotron X-ray diffraction observation of phase transformation during annealing of Si processed by high-pressure torsion, Philos. Mag. Lett. 101 (2021) 223–231.

[1812] Y. Ikoma, T. Yamasaki, T. Shimizu, M. Takaira, M. Kohno, Q. Guo, M. R. McCartney, D.J. Smith, Y. Arai, Z. Horita, Formation of metastable bc8 phase from crystalline $Si_{0.5}Ge_{0.5}$ by high-pressure torsion, Mater. Charact. 169 (2020) 110590.

[1813] J.Z. Hu, L.D. Merkle, C.S. Menoni, I.L. Spain, Crystal data for high pressure phases of silicon, Phys. Rev. B 34 (1986) 4679–4684.

[1814] B.D. Malone, J.D. Sau, M.L. Cohen, *Ab initio* survey of the electronic structure of tetrahedrally bonded phases of silicon, Phys. Rev. B 78 (2008) 035210.

[1815] H. Zhang, H. Liu, K. Wei, O.O. Kurakevych, Y.L. Godec, Z. Liu, J. Martin, M. Guerrette, G.S. Nolas, T.A. Strobel, BC8 silicon (Si-III) is a narrow-gap semiconductor, Phys. Rev. Lett. 118 (2017) 146601.

[1816] R.H. Wentorf Jr., J.S. Kasper, Two new forms of silicon, Science 139 (1963) 338–339.

[1817] J.M. Besson, E.H. Mokhtari, J. Gonzalez, G. Weill, Electrical properties of semimetallic silicon III and semiconductive silicon IV at ambient pressure, Phys. Rev. Lett. 59 (1987) 473–476.

[1818] G. Serghiou, G. Ji, M. Koch-Müller, N. Odling, H.J. Reichmann, J.P. Wright, P. Johnson, Dense Si_xGe_{1-x} ($0 < x < 1$) materials landscape using extreme conditions and precession electron diffraction, Inorg. Chem. 53 (2014) 5656–5662.

[1819] R. Boeker, The mechanics of plastic deformation in crystalline solids, Ver. dtsch. Ing. Mitt. Forsch. 175 (1915) 1–51.

[1820] P.W. Bridgman, Shearing phenomena at high pressures, particularly in inorganic compounds, Proc. Am. Acad. Arts Sci. 71 (1937) 387–460.

[1821] E.S. Larsen, P.W. Bridgman, Shearing experiments on some selected minerals and mineral combinations, Am. J. Sci. 36 (1938) 81–94.

[1822] D.T. Griggs, E.J. Turner, H.C. Heard, Deformation of rocks at 500°C to 800°C, Geol. Soc. Am. Mere. 79 (1960) 39–104.

[1823] P.M. Bell, Aluminum silicate system: experimental determination of the triple point, Science 139 (1963) 1055–1056.

[1824] C.H. Bates, W.B. White, R. Roy, New high-pressure polymorph of zinc oxide, Science 137 (1963) 993.

[1825] F. Dachille, R. Roy, Effectiveness of shearing stresses in accelerating solid-phase reactions at low temperatures and high pressures, J. Geol. 72 (1964) 243–247.

[1826] R.O. Miller, F.F. Dachille, R. Roy, High-pressure phase-equilibrium studies of CdS and MnS by static and dynamic methods, J. Appl. Phys. 37 (1966) 4913–4918.

[1827] L.F. Vereshchagin, E.V. Zubova, K.P. Burdina, G.L. Aparnikov, Behaviour of oxides under the action of high pressure with simultaneous application of shear stresses, Dokl. Akad. Nauk SSSR 196 (1971) 817–818.

[1828] C.E. Weir, E.R. Lippincott, A. Van Valkenburg, E.N. Bunting, Infrared studies in the 1- to I5-micron region to 30,000 atmospheres, J. Res. Nat. Bur. Stand. Sect. A 63 (1959) 55–62.

[1829] V.D. Blank, Y.S. Konyaev, A.I. Kuznetsov, E.I. Estrin, Diamond chamber for examining the effects of shear deformation on the structure and properties of solids at pressures up to 43 GPa, Instrum. Exp. Tech. 27 (1984) 1240–1242.

[1830] V.V. Aksenenkov, V.D. Blank, Y.S. Konyayev, A.I. Kunzetsov, E.I. Estrin, Investigation of phase equilibria in a diamond chamber for shear at pressures up to 25.0 GPa, Phys. Met. Metallogr. 57 (1984) 159–162.

[1831] M. Wang, F. Zhang, L. Chen, B. Xu, Z. Cui, K. Edalati, Influence of Cu doping and high-pressure torsion on electrochemical performance of lithium-rich cathode material, J. Phys. Conf. Ser. 1750 (2021) 012077.

[1832] X. Fang, Mechanical tailoring of dislocations in ceramics at room temperature: a perspective, J. Am. Cera. Soc. 107 (2024) 1425–1447.

[1833] M.A. Meyers, A. Mishra, D.J. Benson, Mechanical properties of nanocrystalline materials, Prog. Mater. Sci. 51 (2006) 427–556.

[1834] H. Wen, Y. Zhao, Y. Li, O. Ertorer, K.M. Nesterov, R.K. Islamgaliev, R.Z. Valiev, E.J. Lavernia, High-pressure torsion-induced grain growth and detwinning in cryomilled Cu powders, Philos. Mag. 90 (2010) 4541–4550.

[1835] D. Setman, E. Schafler, E. Korznikova, M.J. Zehetbauer, The presence and nature of vacancy type defects in nanometals detained by severe plastic deformation, Mater. Sci. Eng. A 493 (2008) 116–122.

[1836] B. Oberdorfer, B. Lorenzoni, K. Unger, W. Sprengel, M. Zehetbauer, R. Pippan, R. Wurschum, Absolute concentration of free volume-type defects in ultrafine-grained Fe prepared by high-pressure torsion, Scr. Mater. 63 (2010) 452–455.

[1837] V. Beloshenko, A. Voznyak, Y. Voznyak, V. Glasunova, T. Konstantinova, Polyamide-6 structure modification by combined solid-phase extrusion, Polym. Eng. Sci. 52 (2012) 1815–1820.

[1838] I. Vozniak, V. Beloshenko, B. Savchenko, A. Voznyak, Improvement of mechanical properties of polylactide by equal channel multiple angular extrusion, J. Appl. Polym. Sci. 138 (2021) 49720.

[1839] F.E. Mamache, A. Mesbah, F. Zaïri, I. Vozniak, A coupled electro-mechanical homogenization-based model for PVDF-based piezo-composites considering α→β phase transition and interfacial damage, Polymers 15 (2023) 5678.

[1840] I. Vozniak, V. Beloshenko, A. Vozniak, F. Zaïri, A. Galeski, A. Rozanski, Interfaces generation via severe plastic deformation – a new way to multiple shape memory polymer composites, Polymer 267 (2023) 125653.

[1841] A. Pawlak, I. Vozniak, J. Krajenta, V. Beloshenko, A. Galeski, Strain-induced consolidation of partially disentangled polypropylene, Express Polym. Let. 15 (2021) 940–956.

[1842] J.I. Weon, H.J. Sue, Effects of clay orientation and aspect ratio on mechanical behavior of nylon-6 nanocomposite, Polymer 46 (2005) 6325–6334.

[1843] J. Ma, G.P. Simon, G.H. Edward, The effect of shear deformation on nylon-6 and two types of nylon-6/clay nanocomposite, Macromolecules 41 (2008) 409–420.

[1844] V.A. Beloshenko, A.V. Voznyak, Y.V. Voznyak, L.A. Novokshonova, V. G. Grinyov, Effect of simple shear induced orientation process on the morphology and properties of polyolefin/graphite nanoplates composites, Compos. Sci. Techn. 139 (2017) 47–56.

[1845] C.K.Y. Li, Z.Y. Xia, H.J. Sue, Simple shear plastic deformation behavior of polycarbonate plate II. mechanical property characterization, Polymer 41 (2000) 6285–6293.

[1846] Z.Y. Xia, H.J. Sue, T.P. Rieker, Morphological evolution of poly(ethylene terephthalate) during equal channel angular extrusion process, Macromolecules 33 (2000) 8746–8755.

[1847] Z. Xia, H.J. Sue, A.J. Hsieh, J.W.L. Huang, Dynamic mechanical behavior of oriented semicrystalline polyethylene terephthalate, J. Polym. Sci. B 39 (2001) 1394–1403.

[1848] A. Phillips, P. Zhu, G. Edward, Simple shear deformation of polypropylene via the equal channel angular extrusion process, Macromolecules 39 (2006) 5796–5803.

[1849] T. Wang, S. Tang, J. Chen, Effect of processing route on morphology and mechanical behavior of polypropylene in equal-channel angular extrusion, J. Appl. Polym. Sci. 122 (2011) 2146–2158.

[1850] R. Boulahia, F. Zaïri, I. Vozniak, J.M. Gloaguen, Repeated equal-channel angular extrusion of polypropylene: processing routes and back-pressure influence, Mater. Today Commun. 26 (2021) 101754.

[1851] Z. Xia, H.J. Sue, A.J. Hsieh, Impact fracture behavior of molecularly oriented polycarbonate sheets, J. Appl. Polym. Sci. 79 (2001) 2060–2066.

[1852] J.I. Weon, T.S. Creasy, H.J. Sue, A.J. Hsieh, Mechanical behavior of polymethylmethacrylate with molecules oriented via simple shear, Polym. Eng. Sci. 45 (2005) 314–324.

[1853] F. Bouaksa, R.C.M. Ovalle, F. Zaïri, G. Stoclet, M. Naït-Abdelaziz, J.M. Gloaguen, T. Tamine, J.M. Lefebvre, Molecular chain orientation in polycarbonate during equal channel angular extrusion: experiments and simulations, Comput. Mater. Sci. 85 (2014) 244–252.

[1854] H. Li, C. Huang, X. Huang, Structure and properties of polypropylene/high-density polyethylene blends by solid equal-channel angular extrusion, J. Appl. Polym. Sci. 131 (2014) 39759.

[1855] V.A. Beloshenko, V.N. Varyukhin, A.V. Voznyak, Y.V. Voznyak, Polyoxymethylene orientation by equal-channel multiple angular extrusion, J. Appl. Polym. Sci. 126 (2012) 837–844.

[1856] V.A. Beloshenko, A.V. Voznyak, Y.V. Voznyak, G.V. Dudarenko, Equal-channel multiple angular extrusion of polyethylene, J. Appl. Polym. Sci. 127 (2013) 1377–1386.

[1857] V.A. Beloshenko, A.V. Voznyak, Y.V. Voznyak, Control of the mechanical and thermal properties of semicrystalline polymers via a new processing route of the equal channel multiple angular extrusion, Polym. Eng. Sci. 54 (2014) 531–539.

[1858] V. Beloshenko, Y. Beygelzimer, Y. Voznyak, B. Savchenko, V. Dmitrenko, Reinforcing effect caused by equal channel multiple angular extrusion of polymers manufactured by the FDM process: experimental investigation and mathematical modelling, J. Appl. Polym. Sci. 135 (2018) 45727.

[1859] V. Beloshenko, Y. Voznyak, V.M. Mikhal`chuk, Microcalorimetric study of crystallizable polymers subjected to severe plastic deformation, Polym. Sci. Ser. A 56 (2014) 269–274.

[1860] V.A. Beloshenko, A.V. Voznyak, Y. Voznyak, Effects of equal-channel, multiple-angular extrusion on the physical and mechanical properties of glassy polymers, J. Appl. Polym. Sci. 132 (2015) 42180.

[1861] V.A. Beloshenko, A.V. Voznyak, I. Vozniak, B. Savchenko, Effects of orientation ordering of low-density polyethylene-multi-walled carbon nanotubes composites determined by severe plastic deformation, Polym. Eng. Sci. 59 (2019) 714–723.

[1862] V.A. Beloshenko, V.N. Varyukhin, A.V. Voznyak, Y.V. Voznyak, Solid-phase extrusion of polyamide-6 by using combined deformation schemes, Polym. Eng. Sci. 51 (2011) 1092–1098.

[1863] V.A. Beloshenko, A.V. Voznyak, Y.V. Voznyak, S.V. Prokhorenko, "Invar effect" in extruded crystallizable polymers, Dokl. Phys. Chem. 449 (2013) 88–90.

[1864] J.I. Weon, Z.Y. Xia, H.J. Sue, Morphological characterization of nylon-6 nanocomposite following a large-scale shear process, J. Polym. Sci. B 43 (2005) 3555–3566.

[1865] V.A. Beloshenko, A.V. Voznyak, Y.V. Voznyak, B. Savchenko, New approach to production of fiber reinforced polymer hybrid composites, Compos. Part B 112 (2017) 22–30.

[1866] X. Zhang, D. Gao, X. Wu, K. Xia, Bulk plastic materials obtained from processing raw powder of renewable natural polymers via back pressure equal-channel angular consolidation (BP-ECAC), Eur. Polym. J. 44 (2008) 780–792.

[1867] Y. Bai, X. Zhang, K. Xia, High strength biocomposites consolidated from hardwood particles by severe plastic deformation, Cellulose 26 (2019) 1067–1084.

[1868] Y. Bai, X. Zhang, K. Xia, Biocomposites produced from hardwood particles by equal channel angular pressing without additives, J. Compos. Sci. 3 (2019) 36.

[1869] Y. Bai, X. Zhang, K. Xia, Biocomposites produced from hardwood particles by equal channel angular pressing: effects of pre-treatment, J. Compos. Sci. 4 (2020) 181.

[1870] Y. Zhu, X. Wu, Perspective on hetero-deformation induced (HDI) hardening and back stress, Mater. Res. Lett. 7 (2019) 393–398.

[1871] A. Kochendörfer, Theorie der Kristallplastizität, Zeitschrift Für, Phys 108 (1938) 244–264.

[1872] P.M. Hazzledine, P.B. Hirsch, A coplanar Orowan loops model for dispersion hardening, Philos. Mag. 30 (1974) 1331–1351.

[1873] X. Feaugas, On the origin of the tensile flow stress in the stainless steel AISI 316L at 300 K: Back stress and effective stress, Acta Mater. 47 (1999) 3617–3632.

[1874] M. Yang, Y. Pan, F. Yuan, Y. Zhu, X. Wu, Back stress strengthening and strain hardening in gradient structure, Mater. Res. Lett. 4 (2016) 145–151.

[1875] Y. Zhu, Introduction to heterostructured materials: a fast emerging field, Metall. Mater. Trans. A 52 (2021) 4715–4726.

[1876] H. Zhou, C. Huang, X. Sha, L. Xiao, X. Ma, H.W. Höppel, M. Göken, X. Wu, K. Ameyama, X. Han, Y. Zhu, In-situ observation of dislocation dynamics near heterostructured interfaces, Mater. Res. Lett. 7 (2019) 376–382.

[1877] F. Mompiou, D. Caillard, M. Legros, H. Mughrabi, In situ TEM observations of reverse dislocation motion upon unloading in tensile-deformed UFG aluminium, Acta Mater. 60 (2012) 3402–3414.

[1878] H. Mughrabi, Deformation-induced long-range internal stresses and lattice plane misorientations and the role of geometrically necessary dislocations, Philos. Mag. 86 (2006) 4037–4054.

[1879] X. Wu, M. Yang, F. Yuan, G. Wu, Y. Wei, X. Huang, Y. Zhu, Heterogeneous lamella structure unites ultrafine-grain strength with coarse-grain ductility, Proc. Natl. Acad. Sci. USA 112 (2015) 14501–14505.

[1880] C.X. Huang, Y.F. Wang, X.L. Ma, S. Yin, H.W. Höppel, M. Göken, X.L. Wu, H.J. Gao, Y.T. Zhu, Interface affected zone for optimal strength and ductility in heterogeneous laminate, Mater. Today 21 (2018) 713–719.

[1881] Z. Cheng, H. Zhou, Q. Lu, H. Gao, L. Lu, Extra strengthening and work hardening in gradient nanotwinned metals, Science 362 (2018) eaau1925.

[1882] X.L. Wu, P. Jiang, L. Chen, J.F. Zhang, F.P. Yuan, Y.T. Zhu, Synergetic strengthening by gradient structure, Mater. Res. Lett. 2 (2014) 185–191.

[1883] X.X. Dong, Y.F. Shen, Y.T. Zhu, Moderating strain hardening rate to produce high ductility and high strength in a medium carbon TRIP steel, Mater. Res. Lett. 11 (2023) 69–75.

[1884] Y. Liu, M. Xu, L. Xiao, X. Chen, Z. Hu, B. Gao, N. Liang, Y. Zhu, Y. Cao, H. Zhou, Dislocation array reflection enhances strain hardening of a dual-phase heterostructured high-entropy alloy, Mater. Res. Lett. 11 (2023) 638–647.

[1885] J.X. Huang, Y. Liu, T. Xu, X.F. Chen, Q.Q. Lai, L.R. Xiao, Z.Y. Pan, B. Gao, H. Zhou, Y.T. Zhu, Dual-phase hetero-structured strategy to improve ductility of a low carbon martensitic steel, Mater. Sci. Eng. A 834 (2022) 142584.

[1886] L. Romero-Resendiz, M. Naeem, Y.T. Zhu, Heterostructured materials by severe plastic deformation: overview and perspectives, Mater. Trans. 64 (2023) 2346–2360.

[1887] L. Romero-Resendiz, Y. Zhu, T. Yang, J.C. Huang, Heterostructured antimicrobial stainless steel and method for synthesizing, Patent Application, 18/161,907, 2023.

[1888] Q. Liu, B. Wu, M. Li, Y. Huang, L. Li, Heterostructures made of upconversion nanoparticles and metal–organic frameworks for biomedical applications, Adv. Sci. 9 (2022) 2103911.

[1889] O. Lupan, N. Magariu, H. Kruger, A. Sereacov, N. Ababii, S. Railean, L. Zimoch, R. Adelung, S. Hansen, Nano-heterostructured materials - based sensors for safety and biomedical applications, In: Proceeding of the 2022 IEEE 12th International Conference "Nanomaterials: Appllications & Properties" 2022 (2022) 1–4.

[1890] L. Romero-Resendiz, H.J. Kong, T. Zhang, H. Ni, S. Chen, M. Naeem, Y.T. Zhu, Achieving antimicrobial and superior mechanical properties in a scalable and cost-effective heterostructured stainless steel, Mater. Sci. Eng. A 886 (2023) 145676.

[1891] L. Wang, X. Zhang, X. Yu, F. Gao, Z. Shen, X. Zhang, S. Ge, J. Liu, Z. Gu, C. Chen, An all-organic semiconductor C3N4/PDINH heterostructure with advanced antibacterial photocatalytic therapy activity, Adv. Mater. 31 (2019) 1901965.

[1892] B. Li, Y. Luo, Y. Zheng, X. Liu, L. Tan, S. Wu, Two-dimensional antibacterial materials, Prog. Mater. Sci. 130 (2022) 100976.

[1893] S. Miao, T. Liu, Y. Du, X. Zhou, J. Gao, Y. Xie, F. Shen, Y. Liu, Y. Cho, 2D material and perovskite heterostructure for optoelectronic applications, Nanomaterials 12 (2022) 2100.

[1894] P.V. Pham, S.C. Bodepudi, K. Shehzad, Y. Liu, Y. Xu, B. Yu, X. Duan, 2D heterostructures for ubiquitous electronics and optoelectronics: principles, opportunities, and challenges, Chem. Rev. 122 (2022) 6514–6613.

[1895] Y. Li, J. Zhang, Q. Chen, X. Xia, M. Chen, Emerging of heterostructure materials in energy storage: a review, Adv. Mater. 33 (2021) 2100855.

[1896] E. Pomerantseva, Y. Gogotsi, Two-dimensional heterostructures for energy storage, Nat. Energy 2 (2017) 17089.

[1897] C. Liu, X. Gao, Z. Han, Y. Sun, Y. Feng, G. Yu, X. Xi, Q. Zhang, Z. Zou, Core-shell heterostructured and visible-light-driven titanoniobate/TiO2 composite for boosting photodegradation performance, Nanomater 9 (2019) 1503.

[1898] Z.C. Guan, H.P. Wang, X. Wang, J. Hu, R.G. Du, Fabrication of heterostructured β-Bi2O3-TiO2 nanotube array composite film for photoelectrochemical cathodic protection applications, Corros. Sci. 136 (2018) 60–69.

[1899] X. Wu, Y. Zhu, Heterostructured materials, Prog. Mater. Sci. 131 (2023) 101019.

[1900] X. Wu, Y. Zhu, Heterostructured Materials: Novel Materials with Unprecedented Mechanical Properties, 1st Edition, Jenny Stanford, 2021.

[1901] G.Y. Liu, B.R. Sun, C.C. Du, S. Lia, S.W. Xin, T.D. Shen, Hierarchically structured powder metallurgy austenitic stainless steel with exceptional strength and ductility, Mater. Sci. Eng. A 861 (2022) 144351.

[1902] R.M. German, Powder Metallurgy Science, 2nd Edition, Metal Powder Federation, Princeton,, 1994.

[1903] F.B. Swinkels, D.S. Wilkinson, E. Arzt, M.F. Ashby, Mechanisms of hot-isostatic pressing, Acta Met. 31 (1983) 1829–1840.

[1904] K. Ameyama, F. Cazes, H. Couque, G. Dirras, S. Kikuchi, J. Li, F. Mompiou, K. Mondal, D. Orlov, B. Sharma, D. Tingaud, S.K. Vajpai, Harmonic structure, a promising microstructure design, Mater. Res. Lett. 10 (2022) 440–471.

[1905] C.C. Koch, Materials Science and Technology, Volume 15, VCH,, Weinheim, Germany, 1991.

[1906] S. Li, K. Wang, L. Sun, Z. Wang, A simple model for refinement of nanocrystalline grain size during ball milling, Scr. Metall. Mater. 27 (1992) 437–442.

[1907] M. Umemoto, Z. Liu, K. Tsuchiya, The development of research and application of mechanical alloying, J. Jpn. Soc. Powder Powder Met. 48 (2001) 929–934.

[1908] Y. Todaka, M. Umemoto, J. Yin, Z. Liu, K. Tsuchiya, Role of strain gradient on grain refinement by severe plastic deformation, Mater. Sci. Eng. A 462 (2007) 264–268.

[1909] K. Edalati, T. Fujioka, Z. Horita, Evolution of mechanical properties and microstructures with equivalent strain in pure Fe processed by high pressure torsion, Mater. Trans. 50 (2009) 44–50.

[1910] C. Borchers, C. Garve, M. Tiegel, M. Deutges, A. Herz, K. Edalati, R. Pippan, Z. Horita, R. Kirchheim, Nanocrystalline steel obtained by mechanical alloying

of iron and graphite subsequently compacted by high-pressure torsion, Acta Mater. 97 (2015) 207–215.

[1911] Z. Horita, D.J. Smith, M. Furukawa, M. Nemoto, R.Z. Valiev, T.G. Langdon, Evolution of grain boundary structure in submicrometer-grained Al-Mg alloy, Mater. Charact. 37 (1996) 285–294.

[1912] X. Huang, N. Tsuji, N. Hansen, Y. Minamino, Microstructural evolution during accumulative roll-bonding of commercial purity aluminum, Mater. Sci. Eng. A 340 (2003) 265–271.

[1913] N. Tsuji, Y. Ito, Y. Saito, Y. Minamino, Strength and ductility of ultrafine-grained aluminum and iron produced by ARB and annealing, Scr. Mater. 47 (2002) 893–899.

[1914] N. Tsuji, R. Ueji, Y. Minamino, Nanoscale crystallographic analysis of ultrafine grained IF steel fabricated by ARB process, Scr. Mater. 47 (2002) 69–76.

[1915] L. Ghalandari, M.M. Moshksar, High-strength and high-conductive Cu/Ag multilayer produced by ARB, J. Alloy. Compd. 506 (2010) 172–178.

[1916] R. Zheng, Z. Zhang, M. Nakatani, M. Ota, X. Chen, C. Ma, K. Ameyama, Enhanced ductility in harmonic structure designed SUS316L produced by high energy ball milling and hot isostatic sintering, Mater. Sci. Eng. A 674 (2016) 212–220.

[1917] I.S. Yasnikov, A. Vinogradov, Y. Estrin, Revisiting the Conside`re criterion from the viewpoint of dislocation theory fundamentals, Scr. Mater. 76 (2014) 37–40.

[1918] X.T. Fang, G.Z. He, C. Zheng, X.L. Ma, D. Kaoumi, Y.S. Li, Y.T. Zhu, Effect of heterostructure and hetero-deformation induced hardening on the strength and ductility of brass, Acta Mater. 186 (2020) 644–655.

[1919] S.C. Song, J. Moon, H.S. Kim, Hetero-deformation-induced strengthening of multi-phase Cu–Fe–Mn medium entropy alloys by dynamic heterostructuring, Mater. Sci. Eng. A 799 (2021) 140275.

[1920] F.J. Guo, Y.F. Wang, M.S. Wang, Q. He, H. Ran, C.X. Huang, Y.T. Zhu, Hetero-deformation induced strengthening and toughening of pure iron with inverse and multi-gradient structures, Mater. Sci. Eng. A 782 (2020) 139256.

[1921] H. Liu, B. Gao, Y. Yang, M. Xu, X. Li, C. Li, H. Pan, J. Yang, X. Hao Zhou, Y. Zhu, Zhu, Strain hardening behavior and microstructure evolution of gradient-structured Cu-Al alloys with low stack fault energy, J. Mater. Res. Technol. 19 (2022) 220–229.

[1922] T.H. Chou, W.P. Li, H.W. Chang, X.H. Du, W.S. Chuang, T. Yang, Y.T. Zhu, J. C. Huang, Quantitative analysis of hetero-deformation induced strengthening in heterogeneous grain structure, Int. J. Plast. 159 (2022) 103482.

[1923] J. Li, J. Liu, G. Dirras, K. Ameyama, F. Cazes, M. Ota, A three-dimensional multi-scale polycrystalline plasticity model coupled with damage for pure Ti with harmonic structure design, Int. J. Plast. 100 (2018) 192–207.

[1924] H.K. Park, K. Ameyama, J. Yoo, H. Hwang, H.S. Kim, Additional hardening in harmonic structured materials by strain partitioning and back stress, Mater. Res. Lett. 6 (2018) 261–267.

[1925] R. Zheng, M. Liu, Z. Zhang, K. Ameyama, C. Ma, Towards strength-ductility synergy through hierarchical microstructure design in an austenitic stainless steel, Scr. Mater. 169 (2019) 76–81.

[1926] S.K. Vajpai, M. Ota, Z. Zhang, K. Ameyama, Three-dimensionally gradient harmonic structure design: an integrated approach for high performance structural materials, Mater. Res. Lett. 4 (2016) 191–197.

[1927] S.K. Vajpai, M. Ota, T. Watanabe, R. Maeda, T. Sekiguchi, T. Kusaka, K. Ameyama, The development of high performance Ti-6Al-4V alloy via a unique microstructural design with bimodal grain size distribution, Metall. Mater. Trans. A 46 (2015) 903–914.

[1928] G. Dirras, D. Ueda, A. Hocini, D. Tingaud, K. Ameyama, Cyclic shear behavior of conventional and harmonic structure-designed Ti-25Nb-25Zr β-titanium alloy: back-stress hardening and twinning inhibition, Scr. Mater. 138 (2017) 44–47.

[1929] G. Dirras, M. Ota, D. Tingaud, K. Ameyama, T. Sekiguchi, Microstructure evolution during direct impact loading of commercial purity α-titanium with harmonic structure design, Mater. Technol. 103 (2015) 311.

[1930] M. Ota Kawabata, K. Ameyama, Harmonic structure design by high pressure gas jet milling process, J. Jpn. Soc. Tech. Plasticity 58 (2017) 563–567.

[1931] G. Li, S. Morinaka, M. Kawabata, C. Ma, K. Ameyama, Improvement of strength with maintaining ductility of harmonic structure pure copper by cold rolling and annealing process, Proc. Manuf. 15 (2018) 1641–1648.

[1932] G. Li, J. Jiang, H. Ma, R. Zheng, S. Gao, S. Zhao, C. Ma, K. Ameyama, B. Ding, X. Li, Superior strength–ductility synergy in three-dimensional heterogeneous-nanostructured metals, Acta Mater. 256 (2023) 119143.

[1933] M. Nagata, N. Horikawa, M. Kawabata, K. Ameyama, Effects of microstructure on mechanical properties of harmonic structure designed pure Ni, Mater. Trans. 60 (2019) 1914–1920.

[1934] D. Orlov, R. Kulagin, Y. Beygelzimer, Strain partitioning and back-stress evaluation in harmonic-structure materials, Mater. Lett. 275 (2020) 128126.

[1935] Z. Zhang, H. Ma, R. Zheng, Q. Hu, M. Nakatani, M. Ota, G. Chen, X. Chen, C. Ma, K. Ameyama, Fatigue behavior of a harmonic structure designed austenitic stainless steel under uniaxial stress loading, Mater. Sci. Eng. A 707 (2017) 287–294.

[1936] S.K. Vajpai, C. Sawangrat, O. Yamaguchi, O.P. Ciuca, K. Ameyama, Effect of bimodal harmonic structure design on the deformation behaviour and mechanical properties of Co-Cr-Mo alloy, Mater. Sci. Eng. C 58 (2016) 1008–1015.

[1937] X. Wang, F. Cazes, J. Li, A. Hocini, K. Ameyama, G. Dirras, A 3D crystal plasticity model of monotonic and cyclic simple shear deformation for commercial-purity polycrystalline Ti with a harmonic structure, Mech. Mater. 128 (2019) 117–128.

[1938] S. Kikuchi, Y. Nukui, Y. Nakatsuka, Y. Nakai, M. Nakatani, M.O. Kawabata, K. Ameyama, Effect of bimodal harmonic structure on fatigue properties of austenitic stainless steel under axial loading, Int. J. Fatigue 127 (2019) 222–228.

[1939] S. Kikuchi, H. Kubozono, Y. Nukui, Y. Nakai, A. Ueno, M.O. Kawabata, K. Ameyama, Statistical fatigue properties and small fatigue crack propagation in bimodal harmonic structured Ti-6Al-4V alloy under four-point bending, Mater. Sci. Eng. A 711 (2018) 29–36.

[1940] P.K. Rai, S. Shekhar, K. Yagi, K. Ameyama, K. Mondal, Fretting wear mechanism for harmonic, non-harmonic and conventional 316L stainless steels, Wear 424–425 (2019) 23–32.

[1941] Q. Pan, L. Lu, Synthesis and deformation mechanics of gradient nanostructured materials, NSO 1 (2022) 20220010.

[1942] X. Li, L. Lu, J. Li, X. Zhang, H. Gao, Mechanical properties and deformation mechanisms of gradient nanostructured metals and alloys, Nat. Rev. Mater. 5 (2020) 706–723.

[1943] M. Vamshi, S.K. Singh, N. Sateesh, D.S. Nagaraju, R. Subbiah, A review on influence of carburizing on ferritic stainless steel, Mater. Today Proc. 26 (2020) 937–943.

[1944] F. Yin, G.J. Cheng, R. Xu, K. Zhao, Q. Li, J. Jian, S. Hu, S. Sun, L. An, Q. Han, Ultrastrong nanocrystalline stainless steel and its Hall-Petch relationship in the nanoscale, Scr. Mater. 155 (2018) 26–31.

[1945] H. Wei, Y. Cui, H. Cui, C. Zhou, L. Hou, Y.H. Wei, Evolution of grain refinement mechanism in Cu-4wt%Ti alloy during surface mechanical attrition treatment, J. Alloy. Compd. 763 (2018) 835–843.

[1946] Y. Lin, J. Pan, H.F. Zhou, H.J. Gao, Y. Li, Mechanical properties and optimal grain size distribution profile of gradient grained nickel, Acta Mater. 153 (2018) 279–289.

[1947] Y. Wei, Y. Li, L. Zhu, Y. Liu, X. Lei, G. Wang, Y. Wu, Z. Mi, J. Liu, H. Wang, H. Gao, Evading the strength-ductility trade-off dilemma in steel through gradient hierarchical nanotwins, Nat. Commun. 5 (2014) 3580.

[1948] K. Lu, Stabilizing nanostructures in metals using grain and twin boundary architectures, Nat. Rev. Mater. 1 (2016) 16019.

[1949] X. Liu, Y. Liu, B. Jin, Y. Lu, J. Lu, Microstructure evolution and mechanical properties of a SMATed Mg alloy under in situ SEM tensile testing, J. Mater. Sci. Technol. 33 (2017) 224–230.

[1950] Q. Pan, L. Zhang, R. Feng, Q. Lu, K. An, A.C. Chuang, J.D. Poplawsky, P.K. Liaw, L. Lu, Gradient cell–structured high-entropy alloy with exceptional strength and ductility, Science 374 (2021) 984–989.

[1951] M. Novelli, P. Bocher, T. Grosdidier, Effect of cryogenic temperatures and processing parameters on gradient-structure of a stainless steel treated by ultrasonic surface mechanical attrition treatment, Mater. Charact. 139 (2018) 197–207.

[1952] J. Ning, B. Xu, M. Sun, C. Zhao, Y. Feng, W. Tong, Strain hardening and tensile behaviors of gradient structure Mg alloys with different orientation relationships, Mater. Sci. Eng. A 735 (2018) 275–287.

[1953] M. Duan, L. Luo, Y. Liu, Microstructural evolution of AZ31 Mg alloy with surface mechanical attrition treatment: grain and texture gradient, J. Alloy. Compd. 823 (2020) 153691.

[1954] J. Moering, X. Ma, G. Chen, P. Miao, G. Li, G. Qian, S. Mathaudhu, Y. Zhu, The role of shear strain on texture and microstructural gradients in low carbon steel processed by surface mechanical attrition treatment, Scr. Mater. 108 (2015) 100–103.

[1955] C. Li, X. Li, Z. Fu, H. Pan, Y. Gong, X. Zhu, An overview on recent works of heterostructured materials fabricated by surface mechanical attrition treatment, Mater. Trans. 64 (2023) 1429–1440.

[1956] S.S. Chakravarthy, W.A. Curtin, Stress-gradient plasticity, Proc. Natl. Acad. Sci. USA 108 (2011) 15716–15720.

[1957] J. Li, S. Chen, X. Wu, A.K. Soh, A physical model revealing strong strain hardening in nano-grained metals induced by grain size gradient structure, Mater. Sci. Eng. A 620 (2015) 16–21.

[1958] Q. Cheng, Y. Wang, W. Wei, F. Guo, Q. He, M. Wang, C. Huang, Superior strength-ductility synergy achieved by synergistic strengthening and strain delocalization in a gradient-structured high-manganese steel, Mater. Sci. Eng. A 825 (2021) 141853.

[1959] Z. Zeng, X. Li, D. Xu, L. Lu, H. Gao, T. Zhu, Gradient plasticity in gradient nano-grained metals, Extrem. Mech. Let. 8 (2016) 213–219.

[1960] Y. Wang, G. Yang, W. Wang, X. Wang, Q. Li, Y. Wei, Optimal stress and deformation partition in gradient materials for better strength and tensile ductility: a numerical investigation, Sci. Rep. 7 (2017) 10954.

[1961] C.Y. He, X.F. Yang, H. Chen, Y. Zhang, G.J. Yuan, Y.F. Jia, X.C. Zhang, Size-dependent deformation mechanisms in copper gradient nano-grained structure: a molecular dynamics simulation, Mater. Today Commun. 31 (2022) 103198.

[1962] X. Wu, Y. Zhu, Heterogeneous materials: a new class of materials with unprecedented mechanical properties, Mater. Res. Lett. 5 (2017) 527–532.

[1963] S. Qu, X.H. An, H.J. Yang, C.X. Huang, G. Yang, Q.S. Zang, Z.G. Wang, S.D. Wu, Z.F. Zhang, Microstructural evolution and mechanical properties of Cu–Al alloys subjected to equal channel angular pressing, Acta Mater. 57 (2009) 1586–1601.

[1964] F. Yuan, D. Yan, J. Sun, L. Zhou, Y. Zhu, X. Wu, Ductility by shear band delocalization in the nano-layer of gradient structure, Mater. Res. Lett. 7 (2018) 12–17.

[1965] H. Wu, G. Fan, An overview of tailoring strain delocalization for strength-ductility synergy, Prog. Mater. Sci. 113 (2020) 100675.

[1966] Y.F. Wang, C.X. Huang, Q. He, F.J. Guo, M.S. Wang, L.Y. Song, Y.T. Zhu, Heterostructure induced dispersive shear bands in heterostructured Cu, Scr. Mater. 170 (2019) 76–80.

[1967] X. Zhang, Heterostructures: new opportunities for functional materials, Mater. Res. Lett. 8 (2019) 49–59.

[1968] M. Umemoto, Y. Todaka, K. Tsuchiya, Formation of nanocrystalline structure in steels by air blast shot peening, Mater. Trans. 44 (2003) 1488–1493.

[1969] J.L. Liu, M. Umemoto, Y. Todaka, K. Tsuchiya, Formation of a nanocrystalline surface layer on steels by air blast shot peening, J. Mater. Sci. 42 (2007) 7716–7720.

[1970] O. Unal, R. Varol, Surface severe plastic deformation of AISI 304 via conventional shot peening, severe shot peening and repeening, Appl. Surf. Sci. 351 (2015) 289–295.

[1971] K. Lu, J. Lu, Nanostructured surface layer on metallic materials induced by surface mechanical attrition treatment, Mater. Sci. Eng. A 375–377 (2004) 38–45.

[1972] N. Tao, H. Zhang, J. Lu, K. Lu, Development of nanostructures in metallic materials with low stacking fault energies during surface mechanical attrition treatment (SMAT), Mater. Trans. 44 (2003) 1919–1925.

[1973] G. Liu, J. Lu, K. Lu, Surface nanocrystallization of 316L stainless steel induced by ultrasonic shot peening, Mater. Sci. Eng. A 286 (2000) 91–95.

[1974] J. Zhou, D. Retraint, Z. Sun, P. Kanouté, Comparative study of the effects of surface mechanical attrition treatment and conventional shot peening on low cycle fatigue of a 316L stainless steel, Surf. Coat. Technol. 349 (2018) 556–566.

[1975] L. Carneiro, X. Wang, Y. Jiang, Cyclic deformation and fatigue behavior of 316L stainless steel processed by surface mechanical rolling treatment, Int. J. Fatigue 134 (2020) 105469.

[1976] C.S. Montross, T. Wei, L. Ye, G. Clark, Y.W. Mai, Laser shock processing and its effects on microstructure and properties of metal alloys: a review, Int. J. Fatigue 24 (2002) 1021–1036.

[1977] Y.K. Zhang, J.Z. Lu, X.D. Ren, H.B. Yao, H.X. Yao, Effect of laser shock processing on the mechanical properties and fatigue lives of the turbojet engine blades manufactured by LY2 aluminum alloy, Mater. Des. 30 (2009) 1697–1703.

[1978] J. Zhao, X. Pan, J. Li, Z. Huang, Q. Kan, G. Kang, L. Zhou, X. Zhang, Laser shock peened Ti-6Al-4 V alloy: experiments and modeling, Int. J. Mech. Sci. 213 (2022) 106874.

[1979] H.F. Lu, K.Y. Luo, L.J. Wu, C.Y. Cui, J.Z. Lu, Effects of service temperature on tensile properties and microstructural evolution of CP titanium subjected to laser shock peening, J. Alloy. Compd. 770 (2019) 732–741.

[1980] P.K. Dwivedi, R. Vinjamuri, A.K. Rai, P. Ganesh, K. Ranganathan, K.S. Bindra, K. Dutta, Effect of laser shock peening on ratcheting strain accumulation, fatigue life and bulk texture evolution in HSLA steel, Int. J. Fatigue 163 (2022) 107033.

[1981] K. Yang, Q. Huang, B. Zhong, Q. Wang, Q. Chen, Y. Chen, N. Su, H. Liu, Enhanced extra-long life fatigue resistance of a bimodal titanium alloy by laser shock peening, Int. J. Fatigue 141 (2020) 105868.

[1982] E. Maawad, H.G. Brokmeier, L. Wagner, Y. Sano, C. Genzel, Investigation on the surface and near-surface characteristics of Ti-2.5Cu after various mechanical surface treatments, Surf. Coat. Technol. 205 (2011) 3644–3650.

[1983] H. Gu, P. Yan, L. Jiao, S. Chen, Y. Song, S. Zou, X. Wang, Effect of laser shock peening on boring hole surface integrity and conformal contact fretting fatigue life of Ti-6Al-4 V alloy, Int. J. Fatigue 166 (2023) 107241.

[1984] Z. Sun, D. Retraint, T. Baudin, A.L. Helbert, F. Brisset, M. Chemkhi, J. Zhou, P. Kanouté, Experimental study of microstructure changes due to low cycle fatigue of a steel nanocrystallised by surface mechanical attrition treatment (SMAT), Mater. Charact. 124 (2017) 117–121.

[1985] Z. Guo, J. Zhou, Z. Sun, D. Retraint, B. Panicaud, Modelling mechanical behaviour of a gradient-microstructured material obtained by surface mechanical attrition treatment accounting for residual stresses, Mech. Mater. 184 (2023) 104713.

[1986] H. Liu, Y. We, C.K.I. Tan, D.T. Ardi, D.C.C. Tan, C.J.J. Lee, XRD and EBSD studies of severe shot peening induced martensite transformation and grain refinements in austenitic stainless steel, Mater. Charact. 168 (2020) 110574.

[1987] Y.B. Lei, Z.B. Wang, J.L. Xu, K. Lu, Simultaneous enhancement of stress- and strain-controlled fatigue properties in 316L stainless steel with gradient nanostructure, Acta Mater. 168 (2019) 133–142.

[1988] Y. Todaka, M. Umemoto, K. Tsuchiya, Comparison of nanocrystalline surface layer in steels formed by air blast and ultrasonic shot peening, Mater. Trans. 45 (2005) 376–379.

[1989] M.S. Kim, S.H. Park, Y.S. Pyun, D.S. Shim, Optimization of ultrasonic nanocrystal surface modification for surface quality improvement of directed energy deposited stainless steel 316L, J. Mater. Res. Technol. 9 (2020) 15102–15122.

[1990] G.H. Farrahi, J.L. Lebrun, D. Couratin, Effect of shot peening on residual stress and fatigue life of a spring steel, Fatigue Fract. Eng. Mater. Struct. 18 (1995) 211–220.

[1991] R.K. Nalla, I. Altenberger, U. Noster, G.Y. Liu, B. Scholtes, R.O. Ritchie, On the influence of mechanical surface treatments-deep rolling and laser shock peening-on the fatigue behavior of Ti-6Al-4V at ambient and elevated temperatures, Mater. Sci. Eng. A 355 (2003) 216–230.

[1992] M.A.S. Torres, H.J.C. Voorwald, An evaluation of shot peening, residual stress and stress relaxation on the fatigue life of AISI 4340 steel, Int. J. Fatigue 24 (2002) 877–886.

[1993] J. Zhou, Z. Sun, Numerical characterization of shot peening induced work hardening gradient and verification based on FEM analysis, Int. J. Solids Struct. 244– 245 (2022) 111586.

[1994] J. Zhou, X. Xu, Z. Sun, D. Retraint, X. Zhang, Predicting gradient mechanical behaviour of a shot-peened structure, Int. J. Solids Struct. 262–263 (2023) 112063.

[1995] J. Zhou, Z. Sun, P. Kanouté, D. Retraint, Effect of surface mechanical attrition treatment on low cycle fatigue properties of an austenitic stainless steel, Int. J. Fatigue 103 (2017) 309–317.

[1996] S. Kumar, K. Chattopadhyay, V. Singh, Effect of ultrasonic shot peening on LCF behavior of the Ti–6Al–4V alloy, J. Alloy. Compd. 724 (2017) 187–197.

[1997] R.C. McClung, A literature survey on the stability and significance of residual stresses during fatigue, Fatigue Fract. Eng. Mater. Struct. 30 (2007) 173–205.

[1998] K. Dalaei, B. Karlsson, L.E. Svensson, Stability of shot peening induced residual stresses and their influence on fatigue lifetime, Mater. Sci. Eng. A 528 (2011) 1008–1015.

[1999] J.W. Tian, L. Shaw, P.K. Liaw, K. Dai, On the ductility of a surface severely plastically deformed nickel alloy, Mater. Sci. Eng. A 498 (2008) 216–224.

[2000] H. Mughrabi, H.W. Höppel, M. Kautz, Fatigue and microstructure of ultrafine-grained metals produced by severe plastic deformation, Scr. Mater. 51 (2004) 807–812.

[2001] H.S. Ho, W.L. Zhou, Y. Li, K.K. Liu, E. Zhang, Low-cycle fatigue behavior of austenitic stainless steels with gradient structured surface layer, Int. J. Fatigue 134 (2020) 105481.

[2002] Z. Sun, J. Zhou, D. Retraint, Mechanical properties of metallic materials processed by surface severe plastic deformation, Mater. Trans. 64 (2023) 1739–1753.

[2003] C.A. Rodopoulos, S.A. Curtis, E.R. De Los Rios, J. SolisRomero, Optimisation of the fatigue resistance of 2024-T351 aluminium alloys by controlled shot peening - methodology, results and analysis, Int. J. Fatigue 26 (2004) 849–856.

[2004] T. Gao, Z. Sun, H. Xue, D. Retraint, Effect of surface mechanical attrition treatment on high cycle and very high cycle fatigue of a 7075-T6 aluminium alloy, Int. J. Fatigue 139 (2020) 105798.

[2005] S.A. Namjoshi, V.K. Jain, S. Mall, Effects of shot-peening on fretting-fatigue behavior of Ti-8Al-4V, J. Eng. Mater. Technol. 124 (2002) 222–228.

[2006] Z. Qin, B. Li, R. Chen, H. Zhang, H. Xue, C. Yao, L. Tan, Effect of shot peening on high cycle and very high cycle fatigue properties of Ni-based superalloys, Int. J. Fatigue 168 (2023) 107429.

[2007] M.K. Khan, Y.J. Liu, Q.Y. Wang, Y.S. Pyun, R. Kayumov, Effect of ultrasonic nanocrystal surface modification on the characteristics of AISI 310 stainless steel up to very high cycle fatigue, Fatigue Fract. Eng. Mater. Struct. 39 (2016) 427–438.

[2008] Q.Y. Wang, C. Bathias, N. Kawagoishi, Q. Chen, Effect of inclusion on subsurface crack initiation and gigacycle fatigue strength, Int. J. Fatigue 24 (2002) 1269–1274.

[2009] K. Nishijima, Stepwise S-N curve and fish-eye failure in gigacycle fatigue, Fatigue Fract. Eng. Mater. Struct. 22 (1999) 601–607.

[2010] Z.B. Wang, N.R. Tao, S. Li, W. Wang, G. Liu, J. Lu, K. Lu, Effect of surface nanocrystallization on friction and wear properties in low carbon steel, Mater. Sci. Eng. A 352 (2003) 144–149.

[2011] J. Zhang, Y. Jian, X. Zhao, D. Meng, F. Pan, Q. Han, The tribological behavior of a surface-nanocrystallized magnesium alloy AZ31 sheet after ultrasonic shot peening treatment, J. Magnes. Alloy. 9 (2021) 1187–1200.

[2012] A. Amanov, O.V. Penkov, Y.S. Pyun, D.E. Kim, Effects of ultrasonic nanocrystalline surface modification on the tribological properties of AZ91D magnesium alloy, Tribol. Int. 54 (2012) 106–113.

[2013] Y.S. Zhang, Z. Han, K. Wang, K. Lu, Friction and wear behaviors of nanocrystalline surface layer of pure copper, Wear 260 (2006) 942–948.

[2014] J. Zou, Y. Liang, Y. Jiang, C. Yin, C. Huang, D. Liu, Z. Zhu, Y. Wu, Fretting fatigue mechanism of 40CrNiMoA steel subjected to the ultrasonic surface rolling process: the role of the gradient structure, Int. J. Fatigue 167 (2022) 107383.

[2015] J. Wang, Y. Gao, X. Wei, Investigations of the effects of combination treatments on the fretting fatigue resistance of GH4169 superalloy at an elevated temperature, Surf. Coat. Technol. 426 (2021) 127758.

[2016] J. Li, S. Chen, W. Zhu, Y. Zhao, L. Liu, Z. Wang, H. Pan, Microstructural response and surface mechanical properties of TC6 titanium alloy subjected to laser peening with different laser energy, Opt. Laser Technol. 158 (2023) 108836.

[2017] S. Alikhani Chamgordani, R. Miresmaeili, M. Aliofkhazraei, Improvement in tribological behavior of commercial pure titanium (CP-Ti) by surface mechanical attrition treatment (SMAT), Tribol. Int. 119 (2018) 744–752.

[2018] W. Yan, L. Fang, K. Sun, Y. Xu, Effect of surface work hardening on wear behavior of Hadfield steel, Mater. Sci. Eng. A 460–461 (2007) 542–549.

[2019] Y. Liu, B. Jin, D.J. Li, X.Q. Zeng, J. Lu, Wear behavior of nanocrystalline structured magnesium alloy induced by surface mechanical attrition treatment, Surf. Coat. Technol. 261 (2015) 219–226.

[2020] T. Hanlon, E.D. Tabachnikova, S. Suresh, Fatigue behavior of nanocrystalline metals and alloys, Int. J. Fatigue 27 (2005) 1147–1158.

[2021] L. Wagner, M. Mhaede, M. Wollmann, I. Altenberger, Y. Sano, Surface layer properties and fatigue behavior in Al 7075-T73 and Ti-6Al-4V Comparing results after laser peening; shot peening and ball-burnishing, Int. J. Struct. Integr. 2 (2011) 185–199.

[2022] M. Benedetti, V. Fontanari, P. Scardi, C.L.A. Ricardo, M. Bandini, Reverse bending fatigue of shot peened 7075-T651 aluminium alloy: the role of residual stress relaxation, Int. J. Fatigue 31 (2009) 1225–1236.

[2023] Y.K. Gao, X.R. Wu, Experimental investigation and fatigue life prediction for 7475-T7351 aluminum alloy with and without shot peening-induced residual stresses, Acta Mater. 59 (2011) 3737–3747.

[2024] Y. Xiang, Y. Liu, Mechanism modelling of shot peening effect on fatigue life prediction, Fatigue Fract. Eng. Mater. Struct. 33 (2010) 116–125.

[2025] J. Zhou, Z. Sun, P. Kanouté, D. Retraint, Reconstruction of residual stress and work hardening and their effects on the mechanical behaviour of a shot peened structure, Mech. Mater. 127 (2018) 100–111.

[2026] V. Schulze, F. Bleicher, P. Groche, Y.B. Guo, Y.S. Pyun, Surface modification by machine hammer peening and burnishing, CIRP Ann. Manuf. Technol. 65 (2016) 809–832.

[2027] S. Bagheri, M. Guagliano, Review of shot peening processes to obtain nanocrystalline surfaces in metal alloys, Surf. Eng. 25 (2009) 3–14.

[2028] Y. Samih, B. Beausir, B. Bolle, T. Grosdidier, In-depth quantitative analysis of the microstructures produced by surface mechanical attrition treatment (SMAT), Mater. Charact. 83 (2013) 129–138.

[2029] G. Proust, D. Retraint, M. Chemkhi, A. Roos, C. Demangel, Electron backscatter diffraction and transmission Kikuchi diffraction analysis of an austenitic stainless steel subjected to surface mechanical attrition treatment and plasma nitriding, Microsc. Microanal. 21 (2015) 919–926.

[2030] S. Bajda, W. Ratuszek, M. Krzyzanowski, D. Retraint, Inhomogeneity of plastic deformation in austenitic stainless steel after surface mechanical attrition treatment, Surf. Coat. Technol. 329 (2017) 202–211.

[2031] S. Shahrezaei, Y. Sun, S.N. Mathaudhu, Strength-ductility modulation via surface severe plastic deformation and annealing, Mater. Sci. Eng. A 761 (2019) 138023.

[2032] J. Peng, Z. Zhang, P. Guo, Z. Liu, Y. Li, W. Zhou, Y. Wu, The effect of surface mechanical attrition treatment on texture evolution and mechanical properties of AZ31 magnesium alloy, Mater. Charact. 148 (2019) 26–34.

[2033] M. Novelli, R. Chulist, W. Skrotzki, E.P. George, T. Grosdidier, Surface hardening of high- and medium- entropy alloys by mechanical attrition at room and cryogenic temperatures Surface hardening of high- and medium-entropy alloys by mechanical attrition at room and cryogenic temperatures, Appl. Phys. Lett. 119 (2021) 201912.

[2034] P. Maurel, L. Weiss, P. Bocher, T. Grosdidier, Effects of SMAT at cryogenic and room temperatures on the kink band and martensite formations with associated fatigue resistance in a β-metastable titanium alloy, Mater. Sci. Eng. A 803 (2020) 140618.

[2035] M.X. Yang, R.G. Li, P. Jiang, F.P. Yuan, Y.D. Wang, Y.T. Zhu, X.L. Wu, Residual stress provides significant strengthening and ductility in gradient structured materials, Mater. Res. Lett. 7 (2019) 433–438.

[2036] P. Maurel, L. Weiss, T. Grosdidier, P. Bocher, How does surface integrity of nanostructured surfaces induced by severe plastic deformation influence fatigue behaviors of Al alloys with enhanced precipitation? Int. J. Fatigue 140 (2020) 105792.

[2037] R. Chen, H. Xue, B. Li, Comparison of SP, SMAT, SMRT, LSP, and UNSM based on treatment on the fatigue properties of metals in the HCF and VHCF regimes, Metals 12 (2022) 642.

[2038] T. Grosdidier, M. Novelli, Recent developments in the application of surface mechanical attrition treatments for improved gradient structures: processing parameters and surface reactivity, Mater. Trans. 60 (2019) 1344–1355.

[2039] W.P. Tong, C.Z. Liu, W. Wang, N.R. Tao, Z.B. Wang, L. Zuo, J.C. He, Gaseous nitriding of iron with a nanostructured surface layer, Scr. Mater. 57 (2007) 533–536.

[2040] W.P. Tong, C.S. He, J.C. He, L. Zuo, N.R. Tao, Z.B. Wang, Strongly enhanced nitriding kinetics by means of grain refinement, Appl. Phys. Lett. 89 (2006) 021918.

[2041] T. Thiriet, T. Czerwiec, D. Hertz, G. Marcos, T. Toll-Duchanoy, S. Migot, B. Brugier, M. Foucault, T. Belmonte, Nitrogen diffusion at low temperature in fcc materials deformed by attrition peening, Defect Diffus. Forum 323–325 (2012) 471–476.

[2042] A.M. Gatey, S.S. Hosmani, C.A. Figueroa, S.B. Arya, R.P. Singh, Role of surface mechanical attrition treatment and chemical etching on plasma nitriding behavior of AISI 304L steel, Surf. Coat. Technol. 304 (2016) 413–424.

[2043] Y. Samih, M. Novelli, T. Thiriet, B. Bolle, N. Allain, J.J. Fundenberger, G. Marcos, T. Czerwiec, T. Grosdidier, Plastic deformation to enhance plasma-assisted nitriding: on surface contamination induced by surface mechanical attrition treatment, IOP Conf. Ser. Mater. Sci. Eng. 63 (2014) 012020.

[2044] M. Chemkhi, D. Retraint, A. Roos, C. Demangel, Role and effect of mechanical polishing on the enhancement of the duplex mechanical attrition/plasma nitriding treatment of AISI 316L steel, Surf. Coat. Technol. 325 (2017) 454–461.

[2045] T. Olugbade, C. Liu, J. Lu, Enhanced passivation layer by Cr diffusion of 301 stainless steel facilitated by SMAT, Adv. Eng. Mater. 21 (2019) 1900125.

[2046] L. Wen, Y. Wang, Y. Jin, X. Ren, Comparison of corrosion behaviour of nanocrystalline 2024-T4 Al alloy processed by surface mechanical attrition treatment with two different mediums, Corros. Eng. Sci. Technol. 50 (2015) 425–432.

[2047] K. Edalati, M. Novelli, S. Itano, H.W. Li, E. Akiba, Z. Horita, T. Grosdidier, Effect of gradient-structure versus uniform nanostructure on hydrogen storage of Ti-V-Cr alloys: Investigation using ultrasonic SMAT and HPT processes, J. Alloy. Compd. 737 (2018) 337–346.

[2048] M. Novelli, K. Edalati, S. Itano, H.W. Li, E. Akiba, Z. Horita, T. Grosdidier, Microstructural details of hydrogen diffusion and storage in Ti–V–Cr alloys activated through surface and bulk severe plastic deformation, Int. J. Hydrog. Energy 45 (2020) 5326–5336.

[2049] N.E. Laadel, M. El Mansori, N. Kang, S. Marlin, Y. Boussant-Roux, Permeation barriers for hydrogen embrittlement prevention in metals – a review on mechanisms, materials suitability and efficiency, Int. J. Hydrog. Energy 47 (2022) 32707–32731.

[2050] T. An, S. Li, J. Qu, J. Shi, S. Zhang, L. Chen, S. Zheng, F. Yang, Effects of shot peening on tensile properties and fatigue behavior of X80 pipeline steel in hydrogen environment, Int. J. Fatigue 129 (2019) 105235.

[2051] K. Makoto, U. Wataru, Y. Satoshi, Improved hydrogen embrittlement resistance of steel by shot peening and subsequent low-temperature annealing, ISIJ Int 61 (2021) 1159–1169.

[2052] Y. Wang, H. Xie, Z. Zhou, X. Li, W. Wu, J. Gong, Effect of shot peening coverage on hydrogen embrittlement of a ferrite-pearlite steel, Int. J. Hydrog. Energy 45 (2020) 7169–7184.

[2053] M. Safyari, M. Moshtaghi, Role of ultrasonic shot peening in environmental hydrogen embrittlement behavior of 7075-T6 alloy, Hydrogen 2 (2021) 377–385.

[2054] U.S. Dixit, S.N. Joshi, J.P. Davim, Incorporation of material behavior in modeling of metal forming and machining processes: a review, Mater. Des. 32 (2011) 3655–3670.

[2055] J. Paulo Davim (Ed.), Materials Forming and Machining, Research and Development, Elsevier,, 2015.

[2056] K. Gupta, J. Paulo Davim, J. Paulo Davim (Eds.), Advanced Welding and Deforming, Elsevier,, 2021.

[2057] P.M. Petkar, V.N. Gaitonde, V.N. Kulkarni, R.S. Karnik, J. Paulo Davim, A comparative study in forming behavior of different grades of steel in cold forging backward extrusion by integrating artificial neural network (ANN) with differential evolution (DE) algorithm, Appl. Sci. 13 (2023) 1276.

[2058] Z. Ge, L. Wang, H. Wu, H. Wang, D. Xia, J. She, G. Huang, W. Cheng, A. Komissarov, K.S. Shin, Effect of Zn addition combined a novel screw twist extrusion technology on the microstructure, texture as well as the ductility of Mg-xZn-1Mn alloys, J. Alloy Compd. 984 (2024) 173995.

[2059] M. Aali Majidabad, A.R. Rezaei, G. Faraji, Simultaneous enhancement of strength and ductility in AM60 tubes using a novel approach of modified tube cyclic expansion extrusion, JOM 76 (2024) 1870–1882.

[2060] Z. Wang, Z. Zhang, J. Yu, Novel severe plastic deformation method for extrusion compression composite processing, Mater. Lett. 355 (2024) 135459.

[2061] Z. Liu, W. Wang, Z. Cui, D. Chen, A new wavy cross-sectional torsion extrusion method with an application to improve the mechanical properties of an aluminum matrix composite, Mater. Sci. Eng. A 889 (2024) 145837.

[2062] A. Hohenwarter, S. Wurster, Uniform strain high-pressure torsion (US-HPT): an approach to reduce strain gradients, J. Mater. Sci. 59 (2024) 6048–6058.

[2063] L.M. Reis, A. Hohenwarter, M. Kawasaki, R.B. Figueiredo, Evaluating high-pressure torsion scale-up, Adv. Eng. Mater. 26 (2024) 2400175.

[2064] F. Zhang, S. Li, P. Zhong, C. Zhang, X. Hao, Z. Zhang, H. Shu, W. Deng, Radial plastic flow machining: a new process for fabricating gradient-structured terminals in one step, Mater. Charact. 207 (2024) 113571.

[2065] N. Li, Q. Wang, W. Niu, P. Han, N. Guo, S. Li, Microstructure and wear behaviors of 17-4 PH stainless steel fabricated by laser cladding with post laser shock peening treatment, Wear 538-539 (2024) 205207.

[2066] R.R. Valiev, A.V. Panin, E.I. Usmanov, Y.N. Savina, R.Z. Valiev, Microstructural transformation and enhanced strength of wire-feed electron-beam additive manufactured Ti–6Al–4V alloy induced by high-pressure torsion, Adv. Eng. Mater. 26 (2024) 2300814.

[2067] S. Sahu, J. Harris, A.R. Hamilton, N. Gao, Interfacial characteristics of multi-material SS316L/IN718 fabricated by laser powder bed fusion and processed by high-pressure torsion, J. Manufact. Process 110 (2024) 52–69.

[2068] P. Kumar, S, D. Babu P, J. Gautam, A.K. Rai, C.P. Paul, Synergistic integration of laser shock peening and heat treatment for refined microstructure and enhanced mechanical properties in additively manufactured 17–4PH stainless steel, J. Mater. Process. Technol. 328 (2024) 118395.

[2069] M. Ozer, O. Yilmaz, L. Subasi, A. Gunaydin, G.M. Bilgin, S. Zulić, J. Kaufman, Enhancement of surface characteristics of additively manufactured γ-TiAl and IN939 alloys after laser shock processing, Opt. Laser Technol. 170 (2024) 110330.

[2070] J.A. Muñoz, L. Huvelle, A. Komissarov, M. Avalos, R.E. Bolmaro, Y. Zhu, J. M. Cabrera, Overcoming the strength-ductility tradeoff of a 3D-printed Al-Si alloy by equal channel angular pressing, J. Alloy. Compd. 987 (2024) 174153.

[2071] J.A. Muñoz, A. Komissarov, M. Avalos, R.E. Bolmaro, Y. Zhu, J.M. Cabrera, Improving density and strength-to-ductility ratio of a 3D-printed Al–Si alloy by high-pressure torsion, J. Mater. Sci. 59 (2024) 6024–6047.

[2072] P.H.F. Oliveira, D.C.C. Magalhães, C.A. Della Rovere, O.M. Cintho, A.M. Kliauga, V.L. Sordi, Unraveling the mechanism for thermal stability of a high-strength Cu alloy produced by a novel cryogenic ECAP route, Mater. Des. 241 (2024) 112931.

[2073] J. Xie, L. Mei, X. Chen, Y. Cao, W. Lu, G. Huang, Strength-ductility synergy via cryogenic severe plastic deformation in an Al–Mg alloy achieved by clustering-induced strengthening, Mater. Res. Lett. 12 (2024) 373–380.

[2074] A. Mohammadi, X. Sauvage, F. Cuvilly, K. Edalati, Enhanced strength-ductility combination in the aluminum-gold system by heterogeneous distribution of nanoparticles via ultra-severe plastic deformation and reactive interdiffusion, *J. Mater. Sci. Technol.* 203 (2024) 269–281.

[2075] R. Lapovok, M.R. Ghandehari Ferdowsi, V. Shterner, P.D. Hodgson, A. Mazilkin, E. Boltynjuk, R. Kulagin, S.L. Semiatin, Refractory high-entropy alloys produced from elemental powders by severe plastic deformation, Adv. Eng. Mater. 26 (2024) 2301949.

[2076] Z.P. Tehrani, T. Fromme, S. Reichenberger, B. Gökcee, T. Ishihara, T. Lippert, K. Edalati, Laser fragmentation of high-entropy oxide for enhanced photocatalytic carbon dioxide (CO$_2$) conversion and hydrogen (H$_2$) production, Adv. Powder Technol. 35 (2024) 104448.

[2077] G. Rogl, V. Bursikova, K. Yubuta, H. Murayama, K. Sato, W. Yamamoto, A. Yasuhara, P. Rogl, In-situ observation of temperature dependent microstructural changes in HPT-produced p-type skutterudites, J. Alloy. Compd. 977 (2024) 173431.

[2078] K.D. Liss, J.K. Han, M. Blankenburg, U. Lienert, S. Harjo, T. Kawasaki, P. Xu, E. Yukutake, M. Kawasaki, Recrystallization of bulk nanostructured magnesium

alloy AZ31 after severe plastic deformation: an in situ diffraction study, J. Mater. Sci. 59 (2024) 5831–5853.

[2079] R.B. Figueiredo, M. Kawasaki, T.G. Langdon, The role of grain size in achieving excellent properties in structural materials, J. Mater. Res. Technol. 30 (2024) 3448–3462.

[2080] I. Lomakin, A. Nigmatullina, X. Sauvage, Nanostructuring of beryllium bronze: contribution of grain boundaries segregation and solid solution, Mater. Lett. 357 (2024) 135632.

[2081] X. Shu, X. Liang, J. Liu, Q. Wen, L. Wan, Severe plastic deformation-induced rapid diffusion behavior at the Al/steel interface, Mater. Lett. 354 (2024) 135328.

[2082] M. Liu, R. Zheng, H. Li, Q. Wei, C. Ma, N. Tsuji, Phase decomposition behavior and its impact on mechanical properties in bulk nanostructured Cu-20 at%Fe supersaturated solid solution, J. Mater. Sci. Technol. 185 (2024) 207–220.

[2083] A. Mazilkin, V. Tavakkoli, O. Davydenko, Y. Beygelzimer, E. Boltynjuk, T. Boll, B. Straumal, B. Baretzky, Y. Estrin, R. Kulagin, Mechanisms of structural evolution of laminates with immiscible components under high-pressure torsion, Acta Mater. 269 (2024) 119804.

[2084] G.S. Davdian, A.S. Gornakova, B.B. Straumal, A. Korneva, N.S. Afonikova, E. A. Novikova, A.I. Tyurin, Effect of pre-annealing on the formation of the ω-phase in the Ti-2 wt%V alloy after high-pressure torsion, J. Mater. Sci. 59 (2024) 5771–5786.

[2085] A. Prakash, Atomistic modeling of idealized equal channel angular pressing process, J. Mater. Sci. 59 (2024) 6097–6114.

[2086] Q. Wang, Y. Tang, A. Miura, K. Miyazaki, Z. Horita, S. Iikubo, Improving thermoelectric properties of Bi_2Te_3 by straining under high pressure: experiment and DFT calculation, Scr. Mater. 243 (2024) 115991.

[2087] A.Y. Morkina, R.I. Babicheva, E.A. Korznikova, N.A. Enikeev, K. Edalati, S. V. Dmitriev, Molecular dynamics simulation to shed insights on mechanical alloying in an Al-Zr alloy induced by severe plastic deformation, Metals 13 (2023) 1595.

[2088] S. Mahato, S. Chandrakar, K. Biswas, N.P. Gurao, An experimental and crystal plasticity simulation study on kink band-assisted grain fragmentation during high-pressure torsion of $(CrFeNi)_{99}Si_1$ medium-entropy alloy, J. Mater. Sci. 59 (2024) 6075–6096.

[2089] Ü. Şimşek, K. Davut, H. Miyamoto, T. Yalçinkaya, Comparison of linear and nonlinear twist extrusion processes with crystal plasticity finite element analysis, Materials 17 (2024) 1139.

[2090] C. Li, A. Amanov, Y. Li, C. Wang, D. Wang, M.A. Wahab, Prediction of residual stress distribution induced by ultrasonic nanocrystalline surface modification using machine learning, Adv. Eng. Softw. 188 (2024) 103570.

[2091] A. Jain, Y. Prabhu, D. Gunderov, J. Bhatt, Micro-indentation-induced deformation studies on high-pressure-torsion-processed $Zr_{62}Cu_{22}Al_{10}Fe_5Dy_1$ metallic glass, J. Mater. Eng. Perform. 33 (2024) 256–263.

[2092] J. Han, S. Nam, Y.T. Choi, T.J. Jang, C. Jung, S.S. Sohn, H.S. Kim, H. Choi, Grain boundary strengthening in nanocrystalline $Mo_{0.2}CoNi$ medium-entropy alloys produced via high-pressure torsion, Int. J. Refract. Met. Hard Mater. 119 (2024) 106535.

[2093] D.I. Sadykov, A.E. Medvedev, M.Y. Murashkin, N.A. Enikeev, D.A. Kirilenko, T. S. Orlova, Influence of ultrafine-grained structure parameters on the annealing-induced hardening and deformation-induced softening effects in pure Al, Int. J. Lightweight Mater. Manuf. 7 (2024) 221–232.

[2094] I.M. Modina, G.S. Dyakonov, A.V. Polyakov, A.G. Stotskiy, I.P. Semenova, Effect of texture on the ductile–brittle transition range and fracture mechanisms of the ultrafine-grained two-phase Ti-6Al-4V titanium alloy, Metals 14 (2024) 36.

[2095] K. Chu, F. Ren, Fatigue-resistant NiTi micropillars with small hysteresis fabricated by micro severe plastic deformation, Mater. Charact. 208 (2024) 113637.

[2096] A. Kopp, J. Werner, N. Kröger, T.E. Weirich, F. D'Elia, Combined severe plastic deformation processing of commercial purity titanium enables superior fatigue resistance for next generation implants, Biomater. Adv. 157 (2024) 213756.

[2097] P. Král, J. Dvořák, M. Kvapilová, A.G. Kadomtsev, V. Sklenička, Enhancement of creep lifetime of aluminum through severe plastic deformation, Crystals 14 (2024) 230.

[2098] W. Skipper, A. Meierhofer, A. Chalisey, K. Six, R. Lewis, Generation of sanded creep curves using the extended creep force model with high pressure torsion data, Wear 542–543 (2024) 205278.

[2099] C. Gurau, F. Tolea, N. Cimpoesu, M. Sofronie, A.C. Ceoromila, C. Stefanescu, G. Gurau, Magnetic shape memory nanocomposites assembled with high speed high pressure torsion, Nanomater 14 (2024) 405.

[2100] M. Mito, N. Mokutani, Y. Tang, K. Matsumoto, T. Tajiri, Z. Horita, Achieving high-T_c superconductivity in Magnéli phase based on Ti oxides: prediction by machine learning and material synthesis by high-pressure torsion processing, J. Mater. Sci. 59 (2024) 5981–5994.

[2101] L. Weissitsch, S. Wurster, H. Krenn, A. Bachmaier, Multistep severe plastic deformation to achieve non-rare earth bulk magnets with high α-MnBi phase content, Mater. Res. Lett. 12 (2024) 226–234.

[2102] F.Y. Wang, T.T. Qi, Q. Wu, Hl Ge, P.Z. Si, Structure and magnetic properties of nanocrystalline $SmCo_5$ and $SmCo_3Cu_2$ prepared by using high-pressure torsion method, AIP Adv. 14 (2024) 015243.

[2103] O. Dabou, T. Baudin, F. Brisset, T. Waeckerlé, Y.A. Betanda, Y. Huang, A. L. Helbert, D. Bradai, T.G. Langdon, Correlation between microstructure, magnetic properties and mechanical behavior of the Permimphy alloy after high-pressure torsion, J. Mater. Sci. 59 (2024) 5968–5980.

[2104] W. Zhang, Z. Su, X. Hu, D. Ju, H. Zhao, The evolution of microstructure and electromagnetic interference shielding effectiveness of Mg-2Mn-1Ce alloy prepared by accumulative roll bonding process, J. Mater. Eng. Perform. 33 (2024) 1672–1684.

[2105] M. Zohrevand, N. Hassanzadeh, R. Alizadeh, T.G. Langdon, Review: recent advances using severe plastic deformation to improve the properties of battery materials, J. Mater. Sci. 59 (2024) 5651–5680.

[2106] P.N. Nguyen, W.J. Kim, Enhancing the electrochemical performance of Sn-Zn alloy anode foil for lithium-ion batteries through microstructure design via accumulative roll bonding technique, J. Power Sources 594 (2024) 233988.

[2107] B. Omranpour Shahreza, J. Ivanisenko, F. Sergejev, H. Omranpour, J. Huot, A novel approach in mechanical nanostructuring synthesis of metal hydride: hydrogen sorption enhancement by high pressure torsion extrusion, Int. J. Hydrog. Energy 51 (2024) 133–142.

[2108] E.P. Silva, G.N.L. Silva, D.C. Knupp, D.R. Leiva, I.N. Bastos, W.J. Botta, H. C. Pinto, V.B. Oliveira, Effect of the addition of 1.5 wt% of mischmetal in the ZK60 alloy processed by friction stir process (FSP) followed by filing on the H-absorption/desorption kinetics, Int. J. Hydrog. Energy 50 (2024) 1542–1554.

[2109] P. Cengeri, Y. Kimoto, M. Janoska, Z. Abbasi, Y. Morisada, H. Fujii, N. Enzinger, C. Sommitsch, G. Boczkal, G. Krexner, M.J. Zehetbauer, E. Schafler, Long term hydrogen storage properties of ZK60 Mg-alloy as processed by different methods of SPD, J. Mater. Sci. 59 (2024) 5906–5922.

[2110] N. Hata, M. Yuasa, H. Miyamoto, K. Edalati, Influence of grain refinement via high-pressure torsion on corrosion behavior of medium- and high-entropy alloys CoCrFeNi and CoCrFeMnNi with various chromium contents, J. Mater. Sci. 59 (2024) 5891–5905.

[2111] A. Tanji, H. Hermawan, C.J. Boehlert, The microstructural evolution and corrosion behavior of Zn-Mg alloys and hybrids processed using high-pressure torsion, Materials 17 (2024) 270.

[2112] R.Z. Valiev, Y. Zheng, K. Edalati, Review: NanoSPD-produced metallic materials for advanced medical devices, J. Mater. Sci. 59 (2024) 5681–5697.

[2113] M.V. Naik, N. Narasaiah, P. Chakravarthy, R.A. Kumar, Microstructure and mechanical properties of friction stir processed Zn-Mg biodegradable alloys, J. Alloy. Compd. 970 (2024) 172160.

[2114] L. Upadhayay, S. Nilawar, C. Kumar, K. Chatterjee, P. Kumar, Effect of processing Mg–6Zn–0.2Ce through high-pressure torsion on its use as a biomaterial, J. Mater. Sci. 59 (2024) 5872–5890.

[2115] X. Sun, D. Xia, M. Zhang, S. Wang, Y. Zhang, Y. Cai, G. Si, S. Li, X. Zhang, J. Zhang, Study on fretting wear properties of GCr15 steel Via ultrasonic surface rolling process, J. Tribol. 146 (2024) 081701.

[2116] F. Yin, P. Han, Q. Han, H. Wang, L. Hua, G.J. Cheng, Ultrastrong gradient M50 bearing steel with lath-shape nano-martensite by ultrasonic shot peening and its enhanced wear resistance at elevated temperature, Mater. Des. 239 (2024) 112786.

[2117] C. Dureau, M. Arzaghi, T. Grosdidier, R. Massion, Y. Nadot, Modeling of the fatigue behavior of functionally graded materials: study of the residual stresses induced by surface severe plastic deformation, Fatigue Fract. Eng. Mater. Struct. 47 (2024) 918–938.

[2118] Y. Wang, S. Huang, J. Sheng, Q. Liu, M. Zhu, S. Zhou, C. Zhao, J. Liu, Y. Lin, J. Wu, Strengthening effect of laser peening on fatigue performance and life extension of laser cladded IN718 nickel-based alloy parts, Int. J. Fatigue 180 (2024) 108081.

[2119] J. Zhang, K. Liu, T. Chen, C. Xu, C. Chen, D. Yan, A.C. Dippel, J. Sun, X. Ding, Inverse gradient nanostructure through gradient cold rolling demonstrated with superelasticity improvement in Ti-50.3Ni shape memory alloy, J. Mater. Sci. Technol. 185 (2024) 233–244.

[2120] P. Ebrahimzadeh, L.B. Peral, R. González-Martínez, E. Mardaras, I. Fernández-Pariente, Influence of severe surface plastic deformation induced by shot peening on microstructure and corrosion resistance of fine grained 316 L stainless steel, Corr. Sci. 231 (2024) 11988.

[2121] Ö. Güler, M. Boyrazlı, M.G. Albayrak, S.H. Güler, T. Ishihara, K. Edalati, Photocatalytic hydrogen evolution of a high-entropy oxide synthesized by mechano-thermal method, Materials 17 (2024) 853.

[2122] K. Edalati, J. Hidalgo-Jiménez, T.T. Nguyen, M. Watanabe, I. Taniguchi, High-pressure torsion processing of serine and glutamic acid: understanding mechanochemical behavior of amino acids under astronomical impacts, Adv. Eng. Mater. 26 (2024) 2302267.

[2123] K. Edalati, Z. Horita, Correlations between hardness and atomic bond parameters of pure metals and semi-metals after processing by high-pressure torsion, Scr. Mater. 64 (2011) 161–164.

[2124] K. Edalati, Q. Wang, H. Razavi-Khosroshahi, H. Emami, M. Fuji, Z. Horita, Low-temperature anatase-to-rutile phase transformation and unusual grain coarsening in titanium oxide nanopowders by high-pressure torsion straining, Scr. Mater. 162 (2019) 341–344.

[2125] Y. Shundo, T.T. Nguyen, S. Akrami, P. Edalati, Y. Itagoe, T. Ishihara, M. Arita, Q. Guo, M. Fuji, K. Edalati, Oxygen vacancy-rich high-pressure rocksalt phase of zinc oxide for enhanced photocatalytic hydrogen evolution, J. Colloid Interf. Sci. 666 (2024) 22–34.

[2126] K. Edalati, I. Taniguchi, R. Floriano, A. Ducati Luchessi, Glycine amino acid transformation under impacts by small solar system bodies, simulated by high-pressure torsion method, Sci. Rep. 12 (2022) 5677.

[2127] K. Kvenvolden, J. Lawless, K. Pering, E. Peterson, J. Flores, C. Ponnamperuma, J. R. Kaplan, C. Moore, Evidence for extraterrestrial amino-acids and hydrocarbons in the Murchison meteorite, Nature 228 (1970) 923–926.

[2128] C.M.O.'D. Alexander, C.D. Cody, B.T. De Gregorio, L.R. Nittler, R.M. Stroud, The nature, origin and modification of insoluble organic matter in chondrites, the major source of Earth's C and N, Gechem 77 (2017) 227–256.

[2129] E. Peterson, F. Horz, S. Chang, Modification of amino acids at shock pressures of 3.5 to 32 GPa, Geochim. Cosmochim. Acta 61 (1997) 3937–3950.

[2130] J.G. Blank, G.H. Miller, R.E. Winans, Experimental shock chemistry of aqueous amino acid solutions and the cometary delivery of prebiotic compounds, Orig. Life Evol. Biosph. 31 (2001) 15–51.

[2131] Z. Martins, M.C. Price, N. Goldman, M.A. Sephton, M.J. Burchell, Shock synthesis of amino acids from impacting cometary and icy planet surface analogues, Nat. Geosci. 6 (2013) 1045–1049.

[2132] D. Davis, Nasa Image, and Video Library, ARC-1991-AC91 0193 (1991).

[2133] P.W. Bridgman, Polymorphic transitions up to 50,000 kg/cm^2 of several organic substances, Proc. Am. Acad. Arts Sci. 72 (1938) 227–268.

[2134] V.A. Zhorin, Y.V. Kissin, Y.V. Luizo, N.M. Fridman, N.S. Yenikolopyan, Structural changes in polyolefins due to the combination of high pressure and shear deformation, Polym. Sci. USSR 18 (1976) 3057–3061.

[2135] Y. Umeda, N. Fukunaga, T. Sekine, Y. Furukawa, T. Kakegawa, T. Kobayashi, H. Nakazawa, Survivability and reactivity of glycine and alanine in early oceans: effects of meteorite impacts, J. Biol. Phys. 42 (2016) 177–198.

[2136] N. Biver, D. Bockelée-Morvan, R. Moreno, J. Crovisier, P. Colom, D.C. Lis, A. Sandqvist, J. Boissier, D. Despois, S.N. Milam, Ethyl alcohol and sugar in comet C/2014 Q2 (Lovejoy), Sci. Adv. 1 (2015) e1500863.

[2137] K. Hadraoui, H. Cottin, S.L. Ivanovski, P. Zapf, K. Altwegg, Y. Benilan, N. Biver, V. Della Corte, N. Fray, J. Lasue, S. Merouane, A. Rotundi, V. Zakharov, Distributed glycine in comet 67P/Churyumov-Gerasimenko, Astron. Astrophys. 630 (2019) A32.

[2138] P.W. Bridgman, The Logic of Modern Physics, Macmillan, New York, 1927.